MOLECULAR MECHANISMS OF BRAIN WATER TRANSPORT

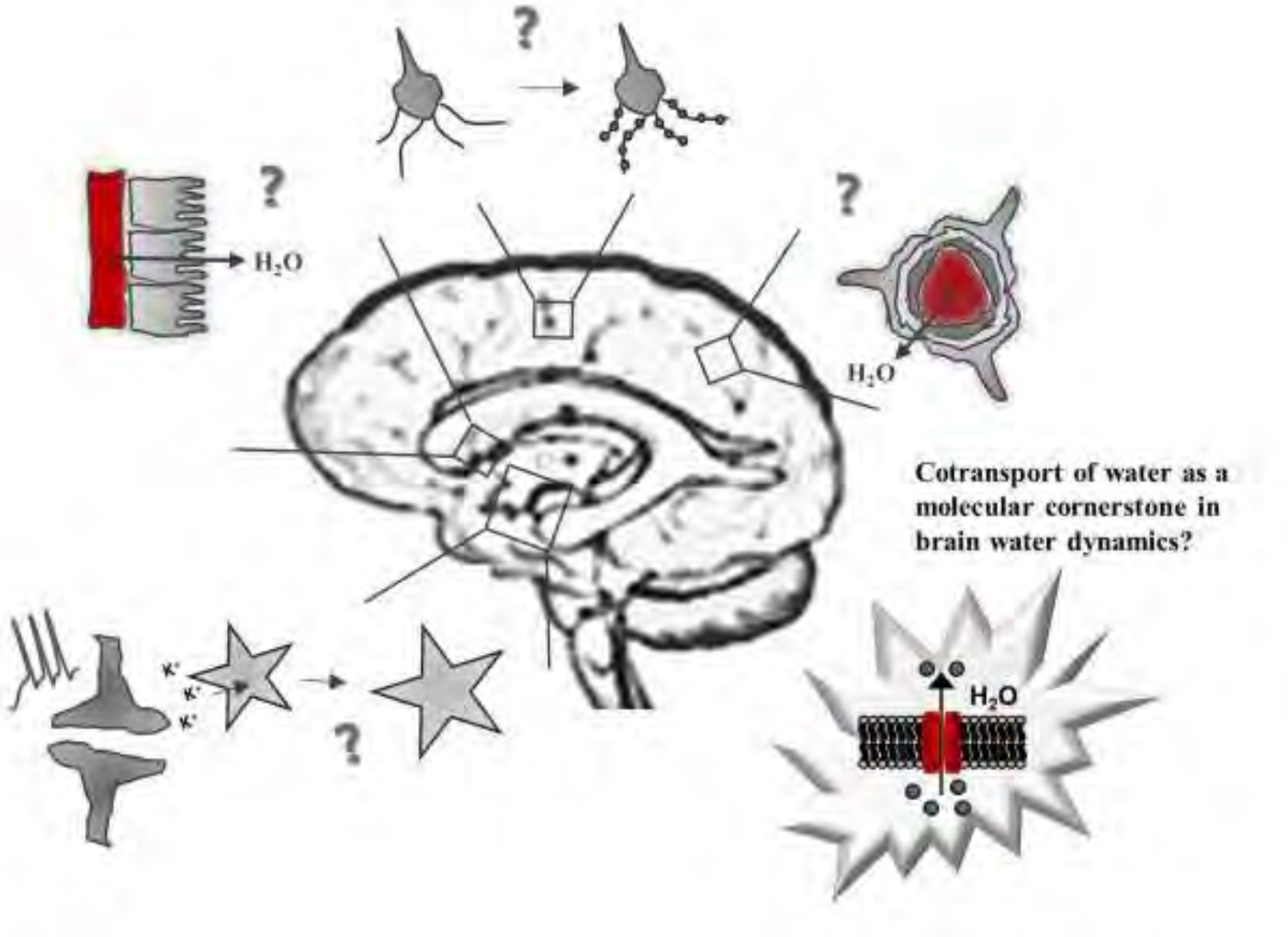

Nanna MacAulay

Doctoral thesis submitted to the Faculty of Health and Medical Sciences
University of Copenhagen

TABLE OF CONTENT

PREFACE

This doctoral thesis is based on experimental work carried out over the last 20 years, some of it by my own hand in the laboratory, but the majority by my dedicated, thorough, and fantastic research group. A lot of our research and understanding of ion and water homeostasis in the brain has a slightly different angle than what is mainstream. While this certainly can be invigourating, fellow researchers (reviewers in journals, visitors at posters, etc) may twist their nose at non-conventional experimental findings and/or ideas. Accordingly, all young scientists in my research group have come to understand the importance of the extra control experiment and/or the inclusion of an additional technical strategy to ensure that our finding was solid. All of you have stood up for your line of research from time to time, which you have done in style! I am so proud of what you have each achieved and what we have accomplished as a research group - thanks to you! For the content contained in this doctoral thesis, my special thanks go to Annette Buur Steffensen, Brian Roland Larsen, Eva Kjer Ørnbo, Kasper Lykke, and Mette Assentoft, most of whom travelled far to learn a new technique and later all established novel techniques in the laboratory in our quest to understand the molecular mechanism underlying a given brain water flux.

The concept of cotransport of water was originally discovered by my former PhD supervisor Professor Thomas Zeuthen, approximately 25 years ago. As with so many other important scientific discoveries, it was unintentional. Thomas spent years trying to disprove his novel, but odd, finding that cotransporters can carry water during their translocation cycle in a manner independent of the osmotic gradient. While the discovery originally was challenged, the concept is becoming accepted and does appear to be the missing molecular building block in many tissues, not least in the brain. Thomas, thank you for being a fantastic mentor. Nobody in the world understands the biophysics of transmembrane water transport better than you! You have been a resourceful source of knowledge and insight (not only scientific) for the 20 years I have known you. Thanks for always having time to discuss and challenge, to motivate and to help - and to cheer with us every time another cotransporter is found to support water movement in brain cells of any kind.

The thesis was nearly completed during a 2-week stay at San Cataldo, Italy, a Danish-owned refuge dedicated to artists, writers, and scientists. I am grateful to the San Cataldo Board for granting me a stipend to visit this fabulous place and thereby providing me with conditions allowing me to delve completely into every little detail of brain water transport and write, literally, from dawn to dusk. Of course a heartfelt thanks to all my fellow San Cataldo guests (group 14th-28th November, 2018) for making the scarce time spent away from the computer enjoyable.

Being a successful researcher requires, amongst other things, time (and travel) and so does being a caring wife and mother. Both these facets of my life are essential and I have aimed to balance the two. I am eternally grateful for the commitment, encouragement and love from my supportive husband and three wonderful children. You will always be the most important thing in my life - even if I am not always there! I appreciate your gracious agreement to my two weeks spent at San Cataldo writing this thesis.

The doctoral thesis is based on the following 11 articles. Much of the research included in these was carried out with valuable contributions from many collaborators, without whom we could not have taken the research topic to the same level. I really enjoy working with talented scientists all over the world, each highly skilled in a certain tecnique or research topic. Sincerely thanks to all of you!

- **Nanna MacAulay**, Thomas Zeuthen & Ulrik Gether (2002) Conformational Basis for the Li^+-Induced Leak Current in the rat g-Aminobutyric Acid (GABA) Transporter-1. *Journal of Physiology 544, 447-458*
- Robert A. Fenton, Hanne B. Moeller, Marina Zelenina, Marteinn T. Snaebjornsson, Torgeir Holen & **Nanna MacAulay** (2010) Differential water permeability and regulation of three AQP4 isoforms. *Cellular and Molecular Life Sciences. 67:829-840*
- Mette Assentoft, Shreyas Kaptan, Robert A. Fenton, Susan Z. Hua, Bert L. de Groot & **Nanna MacAulay** (2013) Phosphorylation of rat aquaporin-4 at Ser^{111} is not required for channel gating. *GLIA 61: 1101-1112*
- Brian Roland Larsen, Mette Assentoft, Maria L. Cotrina, Susan Z. Hua, Maiken Nedergaard, Kai Kaila, Juha Voipio & **Nanna MacAulay** (2014) Contributions of the Na^+/K^+-ATPase, NKCC1, and Kir4.1 to hippocampal K^+-clearance and volume responses. *GLIA 62:608-622*
- Annette B. Steffensen, Jeremy Sword, Deborah Croom, Sergei A. Kirov & **Nanna MacAulay** (2015) Cotransporters as a molecular mechanism underlying spreading depolarization-induced dendritic beading. *Journal of Neuroscience 35:12172-12187*
- Mette Assentoft, Shreyas Kaptan, Hans-Peter Schneider, Joachim W. Deitmer, Bert L. de Groot & **Nanna MacAulay** (2016) Aquaporin 4 as a NH_3 channel. *Journal of Biological Chemistry 291:19184-19195*
- Brian Roland Larsen & **Nanna MacAulay** (2017) Activity-dependent astrocyte swelling is mediated by pH-regulating mechanisms. *GLIA 65:1668-1681*
- Kasper Lykke, Mette Assentoft, Sofie Hørlyck, Hans Christian C. Helms, Anca Stoica, Trine L. Toft-Bertelsen, Katerina Tritsaris, Frederik Vilhardt, Birger Brodin & **Nanna MacAulay** (2017) Evaluating the involvement of cerebralmicrovascular endothelial Na^+/K^+-ATPase and Na^+-K^+-$2Cl^-$ co-transporter (NKCC1) in electrolyte fluxes in an *in vitro*BBB model of dehydration. *Journal of Cerebral Blood Flow and Metabolism, Epub ahead of print.*
- Annette B. Steffensen, Eva K. Oernbo, Anca Stoica, Niklas J. Gerkau, Dagne Barbuskaite, Katerina Tritsaris, Christine R. Rose & **Nanna MacAulay** (2018) Cotransporter-mediated water transport underlying cerebrospinal fluid formation. *Nature Communications 9:2167*
- Eva Kjer Oernbo, Kasper Lykke, Annette B. Steffensen, Kathrin Töllner, Christina Kruuse, Martin Fredensborg Rath, Wolfgang Löscher & **Nanna MacAulay** (2018) Cerebral influx of Na^+ and Cl^- as the osmotherapy-mediated rebound response in rats. *Fluids and Barriers in the CNS 15:27*
- Brian Roland Larsen, Anca Stoica, **NannaMacAulay** (2018) Developmental maturation of activity-induced K^+ and pH transients and the associated extracellular space dynamics in the rat hippocampus. *Journal of Physiology, Epub ahead of print*

SUMMARY

The mammalian brain consists of approximately 80% water, which is continuously replenished by *de novo* secretion of brain fluids at a rate of half a liter per day in the adult human. The water is subsequently shifted between different brain cells and compartments during physiological and pathophysiological processes. Disturbance in the brain water homeostasis can be observed with pathologies involving cerebral water accumulation, such as brain edema formation and hydrocephalus. These conditions can be highly deleterious, and even fatal, due to the confinement of our, otherwise highly protective, cranium. Given the inability to swell beyond the cranial boundaries, brain water accumulation can lead to elevated intracranial pressure and brain tissue compression. Targeted pharmacological treatment aimed at preventing brain water influx in pathology is simply non-existing due to our incomplete *understanding* of the molecular mechanisms governing brain water transport - and will remain so until we unravel the intricate machinery managing the brain water homeostasis in health and disease.

http://artificialbrain.xyz/wp-content/uploads/2016/11/water-and-brain-500x500.jpg

Historically, transmembrane movement of brain water has been assumed to take place according to conventional passive movement of water along the osmotic gradient, greatly accelerated by membranous water channels, the aquaporins, when these are present. While aquaporins govern the majority of the fluid handled by the human kidney, they do not suffice to explain the majority of brain water movement: They are not present in the membranes across which water, nevertheless, does flow (brain capillary endothelium, the basal membrane of choroid plexus, and the neuronal membrane) nor are they required for the observed cell swelling in the neuronal neighbor cells, the glia cells, which swell during neuronal activity and in pathological conditions. Furthermore, a well-documented physiological process, such as brain fluid secretion into a compartment *against* a steep osmotic gradient, cannot take place by conventional passive water flow along an osmotic gradient.

Cotransport of water has recently been described as a novel and unconventional molecular mechanism governing swelling of neuronal dendrites and glia cells as well as brain fluid secretion. The concept of cotransport of water, in which transport proteins carry a fixed number of water molecules along as a ‘cargo’ every time they transport their respective substrate across the membrane, could be the missing building block allowing us to bridge the gap in our understanding of brain water transport.

RESUMÉ

Pattedyrets hjerne består af ca. 80% vand, som kontinuerligt udskiftes ved *de novo* udskillelse af en halv liter hjernevæske dagligt hos det voksne menneske. Vandet flyttes efterfølgende mellem forskellige hjerneceller og hjerneområder under diverse fysiologiske processer og i patologiske tilstande. Forstyrrelse i hjernens vandbalance, som observeret i tilstande, der involverer cerebral vandakkumulering såsom hjerneødemdannelse og hydrocephalus, kan være yderst skadelige og endog dødelige på grund af det begrænsede volumen af vores, ellers meget beskyttende, kranium. På grund af det rigide kranium kan hjernevæskeakkumulering føre til forhøjet intrakranielt tryk og kompression af hjernevævet. Målrettet farmakologisk behandling af hjernevæsketilstrømning i disse patologiske tilstande er simpelthen ikke eksisterende på grund af vores ufuldstændige forståelse af de molekylære mekanismer, der styrer hjernens vandtransport - og vil forblive således, indtil vi afdækker det indviklede maskineri, som forvalter hjernens vandbalance i sundhed og sygdom.

Transport af hjernevæske har historisk set været antaget at foregå ifølge konventionel passiv bevægelse af vand langs den osmotiske gradient, stærkt accelereret af membranøse vandkanaler, aquaporiner, hvis disse er til stede. Mens aquaporiner styrer hovedparten af den væske, der hver dag filtreres af den humane nyre, er de ikke tilstrækkelige til at forklare størstedelen af hjernens vandbevægelser: De er ikke til stede i de membraner, over hvilke vand ikke desto mindre flyder (hjernens kapillærendotel, plexus choroideus' basal membran og nervecellemembranen) ej heller tilsyneladende nødvendige for de observerede cellevolumenændringer i nervecellernes naboceller; gliacellerne, der svulmer når nervecellerne er aktive og i forskellige patologiske tilstande. En veldokumenteret fysiologisk proces, såsom hjernevæskesekretion *mod* en stejl osmotisk gradient, kan derudover ikke ske ved konventionel passiv vandstrømning langs en osmotisk gradient.

http://artificialbrain.xyz/wp-content/uploads/2016/11/water-and-brain-500x500.jpg

Cotransport af vand er således nyligt blevet beskrevet som en alternativ og ukonventionel molekylær mekanisme, der styrer nerve- og gliacellers volumen samt varetager hjernens væskesekretion. Dette nye koncept omkring cotransport af vand, hvor transportproteiner bærer et fast antal vandmolekyler med som en "last", hver gang de transporterer deres respektive substrat over membranen, kunne være den manglende byggesten, der lader os bygge bro over vidensgabet i vores forståelse af hjernens væsketransport.

LIST OF ABBREVIATIONS

AE	Cl^-/HCO_3^- exchanger
AQP	aquaporin
BBB	blood-brain-barrier
CSF	cerebrospinal fluid
DC	direct current
DIDS	4,4'-Diisothiocyano-2,2'-stilbenedisulfonic acid
EAAT	Na^+-coupled glutamate transporter
ENaC	epithelial Na^+ channel
GAT1	Na^+-coupled GABA transporter
IC_{50}	concentration at which the activity is 50% inhibited
i.c.v.	intracerebroventricular
i.p.	intraperitoneal
i.v.	intravenous
ISF	interstitial fluid
KCC	K^+/Cl^- cotransporter
Kir4.1	inwardly rectifying K^+ channel
K_M	concentration at which the activity is half-maximal
LAT	large amino acid transporter
MCT	H^+-coupled monocarboxylate transporter
NBCe1, NBCe2, NCBE, NBCn1	Na^+-coupled bicarbonate cotransporters
NHE	Na^+/H^+ exchanger
NKCC1	$Na^+/K^+/2Cl^-$ cotransporter
PKA	protein kinase A
PKC	protein kinase C
PKG	protein kinase G
RNAseq	ribonucleic acid sequencing
s.c.	subcutaneous
SD	spreading depolarization
SGLT1	Na^+-coupled glucose transporter
TEER	transendothelial electrical resistance

BRAIN FLUIDS IN THE MAMMALIAN BRAIN

The mammalian brain consists of approximately 80% water, divided between cerebrospinal fluid (CSF), blood, interstitial fluid (ISF), and intracellular fluid content. The brain is suspended in the CSF, which fills the central ventricles and the surrounding subarachnoid space (Fig. 1). In this manner, the CSF provides insulation from mechanic insults and allows the brain to float within the cranium, thus preventing the delicate brain tissue from resting on the base of the skull. The CSF is in continuum with the ISF [1–4]. Despite their individual nomenclature, CSF and ISF freely exchange through the gaps between astrocytic endfeet lining the fluid-filled perivascular space [1] and through the ependymal cell lining separating the fluid-filled ventricular cavities from the brain parenchyma [2]. Notably, the ependymal cell layer has no real barrier function, as these cells are not attached to one another by continuous tight junctions [3,4]. Directional flow of CSF along the perivascular space and through the parenchyma has long been proposed to act as a cleansing function, ridding the brain of metabolites and toxic substances [5–7]. The concept was recently reviewed with coining of the 'glymphatic system', named as such due to the proposed implication of glial aquaporins (AQP) [8]. The controversies regarding the existence of the glymphatic system, its underlying driving force, the convective nature of the flow, and the proposed requirement of AQP4 are outside the scope of this review on cerebral *transmembrane* water flow, but have been described and reviewed extensively elsewhere [9–18].

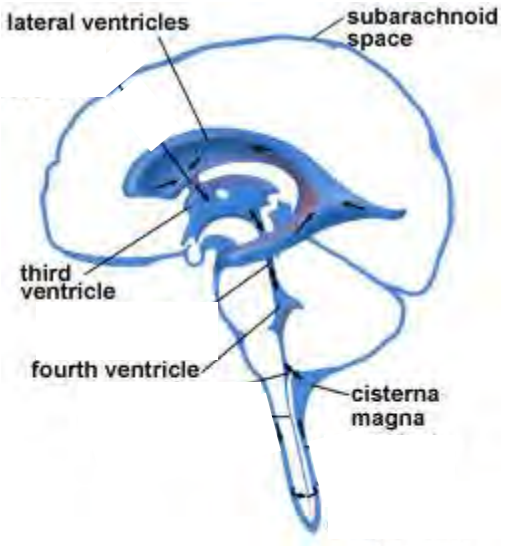

Fig. 1. The fluid-filled ventricular system and subarachnoid space (blue) with choroid plexus marked in red. Adapted from: http://www.mayfieldchiaricenter.com/chiari.php

The continuous fluid secretion into the brain and the intra-cerebral fluid shifts between different compartments and cellular structures have been acknowledged for many decades, or even centuries. Yet, we must not mistake information with understanding; we hardly *understand* how the transmembrane fluid transport in the brain takes place. This knowledge gap prevents targeted pharmacological therapy of the many pathologies involving disturbed brain fluid homeostasis, i.e., 1) dendritic beading during cortical spreading depolarization (SD), 2) glia cell swelling during neuronal activity and in pathologies, such as brain ischemia and liver failure, 3) brain edema formation in association with stroke, traumatic brain injury, acute liver failure, brain tumor, and meningitis and 4) ventriculomegaly observed in the condition known as hydrocephalus, which occurs in association with subarachnoid hemorrhage, as a co-morbidity to neurodegenerative diseases, and as postnatal hydrocephalus. The aberrant lack of pharmacological tools to treat excessive brain fluid content is manifested in the hydro-mechanical principles underlying the neurosurgical approaches to alleviate the symptoms in patients with severe elevation of intracranial pressure. These include surgical implantation of a ventriculo-peritoneal shunt, diverting the excessive fluid from the ventricles into the peritoneal cavity in the abdomen, or a craniectomy, in which part of the skull is temporarily removed to allow the brain to swell outside the confined boundaries of the cranium. A better understanding of brain fluid dynamics is a precondition for better therapeutic approaches with fewer complications. The classic theory for pressure regulation and fluid circulation in the brain is based on considerations, which fail to consider the molecular water transport mechanisms. To control the brain fluid dynamics in pathophysiology, it is imperative to understand the fluid transport at the molecular level.

MOLECULAR MECHANISMS OF TRANSMEMBRANE WATER FLOW

Quantification of brain water movement requires distinction between diffusional exchange of water molecules, which does not necessarily lead to net water transport, and water transport driven by osmotic gradients or hydraulic forces, which does result in net transport. While in some settings this distinction may not be relevant, the body of scientific work utilizing tritiated or heavy water molecules to determine brain water movement cannot necessarily distinguish the two. Intravenous infusion of labelled water leads to rapid exchange with the brain water [19–21], which has occasionally, and mistakenly, been inferred to equal high endothelial water permeability. However, the osmotic water permeability of the endothelium is notoriously low [22–24], due to the complete lack of aquaporin expression in brain endothelial cells [25] and their non-fenestrated nature. These

characteristics are in opposition to the remainder of the mammalian vasculature [26]. Despite the limited endothelial osmotic water permeability, osmotic gradients will, nevertheless, exert a noticeable effect on the brain water content due to the large brain capillary surface [24]. Water can cross cell membranes by different molecular transport routes: Of lowest complexity and limited capacity is water permeation through the lipid bilayer, but osmotically-induced transmembrane water flux is markedly enhanced with expression of aquaporins (Fig. 2). These are transmembrane water channels, of which 13 isoforms exist in the mammalian genome [27]. Aquaporins assemble as tetramers with each subunit as a pore-forming water channel [28] with a pore diameter of 1.5 Å for AQP4 [29]. While all aquaporins are permeable to water, some also allow permeation of other molecules, such as glycerol, urea, and different gaseous compounds [30,31]. Common for all aquaporin-mediated water transport is that the direction of the flow exclusively follows that of the prevailing osmotic gradient; *they conduct passive water transport*.

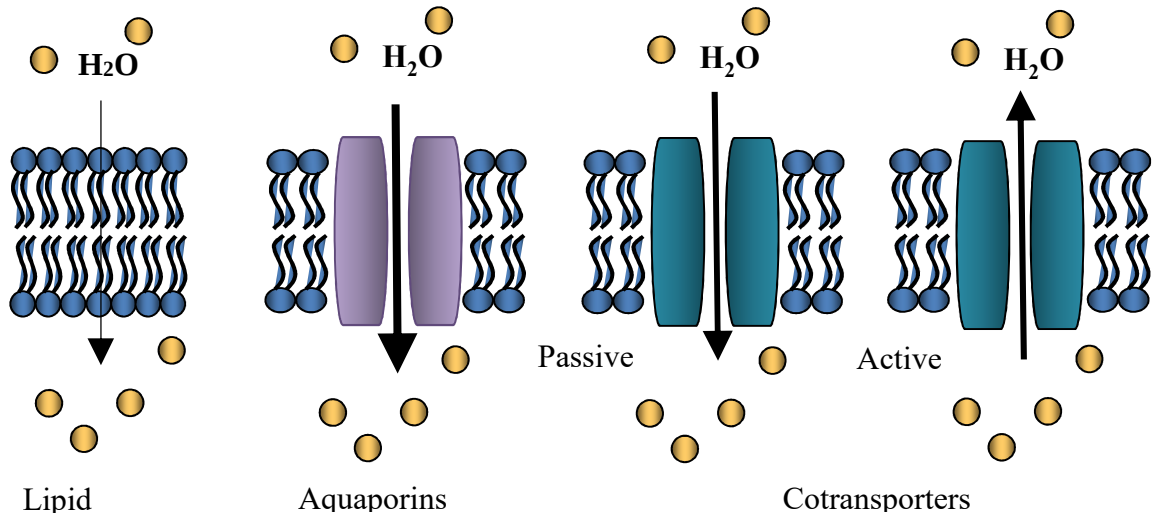

Fig. 2. Water can cross the cell membrane either through the lipid membrane, via aquaporins, or via cotransporters. While the first two types of water transport can occur only passively and in the direction of the osmotic gradient (osmotic particles indicated with yellow circles). Many cotransporters, like-wise, support passive water transport but may also have the inherent ability to transport water in the direction of their solute/ion transport, independently of the osmotic gradient.

A class of membrane transport proteins, known as cotransporters or coupled transporters, has in recent years been established as water-transporting proteins. Some of these support passive water transport analogous to that of the aquaporin-mediated osmotically-driven water flow, just of a smaller capacity. Some, in addition or instead, carry the inherent ability to cotransport water along with their transported solutes in a manner that allows water transport independently of the prevailing transmembrane osmotic gradient; *they conduct active water transport* [31–33], Fig. 2.

AQUAPORIN-MEDIATED WATER TRANSPORT

The aquaporins detected in the brain are mainly AQP1 and AQP4. In brain tissue, AQP1 is most notably localized to the luminal membrane of the choroid plexus epithelium [26,34,35] and is, contrary to the systemic circulation [26], suppressed in the specialized cerebral endothelium [25,36,37]. AQP1 has been reported mostly absent from the rodent brain parenchyma [26,38,39] whereas non-human primates display AQP1 expression in astrocytes of the white matter and glia limitans [40]. Common for human and rodent brain tissue is observations of up-regulation of AQP1 expression under pathological conditions [41–44]. The prominent localization of AQP1 in the luminal membrane of the choroid plexus has implicated the channel in CSF production [45], see later.

AQP4 is the dominant aquaporin in the mammalian brain with a rather selective expression in the ependymal lining of the cerebral ventricles and in glia cells [37,46,47]. In the osmo-sensing areas of the brain, the supraoptic nucleus and the subfornical organ, AQP4 is uniformly expressed in the astrocytic cell membrane, whereas in the remainder of the central nervous system, astrocytic AQP4 is highly polarized to the perivascular endfeet enwrapping the cerebral blood vessels [37]. AQP4 is anchored at this subcellular structure by C-terminal interaction with α-syntrophin, a component of the dystrophin protein complex [48].

AQP4 is largely selective to water permeation [49–51] but is, in addition, permeable to the gaseous form of ammonia (NH_3) [49]. AQP4 exists in different variants, the most prominent of which are the M1, Mz, and the shorter version M23 [46,52]. The latter isoform has been found to either display a reduced [50] or similar [53] unitary water permeability compared to its full length counterparts. M23 is the dominant version in the mammalian brain [54] and is characterized by its ability to form orthogonal arrays of particles, well-structured plaques of protein [55–57]. These arrays cover a substantial fraction of the astrocytic endfeet [58,59] (Fig. 3) and were recognized by freeze-fracture electron microscopy decades prior to identification of their molecular origin [58].

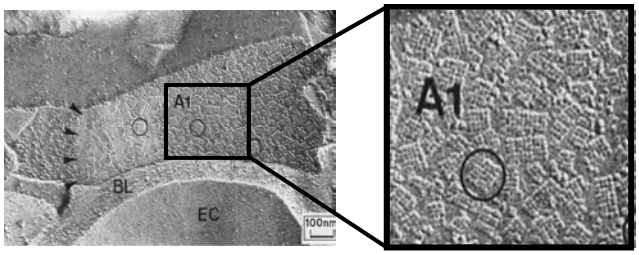

Fig. 3. The perivascular astrocytic endfeet are covered in orthogonal arrays of particles (circled), as detected with freeze-fracture electron microscopy. A1, perivascular astrocytic membrane; EC, endothelial cell; BL, basal lamina. Adapted from [59].

While AQP4 expression evidently increases the osmotic water permeability of the cell membrane in which it is expressed, astrocytes are quite water permeable even in the absence of AQP4 expression: Primary culture of murine astrocytes obtained from WT and AQP4$^{-/-}$ mice displayed only a two-fold difference in osmotic water permeability (when recorded at 37˚C) [60]. As clearly discernable from Fig. 4 (adapted from [60]), with swift introduction of an exceedingly large osmotic gradient (-Δ140 mOsm), astrocytes obtained from WT and knock-out mice swell and completely equilibrate with the surrounding fluid in a few seconds. As is also apparent from the figure; with a given osmotic gradient, cells will generally swell to the *same extent*, regardless of the osmotic water permeability of the cell membrane - just at a slower rate in cells with smaller water permeability, i.e. in AQP4 deficient astrocytes.

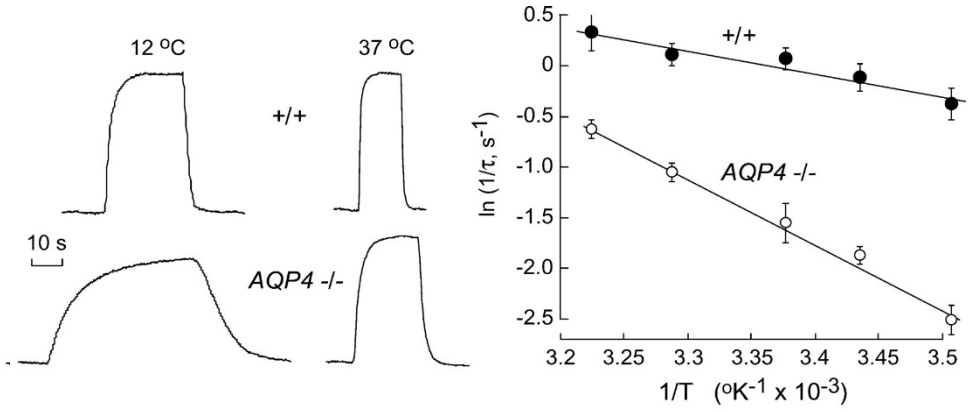

Fig. 4. Exposure of calcein-loaded cultured astrocytes from WT mice (upper left panel) or AQP4$^{-/-}$ mice (lower left panel) to a hyposmotic gradient of 140 mOsm. Rate of cell swelling was recorded with fluorescence microscopy and was halved by genetic deletion of AQP4, when recorded at 37˚C (value obtained from the Arrhenius plot of volume changes as a function of temperature (right panel)). Adapted from [60].

Regulation of AQP4

Despite the very high water permeability of the astrocytic membrane irrespective of its AQP4 abundance, regulation of AQP4 abundance or its unit water permeability has been suggested as a determinant of brain water flux. The astrocytic AQP4-dependent water permeability is notoriously difficult to quantify: Due to the large surface-to-volume ratio of astrocytes and the excessively large osmotic water permeability of the astrocytic membrane, an experimentally inflicted osmotic challenge must be introduced onto the astrocyte membrane surface at a rate that exceeds that of the rate of cell swelling [60–62]. Failure to do so will result in the rate of cellular swelling simply following the rate of entry of the test solution into the experimental chamber. The rate-limiting value

will thus depend on the flow system rather than on the membrane water permeability. Data acquisition must take place swiftly, as the initial linear cell volume change is what provides the osmotic water permeability (prior to initiation of regulatory volume responses and dilution of the transcellular osmotic gradient upon cellular water flux). In the highly water-permeable astrocytes, this rapid initial linear phase (a few seconds) is simply missed at low sampling rates [61].

A line of research has indicated that AQP4 may be regulated in a manner analogous to gating of ion channels: Phosphorylation-dependent gating of AQP4 was proposed to open or close a gate at the intracellularly-facing part of the protein. Specifically, phosphorylation of amino acid residues Ser^{111} and Ser^{180} by protein kinase A, C, or G (PKC, PKA, or PKG) should act as the gating event [63–65]. Subsequent experimental studies in primary culture of astrocytes and AQP4-expressing oocytes revealed no phosphorylation-dependent gating at these residues (or a range of other tested C-terminal serine residues) [61,66,67], the conclusion of which was backed by molecular dynamics simulations [61,68] (Fig. 5).

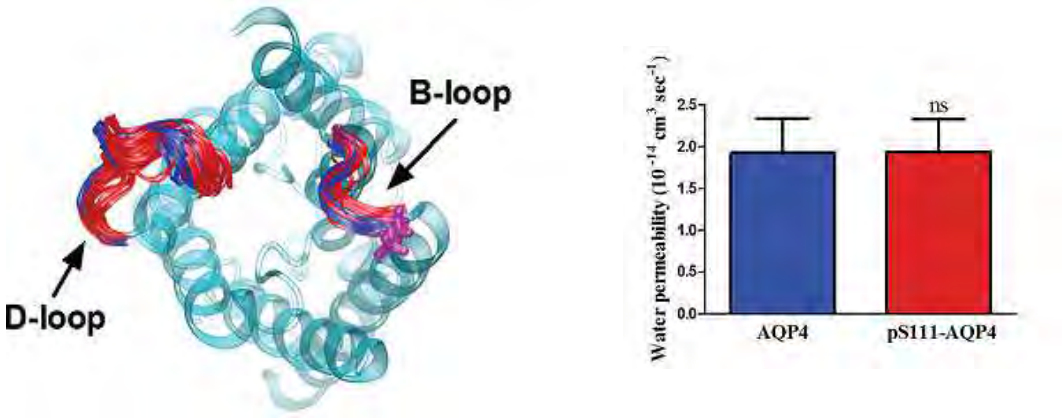

Fig. 5. Phosphorylation of AQP4 at Ser^{111} did not promote movement of the inner gate of AQP4 in molecular dynamics simulations (left panel). Blue is the non-phosphorylated version of AQP4 and red is the Ser^{111}-phosphorylated version. The phosphorylation of Ser^{111} did not affect AQP4-mediated osmotic water permeability (right panel). Adapted from [61].

Accordingly, AQP4 does not change its unit osmotic water permeability in the wake of phosphorylation of the tested amino acid residues. In contrast, AQP4-mediated water permeability can be regulated by pH, in line with several reports on pH-sensitive plant and mammalian aquaporins [69–72]. Although extracellular pH changes had no effect on AQP4-dependent water permeability [70,73] (as opposed to the earlier report on channel opening at alkaline pH [74]), AQP4 is gated by cytosolic pH in a manner involving the His^{95} facing the pore region in the intracellular part of AQP4 [73,75]. Experimental evidence in conjunction with molecular dynamics simulations pinpointed that

acidification of the cytosol caused double protonation of His^{95} in AQP4, which subsequently prompted the histidine side chain to preferentially reside in a position which associates with a larger pore opening [73]. Thus, under pathophysiological conditions, such as brain ischemia, during which astrocytic pH acidifies [76], AQP4-mediated osmotic water permeability increases.

AQP4 and brain edema

AQP4 has been proposed involved in a multitude of aspects of brain (patho)physiology, ranging from brain edema formation, K^+ clearance and associated glia cell swelling, glymphatics, interstitial fluid flow and volume, astrocyte process formation, neuromyelitis optica, brain tumor growth, and memory [8,38,39,67,77–79], despite the lack of an apparent phenotype in the $AQP4^{-/-}$ mice [80]. It is not resolved whether it is altered AQP4-dependent osmotic water permeability, *per se*, that provides the observed experimental changes, or indirect effects of genetic deletion of AQP4. The $AQP4^{-/-}$ mice have, as do many other knock-out animal models, secondary changes in a range of tissue/cellular parameters. These include increased brain water content, increased extracellular space in the brain tissue, reduced glutamate transporter (GLT1) expression, reduced expression of the anchoring proteins α-syntrophin and dystrophin in the astrocytic endfeet [25,79,81,82], the latter of which most likely affects subcellular localization of other membrane proteins. With its remarkably polarized expression at the astrocyte membrane abutting the blood-brain-barrier (BBB), AQP4 was initially assigned a gate for bi-directional blood-to-brain water fluxes [39,47,83]. However, with the complete absence of AQP4 expression in the endothelial cell layer [25,37], which represents the first barrier between blood and brain, water must cross the endothelial barrier by some other means of transport prior to reaching the AQP4-expressing astrocytic endfeet [67]. It is therefore uncertain how AQP4 can act as a *direct* gateway between the vasculature and the brain. Nevertheless, when stressed with conditions promoting brain edema formation, $AQP4^{-/-}$ mice displayed an outcome distinct from that of the WT mice, although the role of AQP4 appeared to depend on the type of brain edema associated with the experimentally-induced pathology. In general, the $AQP4^{-/-}$ mice had improved outcome in conditions associated with cytotoxic brain edema (i.e. cerebral ischemia, acute liver failure, water intoxication, and meningitis), whereas the opposite was the case in experimental approaches causing vasogenic brain edema (i.e. freeze injury, staphylococcal brain abscess, and brain tumor) [39,47,83]. With these findings, the authors indicated that AQP4 may serve distinct roles and transport directionality during edema formation; an entrance route during cytotoxic edema and an exit route during vasogenic edema. For water to enter the brain by osmotic fluid flow in pathologies leading to either of these types of edema, one would generally assume an underlying increase in brain tissue

osmolarity (to attract the water). If that is indeed the case, it is puzzling which driving forces would compel the water to *exit* through AQP4 in conditions of vasogenic edema?

Based on the working hypothesis that increased AQP4-mediated osmotic water flux leads to brain edema, a multitude of studies have aimed at quantifying the AQP4 abundance during conditions promoting brain edema formation. Of these studies, approximately half of those that focus on ischemic insult in rodent animal models observed an up regulation of AQP4 and the other half observed a down regulation (for review, see [67]). The physiological role of AQP4, as well as its impact on pathophysiological conditions leading to brain water accumulation, is clearly not fully established. With astrocytes rendered in osmotic equilibrium with their surroundings on a (sub-) second time scale, even when faced with excessively large osmotic gradients (see above and [60]), the time course of edema formation (hours) suggests that AQP4 alone may not represent the rate-limiting factor in blood-to-brain water fluxes.

AQP4 and extracellular space K^+ clearance

AQP4 co-localizes with the inwardly-rectifying K^+ channel Kir4.1 in astrocytes and retinal Müller cell endfeet, and, although to a much lesser extent, in membranes facing the neuropil [78]. This co-localization led to a proposed functional coupling of the two channels in K^+ management in the extracellular space during neuronal activity and the associated astrocytic cell swelling [38,77,78,84]. Although this concept initially caught interest, it was later demonstrated that Kir4.1 functions independently of AQP4 co-expression [85], although cell swelling activates Kir4.1 [86]. Genetic deletion of AQP4 caused variable effects on the K^+ dynamics between different research groups and across different brain (sub)structures and stimulation paradigms: The peak K^+ increase in the extracellular space during the neuronal activity was either unchanged (cortex, [87], stratum pyramidale [88]), increased (stratum radiatum, [88]), or decreased (stratum pyramidale, [89]), whereas the recovery phase was either unchanged (stratum radiatum/pyramidale, [88]), slowed (cortex, [87]), or slowed only at K^+ rises <1 mM and otherwise unchanged (stratum pyramidale, [89]). Altogether, these non-aligned observations suggest that AQP4, most likely, does not figure as a general requirement for optimal K^+ buffering in the extracellular space of the central nervous system. Lastly, computer-based modelling indicated that Kir4.1-mediated K^+ clearance occurred undisturbed with a gradual decrease of the modelled astrocytic osmotic water permeability, at least until a 10-fold difference from WT [90]. The reported ~2-fold reduction in osmotic water permeability of primary cultures of astrocytes from AQP4$^{-/-}$ mice (at 37˚C, 7-fold at 12 ˚C) [60], should thus suffice for proper clearance of K^+ in the extracellular space of these mice: Kir4.1-mediated K^+ clearance does not

require a neighboring AQP4. It is therefore, most likely, not the altered osmotic water permeability in the AQP4$^{-/-}$ mice, *per se*, that causes increased seizure threshold and prolonged seizure activity in these mice [87,91], but possibly some indirect effect such as the increased extracellular space of the AQP4$^{-/-}$ animals or the reduced glutamate transporter expression [79,82].

TAKEN TOGETHER, AQP4 obviously serves a function in the mammalian brain, otherwise the evolutionary pressure would not favor its substantial coverage of the astrocytic endfeet. It has become apparent that these water channels are not 'gated' by phosphorylation and that passive osmotic aquaporin-mediated water transport simply does not suffice to sustain all water exchange observed in the mammalian brain. Is the concept of cotransport of water the missing link?

COTRANSPORT OF WATER

Cotransporters are transmembrane proteins that support translocation of ions and solutes across the plasma membrane. These transport proteins are able to transport solutes against their (electro)chemical gradient by coupling to a cotransported ion, often, but not exclusively, in the form of Na^+. The cotransported ion is transported 'downhill' with its electrochemical gradient, thereby providing energy to propel the 'uphill' transport of the other ions and/or solutes. The transport direction of these cotransporters is determined by the (electro)chemical ion(solute) gradients across the membrane. With the discovery of an inherent ability of these cotransporters to move water with their translocation cycle, in the direction dictated by the (electro)chemical gradients of their transported ions and solutes, the possibility arose to move water across cell membranes in a manner independently of a transmembrane osmotic driving force. The concept of cotransport of water was originally met with reluctance in the epithelial research field [92–94] but later widely accepted [95,96].

Cotransport of water has been demonstrated in a range of different cell types (choroid plexus epithelial cells, retinal pigment epithelial cells, and *Xenopus laevis* oocytes expressing the protein of interest), by a range of experimental techniques (ion-sensitive microelectrodes in *ex vivo* tissue, fluorescence microscopy of calcein-loaded mammalian cells/tissue, and camera-based quantification of *Xenopus* oocyte volume), and in a range of different cotransporters (amongst others; the Na^+-coupled glucose transporter, SGLT1; the K^+/Cl^- cotransporter, KCC; the $Na^+/K^+/2Cl^-$ cotransporter, NKCC1; the Na^+-coupled glutamate transporter, EAAT1; the Na^+-coupled GABA transporter, GAT1, the H^+-coupled monocarboxylate transporter, MCT1) [97–104], for reviews, see [23,32,33,105]. The

consistent findings across distinct techniques, cell systems, and transporter families exclude that the concept of cotransport of water arose due to a singular artefact in a given experimental approach.

Water transport by the Na^+-coupled GABA transporter

While the biophysical properties of cotransport of water have been dissected for all the above mentioned cotransporters [97–104], the GABA transporter, GAT1, expressed in *Xenopus* oocytes, is uniquely suited to demonstrate the difference between cotransport of water and osmotically obliged water flux in the wake of solute accumulation [100]. The native *Xenopus* oocyte membrane has inherently low water permeability; that is, when exposed to an osmotic gradient, the control oocyte responds with insignificant volume changes [50]. Taken together with their low surface-to-volume ratio and their large diameter (1.3 mm), *Xenopus* oocytes are exceptionally useful for quantitative water measurements of heterologously expressed membrane transport proteins. Abrupt introduction of GABA to the test solution surrounding a GAT1-expressing oocyte led to a swift increase in GAT-mediated membrane currents and an *immediate* onset of cell swelling (jagged line in Fig. 6A). Overlay of the integrated current trace (total amount of accumulated charges) on the cell volume traces (total amount of accumulated fluid) as a function of time illustrated a near-perfect fit (straight line in Fig. 6A). This relation demonstrates that from the very onset, a fixed amount of water molecules are transferred into the cell with each charge; for GAT1 this number amounted to 330 water molecules per turnover [100]. While it may sound substantial, one must bear in mind that each osmotic particle in mammalian fluids is matched with approximately 165 water molecules (to obtain the approximately 300 mOsm tonicity in mammals). Accordingly, one turnover of GAT1 translocates four osmotic particles ($2Na^+$:$1Cl^-$:1GABA [106]), which requires movement of 4×165 (= 660) water molecules, by one molecular route or another. The cotransported water thus contributes to the water translocation required to maintain isotonicity, but does not suffice.

To distinguish between GAT1-mediated cotransport of water and GAT1-mediated accumulation of osmolytes followed by water entry, one can take advantage of the 'ion channel-like' Li^+-leak currents carried by GAT1 in the absence of Na^+ and GABA [107–109]. With replacement of Na^+ with Li^+ in the test solution, GAT1 enters a protein conformation resembling that of an ion channel, in which the transporter supports large inwardly-directed Li^+ fluxes [100]. In this manner, GAT1-expressing oocytes now experience accumulation of osmolytes (in the form of Li^+ instead of Na^+ and GABA) but without swelling on the immediate time scale (Fig. 6B). These observations suggest that it is not GAT-mediated osmolyte accumulation that leads to the immediate volume increase during GABA transport (nor unstirred layers, as these would also occur with the Li^+ transport), but rather the

cotransported water that is translocated in a fixed ratio with each turnover of the transport protein; *the ability of GAT1 to conduct active water transport* [100].

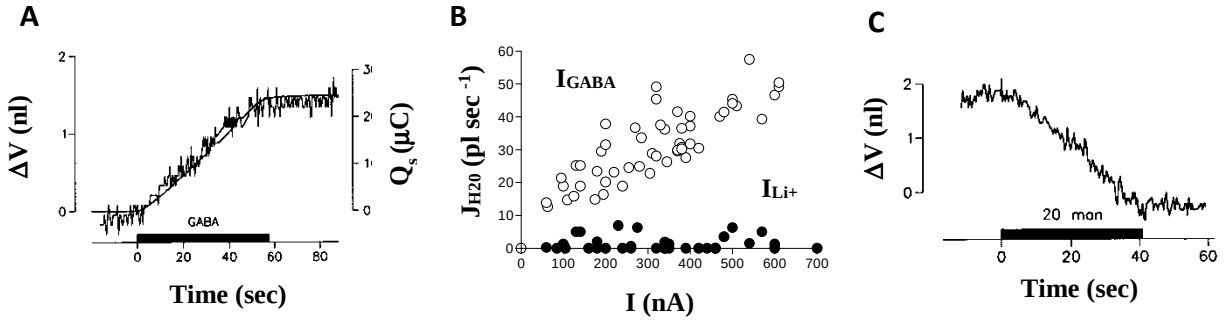

Fig. 6. Water transport in a GAT1-expressing *Xenopus* oocyte observed from below with a sensitive camera during current recordings. A. Cell volume increase in the presence of 100 μM GABA (jagged line) and integrated current depicted as a straight line. B. Water flux presented as a function of current, arising either as GABA-mediated transport activity (open symbols) or as Li^+-mediated leak current (filled symbols). C. Cell volume decrease upon exposure of an osmotic gradient (obtained with addition of mannitol to the test solution). Adapted from [100].

Several of these cotransporters, in addition, act as low-capacity water channels á la the aquaporins. That is, in the absence of substrate and therefore prevention of transporter turnover, an imposed osmotic gradient leads to passive water flux through the transport protein [31,110–114]. Fig. 6C illustrates the cell shrinkage of a GAT-expressing oocyte when exposed to an osmotic gradient; *the ability of GAT1 to conduct passive water transport*. Curiously, the conformation adopted by GAT1 with replacement of Na^+ with Li^+ in the test solution displayed a lower osmotic water permeability than those adopted with Na^+ or choline present [100], indicating that different transporter conformations sustain distinct water permeabilities [31,110–112]. Combination of these two experimental paradigms, as depicted in Fig. 7, sequentially exposes the GAT1-expressing oocyte to just the osmotic gradients (absence of GABA); the passive water transport, and to the osmotic gradients simultaneously with exposure to GABA); the passive plus the active water transport. The oocyte volume change is a linear function of the osmotic challenge, irrespective of the absence/presence of GABA (and thus GABA transport). The parallel shift between the two lines illustrates the GABA-induced cotransported water, which is constant in the face of oppositely directed osmotic challenges of variable sizes [100]. These observations suggest that GAT-mediated cotransport of water takes place independently of the prevailing osmotic gradient, *demonstrating the ability of GAT1 to conduct active water transport*.

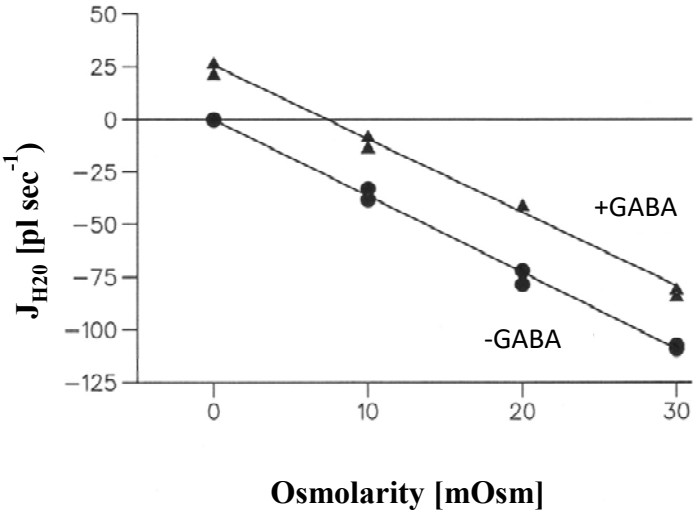

Fig. 7. A GAT1-expressing oocyte was exposed to hyperosmotic solutions (causing oocyte shrinkage) either in the absence of GABA (circles = only passive water transport) or in the presence of 100 µM GABA (triangles = passive + active water transport). The slope of the lines indicates the osmotic water permeability and the shift between them is the fixed amount of water transported inwards via cotransported water. Adapted from [105].

Molecular mechanism underlying cotransport of water

While experimental evidence suggests that cotransport of water *can* occur by a mechanism inherent in the transport protein itself, it is not trivial to elucidate *how* these fluxes occur at a molecular level. Molecular dynamics simulation of a bacterial galactose transporter in *Vibro parahaemolyticus* (resembling the water transporting Na^+-coupled glucose cotransporter, SGLT [104]) provided a working model for cotransport of water [115]. These simulation studies illustrated that with the exit of the galactose molecule, a number of water molecules residing in the inner half of the transporter exited the cavity ahead of the galactose. These water molecules were replaced by water originating in the extracellular space, which transferred to the cytoplasmic side behind the transported substrate. In this manner the water molecules were transported by what the authors coined ‘a Brownian piston’ by a mechanism within the transport protein [33,115].

TAKEN TOGETHER, cotransport of water allows water to be transported in the direction dictated by the ion/solute gradients of a given transport mechanism, and thus independently of required build-up of osmotic gradients.

GLIA CELL VOLUME DYNAMICS

Glia cells swell in response to several pathophysiological conditions, such as brain trauma and ischemia, and may precede the brain edema formation associated with these pathologies [116]. During pathophysiological conditions, the extracellular K^+ concentration may rise to as much as 60 mM, the extracellular glutamate concentration increases, the cells become severely depolarized, and the intracellular osmolarity increases [116–119]. The driving forces for ion, neurotransmitter and water transport are therefore altered [120]. The molecular mechanisms in pathological glia cell swelling are presumably different from the transient volume changes occurring during neuronal activity (see below): In the absence of an active Na^+/K^+-ATPase (such as during prolonged ischemic insult), the Donnan forces dictate a re-distribution of ions across the cell membrane, which - aided by the Cl^-/HCO_3^- and Na^+/H^+ exchangers - presumably leads to an intracellular accumulation of osmolytes [116,120]. The resulting osmotic driving forces will lead to water transport into the cell via the passive water transport pathways, in the form of AQP4 and diverse cotransporters, present in the glia cell membrane. However, a recent study revealed that astrocyte cell swelling observed during peri-infarct depolarizations in a stroke model occurred independently of AQP4 expression [121].

Molecular mechanisms underlying activity-evoked extracellular space shrinkage

During neuronal activity, K^+ is released into the extracellular space of the brain. This elevated K^+ is swiftly removed from the extracellular space, initially by the neighboring glia cells, which then acts as temporary 'K^+ sinks' [122,123] prior to post-stimulus release back into the extracellular space and return to the neuronal compartment [124,125]. This extracellular K^+ transient occurring in the wake of synaptic activity is paralleled by volume changes in the nearby cells, directly monitored as altered intrinsic optical signaling or indirectly as a shrinkage of the extracellular space recorded with ion-sensitive microelectrode [126–134], Fig. 8.

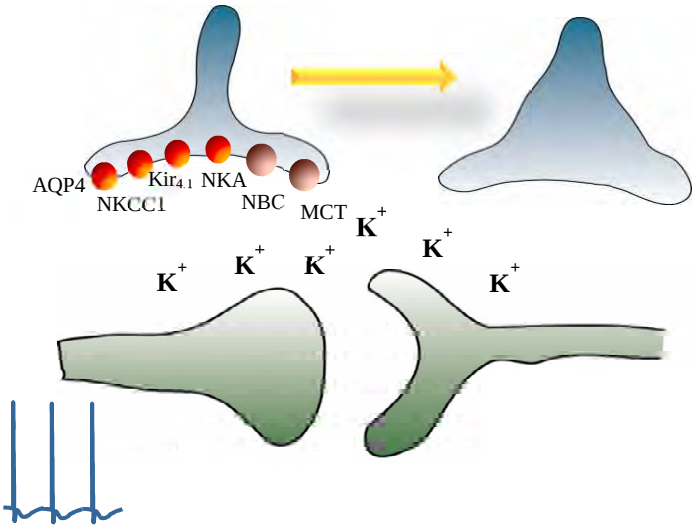

Fig. 8. Activity-evoked K^+ release from neurons into the extracellular space is initially buffered by nearby astrocytes that swell during the process. The swelling takes place, in part, via activation of the astrocytic bicarbonate transporters (labelled NBC) and lactate transporters (labelled MCT). AQP4 and the K^+-transporting proteins are not required for the astrocytic cell swelling. Drawing created by B.R. Larsen.

The cellular origin of the cell swelling has been, partly, assigned to the astrocytic compartment based on direct observation of fluorescently-labelled astrocytes in K^+-exposed rat hippocampal brain slices [135] and on persistent K^+-induced intrinsic optic signaling in the enucleated optic nerve [131]. In support, extracellular space shrinkage is (nearly) absent in rat hippocampus and optic nerve prior to the maturation of glia cells occurring at a later developmental stage [134,136]. Nevertheless, some level of neuronal swelling is likely to contribute to the stimulus-evoked volume dynamics [133].

AQP4

The molecular mechanisms underlying activity-induced extracellular space shrinkage have been debated since its original discovery. With the discovery of aquaporins and the astrocytic expression of AQP4 [37], this water channel was promoted as the required entry-way for water underlying activity-evoked glia cell swelling [47,63,84]. However, experiments conducted on $AQP4^{-/-}$ mice demonstrated identical (stratum pyramidale) or even *increased* (stratum radiatum) shrinkage of the extracellular space during stimulus-induced neuronal activity in hippocampal slices [137]. AQP4, therefore, is not the molecular mediator of activity-evoked glia cell swelling.

NKCC1 and KCC

As the activity-evoked extracellular space shrinkage occurs in parallel with the extracellular K^+ transients (Fig. 9), it was hypothesized that glia cell swelling arises as a direct function of the glia-mediated uptake of K^+ from the extracellular space [78,138–143].

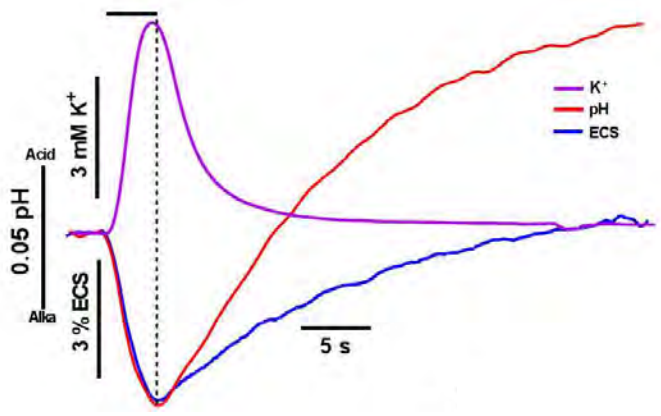

Fig. 9. Activity-evoked changes in K^+ (purple), pH (red), and extracellular space volume changes (blue) recorded with ion-sensitive microelectrodes in rat hippocampus. Black line on top of the traces indicate the electric stimulation of the Schaffer collaterals. Figure adapted from [144].

With the observed facilitation of glia cell volume changes by extracellular Cl^- [130,134,144–148], the family of Cl^--coupled cation transporters (NKCC1/KCC) could be possible transport mechanisms underlying the K^+-induced cell swelling. A body of work on primary culture of astrocytes identified the K^+-transporting $Na^+/K^+/2Cl^-$ cotransporter type 1 (NKCC1) as a molecular candidate underlying K^+-induced cell swelling: It is highly expressed in cultured astrocytes, it belongs to the water-transporting cotransporters, it causes cell swelling when activated, and it transports K^+ with sufficiently low affinity to allow increased transport activity when faced with increased extracellular K^+ (as during neuronal activity) [129,143,149–152]. Nevertheless, slice experiments demonstrated that hippocampal activity-evoked extracellular space shrinkage (and K^+-dynamics) was completely unaffected by inhibition of NKCC1 and KCC (with 10 μM bumetanide and 1 mM furosemide) [129,133,144]. These data suggest that the two K^+-transporters were not involved in the extracellular space dynamics, at least in the hippocampal brain region, although with very high concentrations of the KCC/NKCC inhibitor furosemide (5-10 mM), other research groups have detected reduced activity-evoked glial volume dynamics [130,134,148]. In support of the lack of NKCC1-mediated glia cell swelling *in vivo*; astrocytes *in situ* demonstrate negligible expression of NKCC1 [153,154], despite its prominent transport activity in cultured astrocytes. NKCC1, apparently, is recognized to be severely upregulated upon culturing of native cells of various kinds [155], this list now expanded to include astrocytes [129]. NKCC1, therefore, appears to not contribute to the extracellular space shrinkage during neuronal activity in hippocampus. Curiously, in the optic nerve, in which NKCC1 expression seems to occur, NKCC1 inhibition partly prevented the K^+-induced optical signaling [131]. Different brain regions may thus well employ distinct molecular mechanisms to govern extracellular space dynamics.

The Na^+/K^+-ATPase and Kir4.1

The Na^+/K^+-ATPase represents the key hippocampal astrocytic K^+ uptake machinery [125,129,140,156], acute inhibition of which did not prevent the extracellular space shrinkage [129]. Although with its quantitative contribution questioned [129,140,157], Kir4.1-mediated spatial buffering of K^+ [78,139,158] was proposed as the driving force for osmotically-induced water transport with ensuing AQP4-mediated astrocytic cell swelling [78,139]. However, pharmacological experiments [129] and genetic deletion of Kir4.1 [159] did not prevent activity-dependent glial swelling. These observations align with theoretical considerations based on the premise of Kir4.1-mediated spatial buffering, which relies on 'one-K^+-in-for-every-K^+-out' [127,157,160]. The very essence of spatial buffering thus prevents intracellular build-up of K^+ and thereby an associated

osmotic driving force. In addition, the principle of electro-neutrality dictates that build-up of any charged species requires a counter ion [161]. If a counter ion, possibly in the form of Cl^-, was to enter in parallel to the Kir4.1-mediated K^+ transport, the K^+ flux would no longer qualify as spatial buffering (for further discussion, see [127,140,157]). Taken together, *it thus appears that the well-established extracellular space shrinkage occurring during neuronal activity in rodent hippocampus, is not directly associated with astrocytic K^+ uptake*. This disconnect is further supported by the developmental profile of K^+, pH, and extracellular space dynamics, which illustrates that in hippocampus and optic nerve of young animals, a given neuronal activity (K^+ transient) associates with only sparse extracellular space shrinkage [134,136].

Glutamate transporters and receptors

With the activity-evoked K^+ transients and extracellular space volume dynamics, a range of other solutes (neurotransmitters, metabolites, H^+ (pH)) fluctuates simultaneously (Fig. 9) and could, by modulating transport activity of their assigned cotransporters, lead to the extracellular space shrinkage. Synaptically released glutamate is predominantly absorbed by glutamate transporters of the subtypes 1 and 2 (EAAT1 and EAAT2, human nomenclature) expressed in astrocytes [162] alongside metabotropic glutamate receptors [163]. Studies involving astrocytic cell culture as well as *in vitro*/*ex vivo* preparations have indicated metabotropic glutamate receptor (mGluR)-induced cell swelling [164] and glutamate transporter-mediated cell swelling [147,165–167]. Despite the reported ability of EAAT1 to cotransport water [99], and inhibition of glutamate transport in some studies impairing the stimulus-evoked intrinsic optical signaling [133], neither glutamate transporters nor mGluRs appeared directly implicated in activity-evoked extracellular space shrinkage in rat hippocampal slices [144]. In the latter study, a small contribution of EAAT-mediated extracellular space shrinkage could have gone unheeded with the excessive extracellular space volume dynamics occurring with inhibition of glutamate transporters; the ensuing slowed glutamate clearance caused an amplification and prolongation of the K^+ dynamics [168].

pH-regulating cotransporters contribute to stimulus-evoked extracellular space shrinkage

Neuronal activity associates with an extracellular space alkaline transient [144,169–171], which only in later developmental stages displays similar time course as those of the K^+ transients and the associated extracellular space shrinkage [136], Fig. 9. The molecular origin of the alkaline transient has been debated [172], but may include bicarbonate efflux through GABA-A receptors [169,173,174], uptake of H^+ by the glutamate transporters [175], and possibly bicarbonate

conductance [176] through their anion conductance pathway [177]. However, H^+ uptake from the extracellular space via neuronal plasma membrane Ca^{2+}/H^+-ATPase activity appears to be the most prominent contributor to the alkalization of the extracellular space during neuronal activity [170], while astrocytic transport mechanisms are assigned a role in the re-acidification [172,178]. Astrocytic bicarbonate transport is mainly governed by the electrogenic Na^+-coupled bicarbonate cotransporter, NBCe1, with a proposed symport stoichiometry of $1Na^+:2HCO_3^-$ [154,179,180]. Inward NBCe1-mediated bicarbonate transport is activated by the increased extracellular bicarbonate representing the transient alkalization and by the membrane depolarization arising with the parallel K^+ transient [178,180–185]. According to an earlier proposal [78], inhibition of NBCe1 in rat hippocampal slices (with 4,4'-Diisothiocyano-2,2'-stilbenedisulfonic acid (DIDS) or by removal of bicarbonate) reduced K^+-mediated [135] and activity-evoked [133,144] glia cell swelling without affecting the neuronal activity and thus the K^+ transient [144]. However, the activity-evoked intrinsic optical signal was not disturbed in nominally bicarbonate-free solutions [130], which could be assigned to the exceedingly high bicarbonate affinity of the astrocytic NBCe1; a low concentration of bicarbonate, generated within the slice, would suffice to activate the bicarbonate transport even in a nominally bicarbonate-free test solution [180].

Astrocytic Na^+-coupled bicarbonate transport thus serves as a mediator of the activity-evoked extracellular space shrinkage prompted by the neuronally-induced extracellular space alkalization and the K^+-mediated depolarization of the astrocytic membrane. It remains, however, to be resolved whether NBCe1 belongs to the water-transporting cotransporters.

The extracellular lactate concentration fluctuates with neuronal activity, and may briefly decrease in the first few seconds of neuronal activity [186–188]; that is, on a similar time scale as activity-evoked K^+ transients, pH transients, and extracellular space volume dynamics. Accordingly, inhibition of the lactate-transporting MCTs, of which MCT1 and -4 are expressed in astrocytes and MCT2 in neurons [189–193], reduced the activity-evoked extracellular space shrinkage in rat hippocampal slices without affecting the K^+ transients [144]. The initial activity-evoked brief dip in extracellular lactate concentration may thus be assigned to MCT-mediated uptake of lactate (prior to the onset of stimulus-induced glial lactate production), leading to extracellular space shrinkage, possibly via their ability to cotransport water [103]. In support of glial MCT-mediated cotransport of water, a 200 mOsm opposing osmotic gradient was required to prevent lactate-dependent swelling of primary cultured rat astrocytes [194].

TAKEN TOGETHER, activity-evoked extracellular space shrinkage predominantly originates from glia cell swelling, which does not occur via AQP4-dependent osmotic water transport and not in direct connection with any of the astrocytic K^+-transporting mechanisms implicated in removal of K^+ from the extracellular space (at least in rodent hippocampus). Rather, pH-modulating cotransporters (currently identified as NBCe1 and MCTs) are activated by the membrane depolarization prompted by the K^+ transient, by the neuronally-induced extracellular alkalization, and presumably by activity-induced metabolism. Their transport activity contributes to astrocytic cell swelling in a manner *not directly* coupled to the K^+ uptake mechanisms, as originally proposed, but in their own right (Fig. 8). The ensuing activity-evoked shrinkage of the extracellular space, which arises with developmental maturity, is predicted to ensure synaptic precision during neuronal activity.

NEURONAL SWELLING

Osmotic challenges lead to volume changes of brain cells *in vitro* and *in vivo* [195–198]. The volume changes take place exclusively in the astrocytic compartment, with the neighboring neurons resisting osmotic cell swelling [195–199]. The complete lack of aquaporin expression in most neuronal membranes provides their low osmotic water permeability [37,39,56]. An alternative, but yet unexplored, possibility could be that the neuronal volume regulatory machinery is sufficiently sensitive and initiates prior to detectable cell swelling, thus preventing noticable cell volume changes during osmotic stress [196,197]. Upon cell culturing, neurons attain the ability to respond to osmotic challenges with cell volume changes, and are, interestingly, capable of returning to their initial volume despite continuous presence of the imposed osmotic gradient [200,201]. Nevertheless, neuronal dendrites (as well as astrocytes [198,202]) readily swell when exposed to high $[K^+]_o$, glutamate agonists, or oxygen/glucose deprivation and during spreading depolarization (SD) [195–197].

Spreading depolarization-induced dendritic beading

Spreading depolarization occurs in connection with various pathological events, such as stroke, traumatic brain injury, and migraine [203–206] and can inflict secondary neuronal damage in patients experiencing these events in connection with their brain injury [207–209]. SD presents as a spreading wave of cell depolarization travelling at a speed of 2–6 mm/min across the brain tissue [210,211]. The SD associates with large shifts in the ion gradients, most notably a fall in extracellular $[Na^+]$ and

[Cl^-] and a concomitant rise in $[K^+]_o$ [212–217]. The shifted K^+ gradient causes its equilibrium potential to approach 0 mV and hence leads to severe membrane depolarization [218].

The membrane conductance responsible for initiation and propagation of SD has remained unresolved, possibly due to cooperation of several channels [219]. The machinery required for SD propagation appears to be identical irrespective of what triggered the SD in the first place [210]; one of several noxious events such as hypoxia, elevated glutamate or K^+, or inhibition of the Na^+/K^+-ATPase [220,221]. During SD, fluid shifts between the different compartments, as indicated by experiments conducted with ion-sensitive microelectrodes, with tissue light transmission, with two-photon laser scanning microscopy of fluorescent dendrites, and by electron microscopy [218,222–227]. Despite their resistance to osmotically-induced cell volume changes, neurons and their dendrites readily swell during pathological conditions or experimental conditions mimicking these [195–197,199,228–230]. Dendritic swelling has been assigned the main contributor to the initial SD-induced cell swelling [227], although astrocytic swelling may occur on a slightly different time course [202,228]. The focal dendritic swelling, oddly, presents with segmented cell volume increase separated by areas of cell shrinkage (Fig. 10). This phenomenon makes fluorescent protein-expressing dendrites, observed with two-photon laser scanning microscopy, appear as beads on a string, rather than a continuous dendritic structure; hence the term 'dendritic beading' [197,222]. As evident in Fig. 10, with each passing SD wave the dendrites instantly 'bead' and if the tissue is not metabolically compromised, the dendrites swiftly return to their original volume and shape [199].

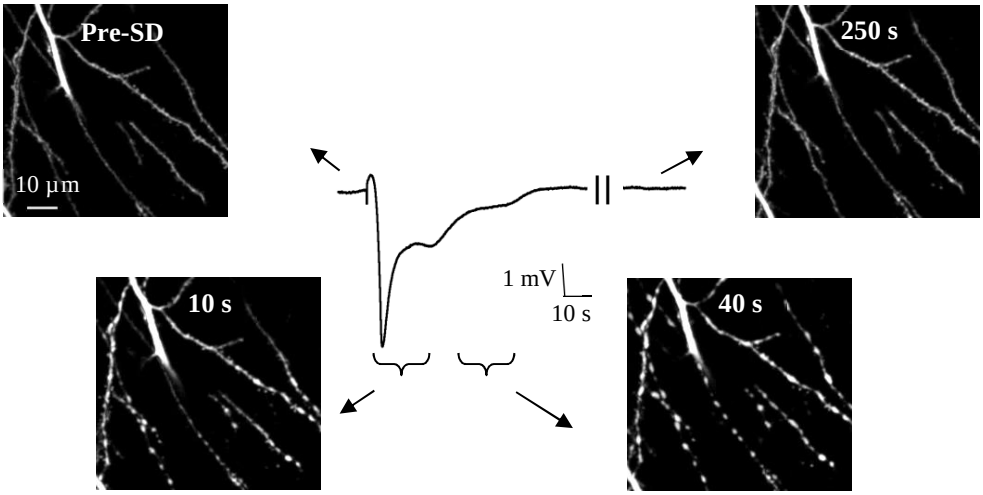

Fig. 10. Time course of dendritic beading arising with K^+-induced SD (indicated with the central trace recording the DC potential shift) in hippocampal slices from eGFP-expressing mice. Adapted from [199].

The large shift in ionic gradients prompted the proposal of an accompanying transmembrane osmotic gradient leading to passive water influx in nearby dendrites. However, mimicking such an osmotic gradient (by exposing the brain slice to a hyposmotic challenge) indicated that an osmotic gradient, in itself, failed to induce dendritic beading [197,199]. SD-induced disturbance in cytoskeletal organization was proposed as an alternative means of dendritic bead formation [231–233], although reorganization of the cytoskeletal elements were not required to inflict SD-induced dendritic beading [199,234], and neither was the large-pore channel pannexin 1 [235].

Cotransport of water as the molecular mechanism of SD-induced dendritic beading

The Cl^- concentration in the extracellular space declines during the SD wave, due to dendritic Cl^- accumulation [236]. Extracellular Cl^- is not required for the SD itself in normoxic slices, but essential for occurrence of dendritic beading when assessed directly with two-photon laser scanning microscopy of fluorescent dendrites, light scattering, or tissue electrical resistance, but not when recorded with TMA^+-sensitive microelectrodes [199,227,237]. The large shifts in ionic gradients (and pH) are bound to alter driving forces and activity of a range of cotransporters expressed on the dendrites, such as the Cl^--coupled NKCC1, KCC2, and the Cl^-/HCO_3^- exchanger AE3 [153,238,239], in addition to the H^+-coupled monocarboxylate transporter MCT2 [240]. Several of these transporters belong amongst the water transporting cotransporters (see above or [105]). Their combined SD-induced activity, indeed, did promote dendritic beading without contributing to the SD amplitude itself both *in vitro* and *in vivo* [199]. Singular inhibition of KCC2/NKCC1 (with furosemide) slightly reduced the intrinsic optical signal while DIDS did not (and the SD-induced extracellular space shrinkage as recorded with TMA-sensitive microelectrodes was unaffected with both inhibitors) [227,237]. In contrast to the findings by Steffensen and colleagues [199], these studies observed a direct effect of these inhibitors on the underlying SD-induced extracellular direct current (DC) potential shift [227,237], which could complicate direct assessment of inhibitor-mediated effect on the SD-induced dendritic beading. While its implication in SD-mediated dendritic beading and the associated means of water entry remains to be determined, the Cl^- channel SLC26A11 is reported as a novel contributor to neuronal cell body swelling prompted by a pharmacologically-mediated increase in neuronal Na^+ concentration [241].

TAKEN TOGETHER, the mechanisms promoting the wave of spreading depolarization are anticipated to be of ion channel origin. The large shifts in ionic gradients and pH arising with the SD promotes dendritic beading - not by conventional osmotic water transport but by cotransporter-mediated water transport, which occurs independently of an osmotic gradient, thus overcoming the inherently low neuronal osmotic water permeability. These transporters reverse their transport direction with normalization of the transmembrane ionic gradients, and could in this manner aid the reversal of the process.

CEREBROSPINAL FLUID SECRETION

The cerebral water content is continuously renewed by *de novo* secretion of CSF at a rate of ~350 µl /min in man, 50 µl/min in dog, 25 µl/min in cat, 9 µl/min in rabbit, 3 µl/min in rat, and 0.7 µl/min in mouse [101,242–252]. The CSF secretion capacity is similar in all tested species both when illustrated as percentage replenishment of total CSF volume (~0.5%/min) or as volume CSF produced per tissue mass (~0.5 µl/min/mg CP) [249,253,254].

CSF is produced predominantly (although not exclusively, see later) by the choroid plexuses [253,255–258]. Four of these highly vascularized structures of monolayered epithelial cells float in the ventricular cavities with an attachment to the ventricular wall. The choroid plexuses are distributed with two in the lateral ventricles, one in the third ventricle, and one in the fourth ventricle (Fig. 1).

Direct evidence of choroidal fluid secretion was obtained a century ago by an elegant set of experiments in dog [255]: i) unilateral blockage of the foramen of Monro (the passage between the lateral and the third ventricle) gave rise to a one-sided expansion of the lateral ventricle; ii) unilateral removal of a lateral choroid plexus followed by blockage of the ipsilateral foramen of Monroe lead to a collapse of the ventricle; and iii) combination of the two on individual sides of the ventricular system led to expansion of one ventricle and collapse of the other. From these sets of experiments the author concluded that the choroid plexus, rather than the ependymal cell lining, secretes the majority of the CSF [255]. This notion was later supported by several independent lines of evidence, including fluid collection at the exposed luminal choroidal membrane [259], determination of fluid lost from the choroidal vasculature during its passage through the tissue [258], and the observation of active secretion of Na^+ and Cl^- from the vasculature into the ventricular lumen (at a much faster rate than

the secretion across the capillary endothelium in cerebral cortex) [256,260,261]. The choroid plexus is thus a prominent site of CSF secretion.

The CSF contains higher concentration of Na^+ and lower concentration of K^+ than expected from an ultrafiltrate from plasma [259,262], suggesting the CSF is produced by active transport mechanisms [249,262]. The secreted fluid is practically identical to bulk CSF [9,256,259,263,264] and is secreted at a rate comparable to other efficient secretory epithelia in the mammalian body [265].

CSF secretion independently of the transepithelial osmotic gradient

It is generally assumed that CSF is produced by osmotically obliged water transport following Na^+ secretion [256,257,266]. However, several obstacles to this model present themselves. The CSF osmolarity in rats and rabbits is only slightly elevated compared to that of plasma (315 mOsm in CSF vs. 308 mOsm in plasma in rabbits and 302 mOsm in CSF vs. 298 mOsm in plasma in rats) [242,267], but nearly isotonic in cats (320-321 mOsm in CSF vs. 319-323 mOsm in plasma) [243,252,268] and humans (289 mOsm in CSF_{lumbar} vs. 289 mOsm in plasma) [269]. With such small, if any, transchoroidal osmotic gradient, the transepithelial osmotic water permeability of the choroid plexus therefore does not suffice to support the rates of CSF production consistently observed in mammals of different species [105,249,270]. To overcome this challenge, it has been speculated that the presence of unstirred layers in the immediate vicinity of the luminal choroidal membrane could create favorable conditions for passive movement of water across the choroidal membrane [249,254]. However, such unstirred layers have never been documented experimentally and the reversed organization of the choroid plexus epithelium prevents local build-up of osmolytes in the (putatively diffusion-restricted) lateral spaces [271], for details, see (Zeuthen and Steffensen, in review).

Of interest, several research teams have documented the ability of CSF secretion to take place independently of, and even against, an osmotic gradient in rabbit, cat, and goat [243,252,253,270,272–274]. Similar results were obtained with different osmolytes (sucrose, glucose, NaCl) generating the blood-to-CSF osmotic gradient and with both addition/removal of different osmolytes to/from either the ventricular fluid or to/from the vascular compartment. Common across all experiments was the linear correlation of CSF secretion with the osmotic gradient (Fig. 11), suggesting the ability of the choroidal tissue/ependymal lining to support passive water transport along an imposed osmotic challenge. *Most notably, however, is that all experimental approaches very clearly demonstrated robust CSF production during isotonic conditions - and especially; continued CSF secretion even during an oppositely directed osmotic gradient (indicated by red squares in Fig.*

11). According to the generally held assumption of osmotically obliged water flow following transport of electrolytes, the oppositely directed osmotic gradient should favor fluid transport in the opposite direction; from the ventricles to the vasculature (Fig. 11). In fact, an oppositely directed osmotic gradient of 60-120 mOsm was required to balance CSF secretion and render the fluid production zero [252,253,273]. Although CSF secretion correlated with large experimentally imposed osmotic gradients, at physiologically relevant osmolarities; the greater part of CSF secretion appears to occur by water transport occurring in the absence of a transchoroidal osmotic gradient and therefore not as osmotically obliged flow secondary to electrolyte secretion [253,270,272,273], Fig. 11.

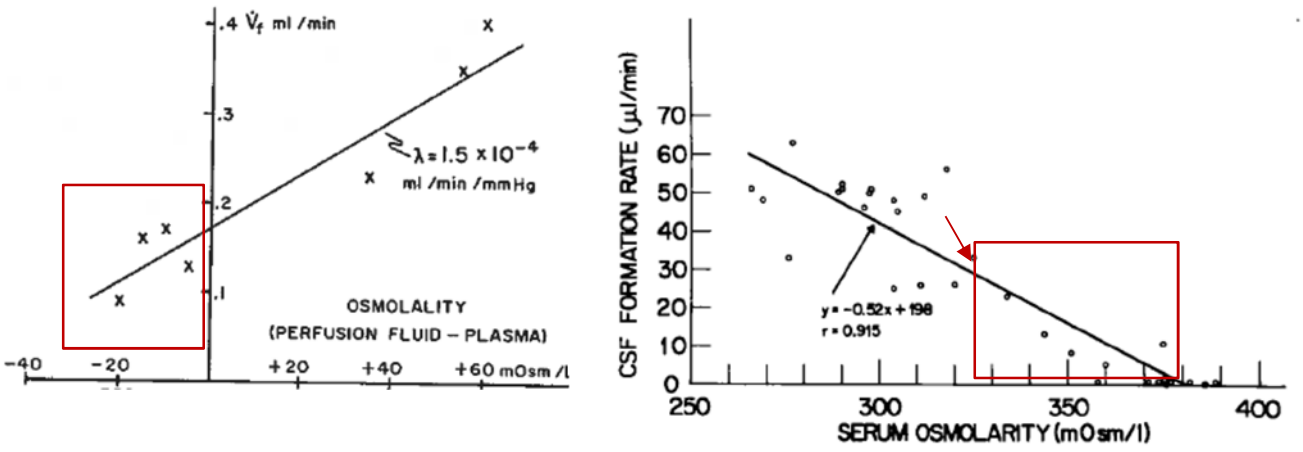

Fig. 11. CSF secretion rate measured in goat (left panel) upon changing of CSF osmolarity and in cat (right panel) upon changing serum osmolarity. Marked with red squares are the transepithelial osmotic gradients that would favor osmotic flow of water in the opposite direction, and yet CSF secretion continues. The red arrow indicates the physiological serum osmolarity in cats (isotonic with CSF [252]). Figures adapted from [243,253].

Quantitative assignment of the portion of the CSF secretion originating from choroid plexus versus the ependymal cell layer could not be definitely revealed from these studies. Notably, a diffusion-open cell layer, such as the junction-free ependymal layer, generally does not support osmotically induced water flow (which requires the presence of a semi-permeable membrane). Taken together, already half a century ago, research groups detected the first indications of active water transport as an underlying mechanism of CSF production (in analogy to observations in other epithelia, see [270] for references).

Molecular mechanisms of CSF secretion

The choroid plexus possesses general features resembling those of other secretory epithelia; microvilli on the luminal (ventricular) side, tight junctions sealing off the interstitial fluid from the CSF, and an array of transport mechanisms expressed in a polarized fashion on the two sides of the epithelium, some of which are indicated in Fig. 12, for review, see [275]. Decades of experimentation have implied these different transport mechanisms in CSF secretion. The quantitative contribution of each of these remain unresolved, as does, for the most part, their ability to sustain the uphill movement of water, as demonstrated in the various animal models.

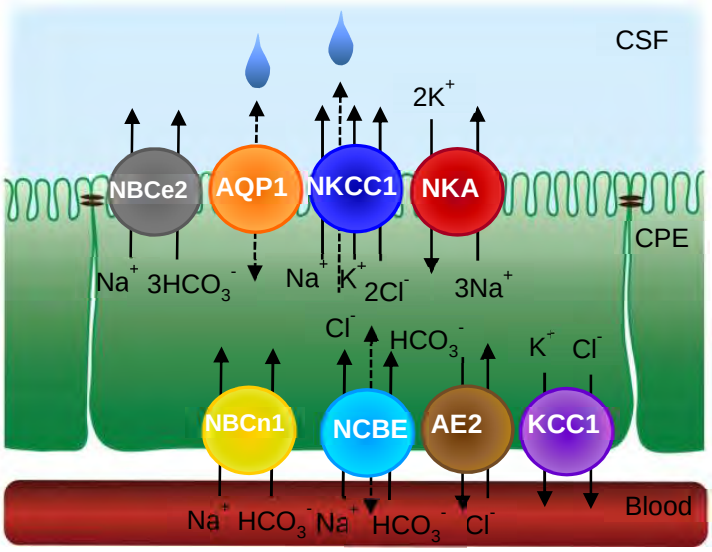

Fig. 12. Localization of select transporters in the choroid plexus epithelium (CPE). Modified from [101].

AQP1

The water channel AQP1 is located in the luminal membrane of the choroid plexus with little or no aquaporin expression in the basal membrane facing the blood vessel [35,45,276]. AQP1 contributes to the osmotic water permeability of the membrane separating the choroid plexus epithelial interior from the CSF; genetic deletion of AQP1 caused an 80% reduction in the osmotic water permeability of the luminal membrane [45]. Notably, the absence of aquaporins in the basal membrane predicts this membrane to be rate limiting for osmotic water flux and the AQP1-mediated osmotic water permeability therefore does not reflect the choroidal transepithelial water permeability. The CSF production in AQP1$^{-/-}$ mice was 20% lower than their wild type counterparts and their intracranial

pressure reduced by 50%, despite identical brain water content [45]. The AQP1$^{-/-}$ mice had a dramatic 80% drop in central venous pressure (measured in the jugular vein [45]), which may, indirectly, affect both CSF production and ICP. A group of patients with homozygous mutations in the gene encoding AQP1 lack functional expression of this water channel. Nevertheless, these individuals display no overt signs of neurological dysfunction [277,278], as is also the case with the AQP1$^{-/-}$ mice [279]. AQP1-mediated choroidal passive osmotic water flux may thus be dispensable for CSF production and brain function in mice and men, a notion supported by the above-mentioned choroidal CSF secretion near-independently of an osmotic gradient.

Na^+/K^+-ATPase

The Na^+/K^+-ATPase is located on the luminal membrane of the choroid plexus [276,280], in which it secretes Na^+ into the ventricular lumen in exchange for K^+. The pump thereby contributes both to transepithelial Na^+ fluxes from blood to brain and to exit of K^+ from the CSF, especially in conditions of elevated $[K^+]_{CSF}$, during which the Na^+/K^+-ATPase activity is increased [281–283]. The choroidal Na^+/K^+-ATPase activity (approximately 15 mol/kg/h in dog/rabbit [257]) arises predominantly from the catalytic α1 isoform [276], with several different isoforms of the accessory subunit β detected in choroid plexus tissue [284].

The contribution of the Na^+/K^+-ATPase to CSF production has been assessed in a variety of experimental animal species, predominantly with the ventricular-cisternal perfusion method [249]. This methodology relies on infusion of artificial CSF containing a fluorescent dextran (or other large molecules with limited parenchymal exchange) into the lateral ventricle of the anesthetized animal with subsequent collection at a downstream location, often the cisterna magna. The dilution of the fluorescent dextran represents the newly formed CSF. This approach, however, does not distinguish between fluid secreted by the choroid plexus and the fluid arising from endothelial secretion and subsequent entry into the ventricles via the ependymal cell layer. Detailed studies on rabbit, cats, and dogs demonstrated 50-70% reduction of CSF production upon inhibition of the Na^+/K^+-ATPase from the luminal side with 10^{-6} to 10^{-4} M ouabain [256–258,263,285–287]. Most reports observed an effect of ouabain treatment only when the inhibitor was delivered intracerebroventricularly (i.c.v.) in accordance with the luminal expression of the Na^+/K^+-ATPase in choroid plexus, although a few reports observed reduced CSF production upon intravenous (i.v.) or subcutaneous (s.c.) delivery of the inhibitor [285,288]. Ouabain affects a multitude of cellular functions and may lead to high mortality rates of the experimental animals, disturbances in cardiovascular parameters at higher concentrations, or indirect effects on other transport mechanisms by disturbance of the Na^+ and K^+

gradients [257,287]. The latter notion is supported by observations of ouabain-induced increase in $[K^+]_{CSF}$ to 5 mM [263] and an ouabain-induced reduction (30%) of choroidal $^{36}Cl^-$ flux in rats [289]. Accordingly, while it is undisputed that Na^+/K^+-ATPase activity is an ultimate requirement for CSF production, it remains unresolved to what extent it partakes *directly* in CSF secretion and to what extent it creates the electrochemical gradients for other transporters involved in this process. As an example; increased $[K^+]_{CSF}$ will have a severe impact on the transport direction of NKCC1 and thus the CSF production rate, see later.

Bicarbonate transporters

A range of bicarbonate transporters are expressed in the choroid plexus; the Na^+-coupled NCBE, NBCe2, NBCn1, and the Cl^-/HCO_3^--exchanger AE2 [275,290,291]. The transcript level of NBCn1 was less abundant than the other three bicarbonate transporters in RNA sequencing analysis of the mouse choroid plexus [284] and its choroidal function not yet revealed [292]. While the electrogenic Na^+-coupled bicarbonate cotransporter NBCe2 acts as the prominent luminal bicarbonate transporter, the remaining bicarbonate-transporting proteins reside in the basal membrane of choroid plexus [290–293], Fig. 12.

Quantification of the bicarbonate transporter contribution to CSF production and electrolyte secretion has been obtained with DIDS (inhibitor of bicarbonate transporters and anion channels [294]) and indirectly with acetazolamide (membrane permeable inhibitor of carbonic anhydrase), which is widely recognized for its ability to affect CSF production. Direct inhibition of the bicarbonate transporters with DIDS (i.c.v.) reduced CSF secretion and $^{36}Cl^-$ secretion by 25-30% [295]. The i.v. DIDS treatment led to decreased choroidal $[Cl^-]_i$ [295], supporting the generally accepted notion of bicarbonate transporters as the basal membrane Cl^- loaders [296], coupled to the inwardly-directed Na^+ transport from blood to choroidal epithelial cell interior [260]. These findings are corroborated by studies with acetazolamide, where in man, the carbonic anhydrase inhibitor had only a brief (30 min), and highly variable, effect on CSF production of around 10-50% [248]. In experimental animals, application of acetazolamide generally reduced CSF production (to a variable degree but generally by at least 50%), irrespective of experimental animal or inhibitor delivery route (i.v., intraperitoneal (i.p.), or i.c.v.) [45,250,251,263,285,286,297–300]. The acetazolamide-induced reduction in CSF production is mirrored by its effect on entry of radiolabeled Na^+ and Cl^- into the ventricle of all tested species of experimental animals [250,256,264,266,297,301–303]. Notably, no effect of acetazolamide was detected on BBB transendothelial Na^+ permeation [256,303], suggesting that the

origin of the observed acetazolamide-induced reduction of CSF secretion resides in the choroid plexus.

Acetazolamide only served its full inhibitory potential at concentrations leading to >99% inhibition of carbonic anhydrase [298]. While no changes was observed in CSF electrolyte concentration [250,263,264], acetazolamide treatment led to reduced choroidal $[Na^+]_i$ and elevated choroidal $[K^+]_i$ [250,302,304], same pattern as observed with Na^+/K^+-ATPase inhibition [250]. With experimental correction of the acetazolamide-induced blood pH change, the Na^+ and K^+ redistribution was reversed, however, with no effect on the acetazolamide-mediated reduction of CSF production [250].

In addition, acetazolamide may indirectly affect CSF secretion by its proposed vasoconstrictive action, especially on choroidal blood vessels [305], with an ensuing reduction of choroidal blood flow and thus CSF production [306]. Acetazolamide has also been observed to exert no effect on arterial blood pressure or choroidal blood flow [266,300], and may even act as a vasodilator [307]. Taken together with the lack of additive effect of ouabain and acetazolamide treatment [250,256], the quantitative mismatch in acetazolamide inhibitory effect on $^{22}Na^+$ flux (35%) versus CSF production (65%) [256], its proposed effect on oxidative metabolism [308], Cl^- channels [309,310], and cellular cGMP content [311], it remains unresolved what fraction of the acetazolamide-mediated effects occurs via *direct* inhibition of transchoroidal bicarbonate transport and what fraction is due to indirect effects on other membrane transport mechanisms contributing to CSF secretion.

In an attempt to quantify the contribution of individual bicarbonate transporters and circumventing the indirect effects of carbonic anhydrase inhibitors, the bicarbonate transporters NCBE and NBCe2 were successfully removed in mouse choroid plexus by genetic deletion. The small ventricular size of these genetically modified mice supported the pharmacological evidence of bicarbonate transport as an important mediator of choroid plexus-mediated ion and fluid transport from blood to brain [312,313]. It was, however, demonstrated that several choroidal membrane transport proteins were mislocalized in these transgenic animals and that their diminished ventricle size therefore could not be directly assigned to NCBE and/or NBCe2 by this experimental strategy [292,313,314].

Chloride-coupled cation transporters

Of the family of Cl^--coupled cation transporters, the K^+/Cl^- cotransporters (KCCs) and the $Na^+/K^+/2Cl^-$ cotransporter 1 (NKCC1) have been detected in choroid plexus. While there is general agreement of robust NKCC1 expression in the luminal membrane of both human and rodent choroid plexus, observed with immunohistochemical approaches [101,153,276] and upon functional isotope-

flux experiments [101,315,316], reports on KCC isoform expression are incongruent. Transcript analysis in mouse and rat choroid plexus indicates expression of the KCC1 isoform, with KCC2-4 transcript levels below or near detection levels [101,284,317]. Nevertheless, two immunohistochemical studies have indicated presence of KCC3 in the basolateral membrane and KCC4 in the luminal membrane of murine choroid plexus [318,319]. Neither of these observations could be confirmed by protein quantification or functional studies [101,316], which suggest that KCC1, as the only choroidal KCC isoform, is localized at the basolateral membrane [101], Fig. 12.

Commonly used inhibitors of KCCs and NKCCs generally act as diuretics, due to the established roles of these transporters in kidney fluid management. Accordingly, results obtained with i.v. delivery of furosemide (KCC and NKCC inhibitor) and bumetanide (NKCC inhibitor) appear to depend largely on whether or not the experimental animals were nephrectomized during the experimental procedure. In non-nephrectomized animals, i.v. delivery of furosemide reduced CSF production by 50-70% [274,298,299], possibly due to the furosemide-induced 8-fold increase in urine volume and the ensuing systemic water loss [274] with a predicted drop in blood pressure. With high concentrations of furosemide, a part of the effect observed with this inhibitor may be assigned to its parallel action as a carbonic anhydrase inhibitor [251,298]. In experimental conditions with abolished kidney function, neither furosemide nor bumetanide affected CSF production, $^{22}Na^+$ flux, or CSF ion composition when delivered i.v. or i.p. [244,251,320–322]. In contrast, and in congruence with the luminal localization of choroidal NKCC1, i.c.v. delivery of bumetanide or furosemide caused at least 50% reduction of CSF production in mouse, cat, and dog [101,244,274], with no effect on the measured systemic physiological parameters [244]. This inhibitor-mediated reduction in CSF secretion was paralleled by a comparable reduction in $^{36/38}Cl^-$ flux across choroid plexus *in vivo* and *ex vivo* [310,323], near-complete blockage of $^{86}Rb^+$ (as congener of K^+) efflux *ex vivo* [101,316], and reduced Na^+ and K^+ CSF content [320]. Notably, the inhibitory action of bumetanide and furosemide was quantitatively similar on the tested parameters [101,310,323], supporting the lack of functional KCC expression in the luminal membrane of mammalian choroid plexus [101].

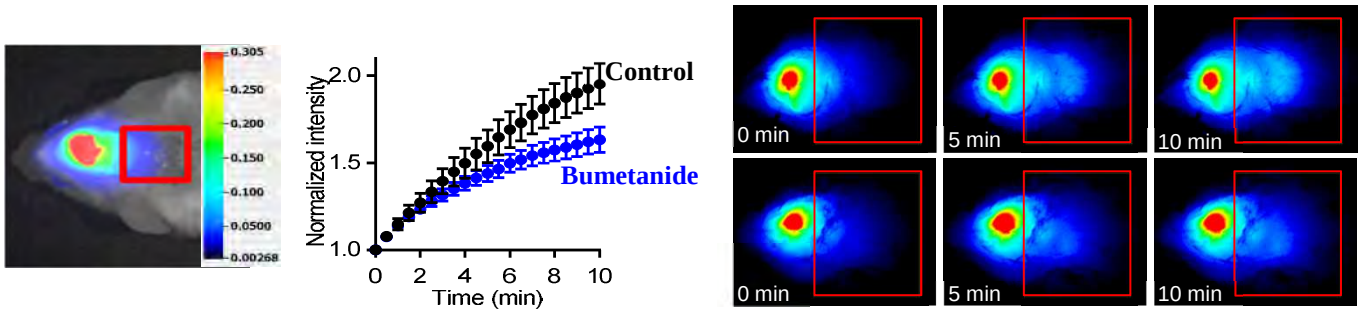

Fig. 13 Measurement of CSF production with Pearl Small Animal Imaging, LI-COR. Fluorescent dye, injected into the lateral ventricle, moves caudally with the CSF flow through the ventricular system as a function of time. This movement is slowed by inhibition of the CSF secreting $Na^+/K^+/2Cl^-$ cotransporter. Adapted from [104].

The NKCC1 transport direction depends on the transmembrane substrate gradients and thus varies with the prevailing ion concentrations. In most tissues, NKCC1 transports its substrates *into* the cells [324], but the high choroidal concentrations of Na^+ and Cl^- [101,325,326] provide the driving forces for the unusual outward transport direction of NKCC1 in rat and mouse *ex vivo* choroid plexus isotope studies [101,316]. NKCC1 is able to cotransport water independently of the osmotic gradient both in NKCC1-expressing oocytes, in primary cultures of human pigmented epithelial cells, and in *ex vivo* mouse choroid plexus [98,101,152]. It appears to contribute approximately 50% of the CSF secretion in mouse, cat, and dog, as determined by ventriculocisternal perfusion and ventricular flow of intraventricularly-delivered fluorescent dye [101,244,274], Fig. 13. These findings point to NKCC1 as an important contributor to the fluid secretion across the luminal choroidal membrane in a manner that could sustain the CSF production independently of, and even against, an imposed osmotic gradient [243,252,253,270,272–274].

TAKEN TOGETHER, the limited transepithelial water permeability of the choroid plexus and the small, if not negligible, transchoroidal osmotic gradient do not suffice to maintain the CSF secretion rates that are so well established across many animal species. Electrolyte transport and osmotically obliged water flow cannot support the experimentally documented CSF secretion against an oppositely directed osmotic gradient. Cotransport of water, at least in part by the NKCC1 expressed in the luminal membrane of choroid plexus, provides a novel molecular building block that sustains CSF secretion independently of the prevailing osmotic gradient.

BLOOD-BRAIN-BARRIER ION AND WATER TRANSPORT

While the majority of brain fluid accumulation generally is attributed to the choroid plexus [255–258], see above, a portion of the brain fluid flow can be assigned to secretion across the endothelial cell layer of the blood-brain-barrier (following entry into the ventricles via the ependymal cell layer) [267,272,327–330]. The majority of the endothelial water flux is transcellular [331] and has been assumed to arise as osmotically obliged water transport subsequent to ionic transport across the endothelium [12,332]. However, the low osmotic water permeability of the endothelial cell layer [22–24], due to complete lack of aquaporin-expression [25], would require a considerable build-up of osmotic particles in the space between the endothelial cell layer and the astrocytic endfeet. An increased osmolarity in such compartment would, via conventional osmosis, extract water across all adjacent membranes, not only the endothelial membrane but also the AQP4-rich and highly water-permeable neighboring astrocytic endfoot membrane. With this cellular organization, it is puzzling to envision exactly how water would be transferred selectively across the endothelial membranes to promote the desired directional flow of water from blood to brain. The mechanisms governing the trans-endothelial contribution to CSF/ISF secretion currently remain unidentified and are notoriously difficult to address experimentally. Future experiments will reveal the quantitative contribution of conventional passive osmotic water flux and cotransport of water in trans-endothelial water flux, but either way, the directional water flux arises with some form of transport of electrolytes from plasma to the brain.

Transport mechanisms in cerebral endothelium

The brain is highly vascularized with all cells being within less than 100 µm distance from the nearest capillary. Consequently, each cm^3 of brain contains approximately 100 cm^2 of endothelial membrane [24], which efficiently ensures passage of nutrients and gasses into and out of the brain. Brain endothelium belongs to the tight barrier layers with tight junctions ensuring a transendothelial electrical resistance (TEER) of approx. 1500-2000 $\Omega \cdot cm^2$ [333–335]. This high resistance testifies to the low ionic permeability of the BBB tight junctions and supports the notion of the majority of the BBB ion flux occurring via a transcellular route [331,332,336]. Accordingly, a range of endothelial transport mechanisms has been identified, although their quantitative distribution and their polarized expression to a large extent await clarification. Amongst the highlighted membrane transport mechanisms are the glucose transporter 1 (GLUT1), the monocarboxylate transporter 1 (MCT1), the glutamate transporter 1 (EAAT1), the amino acid transporters, most prominently the large amino acid transporter 1 (LAT1), different bicarbonate transporter isoforms, and the Na^+/K^+-ATPase (see e.g.

[329,337–339]). Most reports assign the Na^+/K^+-ATPase to the abluminal membrane [340–343], more specifically with protein and transcript expression of the α1 catalytic isoform in predicted combination with the accessory subunit of the β1 or β3 isoform [154,342]. The ouabain sensitivity of rat endothelial Na^+/K^+-ATPase activity ($IC_{50} \approx 10$ μM [344]) supports its α1 origin [345]. The Na^+/K^+-ATPase is thus ideally located at the abluminal endothelial membrane to ensure that the brain extracellular K^+ concentration remains at the 3 mM, even in the face of large and prolonged fluctuations in plasma K^+ concentrations [281,344,346,347]. With the reported endothelial Na^+/K^+-ATPase K^+ affinity (K_M of 2-3 mM, [342,344,348,349]), the endothelial combination of Na^+/K^+-ATPase isoforms provides the pump with the ability to increase its activity, and thus lower the $[K^+]_{ISF}$, when faced with elevated K^+ concentration in the interstitial fluid. Increased Na^+/K^+-ATPase activity would, in this manner, remove excess K^+ and lead to concomitant transfer of Na^+ into the brain tissue, and could, given an appropriate counter ion, promote electrolyte and water accumulation.

The mechanisms supporting Na^+ transport across the luminal (blood-facing) endothelial membrane prior to exciting via the abluminal Na^+/K^+-ATPase are more elusive. While many Na^+-coupled transporters have been identified in brain endothelium [154,329,339,350,351], several of these may be upregulated and/or mislocalized during culturing of the endothelial cells. Most debated is endothelial expression of NKCC1, which a research group assigned to the luminal membrane of cultured endothelial cells (by functional studies) and of tissue (by electron microscopy) [352,353]. Other research groups mainly detected NKCC1 activity at the abluminal membrane [342,354]. The tightness of the endothelial monolayer in the *in vitro* BBB model, and thus its resemblance to *in vivo* conditions, likely determines the NKCC1 activity in the model systems [342]. Taken together with the sparse endothelial NKCC1 protein/mRNA expression in cerebral endothelium *in vivo* [153,154,339], and functional absence in acutely isolated corneal endothelium, cortical microvessels, and in *in vivo* experimentation [355–357], the discrepancy may originate in NKCC1's general upregulation in cultured cell systems [129,155]. During ischemic conditions, inclusion of the NKCC inhibitor bumetanide limited brain edema formation [352], pointing to a possible upregulation in pathology and a role for this transport system in brain electrolyte and water accumulation under these conditions. Curiously, while ischemic conditions promote robust brain Na^+ and Cl^- accumulation, it associates with reduced K^+ brain content: In early stages of ischemia with intact BBB, this ion accumulation was assigned to elevated endothelial Na^+/K^+-ATPase activity spurred on by the ischemia-mediated increase in $[K^+]_{ISF}$ [358,359], although impaired efflux pathways may be an aiding parameter [360]. The selective Na^+ and Cl^- accumulation cannot directly be reconciled with NKCC1-

mediated ion transport, the activity of which should lead to increased brain accumulation of all three cotransported ions.

Brain volume regulation during osmotic challenges

Despite the complete absence of aquaporins in the brain endothelium [25,37] and thus one of the lowest reported osmotic water membrane permeabilities per cm^2 [23], the substantial capillary area-to-brain volume [24] allows significant water transport across the endothelial barrier with fluctuating plasma osmolarity. Accordingly, when faced with altered systemic plasma osmolarity, brain water increases with reduced plasma osmolarity and decreases with elevated plasma osmolarity [268,357,361–364]. Notably, the amount of brain water gained or lost is less than what is predicted from the imposed osmotic gradient; that is, when faced with the danger of brain water fluctuation and thus altered ion concentrations, especially K^+ with its direct influence of neuronal excitability, a volume regulatory machinery is set in place [357,361,362], Fig. 14. Elevated rat plasma osmolarity promoted brain Na^+ and Cl^- accumulation (not amino acids) in brain tissue [268,357,361]. These mechanisms ensure brain accumulation of electrolytes, the increased content of which can account for the protective limitation of the osmotically-induced water loss [268,357,361]. The electrolytes are hypothesized to be actively transported into the brain across the BBB upon dehydration-induced activation of some regulatory mechanism, yet unidentified [268,357,361]. An alternative manner could be via bulk flow from ventricular CSF to brain tissue [242,247,365] or via choroid plexus; elevation of cat ventricular osmolarity above the nascent 320 mOsm, promoted increased ventricular Na^+ influx [366].

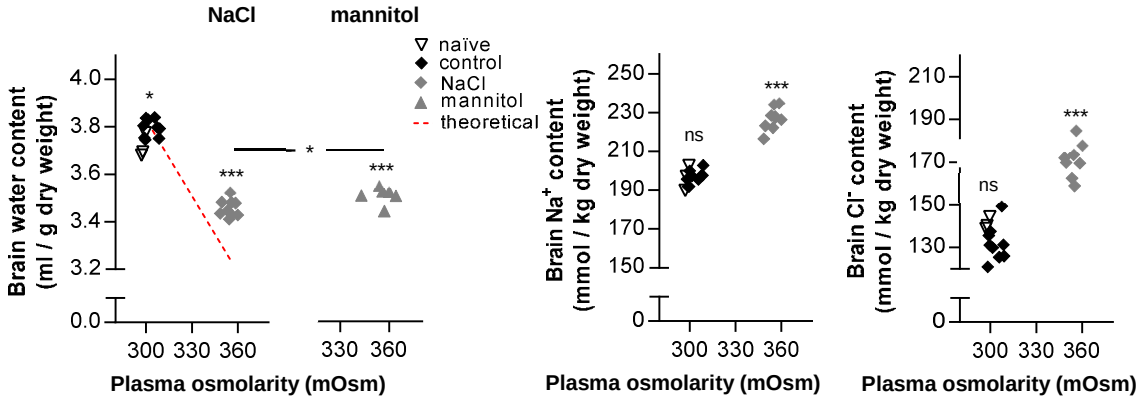

Fig. 14. Brain content of water, Na^+ and Cl^- after 60 min elevated plasma osmolarity (approx. 50 mOsm) in rats. The brain loses less water than anticipated from osmotic considerations, indicated by a red line (whether the osmolarity is raised with NaCl or mannitol i.p.). This limited water loss originates from brain accumulation of Na^+ and Cl^-. Adapted from [357].

K^+- and cell shrinkage-mediated activation of the endothelial abluminal Na^+/K^+-ATPase [342] could contribute to the elevated plasma osmolarity-induced brain electrolyte accumulation leading to brain protection against excessive water loss. On the blood-facing luminal membrane of the endothelium, the Na^+-transporting mechanisms NKCC1, the bicarbonate transporters, the Na^+/H^+ exchanger (NHE), and the epithelial Na^+ channel (ENaC) apparently did not contribute to the observed electrolyte accumulation in experimental animals exposed to elevated plasma osmolarity [357], leaving the Na^+ entry pathways across the luminal membrane unresolved. The cell shrinkage bound to follow elevated osmolarity in surrounding fluid is recognized to activate NKCC1 in heterologous expression systems and cell lines, including brain endothelial cell culture (immortalized and primary) [342,367–369]. Nevertheless, in parallel experiments, cell shrinkage did not activate NKCC1 in the tight *in vitro* co-culture BBB model from acutely isolated endothelial cells [342]. NKCC1 may therefore, if indeed expressed, be fully active at basal conditions in the brain endothelium. Although cell lines and heterologous expression systems are highly useful for biophysical characterization of transport proteins, they may not recapitulate observations from *in vivo* systems (or *in vitro* systems approximating *in vivo* conditions).

Elevated plasma osmolarity and acute brain insults are both associated with release of vasopressin systemically and centrally [370–372]. Vasopressin may increase endothelial water flux and pathologic brain water accumulation through activation of its G-protein coupled receptor $V1_aR$ [373–377]. $V_{1a}R$-mediated activation of luminally expressed NKCC1 in primary brain capillary endothelial cell culture has been proposed; elevated plasma osmolarity (or stroke) could in this manner promote dehydration-induced brain electrolyte accumulation [378]. However, vasopressin failed to activate NKCC1 in both a tight *in vitro* co-culture BBB model, in primary culture of brain capillary endothelial cells, and in *Xenopus* oocytes co-expressing NKCC1 and the vasopressin receptor [342]. Low levels of $V_{1a}R$ transcript are detected in cerebral endothelium [379–381], which aligns well with lack of detectable $V_{1a}R$ protein expression in capillary endothelial membranes in most brain regions [154,382,383]. Under physiological conditions, endothelial NKCC1 may therefore not act as the regulator of capillary electrolyte and water flux, and thus brain water homeostasis, but may be upregulated and implicated in stroke-induced edema formation [154,352,382–384].

Other BBB transporters as contributors to endothelial CSF secretion

It is currently not resolved which transport proteins support the endothelial contribution to CSF/ISF secretion. The exact catalogue of transport proteins expressed in the individual membranes of brain capillaries is not fully mapped, as many of the studies do not address their luminal/abluminal location

and are, in addition, done on cultured cells with distinct expression profile or with purified capillaries, containing remnants of astrocytic endfeet. Only few of the established endothelial cotransporters have been investigated for their ability to cotransport water. In addition to the water cotransporting NKCC1 [152], which may or may not be involved in endothelial water flux in physiology [342,352,357,378,384], the glucose transporter GLUT1 is highly expressed in both endothelial membranes [337,339,385] and is the major transport route for glucose transfer from blood to brain, driven by the concentration difference across the endothelium. The water transport capabilities of GLUT1 and its homologue isoform GLUT2 have been determined upon heterologous expression in *Xenopus* oocyte [386] and unpublished results (Zeuthen T). Their individual inherent capacity for both passive and active water transport are in the lower range [105,386] but with the large number of GLUT1s required to supply the brain with glucose, their contribution to brain water flux is likely significant [105]. The monocarboxylate transporter MCT1 and the glutamate transporter EAAT1 are both highly expressed in the brain capillary endothelium [339,387,388] and both belong to the water-transporting cotransporters [99,103]. Continuous supply of lactate and glutamate, and possibly other amino acids [379–381] to and from the brain tissue may, by means of cotransport of water, contribute to the endothelial contribution to CSF/ISF secretion.

TAKEN TOGETHER, in contrast to the systemic vasculature, the brain capillary endothelium does not express aquaporins and therefore has low osmotic water permeability. Nevertheless, a portion of the CSF is secreted across this cell layer, presumably at augmented rate under conditions of elevated plasma osmolarity and in edema-promoting pathologies. With the scarce knowledge of quantitative and polarized transporter expression in the endothelial membranes and the challenges with the associated experimentation (partly due to the altered protein expression in endothelium upon culturing), these transport mechanisms remain unresolved.

CONCLUSION

Although it is imperative to control the systemic water homeostasis, it is even more crucial to ensure precise volume regulation for the mammalian brain and its cellular structures; disturbance in the ion concentrations alters neuronal activity and with the rigidity of the cranium, excessive fluid accumulation leads to compression of the delicate brain tissue. We simply cannot rely solely on osmotic water transport in the brain; with every systemic dehydration due to thirst, sport, heat, etc., ion concentrations in the brain would immediately change if all volume regulation was pinned on

aquaporin-mediated passive osmotic water flow. This notion is supported by the lack of aquaporin expression on cerebral endothelium, contrasting the systemic vasculature, and in the basal membrane of choroid plexus. Growing evidence obtained in choroid plexus epithelial cells, neuronal dendrites, and glia cells points to cotransport of water as a manner in which the brain fluid dynamics can be precisely regulated without the required build-up of large osmotic gradients to drive the observed directional water fluxes.

With proteomics, the molecular knowledge of cerebral transport mechanisms, and the novel concept of cotransport of water as additional tools, it is timely to return to the volume of extraordinary work conducted by our predecessors in the past century and solve the molecular mechanisms underlying the intricate brain fluid flow in health and disease. Regrettably, few research laboratories nowadays address these issues and master the experimental techniques employed to obtain quantitative read-out of fluid movements. Much of the brain fluid research conducted last century was of the highest level of physiological experimentation, and conducted by very insightful and careful researchers. Despite my best efforts, I may have unintentionally overlooked some valuable findings but their results and experimental techniques will be a great aid on our path towards understanding the molecular mechanisms of brain water transport.

REFERENCES

** indicates articles included in the thesis*

1. Mathiisen TM, Lehre KP, Danbolt NC, Ottersen OP (2010) The perivascular astroglial sheath provides a complete covering of the brain microvessels: an electron microscopic 3D reconstruction. Glia 58: 1094-1103.

2. Brightman MW (1965) The distribution within the brain of ferritin injected into cerebrospinal fluid compartments. I. Ependymal distribution. J Cell Biol 26: 99-123.

3. Brightman MW, Reese TS (1969) Junctions between intimately apposed cell membranes in the vertebrate brain. J Cell Biol 40: 648-677.

4. Mollgard K, Balslev Y, Lauritzen B, Saunders NR (1987) Cell junctions and membrane specializations in the ventricular zone (germinal matrix) of the developing sheep brain: a CSF-brain barrier. J Neurocytol 16: 433-444.

5. Cserr HF, Cooper DN, Suri PK, Patlak CS (1981) Efflux of radiolabeled polyethylene glycols and albumin from rat brain. Am J Physiol 240: F319-F328.

6. His W (1865) Über ein perivasculäres canalsystem in den nervösen centralorganen und über dessen beziehungen sum lymphsystem. Zeitschrift für wissenschaftliche Zoologie 15: 127-141.

7. Rennels ML, Blaumanis OR, Grady PA (1990) Rapid solute transport throughout the brain via paravascular fluid pathways. Adv Neurol 52: 431-439.

8. Iliff JJ, Wang M, Liao Y, Plogg BA, Peng W, Gundersen GA, Benveniste H, Vates GE, Deane R, Goldman SA, Nagelhus EA, Nedergaard M (2012) A paravascular pathway facilitates CSF flow through the brain parenchyma and the clearance of interstitial solutes, including amyloid beta. Sci Transl Med 4: 147ra111.

9. Abbott NJ, Pizzo ME, Preston JE, Janigro D, Thorne RG (2018) The role of brain barriers in fluid movement in the CNS: is there a 'glymphatic' system? Acta Neuropathol 135: 387-407.

10. Asgari M, de ZD, Kurtcuoglu V (2016) Glymphatic solute transport does not require bulk flow. Sci Rep 6: 38635.

11. Faghih MM, Sharp MK (2018) Is bulk flow plausible in perivascular, paravascular and paravenous channels? Fluids Barriers CNS 15: 17.

12. Hladky SB, Barrand MA (2014) Mechanisms of fluid movement into, through and out of the brain: evaluation of the evidence. Fluids Barriers CNS 11: 26.

13. Hladky SB, Barrand MA (2018) Elimination of substances from the brain parenchyma: efflux via perivascular pathways and via the blood-brain barrier. Fluids Barriers CNS 15: 30.

14. Holter KE, Kehlet B, Devor A, Sejnowski TJ, Dale AM, Omholt SW, Ottersen OP, Nagelhus EA, Mardal KA, Pettersen KH (2017) Interstitial solute transport in 3D reconstructed neuropil occurs by diffusion rather than bulk flow. Proc Natl Acad Sci U S A 114: 9894-9899.

15. Jin BJ, Smith AJ, Verkman AS (2016) Spatial model of convective solute transport in brain extracellular space does not support a "glymphatic" mechanism. J Gen Physiol 148: 489-501.

16. Smith AJ, Yao X, Dix JA, Jin BJ, Verkman AS (2017) Test of the 'glymphatic' hypothesis demonstrates diffusive and aquaporin-4-independent solute transport in rodent brain parenchyma. Elife 6.

17. Smith AJ, Verkman AS (2017) The "glymphatic" mechanism for solute clearance in Alzheimer's disease: game changer or unproven speculation? FASEB J 32.

18. Spector R, Robert SS, Johanson CE (2015) A balanced view of the cerebrospinal fluid composition and functions: Focus on adult humans. Exp Neurol 273: 57-68.

19. Bering EA, Jr. (1952) Water exchange of central nervous system and cerebrospinal fluid. J Neurosurg 9: 275-287.

20. Eichling JO, Raichle ME, Grubb RL, Jr., Ter-Pogossian MM (1974) Evidence of the limitations of water as a freely diffusible tracer in brain of the rhesus monkey. Circ Res 35: 358-364.

21. Raichle ME, Eichling JO, Straatmann MG, Welch MJ, Larson KB, Ter-Pogossian MM (1976) Blood-brain barrier permeability of 11C-labeled alcohols and 15O-labeled water. Am J Physiol 230: 543-552.

22. Fenstermacher JD, Johnson JA (1966) Filtration and reflection coefficients of the rabbit blood-brain barrier. Am J Physiol 211: 341-346.

23. MacAulay N, Hamann S, Zeuthen T (2009) Chloride transporters as water pumps: Elements in a new model of epithelial water transport. In: FJ Alvarez-Leefmans & E Delpire, editors. Physiology and pathology of chloride transporters and channels in the nervous system. Academic Press, Elsevier. pp. 547-568.

24. Paulson OB, Hertz MM, Bolwig TG, Lassen NA (1977) Filtration and diffusion of water across the blood-brain barrier in man. Microvasc Res 13: 113-124.

25. Haj-Yasein NN, Vindedal GF, Eilert-Olsen M, Gundersen GA, Skare O, Laake P, Klungland A, Thoren AE, Burkhardt JM, Ottersen OP, Nagelhus EA (2011) Glial-conditional deletion of aquaporin-4 (Aqp4) reduces blood-brain water uptake and confers barrier function on perivascular astrocyte endfeet. Proc Natl Acad Sci U S A 108: 17815-17820.

26. Nielsen S, Smith BL, Christensen EI, Agre P (1993) Distribution of the aquaporin CHIP in secretory and resorptive epithelia and capillary endothelia. Proc Natl Acad Sci U S A 90: 7275-7279.

27. Agre P (1997) Molecular physiology of water transport: aquaporin nomenclature workshop. Mammalian aquaporins. Biol Cell 89: 255-257.

28. Wang Y, Tajkhorshid E (2007) Molecular mechanisms of conduction and selectivity in aquaporin water channels. J Nutr 137: 1509S-1515S.

29. Ho JD, Yeh R, Sandstrom A, Chorny I, Harries WE, Robbins RA, Miercke LJ, Stroud RM (2009) Crystal structure of human aquaporin 4 at 1.8 A and its mechanism of conductance. Proc Natl Acad Sci U S A 106: 7437-7442.

30. Litman T, Sogaard R, Zeuthen T (2009) Ammonia and urea permeability of mammalian aquaporins. Handb Exp Pharmacol 327-358.

31. Zeuthen T, MacAulay N (2002) Passive water transport in biological pores. Int Rev Cytol 215: 203-230.

32. Zeuthen T, MacAulay N (2002) Cotransporters as molecular water pumps. Int Rev Cytol 215: 259-284.

33. Zeuthen T (2010) Water-transporting proteins. J Membr Biol 234: 57-73.

34. Badaut J, Lasbennes F, Magistretti PJ, Regli L (2002) Aquaporins in brain: distribution, physiology, and pathophysiology. J Cereb Blood Flow Metab 22: 367-378.

35. Speake T, Freeman LJ, Brown PD (2003) Expression of aquaporin 1 and aquaporin 4 water channels in rat choroid plexus. Biochim Biophys Acta 1609: 80-86.

36. Dolman D, Drndarski S, Abbott NJ, Rattray M (2005) Induction of aquaporin 1 but not aquaporin 4 messenger RNA in rat primary brain microvessel endothelial cells in culture. J Neurochem 93: 825-833.

37. Nielsen S, Nagelhus EA, miry-Moghaddam M, Bourque C, Agre P, Ottersen OP (1997) Specialized membrane domains for water transport in glial cells: high-resolution immunogold cytochemistry of aquaporin-4 in rat brain. J Neurosci 17: 171-180.

38. Amiry-Moghaddam M, Ottersen OP (2003) The molecular basis of water transport in the brain. Nat Rev Neurosci 4: 991-1001.

39. Papadopoulos MC, Verkman AS (2013) Aquaporin water channels in the nervous system. Nat Rev Neurosci 14: 265-277.

40. Arcienega II, Brunet JF, Bloch J, Badaut J (2010) Cell locations for AQP1, AQP4 and 9 in the non-human primate brain. Neuroscience 167: 1103-1114.

41. Misawa T, Arima K, Mizusawa H, Satoh J (2008) Close association of water channel AQP1 with amyloid-beta deposition in Alzheimer disease brains. Acta Neuropathol 116: 247-260.

42. Nesic O, Lee J, Unabia GC, Johnson K, Ye Z, Vergara L, Hulsebosch CE, Perez-Polo JR (2008) Aquaporin 1 - a novel player in spinal cord injury. J Neurochem 105: 628-640.

43. Oliva AA, Jr., Kang Y, Truettner JS, Sanchez-Molano J, Furones C, Yool AJ, Atkins CM (2011) Fluid-percussion brain injury induces changes in aquaporin channel expression. Neuroscience 180: 272-279.

44. Satoh J, Tabunoki H, Yamamura T, Arima K, Konno H (2007) Human astrocytes express aquaporin-1 and aquaporin-4 in vitro and in vivo. Neuropathology 27: 245-256.

45. Oshio K, Watanabe H, Song Y, Verkman AS, Manley GT (2005) Reduced cerebrospinal fluid production and intracranial pressure in mice lacking choroid plexus water channel Aquaporin-1. FASEB J 19: 76-78.

46. Jung JS, Bhat RV, Preston GM, Guggino WB, Baraban JM, Agre P (1994) Molecular characterization of an aquaporin cDNA from brain: Candidate osmoreceptor and regulator of water balance. Proc Natl Acad Sci USA 91: 13052-13056.

47. Nagelhus EA, Ottersen OP (2013) Physiological roles of aquaporin-4 in brain. Physiol Rev 93: 1543-1562.

48. Neely JD, miry-Moghaddam M, Ottersen OP, Froehner SC, Agre P, Adams ME (2001) Syntrophin-dependent expression and localization of Aquaporin-4 water channel protein. Proc Natl Acad Sci U S A 98: 14108-14113.

49.* Assentoft M, Kaptan S, Schneider HP, Deitmer JW, de Groot BL, MacAulay N (2016) Aquaporin 4 as a NH3 Channel. J Biol Chem 291: 19184-19195.

50.* Fenton RA, Moeller HB, Zelenina M, Snaebjornsson MT, Holen T, MacAulay N (2010) Differential water permeability and regulation of three aquaporin 4 isoforms. Cell Mol Life Sci 67: 829-840.

51. Meinild A-K, Klaerke DA, Zeuthen T (1998) Bidirectional water fluxes and specificity for small hydrophilic molecules in aquaporins 0-5. Journal of Biological Chemistry 273: 32446-32451.

52. Moe SE, Sorbo JG, Sogaard R, Zeuthen T, Petter OO, Holen T (2008) New isoforms of rat Aquaporin-4. Genomics 91: 367-377.

53. Rossi A, Ratelade J, Papadopoulos MC, Bennett JL, Verkman AS (2012) Neuromyelitis optica IgG does not alter aquaporin-4 water permeability, plasma membrane M1/M23 isoform content, or supramolecular assembly. Glia 60: 2027-2039.

54. Neely JD, Christensen BM, Nielsen S, Agre P (1999) Heterotetrameric composition of aquaporin-4 water channels. Biochemistry 38: 11156-11163.

55. Furman CS, Gorelick-Feldman DA, Davidson KG, Yasumura T, Neely JD, Agre P, Rash JE (2003) Aquaporin-4 square array assembly: opposing actions of M1 and M23 isoforms. Proc Natl Acad Sci U S A 100: 13609-13614.

56. Rash JE, Yasumura T, Hudson CS, Agre P, Nielsen S (1998) Direct immunogold labeling of aquaporin-4 in square arrays of astrocyte and ependymocyte plasma membranes in rat brain and spinal cord. Proc Natl Acad Sci U S A 95: 11981-11986.

57. Yang B, Brown D, Verkman AS (1996) The mercurial insensitive water channel (AQP-4) forms orthogonal arrays in stably transfected Chinese hamster ovary cells. J Biol Chem 271: 4577-4580.

58. Landis DM, Reese TS (1974) Arrays of particles in freeze-fractured astrocytic membranes. J Cell Biol 60: 316-320.

59. Neuhaus J (1990) Orthogonal arrays of particles in astroglial cells: quantitative analysis of their density, size, and correlation with intramembranous particles. Glia 3: 241-251.

60. Solenov E, Watanabe H, Manley GT, Verkman AS (2004) Sevenfold-reduced osmotic water permeability in primary astrocyte cultures from AQP-4-deficient mice, measured by a fluorescence quenching method. Am J Physiol Cell Physiol 286: C426-C432.

61.* Assentoft M, Kaptan S, Fenton RA, Hua SZ, de Groot BL, MacAulay N (2013) Phosphorylation of rat aquaporin-4 at Ser(111) is not required for channel gating. Glia 61: 1101-1112.

62. Heo J, Meng F, Hua SZ (2008) Contribution of aquaporins to cellular water transport observed by a microfluidic cell volume sensor. Anal Chem 80: 6974-6980.

63. Gunnarson E, Zelenina M, Axehult G, Song Y, Bondar A, Krieger P, Brismar H, Zelenin S, Aperia A (2008) Identification of a molecular target for glutamate regulation of astrocyte water permeability. Glia 56: 587-596.

64. Song Y, Gunnarson E (2012) Potassium dependent regulation of astrocyte water permeability is mediated by cAMP signaling. PLoS One 7: e34936.

65. Zelenina M, Zelenin S, Bondar AA, Brismar H, Aperia A (2002) Water permeability of aquaporin-4 is decreased by protein kinase C and dopamine. Am J Physiol Renal Physiol 283: F309-F318.

66. Assentoft M, Larsen BR, Olesen ET, Fenton RA, MacAulay N (2014) AQP4 plasma membrane trafficking or channel gating is not significantly modulated by phosphorylation at COOH-terminal serine residues. Am J Physiol Cell Physiol 307: C957-C965.

67. Assentoft M, Larsen BR, MacAulay N (2015) Regulation and Function of AQP4 in the Central Nervous System. Neurochem Res 40: 2615-2627.

68. Sachdeva R, Singh B (2014) Phosphorylation of Ser-180 of rat aquaporin-4 shows marginal affect on regulation of water permeability: molecular dynamics study. J Biomol Struct Dyn 32: 555-566.

69. Fischer M, Kaldenhoff R (2008) On the pH regulation of plant aquaporins. J Biol Chem 283: 33889-33892.

70. Nemeth-Cahalan KL, Hall JE (2000) pH and calcium regulate the water permeability of aquaporin 0. J Biol Chem 275: 6777-6782.

71. Verdoucq L, Grondin A, Maurel C (2008) Structure-function analysis of plant aquaporin AtPIP2;1 gating by divalent cations and protons. Biochem J 415: 409-416. B

72. Zeuthen T, Klaerke DA (1999) Transport of water and glycerol in aquaporin 3 is gated by H(+). J Biol Chem 274: 21631-21636.

73. Kaptan S, Assentoft M, Schneider HP, Fenton RA, Deitmer JW, MacAulay N, de Groot BL (2015) H95 Is a pH-Dependent Gate in Aquaporin 4. Structure 23: 2309-2318.

74. Nemeth-Cahalan KL, Kalman K, Hall JE (2004) Molecular basis of pH and Ca2+ regulation of aquaporin water permeability. J Gen Physiol 123: 573-580.

75. Alberga D, Nicolotti O, Lattanzi G, Nicchia GP, Frigeri A, Pisani F, Benfenati V, Mangiatordi GF (2014) A new gating site in human aquaporin-4: Insights from molecular dynamics simulations. Biochim Biophys Acta 1838: 3052-3060.

76. Kraig RP, Chesler M (1990) Astrocytic acidosis in hyperglycemic and complete ischemia. J Cereb Blood Flow Metab 10: 104-114.

77. Amiry-Moghaddam M, Williamson A, Palomba M, Eid T, de Lanerolle NC, Nagelhus EA, Adams ME, Froehner SC, Agre P, Ottersen OP (2003) Delayed K+ clearance associated with aquaporin-4 mislocalization: phenotypic defects in brains of alpha-syntrophin-null mice. Proc Natl Acad Sci U S A 100: 13615-13620.

78. Nagelhus EA, Mathiisen TM, Ottersen OP (2004) Aquaporin-4 in the central nervous system: cellular and subcellular distribution and coexpression with KIR4.1. Neuroscience 129: 905-913.

79. Yao X, Hrabetova S, Nicholson C, Manley GT (2008) Aquaporin-4-deficient mice have increased extracellular space without tortuosity change. J Neurosci 28: 5460-5464.

80. Ma T, Yang B, Gillespie A, Carlson EJ, Epstein CJ, Verkman AS (1997) Generation and phenotype of a transgenic knockout mouse lacking the mercurial-insensitive water channel aquaporin-4. J Clin Invest 100: 957-962.

81. Eilert-Olsen M, Haj-Yasein NN, Vindedal GF, Enger R, Gundersen GA, Hoddevik EH, Petersen PH, Haug FM, Skare O, Adams ME, Froehner SC, Burkhardt JM, Thoren AE, Nagelhus EA (2012) Deletion of aquaporin-4 changes the perivascular glial protein scaffold without disrupting the brain endothelial barrier. Glia 60: 432-440.

82. Zeng XN, Sun XL, Gao L, Fan Y, Ding JH, Hu G (2007) Aquaporin-4 deficiency down-regulates glutamate uptake and GLT-1 expression in astrocytes. Mol Cell Neurosci 34: 34-39.

83. Zador Z, Stiver S, Wang V, Manley GT (2009) Role of aquaporin-4 in cerebral edema and stroke. Handb Exp Pharmacol 159-170.

84. Nagelhus EA, Horio Y, Inanobe A, Fujita A, Haug FM, Nielsen S, Kurachi Y, Ottersen OP (1999) Immunogold evidence suggests that coupling of K+ siphoning and water

transport in rat retinal Muller cells is mediated by a coenrichment of Kir4.1 and AQP4 in specific membrane domains. Glia 26: 47-54.

85. Ruiz-Ederra J, Zhang H, Verkman AS (2007) Evidence against functional interaction between aquaporin-4 water channels and Kir4.1 potassium channels in retinal Muller cells. J Biol Chem 282: 21866-21872.

86. Soe R, MacAulay N, Klaerke DA (2009) Modulation of Kir4.1 and Kir4.1-Kir5.1 channels by small changes in cell volume. Neurosci Lett 457: 80-84.

87. Binder DK, Yao X, Zador Z, Sick TJ, Verkman AS, Manley GT (2006) Increased seizure duration and slowed potassium kinetics in mice lacking aquaporin-4 water channels. Glia 53: 631-636.

88. Haj-Yasein NN, Bugge CE, Jensen V, Ostby I, Ottersen OP, Hvalby O, Nagelhus EA (2014) Deletion of aquaporin-4 increases extracellular K concentration during synaptic stimulation in mouse hippocampus. Brain Struct Funct 220:2469-74.

89. Strohschein S, Huttmann K, Gabriel S, Binder DK, Heinemann U, Steinhauser C (2011) Impact of aquaporin-4 channels on K+ buffering and gap junction coupling in the hippocampus. Glia 59: 973-980.

90. Jin BJ, Zhang H, Binder DK, Verkman AS (2013) Aquaporin-4-dependent K(+) and water transport modeled in brain extracellular space following neuroexcitation. J Gen Physiol 141: 119-132.

91. Binder DK, Yao X, Verkman AS, Manley GT (2006) Increased seizure duration in mice lacking aquaporin-4 water channels. Acta Neurochir Suppl 96: 389-392.

92. Diamond JM (1996) Wet transport proteins. Nature 384: 611-612.

93. Lapointe JY, Gagnon MP, Gagnon DG, Bissonnette P (2002) Controversy regarding the secondary active water transport hypothesis. Biochem Cell Biol 80: 525-533.

94. Spring KR (1999) Epithelial Fluid Transport--A Century of Investigation. News Physiol Sci 14: 92-98.

95. Agre P, Nielsen S, Ottersen OP (2004) Towards a molecular understanding of water homeostasis in the brain. Neuroscience 129: 849-850.

96. King LS, Kozono D, Agre P (2004) From structure to disease: the evolving tale of aquaporin biology. Nat Rev Mol Cell Biol 5: 687-698.

97. Hamann S, Kiilgaard JF, la CM, Prause JU, Zeuthen T (2003) Cotransport of H+, lactate, and H2O in porcine retinal pigment epithelial cells. Exp Eye Res 76: 493-504.

98. Hamann S, Herrera-Perez JJ, Zeuthen T, Alvarez-Leefmans FJ (2010) Cotransport of water by the Na+-K+-2Cl- cotransporter NKCC1 in mammalian epithelial cells. J Physiol 588: 4089-4101.

99. MacAulay N, Gether U, Klaerke DA, Zeuthen T (2001) Water transport by the human Na+-coupled glutamate cotransporter expressed in Xenopus oocytes. J Physiol 530: 367-378.

100.* MacAulay N, Zeuthen T, Gether U (2002) Conformational basis for the Li(+)-induced leak current in the rat gamma-aminobutyric acid (GABA) transporter-1. J Physiol 544: 447-458.

101.* Steffensen AB, Oernbo EK, Stoica A, Gerkau NJ, Barbuskaite D, Tritsaris K, Rose CR, MacAulay N (2018) Cotransporter-mediated water transport underlying cerebrospinal fluid formation. Nat Commun 9: 2167.

102. Zeuthen T (1994) Cotransport of K+, Cl- and H2O by membrane proteins from choroid plexus epithelium of Necturus maculosus. J Physiol 478 (Pt 2): 203-219.

103. Zeuthen T, Hamann S, la Cour M (1996) Cotransport of H+, lactate and H2O by membrane proteins in retinal pigment epithelium of bullfrog. J Physiol 497: 3-17.

104. Zeuthen T, Meinild AK, Klaerke DA, Loo DD, Wright EM, Belhage B, Litman T (1997) Water transport by the Na+/glucose cotransporter under isotonic conditions. Biol Cell 89: 307-312.

105. MacAulay N, Zeuthen T (2010) Water transport between CNS compartments: contributions of aquaporins and cotransporters. Neuroscience 168: 941-956.

106. Kavanaugh MP, Arriza JL, North RA, Amara SG (1992) Electrogenic uptake of gamma-aminobutyric acid by a cloned transporter expressed in Xenopus oocytes. J Biol Chem 267: 22007-22009.

107. Bismuth Y, Kavanaugh MP, Kanner BI (1997) Tyrosine 140 of the gamma-aminobutyric acid transporter GAT-1 plays a critical role in neurotransmitter recognition. J Biol Chem 272: 16096-16102.

108. MacAulay N, Bendahan A, Loland CJ, Zeuthen T, Kanner BI, Gether U (2001) Engineered Zn(2+) switches in the gamma-aminobutyric acid (GABA) transporter-1. Differential effects on GABA uptake and currents. J Biol Chem 276: 40476-40485.

109. Mager S, Kleinberger-Doron N, Keshet GI, Davidson N, Kanner BI, Lester HA (1996) Ion binding and permeation at the GABA transporter GAT1. J Neurosci 16: 5405-5414.

110. Enkavi G, Li J, Wen P, Thangapandian S, Moradi M, Jiand T, Han W, Tajkhorshid E (2014) A microscopic view of the mechanisms of active transport across the cellular membrane. Annual Reports in Computational Chemistry 10: 77-125.

111. Li J, Shaikh SA, Enkavi G, Wen PC, Huang Z, Tajkhorshid E (2013) Transient formation of water-conducting states in membrane transporters. Proc Natl Acad Sci U S A 110: 7696-7701.

112. MacAulay N, Gether U, Klaeke DA, Zeuthen T (2002) Passive water and urea permeability of a human Na(+)-glutamate cotransporter expressed in Xenopus oocytes. J Physiol 542: 817-828.

113. Sasseville LJ, Cuervo JE, Lapointe JY, Noskov SY (2011) The structural pathway for water permeation through sodium-glucose cotransporters. Biophys J 101: 1887-1895.

114. Zeuthen T, Belhage B, Zeuthen E (2006) Water transport by Na+-coupled cotransporters of glucose (SGLT1) and of iodide (NIS). The dependence of substrate size studied at high resolution. J Physiol 570: 485-499.

115. Choe S, Rosenberg JM, Abrahamson J, Wright EM, Grabe M (2010) Water permeation through the sodium-dependent galactose cotransporter vSGLT. Biophysical Journal - Biophysical Letters 99: 56-58.

116. Kimelberg HK (1995) Current concepts of brain edema. Review of laboratory investigations. J Neurosurg 83: 1051-1059.

117. Davalos A, Shuaib A, Wahlgren NG (2000) Neurotransmitters and pathophysiology of stroke: evidence for the release of glutamate and other transmitters/mediators in animals and humans. J Stroke Cerebrovasc Dis 9: 2-8.

118. Hossmann KA, Sakaki S, Zimmerman V (1977) Cation activities in reversible ischemia of the cat brain. Stroke 8: 77-81.

119. Walz W, Wuttke W, Hertz L (1984) Astrocytes in primary cultures: membrane potential characteristics reveal exclusive potassium conductance and potassium accumulator properties. Brain Res 292: 367-374.

120. Walz W, Mukerji S (1988) KCl movements during potassium-induced cytotoxic swelling of cultured astrocytes. Exp Neurol 99: 17-29.

121. Rakers C, Schmid M, Petzold GC (2017) TRPV4 channels contribute to calcium transients in astrocytes and neurons during peri-infarct depolarizations in a stroke model. Glia 65: 1550-1561.

122. Ballanyi K, Grafe P, Ten Bruggencate G (1987) Ion activities and potassium uptake mechanisms of glial cells in guinea-pig olfactory cortex slices. J Physiol 382: 159-174.

123. Grafe P, Ballanyi K (1987) Cellular mechanisms of potassium homeostasis in the mammalian nervous system. Can J Physiol Pharmacol 65: 1038-1042.

124. Coles JA, Schneider-Picard G (1989) Increase in glial intracellular K+ in drone retina caused by photostimulation but not mediated by an increase in extracellular K+. Glia 2: 213-222.

125. Larsen BR, Stoica A, MacAulay N (2016) Managing Brain Extracellular K(+) during Neuronal Activity: The Physiological Role of the Na(+)/K(+)-ATPase Subunit Isoforms. Front Physiol 7: 141.

126. Connors BW, Ransom BR, Kunis DM, Gutnick MJ (1982) Activity-dependent K+ accumulation in the developing rat optic nerve. Science 216: 1341-1343.

127. Dietzel I, Heinemann U, Hofmeier G, Lux HD (1980) Transient changes in the size of the extracellular space in the sensorimotor cortex of cats in relation to stimulus-induced changes in potassium concentration. Exp Brain Res 40: 432-439.

128. Hochman DW, Baraban SC, Owens JW, Schwartzkroin PA (1995) Dissociation of synchronization and excitability in furosemide blockade of epileptiform activity. Science 270: 99-102.

129.* Larsen BR, Assentoft M, Cotrina ML, Hua SZ, Nedergaard M, Kaila K, Voipio J, MacAulay N (2014) Contributions of the Na(+) /K(+) -ATPase, NKCC1, and Kir4.1 to hippocampal K(+) clearance and volume responses. Glia 62: 608-622.

130. MacVicar BA, Hochman D (1991) Imaging of synaptically evoked intrinsic optical signals in hippocampal slices. J Neurosci 11: 1458-1469.

131. MacVicar BA, Feighan D, Brown A, Ransom B (2002) Intrinsic optical signals in the rat optic nerve: role for K(+) uptake via NKCC1 and swelling of astrocytes. Glia 37: 114-123.

132. Orkand RK, Dietzel I, Coles JA (1984) Light-induced changes in extracellular volume in the retina of the drone, Apis mellifera. Neurosci Lett 45: 273-278.

133. Pal I, Nyitrai G, Kardos J, Heja L (2013) Neuronal and astroglial correlates underlying spatiotemporal intrinsic optical signal in the rat hippocampal slice. PLoS One 8: e57694.

134. Ransom BR, Yamate CL, Connors BW (1985) Activity-dependent shrinkage of extracellular space in rat optic nerve: a developmental study. J Neurosci 5: 532-535.

135. Florence CM, Baillie LD, Mulligan SJ (2012) Dynamic volume changes in astrocytes are an intrinsic phenomenon mediated by bicarbonate ion flux. PLoS One 7: e51124.

136.* Larsen BR, Stoica A, MacAulay N (2018) Developmental maturation of activity-induced K(+) and pH transients and the associated extracellular space dynamics in the rat hippocampus. J Physiol, Epub ahead of print.

137. Haj-Yasein NN, Jensen V, Ostby I, Omholt SW, Voipio J, Kaila K, Ottersen OP, Hvalby O, Nagelhus EA (2012) Aquaporin-4 regulates extracellular space volume dynamics during high-frequency synaptic stimulation: a gene deletion study in mouse hippocampus. Glia 60: 867-874.

138. Hertz L, Xu J, Song D, Yan E, Gu L, Peng L (2013) Astrocytic and neuronal accumulation of elevated extracellular K(+) with a 2/3 K(+)/Na(+) flux ratio-consequences for energy metabolism, osmolarity and higher brain function. Front Comput Neurosci 7: 114.

139. Kofuji P, Newman EA (2004) Potassium buffering in the central nervous system. Neuroscience 129: 1045-1056.

140. MacAulay N, Zeuthen T (2012) Glial K(+) clearance and cell swelling: key roles for cotransporters and pumps. Neurochem Res 37: 2299-2309.

141. Su G, Kintner DB, Flagella M, Shull GE, Sun D (2002) Astrocytes from Na(+)-K(+)-Cl(-) cotransporter-null mice exhibit absence of swelling and decrease in EAA release. Am J Physiol Cell Physiol 282: C1147-C1160.

142. Tas PW, Massa PT, Kress HG, Koschel K (1987) Characterization of an Na+/K+/Cl- co-transport in primary cultures of rat astrocytes. Biochim Biophys Acta 903: 411-416.

143. Walz W (1992) Role of Na/K/Cl cotransport in astrocytes. Can J Physiol Pharmacol 70 Suppl: S260-S262.

144.* Larsen BR, MacAulay N (2017) Activity-dependent astrocyte swelling is mediated by pH-regulating mechanisms. Glia 65: 1668-1681.

145. Bourke RS (1969) Studies of the development and subsequent reduction of swelling of mammalian cerebral cortex under isosmotic conditions in vitro. Exp Brain Res 8: 232-248.

146. Bourke RS, Nelson KM (1972) Further studies on the K + -dependent swelling of primate cerebral cortex in vivo: the enzymatic basis of the K + -dependent transport of chloride. J Neurochem 19: 663-685.

147. Lund-Andersen H, Hertz L (1970) Effects of potassium content in brain-cortex slices from adult rats. Exp Brain Res 11: 199-212.

148. Holthoff K, Witte OW (1996) Intrinsic optical signals in rat neocortical slices measured with near-infrared dark-field microscopy reveal changes in extracellular space. J Neurosci 16: 2740-2749.

149. Su G, Kintner DB, Sun D (2002) Contribution of Na(+)-K(+)-Cl(-) cotransporter to high-[K(+)](o)- induced swelling and EAA release in astrocytes. Am J Physiol Cell Physiol 282: C1136-C1146.

150. Walz W, Hertz L (1984) Intense furosemide-sensitive potassium accumulation in astrocytes in the presence of pathologically high extracellular potassium levels. J Cereb Blood Flow Metab 4: 301-304.

151. Walz W, Hinks EC (1985) Carrier-mediated KCl accumulation accompanied by water movements is involved in the control of physiological K+ levels by astrocytes. Brain Res 343: 44-51.

152. Zeuthen T, MacAulay N (2012) Cotransport of water by Na(+)-K(+)-2Cl(-) cotransporters expressed in Xenopus oocytes: NKCC1 versus NKCC2. J Physiol 590: 1139-1154.

153. Plotkin MD, Kaplan MR, Peterson LN, Gullans SR, Hebert SC, Delpire E (1997) Expression of the Na(+)-K(+)-2Cl- cotransporter BSC2 in the nervous system. Am J Physiol 272: C173-C183.

154. Zhang Y, Chen K, Sloan SA, Bennett ML, Scholze AR, O'Keeffe S, Phatnani HP, Guarnieri P, Caneda C, Ruderisch N, Deng S, Liddelow SA, Zhang C, Daneman R, Maniatis T, Barres BA, Wu JQ (2014) An RNA-sequencing transcriptome and splicing database of glia, neurons, and vascular cells of the cerebral cortex. J Neurosci 34: 11929-11947.

155. Raat NJ, Delpire E, Van Os CH, Bindels RJ (1996) Culturing induced expression of basolateral Na+-K+-2Cl- cotransporter BSC2 in proximal tubule, aortic endothelium, and vascular smooth muscle. Pflugers Arch 431: 458-460.

156. D'Ambrosio R, Gordon DS, Winn HR (2002) Differential role of KIR channel and Na(+)/K(+)-pump in the regulation of extracellular K(+) in rat hippocampus. J Neurophysiol 87: 87-102.

157. Larsen BR, MacAulay N (2014) Kir4.1-mediated spatial buffering of K(+): experimental challenges in determination of its temporal and quantitative contribution to K(+) clearance in the brain. Channels (Austin) 8: 544-550.

158. Walz W (2000) Role of astrocytes in the clearance of excess extracellular potassium. Neurochem Int 36: 291-300.

159. Haj-Yasein NN, Jensen V, Vindedal GF, Gundersen GA, Klungland A, Ottersen OP, Hvalby O, Nagelhus EA (2011) Evidence that compromised K(+) spatial buffering contributes to the epileptogenic effect of mutations in the human kir4.1 gene (KCNJ10). Glia 59: 1635-1642.

160. Orkand RK, Nicholls JG, Kuffler SW (1966) Effect of nerve impulses on the membrane potential of glial cells in the central nervous system of amphibia. J Neurophysiol 29: 788-806.

161. Blaustein, M. P., Kao, J. P. Y., and Matteson D.R. (2004) Cellular Physiology. Elsevier, USA.

162. Danbolt NC (2001) Glutamate uptake. Prog Neurobiol 65: 1-105.

163. Schools GP, Kimelberg HK (1999) mGluR3 and mGluR5 are the predominant metabotropic glutamate receptor mRNAs expressed in hippocampal astrocytes acutely isolated from young rats. J Neurosci Res 58: 533-543.

164. Hansson E (1994) Metabotropic glutamate receptor activation induces astroglial swelling. J Biol Chem 269: 21955-21961.

165. Izumi Y, Kirby CO, Benz AM, Olney JW, Zorumski CF (1999) Muller cell swelling, glutamate uptake, and excitotoxic neurodegeneration in the isolated rat retina. Glia 25: 379-389.

166. Koyama Y, Ishibashi T, Okamoto T, Matsuda T, Hashimoto H, Baba A (2000) Transient treatments with L-glutamate and threo-beta-hydroxyaspartate induce swelling of rat cultured astrocytes. Neurochem Int 36: 167-173.

167. Schneider GH, Baethmann A, Kempski O (1992) Mechanisms of glial swelling induced by glutamate. Can J Physiol Pharmacol 70 Suppl: S334-S343.

168. Larsen BR, Holm R, Vilsen B, MacAulay N (2016) Glutamate transporter activity promotes enhanced Na+ /K+ -ATPase-mediated extracellular K+ management during neuronal activity. J Physiol 594: 6627-6641.

169. Chen JC, Chesler M (1992) Modulation of extracellular pH by glutamate and GABA in rat hippocampal slices. J Neurophysiol 67: 29-36.

170. Makani S, Chesler M (2010) Rapid rise of extracellular pH evoked by neural activity is generated by the plasma membrane calcium ATPase. J Neurophysiol 103: 667-676.

171. Voipio J, Kaila K (1993) Interstitial PCO2 and pH in rat hippocampal slices measured by means of a novel fast CO2/H(+)-sensitive microelectrode based on a PVC-gelled membrane. Pflugers Arch 423: 193-201.

172. Chesler M (2003) Regulation and modulation of pH in the brain. Physiol Rev 83: 1183-1221.

173. Kaila K, Voipio J (1987) Postsynaptic fall in intracellular pH induced by GABA-activated bicarbonate conductance. Nature 330: 163-165.

174. Kaila K, Paalasmaa P, Taira T, Voipio J (1992) pH transients due to monosynaptic activation of GABAA receptors in rat hippocampal slices. Neuroreport 3: 105-108.

175. Zerangue N, Kavanaugh MP (1996) Flux coupling in a neuronal glutamate transporter. Nature 383: 634-637.

176. Kunzelmann K, Gerlach L, Frobe U, Greger R (1991) Bicarbonate permeability of epithelial chloride channels. Pflugers Arch 417: 616-621.

177. Kanai Y, Trotti D, Berger UV, Hediger MA (2002) The High-Affinity Glutamate and Neutral Amino-Acid Transporter Family. in Neurotransmitter Transporters - Structure, Function, and Regulation (2nd edition), Ed.; Reit MEA, Springer Science+Business Media.

178. Chesler M, Kraig RP (1989) Intracellular pH transients of mammalian astrocytes. J Neurosci 9: 2011-2019.

179. Deitmer JW, Schlue WR (1989) An inwardly directed electrogenic sodium-bicarbonate co-transport in leech glial cells. J Physiol 411: 179-194.

180. Theparambil SM, Ruminot I, Schneider HP, Shull GE, Deitmer JW (2014) The electrogenic sodium bicarbonate cotransporter NBCe1 is a high-affinity bicarbonate carrier in cortical astrocytes. J Neurosci 34: 1148-1157.

181. Brookes N, Turner RJ (1994) K(+)-induced alkalinization in mouse cerebral astrocytes mediated by reversal of electrogenic Na(+)-. Am J Physiol 267: C1633-C1640.

182. Deitmer JW, Szatkowski M (1990) Membrane potential dependence of intracellular pH regulation by identified glial cells in the leech central nervous system. J Physiol 421: 617-631.

183. Pappas CA, Ransom BR (1994) Depolarization-induced alkalinization (DIA) in rat hippocampal astrocytes. J Neurophysiol 72: 2816-2826.

184. Theparambil SM, Naoshin Z, Thyssen A, Deitmer JW (2015) Reversed electrogenic sodium bicarbonate cotransporter 1 is the major acid loader during recovery from cytosolic alkalosis in mouse cortical astrocytes. J Physiol 593: 3533-3547.

185. Theparambil SM, Deitmer JW (2015) High effective cytosolic H+ buffering in mouse cortical astrocytes attributable to fast bicarbonate transport. Glia 63: 1581-1594.

186. Barros LF (2013) Metabolic signaling by lactate in the brain. Trends Neurosci 36: 396-404.

187. Hu Y, Wilson GS (1997) Rapid changes in local extracellular rat brain glucose observed with an in vivo glucose sensor. J Neurochem 68: 1745-1752.

188. Mangia S, Garreffa G, Bianciardi M, Giove F, Di SF, Maraviglia B (2003) The aerobic brain: lactate decrease at the onset of neural activity. Neuroscience 118: 7-10.

189. Bergersen L, Waerhaug O, Helm J, Thomas M, Laake P, Davies AJ, Wilson MC, Halestrap AP, Ottersen OP (2001) A novel postsynaptic density protein: the monocarboxylate transporter MCT2 is co-localized with delta-glutamate receptors in postsynaptic densities of parallel fiber-Purkinje cell synapses. Exp Brain Res 136: 523-534.

190. Chiry O, Pellerin L, Monnet-Tschudi F, Fishbein WN, Merezhinskaya N, Magistretti PJ, Clarke S (2006) Expression of the monocarboxylate transporter MCT1 in the adult human brain cortex. Brain Res 1070: 65-70.

191. Leino RL, Gerhart DZ, Drewes LR (1999) Monocarboxylate transporter (MCT1) abundance in brains of suckling and adult rats: a quantitative electron microscopic immunogold study. Brain Res Dev Brain Res 113: 47-54.

192. Pierre K, Pellerin L, Debernardi R, Riederer BM, Magistretti PJ (2000) Cell-specific localization of monocarboxylate transporters, MCT1 and MCT2, in the adult mouse brain revealed by double immunohistochemical labeling and confocal microscopy. Neuroscience 100: 617-627.

193. Rafiki A, Boulland JL, Halestrap AP, Ottersen OP, Bergersen L (2003) Highly differential expression of the monocarboxylate transporters MCT2 and MCT4 in the developing rat brain. Neuroscience 122: 677-688.

194. Bender AS, Young LP, Norenberg MD (1997) Effect of lactic acid on L-glutamate uptake in cultured astrocytes: mechanistic considerations. Brain Res 750: 59-66.

195. Andrew RD, MacVicar BA (1994) Imaging cell volume changes and neuronal excitation in the hippocampal slice. Neuroscience 62: 371-383.

196. Andrew RD, Lobinowich ME, Osehobo EP (1997) Evidence against volume regulation by cortical brain cells during acute osmotic stress. Exp Neurol 143: 300-312.

197. Andrew RD, Labron MW, Boehnke SE, Carnduff L, Kirov SA (2007) Physiological evidence that pyramidal neurons lack functional water channels. Cereb Cortex 17: 787-802.

198. Risher WC, Andrew RD, Kirov SA (2009) Real-time passive volume responses of astrocytes to acute osmotic and ischemic stress in cortical slices and in vivo revealed by two-photon microscopy. Glia 57: 207-221.

199.* Steffensen AB, Sword J, Croom D, Kirov SA, MacAulay N (2015) Chloride Cotransporters as a Molecular Mechanism underlying Spreading Depolarization-Induced Dendritic Beading. J Neurosci 35: 12172-12187.

200. Aitken PG, Borgdorff AJ, Juta AJ, Kiehart DP, Somjen GG, Wadman WJ (1998) Volume changes induced by osmotic stress in freshly isolated rat hippocampal neurons. Pflugers Arch 436: 991-998.

201. Pasantes-Morales H, Maar TE, Moran J (1993) Cell volume regulation in cultured cerebellar granule neurons. J Neurosci Res 34: 219-224.

202. Zhou N, Gordon GR, Feighan D, MacVicar BA (2010) Transient Swelling, Acidification, and Mitochondrial Depolarization Occurs in Neurons but not Astrocytes during Spreading Depression. Cereb Cortex 20:2614-2624.

203. Dreier JP, Reiffurth C (2015) The Stroke-Migraine Depolarization Continuum. Neuron 86: 902-922.

204. Hadjikhani N, Sanchez Del RM, Wu O, Schwartz D, Bakker D, Fischl B, Kwong KK, Cutrer FM, Rosen BR, Tootell RB, Sorensen AG, Moskowitz MA (2001) Mechanisms of migraine aura revealed by functional MRI in human visual cortex. Proc Natl Acad Sci U S A 98: 4687-4692.

205. Hartings JA, Bullock MR, Okonkwo DO, Murray LS, Murray GD, Fabricius M, Maas AI, Woitzik J, Sakowitz O, Mathern B, Roozenbeek B, Lingsma H, Dreier JP, Puccio AM, Shutter LA, Pahl C, Strong AJ (2011) Spreading depolarisations and outcome after traumatic brain injury: a prospective observational study. Lancet Neurol 10: 1058-1064.

206. Oliveira-Ferreira AI, Milakara D, Alam M, Jorks D, Major S, Hartings JA, Luckl J, Martus P, Graf R, Dohmen C, Bohner G, Woitzik J, Dreier JP (2010) Experimental and preliminary clinical evidence of an ischemic zone with prolonged negative DC shifts surrounded by a normally perfused tissue belt with persistent electrocorticographic depression. J Cereb Blood Flow Metab 30: 1504-1519.

207. Dreier JP, Woitzik J, Fabricius M, Bhatia R, Major S, Drenckhahn C, Lehmann TN, Sarrafzadeh A, Willumsen L, Hartings JA, Sakowitz OW, Seemann JH, Thieme A, Lauritzen M, Strong AJ (2006) Delayed ischaemic neurological deficits after subarachnoid haemorrhage are associated with clusters of spreading depolarizations. Brain 129: 3224-3237.

208. Lauritzen M, Dreier JP, Fabricius M, Hartings JA, Graf R, Strong AJ (2011) Clinical relevance of cortical spreading depression in neurological disorders: migraine, malignant stroke, subarachnoid and intracranial hemorrhage, and traumatic brain injury. J Cereb Blood Flow Metab 31: 17-35.

209. Hartings JA, Watanabe T, Bullock MR, Okonkwo DO, Fabricius M, Woitzik J, Dreier JP, Puccio A, Shutter LA, Pahl C, Strong AJ (2011) Spreading depolarizations have prolonged direct current shifts and are associated with poor outcome in brain trauma. Brain 134: 1529-1540.

210. Dreier JP (2011) The role of spreading depression, spreading depolarization and spreading ischemia in neurological disease. Nat Med 17: 439-447.

211. Leao AA (1944) Spreading depression of activity in the cerebral cortex. Journal of Neurophysiology 7: 359-390.

212. Hansen AJ, Zeuthen T (1981) Extracellular ion concentrations during spreading depression and ischemia in the rat brain cortex. Acta Physiol Scand 113: 437-445.

213. Kraig RP, Nicholson C (1978) Extracellular ionic variations during spreading depression. Neuroscience 3: 1045-1059.

214. Menna G, Tong CK, Chesler M (2000) Extracellular pH changes and accompanying cation shifts during ouabain-induced spreading depression. J Neurophysiol 83: 1338-1345.

215. Mutch WA, Hansen AJ (1984) Extracellular pH changes during spreading depression and cerebral ischemia: mechanisms of brain pH regulation. J Cereb Blood Flow Metab 4: 17-27.

216. Somjen GG (2001) Mechanisms of spreading depression and hypoxic spreading depression-like depolarization. Physiol Rev 81: 1065-1096.

217. Windmuller O, Lindauer U, Foddis M, Einhaupl KM, Dirnagl U, Heinemann U, Dreier JP (2005) Ion changes in spreading ischaemia induce rat middle cerebral artery constriction in the absence of NO. Brain 128: 2042-2051.

218. Snow RW, Taylor CP, Dudek FE (1983) Electrophysiological and optical changes in slices of rat hippocampus during spreading depression. J Neurophysiol 50: 561-572.

219. Somjen, G. G. (2004) Ions in the brain: normal function, seizures, and stroke. Oxford University Press, USA.

220. Balestrino M, Young J, Aitken P (1999) Block of (Na+,K+)ATPase with ouabain induces spreading depression-like depolarization in hippocampal slices. Brain Res 838: 37-44.

221. Hasbani MJ, Schlief ML, Fisher DA, Goldberg MP (2001) Dendritic spines lost during glutamate receptor activation reemerge at original sites of synaptic contact. J Neurosci 21: 2393-2403.

222. Risher WC, Ard D, Yuan J, Kirov SA (2010) Recurrent spontaneous spreading depolarizations facilitate acute dendritic injury in the ischemic penumbra. J Neurosci 30: 9859-9868.

223. Phillips JM, Nicholson C (1979) Anion permeability in spreading depression investigated with ion-sensitive microelectrodes. Brain Res 173: 567-571.

224. Van Harrevald A, Khattab FI (1967) Electron microscopy of asphyxiated spinal cords of cats. J Neuropathol Exp Neurol 26: 521-536.

225. Van Harrevald A (1957) Changes in volume of cortical neuronal elements during asphyxiation. Am J Physiol 191: 233-242.

226. Jing J, Aitken PG, Somjen GG (1994) Interstitial volume changes during spreading depression (SD) and SD-like hypoxic depolarization in hippocampal tissue slices. J Neurophysiol 71: 2548-2551.

227. Muller M, Somjen GG (1999) Intrinsic optical signals in rat hippocampal slices during hypoxia-induced spreading depression-like depolarization. J Neurophysiol 82: 1818-1831.

228. Risher WC, Croom D, Kirov SA (2012) Persistent astroglial swelling accompanies rapid reversible dendritic injury during stroke-induced spreading depolarizations. Glia 60: 1709-1720.

229. Takano T, Tian GF, Peng W, Lou N, Lovatt D, Hansen AJ, Kasischke KA, Nedergaard M (2007) Cortical spreading depression causes and coincides with tissue hypoxia. Nat Neurosci 10: 754-762.

230. Murphy TH, Li P, Betts K, Liu R (2008) Two-photon imaging of stroke onset in vivo reveals that NMDA-receptor independent ischemic depolarization is the major cause of rapid reversible damage to dendrites and spines. J Neurosci 28: 1756-1772.

231. Kirov SA, Petrak LJ, Fiala JC, Harris KM (2004) Dendritic spines disappear with chilling but proliferate excessively upon rewarming of mature hippocampus. Neuroscience 127: 69-80.

232. Hoskison MM, Yanagawa Y, Obata K, Shuttleworth CW (2007) Calcium-dependent NMDA-induced dendritic injury and MAP2 loss in acute hippocampal slices. Neuroscience 145: 66-79.

233. Gisselsson LL, Matus A, Wieloch T (2005) Actin redistribution underlies the sparing effect of mild hypothermia on dendritic spine morphology after in vitro ischemia. J Cereb Blood Flow Metab 25: 1346-1355.

234. Hoskison MM, Shuttleworth CW (2006) Microtubule disruption, not calpain-dependent loss of MAP2, contributes to enduring NMDA-induced dendritic dysfunction in acute hippocampal slices. Exp Neurol 202: 302-312.

235. Sword J, Croom D, Wang PL, Thompson RJ, Kirov SA (2017) Neuronal pannexin-1 channels are not molecular routes of water influx during spreading depolarization-induced dendritic beading. J Cereb Blood Flow Metab 37: 1626-1633.

236. Van Harrevald A, Schade JP (1959) Chloride movements in cerebral cortex after circulatory arrest and during spreading depression. J Cell Comp Physiol 54: 65-84.

237. Muller M (2000) Effects of chloride transport inhibition and chloride substitution on neuron function and on hypoxic spreading-depression-like depolarization in rat hippocampal slices. Neuroscience 97: 33-45.

238. Kopito RR, Lee BS, Simmons DM, Lindsey AE, Morgans CW, Schneider K (1989) Regulation of intracellular pH by a neuronal homolog of the erythrocyte anion exchanger. Cell 59: 927-937.

239. Payne JA (1997) Functional characterization of the neuronal-specific K-Cl cotransporter: implications for [K+]o regulation. Am J Physiol 273: C1516-C1525.

240. Pierre K, Magistretti PJ, Pellerin L (2002) MCT2 is a major neuronal monocarboxylate transporter in the adult mouse brain. J Cereb Blood Flow Metab 22: 586-595.

241. Rungta RL, Choi HB, Tyson JR, Malik A, Dissing-Olesen L, Lin PJC, Cain SM, Cullis PR, Snutch TP, MacVicar BA (2015) The cellular mechanisms of neuronal swelling underlying cytotoxic edema. Cell 161: 610-621.

242. DePasquale M, Patlak CS, Cserr HF (1989) Brain ion and volume regulation during acute hypernatremia in Brattleboro rats. Am J Physiol 256: F1059-F1066.

243. Hochwald GM, Wald A, DiMattio J, Malhan C (1974) The effects of serum osmolarity on cerebrospinal fluid volume flow. Life Sci 15: 1309-1316.

244. Javaheri S, Wagner KR (1993) Bumetanide decreases canine cerebrospinal fluid production. In vivo evidence for NaCl cotransport in the central nervous system. J Clin Invest 92: 2257-2261.

245. Nilsson C, Stahlberg F, Thomsen C, Henriksen O, Herning M, Owman C (1992) Circadian variation in human cerebrospinal fluid production measured by magnetic resonance imaging. Am J Physiol 262: R20-R24.

246. Pollay M, Davson H (1963) The passage of certain substances out of the cerebrosphinal fluid. Brain 86: 137-150.

247. Pullen RG, DePasquale M, Cserr HF (1987) Bulk flow of cerebrospinal fluid into brain in response to acute hyperosmolality. Am J Physiol 253: F538-F545.

248. Rubin RC, Henderson ES, Ommaya AK, Walker MD, Rall DP (1966) The production of cerebrospinal fluid in man and its modification by acetazolamide. J Neurosurg 25: 430-436.

249. Segal MB, Pollay M (1977) The secretion of cerebrospinal fluid. Exp Eye Res 25 Suppl: 127-148.

250. Smith QR, Johanson CE (1980) Effect of carbonic anhydrase inhibitors and acidosis in choroid plexus epithelial cell sodium and potassium. J Pharmacol Exp Ther 215: 673-680.

251. Vogh BP, Langham MR, Jr. (1981) The effect of furosemide and bumetanide on cerebrospinal fluid formation. Brain Res 221: 171-183.

252. Wald A, Hochwald GM, Malhan C (1976) The effects of ventricular fluid osmolality on bulk flow of nascent fluid into the cerebral ventricles of cats. Exp Brain Res 25: 157-167.

253. Heisey SR, Held D, Pappenheimer JR (1962) Bulk flow and diffusion in the cerebrospinal fluid system of the goat. Am J Physiol 203: 775-781.

254. Pollay M (1975) Formation of cerebrospinal fluid. Relation of studies of isolated choroid plexus to the standing gradient hypothesis. J Neurosurg 42: 665-673.

255. Dandy WE (1919) Experimental hydrocephalus. Ann Surg 70: 129-142.

256. Davson H, Segal MB (1970) The effects of some inhibitors and accelerators of sodium transport on the turnover of 22Na in the cerebrospinal fluid and the brain. J Physiol 209: 131-153.

257. Pollay M, Hisey B, Reynolds E, Tomkins P, Stevens FA, Smith R (1985) Choroid plexus Na+/K+-activated adenosine triphosphatase and cerebrospinal fluid formation. Neurosurgery 17: 768-772.

258. Welch K (1963) Secretion of cerebrospinal fluid by choroid plecus of the rabbit. Am J Physiol 205: 617-624.

259. de Rougemont J, Ames A, III, Nesbett FB, Hofmann HF (1960) Fluid formed by choroid plexus; a technique for its collection and a comparison of its electrolyte composition with serum and cisternal fluids. J Neurophysiol 23: 485-495.

260. Smith QR, Johanson CE, Woodbury DM (1981) Uptake of 36Cl and 22Na by the brain-cerebrospinal fluid system: comparison of the permeability of the blood-brain and blood-cerebrospinal fluid barriers. J Neurochem 37: 117-124.

261. Smith QR, Rapoport SI (1986) Cerebrovascular permeability coefficients to sodium, potassium, and chloride. J Neurochem 46: 1732-1742.

262. Davson H (1955) A comparative study of the aqueous humour and cerebrospinal fluid in the rabbit. J Physiol 129: 111-133.

263. Ames A, III, Higashi K, Nesbett FB (1965) Effects of Pco2 acetazolamide and ouabain on volume and composition of choroid-plexus fluid. J Physiol 181: 516-524.

264. Vogh BP, Maren TH (1975) Sodium, chloride, and bicarbonate movement from plasma to cerebrospinal fluid in cats. Am J Physiol 228: 673-683.

265. Damkier HH, Brown PD, Praetorius J (2013) Cerebrospinal fluid secretion by the choroid plexus. Physiol Rev 93: 1847-1892.

266. Knuckey NW, Fowler AG, Johanson CE, Nashold JR, Epstein MH (1991) Cisterna magna microdialysis of 22Na to evaluate ion transport and cerebrospinal fluid dynamics. J Neurosurg 74: 965-971.

267. Pollay M, Curl F (1967) Secretion of cerebrospinal fluid by the ventricular ependyma of the rabbit. Am J Physiol 213: 1031-1038.

268. Bradbury MW, Kleeman CR (1969) The effect of chronic osmotic disturbance on the concentrations of cations in cerebrospinal fluid. J Physiol 204: 181-193.

269. Hendry EB (1962) The osmotic pressure and chemical composition of human body fluids. Clin Chem 8: 246-265.

270. Welch K, Sadler K, Gold G (1966) Volume flow across choroidal ependyma of the rabbit. Am J Physiol 210: 232-236.

271. Zeuthen T (1991) Water permeability of ventricular cell membrane in choroid plexus epithelium from Necturus maculosus. J Physiol 444: 133-151.

272. Curl FD, Pollay M (1968) Transport of water and electrolytes between brain and ventricular fluid in the rabbit. Exp Neurol 20: 558-574.

273. Hochwald GM, Wald A, Malhan C (1976) The sink action of cerebrospinal fluid volume flow. Effect on brain water content. Arch Neurol 33: 339-344.

274. Sahar A, Tsipstein E (1978) Effects of mannitol and furosemide on the rate of formation of cerebrospinal fluid. Exp Neurol 60: 584-591.

275. Damkier HH, Brown PD, Praetorius J (2010) Epithelial pathways in choroid plexus electrolyte transport. Physiology (Bethesda) 25: 239-249.

276. Praetorius J, Nielsen S (2006) Distribution of sodium transporters and aquaporin-1 in the human choroid plexus. Am J Physiol Cell Physiol 291: C59-C67.

277. Chretien S, Catron JP (1999) A single mutation inside the NPA motif of aquaporin-1 found in a Colton-null phenotype. Blood 93: 4021-4023.

278. Preston GM, Smith BL, Zeidel ML, Moulds JJ, Agre P (1994) Mutations in aquaporin-1 in phenotypically normal humans without functional CHIP water channels. Science 265: 1585-1587.

279. Ma T, Yang B, Gillespie A, Carlson EJ, Epstein CJ, Verkman AS (1998) Severely impaired urinary concentrating ability in transgenic mice lacking aquaporin-1 water channels. J Biol Chem 273: 4296-4299.

280. Quinton PM, Wright EM, Tormey JM (1973) Localization of sodium pumps in the choroid plexus epithelium. J Cell Biol 58: 724-730.

281. Bradbury MW, Kleeman CR (1967) Stability of the potassium content of cerebrospinal fluid and brain. Am J Physiol 213: 519-528.

282. Bradbury MW, Stulcova B (1970) Efflux mechanism contributing to the stability of the potassium concentration in cerebrospinal fluid. J Physiol 208: 415-430.

283. Smith QR, Johanson CE (1980) Effect of ouabain and potassium on ion concentrations in the choroidal epithelium. Am J Physiol 238: F399-F406.

284. Lun MP, Johnson MB, Broadbelt KG, Watanabe M, Kang YJ, Chau KF, Springel MW, Malesz A, Sousa AM, Pletikos M, Adelita T, Calicchio ML, Zhang Y, Holtzman MJ, Lidov HG, Sestan N, Steen H, Monuki ES, Lehtinen MK (2015) Spatially heterogeneous choroid plexus transcriptomes encode positional identity and contribute to regional CSF production. J Neurosci 35: 4903-4916.

285. Holloway LS, Jr., Cassin S (1972) Effect of acetazolamide and ouabain on CSF production rate in the newborn dog. Am J Physiol 223: 503-506.

286. Segal MB, Burgess AM (1974) A combined physiological and morphological study of the secretory process in the rabbit choroid plexus. J Cell Sci 14: 339-350.

287. Vates TS, Jr., Bonting SL, Oppelt WW (1964) NA-K activated adenosine thiphosphatase formation of cerebrospinal fluid in the cat. Am J Physiol 206: 1165-1172.

288. Bass NH, Fallstrom SP, Lundborg P (1979) Digoxin-induced arrest of the cerebrospinal fluid circulation in the infant rat: implications for medical treatment of hydrocephalus during early postnatal life. Pediatr Res 13: 26-30.

289. Deng QS, Johanson CE (1992) Cyclic AMP alteration of chloride transport into the choroid plexus-cerebrospinal fluid system. Neurosci Lett 143: 146-150.

290. Lindsey AE, Schneider K, Simmons DM, Baron R, Lee BS, Kopito RR (1990) Functional expression and subcellular localization of an anion exchanger cloned from choroid plexus. Proc Natl Acad Sci U S A 87: 5278-5282.

291. Praetorius J, Nejsum LN, Nielsen S (2004) A SCL4A10 gene product maps selectively to the basolateral plasma membrane of choroid plexus epithelial cells. Am J Physiol Cell Physiol 286: C601-C610.

292. Praetorius J, Damkier HH (2017) Transport across the choroid plexus epithelium. Am J Physiol Cell Physiol 312: C673-C686.

293. Bouzinova EV, Praetorius J, Virkki LV, Nielsen S, Boron WF, Aalkjaer C (2005) Na+-dependent HCO-3 uptake into the rat choroid plexus epithelium is partially DIDS sensitive. Am J Physiol Cell Physiol 289: C1448-C1456.

294. McAlear SD, Liu X, Williams JB, McNicholas-Bevensee CM, Bevensee MO (2006) Electrogenic Na/HCO3 cotransporter (NBCe1) variants expressed in Xenopus oocytes: functional comparison and roles of the amino and carboxy termini. J Gen Physiol 127: 639-658.

295. Deng QS, Johanson CE (1989) Stilbenes inhibit exchange of chloride between blood, choroid plexus and cerebrospinal fluid. Brain Res 501: 183-187.

296. Smith QR, Johanson CE (1985) Active transport of chloride by lateral ventricle choroid plexus of the rat. Am J Physiol 249: F470-F477.

297. Maren TH, Broder LE (1970) The role of carbonic anhydrase in anion secretion into cerebrospinal fluid. J Pharmacol Exp Ther 172: 197-202.

298. McCarthy KD, Reed DJ (1974) The effect of acetazolamide and furosemide on cerebrospinal fluid production and choroid plexus carbonic anhydrase activity. J Pharmacol Exp Ther 189: 194-201.

299. Melby JM, Miner LC, Reed DJ (1982) Effect of acetazolamide and furosemide on the production and composition of cerebrospinal fluid from the cat choroid plexus. Can J Physiol Pharmacol 60: 405-409.

300. Pollay M, Stevens A, Estrada E, Kaplan R (1972) Extracorporeal perfusion of choroid plexus. J Appl Physiol 32: 612-617.

301. Fishman RA (1959) Factors influencing the exchange of sodium between plasma and cerebrospinal fluid. J Clin Invest 38: 1698-1708.

302. Johanson CE, Murphy VA (1990) Acetazolamide and insulin alter choroid plexus epithelial cell [Na+], pH, and volume. Am J Physiol 258: F1538-F1546.

303. Murphy VA, Johanson CE (1989) Acidosis, acetazolamide, and amiloride: effects on 22Na transfer across the blood-brain and blood-CSF barriers. J Neurochem 52: 1058-1063.

304. Koch A, Woodbury DM (1960) Carbonic anhydrase inhibition and brain electrolyte composition. Am J Physiol 198: 434-440.

305. Macri FJ, Politoff A, Rubin R, Dixon R, Rall D (1966) Preferential vasoconstrictor properties of acetazolamide on the arteries of the choroid plexus. Int J Neuropharmacol 5: 109-115.

306. Carey ME, Vela AR (1974) Effect of systemic arterial hypotension on the rate of cerebrospinal fluid formation in dogs. J Neurosurg 41: 350-355.

307. Swenson ER (2014) New insights into carbonic anhydrase inhibition, vasodilation, and treatment of hypertensive-related diseases. Curr Hypertens Rep 16: 467.

308. Francois C, Deprez C (1971) Ion transport and oxidative metabolism. I. The inhibition of mitochondrial oxidative metabolism by the unsubstituted aromatic sulfonamides (carbonic anhydrase inhibitors). Arch Int Physiol Biochim 79: 993-1007.

309. Johanson CE (1984) Differential effects of acetazolamide, benzolamide and systemic acidosis on hydrogen and bicarbonate gradients across the apical and basolateral membranes of the choroid plexus. J Pharmacol Exp Ther 231: 502-511.

310. Smith QR, Johanson CE (1991) Chloride efflux from isolated choroid plexus. Brain Res 562: 306-310.

311. Osswald H, Hawlina A (1979) Effects of acetazolamide and changes of acid-base balance on the content of cyclic nucleotides in the rat kidney. Pharmacology 19: 44-50.

312. Jacobs S, Ruusuvuori E, Sipila ST, Haapanen A, Damkier HH, Kurth I, Hentschke M, Schweizer M, Rudhard Y, Laatikainen LM, Tyynela J, Praetorius J, Voipio J, Hubner CA (2008) Mice with targeted Slc4a10 gene disruption have small brain ventricles and show reduced neuronal excitability. Proc Natl Acad Sci U S A 105: 311-316.

313. Kao L, Kurtz LM, Shao X, Papadopoulos MC, Liu L, Bok D, Nusinowitz S, Chen B, Stella SL, Andre M, Weinreb J, Luong SS, Piri N, Kwong JM, Newman D, Kurtz I (2011) Severe neurologic impairment in mice with targeted disruption of the electrogenic sodium bicarbonate cotransporter NBCe2 (Slc4a5 gene). J Biol Chem 286: 32563-32574.

314. Damkier HH, Praetorius J (2012) Genetic ablation of Slc4a10 alters the expression pattern of transporters involved in solute movement in the mouse choroid plexus. Am J Physiol Cell Physiol 302: C1452-C1459.

315. Bairamian D, Johanson CE, Parmelee JT, Epstein MH (1991) Potassium cotransport with sodium and chloride in the choroid plexus. J Neurochem 56: 1623-1629.

316. Keep RF, Xiang J, Betz AL (1994) Potassium cotransport at the rat choroid plexus. Am J Physiol 267: C1616-C1622.

317. Kanaka C, Ohno K, Okabe A, Kuriyama K, Itoh T, Fukuda A, Sato K (2001) The differential expression patterns of messenger RNAs encoding K-Cl cotransporters (KCC1,2) and Na-K-2Cl cotransporter (NKCC1) in the rat nervous system. Neuroscience 104: 933-946.

318. Karadsheh MF, Byun N, Mount DB, Delpire E (2004) Localization of the KCC4 potassium-chloride cotransporter in the nervous system. Neuroscience 123: 381-391.

319. Pearson MM, Lu J, Mount DB, Delpire E (2001) Localization of the K(+)-Cl(-) cotransporter, KCC3, in the central and peripheral nervous systems: expression in the choroid plexus, large neurons and white matter tracts. Neuroscience 103: 481-491.

320. Ishikawa A, Kono K, Sakae R, Aiba T, Kawasaki H, Kurosaki Y (2010) Altered electrolyte handling of the choroid plexus in rats with glycerol-induced acute renal failure. Biopharm Drug Dispos 31: 455-463.

321. Miller TB, Wilkinson HA, Rosenfeld SA, Furuta T (1986) Intracranial hypertension and cerebrospinal fluid production in dogs: effects of furosemide. Exp Neurol 94: 66-80.

322. Vogh BP, Doyle AS (1981) The effect of carbonic anhydrase inhibitors and other drugs on sodium entry to cerebrospinal fluid. J Pharmacol Exp Ther 217: 51-56.

323. Johnson DC, Singer S, Hoop B, Kazemi H (1987) Chloride flux from blood to CSF: inhibition by furosemide and bumetanide. J Appl Physiol (1985) 63: 1591-1600.

324. Haas M, Forbush B, III (2000) The Na-K-Cl cotransporter of secretory epithelia. Annu Rev Physiol 62: 515-534.

325. Johanson CE, Reed DJ, Woodbury DM (1974) Active transport of sodium and potassium by the choroid plexus of the rat. J Physiol 241: 359-372.

326. Murphy VA, Johanson CE (1990) Na(+)-H+ exchange in choroid plexus and CSF in acute metabolic acidosis or alkalosis. Am J Physiol 258: F1528-F1537.

327. Milhorat TH (1969) Choroid plexus and cerebrospinal fluid production. Science 166: 1514-1516.

328. Milhorat TH, Hammock MK, Fenstermacher JD, Levin VA (1971) Cerebrospinal fluid production by the choroid plexus and brain. Science 173: 330-332.

329. Mokgokong R, Wang S, Taylor CJ, Barrand MA, Hladky SB (2014) Ion transporters in brain endothelial cells that contribute to formation of brain interstitial fluid. Pflugers Arch 466: 887-901.

330. Oreskovic D, Klarica M (2010) The formation of cerebrospinal fluid: nearly a hundred years of interpretations and misinterpretations. Brain Res Rev 64: 241-262.

331. Rooney WD, Li X, Sammi MK, Bourdette DN, Neuwelt EA, Springer CS, Jr. (2015) Mapping human brain capillary water lifetime: high-resolution metabolic neuroimaging. NMR Biomed 28: 607-623.

332. Betz AL, Goldstein GW (1986) Specialized properties and solute transport in brain capillaries. Annu Rev Physiol 48: 241-250.

333. Butt AM, Jones HC, Abbott NJ (1990) Electrical resistance across the blood-brain barrier in anaesthetized rats: a developmental study. J Physiol 429: 47-62.

334. Crone C, Olesen SP (1982) Electrical resistance of brain microvascular endothelium. Brain Res 241: 49-55.

335. Reese TS, Karnovsky MJ (1967) Fine structural localization of a blood-brain barrier to exogenous peroxidase. J Cell Biol 34: 207-217.

336. Smith QR, Rapoport SI (1984) Carrier-mediated transport of chloride across the blood-brain barrier. J Neurochem 42: 754-763.

337. Cornford EM, Hyman S (2005) Localization of brain endothelial luminal and abluminal transporters with immunogold electron microscopy. NeuroRx 2: 27-43.

338. Nicola PA, Taylor CJ, Wang S, Barrand MA, Hladky SB (2008) Transport activities involved in intracellular pH recovery following acid and alkali challenges in rat brain microvascular endothelial cells. Pflugers Arch 456: 801-812.

339. Shawahna R, Uchida Y, Decleves X, Ohtsuki S, Yousif S, Dauchy S, Jacob A, Chassoux F, Daumas-Duport C, Couraud PO, Terasaki T, Scherrmann JM (2011) Transcriptomic and quantitative proteomic analysis of transporters and drug metabolizing enzymes in freshly isolated human brain microvessels. Mol Pharm 8: 1332-1341.

340. Betz AL, Firth JA, Goldstein GW (1980) Polarity of the blood-brain barrier: distribution of enzymes between the luminal and antiluminal membranes of brain capillary endothelial cells. Brain Res 192: 17-28.

341. Kato S, Nakamura H (1989) Ultrastructural and ultracytochemical studies on the blood-brain barrier in chronic relapsing experimental allergic encephalomyelitis. Acta Neuropathol 77: 455-464.

342.* Lykke K, Assentoft M, Horlyck S, Helms HC, Stoica A, Toft-Bertelsen TL, Tritsaris K, Vilhardt F, Brodin B, MacAulay N (2017) Evaluating the involvement of cerebral microvascular endothelial Na+/K+-ATPase and Na+-K+-2Cl- co-transporter in electrolyte fluxes in an in vitro blood-brain barrier model of dehydration. J Cereb Blood Flow Metab, Epub ahead of publication, 10.1177/0271678X17736715 [doi].

343. Vorbrodt AW, Trowbridge RS (1991) Ultracytochemical characteristics of cultured goat brain microvascular endothelial cells [corrected]. J Histochem Cytochem 39: 1555-1563.

344. Goldstein GW (1979) Relation of potassium transport to oxidative metabolism in isolated brain capillaries. J Physiol 286: 185-195.

345. Jewell EA, Lingrel JB (1991) Comparison of the substrate dependence properties of the rat Na,K-ATPase alpha 1, alpha 2, and alpha 3 isoforms expressed in HeLa cells. J Biol Chem 266: 16925-16930.

346. Bradbury MW (1970) The effect of rubidium on the distribution and movement of potassium between blood, brain and cerebrospinal fluid in the rabbit. Brain Res 24: 311-321.

347. Katzman R (1976) Maintenance of a constant brain extracellular potassium. Fed Proc 35: 1244-1247.

348. Lin JD (1985) Potassium transport in isolated cerebral microvessels from the rat. Jpn J Physiol 35: 817-830.

349. Schielke GP, Moises HC, Betz AL (1990) Potassium activation of the Na,K-pump in isolated brain microvessels and synaptosomes. Brain Res 524: 291-296.

350. Al Feteisi H, Al-Majdoub ZM, Achour B, Couto N, Rostami-Hodjegan A, Barber J (2018) Identification and quantification of blood-brain barrier transporters in isolated rat brain microvessels. J Neurochem 146: 670-685.

351. Kubo Y, Ohtsuki S, Uchida Y, Terasaki T (2015) Quantitative Determination of Luminal and Abluminal Membrane Distributions of Transporters in Porcine Brain Capillaries by Plasma Membrane Fractionation and Quantitative Targeted Proteomics. J Pharm Sci 104: 3060-3068.

352. O'Donnell ME, Tran L, Lam TI, Liu XB, Anderson SE (2004) Bumetanide inhibition of the blood-brain barrier Na-K-Cl cotransporter reduces edema formation in the rat middle cerebral artery occlusion model of stroke. J Cereb Blood Flow Metab 24: 1046-1056.

353. Sun D, Lytle C, O'Donnell ME (1995) Astroglial cell-induced expression of Na-K-Cl cotransporter in brain microvascular endothelial cells. Am J Physiol 269: C1506-C1512.

354. Abbruscato TJ, Lopez SP, Roder K, Paulson JR (2004) Regulation of blood-brain barrier Na,K,2Cl-cotransporter through phosphorylation during in vitro stroke conditions and nicotine exposure. J Pharmacol Exp Ther 310: 459-468.

355. Betz AL (1983) Sodium transport from blood to brain: inhibition by furosemide and amiloride. J Neurochem 41: 1158-1164.

356. Lane JR, Wigham CG, Hodson SA (1997) Determination of Na+/Cl-, Na+/HCO3- and Na+/K+/2Cl- co-transporter activity in corneal endothelial cell plasma membrane vesicles. Biochim Biophys Acta 1328: 237-242.

357.* Oernbo EK, Lykke K, Steffensen AB, Tollner K, Kruuse C, Rath MF, Loscher W, MacAulay N (2018) Cerebral influx of Na(+) and Cl(-) as the osmotherapy-mediated rebound response in rats. Fluids Barriers CNS 15: 27.

358. Betz AL, Keep RF, Beer ME, Ren XD (1994) Blood-brain barrier permeability and brain concentration of sodium, potassium, and chloride during focal ischemia. J Cereb Blood Flow Metab 14: 29-37.

359. Schielke GP, Moises HC, Betz AL (1991) Blood to brain sodium transport and interstitial fluid potassium concentration during early focal ischemia in the rat. J Cereb Blood Flow Metab 11: 466-471.

360. Betz AL, Ennis SR, Schielke GP, Hoff JT (1990) Blood-to-brain sodium transport in ischemic brain edema. Adv Neurol 52: 73-80.

361. Cserr HF, DePasquale M, Patlak CS (1987) Regulation of brain water and electrolytes during acute hyperosmolality in rats. Am J Physiol 253: F522-F529.

362. Melton JE, Patlak CS, Pettigrew KD, Cserr HF (1987) Volume regulatory loss of Na, Cl, and K from rat brain during acute hyponatremia. Am J Physiol 252: F661-F669.

363. Wasterlain CG, Posner JB (1968) Cerebral edema in water intoxication. I. Clinical and chemical observations. Arch Neurol 19: 71-78.

364. Rymer MM, FISHMAN RA (1973) Protective adaptation of brain to water intoxication. Arch Neurol 28: 49-54.

365. Cserr HF, DePasquale M, Nicholson C, Patlak CS, Pettigrew KD, Rice ME (1991) Extracellular volume decreases while cell volume is maintained by ion uptake in rat brain during acute hypernatremia. J Physiol 442: 277-295.

366. Wald A, Hochwald GM, Malhan C (1975) The relationship between sodium influx and volume flow into the cerebral ventricles of cats. J Neurochem 25: 151-154.

367. Alessi DR, Zhang J, Khanna A, Hochdorfer T, Shang Y, Kahle KT (2014) The WNK-SPAK/OSR1 pathway: master regulator of cation-chloride cotransporters. Sci Signal 7.

368. Gagnon KB, England R, Delpire E (2006) Characterization of SPAK and OSR1, regulatory kinases of the Na-K-2Cl cotransporter. Mol Cell Biol 26: 689-698.

369. Vigne P, Lopez FA, Frelin C (1994) Na(+)-K(+)-Cl- cotransporter of brain capillary endothelial cells. Properties and regulation by endothelins, hyperosmolar solutions, calyculin A, and interleukin-1. J Biol Chem 269: 19925-19930.

370. Barreca T, Gandolfo C, Corsini G, Del SM, Cataldi A, Rolandi E, Franceschini R (2001) Evaluation of the secretory pattern of plasma arginine vasopressin in stroke patients. Cerebrovasc Dis 11: 113-118.

371. Miura M, Takagi S, Matsukado Y, Ushio Y (1989) Influence of vasopressin level on osmotic pressure and sodium concentration in plasma and cerebrospinal fluid in patients with intracranial lesions. Neurol Med Chir (Tokyo) 29: 806-810.

372. Demotes-Mainard J, Chauveau J, Rodriguez F, Vincent JD, Poulain DA (1986) Septal release of vasopressin in response to osmotic, hypovolemic and electrical stimulation in rats. Brain Res 381: 314-321.

373. Liu X, Nakayama S, Amiry-Moghaddam M, Ottersen OP, Bhardwaj A (2010) Arginine-vasopressin V1 but not V2 receptor antagonism modulates infarct volume, brain water content, and aquaporin-4 expression following experimental stroke. Neurocrit Care 12: 124-131.

374. Liu XF, Shi YM, Lin BC (1991) Mechanism of action of arginine vasopressin on acute ischemic brain edema. Chin Med J (Engl) 104: 480-483.

375. Rosenberg GA, Kyner WT, Fenstermacher JD, Patlak CS (1986) Effect of vasopressin on ependymal and capillary permeability to tritiated water in cat. Am J Physiol 251: F485-F489.

376. Rosenberg GA, Estrada E, Kyner WT (1990) Vasopressin-induced brain edema is mediated by the V1 receptor. Adv Neurol 52: 149-154.

377. Kleindienst A, Dunbar JG, Glisson R, Marmarou A (2013) The role of vasopressin V1A receptors in cytotoxic brain edema formation following brain injury. Acta Neurochir (Wien) 155: 151-164.

378. O'Donnell ME, Duong V, Suvatne J, Foroutan S, Johnson DM (2005) Arginine vasopressin stimulation of cerebral microvascular endothelial cell Na-K-Cl cotransporter activity is V1 receptor and [Ca] dependent. Am J Physiol Cell Physiol 289: C283-C292.

379. Smith QR, Momma S, Aoyagi M, Rapoport SI (1987) Kinetics of neutral amino acid transport across the blood-brain barrier. J Neurochem 49: 1651-1658.

380. Smith QR (2000) Transport of glutamate and other amino acids at the blood-brain barrier. J Nutr 130: 1016S-1022S.

381. Ohtsuki S (2004) New aspects of the blood-brain barrier transporters; its physiological roles in the central nervous system. Biol Pharm Bull 27: 1489-1496.

382. Kretzschmar R, Landgraf R, Gjedde A, Ermisch A (1986) Vasopressin binds to microvessels from rat hippocampus. Brain Res 380: 325-330.

383. Szmydynger-Chodobska J, Chung I, Kozniewska E, Tran B, Harrington FJ, Duncan JA, Chodobski A (2004) Increased expression of vasopressin v1a receptors after traumatic brain injury. J Neurotrauma 21: 1090-1102.

384. Foroutan S, Brillault J, Forbush B, O'Donnell ME (2005) Moderate-to-severe ischemic conditions increase activity and phosphorylation of the cerebral microvascular endothelial cell Na+-K+-Cl- cotransporter. Am J Physiol Cell Physiol 289: C1492-C1501.

385. Lund-Andersen H (1979) Transport of glucose from blood to brain. Physiol Rev 59: 305-352.

386. Zeuthen T, Zeuthen E, MacAulay N (2007) Water transport by GLUT2 expressed in Xenopus laevis oocytes. J Physiol 579: 345-361.

387. Simpson IA, Carruthers A, Vannucci SJ (2007) Supply and demand in cerebral energy metabolism: the role of nutrient transporters. J Cereb Blood Flow Metab 27: 1766-1791.

388. Helms HCC, Nielsen CU, Waagepetersen HS, Brodin B (2017) Glutamate Transporters in the Blood-Brain Barrier. Adv Neurobiol 16: 297-314.

APPENDIX

Articles included in the thesis:

- **Nanna MacAulay**, Thomas Zeuthen & Ulrik Gether (2002) Conformational Basis for the Li^+-Induced Leak Current in the rat g-Aminobutyric Acid (GABA) Transporter-1. *Journal of Physiology 544, 447-458*
- Robert A. Fenton, Hanne B. Moeller, Marina Zelenina, Marteinn T. Snaebjornsson, Torgeir Holen & **Nanna MacAulay** (2010) Differential water permeability and regulation of three AQP4 isoforms. *Cellular and Molecular Life Sciences. 67:829-840*
- Mette Assentoft, Shreyas Kaptan, Robert A. Fenton, Susan Z. Hua, Bert L. de Groot & **Nanna MacAulay** (2013) Phosphorylation of rat aquaporin-4 at Ser^{111} is not required for channel gating. *GLIA 61: 1101-1112*
- Brian Roland Larsen, Mette Assentoft, Maria L. Cotrina, Susan Z. Hua, Maiken Nedergaard, Kai Kaila, Juha Voipio & **Nanna MacAulay** (2014) Contributions of the Na^+/K^+-ATPase, NKCC1, and Kir4.1 to hippocampal K^+-clearance and volume responses. *GLIA 62:608-622*
- Annette B. Steffensen, Jeremy Sword, Deborah Croom, Sergei A. Kirov & **Nanna MacAulay** (2015) Cotransporters as a molecular mechanism underlying spreading depolarization-induced dendritic beading. *Journal of Neuroscience 35:12172-12187*
- Mette Assentoft, Shreyas Kaptan, Hans-Peter Schneider, Joachim W. Deitmer, Bert L. de Groot & **Nanna MacAulay** (2016) Aquaporin 4 as a NH_3 channel. *Journal of Biological Chemistry 291:19184-19195*
- Brian Roland Larsen & **Nanna MacAulay** (2017) Activity-dependent astrocyte swelling is mediated by pH-regulating mechanisms. *GLIA 65:1668-1681*
- Kasper Lykke, Mette Assentoft, Sofie Hørlyck, Hans Christian C. Helms, Anca Stoica, Trine L. Toft-Bertelsen, Katerina Tritsaris, Frederik Vilhardt, Birger Brodin & **Nanna MacAulay** (2017) Evaluating the involvement of cerebralmicrovascular endothelial Na^+/K^+-ATPase and Na^+-K^+-$2Cl^-$ co-transporter (NKCC1) in electrolyte fluxes in an *in vitro*BBB model of dehydration. *Journal of Cerebral Blood Flow and Metabolism, Epub ahead of print.*
- Annette B. Steffensen, Eva K. Oernbo, Anca Stoica, Niklas J. Gerkau, Dagne Barbuskaite, Katerina Tritsaris, Christine R. Rose & **Nanna MacAulay** (2018) Cotransporter-mediated water transport underlying cerebrospinal fluid formation. *Nature Communications 9:2167*
- Eva Kjer Oernbo, Kasper Lykke, Annette B. Steffensen, Kathrin Töllner, Christina Kruuse, Martin Fredensborg Rath, Wolfgang Löscher & **Nanna MacAulay** (2018) Cerebral influx of Na^+ and Cl^- as the osmotherapy-mediated rebound response in rats. *Fluids and Barriers in the CNS 15:27*
- Brian Roland Larsen, Anca Stoica, **Nanna MacAulay** (2018) Developmental maturation of activity-induced K^+ and pH transients and the associated extracellular space dynamics in the rat hippocampus. *Journal of Physiology, Epub ahead of print*

Journal of Physiology (2002), **544.2**, *pp.* 447–458
DOI: 10.1113/jphysiol.2002.022897

www.jphysiol.org

Conformational basis for the Li^+-induced leak current in the rat γ-aminobutyric acid (GABA) transporter-1

Nanna MacAulay, Thomas Zeuthen * and Ulrik Gether *†

Department of Medical Physiology and † Department of Pharmacology, The Panum Institute, University of Copenhagen, DK-2200 Copenhagen N, Denmark

The rat γ-aminobutyric acid transporter-1 (GAT-1) was expressed in *Xenopus laevis* oocytes and the substrate-independent Li^+-induced leak current was examined using two-electrode voltage clamp. The leak current was not affected by the addition of GABA and was not due to H^+ permeation. The Li^+-bound conformation of the protein displayed a lower passive water permeability than that of the Na^+- and choline (Ch^+)-bound conformations and the leak current did not saturate with increasing amounts of Li^+ in the test solution. The mechanism that gives rise to the leak current did not support active water transport in contrast to the mechanism responsible for GABA translocation (~330 water molecules per charge). Altogether, these data support the distinct nature of the leak conductance in relation to the substrate translocation process. It was observed that the leak current was inhibited by low millimolar concentrations of Na^+ (the apparent affinity constant, $K'_{0.5}$ = 3 mM). In addition, it was found that the GABA transport current was sustained at correspondingly low Na^+ concentrations if Li^+ was present instead of choline. This is consistent with a model in which Li^+ can bind and substitute for Na^+ at the putative 'first' apparently low-affinity Na^+ binding site. In the absence of Na^+, this allows a Li^+-permeable channel to open at hyperpolarized potentials. Occupancy of the 'second' apparently high-affinity Na^+ binding site by addition of low millimolar concentrations of Na^+ restrains the transporter from moving into a leak conductance mode as well as allowing maintenance of GABA-elicited transport-associated current.

(Received 19 April 2002; accepted after revision 13 August 2002; first published online 30 August 2002)
Corresponding author N. MacAulay: Division of Cellular and Molecular Physiology, Department of Medical Physiology 12.5, The Panum Institute, University of Copenhagen, DK-2200 Copenhagen N, Denmark. Email: nmacaulay@mfi.ku.dk

The major role of the γ-aminobutyric acid (GABA) transporters is termination of the synaptic response by re-uptake of GABA released into the synaptic cleft during neuronal activity. Four different GABA transporter subtypes have been described (GAT-1, GAT-2, GAT-3 and the betaine–GABA transporter-1 (BGT-1)), which are characterized by distinct localization patterns in the mammalian body and central nervous system (for review see Borden, 1996). GAT-1 was the first cloned member of the family of Na^+–Cl^- neurotransmitter transporters (Guastella *et al.* 1990). The uptake process is driven by the transmembrane Na^+ gradient with the co-transport of two Na^+ and one Cl^- ions, thereby rendering the translocation electrogenic (Radian & Kanner, 1983; Keynan & Kanner, 1988). Many electrophysiological studies of heterologously expressed GAT-1, both in mammalian cell lines and in *Xenopus laevis* oocytes, have been carried out and four current-generating modes of the transporter have been described: the Na^+-coupled GABA transport, the leak current, the capacitive Na^+-dependent transient currents, and a not fully documented uncoupled substrate-induced channel activity (Kavanaugh *et al.* 1992; Mager *et al.* 1993, 1996; Cammack *et al.* 1994; Cammack & Schwartz, 1996; Risso *et al.* 1996; Bismuth *et al.* 1997; Lu & Hilgemann, 1999; Forlani *et al.* 2001; MacAulay *et al.* 2001*a*).

The GABA transporter and several related transporters sustain an inward uncoupled leak current in the absence of their substrates. The cationic permeability differs for the different family members, with Li^+, and to a smaller extent Cs^+, being the only ions found to permeate through GAT-1 (Mager *et al.* 1996; Bismuth *et al.* 1997; MacAulay *et al.* 2001*a*). The dopamine and serotonin transporters (DAT and SERT) are less restrictive, allowing permeation of Na^+, K^+, Li^+ and possibly H^+ (Mager *et al.* 1994; Cao *et al.* 1997; Sonders *et al.* 1997). The molecular mechanism underlying the leak currents remains poorly understood. It has been suggested that the leak current in the neurotransmitter transporters is a channel-mode conductance (Cammack & Schwartz, 1996; Lin *et al.* 1996) and that it might (Sonders & Amara, 1996; Petersen & DeFelice, 1999;) or might not (Mager *et al.* 1994) share a common permation pathway

* These authors contributed equally to this work.

with the substrate. In contrast, the Na^+ leak current in the functionally related Na^+-coupled glucose transporter (SGLT) was suggested to involve the same pathway as and a similar mechanism to the Na^+-coupled glucose transporter (Loo *et al.* 1999).

Recently, we have structurally and functionally probed the GAT-1 by introducing engineered Zn^{2+} binding sites in the transporter molecule. Intriguingly, we observed that although Zn^{2+} binding at one site resulted in strong inhibition of both GABA translocation and the Li^+-induced leak conductance, Zn^{2+} binding to a closely related site only blocked translocation without any effect on the leak current (MacAulay *et al.* 2001*a*). It was therefore suggested that the leak current represents a unique operational mode of the transporter involving conformational changes and/or states different from those of the substrate translocation process. In the present paper, we have obtained additional new insight into the molecular basis of the leak current of the GABA transporter. We have used the *Xenopus laevis* expression system and two-electrode voltage clamp to assess the transporter-mediated currents and volume measurements to monitor the water transport properties of the GAT-1. Most significantly, we observe that the mechanism underlying the leak current is distinct from that underlying the GABA-induced current and that the leak current is inhibited by low millimolar concentrations of Na^+ ($K'_{0.5}$ = 3 mM). In addition, we find that transport is sustained at correspondingly low Na^+ concentrations if Li^+ is present instead of choline. The data suggest that Li^+ can replace Na^+ at the putative 'first' apparently low-affinity Na^+ binding site while Na^+ occupancy of the putative 'second' apparently high-affinity Na^+ binding site is sufficient to restrain the transporter from moving into a leak conductance mode.

METHODS

Molecular biology and oocytes

The rGAT-1 construct was cloned into a vector optimized for oocyte expression (pNB1) as earlier described (MacAulay *et al.* 2001*a*). The cDNA was linearized downstream of the poly-A segment and *in vitro* transcribed with the T7 RNA polymerase using the mCAP mRNA capping kit (Stratagene, La Jolla, CA, USA) and 50 ng cRNA was injected into defolliculated *Xenopus laevis* oocytes (MacAulay *et al.* 2001*a*). *Xenopus* oocytes were collected under anaesthesia (Tricain, 2 g l^{-1}) and the frogs were observed for a period of 3 h after the operation. After the final collection the frogs were humanely killed by decapitation. The surgical procedures complied with Danish legislation and were approved by the controlling body under the Ministry of Justice. The oocytes were incubated in Kulori medium (90 mM NaCl, 1 mM KCl, 1 mM $CaCl_2$, 1 mM $MgCl_2$, 5 mM Hepes, pH 7.4) at 19 °C for 3–7 days before experiments were performed.

[^{3}H]GABA uptake experiments in oocytes

The uptake experiments were performed in 24-well plates with 100 μM GABA and 50 nM [^{3}H]GABA (4-amino-*n*-[2, 3-^{3}H]butyric acid, 81 Ci $mmol^{-1}$, Amersham, Little Chalfont, UK) added to a total of 400 μl test solution (0–100 mM NaCl, 2 mM KCl, 1 mM $CaCl_2$, 1 mM $MgCl_2$, 10 mM Hepes, pH 7.4, NaCl substituted with equimolar LiCl or ChCl). Oocytes were incubated for 30 min at room temperature, washed 3 times in 1 ml test solution with 100 mM ChCl (100 mM ChCl, 2 mM KCl, 1 mM $CaCl_2$, 1 mM $MgCl_2$, 10 mM Hepes, pH 7.4), and dissolved in 200 μl 10 % SDS. Before counting, 2.0 ml scintillation fluid were added to the samples.

Electrophysiology

The oocytes were impaled by two microelectrodes in recording solution containing 100 mM NaCl, 2 mM KCl, 1 mM $CaCl_2$, 1 mM $MgCl_2$ and 10 mM Hepes (pH 7.4). In substitution experiments, sodium ions were replaced by equimolar lithium or choline ions. The data presented are subtractive currents, i.e. ($I_{Na+GABA} - I_{Na}$) or ($I_{Li} - I_{Ch}$). Two-electrode voltage clamp recordings were performed at room temperature with a Dagan clampator interfaced to an IBM-compatible PC using a DigiData 1200 A/D converter and pCLAMP 6.0 (Axon Instruments). Electrodes were pulled from borosilicate glass capillaries to a resistance of 0.5–2 MΩ and were filled with 1 M KCl.

Volume measurements

The volume measurements have previously been described in detail (Zeuthen *et al.* 1997; Meinild *et al.* 1998). The impaled oocyte was observed from below via a low magnification objective and a charge-coupled device camera. To achieve a high stability of the oocyte image, the upper surface of the bathing solution was determined by the flat end of a perspex rod, which also provided an illuminated background. Images were captured directly from the camera to the random access memory of a computer. The oocyte was focused at the circumference and assumed to be spherical. The volume was recorded and calculated on-line at a rate of one point per second with an accuracy of 3 in 10 000. The osmotic water permeability, L_p, was calculated per true membrane surface area (Loo *et al.* 1996), which is about 9 times the apparent area due to membrane foldings (Zampighi *et al.* 1995). The data were corrected for the batch-specific L_p of the native oocytes. L_p values are given in units of cm s^{-1} (osmol l^{-1})$^{-1}$ and were equal to $J_{H_2O}/A\,\Delta\pi$, where J_{H_2O} is the water flux, A is the surface area of the oocyte, and $\Delta\pi$ is the osmotic difference. The coupling ratio of the GAT-1 is taken as the number of water molecules cotransported per unit charge by the protein during GABA transport. Accordingly, the coupling ratio equals $F\,J_{H_2O}\,(V_w\,I_s)^{-1}$, where J_{H_2O} is the water flux, V_w is the partial molal volume of water (18 cm^3 mol^{-1}), I_s is the clamp current induced by application of GABA, and F is Faraday's constant. The coupling ratio was calculated by linear regression of the data from each oocyte and the average of these numbers is stated in the text.

Calculations

The data were analysed by linear and non-linear regression analysis using Prism 3.0 from GraphPad Software (San Diego, CA, USA). All numbers are given as means ± S.E.M. with n equal to the number of oocytes tested unless otherwise stated.

RESULTS

Current–voltage relationship

Addition of 100 μM GABA to GAT-1-expressing *Xenopus laevis* oocytes under voltage clamp (−50 mV) yielded currents in the range 100–350 nA. The GABA transport is strictly dependent on Na^+ as the cotransported cation

(Radian & Kanner, 1983; Keynan & Kanner, 1988) but in the absence of GABA and Na^+, addition of Li^+ generates a large inward current (Fig. 1 and Mager *et al.* 1996; Bismuth *et al.* 1997). As seen in Fig. 1, the *I–V* relationship of the GABA-induced current was distinct from that of the Li^+-induced leak current, which showed stronger inward rectification and occurred only at membrane potentials more negative than ~ −75 mV. At membrane potentials more negative than ~ −135 mV the leak current was larger than the GABA-induced current. The addition of GABA had no effect on the Li^+ current (Fig. 1). No Na^+ leak current was apparent in the GAT-1-expressing oocytes, as reported earlier (Mager *et al.* 1993; Loo *et al.* 1999; MacAulay *et al.* 2001*a*) and non-injected oocytes supported no Na^+/Li^+ leak current (data not shown and Fig. 1). The specific inhibitor of GAT-1, SKF89976A (50 μM), partly inhibited the Li^+-induced leak current of GAT-1 (about 50 %) and 100 μM Zn^{2+} inhibited the leak current of a Zn^{2+}-sensitive mutant of GAT-1 to the same extent (MacAulay *et al.* 2001*a*).

pH dependence

The Li^+-bound conformation of GAT-1 may support Li^+ flux and/or it may allow permeation of other ions, such as H^+. The *I–V* relationship of the leak current was not affected by changes in the pH of the LiCl solution (data not shown). At a clamp potential of –160 mV the leak current obtained at pH 6.5 was 103 ± 6 % of the current obtained in control solution at pH 7.5. At pH 8.5 the leak current was 116 ± 12 % of control (n = 6). These data suggest that H^+ is not the major permeant ion in a Li^+ test solution. It has not been possible to determine if Li^+ carries all the current, as the leak current does not reverse at the tested clamp potentials.

Activation energy and saturation profile

The leak currents of the neurotransmitter transporters have been suggested to be a channel mode of conductance (Cammack & Schwartz, 1996; Lin *et al.* 1996) as opposed to that of the SGLT in which a transporter mode has been proposed (Loo *et al.* 1999). In an attempt to obtain more information about the mechanism by which Li^+ permeates through the transporter, we measured the Arrhenius activation energy (E_a) of the transport processes. The E_a values were determined from the slope of the Arrhenius plot (Fig. 2). The E_a value of the leak current (obtained in the range 15–27 °C) was 26 ± 1 kcal mol^{-1} at –80 mV (109 ± 4 kJ mol^{-1}; n = 4), which is not statistically different from that of the GABA-induced current, 23 ± 2 kcal mol^{-1} at –50 mV (96 ± 8 kJ mol^{-1}; n = 5).

We tested for saturation of the leak current at increasing concentrations of Li^+ at different clamp potentials (data not shown). At the most negative clamp potential (−160 mV) there was a barely detectable saturation of the current, whereas the current was a linear function of the Li^+ concentration at less negative potentials.

Water permeability measurements

The existence of a passive water permeability (L_p) through the transporter has been demonstrated previously for the

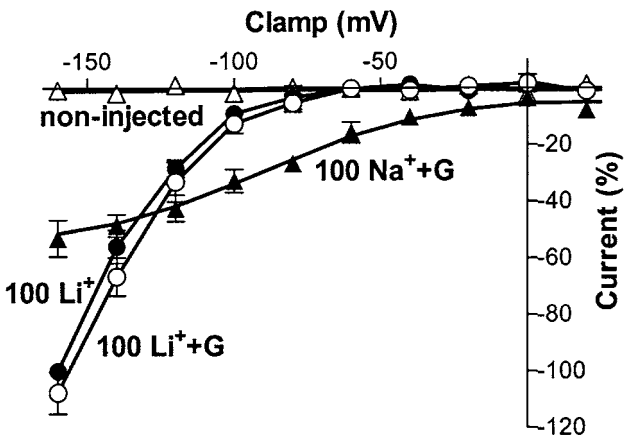

Figure 1. Li^+-induced leak current *versus* GABA-induced current

Non-injected and GAT-1-expressing oocytes were clamped to a holding potential of –50 mV before the membrane potential was jumped to the test potential for 300 ms (from +40 to –160 mV with intervals of 20 mV). Data are presented as a percentage of the Li^+-induced leak current obtained in the GAT-1-expressing oocytes with 100 mM LiCl at –160 mV and have been averaged for 5 oocytes. ▲, GABA-induced current ($I_{Na+GABA} - I_{Na}$); ●, the leak current ($I_{Li} - I_{Ch}$); ○, the leak current in the presence of 100 μM GABA ($I_{Li+GABA} - I_{Ch}$); and △, the Li^+-induced leak current in a non-injected oocyte.

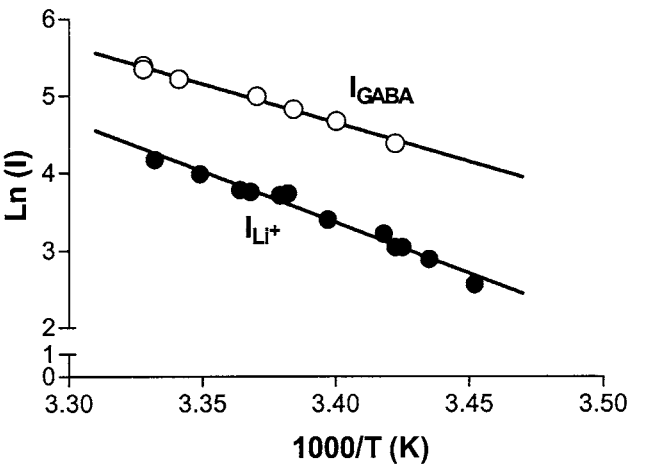

Figure 2. Arrhenius activation energy of the leak current and the GABA-induced current

For the GABA-induced current, GAT-1-expressing oocytes were clamped to a holding potential of –50 mV in Na^+ solution and 100 μM GABA was added to the test solution at different bath temperatures (I_{GABA}). For the leak current, the oocytes were clamped to –80 mV in Ch^+ solution which was replaced with the Li^+ solution to obtain the leak current (I_{Li}) at the different bath temperatures. Data are presented as Ln of the current obtained by either GABA or Li^+ as a function of temperature (K). The present experiment is a representative example of 4.

GAT-1 as well as for several other Na^+-coupled transporters (Zeuthen, 1991; Zeuthen *et al.* 1996; Loike *et al.* 1996; Loo *et al.* 1996, 1999; Meinild *et al.* 2000; MacAulay *et al.* 2001*b*). Since an alteration of this permeability reflects a change in transporter conformation, we compared the L_p value in the presence of Na^+, Li^+ or Ch^+. The water permeability measurements were performed in the two-electrode voltage clamp set-up with simultaneous monitoring of the oocyte from beneath with a sensitive camera, which gives an accurate read-out of the volume of the oocyte (Zeuthen *et al.* 1997; Meinild *et al.* 1998). Application of a hyperosmotic gradient in the surrounding test solution (which contained Na^+, Li^+ or Ch^+, but no GABA) caused the oocyte to shrink as water osmotically escaped the cytoplasm of the oocyte (Fig. 3*A*; see Methods for the calculation of the L_p). In agreement with earlier studies (Loo *et al.* 1999), we observed in GAT-1 an inherent passive water permeability (L_p) as reflected by the ability of the GAT-1-expressing oocyte to shrink at a higher rate than the non-injected oocyte. Subtraction of the contribution from the non-injected oocyte membrane ($2.19 \pm 0.23 \times 10^{-6}$ cm s^{-1} (osmol l^{-1})$^{-1}$, $n = 4$) allowed for

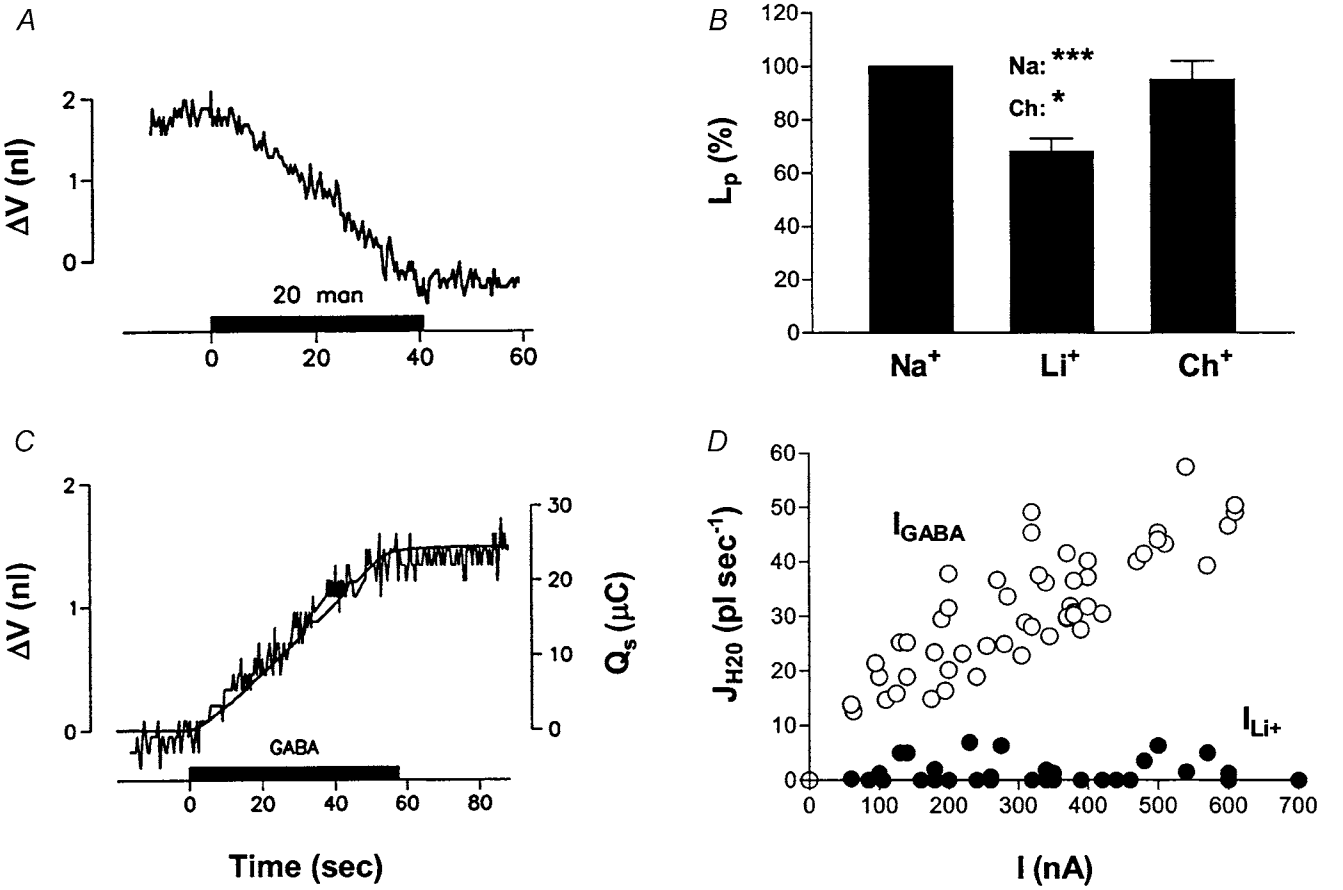

Figure 3. Water transport properties of GAT-1

A, a GAT-1-expressing oocyte was clamped to –30 mV and was superfused for 40 s with a test solution of the same ionic composition as the control solution (no GABA) but with the addition of 20 mosmol l^{-1} mannitol (man) to obtain a hyperosmolar solution (filled bar). ΔV is the change in volume of the oocyte. The L_p was calculated from the rate of shrinkage of the oocyte volume (see Methods). *B*, the oocytes were bathed in a control solution containing either 100 mM Na^+, Li^+ or Ch^+ as indicated and were superfused with the hyperosmolar test solution for 40 s. The L_p was calculated for each oocyte as a percentage of the L_p obtained in 100 mM Na^+. The data are presented as an average of these percentages ($n = 5$). * $0.01 < P < 0.05$; *** $P < 0.001$. The contribution from the native oocyte membrane has been subtracted. *C*, a GAT-1-expressing oocyte was clamped to –50 mV and 100 μM GABA was isotonically added to the test solution (filled bar). Accordingly, there was no osmotic driving force across the membrane. The jagged line in the figure represents the volume of the oocyte and the straight line represents the total amount of charges translocated by the GABA transport (Q_s). *D*, GAT-1-expressing oocytes were clamped to varying potentials (from –30 to –140 mV). The leak current (I_{Li}) obtained with 100 mM Li^+ ($I_{Li} - I_{Ch}$) or the GABA current I_{GABA} obtained with 100 μM GABA ($I_{Na+GABA} - I_{Na}$) gave currents in the range 50–700 nA ($n = 6$–7). The accompanying water flux (J_{H_2O}) is plotted *versus* this current for the leak current (●) and the GABA-induced current (○). See Methods for calculation of the coupling ratio.

a determination of the L_p of the expressed GABA transporters (in the present study $2.92 \pm 0.57 \times 10^{-6}$ cm s^{-1} (osmol $l^{-1})^{-1}$ in Na^+ ($n = 5$)). The L_p of the non-injected oocyte was not affected by the choice of cation in the solution (data not shown). The passive water permeability of GAT-1 is completely abolished in the presence of the inhibitor SKF89976A (Loo *et al.* 1999). Interestingly, GAT-1 displayed a significantly smaller L_p when Li^+ was present in the solution (68 ± 5 % of the L_p obtained in the Na^+ solution, $n = 5$) as compared with when Na^+ or Ch^+ was the main cation present (Fig. 3*B*). The water permeability observed in the presence of Ch^+ was not significantly different from the L_p in the presence of Na^+ (95 ± 7 %, $n = 5$), although it was significantly different from the L_p obtained in Li^+. The L_p was determined for each oocyte with all three cations, which made the oocyte its own control; therefore differences in the size of the oocytes can be neglected. The difference among the data was significant even when the contribution from the non-injected oocyte was not subtracted from the L_p obtained with the GAT-1-expressing oocytes, which indicates that variability between batches does not affect the confidence of the calculated results. These data support the notion that the Li^+-bound state of GAT-1 is structurally distinct.

Active water transport

Several cotransporters have been shown not only to possess a passive water permeability but also to transport water along with their substrate in a secondarily active mode (with coupling ratios of 50–500 water molecules per charge; for review see Zeuthen, 2000; Zeuthen & MacAulay, 2002). Active water transport has been shown previously in GAT-1 (Loo *et al.* 1996), although the exact coupling ratio was not determined. As seen in Fig. 3*C* (jagged line), the volume of the clamped oocyte increased linearly with time in the presence of GABA. It should be noted that there is no osmotic driving force across the membrane under these experimental conditions. The straight line is the integrated GABA-induced current, which reflects the total amount of charges entering the cell. Comparison of these two traces indicates a fixed amount of water molecules entering the cell per translocated charge. The coupling ratio was calculated from the slope of the volume trace (the water flux; see Methods), and was a linear function of the GABA-induced current (Fig. 3*D*). The calculated coupling ratio was 330 ± 49 water molecules per charge ($n = 7$). The increase in current (along the abscissa in the Fig. 3*D*) was obtained by varying the clamp potential from –30 to –140 mV. Li^+-induced leak currents of the same amplitude did not give rise to a similar water transport (the same oocytes were used to obtain both the GABA-induced current and the Li^+-induced leak current). In fact, little water followed the current, 33 ± 19 water molecules per charge, which was not significantly different from zero ($n = 6$), and there was no increase in water flux with increasing current. These data underline the distinctive nature of the leak conductance in comparison to the substrate-transporting mode.

Effect of Na^+ on the leak current

We wished to explore the effect of Na^+ on the Li^+-induced leak current of GAT-1 by generating *I–V* curves with

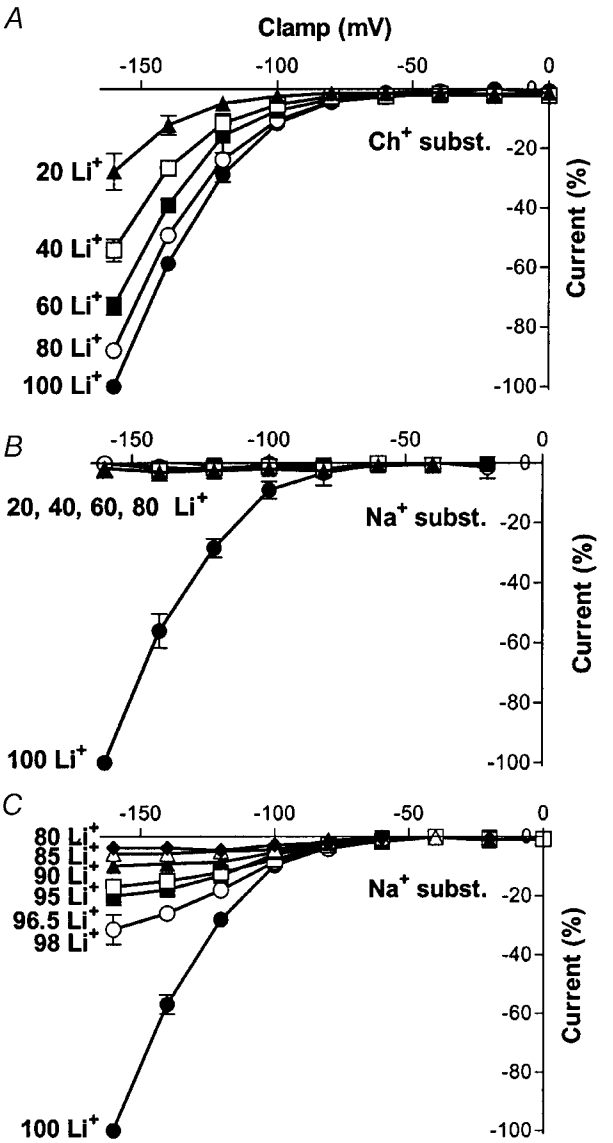

Figure 4. The effect of Na^+ on the Li^+-induced leak current

GAT-1-expressing oocytes were clamped to a holding potential of – 50 mV before the membrane potential was jumped to the test potential for 300 ms (0 to –160 mV with intervals of 20 mV) at different Li^+ concentrations. Data are presented as a percentage of the leak current obtained with 100 mM LiCl at –160 mV and have been averaged for 5 oocytes. *A*, Li^+ was substituted with equimolar Ch^+ and the leak current ($I_{Li} - I_{Ch}$) at different Li^+ concentrations are plotted. ▲, 20 mM Li^+; □, 40 mM Li^+; ■, 60 mM Li^+; ○, 80 mM Li^+; ●, 100 mM Li^+. *B*, Li^+ was substituted with equimolar Na^+, otherwise as above. *C*, Li^+ was substituted with equimolar Na^+, as in *B*, but the Li^+ concentrations were as follows: ◆, 80 mM Li^+; △, 85 mM Li^+; ▲, 90 mM Li^+, □, 95 mM Li^+; ■, 96.5 mM Li^+; ○, 98 mM Li^+; ●, 100 mM Li^+.

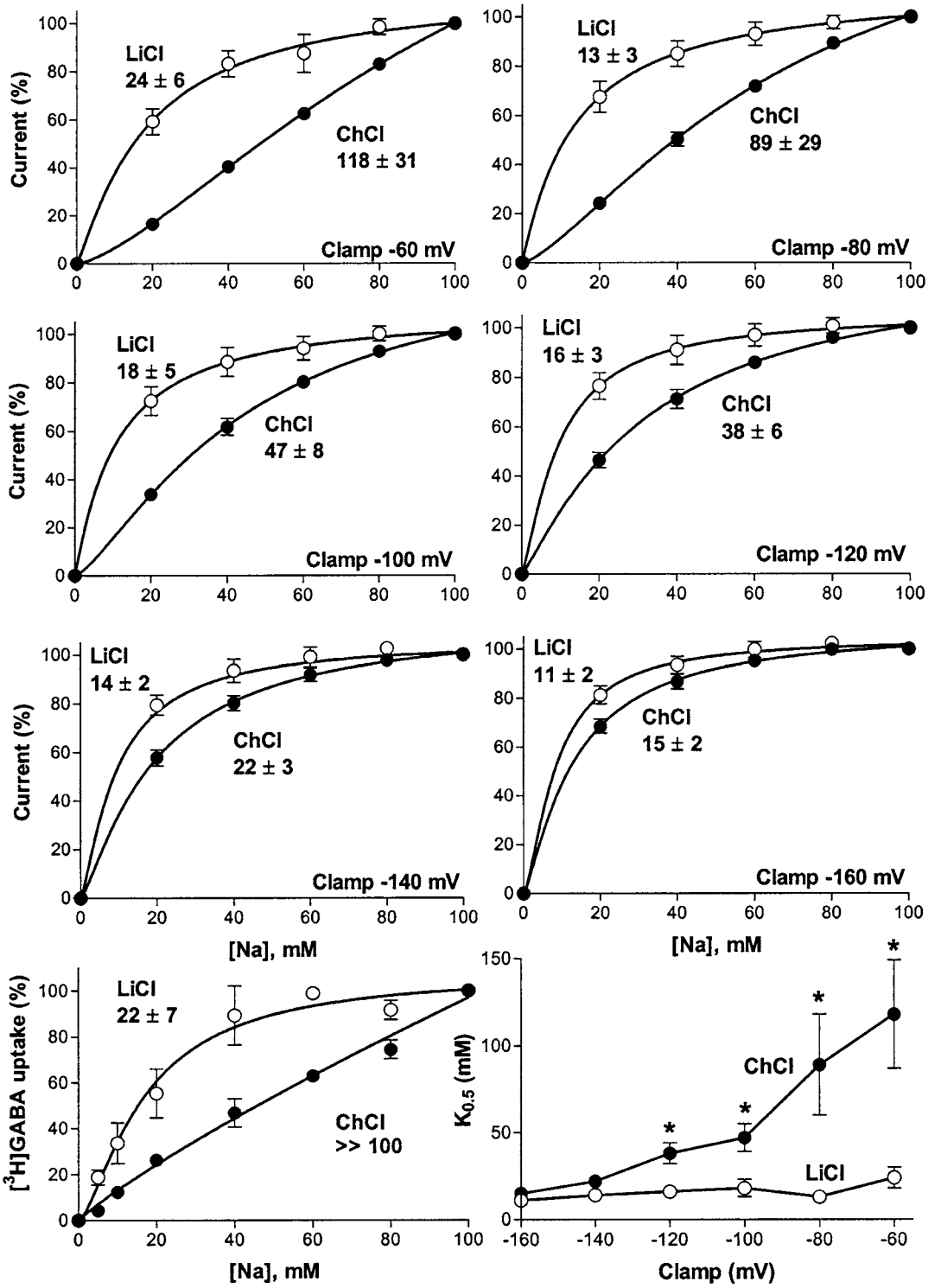

Figure 5. Apparent Na^+ affinity with different substituting cations

GAT-1-expressing oocytes were clamped to a holding potential of –50 mV before the membrane potential was jumped to the test potential for 300 ms (0 to –160 mV with intervals of 20 mV) at different Na^+ concentrations +/- 100 μM GABA (Ch^+ or Li^+ substitution). Data are presented as the GABA-induced current (% of the current obtained at 100 mM Na^+) with Li^+ substitution (○) or with Ch^+ substitution (●) at different clamp potentials as stated. Data are average of 4 oocytes. The data were fitted to the Hill equation and the resulting $K'_{0.5}$ values (mM) are stated in the figure and plotted in the lower right panel. * $0.01 < P < 0.05$. The identical experimental conditions were repeated with [^{3}H]GABA uptake in unclamped oocytes where the data are presented as the percentage of the uptake at 100 mM Na^+. The average of 3 experiments (performed in quadruplicate) is shown in the lower left panel with the $K'_{0.5}$ values of the experiment. The Ch^+-substituted Na^+ curve did not reach saturation at the Na^+ concentrations used, so a reliable $K'_{0.5}$ could not be calculated for this curve.

increasing amounts of Li^+ (0–100 mM), substituted with equimolar Ch^+ (Fig. 4*A*) or Na^+ (Fig. 4*B* and *C*). With Ch^+ as the substituting cation, the leak current increased essentially linearly with increasing Li^+ concentration at all potentials tested (Fig. 4*A*). With Na^+ as the substituting ion, however, this was not the case. The presence of even small concentrations of Na^+ reduced the leak current substantially (compare Fig. 4*A* and *B*). In Fig. 4*C*, even smaller concentrations of Na^+ were used to determine the concentration of Na^+ that led to 50 % inhibition of the leak current: 2.7 ± 0.1 mM at –120 mV ($n = 5$). These data show that Na^+ has an inhibitory effect on the Li^+ -induced leak current.

GABA transport is dependent on the binding of two Na^+ ions prior to GABA translocation (Radian & Kanner, 1983; Keynan & Kanner, 1988). Modelling of the GABA transporter led Hilgeman & Lu (1999) to propose two different affinities by which these two Na^+ ions bind to the transporter. According to this model, the transporter releases its substrate to the cytoplasm of the cell, after which an apparently low-affinity Na^+ binding site (K_d of 920 mM) opens up facing the outside of the membrane. Na^+ binding to this apparently low-affinity 'first' Na^+ binding site leads to the formation of the outward-facing conformation by a voltage-dependent step and during this process a 'second' apparently high-affinity binding site (K_d of 10 mM) becomes accessible from the extracellular side, leading to binding of the second Na^+ ion and subsequently to GABA binding and translocation (Hilgemann & Lu, 1999). The sequential and co-operative binding of the two sodium ions was reflected in a characteristic sigmoidal Na^+ dependence curve of the GABA-induced current with a Hill coefficient of 1.4 ± 0.1 at –120 mV ($n = 5$, data not shown and Martin & Smith, 1972; Keynan *et al.* 1992; Mager *et al.* 1993).

A conceivable explanation for the above data would be that Li^+ interacts with the first, apparently low-affinity cation binding site in the absence of Na^+, allowing not only the transporter to go into a leak-conducting mode but also leading to exposure of the second apparently high-affinity Na^+ binding site. Binding of Na^+ to this site could then lead to a conformational change causing inhibition of the leak current with a half-maximal effect at 2.7 mM. Thus, Na^+ may bind to the second site with the same apparently high affinity whether it is to 'pull' the transporter out of its leak-conducting mode or whether it is to support GABA-induced current. This leads to the question: if Li^+ can substitute for the first Na^+ ion, and still allow for the second Na^+ to bind, can the Li^+–Na^+ transporter complex support GABA binding and translocation? We determined the Na^+ dependence of the GABA-induced current with the substituting ion being either Ch^+ or Li^+. As seen from the upper six panels in Fig. 5, the GABA-induced current reached saturation at lower Na^+ concentrations when Li^+ was the substituting ion than when Ch^+ replaced the Na^+, that is, lower concentrations of Na^+ were required to obtain half-maximal GABA currents when Li^+ was present in the bath (for $K'_{0.5}$ values, see Fig. 5). We verified that this current was indeed due to GABA transport by performing the identical experiment with [^{3}H]GABA uptake into unclamped oocytes (Fig. 5, lower left panel). This finding indicates that Li^+ inclusion in the buffer markedly reduces the voltage dependence of the apparent Na^+ affinity and thereby suggests a contribution of Li^+ to the Na^+ activation of the GABA-induced current. The Li^+-induced leak current does not contribute to the generated current under these experimental conditions since no Li^+-induced leak current is observed in the presence of 20 mM Na^+ (see Fig. 4). The lowest Na^+ concentration used therefore was 20 mM (lower concentrations were used in the uptake experiment, where the leak current is not an issue). As GABA translocation is strictly dependent on the presence of Na^+ (data not shown and Radian & Kanner, 1983; Keynan & Kanner, 1988), the GABA-induced current is set to zero in the absence of Na^+. The difference between the $K'_{0.5}$ values obtained with Ch^+ and Li^+ decreased as the membrane potential became more hyperpolarized (lower right panel in Fig. 5). While the $K'_{0.5}$ values for Na^+ with Li^+ substitution did not change significantly with the membrane potential ($P > 0.05$, two-tailed t test, $n = 4$), the voltage-dependent apparent Na^+ affinity obtained with Ch^+ substitution markedly increased at more negative membrane potentials (Fig. 5 and Mager *et al.* 1993). Altogether, with Li^+ as the substituting ion, the transporter appears to sense a high cation concentration, even at low Na^+ concentrations, consistent with the notion that Li^+ may substitute for the first apparently low-affinity Na^+ binding in the GABA translocation cycle.

DISCUSSION

Originally a Na^+-coupled cotransporter was thought of as a protein whose sole role was the translocation of its substrate, often against large electrochemical gradients. However, increasing evidence suggests that transport proteins show resemblance to ion channels by also carrying currents unrelated to translocation of their substrate. The glutamate transporters have for example been shown to carry a large glutamate-gated Cl^- conductance and can thus also be considered substrate-gated anion channels (Fairman *et al.* 1995; Wadiche *et al.* 1995; Eliasof & Jahr, 1996). In addition, several cotransporters, among them the GABA transporters as well as the monoaminergic transporters, were shown to support uncoupled leak currents (Umbach *et al.* 1990; Mager *et al.* 1994, 1996; Galli *et al.* 1995; Vandenberg *et al.* 1995; Sonders *et al.* 1997). The leak permeability differs between the transporters with GAT-1 being permeable to Li^+ and to a lesser extent Cs^+, but not to Na^+ (Mager *et al.* 1996; Bismuth *et al.* 1997; Loo *et al.* 1999;

MacAulay *et al.* 2001*a*), whereas other functionally related transporters, such as SERT, DAT, the noradrenaline transporter (NET), the glutamate transporter-1 or the excitatory amino acid transporter-1 (EAAT1) and SGLT, also sustain Na^+ leak currents (Umbach *et al.* 1990; Mager *et al.* 1994; Vandenberg *et al.* 1995; Galli *et al.* 1995; Sonders *et al.* 1997). This Na^+ leak current is often smaller than the Li^+-induced leak current (Mager *et al.* 1994; Sonders *et al.* 1997; Panayotova-Heiermann *et al.* 1998; Petersen & DeFelice, 1999). In this study, we ruled out the possibility of Li^+ serving a permissive role for subsequent H^+ permeation in GAT-1, although H^+ has been shown to permeate GAT-1 and SERT in a NMDG test solution (Cao *et al.* 1997). Under their experimental conditions, with both Na^+ and Li^+ absent, protons may replace the role of Li^+ (although at less negative potentials, −40 mV) or they may permeate via a proton wire through a water-filled pore (Cao *et al.* 1997). Cl^- is not carried through the leak current pathway in SERT and DAT (Lin *et al.* 1996; Sonders *et al.* 1997), although its presence in the test solution is necessary to obtain maximal leak currents in SERT, DAT and GAT-1 (Lin *et al.* 1996; Mager *et al.* 1996; Sonders *et al.* 1997).

The substrate translocation in the monoaminergic transporters and GAT-1 is strictly dependent on the presence of Na^+ and cannot transport their substrates with Li^+ as the cationic ligand (Radian & Kanner, 1983; Keynan & Kanner, 1988; Gu *et al.* 1994; Galli *et al.* 1995, 1997; Lin *et al.* 1996; Sonders *et al.* 1997; Petersen & DeFelice, 1999), although it appears as if substrates can interact with the Li^+-bound state in SERT and DAT (Mager *et al.* 1994; Sonders *et al.* 1997; Petersen & DeFelice, 1999). This transporter–substrate interaction inhibits the Li^+ leak current in these two transporters, whereas the leak current of GAT-1 is completely unaffected by the presence of substrate. The Li^+-bound conformation may therefore not support GABA binding.

Mechanism of the Li^+-induced leak current

Based on a high Arrhenius activation energy (19 kcal mol^{-1} (79 kJ mol^{-1})), a Hill coefficient of 2 and the same apparent Na^+ affinity (2.5 mM) of the leak current and the glucose transport (Loo *et al.* 1999), it was suggested for the SGLT that the leak current is carried through this transporter in the 'transporter mode', i.e. the leak is a consequence of the transporter moving through its transport cycle even in the absence of substrate. Another possibility is that the current arises as a channel mode of conductance as was suggested for SERT and GAT-1 (Cammack & Schwartz, 1996; Lin *et al.* 1996). Previously, we have observed distinct Zn^{2+} sensitivities of the GABA-induced current and the Li^+-induced leak current in a mutant GAT-1 containing a bidentate Zn^{2+} binding site between transmembrane segments 7 and 8 (T349H/Q374C; MacAulay *et al.* 2001*a*). Based on these findings we were able to conclude that either the conformational changes responsible for the Li^+ conductance are different from those involved in GABA translocation and/or the conformational states adopted by the Li^+-bound transporter are distinct from those adopted in the presence of Na^+–GABA. The current data provide additional support for an altered conformational state of the Li^+-bound transporter, as reflected in the reduced passive water permeability of the transporter in the presence of Li^+ as compared with that in the presence of Na^+ or Ch^+. Most probably this lower water permeability is a result of a smaller aqueous pore in the Li^+-bound conformation. Of notable interest, the SGLT did not show this Li^+-induced reduction in the passive water permeability (Loo *et al.* 1999). However, covalent modification with sulfhydryl-reactive methanethiosulphonate (MTS) reagents of the closely related SERT and the glycine transporter has shown a distinct Li^+-bound conformation, similar to the findings in GAT-1, suggesting that it is not the lack of Na^+ binding that renders the conformational occupancy distinct but it is the Li^+ binding *per se* (Chen *et al.* 1997; Lopez-Corcuera *et al.* 2001; Ni *et al.* 2001). The distinct nature of the leak current and the substrate translocation process is also supported by the number of mutated or modified transporters in which the leak current is intact but the transport current is abolished (Mager *et al.* 1996; Bismuth *et al.* 1997; Yu *et al.* 1998; MacAulay *et al.* 2001*a*).

Several Na^+- and H^+-coupled cotransporters have been shown to translocate water across the membrane together with their substrates. This has been found for the K^+–Cl^- cotransporter (Zeuthen, 1994), the lactate transporter MCT-1 (Zeuthen *et al.* 1996), SGLT (Loo *et al.* 1996; Meinild *et al.* 1998), the dicarboxylate transporter NaDC-1 (Meinild *et al.* 2000), the glutamate transporter EAAT1 (MacAulay *et al.* 2001*b*), GAT-1 (Loo *et al.* 1996), and the plant H^+-amino acid transporter APP5 (Loo *et al.* 1996). In each of these cotransporters, water is transported with a fixed coupling ratio with a value in the range of 50–500 water molecules per charge. The water transport is independent of external parameters, such as ligand concentrations, osmolarity and temperature, and even takes place uphill, against an imposed water–chemical gradient favouring water transport the opposite way (Zeuthen, 1994; Meinild *et al.* 1998, 2000; MacAulay *et al.* 2001*b*). These studies suggest that the active and passive water transport are two independent modes of transport that proceed in parallel. The active water transport is stoichiometrically coupled to the substrate translocation and is *not* due to a build-up of an osmotic gradient as Na^+ and other ligands are transported into the cell (Zeuthen *et al.* 2002; for review see Zeuthen, 2000; Zeuthen & MacAulay, 2002). The GABA transport led to the translocation of 330 ± 49 water molecules per translocated charge ($n = 7$). If GABA transport leads to translocation of only one charge

(Kavanaugh *et al.* 1992), the coupling ratio reflects the number of water molecules being transported per turnover. If two charges are being translocated per GABA molecule, as was recently suggested (Loo *et al.* 2000), it follows that 660 water molecules are transported per turnover. It is noted that the water flux as a function of current does not appear to be a straight line through 0.0. A previous study on EAAT1 showed a similar pattern in the *presence* of the permeable anion, whereas the water flux was a linear function of the glutamate transport (through 0.0) in the *absence* of the permeable anion (MacAulay *et al.* 2001*b*). In analogy to this, the GABA-induced current may be made up of two components – the transport-associated current and an uncoupled current. The existence of a substrate-induced uncoupled current component has been proposed for GAT-1 (Cammack *et al.* 1994; Risso *et al.* 1996) and for the monoaminergic transporters (Mager *et al.* 1994; Galli *et al.* 1995, 1997; Sonders *et al.* 1997; Petersen & DeFelice, 1999).

Currents of the same amplitude as the GABA-induced current could be obtained with the leak current, yet no significant water flux was observed ($n = 6$). This clearly distinguishes the mechanism of Li^+ permeation from that of the GABA translocation. As mentioned above, it has been shown that the water transport is *not* driven by the osmotic build-up of ions and substrate (Meinild *et al.* 1998; MacAulay *et al.* 2001*b*; Zeuthen *et al.* 2001, 2002). Even so, it could be argued that four molecules are transported into the cytoplasm per charge translocated by the GABA transport while only one Li^+ enters the cytoplasm per charge during the leak-current process, and that this might cause the increased water flux with the GABA transport. One should then multiply the number of water molecules transported with the leak current by four ($33 \times 4 = 132$) in order to compare with the number of water molecules translocated with GABA into the cell (330). Thus, osmotic build-up would still not explain the difference in the water transport properties of these two current modes.

The E_a of the leak current in GAT-1 was not significantly different from that of the GABA-induced current. At first this would indicate the involvement of large conformational changes in the mechanism with which the leak current takes place. However, as the leak current barely showed any saturation with increased Li^+ concentration and did not carry any water, we propose that the permeation of Li^+ takes place in a channel mode of conductance but that the actual opening of the pore requires conformational changes. In support of this, the voltage dependence of the leak current is quite steep and the permeation does not take place until the membrane potential is more hyperpolarized than −75 mV. The driving force for Li^+ would in itself allow Li^+ to permeate at much more depolarized potentials, which suggests that at hyperpolarized potentials, Li^+ leads to an increase in the single-channel open probability, as was proposed for SERT (Lin *et al.* 1996). It follows that in GAT-1, the conformational change leading to channel opening does not take place until the membrane potential is hyperpolarized below −75 mV. The high E_a may then reflect upon the opening of the channel and not on the permeation through the pore (Hille, 2001). In analogy with this, the *Shaker* K^+ channel has low activation energies for the conducting current and high activation energies for the opening and closing of the channel (Nobile *et al.* 1997).

Conformational basis of the leak current

The GABA transporter translocates two Na^+ ions per GABA ion (Radian & Kanner, 1983; Keynan & Kanner, 1988) and by a model proposed by Hilgeman & Lu (1999), these two Na^+ ions bind to the transporter with distinct affinities in a co-operative manner. According to this model, the apparent affinity of the first Na^+ binding site is around 900 mM and that of the second Na^+ binding site around 10 mM. The Na^+ activation curve showed a strong voltage dependence of the apparent Na^+ affinity from around 15 mM at −160 mV, 40 mM at −120 mV to > 100 mM at −60 mV (Fig. 5 and Mager *et al.* 1993). This voltage dependence may well reflect on the binding of the first Na^+ as this binding step has been associated with the voltage-dependent return step of the empty transporter from inward-facing to outward-facing (Parent *et al.* 1992; Hilgemann & Lu, 1999). Interestingly, Na^+ inhibited the Li^+-induced leak current with a half-maximal effect at 2.7 mM Na^+, suggesting that the binding of Na^+ (with an apparent affinity constant of around 2.7 mM) constrains GAT-1 in a conformation that does not support a leak current. An intriguing explanation is that Li^+ is able to substitute for the first Na^+ ion and thereby allow Na^+ to bind with the apparently high affinity that is characteristic of the second Na^+ binding site. As Li^+ replaced Na^+ in the first binding site, GABA transport took place with a significantly higher apparent Na^+ affinity than when Na^+ was substituted with Ch^+ (Fig. 5), as has also been found in the glutamate transporter, GLT-1 (Grunewald & Kanner, 1995). At potentials from −60 to −120 mV, the apparent affinity for Na^+ was significantly different with the two different cation substitutes (Ch^+ or Li^+). The apparent Na^+ affinities obtained with the two different substituting cations approached each other at the more hyperpolarized test potentials (−140 and −160 mV), most probably because the apparent Na^+ affinity of the voltage-dependent binding of the first Na^+ is so high at this potential that the two Na^+ binding sites most likely approach the same apparent Na^+ affinity, and the Li^+ substitution is no longer stimulatory.

Altogether, we propose that Li^+ can bind to the first cation binding site of the transporter (C_1Li) as depicted in the simplified model in Fig. 6. At hyperpolarized potentials, a

Li^+-permeable channel opens (C_1LiO) and gives rise to the leak current. Na^+ may bind to the Li^+-bound state (C_2LiNa) in a similar manner as it would bind to the 'normal' Na^+-bound state ($C_1Na_1 \rightarrow C_2Na_2$) before GABA (S) binds to either of those two states (C_3LiNaS or C_3Na_2S) and the complex gets translocated (C_4LiNaS or C_4Na_2S). In theory, the pore may also be permeable to Na^+, as is the case for DAT, SERT, NET, SGLT and EAAT1 (Umbach *et al.* 1990; Mager *et al.* 1994; Galli *et al.* 1995; Vandenberg *et al.* 1995; Sonders *et al.* 1997), but since low concentrations of Na^+ transfer the protein into the C_2Na_2 conformation which is not permeable, no Na^+ permeation would be detected. In support of this, covalent modification with sulfhydryl-reactive methanethiosulphonate (MTS) reagents of the first external loop in GAT-1 renders the transporter permeable to Na^+ as well as Li^+ (Yu *et al.* 1998), which could be interpreted as the transporter getting 'stuck' in the C_1 conformation and thereby allowing Na^+ to permeate. Non-additive Na^+- and Li^+-induced leak currents have also been observed in SERT (Petersen & DeFelice, 1999; Ni *et al.* 2001) and an idea similar to the one presented in this paper was introduced (Ni *et al.* 2001). The authors suggested that Na^+ stabilized a conformation of the protein that was different from that of the Li^+-bound conformation. Another possibility is that Na^+ and Li^+ may interact in a common pore with anomalous mole fractions, as was suggested for the *Drosophila* SERT, with 6 mM Na^+ inhibiting the Li^+ current down to 50 % (Petersen & DeFelice, 1999), instead of the 3 mM found in the present study with GAT-1.

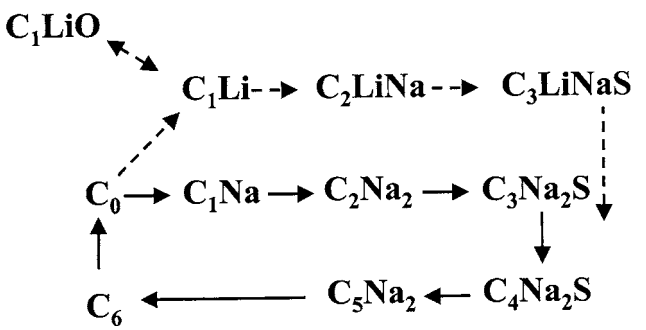

Figure 6. The GAT-1 reaction scheme

The simplified GAT-1 reaction scheme shows the empty inward-facing transporter (C6) returning to the empty outward-facing state (C_0) where 2 Na^+ are bound to the transporter sequentially ($C_0 \rightarrow C_1Na \rightarrow C_2Na_2$) before substrate (S) is bound ($C_2Na_2 \rightarrow C_3Na_2S$) and the complex is translocated (C_4Na_2S). An alternative pathway is shown with dotted arrows where Li^+ can replace the first Na^+ and enter into a conformationally distinct state (C_1Li) from which the Li^+ leak channel may open (C_1LiO). Na^+ can bind to the second apparently high-affinity Na^+ binding site (C_2LiNa) and the transporter can no longer sustain the Li^+-induced leak current. According to our model, the Li^+–Na^+- bound complex binds substrate (C_3LiNaS) and the translocation takes place.

REFERENCES

Bismuth, Y., Kavanaugh, M. P. & Kanner, B. I. (1997). Tyrosine 140 of the gamma-aminobutyric acid transporter GAT-1 plays a critical role in neurotransmitter recognition. *Journal of Biological Chemistry* **272**, 16096–16102.

Borden, L. A. (1996). GABA transporter heterogeneity: pharmacology and cellular localization. *Neurochemistry International* **29**, 335–356.

Cammack, J. N., Rakhilin, S. V. & Schwartz, E. A. (1994). A GABA transporter operates asymmetrically and with variable stoichiometry. *Neuron* **13**, 949–960.

Cammack, J. N. & Schwartz, E. A. (1996). Channel behavior in a gamma-aminobutyrate transporter. *Proceedings of the Naional Academy of Sciences of the USA* **93**, 723–727.

Cao, Y., Mager, S. & Lester, H. A. (1997). H^+ permeation and pH regulation at a mammalian serotonin transporter. *Journal of Neuroscience* **17**, 2257–2266.

Chen, J.-G., Lui-Chen, S. & Rudnick, G. (1997). External cysteine residues in the serotonin transporter. *Biochemistry* **36**, 1479–1486.

Eliasof, S. & Jahr, C. E. (1996). Retinal glial cell glutamate transporter is coupled to an anionic conductance. *Proceedings of the Naional Academy of Sciences of the USA* **93**, 4153–4158.

Fairman, W. A., Vandenberg, R. J., Arriza, J. L., Kavanaugh, M. P. & Amara, S. G. (1995). An excitatory amino-acid transporter with properties of a ligand-gated chloride channel. *Nature* **375**, 599–603.

Forlani, G., Bossi, E., Ghirardelli, R., Giovannardi, S., Binda, F., Bonadiman, L., Ielmini, L. & Peres, A. (2001). Mutation K448E in the external loop 5 of rat GABA transporter rGAT1 induces pH sensitivity and alters substrate interactions. *Journal of Physiology* **536**, 479–494.

Galli, A., DeFelice, L. J., Duke, B. J., Moore, K. R. & Blakely, R. D. (1995). Sodium-dependent norepinephrine-induced currents in norepinephrine-transporter-transfected HEK-293 cells blocked by cocaine and antidepressants. *Journal of Experimental Biology* **198**, 2197–2212.

Galli, A., Petersen, C. I., Deblaquiere, M., Blakely, R. D. & Defelice, L. J. (1997). *Drosophila* serotonin transporters have voltage-dependent uptake coupled to a serotonin-gated ion channel. *Journal of Neuroscience* **17**, 3401–3411.

Grunewald, M. & Kanner, B. (1995). Conformational changes monitored on the glutamate transporter GLT-1 indicate the existence of two neurotransmitter-bound states. *Journal of Biological Chemistry* **270**, 17017–17024.

Gu, H., Wall, S. C. & Rudnick, G. (1994). Stable expression of biogenic amine transporters reveals differences in inhibitor sensitivity, kinetics, and ion dependence. *Journal of Biological Chemistry* **269**, 7124–7130.

Guastella, J., Nelson, N., Nelson, H., Czyzyk, L., Keynan, S., Miedel, M. C., Davidson, N., Lester, H. A. & Kanner, B. I. (1990). Cloning and expression of a rat brain GABA transporter. *Science* **249**, 1303–1306.

Hilgemann, D. W. & Lu, C. C. (1999). GAT1 (GABA:Na^+:Cl^-). cotransport function. Database reconstruction with an alternating access model. *Journal of General Physiology* **114**, 459–475.

Hille, B. (2001). Ionic Channels of Excitable Membranes, 3rd edn. Singauer, Sunderland, MA, USA.

Kavanaugh, M. P., Arriza, J. L., North, R. A. & Amara, S. G. (1992). Electrogenic uptake of gamma-aminobutyric acid by a cloned transporter expressed in Xenopus oocytes. *Journal of Biological Chemistry* **267**, 22007–22009.

Keynan, S. & Kanner, B. I. (1988). gamma-Aminobutyric acid transport in reconstituted preparations from rat brain: coupled sodium and chloride fluxes. *Biochemistry* **27**, 12–17.

Keynan, S., Suh, Y. J., Kanner, B. I. & Rudnick, G. (1992). Expression of a cloned gamma-aminobutyric acid transporter in mammalian cells. *Biochemistry* **31**, 1974–1979.

Lin, F., Lester, H. A. & Mager, S. (1996). Single-channel currents produced by the serotonin transporter and analysis of a mutation affecting ion permeation. *Biophysical Journal* **71**, 3126–3135.

Loike, J., Hickman, S., Kuang, K., Xu, M., Cao, L., Vera, J. C., Silverstein, S. C. & Fischbarg, J. (1996). Sodium-glucose cotransporters display sodium- and phlorizin-dependent water permeability. *American Journal of Physiology* **271**, C1774–1779.

Loo, D. D., Eskandari, S., Boorer, K. J., Sarkar, H. K. & Wright, E. M. (2000). Role of Cl^- in electrogenic Na^+-coupled cotransporters GAT1 and SGLT1. *Journal of Biological Chemistry* **275**, 37414–37422.

Loo, D. D., Zeuthen, T., Chandy, G. & Wright, E. M. (1996). Cotransport of water by the Na^+/glucose cotransporter. *Proceedings of the National Academy of Sciences of the USA* **93**, 13367–13370.

Loo, D. D. F., Hirayama, B. A., Meinild, A.-K., Chandy, G., Zeuthen, T. & Wright, E. M. (1999). Passive water and ion transport by cotransporters. *Journal of Physiology* **518**, 195–202.

Lopez-Corcuera, B., Nunez, E., Martinez-Maza, R., Geerlings, A. & Aragon, C. (2001). Substrate-induced conformational changes of extracellular loop one in the glycine transporter GLYT2. *Journal of Biological Chemistry* **276**, 43463–43470.

Lu, C. C. & Hilgemann, D. W. (1999). GAT1 (GABA:Na^+:Cl^-) cotransport function. Steady state studies in giant Xenopus oocyte membrane patches. *Journal of General Physiology* **114**, 429–444.

MacAulay, N., Bendahan, A., Loland, C. J., Kanner, B. I., Zeuthen, T. & Gether, U. (2001*a*). Engineered Zn^{2+} Switches in the GABA transporter-1: differential effects on GABA uptake and currents. *Journal of Biological Chemistry* **276**, 40476–40485.

MacAulay, N., Gether, U., Klaerke, D. A. & Zeuthen, T. (2001*b*). Water transport by the human Na^+-coupled glutamate cotransporter expressed in *Xenopus* oocytes. *Journal of Physiology* **530**, 367–378.

Mager, S., Kleinberger-Doron, N., Keshet, G. I., Davidson, N., Kanner, B. I. & Lester, H. A. (1996). Ion binding and permeation at the GABA transporter GAT1. *Journal of Neuroscience* **16**, 5405–5414.

Mager, S., Min, C., Henry, D. J., Chavkin, C., Hoffman, B. J., Davidson, N. & Lester, H. A. (1994). Conducting states of a mammalian serotonin transporter. *Neuron* **12**, 845–859.

Mager, S., Naeve, J., Quick, M., Labrace, C., Davidson, N. & Lester, H. A. (1993). Steady states, charge movements, and rates for a cloned GABA transporter expressed in Xenopus oocytes. *Neuron* **10**, 177–188.

Martin, D. L. & Smith, A. A. III (1972). Ions and the transport of gamma-aminobutyric acid by synaptosomes. *Journal of Neurochemistry* **19**, 841–855.

Meinild, A.-K., Klaerke, D. A., Loo, D. D. F., Wright, E. M. & Zeuthen, T. (1998). The human Na^+–glucose cotransporter is a molecular water pump. *Journal of Physiology* **508**, 15–21.

Meinild, A. K., Loo, D. D., Pajor, A. M., Zeuthen, T. & Wright, E. M. (2000). Water transport by the renal Na(+)–dicarboxylate cotransporter. *American Journal of Physiology – Renal Physiology* **278**, F777–783.

Ni, Y. G., Chen, J. G., Androutsellis-theotokis, A., Huang, C. J., Moczydlowski, E. & Rudnick, G. (2001). A lithium-induced conformational change in serotonin transporter alters cocaine binding, ion conductance, and reactivity of Cys-109. *Journal of Biological Chemistry* **276**, 30942–30947.

Nobile, M., Olcese, R., Toro, L. & Stefani, E. (1997). Fast inactivation of Shaker K^+ channels is highly temperature dependent. *Experimental Brain Research* **114**, 138–142.

Panayotova-Heiermann, M., Loo, D. D. F., Lam, J. T. & Wright, E. M. (1998). Neutralization of conservative charged transmembrane residues in the Na^+/glucose cotransporter SGLT1. *Biochemistry* **37**, 10522–10528.

Parent, L., Supplisson, S., Loo, D. D. F. & Wright, E. M. (1992). Electrogenic properties of the cloned Na^+/glucose cotransporter: II. A transport model under nonrapid equilibrium conditions. *Journal of Membrane Biology* **125**, 63–79.

Petersen, C. I. & Defelice, L. J. (1999). Ionic interactions in the *Drosophila* serotonin transporter identify it as a serotonin channel. *Nature Neuroscience* **2**, 605–610.

Radian, R. & Kanner, B. I. (1983). Stoichiometry of sodium- and chloride-coupled gamma-aminobutyric acid transport by synaptic plasma membrane vesicles isolated from rat brain. *Biochemistry* **22**, 1236–1241.

Risso, S., Defelice, L. J. & Blakely, R. D. (1996). Sodium-dependent GABA-induced currents in GAT1-transfected HeLa cells. *Journal of Physiology* **490**, 691–702.

Sonders, M. S. & Amara, S. G. (1996). Channels in transporters. *Current Opinion in Neurobiology* **6**, 294–302.

Sonders, M. S., Zhu, S. J., Zahniser, N. R., Kavanaugh, M. P. & Amara, S. G. (1997). Multiple ionic conductances of the human dopamine transporter: the actions of dopamine and psychostimulants. *Journal of Neuroscience* **17**, 960–974.

Umbach, J. A., Coady, M. J. & Wright, E. M. (1990). Intestinal Na^+/glucose cotransporter expressed in Xenopus oocytes is electrogenic. *Biophysical Journal* **57**, 1217–1224.

Vandenberg, R. J., Arriza, J. L., Amara, S. G. & Kavanaugh, M. P. (1995). Constitutive ion fluxes and substrate binding domains of human glutamate transporters. *Journal of Biological Chemistry* **270**, 17668–17671.

Wadiche, J. I., Amara, S. G. & Kavanaugh, M. P. (1995). Ion fluxes associated with excitatory amino acid transport. *Neuron* **15**, 721–728.

Yu, N., Cao, Y., Mager, S. & Lester, H. A. (1998). Topological localization of cysteine 74 in the GABA transporter, GAT1, and its importance in ion binding and permeation. *FEBS Letters* **426**, 174–178.

Zampighi, G. A., Kreman, M., Boorer, K. J., Loo, D. D. F., Bezanilla, F., Chandy, G., Hall, J. E. & Wright, E. M. (1995). A method for determining the unitary functional capacity of cloned channels and transporters expressed in *Xenopus laevis* oocytes. *Journal of Membrane Biology* **148**, 65–78.

Zeuthen, T. (1991). Water permeability of ventricular cell membrane in choroid plexus epithelium from *Necturus maculosus*. *Journal of Physiology* **444**, 133–151.

Zeuthen, T. (1994). Cotransport of K^+, Cl^- and $_{H_2O}$ by the membrane proteins from choroid plexus epithelium of *Necturus maculosus*. *Journal of Physiology* **478**, 203–219.

Zeuthen, T. (2000). Molecular water pumps. *Reviews of Physiology Biochemistry and Pharmacology* **141**, 97–151.

Zeuthen, T., Hamann, S. & La Cour, M. (1996). Cotransport of H^+, lactate and H_2O by membrane proteins in retinal pigment epithelium of bullfrog. *Journal of Physiology* **497**, 3–17.

Zeuthen, T. & MacAulay, N. (2002). Cotransporters as molecular water pumps. In *International Review of Cytology,* vol. 215, ed. Zeuthen, T. & Stein, W. D., pp. 259–284. Academic Press, San Diego.

Zeuthen, T., Meinild, A. K., Klaerke, D. A., Loo, D. D., Wright, E. M., Belhage, B. & Litman, T. (1997). Water transport by the Na^+/glucose cotransporter under isotonic conditions. *Biology of the Cell* **89**, 307–312.

Zeuthen, T., Meinild, A. K., Loo, D. D., Wright, E. M. & Klaerke, D. A. (2001). Isotonic transport by the Na^+–glucose cotransporter SGLT1 from humans and rabbit. *Journal of Physiology* **531**, 631–644.

Zeuthen, T., Zeuthen, E. & Klaerke, D.A. (2002). Mobility of ions, sugar, and water in the cytoplasm of *Xenopus* oocytes expressing Na^+-coupled sugar transporters (SGLT1). *Journal of Physiology* **542**, 71–87.

Acknowledgements

The GAT-1 clone was a kind gift from Baruch Kanner. We are grateful for the technical assistance of B. Lynderup and T. Soland and for the critical reading of the manuscript by Drs Mark Sonders, Erika Adkins and Anne-Kristine Meinild. This study was supported by the Lundbeck Foundation and the Danish Research Council.

Cell. Mol. Life Sci. (2010) 67:829–840
DOI 10.1007/s00018-009-0218-9

Cellular and Molecular Life Sciences

RESEARCH ARTICLE

Differential water permeability and regulation of three aquaporin 4 isoforms

Robert A. Fenton · Hanne B. Moeller · Marina Zelenina · Marteinn T. Snaebjornsson · Torgeir Holen · Nanna MacAulay

Received: 29 September 2009 / Revised: 3 November 2009 / Accepted: 16 November 2009 / Published online: 15 December 2009

Abstract Aquaporin 4 (AQP4) is expressed in the perivascular glial endfeet and is an important pathway for water during formation and resolution of brain edema. In this study, we examined the functional properties and relative unit water permeability of three functional isoforms of AQP4 expressed in the brain (M1, M23, Mz). The M23 isoform gave rise to square arrays when expressed in *Xenopus laevis* oocytes. The relative unit water permeability differed significantly between the isoforms in the order of M1 > Mz > M23. None of the three isoforms were permeable to small osmolytes nor were they affected by changes in external K^+ concentration. Upon protein kinase C (PKC) activation, oocytes expressing the three isoforms demonstrated rapid reduction of water permeability, which correlated with AQP4 internalization. The M23 isoform was more sensitive to PKC regulation than the longer isoforms and was internalized significantly faster. Our results suggest a specific role for square array formation.

Keywords Aquaporin · Glial cells · Water permeability · Regulation · Protein kinase C · Isoforms

All authors belong to Nordic Center of Excellence for Water Imbalance Related Disorders.

Electronic supplementary material The online version of this article (doi:10.1007/s00018-009-0218-9) contains supplementary material, which is available to authorized users.

R. A. Fenton · H. B. Moeller
The Water and Salt Research Center, Department of Anatomy, University of Aarhus, 8000 Aarhus, Denmark

M. Zelenina
Department of Women's and Children's Health, Karolinska Institutet, 171-77 Stockholm, Sweden

M. Zelenina
Department of Applied Physics, Royal Institute of Technology, Stockholm, Sweden

M. T. Snaebjornsson
Department of Anatomy, University of Iceland, Reykjavik, Iceland

M. T. Snaebjornsson · T. Holen
Department of Anatomy, University of Oslo, PO Box 1105, Blindern, 0317 Oslo, Norway

N. MacAulay (✉)
Department of Cellular and Molecular Medicine, The Panum Institute, University of Copenhagen, Blegdamsvej 3, 12.6, 2200 Copenhagen, Denmark
e-mail: macaulay@sund.ku.dk

Introduction

Aquaporin 4 (AQP4) is the principal water channel in the central nervous system. It is predominantly expressed in areas with close contact to the blood vessels or to the cerebrospinal fluid, such as the pericapillary glial endfeet and the ventricular ependymal cell lining, in which fluid exchange takes place between the brain and the blood/cerebrospinal fluid [1, 2]. The distinct polarized expression of AQP4 appears to be promoted by the basal lamina-associated extracellular matrix component, agrin [3]. During pathophysiological conditions leading to brain edema, AQP4 plays a role in the underlying brain water accumulation, either by permitting water entry into the brain parenchyma or by allowing accumulated water to exit, depending on whether the edema is of cytotoxic or vasogenic origin (reviewed in [4]).

AQP4 in brain tissue, cultured primary astrocytes, or expressed in various heterologous expression systems is

reported to be regulated by numerous protein kinases, such as protein kinase C (PKC), protein kinase A (PKA), Ca^{2+}/calmodulin-dependent kinase II (CamKII), casein kinase II (CKII), and protein kinase G (PKG) [5–11]. Phosphorylation-dependent regulation of AQP4 might thus encompass several processes, including gating, protein internalization, lysosomal targeting, and Golgi transition.

Three of the AQP4 isoforms have been demonstrated to transport water: M1 (AQP4a) consisting of 323 amino acids, the shorter M23 (AQP4c) consisting of 301 amino acids, and Mz (AQP4e) consisting of 364 amino acids [12–14]. M23 is the prevalent isoform in the mammalian brain [15] and gives rise to the square arrays detected in the astrocytic endfeet [16–18]. The isoform composition of these square arrays is currently debated [19–21]. Co-transfection of the M1 and M23 isoforms modulate the size of square arrays [16], possibly due to palmitoylation of two cysteines at positions 13 and 17, which are lacking in the shorter M23 isoform [21, 22]. The importance of these two residues for square array formation was recently challenged and new molecular determinants put forth [23].

The rationale for endogenous expression of distinct isoforms of AQP4 in the brain and the function of square arrays have remained elusive, although the adhesive properties of AQP4 between adjoining membranes expressing the M23 isoform may provide a possible explanation [24]. Previously, two conflicting reports have estimated the unit water permeability of M1 and M23 to be either identical [15] or eightfold higher in M23 compared to M1 [25]. In this study, we aimed to resolve this discrepancy, in addition to investigating possible differences in the permeability profile and phosphorylation-dependent regulation of all three AQP4 isoforms.

Materials and methods

Oocyte preparation and expression of AQP4 isoforms

Xenopus laevis frogs were obtained from Nasco (USA) or National Center for Scientific Research (France). After surgical removal of the oocytes from anesthetized frogs, the follicular membrane was removed by incubation in Kulori medium (90 mM NaCl, 1 mM KCl, 1 mM $CaCl_2$, 1 mM $MgCl_2$, 5 mM HEPES, pH 7.4, 182 mOsm) containing 10 mg/ml collagenase (type 1; Worthington, NJ, USA) and trypsin inhibitor (1 mg/ml; Sigma, Denmark) for 1 h. Subsequently, the oocytes were washed five times in Kulori medium containing 0.1% bovine serum albumin (Sigma) and incubated in 100 mM K_2HPO_4 with 0.1% BSA for 1 h. After the final oocyte collection, the frogs were anesthetized and killed by decapitation. The protocol complies with the European Community guidelines for the use of experimental animals, and the experiments were approved by The Danish National Committee for Animal Studies. The three isoforms of rat AQP4 (AQP4a, AQP4c, and AQP4e) will in the remainder of the paper be referred to as M1, M23, and Mz, respectively. Note that it is not fully resolved whether the AQP4e cDNA encodes the Mz band detected in brain lysate [14]. The cDNAs encoding the isoforms in the oocyte expression vector pXOOM were linearized downstream from the poly-A segment, and in vitro transcribed using mMessage Machine according to manufacturer's instruction (Ambion). cRNA was extracted with MEGAclear (Ambion) and microinjected into defolliculated *Xenopus* oocytes (25 ng RNA/oocyte).

Freeze fracture electron microscopy

AQP4-expressing oocytes were fixed in 0.1 M sodium cacodylate (NaCac), 2.5% glutaraldehyde, pH 7.4 for 80 min with slow shaking and subsequently stored in 0.12 M NaCac, 34% glycerol, 0.12% gluteraldehyde at 4°C. Freeze fracture was performed essentially as previously described [26]. In brief, fixed oocytes were equilibrated overnight in 25% glycerol at 4°C, attached to gold holders, and snap frozen in Freon 22 cooled in liquid nitrogen. Oocytes were fractured in a Balzer's freeze fracture apparatus (BAF 300; Balzers) at −100°C. Samples were immediately rotary shadowed at an angle of 25° with platinum and carbon replicated. The replicas were cleaned overnight in 40% chrome oxide, rinsed with water, and analyzed with a CM100 TEM microscope (FEI).

Blue native gel electrophoresis (BN-PAGE) of AQP4 isoforms expressed in HeLa cells and *Xenopus* oocytes

HeLa cells were grown in 75-cm^2 culture flasks using Dulbecco's modified Eagle medium (DMEM; Invitrogen) supplemented with 10% fetal bovine serum (FBS; Gibco) and 1% L-glutamine (Lonza). At 24 h prior to transfection, cells were seeded at a density of 20,000 cells/cm^2. FuGENE6 transfection reagent (Roche) was used at the ratio of 3:1 (FuGENE6:DNA) in accordance with the manufacturer's instructions. Then, 24 h post-transfection cells were trypsinized and suspended in 9 ml of medium before centrifugation at 1,000*g* for 10 min. Subsequently, cells were washed in 10 ml of phosphate buffered saline (PBS) and centrifuged again at 1,000*g* for 10 min. Cells from one 75-cm^2 culture flask were homogenized in 200 µl of HEPES buffer (10 mM HEPES, pH 7.4, 2 mM EDTA, 333 mM sucrose, and complete protease inhibitor cocktail; Roche) using cold mortar and pestle. The lysate was centrifuged at 1,000*g* for 10 min and the supernatant used for BN-PAGE electrophoresis. *Xenopus* oocytes and cerebellum from rat were homogenized in the HEPES buffer in the

ratio 1:10 (mg tissue: µl buffer) and the lysate was then treated as described above for the cell lysate. Next, 2–10 µg of total protein sample was mixed with 4× native PAGE sample buffer (Invitrogen) and 5% dodecyl β-D-maltoside (DDM) to a final concentration of 1× sample buffer and 1% DDM in a volume of 20 µl. Samples were incubated at RT for 10 min and then centrifuged for 10 min at 10,000*g*. After centrifugation, the supernatant was mixed with Coomassie G-250 1:4 (Coomassie G-250:DDM). Samples were loaded on a 4–16% BN-PAGE Bis–Tris gradient gel. NativeMark unstained protein standard (Invitrogen) was used as a molecular weight marker. Electrophoresis was carried out at 150 V, with the dark cathode buffer (5% 20× running buffer and 5% cathode additive; both Invitrogen) for the first 20 min, and with the light cathode buffer (5% 20× running buffer, 0.5% cathode additive) for the next 140 min. The anode buffer was the same as the cathode buffer but contained no cathode additive. Gels were then blotted to PVDF membranes and probed with AQP4 antibodies, as described previously [20].

Osmotic water permeability measurements on *Xenopus* oocytes

The osmotic water permeability measurements were performed as previously described [27]. During the measurements, the membrane potential of the oocytes was measured by two-electrode voltage clamp with a Dagan Clampator interfaced to an IBM-compatible PC using a Digidata 1322 A/D converter and pClamp 9.2 (Axon Instruments). The oocyte was placed in a small chamber with a glass bottom, through which the oocyte could be viewed via a long distance objective (×4) and a CCD camera. To quantify the oocyte volume changes, oocyte images were captured and processed as previously described in detail [27]. The experimental chamber was perfused by a control solution (100 mM NaCl, 2 mM KCl, 1 mM $CaCl_2$, 1 mM $MgCl_2$, 10 mM HEPES, pH 7.4) and hypertonic test solution which was obtained by adding 20 mOsm of mannitol to the control solution. For measurements of the reflection coefficients, the mannitol was replaced with equiosmolar urea, glycerol, or formamide. Osmolarities of the test solutions were determined with an accuracy of 1 mOsm by a cryoscopic osmometer (Gonotec, Berlin, Germany). For the experiments with 8 mM K^+, the control 2 mM K^+ solution contained an additional 6 mM choline chloride to keep the two control solutions equiosmolar. Phorbol 12-myristate 13-acetate (PMA) was obtained from Sigma–Aldrich. The osmotic water permeability is given in units of (cm/s) and was calculated as $L_p = -J_v/A \times \Delta\pi \times V_w$, where J_v is the water flux during the osmotic challenge, A is the true membrane surface area (about nine times the apparent area due to membrane foldings [28]), $\Delta\pi$ is the osmotic challenge, and V_w is the partial molal volume of water, 18 cm^3/mol.

Immunoblotting on *Xenopus* oocytes

The preparation of oocyte plasma membranes was modified from [29] and has been recently described in detail [30]. In brief, total oocyte membranes were obtained by homogenization (with a p200 pipette) of two oocytes in 1 ml HbA+ buffer: 5 mM $MgCl_2$, 5 mM NaH_2PO_4, 1 mM EDTA, 80 mM sucrose, 20 mM Tris, pH 7.48, containing the protease inhibitors leupeptin (8 µM) and pefabloc (0.4 mM). The supernatant was recovered following 10 min centrifugation at 250*g* and subsequently centrifuged at 14,000*g* for 20 min to obtain the total membrane fraction. The pellets were resuspended in 20 µl HbA+ followed by addition of 5 µl of 5× sample buffer (7.5% SDS, 250 mM Tris (pH 6.8), 30% glycerol, bromphenol blue, and 60 mg/ml DTT) and heated at 65°C for 15 min. Plasma membranes were obtained from a minimum of 15 oocytes for each construct/condition. The oocytes were treated as previously described [29] prior to homogenization and consecutive centrifugation steps [30]. Total oocyte membranes and purified plasma membranes were subjected to immunoblotting using rabbit polyclonal anti-AQP4 antibody (Alamone Labs, Israel), 1:1,000. Sites of antibody–antigen reaction were visualized using an enhanced chemiluminescence substrate (GE Healthcare, Denmark) before exposure to light-sensitive film. Numerous film exposures were performed to be certain that the linearity of the film was not exceeded. The band densities were quantified by densitometry.

Immunocytochemistry and confocal laser scanning microscopy on *Xenopus* oocytes

The oocytes were fixed for 1 h in 3% paraformaldehyde in Kulori medium, rinsed in Kulori medium, dehydrated in a series of ethanol concentrations (40 min in 70, 96, and 99% ethanol) and incubated in xylene for 1 h. Oocytes were infiltrated with paraffin for 1 h at 50°C before embedding. Next, 2-µm sections were cut on a Leica RM 2126 microtome and immunostained as described previously [31] using rabbit polyclonal anti-AQP4 antibody. An Alexa 488-conjugated secondary antibody was used for visualization (DAR; Invitrogen). A Leica TCS SL confocal microscope and Leica confocal software were used for imaging of the oocytes. Control AQP4-expressing oocytes were used to set laser intensity and capture settings on the microscope such that saturation of images for each condition was avoided. The microscope and laser settings were kept constant within each experiment. Images were taken

using an HCX PL APO ×63 oil objective lens. A minimum of two images per oocyte, with 3–5 oocytes per experiment, were used for statistical analysis. Image semi-quantification and validation has recently been described in detail [30]. To facilitate comparisons between experiments and between individual oocytes, plasma membrane fluorescence was normalized to total oocyte fluorescence.

Water permeability measurements in mammalian cells

A human bronchial epithelial cell line BEAS-2b (European Collection of Cell Cultures, Center for Applied Microbiology and Research, Salisbury, Wiltshire, UK; subpassages 8–16) was cultured on coverslips (Bioptechs, Butler, PA) coated with collagen type I and fibronectin (Sigma–Aldrich Sweden) in Dulbecco's MEM/NUT MIX F-12 (1:1) medium (Gibco, Paisley, Scotland, UK) containing 0.5 U/ml penicillin, 50 μg/ml streptomycin, and supplemented with 10% heat-inactivated FBS and 2 mM L-glutamine. On the second day of culture, the cells were transiently transfected using CLONfectin (Clontech) according to the manufacturer's protocol. cDNA constructs used for the transfection were described previously [32]. cDNA fragments encoding human AQP4 M1 and AQP4 M23 were subcloned into the pIRES2-EGFP vector (Clontech). The resulting constructs expressed AQP4 and GFP as separate proteins in the same cell. Experiments were performed on the fourth day of culture. Cells positive for AQP4 M1 and M23 were identified by GFP fluorescence. The GFP signal was distributed evenly in the cytoplasm of the cells. The cells positive for AQP4 M1 and M23 were not different in morphology compared to each other or to the untransfected cells.

Water permeability of the cells was measured as previously described [7, 11, 33]. Briefly, the cells were mounted in a closed chamber on the stage of an inverted confocal laser scanning microscope in isoosmotic, 300 mOsm PBS. The cells were loaded with 20 μM calcein-AM (Molecular Probes; Invitrogen) for 5 min at RT. Loading with calcein was similar in transfected and untransfected cells. The cells were perfused with isosmotic PBS and scanned every 1.8 s with excitation at 488 nm. The fluorescent signal was collected at 515–525 nm from an optical slice within the cell body. The cells were then subjected to an osmotic shock by switching the perfusate to a hypoosmotic, 200 mOsm, PBS, obtained by omission of 50 mM NaCl from the isosmotic solution. The swelling of the cells was monitored as a decrease of calcein fluorescence, which occurred due to the dilution of the fluorophore and a reduction in self-quenching. The initial slope of the fluorescence intensity curve was used to calculate water permeability (P_f) of each cell as described in detail previously [7, 11, 32, 33]. The P_f of all cells in each experiment was expressed relative to the mean maximal P_f in cells transfected with M1.

Osmolyte uptake measurements in *Xenopus* oocytes

The uptake of osmolytes was measured using radioactively labeled compounds. The experiments were performed in 24-well plates (five oocytes/condition) containing 500 μl test solution (100 mM NaCl, 2 mM KCl, 1 mM $CaCl_2$, 1 mM $MgCl_2$, 10 mM HEPES, pH 7.4) containing 20 mOsm of the unlabeled osmolyte and trace amounts of [^{14}C]mannitol, [^{14}C]urea, [^{14}C]glycerol, or [^{14}C]formamide (Amersham, UK). The oocytes were pre-incubated in control solution containing 20 mOsm of non-permeable sucrose in order to avoid imposing an osmotic challenge at the initiation of the uptake experiment. The oocytes were incubated in the test solution for 5 min at RT with gentle shaking, washed four times in ice-cold test solution without the radioactive osmolytes, and dissolved individually in 200 μl 10% SDS. Finally, 2 ml scintillation fluid (Opti-fluor; Packard, Netherlands) was added and the samples counted in a scintillation counter (Packard Tri-Carb).

Data are presented as mean ± SE for n = number of cells. Student's t test has been used for the statistical analysis.

Results

Three isoforms of AQP4 (M1, M23, and Mz) were individually expressed in *Xenopus* oocytes to investigate possible differences in their functional properties. This expression system is widely used to assess relative unit water permeability and solute permeability of different aquaporins (see, e.g., [30, 34]). Expression of the AQP4 isoforms increased the water permeability of the oocytes from (in $\times 10^{-3}$ cm/s) 0.10 ± 0.01 ($n = 19$) for the non-injected oocytes to 1.47 ± 0.05 ($n = 37$) for M1, 1.60 ± 0.11 ($n = 37$) for M23, and 1.31 ± 0.06 ($n = 37$) for Mz.

Formation of square arrays

To validate the use of *Xenopus* oocytes as an expression system for this comparative study, we explored the ability of AQP4 isoforms to form square arrays in oocytes by performing freeze fracture electron microscopy. As shown in Fig. 1a, b, and c, highly ordered structures characteristic of square arrays were visible in M23-expressing oocytes (P-face as well as E-face). These arrays were only apparent at the oocyte plasma membrane (electronic

supplementary material, Fig. 1). Due to the extensive invaginations of the *Xenopus* oocyte membrane [28], only sporadic patches of plasma membrane were in the plane of the fracture, which excluded quantitative studies of the array formation. No ordered structures were observed in oocytes expressing M1 and Mz (Fig. 1d, e). In addition, we analyzed M1-, M23-, and Mz-expressing oocytes using blue native poly-acryl gel electrophoresis (BN-PAGE) that was recently established as a biochemical assay to visualize AQP4 higher order structures [20]. As shown in Fig. 1f, the M23 isoform, whether heterologously expressed in HeLa cells or *Xenopus* oocytes, gave rise to the higher order structures that are the hallmark of the square arrays and also apparent in rat cerebellum. The M1 and Mz isoforms did not form higher order structures when expressed in HeLa cells or in *Xenopus* oocytes. Thus, in *Xenopus* oocytes, AQP4 assembles similarly to native tissue, making oocytes a suitable model for functional studies.

Relative unit water permeability of AQP4 isoforms expressed in *Xenopus* oocytes

The relative unit water permeability of M1 and M23 is debated [15, 25] and we therefore set out to resolve this issue. We have recently established sensitive methods to estimate the relative unit water permeability of different aquaporins [30] in which the water permeability of the AQP-expressing oocyte is normalized to the abundance of the AQP in the oocyte plasma membrane. We determined the water permeability of oocytes expressing M1, M23, or Mz by exposing the oocytes to an osmotic challenge of 20 mOsm mannitol (added to the control solution) (Fig. 2a). The water permeability of the native oocyte membrane (<10% of the total L_p) was deducted in order to obtain the contribution from each AQP4 (in $\times 10^{-3}$ cm/s): 1.15 ± 0.04 for M1 ($n = 25$), 1.17 ± 0.09 for M23 ($n = 25$), and 1.07 ± 0.05 for Mz ($n = 20$) for a total of 4–5 batches, which were not significantly different from

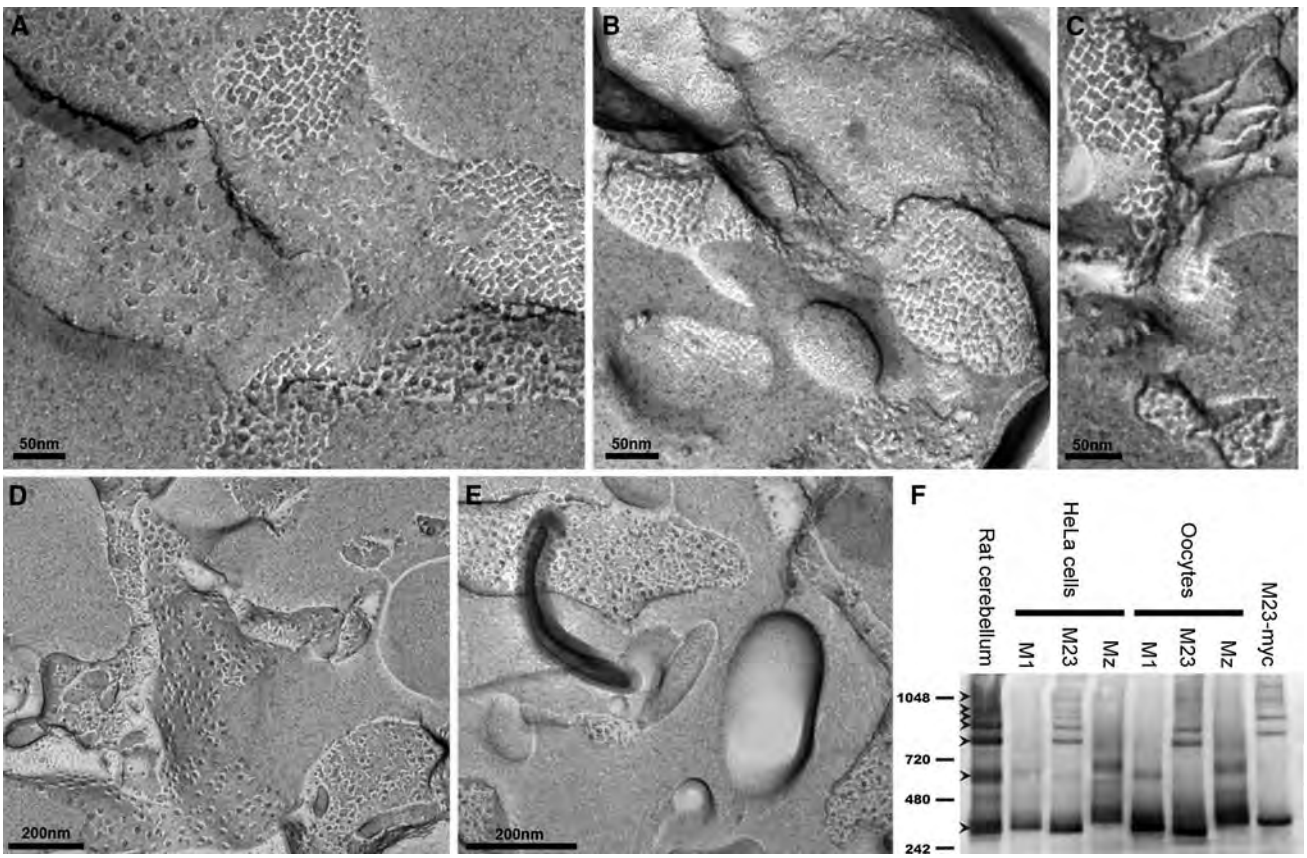

Fig. 1 The M23 isoform forms square arrays in *Xenopus laevis* oocytes. **a–c** At the plasma membrane, highly ordered structures characteristic of square arrays are observed for the M23 isoform. In contrast, neither the M1 isoform (**d**) nor the Mz isoform (**e**) show similar ordered structures. **f** BN-PAGE analysis of AQP4. In contrast to the M1 and Mz isoforms, the M23 isoform forms higher molecular weight moieties in both HeLa cells and *Xenopus* oocytes. *Lane 1* brain lysate (rat cerebellum), *lanes 2–4* M1, M23, and Mz expressed in HeLa cells, *lanes 5–7* M1, M23, and Mz expressed in *Xenopus* oocytes. Control M23-myc expressed in HeLa cells also exhibited higher order bands (*lane 8*). Molecular weight markers are indicated to the *left*, in kDa. The lower tetramer band and six higher order bands are indicated by *arrowheads*

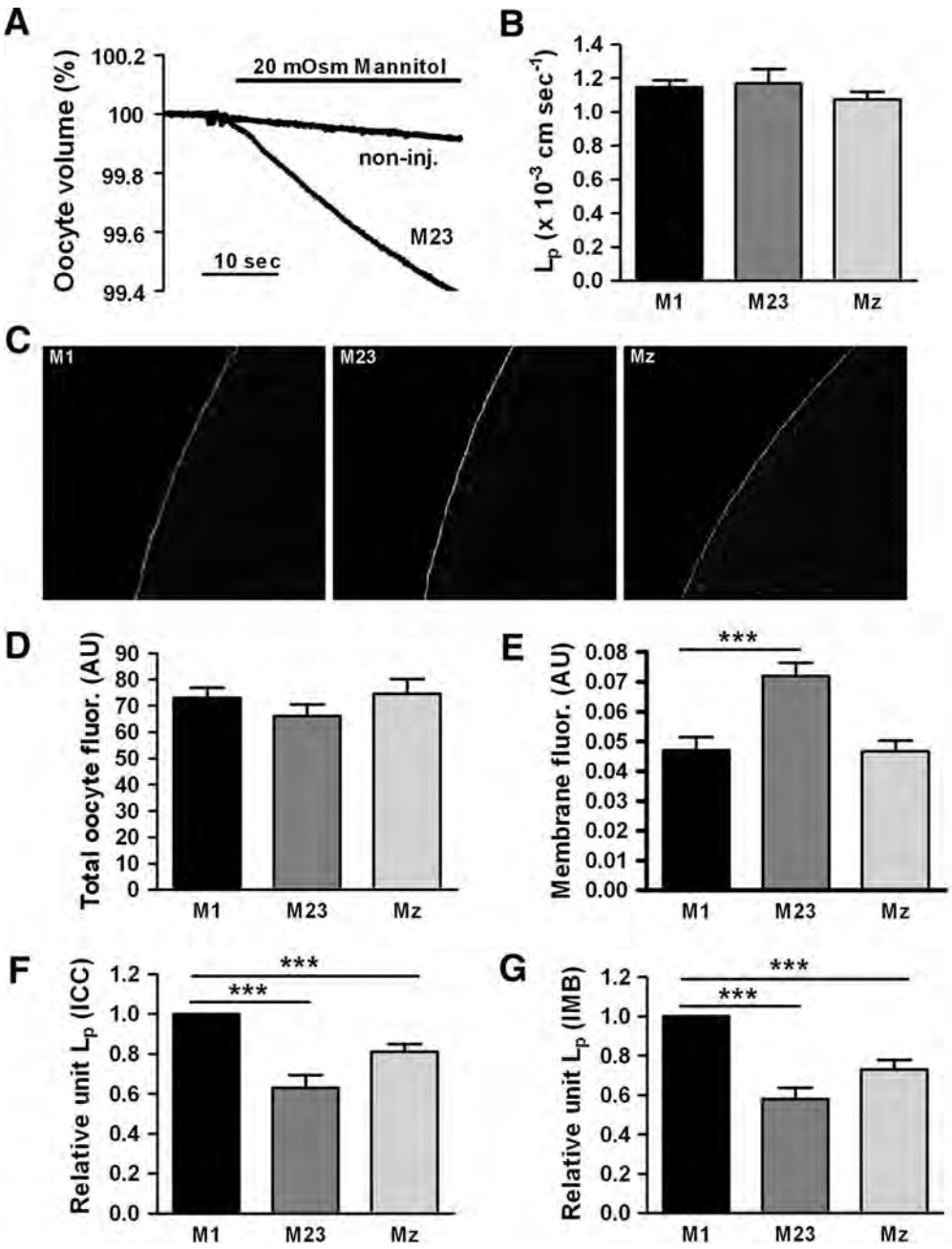

Fig. 2 The relative unit water permeability of M1, M23, and Mz expressed in oocytes. **a** An oocyte expressing the M23 isoform and a non-injected oocyte (with L_ps of 1.14 and 0.11×10^{-3} cm/s, respectively) were challenged with an osmotic gradient of 20 mOsm mannitol for 30 s. **b** The average water permeability of oocytes expressing M1, M23, or Mz with the contribution of the native oocyte membrane deducted ($n = 20$–25 of each). **c** Representative confocal laser scanning microscopy of oocytes expressing M1, M23 and Mz immunolabeled for AQP4. **d** Oocyte total fluorescent counts (in arbitrary units) were used to asses the abundance of AQP4 in oocytes expressing the three isoforms ($n = 15$–20 of each). **e** Oocyte plasma membrane fluorescent counts (in arbitrary units) were used to asses the AQP4 abundance in the plasma membrane of oocytes expressing the three isoforms ($n = 15$–20 of each). **f** Normalized relative unit water permeability of the three isoforms based on quantification by immunocytochemistry ($n = 4$–5 experiments based on 3–5 oocytes of each). **g** Normalized relative unit water permeability of the three isoforms based on quantification by immunoblotting of purified plasma membranes ($n = 3$ experiments, each based on $n = 5$ oocytes of each isoform for the L_p determination and $n = 20$ oocytes of each isoform for the plasma membrane purification). ***$P < 0.001$ (compared to M1)

each other (Fig. 2b). Subsequently, we determined the relative abundance of AQP4 protein in each oocyte (total abundance and plasma membrane abundance) by immunolabeling of the same oocytes employed for the L_p measurements using an anti-AQP4 antibody that recognizes the C-terminal part of the protein. Representative confocal images of the immunostained oocytes are shown in Fig. 2c. Semi-quantification of the images for each isoform revealed a similar amount of total fluorescent counts corresponding to total AQP4 protein in the oocytes (Fig. 2d), whereas the plasma membrane abundance differed between the isoforms, with M23 demonstrating a significantly larger fraction of the total protein in the plasma membrane ($P < 0.001$): (in arbitrary units, average of all oocytes used in the 4–5 batches of oocytes used in the dataset): 0.047 ± 0.004 for M1 ($n = 20$), 0.072 ± 0.004 for M23 ($n = 18$), and 0.047 ± 0.004 for Mz ($n = 18$) (Fig. 2e).

To compare the unit water permeability of the three isoforms, the water permeability relative to the plasma membrane abundance was calculated for *each* experiment (batch of oocytes) after which it was normalized to M1 and

then averaged. As shown in Fig. 2f, the relative unit water permeability of M23 was significantly lower than M1 ($P < 0.001$). The relative unit water permeability of Mz was intermediate and significantly lower than M1 ($P < 0.001$): 1.00 ± 0.00 for M1, 0.63 ± 0.07 for M23, and 0.81 ± 0.04 for Mz ($n = 4$–5 experiments with 3–5 oocytes expressing each isoform). To verify these results, we performed immunoblotting of total oocyte membranes and purified plasma membranes from M1-, M23-, and Mz-expressing oocytes day-matched with water permeability measurements on the same batch of oocytes. The total expression of AQP4 was similar for M1-, M23-, and Mz-expressing oocytes (data not shown) but in accordance with the immunostaining data, the M23 abundance was increased in the plasma membrane (data not shown). The relative unit water permeability of the different isoforms was calculated based on the densitometry of the immunoblotting of the purified plasma membranes (Fig. 2g): 1.00 ± 0.00 for M1, 0.58 ± 0.06 for M23, and 0.73 ± 0.05 for Mz ($n = 3$ experiments, each based on $n = 5$ oocytes for L_p measurement and $n = 20$ oocytes for membrane preparation for each isoform), thus confirming the reduced relative unit water permeability of the M23 isoform.

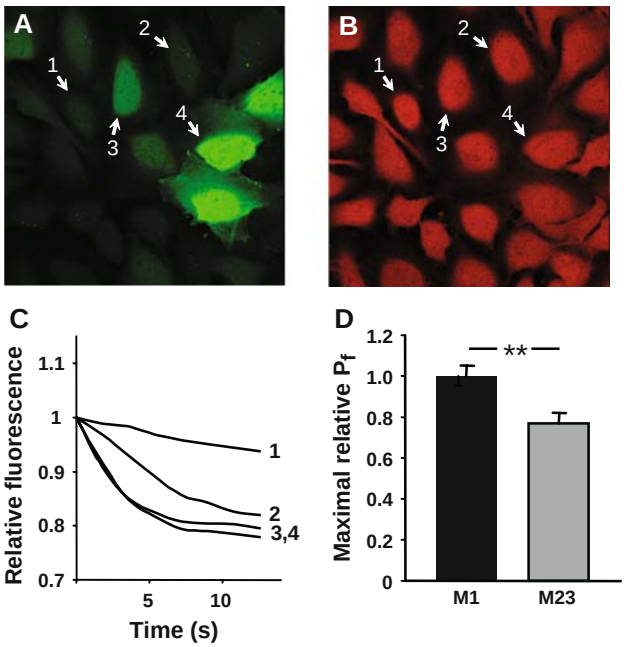

Fig. 3 The relative unit water permeability of M1 and M23 in transfected human bronchial epithelial cell line. **a** The level of GFP fluorescence within the cells. **b** Loading with calcein, which was used for water permeability measurements, was similar in AQP4-positive and AQP4-negative cells. *Numbers* indicate the same cells before (**a**) and after (**b**) calcein loading. **c** Single cell traces showing the dilution of calcein due to the cell swelling after an osmotic challenge. In cells with low GFP (and hence AQP4) expression (cells 1–3 in **a**), the swelling rate was increasing (*line 1* through *line 3* in **c**) with the increase in GFP (AQP4) level. The swelling of the cells 3 and 4 occurred at practically identical speed, probably due to saturation of the plasma membrane with AQP4. **d** Maximal relative water permeability in cells expressing M1 ($n = 22$) and M23 ($n = 13$), $^{**}P < 0.01$

Water permeability of AQP4 isoforms expressed in mammalian cells

To exclude the possibility that the reduced water permeability of M23 compared to M1 was specific to *Xenopus* oocytes as an expression system, we compared the relative water permeability of M1 and M23 in a bronchial epithelial cell line. The cells were transiently transfected with cDNA constructs that in each transfected cell produced two separate proteins, AQP4 and green fluorescent protein (GFP). GFP, which is a compact water soluble protein, was distributed throughout the cytoplasm and the nucleus of transfected cells (Fig. 3a). The cells with a weaker GFP signal demonstrated low water permeability, as judged from a low rate of swelling after hypoosmotic challenge (Fig. 3a, cell 1, and Fig. 3c, line 1). The cells with a stronger GFP signal had a higher water permeability (Fig. 3a, cells 2, 3, and Fig. 3c, lines 2, 3). With further increase in GFP expression, the rate of the swelling did not increase any further and the swelling of the cells 3 and 4 (Fig. 3a) occurred at practically identical speed (Fig. 3c), probably due to a saturation of the capacity of the plasma membrane to accommodate the water channels. The relative maximal P_f values that could be achieved in cells transfected with the M1 isoform were significantly higher than those in cells transfected with M23: 1.00 ± 0.05 for M1 ($n = 22$ cells) and 0.77 ± 0.05 for M23 ($n = 13$ cells), $P < 0.01$ (Fig. 3d).

Sensitivity to external K^+-concentration

To investigate a possible effect of K^+ on the water permeability of M1-, M23-, and Mz-expressing oocytes, we compared the water permeability in test solutions containing 8 mM KCl to the water permeability obtained in the presence of 2 mM KCl. In this experiment, oocytes had L_ps of (in $\times 10^{-3}$ cm/s) 1.63 ± 0.19 for M1, 2.38 ± 0.19 for M23, 1.37 ± 0.25 for Mz ($n = 5$ of each), and 0.10 ± 0.01 for non-injected oocytes ($n = 4$). The L_p of each oocyte was assessed at both K^+ concentrations and thereby served as its own control. The data are therefore presented as the ratio between the L_p obtained at 8 mM KCl and the L_p obtained at 2 mM KCl (Fig. 4). The water permeability of the three isoforms and the non-injected oocytes showed no significant degree of K^+-dependence; $L_{p(8K)}/L_{p(2K)}$: 0.98 ± 0.02 for M1, 1.01 ± 0.01 for M23, 1.05 ± 0.02 for Mz ($n = 5$ of each), and 1.02 ± 0.02 for non-injected oocytes ($n = 4$).

Solute permeability profile

To explore if M1-, M23-, or Mz-expressing oocytes were permeable to urea, glycerol, or formamide, we determined the L_p with 20 mOsm of each of these osmolytes and related them to the L_p obtained with the larger osmolyte, mannitol, to obtain the reflection coefficient, σ. These oocytes had L_ps of (in $\times 10^{-3}$ cm/s) 1.93 ± 0.12 for M1, 2.10 ± 0.41 for M23, 1.78 ± 0.33 for Mz ($n = 4$ of each), and 0.09 ± 0.02 for non-injected oocytes ($n = 3$). The reflection coefficients were identical for the three isoforms and the non-injected oocytes, which indicated that AQP4, independent of the isoform, was not permeable to these small molecules (Fig. 5a). The reflection coefficient was reduced for formamide, both for AQP4-expressing oocytes and for the non-injected oocytes, indicating that the native oocyte plasma membrane is slightly permeable to formamide. As a very low permeability to the osmolyte would not be detectable by this method, we performed uptake experiments using radio-labeled ^{14}C-mannitol, ^{14}C-urea, ^{14}C-glycerol, and ^{14}C-formamide (Fig. 5b). The pattern of the solute uptake by oocytes expressing M1, M23, Mz, and non-injected oocytes was identical to that observed for the reflection coefficients; expression of any of the three isoforms did not confer an increased permeability of the oocyte to any of these solutes ($n = 4$ experiments, 5 oocytes per condition).

PKC-dependent regulation

AQP4 is downregulated by PKC [8, 11, 35, 36] which we have found to be due to internalization of the protein [35].

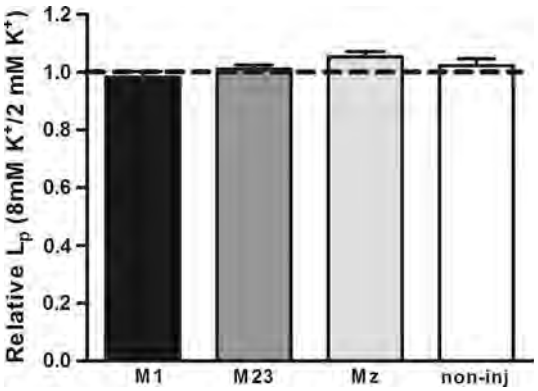

Fig. 4 Lack of K^+-dependent water permeability in M1, M23, and Mz-expressing oocytes. Oocytes expressing the three different isoforms were voltage-clamped to −50 mV to avoid K^+-dependent changes in membrane potential and exposed to test solution containing the standard 2 mM K^+ (+6 mM Ch^+) in which the L_p was determined. Subsequently the same oocyte was exposed to a test solution containing 8 mM K^+ in which the L_p was determined. The data are presented as the L_p obtained in 8 mM K^+ relative to that obtained in 2 mM K^+ ($n = 4$ of each)

Here, we investigated the rate of PKC-dependent downregulation of the three different isoforms. For each oocyte, the membrane-permeable PKC-activator, PMA (1 nM), was added to the test solution after determination of the oocyte basal water permeability. In this way, each oocyte was its own control and variations in the expression level did not affect the data. The L_p of the oocytes employed in this set of experiments was (in $\times 10^{-3}$ cm/s): 1.36 ± 0.07

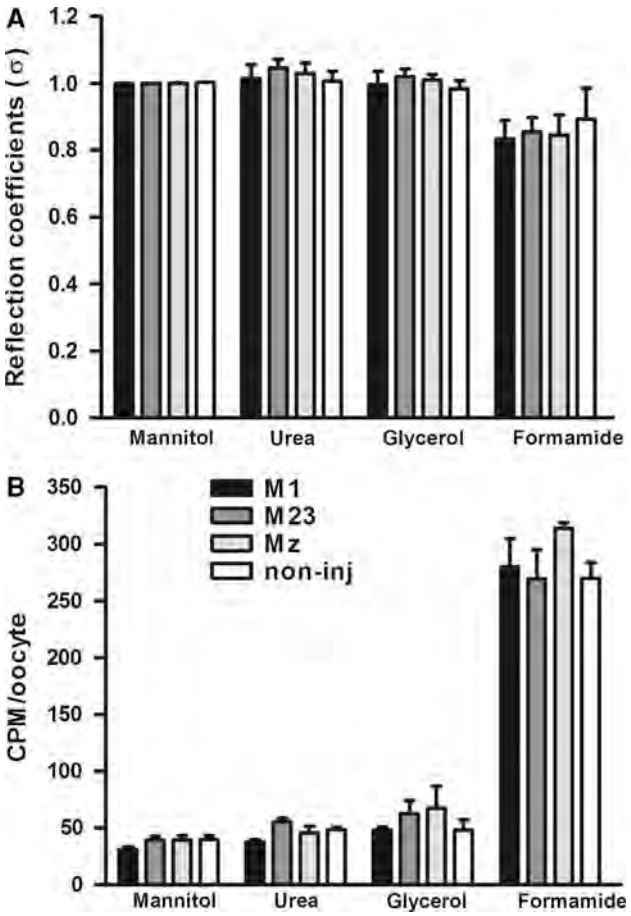

Fig. 5 Lack of permeability to small osmolytes in M1, M23, and Mz-expressing oocytes. **a** The L_p of oocytes expressing M1, M23, and Mz as well as non-injected oocytes was determined with different osmolytes; mannitol, urea, glycerol, and formamide (20 mOsm of each). The L_p obtained with urea, glycerol, and formamide was plotted relative to that obtained with mannitol for each oocyte (reflection coefficient, σ). The reflection coefficients for oocytes expressing M1, M23, or Mz were not significantly different from that of the non-injected oocytes ($n = 4$ of each isoform and $n = 3$ for the non-injected oocytes). **b** Oocytes expressing M1, M23, and Mz as well as non-injected oocytes were exposed to test solution containing different osmolytes; mannitol, urea, glycerol, and formamide (20 mOsm of each) in addition to trace amounts of the [^{14}C]-labeled osmolyte. The data are presented as the average uptake of four experiments performed in pentaplicate, with no significant difference between oocytes expressing the three isoforms and the non-injected oocytes

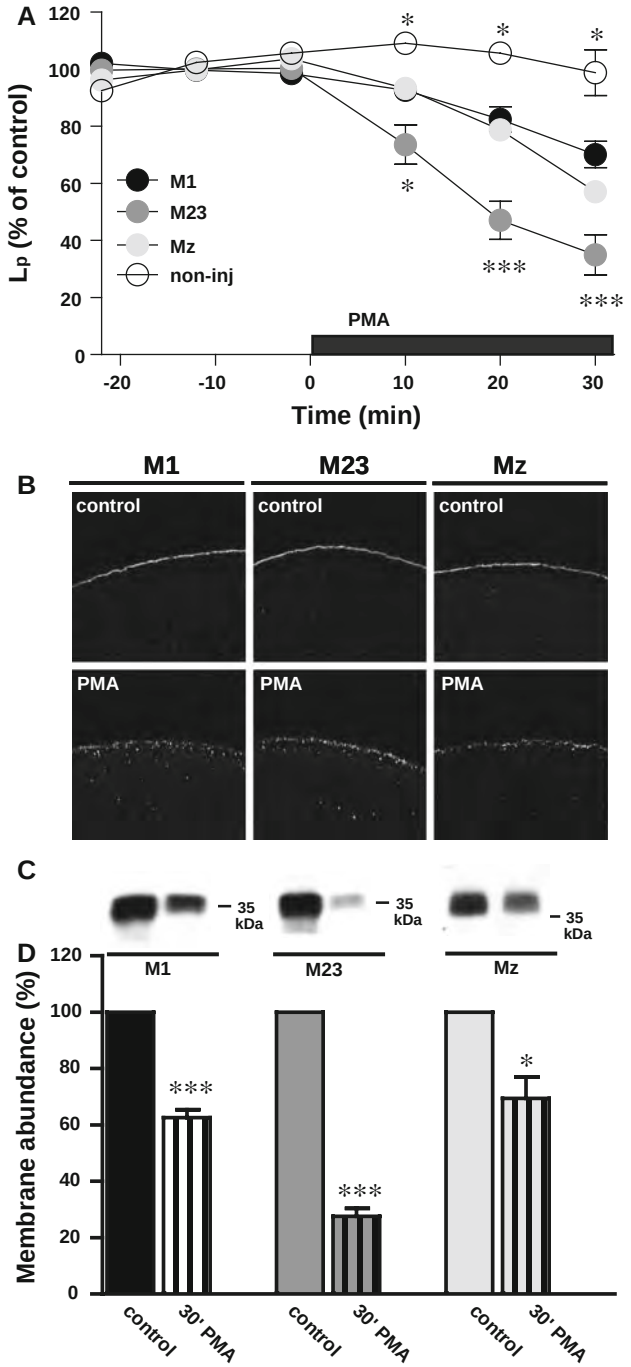

◀ **Fig. 6** PKC-dependent down-regulation of AQP4. **a** The relative water permeability of oocytes expressing M1, M23, or Mz or non-injected oocytes as a function of time. 1 nM PMA was included in the external solution as marked by the *black bar*. After 30 min of PMA treatment, the L_p was reduced to (in % of control) for M1; 70 ± 5 ($n = 8$), M23; 35 ± 7 ($n = 7$), Mz; 57 ± 4, error bar within the symbol ($n = 9$), and non-injected; 99 ± 8 ($n = 3$). The significance levels on the graph refer to M1, $^*P < 0.05$, $^{***}P < 0.001$. **b** Representative confocal laser scanning microscopy of oocytes expressing M1, M23, and Mz immunolabeled for AQP4 without (*upper panels*) or with (*lower panels*) 30 min PMA treatment (1 nM). **c** Representative immunoblot of plasma membrane purification of oocytes expressing M1, M23, or Mz in control condition and after 30 min of PMA treatment (1 nM), minimum 15 oocytes for each condition. **d** Relative membrane abundance of M1, M23, and Mz was assessed by densitometry of the immunoblots as presented in panel (**c**) of oocytes with control treatment or 30 min PMA treatment (1 nM). 15–20 oocytes were used for each condition ($n = 3$ experiments), $^*P < 0.05$, $^{***}P < 0.001$. The M23-expressing oocytes had a significantly lower AQP4 abundance in the plasma membrane after PMA treatment compared to M1 and Mz, $P < 0.01$

for M1 ($n = 8$), 1.40 ± 0.15 for M23 ($n = 8$), 1.19 ± 0.08 for Mz ($n = 9$), and 0.05 ± 0.01 for non-injected oocytes ($n = 3$). Figure 6a shows the PMA-dependent reduction of the L_p for the various isoforms of AQP4. The water permeability of oocytes expressing the three isoforms were down-regulated in response to PMA, but M23-expressing oocytes showed a faster and more pronounced down-regulation than M1- and Mz-expressing oocytes, with the non-injected oocytes being insensitive to PMA treatment. The significance levels on the graph refer to the M1 isoform. After 30 min of PMA treatment, the L_p was (in % of control); 70 ± 5 ($n = 8$) for M1, 35 ± 7 ($n = 7$) for M23, 57 ± 4 ($n = 9$) for Mz, and 99 ± 8 ($n = 3$) for the non-injected oocytes. To visualize the predicted PMA-dependent internalization of AQP4, immunocytochemistry was performed with the C-terminal anti-AQP4 antibody on oocytes expressing M1, M23, or Mz incubated for 30 min in control solution with or without 1 nM PMA ($n = 11$–14 of each). Representative confocal images clearly demonstrate appearance of AQP4 in intracellular vesicles, indicating PMA-dependent internalization of all three isoforms (Fig. 6b). In order to quantify the level of internalization, we prepared purified plasma membranes of M1-, M23-, and Mz-expressing oocytes after 30 min incubation in control solution with or without 1 nM PMA. The purified plasma membranes were immunoblotted with the anti-AQP4 antibody, representatives of which are shown in Fig. 6c. A summary of the densitometry is shown in Fig. 6d. After 30 min of PMA treatment, the amount of AQP4 left in the plasma membrane (in % of control) was 63 ± 3 for M1, 28 ± 3 for M23, and 69 ± 8 for Mz ($n = 3$ experiments with 15–20 oocytes for each condition per experiment). For all isoforms, PMA-dependent reduction in plasma membrane abundance was significantly different from control ($P < 0.001$ for M1 and M23 and $P < 0.05$ for Mz) and the PMA-dependent internalization of M23 was in addition significantly more pronounced than that of M1 and Mz ($P < 0.01$). PMA reduced the water permeability (Fig. 6a) and the membrane abundance of AQP4 (Fig. 6d) to the same extent for all three isoforms, suggesting that the effect of PKC on AQP4 may be due to the level of AQP4 internalization and not to a direct effect on channel function.

Discussion

In the present study, we investigated functional parameters of three isoforms of AQP4. All three isoforms were strictly permeable to water and did not allow permeation of smaller osmolytes, which is in agreement with previous studies performed on M1 and/or M23 [13, 34, 37], but has not previously been shown for Mz. The water permeability did not alter with the membrane potential and electrophysiological experiments were unable to detect any ionic conductance through either of the three isoforms (data not shown).

The large square arrays observed in freeze fracture replicas of perivascular glial endfeet [17] can be reconstituted in cell-line models by transfection of the M23 isoform of AQP4 [16, 18]. To validate the *Xenopus* expression system used here for functional comparison of AQP4 isoforms, it was necessary to investigate the formation of square arrays in this cell type. To this end, we performed freeze fracture studies of oocytes expressing the three isoforms. Expression of the M23 isoform in oocytes gave rise to square arrays, while the M1 or Mz failed to induce the formation of these higher order structures. To exclude the possibility that putative square arrays could have been overlooked in the M1- and Mz-expressing oocytes due to the membrane invaginations [28], we employed a newly developed biochemical assay for studying higher order AQP4 structures, BN-PAGE [20]. This method confirmed that M23, but not M1 and Mz, was organized in the high-molecular weight complexes when expressed in either *Xenopus* oocytes or HeLa cells. Taken together, our freeze fracture and BN-PAGE experiments validated our use of *Xenopus* oocytes for functional analysis of the three AQP4 isoforms.

The relative unit water permeability of the M1 and M23 isoforms has been debated in several studies. Experiments using heterologous expression of M1 and M23 in *Xenopus* oocytes have demonstrated identical water permeability of oocytes expressing M1 or M23 [13, 15], although the membrane abundance of AQP4 was not quantified in these studies. A conflicting study has reported an eightfold higher water permeability of the M23 isoform compared to the M1 isoform LLC-PK1 cells [25]. Comparative determination of the water permeability in the latter study may have been complicated by the large variability in size of the LLC-PK1 cells, which was dependent on the AQP4 isoform expressed, and the fact that the calculation of the water permeability was based on an assumption of the LLC-PK1 cells being spherical. In the present study, the overall water permeability of oocytes expressing the different AQP4 isoforms was similar, which is in agreement with the previous studies performed on *Xenopus* oocytes [13, 15]. In addition, the *total* abundance of AQP4 was similar for the three isoforms, although the M23 isoform had a significantly higher *plasma membrane* abundance compared to the other isoforms. The plasma membrane abundance was assessed with immunocytochemistry as well as with immunoblotting of purified plasma membranes to rule out possible isoform-specific differences in antibody binding, i.e., steric hindrance upon square array formation. Relating the water permeability of M1-, M23-, and Mz-expressing oocytes to the amount of AQP4 in the plasma membrane revealed that the relative unit water permeability of the M23 isoform was $\sim$40% lower than that of M1 while Mz was intermediate in its water permeability ($\sim$20% lower than M1).

To exclude the possibility that the lower relative water permeability of M23 was specific to the oocyte expression system, the difference between the water permeability of M1 and M23 was investigated in a mammalian expression system. In these experiments, the maximal water permeability of M23-expressing cells was also lower than that of M1-expressing cells, which is in agreement with our oocyte data. However, the membrane abundance of the two isoforms was not quantified in this set of data nor in a previous study on COS-7 cells transfected with c-myc-tagged M1 or M23 [19] in which a similar result was obtained. Taken together, in contrast to [25], but in agreement with [19], our results suggest that the unit water permeability of M23 is lower than the other isoforms.

In astrocytes and retinal Müller cells, AQP4 is extensively co-localized with the inwardly rectifying K^+ channel Kir4.1 [38, 39]. The co-localization of a K^+ channel with an aquaporin has warranted suggestions that AQP4 might facilite K^+ clearance from the perisynaptic space [38, 39]. To that effect, it has indeed been shown that mice lacking either AQP4 itself [40] or the endfoot-specific localization of AQP4 [41] had a slower K^+ clearance and therefore more intense and longer lasting experimentally induced seizures. However, the functional characteristics of Kir4.1 in freshly isolated glial cells were not altered by genetic deletion of AQP4, which suggests that Kir4.1 is not directly affected by its co-localization with AQP4 [42, 43]. Our recent studies showed that Kir4.1 was activated by cell swelling, and that AQP4 thereby may pose an indirect effect on the activity of Kir4.1 [44]. The question then arose if the water permeability of AQP4 could be affected by the increase in external K^+ concentration that inevitably leads to glial cell swelling [45, 46]. Increasing the K^+ concentration in the test solution from 2 to 8 mM did not alter the water permeability of M1-, M23-, or Mz-expressing oocytes, which bears evidence of AQP4 being insensitive to increase in external K^+ concentration (at least in the range tested).

AQP4 is regulated by several protein kinases with various effects on the protein, such as gating, internalization,

trafficking to the plasma membrane, and lysosomal targeting [5–11]. PKC has been shown to phosphorylate AQP4 directly in rat brain homogenate [8] and in AQP4-expressing glioma cells [36], although this was not apparent in mouse primary cultured astrocytes [9]. PKC activation down-regulates the water permeability of AQP4 expressed in a mammalian cell line, glioma cells, or in *Xenopus* oocytes [8, 11, 35, 36]. We recently showed that the PKC-dependent reduction of the water permeability of AQP4-expressing *Xenopus* oocytes was due to internalization of AQP4 [35]. In the present study, it was evident that the water permeability of the M23-expressing oocytes was significantly more sensitive to PKC activation than oocytes expressing the longer isoforms. Importantly, PKC-dependent AQP4 internalization was also more prominent with the M23 isoform. There was no significant difference between the PMA-dependent reduction in water permeability and the PMA-dependent level of internalization for any of the three isoforms, suggesting that the effect of PKC on AQP4 is primarily due to the level of AQP4 internalization and not to a direct effect on channel function. The increased PKC sensitivity of the M23 isoform suggests a function for the organization of AQP4 isoforms into large square arrays. One may speculate that, after phosphorylation of AQP4, the internalization machinery will be able to retrieve more units of AQP4 per unit of adaptor proteins if AQP4 is organized into square arrays. The more efficient internalization of large amounts of AQP4 with square arrays would thus increase dynamic regulation of AQP4 in vivo, and therefore we may have revealed the first functional rationale for maintaining the elaborate square arrays. Disruption of square arrays in the glial endfeet within minutes after the onset of cerebral ischemia has indeed been demonstrated [47–49], although a conflicting study identifies square arrays present in the astrocytic endfeet 60 min after the onset of hypoxia [50]. One may speculate whether the putative hypoxia-induced disruption of square arrays may be indicative of phosphorylation-dependent internalization of AQP4, i.e., via the G-protein coupled vasopressin receptor, $V1_aR$ [35].

Acknowledgments Technical assistance was provided by Charlotte G. Iversen, Mikkel Olsen, and Inger Merete Paulsen. The authors wish to give special thanks to Karen Thomsen for expert freeze fracture studies. The study was supported by the Nordic Centre of Excellence in Water-Imbalance Related Disorders, the Lundbeck Foundation (to N.M.), the Danish Medical Research Council (FSS) (to N.M., R.A.F.), E. Danielsen's Foundation (to N.M.), the Augustinus Foundation (to N.M.), the Michaelsen's Foundation (to N.M.), the Novo Nordisk Foundation (to R.A.F.), the Carlsberg Foundation (to R.A.F.) and the L'Oreal/UNESCO/Royal Danish Academy of Sciences Scholarship to Young Women in Science (to N.M.), Heart–Lung Foundation (to M.Z.), and the Functional genomics program of the Norwegian Research Council, FUGE (to T.H.). Additional funding to R.A.F was provided by a Marie Curie Intra-European Fellowship. The Water and Salt Research Center at the University of Aarhus is established and supported by the Danish National Research Foundation (Danmarks Grundforskningsfond).

References

1. Amiry-Moghaddam M, Ottersen OP (2003) The molecular basis of water transport in the brain. Nat Rev Neurosci 4:991–1001
2. Nielsen S, Nagelhus EA, Amiry-Moghaddam M, Bourque C, Agre P, Ottersen OP (1997) Specialized membrane domains for water transport in glial cells: high-resolution immunogold cytochemistry of aquaporin-4 in rat brain. J Neurosci 17:171–180
3. Noell S, Fallier-Becker P, Beyer C, Kroger S, Mack AF, Wolburg H (2007) Effects of agrin on the expression and distribution of the water channel protein aquaporin-4 and volume regulation in cultured astrocytes. Eur J Neurosci 26:2109–2118
4. Zador Z, Stiver S, Wang V, Manley GT (2009) Role of aquaporin-4 in cerebral edema and stroke. Handb Exp Pharmacol 190:159–170
5. Carmosino M, Procino G, Tamma G, Mannucci R, Svelto M, Valenti G (2007) Trafficking and phosphorylation dynamics of AQP4 in histamine-treated human gastric cells. Biol Cell 99:25–36
6. Gunnarson E, Axehult G, Baturina G, Zelenin S, Zelenina M, Aperia A (2005) Lead induces increased water permeability in astrocytes expressing aquaporin 4. Neuroscience 136:105–114
7. Gunnarson E, Zelenina M, Axehult G, Song Y, Bondar A, Krieger P, Brismar H, Zelenin S, Aperia A (2008) Identification of a molecular target for glutamate regulation of astrocyte water permeability. Glia 56:587–596
8. Han Z, Wax MB, Patil RV (1998) Regulation of aquaporin-4 water channels by phorbol ester-dependent protein phosphorylation. J Biol Chem 273:6001–6004
9. Kadohira I, Abe Y, Nuriya M, Sano K, Tsuji S, Arimitsu T, Yoshimura Y, Yasui M (2008) Phosphorylation in the C-terminal domain of aquaporin-4 is required for Golgi transition in primary cultured astrocytes. Biochem Biophys Res Commun 377:463–468
10. Madrid R, Le MS, Barrault MB, Janvier K, Benichou S, Merot J (2001) Polarized trafficking and surface expression of the AQP4 water channel are coordinated by serial and regulated interactions with different clathrin-adaptor complexes. EMBO J 20:7008–7021
11. Zelenina M, Zelenin S, Bondar AA, Brismar H, Aperia A (2002) Water permeability of aquaporin-4 is decreased by protein kinase C and dopamine. Am J Physiol Ren Physiol 283:F309–F318
12. Hasegawa H, Ma T, Skach W, Matthay MA, Verkman AS (1994) Molecular cloning of a mercurial-insensitive water channel expressed in selected water-transporting tissues. J Biol Chem 269:5497–5500
13. Jung JS, Bhat RV, Preston GM, Guggino WB, Baraban JM, Agre P (1994) Molecular characterization of an aquaporin cDNA from brain: Candidate osmoreceptor and regulator of water balance. Proc Natl Acad Sci USA 91:13052–13056
14. Moe SE, Sorbo JG, Sogaard R, Zeuthen T, Ottersen OP, Holen T (2008) New isoforms of rat aquaporin-4. Genomics 91:367–377
15. Neely JD, Christensen BM, Nielsen S, Agre P (1999) Heterotetrameric composition of aquaporin-4 water channels. Biochemistry 38:11156–11163
16. Furman CS, Gorelick-Feldman DA, Davidson KG, Neely Yasumura T, JD Agre P, Rash JE (2003) Aquaporin-4 square array assembly: opposing actions of M1 and M23 isoforms. Proc Natl Acad Sci USA 100:13609–13614
17. Rash JE, Yasumura T, Hudson CS, Agre P, Nielsen S (1998) Direct immunogold labeling of aquaporin-4 in square arrays of

astrocyte and ependymocyte plasma membranes in rat brain and spinal cord. Proc Natl Acad Sci USA 95:11981–11986
18. Yang B, Brown D, Verkman AS (1996) The mercurial insensitive water channel (AQP-4) forms orthogonal arrays in stably transfected Chinese hamster ovary cells. J Biol Chem 271:4577–4580
19. Crane JM, Van Hoek AN, Skach WR, Verkman AS (2008) Aquaporin-4 dynamics in orthogonal arrays in live cells visualized by quantum dot single particle tracking. Mol Biol Cell 19:3369–3378
20. Sorbo JG, Moe SE, Ottersen OP, Holen T (2008) The molecular composition of square arrays. Biochemistry 47:2631–2637
21. Strand L, Moe SE, Solbu TT, Vaadal M, Holen T (2009) Roles of aquaporin-4 isoforms and amino acids in square array assembly. Biochemistry 48:5785–5793
22. Suzuki H, Nishikawa K, Hiroaki Y, Fujiyoshi Y (2008) Formation of aquaporin-4 arrays is inhibited by palmitoylation of N-terminal cysteine residues. Biochim Biophys Acta 1778:1181–1189
23. Crane JM, Verkman AS (2009) Determinants of aquaporin-4 assembly in orthogonal arrays revealed by live-cell single-molecule fluorescence imaging. J Cell Sci 122:813–821
24. Hiroaki Y, Tani K, Kamegawa A, Gyobu N, Nishikawa K, Suzuki H, Walz T, Sasaki S, Mitsuoka K, Kimura K, Mizoguchi A, Fujiyoshi Y (2006) Implications of the aquaporin-4 structure on array formation and cell adhesion. J Mol Biol 355:628–639
25. Silberstein C, Bouley R, Huang Y, Fang P, Pastor-Soler N, Brown D, Van Hoek AN (2004) Membrane organization and function of M1 and M23 isoforms of aquaporin-4 in epithelial cells. Am J Physiol Ren Physiol 287:F501–F511
26. Zeidel ML, Nielsen S, Smith BL, Ambudkar SV, Maunsbach AB, Agre P (1994) Ultrastructure, pharmacologic inhibition, and transport selectivity of aquaporin channel-forming integral protein in proteoliposomes. Biochemistry 33:1606–1615
27. Zeuthen T, Belhage B, Zeuthen E (2006) Water transport by Na+-coupled cotransporters of glucose (SGLT1) and of iodide (NIS). The dependence of substrate size studied at high resolution. J Physiol 570:485–499
28. Zampighi GA, Kreman M, Boorer KJ, Loo DD, Bezanilla F, Chandy G, Hall JE, Wright EM (1995) A method for determining the unitary functional capacity of cloned channels and transporters expressed in *Xenopus laevis* oocytes. J Membr Biol 148:65–78
29. Leduc-Nadeau A, Lahjouji K, Bissonnette P, Lapointe JY, Bichet DG (2007) Elaboration of a novel technique for purification of plasma membranes from *Xenopus laevis* oocytes. Am J Physiol Cell Physiol 292:C1132–C1136
30. Moeller HB, MacAulay N, Knepper MA, Fenton RA (2009) Role of multiple phosphorylation sites in the COOH-terminal tail of aquaporin-2 for water transport: evidence against channel gating. Am J Physiol Ren Physiol 296:F649–F657
31. Fenton RA, Brond L, Nielsen S, Praetorius J (2007) Cellular and subcellular distribution of the type-2 vasopressin receptor in the kidney. Am J Physiol Ren Physiol 293:F748–F760
32. Zelenina M, Bondar AA, Zelenin S, Aperia A (2003) Nickel and extracellular acidification inhibit the water permeability of human aquaporin-3 in lung epithelial cells. J Biol Chem 278:30037–30043
33. Zelenina M, Brismar H (2000) Osmotic water permeability measurements using confocal laser scanning microscopy. Eur Biophys J 29:165–171
34. Yang B, Verkman AS (1997) Water and glycerol permeabilities of aquaporin 1–5 and MIP determined quantitatively by expression of epitope-tagged constructs in *Xenopus* oocytes. J Biol Chem 272:16140–16146
35. Moeller HB, Fenton RA, Zeuthen T, MacAulay N (2009) Vasopressin-dependent short-term regulation of AQP4 expressed in *Xenopus* oocytes. Neuroscience 164:1674–1684
36. McCoy ES, Haas BR, Sontheimer H (2009) Water permeability through aquaporin-4 is regulated by protein kinase C and becomes rate-limiting for glioma invasion. Neuroscience (in press)
37. Meinild AK, Klaerke DA, Zeuthen T (1998) Bidirectional water fluxes and specificity for small hydrophilic molecules in aquaporins 0–5. J Biol Chem 273:32446–32451
38. Nagelhus EA, Horio Y, Inanobe A, Fujita A, Haug FM, Nielsen S, Kurachi Y, Ottersen OP (1999) Immunogold evidence suggests that coupling of K+ siphoning and water transport in rat retinal Muller cells is mediated by a coenrichment of Kir4.1 and AQP4 in specific membrane domains. Glia 26:47–54
39. Nagelhus EA, Mathiisen TM, Ottersen OP (2004) Aquaporin-4 in the central nervous system: cellular and subcellular distribution and coexpression with KIR4.1. Neuroscience 129:905–913
40. Binder DK, Yao X, Zador Z, Sick TJ, Verkman AS, Manley GT (2006) Increased seizure duration and slowed potassium kinetics in mice lacking aquaporin-4 water channels. Glia 53:631–636
41. Amiry-Moghaddam M, Williamson A, Palomba M, Eid T, de Lanerolle NC, Nagelhus EA, Adams ME, Froehner SC, Agre P, Ottersen OP (2003) Delayed K+ clearance associated with aquaporin-4 mislocalization: phenotypic defects in brains of alpha-syntrophin-null mice. Proc Natl Acad Sci USA 100:13615–13620
42. Ruiz-Ederra J, Zhang H, Verkman AS (2007) Evidence against functional interaction between aquaporin-4 water channels and Kir4.1 potassium channels in retinal Muller cells. J Biol Chem 282:21866–21872
43. Zhang H, Verkman AS (2008) Aquaporin-4 independent Kir4.1 K+ channel function in brain glial cells. Mol Cell Neurosci 37:1–10
44. Soe R, MacAulay N, Klaerke DA (2009) Modulation of Kir4.1 and Kir4.1-Kir5.1 channels by small changes in cell volume. Neurosci Lett 457:80–84
45. MacVicar BA, Feighan D, Brown A, Ransom B (2002) Intrinsic optical signals in the rat optic nerve: role for K(+) uptake via NKCC1 and swelling of astrocytes. Glia 37:114–123
46. Walz W, Hinks EC (1985) Carrier-mediated KCl accumulation accompanied by water movements is involved in the control of physiological K+ levels by astrocytes. Brain Res 343:44–51
47. Cuevas P, Gutierrez Diaz JA, Dujovny M, Diaz FG, Ausman JI (1985) Disturbance of plasmalemmal astrocytic assemblies in focal and selective cerebral ischemia. Anat Embryol (Berl) 172:171–175
48. Landis DM, Reese TS (1981) Astrocyte membrane structure: changes after circulatory arrest. J Cell Biol 88:660–663
49. Suzuki M, Iwasaki Y, Yamamoto T, Konno H, Yoshimoto T, Suzuki J (1984) Disintegration of orthogonal arrays in perivascular astrocytic processes as an early event in acute global ischemia. Brain Res 300:141–145
50. Neuhaus J, Schmid EM, Wolburg H (1990) Stability of orthogonal arrays of particles in murine skeletal muscle and astrocytes after circulatory arrest, and human gliomas. Neurosci Lett 109:163–168

Phosphorylation of Rat Aquaporin-4 at Ser^{111} Is Not Required for Channel Gating

Mette Assentoft,[1] Shreyas Kaptan,[2] Robert A. Fenton,[3] Susan Z. Hua,[4,5] Bert L. de Groot,[2] and Nanna MacAulay[1]

Aquaporin 4 (AQP4) is the predominant water channel in the mammalian brain and is mainly expressed in the perivascular glial endfeet at the brain-blood interface. AQP4 has been described as an important entry and exit site for water during formation of brain edema and regulation of AQP4 is therefore of therapeutic interest. Phosphorylation of some aquaporins has been proposed to regulate their water permeability via gating of the channel itself. Protein kinase (PK)-dependent phosphorylation of Ser^{111} has been reported to increase the water permeability of AQP4 expressed in an astrocytic cell line. This possibility was, however, questioned based on the crystal structure of the human AQP4. Our study aimed to resolve if Ser^{111} was indeed a site involved in phosphorylation-mediated gating of AQP4. The water permeability of AQP4-expressing *Xenopus* oocytes was not altered by a range of activators and inhibitors of PKG and PKA. Mutation of Ser^{111} to alanine or aspartate (to prevent or mimic phosphorylation) did not change the water permeability of AQP4. PKG activation had no effect on the water permeability of AQP4 in primary cultures of rat astrocytes. Molecular dynamics simulations of a phosphorylation of AQP4.Ser^{111} recorded no phosphorylation-induced change in water permeability. A phospho-specific antibody, exclusively recognizing AQP4 when phosphorylated on Ser^{111}, failed to detect phosphorylation in cell lysate of rat brain stimulated by conditions proposed to induce phosphorylation of this residue. Thus, our data indicate a lack of phosphorylation of Ser^{111} and of phosphorylation-dependent gating of AQP4.

GLIA 2013;61:1101–1112

Key words: regulation; astrocytic swelling; AQP4; protein kinase G; molecular dynamics simulations

Introduction

Aquaporins possess intrinsic water permeability when faced with an osmotic gradient and a subset of the 13 isoforms identified in humans displays additional permeability toward glycerol, urea, and ammonium (reviewed by Gomes et al. (2009)). AQP4 is the predominant aquaporin in the mammalian brain and is localized in the perivascular glial endfeet, the ependymal cell lining, and osmosensing areas such as the supraoptic nucleus and subfornical organ (Nielsen et al., 1997). AQP4 exists as three functional isoforms with different length of their N-termini and distinct isoform-specific water permeability (Fenton et al., 2010; Moe et al., 2008). The shortest isoform (M23) is the dominant AQP4 isoform in the brain (Moe et al., 2008).

AQP4 has been proposed to be involved in brain edema formation based on its distinct expression pattern at the brain-blood interface and the altered outcome of AQP4 knock-out mice following experimentally inflicted brain edema formation (reviewed by Zador et al. (2009)). Short-term regulation of AQP4 under pathophysiological conditions promoting brain edema has therefore attracted scientific interest. Dynamic regulation of AQP4 could be achieved by changes in levels of AQP4 membrane expression or by changes in the water permeability of AQP4 already present in

View this article online at wileyonlinelibrary.com. DOI: 10.1002/glia.22498

Published online Apr 25, 2013 in Wiley Online Library (wileyonlinelibrary.com). Received Sep 6, 2012, Accepted for publication Feb 27, 2013.

Address correspondence to Nanna MacAulay, Department of Cellular and Molecular Medicine, University of Copenhagen, Blegdamsvej 3, Bldg. 12.6, 2200 Copenhagen N, Denmark. E-mail: macaulay@sund.ku.dk

From the [1]Department of Cellular and Molecular Medicine, University of Copenhagen, Copenhagen, Denmark; [2]Computational Biomolecular Dynamics Group, Max Planck Institute for Biophysical Chemistry, Gottingen, Germany; [3]Department of Biomedicine and InterPrET Center, Aarhus University, Aarhus, Denmark; [4]Department of Physiology and Biophysics, State University of New York in Buffalo, Buffalo, NY; [5]Department of Mechanical and Aerospace Engineering, State University of New York in Buffalo, Buffalo, NY.

the membrane, i.e., "gating." The possibility of altered membrane expression of AQP4 following experimentally inflicted brain edema has remained inconclusive based on divergent reports of up-regulation (Papadopoulos and Verkman 2005; Ribeiro Mde et al., 2006; Saadoun et al., 2003) and down-regulation (Friedman et al., 2009; Frydenlund et al., 2006; Meng et al., 2004; Zhao et al., 2005) of AQP4 expression during edema formation. Activation of PKC leads to down-regulation of AQP4 function (Zelenina et al., 2002) possibly by internalization of the protein (Moeller et al., 2009a). Other protein kinases such as PKG and PKA have been proposed to phosphorylate Ser^{111} in AQP4 and thereby provoke a gating event leading to increased osmotic water permeability (Gunnarson et al., 2008; Song and Gunnarson, 2012). Phosphorylation-dependent gating of aquaporins has been promoted further following molecular dynamics simulations performed on the crystallized spinach aquaporin, SoPIP2;1. In the study, the authors added, *in silico,* a phosphate-moiety to the Ser^{115} (Tornroth-Horsefield et al., 2006), which corresponds to Ser^{111} in AQP4. The molecular dynamics recorded an open conformation of SoPIP2;1 upon this phosphorylation.

Despite the beauty of this gating model, concerns have been raised: Crystallization of the human AQP4 yielded an open conformation, despite the lack of a phosphate group at Ser^{111}, and a D-loop too short to act as the gate (Ho et al., 2009). *In vivo* phosphorylation of Ser^{115} on SoPIP2;1 was not detected despite experimental activation of a range of protein kinases (Johansson et al., 1998). In addition, the open structure of the spinach aquaporin, on which the molecular modeling was based, was obtained at a pH promoting a closed structure and vice versa (Tornroth-Horsefield et al., 2006; Walz et al., 2009). In this study we aimed to determine the extent to which AQP4 is gated by phosphorylation of Ser^{111}. We found no evidence in favor of phosphorylation-dependent gating of AQP4 in its native setting in primary culture of astrocytes, upon heterologous expression in *Xenopus* oocytes, or by molecular dynamics simulations. Nor did we detect *in vivo* phosphorylation of the Ser^{111} in rat brain.

Materials and Methods

Molecular Biology

Rat AQP4.M23, human KCNQ1, KCNE1, and ENaC were subcloned into the oocyte expression vector pXOOM (AQP4.M23, KCNQ1, and KCNE1) or pBS (ENaC), linearized downstream from the poly-A segment, and *in vitro* transcribed using T7 mMessage Machine (Ambion, Austin, TX). cRNA was extracted with MEGAclear (Ambion, Austin, TX) and micro-injected into defolliculated *Xenopus laevis* oocytes (25 ng AQP4 or ENaC (1:1:1 of the α, β, and γ subunit) RNA/oocyte or 5 ng KCNQ1/KCNE1 (4:1) RNA/oocyte). Mutations were introduced into AQP4 with Quick Change site-directed mutagenesis kit (Stratagene, Santa Clara, CA) and verified with DNA sequencing. Numbering of the AQP4 amino acids is kept according to that of AQP4.M1.

Oocyte Preparation

Xenopus laevis frogs were obtained from Nasco (Fort Atkinson, WI) or National Center for Scientific Research (France). Oocytes were surgically removed from anesthetized frogs and prepared as previously described (Fenton et al., 2010). The protocol complies with the European Community guidelines for the use of experimental animals and the experiments were approved by The Danish National Committee for Animal Studies.

Oocyte Volume Measurements

The experimental setup for measuring water permeability of oocytes has been described in detail previously (Zeuthen et al., 2006). Briefly, the oocyte was placed in a small chamber with a glass bottom and perfused with a control solution (100 mM NaCl, 2 mM KCl, 1 mM $CaCl_2$, 1 mM $MgCl_2$, 10 mM HEPES, pH 7.4) at room temperature. Oocyte images were captured continuously from below at a rate of 25 images/s. To determine the water permeability, the oocytes were challenged with a hypertonic solution (control solution with additional 20 mOsm mannitol).

Immunocytochemistry and Confocal Laser Scanning Microscopy

Fixed oocytes were prepared for immunocytochemistry as previously described (Moeller et al., 2009b) and the 2 μm sections were immunostained with an anti-AQP4 antibody 1:5,000 (Alomone Laboratories, Israel) while an Alexa 488-conjugated secondary antibody 1:1,000 was used for visualization (DAR, Invitrogen, Denmark). Imaging, image semi-quantification, and validation was performed as recently described in detail (Moeller et al., 2009b).

Electrophysiology

Conventional two-electrode voltage clamp studies were performed with a DAGAN CA-1B High Performance oocyte clamp (DAGAN, Minneapolis, MN) with DigiData 1322A interface controlled by pCLAMP software, version 9.2 (Axon Instruments, Burlingame, CA). For ENaC measurements the membrane potential was clamped at -50 mV and the current–voltage (I–V) relationship was determined by stepping the clamp potential from -50 mV to test potentials ranging from $+40$ mV to -120 mV in 20 mV increments (100 ms pulses). For KCNQ1/KCNE1 measurements, the membrane potential was clamped at -80 mV. The I–V relationship was obtained with a 2 s pulse to a range of voltages between -80 mV and $+60$ mV in 20 mV steps followed by a 1 s pulse to -40 mV.

Astrocyte Preparation

Adult male Sprague-Dawley rats (250–300 g) were used for the astrocytic preparation. The procedure has earlier been described in detail (Langan et al., 1995) and these cultured astrocytes have previously been used for volume measurements (see below and Ateya et al. (2005)). In brief, adult astrocytes were isolated from gelatin-sponge implants left in the animal for three days. Sponges were subsequently removed, minced and triturated followed by trypsination

and passage through a nylon mesh with pore diameter of 20 μm. The astrocytes were maintained in Dulbecco's Modified Eagle Medium (DMEM) supplemented with 10% fetal bovine serum and 1% penicillin/streptomycin. Cells were used in experiments two to five days after passage. Cells between passage 5 and 15 were used and expression of AQP4 verified with Western blotting (data not shown).

Astrocyte Volume Measurements

A microfluidic volume sensor was used to study volume changes in astrocytes, as previously described (Ateya et al., 2005). Astrocytes were grown on a microscope slide that was inverted over the sensor chip thereby creating a flow chamber with a fixed volume of 60 nL. A sinusoidal current of 50 Hz, 1 μA was provided to the two outer electrodes in the chamber and the voltage was measured between the two inner electrodes. An increase in cell volume will increase the chamber resistance and thus an increase in voltage serves as the functional read-out of cell swelling. The chamber was perfused with an isotonic solution (95 mM NaCl, 5 mM KCl, 1.2 mM $CaCl_2$, 1 mM $MgCl_2$, 5 mM HEPES, 20 mM glucose, 100 mM mannitol, pH 7.4), 310 mOsm at room temperature. The flow rate of the solution ($\sim$30 μL/min) was controlled by adjusting hydraulic pressure at the inlet. To study the water permeability, the astrocytes were challenged with a hypotonic solution (isotonic solution with 60 mM less mannitol), 250 mOsm.

Molecular Dynamics Simulations

The starting structure of AQP4 was obtained from the protein data bank, entry 3GD8 (Ho et al., 2009). The protein was embedded in a membrane bilayer made up of 294 dimyristoylphosphotidylcholine (DMPC) lipids, using the Gromacs tool g_membed (Wolf et al., 2010). An ion concentration of 150 mM NaCl was chosen to simulate a neutral system. All the simulations were performed using the Gromacs simulation package version 4.5 (Hess et al., 2008). The AMBER99SB-ILDN force field was used for the protein and the ions (Lindorff-Larsen et al., 2010) and the parameters for the lipids were derived from Berger et al. (1997). The box was hydrated with 22,010 molecules of SPC water (Berendsen et al., 1987). The electrostatics in the system were treated explicitly within a cut-off of 1.0 nm and with the Particle Mesh Ewald method for the rest of the system (Darden et al., 1993). A cut-off of 1.0 nm was used for the calculation of Lennard-Jones interactions. The LINCS algorithm was used to constrain the bonds in the system (Hess 2008) along with v-sites for the protein hydrogens (Feenstra et al., 1999) allowing a time-step of 4 fs. The simulation temperature was held constant at 300 K using velocity-rescale thermostat (Bussi et al., 2007) with a coupling constant of 0.5 ps. The pressure was maintained at 1 atm with the Parrinello-Rahman barostat. AQP4 was simulated under two conditions: with no modifications to the amino acid sequence and with phosphorylation of Ser^{111}. The parameters for the phosphorylated serine residue were obtained from Homeyer et al. (2006). The simulations were carried out for 500 ns each and the water permeability was calculated using the collective diffusion method (Zhu et al., 2004). The first 100 ns of the simulations were discarded to account for equilibration. The osmotic water permeability was then calculated for a 50 ns window, dividing the simulation into eight slices for each monomer. The average over the eight windows and four monomers was used to compare the water permeability of AQP4 with its phosphorylated form.

Preparation of Rat Brain Lysate and Immunoblotting

Male Sprague–Dawley rats (3–4 weeks) were anesthetized and decapitated. The brains were immediately removed and placed in ice-cold artificial cerebrospinal fluid (aCSF) (125 mM NaCl, 2.5 mM KCl, 26 mM $NaHCO_3$, 1.25 mM NaH_2PO_4, 1 mM $MgCl_2$, 2 mM $CaCl_2$, 25 mM glucose, pH 7.4). The brains were cut into 0.5 mm thick slices and incubated in the presence or absence of the group I mGluR agonist (*S*)-3,5 dihydroxyphenylglycine (DHPG) (50 μM) for 60 min at 35°C in aCSF bubbled with 95% O_2 and 5% CO_2. The slices were homogenized on ice in cold homogenizing buffer (50 mM Tris pH 7.4, 2.5 mM Na-EGTA, 5 mM Na-EDTA, 10 mM NaCl, 10 mM KCl, 100 mM NaFl, 320 mM sucrose, 200 μg/mL pefabloc, 2 μg/mL aprotinin, 1 μg/mL leupeptin, 2 μg/mL antipain, 10 μg/mL benzamidine and PhosSTOP Phosphatase Inhibitor Cocktail 1 tablet per 10 mL), and cell debris was pelleted at 800*g*, 4°C x 10 min. The supernatant was subsequently centrifuged at 15,500*g*, 4°C $\times$ 90 min and pellet was resuspended in cold lysis buffer (50 M Tris pH 8.5, 150 mM NaCl, 5 mM EDTA, 1% Nonidet P40, 8 μM leupeptin, 0.4 mM pefablock, and PhosSTOP Phosphatase Inhibitor Cocktail, 1 tablet per 10 mL) and snap frozen. Immunoblotting was performed (10 μg protein/lane) with rabbit anti-AQP4 antibody, 1:1,000 (Alomone Laboratories, Jerusalem, Israel) or a custom-made rabbit anti-pS111-AQP4 antibody, 1:1,000 (PhosphoSolutions®, Aurora, CO). Two peptides (CTRKISIAK either phosphorylated at the serine residue (the epitope) or non-phosphorylated) were synthesized by Phosphosolutions® and are published with their permission (Aurora, CO). For dot blot, the peptides (20 ng) were spotted onto a membrane and probed with the custom-made rabbit anti-pS111-AQP4 antibody, 1:1,000. A horseradish peroxidase-conjugated secondary antibody (P448, Dako, Denmark) was used at 1:3,000. Visualization was obtained with SuperSignal West Pico Chemiluminescent Substrate (Thermo Fisher Scientific, Waltham, MA) and imaged with BioSpectrum AC imaging system (UVP, Upland, CA).

Drugs

Dihydroxyphenylglycine, DHPG (50 μM), 8-Br-cGMP (100 μM), 8-pCPT-cGMP (100 μM), H89 (50 μM), pefabloc (200 μg/mL), leupeptin (1 μg/mL), aprotinin (2 μg/mL), antipain (2 μg/mL), and benzamidine (10 μg/ml) were all dissolved in water. Amiloride (100 μM) and K252a (1 μM) were dissolved in DMSO (0.067% or 0.05% DMSO in both control and test solution) while 8-Br-cAMP (300 μM) was dissolved in water containing 100 mM TRIS-base. All were obtained from Sigma Aldrich, Denmark. PhosSTOP Phosphatase Inhibitor Cocktail Tablets (1 tablet per 10 mL) and Nonidet P40 (1%) were obtained from Roche, Germany.

Statistics

Data are presented as means $\pm$ SEM. Student's *t*-test or analysis of variance (ANOVA) followed by Dunnett's multiple comparison test

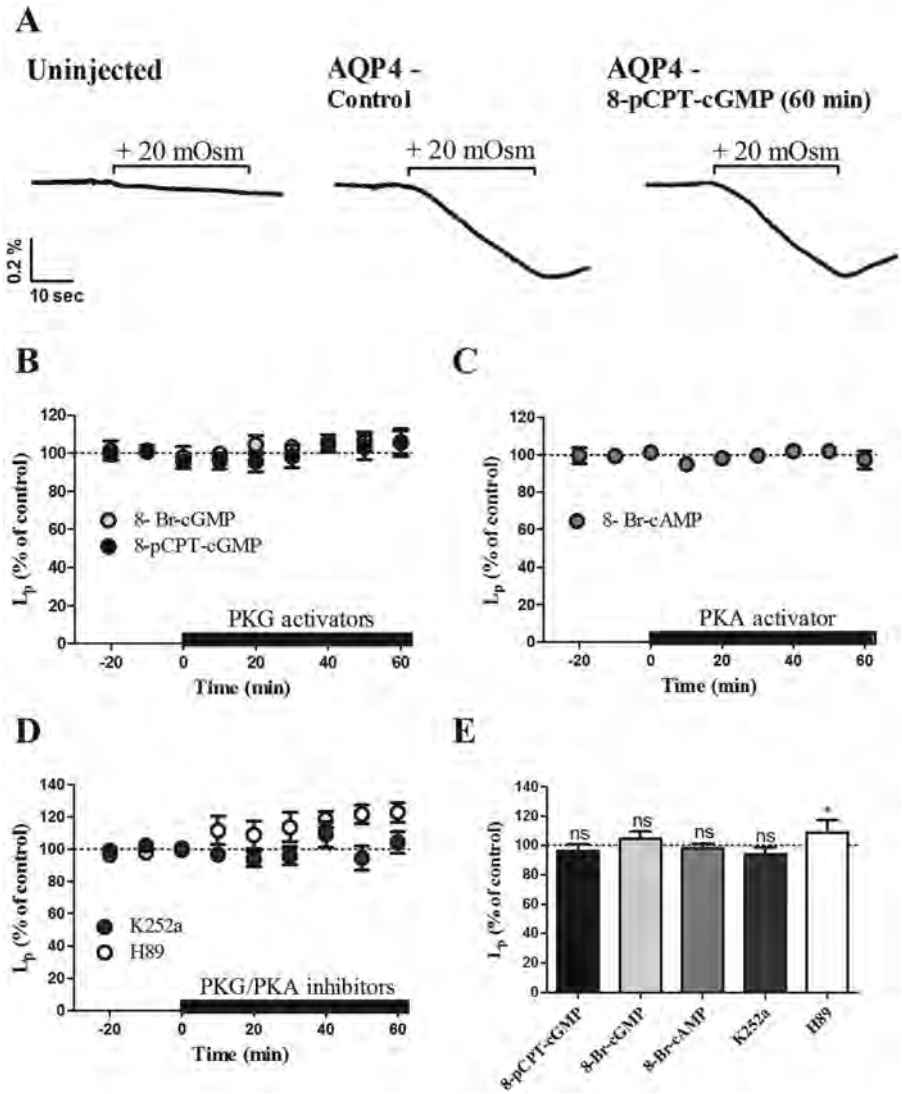

FIGURE 1: No PKG/PKA-dependent regulation of AQP4 expressed in oocytes. (A) Volume traces from an uninjected oocyte challenged with a hyperosmotic gradient (left panel) and an AQP4-expressing oocyte challenged with a hyperosmotic gradient before and after exposure to 100 μM 8-pCPT-cGMP for 60 min (middle and right panel). (B–D) The relative water permeability of AQP4-expressing oocytes determined as a function of time. Three control measurements were taken prior to addition of either (B) PKG activators (8-pCPT-cGMP, 100 μM or 8-Br-cGMP, 100 μM), (C) a PKA activator (8-Br-cAMP, 300 μM) or (D) PKG and PKA inhibitors (K252a, 1 μM or H89, 50 μM) to the external solution (black bar) (n = 7–12). (E) A summary of the water permeability of AQP4-expressing oocytes after 20 min exposure to various PKG and PKA activators and inhibitors relative to the control measurements. In % of control; 96.2 ± 4.6 for 8-pCPT-cGMP, n = 12, 104.4 ± 4.8 for 8-Br-cGMP, n = 7, 98.2 ± 3.3 for 8-Br-cAMP, n = 7, 93.9 ± 5.0 for K252a, n = 8, and 108.8 ± 8.5 for H89, n = 8. Repeated measures ANOVA followed by Dunnett's multiple comparison test was used as statistical test. *P < 0.05.

were used for the statistical analysis. A probability level of <0.05 was considered statistically significant.

Results

To determine the effect of a putative PKG-dependent phosphorylation of AQP4, the M23 isoform of AQP4 was heterologously expressed in *Xenopus laevis* oocytes. The osmotic water permeability of the oocytes was evaluated upon an abrupt challenge with a hypertonic test solution containing an additional 20 mM mannitol (20 mOsm). This osmotic challenge caused a ~15-fold faster shrinkage of AQP4-expressing oocytes compared to that of the native uninjected oocytes (compare $1.48 \pm 0.05 \times 10^{-3}$ cm/s ($n = 77$) with $0.09 \pm 0.01 \times 10^{-3}$ cm/s ($n = 34$), $P < 0.05$), representative traces shown in Fig. 1A, left and middle trace. This experimental system thus provides us with a clear read-out of AQP4 function with a negligible background due to the low inherent water permeability of the oocyte membrane. Following three water permeability measurements in control solution to ensure a stable baseline, PKG was activated by addition of membrane-permeable cGMP analogs (100 μM 8-Br-cGMP or 8-pCPT-cGMP) to the test solutions. The water permeability

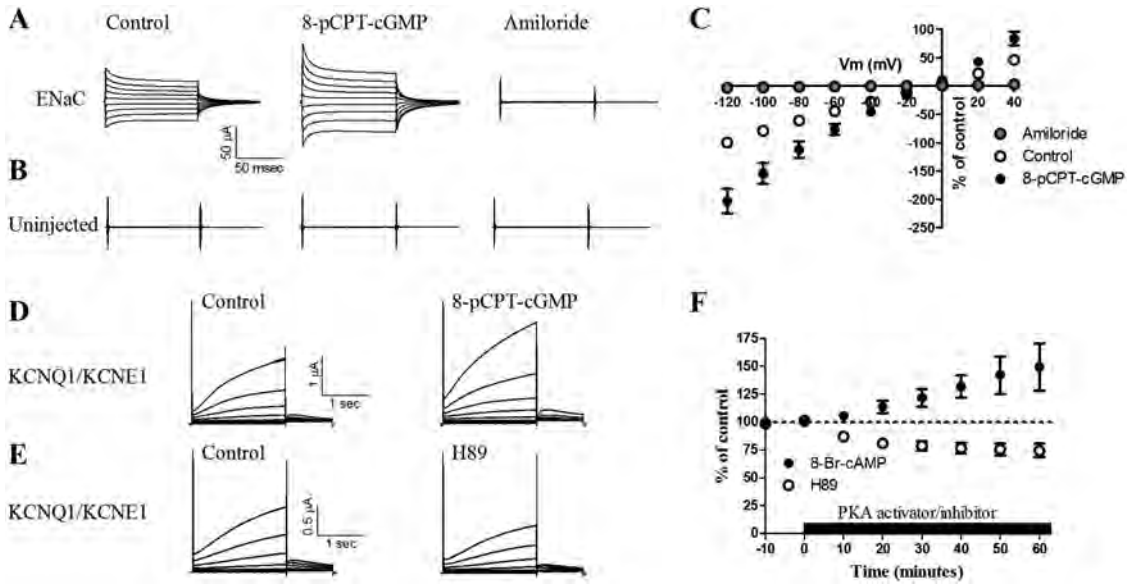

FIGURE 2: PKG/PKA activation in oocytes. (A, B) *I/V* relationship of an oocyte expressing ENaC (A) or an uninjected oocyte (B) before and after 5 min treatment with a PKG-activator (8-pCPT-cGMP, 100 μM), left and middle panel. The same oocyte was subsequently exposed to 100 μM of the ENaC blocker amiloride (right panel). (C) A summary of the *I/V* relationship of ENaC-expressing oocytes (n = 4) before and after treatment with 8-pCPT-cGMP and amiloride relative to the control measurement at −120 mV. In % of control at V_m = −120 mV: 203.5 ± 20.4 for 8-pCPT-cGMP ($P < 0.05$) and 3.8 ± 1.5 for amiloride ($P < 0.05$). (D, E) *I/V* relationship of oocytes expressing KCNQ1/KCNE1 before and after 60 min treatment with either a PKA-activator (8-Br-cAMP, 300 μM) (D) or PKA/PKG inhibitor (H89, 50 μM) (E). (F) Summary of the membrane currents obtained in KCNQ1/KCNE1-expressing oocytes after 60 min exposure to either 8-Br-cAMP (n = 5) or H89 (n = 3) relative to the control measurements. In % of control at V_m = 20 mV: 149.5 ± 21.3 for 8-Br-cAMP ($P < 0.05$) and 74.4 ± 6.1 for H89 ($P < 0.05$). Repeated measures ANOVA followed by Dunnett's multiple comparison test was used as statistical test.

was then measured in 10-min intervals for 60 min. The rate of shrinkage of the same AQP4-expressing oocyte following 60 min exposure to 8-pCPT-cGMP is illustrated in Fig. 1A, right trace. Figure 1B shows the water permeability as a function of time for AQP4-expressing oocytes, with the addition of 8-pCPT-cGMP or 8-Br-cGMP marked with a black bar. No significant change in AQP4-induced water permeability was observed upon activation of PKG (n = 12 and 7), data for 20 min PKG-activation are summarized in Fig. 1E. The amino acid sequence surrounding Ser^{111} encodes a consensus sequence for PKG as well as PKA. Thus the effect on AQP4 function by activation of PKA was determined by addition of a membrane-permeable cAMP analog (300 μM 8-Br-cAMP). The water permeability of AQP4-expressing oocytes was not altered upon this treatment, n = 8 (Fig. 1C), summarized for 20 min PKA activation in Fig. 1E. To rule out the possibility that the steady-state level of Ser^{111} phosphorylation in oocytes was too high to allow for further kinase-dependent activation, similar experiments were performed with membrane-permeable inhibitors of PKA and PKG; 50 μM H89 or 1 μM K252a (Johansson et al., 1998; Rusinova et al., 2009), n = 8 (Fig. 1D). K252a had no significant effect on the water permeability but kinase inhibition with H89 produced a slight increase in AQP4-mediated water permeability (n = 8, $P < 0.05$), which may be due to its inhibitory action on PKC, the activation of which leads to down-regulation of AQP4 (Moeller et al., 2009a). The intrinsic water permeability of batch-matched uninjected oocytes was not affected by any of the above treatments (data not shown). Thus, we observed no indication of kinase activation leading to the proposed increase in AQP4-mediated water permeability nor of kinase inhibition leading to reduction thereof.

With the lack of both PKG- and PKA-induced increase in AQP4-dependent water permeability, we verified the kinase activity in the oocytes by expressing either the epithelial Na^+ channel (ENaC) known to be activated by PKG (Nie et al., 2009) or the PKA-regulated voltage-gated potassium channel KCNQ1, with its ancillary subunit KCNE1 (Dilly et al., 2004; Grunnet et al., 2003). ENaC-expressing oocytes were voltage clamped and the *I–V* relation was determined (Fig. 2A, left trace). Subsequently, the same ENaC-expressing oocyte was exposed to 8-pCPT-cGMP (100 μM) for 5 min with a subsequent determination of the *I–V* relation (Fig. 2A, middle trace). PKG activation increased the ENaC-mediated current obtained at −120 mV to 203.5 ± 20.4% of control, n = 4 (Fig. 2C) but had no effect on the uninjected oocytes, 91.7 ± 3.3% of control, n = 3 (Fig. 2B). The ENaC blocker amiloride (100 μM) completely abolished the ENaC current (Fig. 2A, right trace and 2C). The *I–V* relation of KCNQ1/KCNE1-expressing oocytes was determined before

(Fig. 2D,E, left traces) and after exposure to the PKA activator 8-Br-cAMP (300 μM) for 60 min (Fig. 2D, right trace) or to the PKA/PKG inhibitor H89 (50 μM) for 60 min (Fig. 2E, right trace). PKA activation increased the KCNQ1/KCNE1 current in a time-dependent manner and 60 min of activation increased the current obtained at 20 mV to 149.5 $\pm$ 21.5% of control, $n = 5$ (Fig. 2F). Inhibition of PKA by H89 reduced the current obtained at 20 mV to 74.4 $\pm$ 6.1%, $n = 3$, which suggests a basal level of PKA activity. Thus, PKG and PKA inhibition and activation by membrane-permeable inhibitors and cGMP- or cAMP analogs is robust and efficient in *Xenopus laevis* oocytes.

A mutational strategy was adopted to further deduce a possible involvement of Ser^{111} in a gating mechanism of AQP4. Ser^{111} was mutated to an alanine (S111A) to abolish potential phosphorylation of this residue and to an aspartate (S111D) in an attempt to mimic a phosphorylated serine (Maciejewski et al., 1995). The wild type AQP4 and the two mutant constructs, AQP4.S111A and AQP4.S111D, were expressed in oocytes and the water permeability was determined. The water permeabilities of these constructs in a representative batch of oocytes ($n = 5$ of each construct) are shown in Fig. 3A with water permeabilities of (in $\times 10^{-3}$ cm/s): 1.67 $\pm$ 0.18 for wild-type AQP4, 1.47 $\pm$ 0.10 for AQP4.S111A, and 1.20 $\pm$ 0.20 for AQP4.S111D, $n = 5$. As membrane expression levels vary between batches of oocytes and between constructs, we semiquantified the membrane abundance of oocytes from each day-matched batch of oocytes ($n = 5$ of each construct) by immunocytochemistry. Representative confocal images are shown in Fig. 3B and the membrane abundance of the different constructs in the representative batch from Fig. 3A is summarized in Fig. 3C. AQP4.S111A and AQP4.S111D both act as functional water channels at the plasma membrane. Based on the water permeability and the membrane abundance of each individual construct, the relative unit water permeability was obtained for each batch of oocytes. The relative unit water permeability was normalized to that of the wild-type AQP4 and averaged across four to five experimental batches of oocytes (Fig. 3D). There was no significant difference between the relative unit water permeability of AQP4 and the two mutants AQP4.S111A and AQP4.S111D (in % of AQP4 WT): 109 $\pm$ 10.5% for AQP4.S111A, $n = 5$ and 117 $\pm$ 9.4% for AQP4.S111D, $n = 4$. Therefore a phosphorylated Ser^{111} is not required for AQP4 to be fully functional and an attempt to mimic a phosphorylation at Ser^{111} does not significantly increase the water permeability of AQP4.

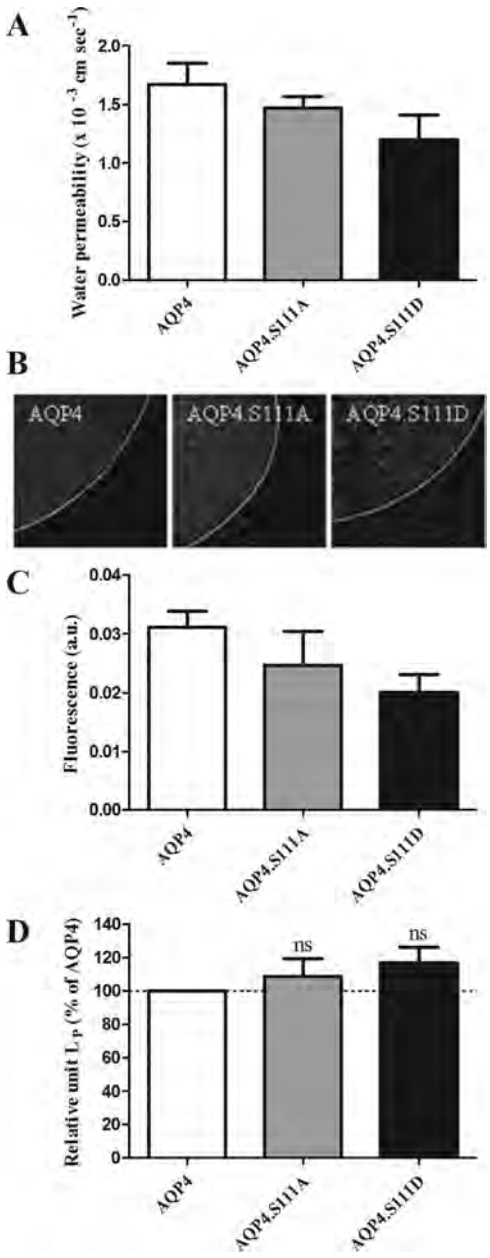

FIGURE 3: No change in the relative unit water permeability by mutation of Ser^{111}. (A) A representative experiment of the average water permeability of oocytes expressing AQP4, AQP4.S111A, or AQP4.S111D obtained as in Fig. 1 ($n = 5$). The contribution from the native oocyte membrane was deducted prior to quantification of the AQP4-mediated water permeability. (B) Representative confocal laser scanning microscopy of oocytes expressing either AQP4 (left panel), AQP4.S111A (middle panel), or AQP4.S111D (right panel) after immunolabeling with anti-AQP4 antibodies. (C) Oocyte plasma membrane fluorescent counts of oocytes from the same experiment as in panel A, were used to assess the AQP4 abundance in the plasma membrane of AQP4-, AQP4.S111A-, and AQP4.S111D-expressing oocytes ($n = 5$). (D) Relative unit water permeability (values obtained as in panel A divided by values obtained as in C) of AQP4.S111A and AQP4.S111D was normalized to that of AQP4 and averaged across 4-5 experiments. In % of control; 109 $\pm$ 10.5 for AQP4.S111A, $n = 5$ and 117 $\pm$ 9.4 for AQP4.S111D, $n = 4$. ANOVA followed by Dunnett's multiple comparison test was used as statistical test.

Astrocytic Water Permeability

AQP4 is native to the astrocytes of the mammalian central nervous system where it is highly expressed in the perivascular

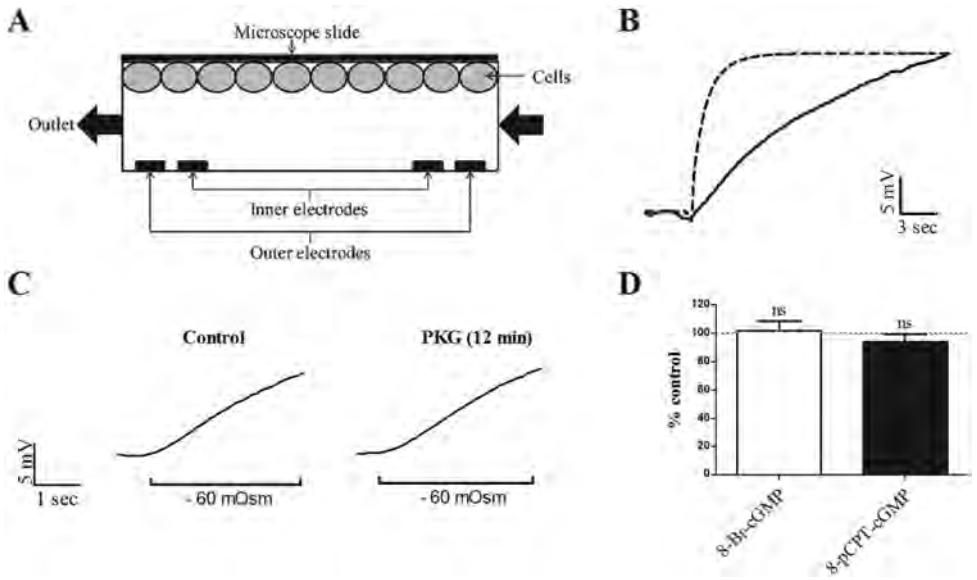

FIGURE 4: Astrocytic water permeability was not affected by PKG activation. (A) Schematic representation of the microfluidic volume sensor with the sensing chamber, electrodes, and cell-containing slide. (B) The speed of solution change (dashed line) precedes the osmotically induced change in astrocytic cell volume (solid line). (C) Representative traces from astrocytes in primary culture challenged with a hyposmotic gradient prior to (left panel) and after (right panel) exposure of a PKG-activator (8-Br-cGMP, 100 μM). Measurements were performed in duplicates prior to and after addition of either 8-pCPT-cGMP or 8-Br-cGMP (both 100 μM). (D) Summarized astrocytic water permeabilities after stimulation with the PKG activators normalized to the control measurements, n = 5–6 based on three batches of astrocyte culture for each cGMP-analog. In % of control; 101.7 ± 7.1 for 8-Br-cGMP, n = 5 and 93.9 ± 5.4 for 8-pCPT-cGMP, n = 6. Paired Student's t-test was used as statistical test.

endfeet (Nielsen et al., 1997). In primary culture of astrocytes, AQP4 loses its distinct expression pattern and disperses throughout the entire plasma membrane (Nicchia et al., 2000). The entire astrocytic surface is thus provided with an AQP4-dependent osmotic water permeability. We used primary cultures of astrocytes to determine the effect of PKG activation on AQP4. We employed a microfluidic cell volume sensor (Ateya et al., 2005), which meets the required experimental criteria of swift solution change and fast sampling rate, to measure the osmotic water permeability of the astrocytic culture (Fig. 4A). The premise is based on placing the cells in a small sensing chamber and applying a constant current through the chamber. Upon cell swelling, the free volume of the sensing chamber is reduced and the electric resistance therefore increased. The change in voltage is thus a sensitive and robust read-out of cell volume changes and is stable over the entire duration of the experiment. Upon a swift solution change to a test solution containing 60 mOsm less mannitol than the control solution, the astrocytes swelled immediately as illustrated by the solid trace in Fig. 4B. The dotted line indicates the rate of solute change which clearly precedes the rate of cell swelling. The astrocytes were exposed to two consecutive hyposmotic challenges, a representative trace of which is shown in Fig. 4C, left trace. Subsequently, the astrocytes were exposed to the membrane-permeable cGMP analog (8-Br-cGMP, 100 μM, 12 min) before exposure to hyposmotic challenges identical to those of the control except the presence of 8-Br-cGMP in both control and hyposmotic test solution (Fig. 4C, right trace). PKG has repeatedly been shown to be activated in cultured astrocytes by membrane-permeable analogs of cGMP (Brahmachari et al., 2006; Konopacka et al., 2009; Sporbert et al., 1999). The rate of osmotically-induced astrocytic swelling was identical before and after exposure to the PKG activator. The data, along with those obtained with the alternative PKG activator, 8-pCPT-cGMP, are summarized in Fig. 4D where the rate of astrocytic cell swelling upon exposure to cGMP analogs is presented as % of that of the control; 101.7 ± 7.1, n = 5 for 8-Br-cGMP and 93.9 ± 5.4, n = 6 for 8-pCPT-cGMP.

Molecular Dynamics Simulations

Molecular dynamics simulations were performed on AQP4 to obtain a scenario in which a phosphate-group was attached to Ser^{111} (Fig. 5A). In the simulation time window, we observed no significant effect of the phosphorylation of Ser^{111} (pS111-AQP4) on the conformation of the Ser^{111}-containing loop B or of the loop D (Fig. 5B). Nor did the phosphorylation of Ser^{111} affect the water permeability of AQP4, (in $\times 10^{-14}$ cm^3/sec); 1.93 ± 0.41 for AQP4 and 1.94 ± 0.39 for pS111-AQP4, n = 8 (Fig. 5C). To determine the effect of a phosphorylation of Ser^{111} on the flexibility of the B-loop, we compared the Root Mean Square Fluctuations (RMSF) of the

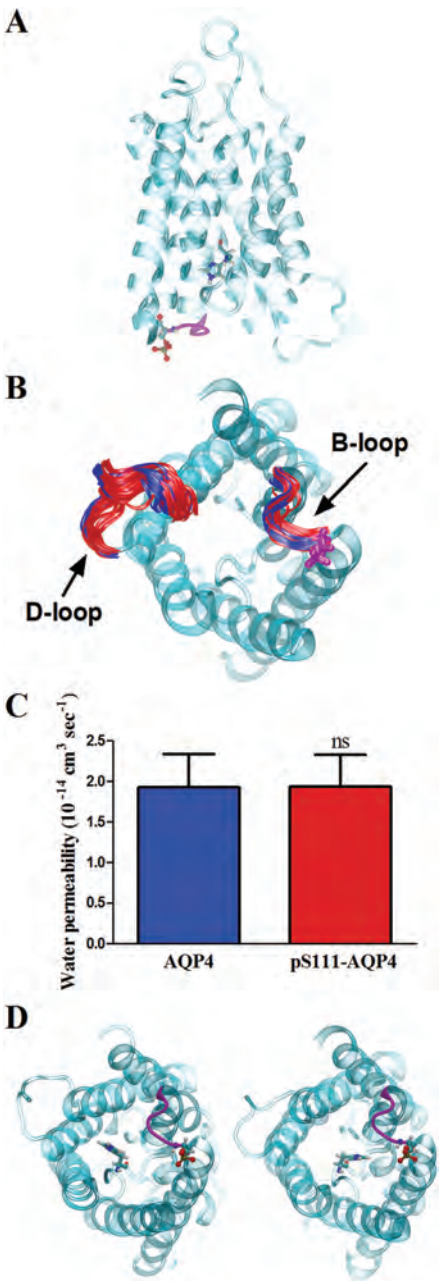

FIGURE 5: Molecular dynamics simulation on AQP4 revealed no functional effect of phosphorylation of Ser^{111} on the water permeability of AQP4. (A) Side-view of an AQP4 monomer with the B loop in magenta and with a phosphate-group (shown in ball and stick model) attached to Ser^{111}. His^{95} is emphasized in licorice representation. (B) Recorded conformations of the B and D loop in the non-phosphorylated (blue) and the phosphorylated form (red), viewed from the intracellular side. The average position of phosphorylated Ser^{111} is shown in licorice representation. The phosphorylated and non-phosphorylated conformations largely overlap and neither blocked the channel. (C) The summarized recorded water permeability of AQP4 whether non-phosphorylated (blue) or phosphorylated (red) was not statistically different (n = 8 blocks, Student's t-test). (D) View of an AQP4 monomer from the intracellular side with loop B in magenta and the phosphorylated Ser^{111} depicted in ball and stick representation. His^{95}, shown in licorice representation, transiently moves into (left panel) and out of (right panel) the pore during the simulation.

backbone atoms of the loop residues over 400 ns of the simulation. There was no significant change in the motion of the loop between the phosphorylated and the non-phosphorylated forms (data not shown). During the simulation, His^{95} was discovered to transiently move in and out of the channel pore of the AQP4 (Fig. 5D). In the initial simulations, we had predicted this residue to have a single protonation and thus be neutral. Since this residue was placed within 1 nm distance of the Ser^{111}, a protonation of this His^{95} could possibly prevent it from blocking the channel pore by electrostatic interaction with the negatively charged phosphate-moiety attached to Ser^{111}. His^{95} might thus become doubly protonated, due to a pK_a shift upon phosphorylation, and thereby change its conformation and transiently block the water pore. To test this hypothesis, we used both the doubly protonated and the neutral (singly protonated at epsilon nitrogen) forms of this histidine in simulations. However, also in the simulations with a doubly protonated His^{95} did we observe no significant difference in the water permeability between the two forms of AQP4 (data not shown).

No Detectable In Vivo *Phosphorylation of Ser^{111}*

Phosphorylation of Ser^{111} is the proposed molecular determinant for the putative gating mechanism for AQP4. A PKG-dependent phosphorylation of a *peptide* encoding the respective consensus sequence has been demonstrated (Gunnarson et al., 2008) but *in vivo* or *in vitro* phosphorylation of whole-length AQP4 at this residue has not. We generated a phospho-specific antibody that recognizes an epitope surrounding the Ser^{111} *solely* when the Ser^{111} is phosphorylated, pS111-AQP4 (Fig. 6A). The selectivity toward the phosphorylated peptide is demonstrated by dot blot with the native and the phosphorylated peptides encoding the region in question, i.e., the antibody epitope (Fig. 6B).

Rat brain slices were incubated 60 min in the presence or absence of the mGluR agonist DHPG, which has been proposed to induce downstream PKG-dependent phosphorylation of AQP4 at Ser^{111} (Gunnarson et al., 2008). Brain homogenate was subsequently prepared in the presence of a cocktail of phosphatase inhibitors to preserve possible phosphorylation of AQP4. Immunoblots of the brain homogenate were performed with either the conventional C-terminal AQP4 antibody (Fig. 6C, left panel) or the pS111-AQP4 antibody (Fig 6C, right panel). The left lane in both panels is loaded with the brain homogenate of slices kept in control solution and the right lane in both panels is loaded with the homogenate of slices exposed to DHPG. The three different isoforms of AQP4, M1, M23, and Mz (Moe et al., 2008), were visible on the immunoblot based on the conventional AQP4 antibody (Fig. 6C, left panel) whereas no immunoreactivity was detected with the pS111-AQP4 antibody

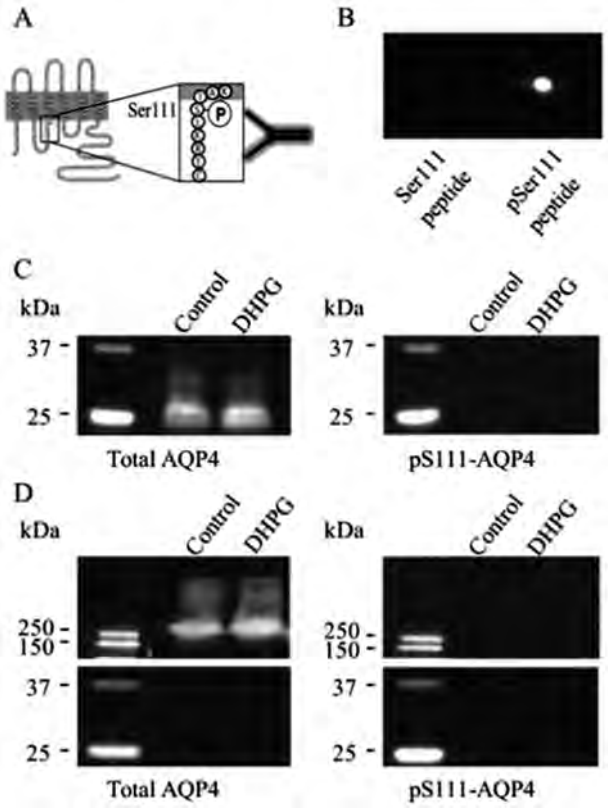

FIGURE 6: No evidence in favor of *in vivo* phosphorylation of Ser^{111} on AQP4 in rat brain. (A) A schematic diagram depicting the epitope recognized by the phospho-specific antibody pS111-AQP4. (B) Dot blot analysis demonstrates that the anti-pS111-AQP4 antibody recognizes exclusively the AQP4 peptide encoding the *phosphorylated* Ser^{111} and not the peptide encoding the non-phosphorylated Ser^{111}. (C, D) Immunoblotting of whole rat brain lysate incubated 60 min in either a control solution (lane 1) or a solution containing 50 μM of the mGluR1/5 agonist DHPG (lane 2); left panel with a conventional C-terminal anti-AQP4 antibody and right panel with the custom-made pS111-AQP4 antibody (size marker on left side of all blots). Before loading, samples were (C) kept at room temperature or (D) heated to 90°C. The total amount of AQP4 was unaffected by treatment with DHPG (left panels) and no immuno-reactivity was detected with the pS111-AQP4 antibody regardless of DHPG treatment (right panels), $n = 3$.

(Fig. 6C, right panel), $n = 3$. As steric hindrance of the antibody to its epitope cannot be ruled out, we attempted to alter the accessibility of the epitope by complete denaturation of AQP4: a separate sample of the brain homogenate was heated to 90°C before immunoblotting. This treatment, in association with the denaturing process, promotes aggregation of AQP4 (Sorbo et al., 2007), which is thus detected at higher molecular weight when immunoblotted with the conventional antibody (Fig. 6D, left panel). No immuno-reactivity of the pS111-AQP4 antibody was observed under these conditions (Fig. 6D, right panel). Exposure of the brain slice to DHPG did not induce detectable phosphorylation of AQP4 on Ser^{111}, indicating that AQP4 may not be phosphorylated in this manner *in vivo*.

Discussion

In the present work we have addressed the controversial issue of phosphorylation-dependent gating of AQP4 as a physiological mechanism for regulation of the osmotic water permeability of AQP4-expressing astrocytes. The low intrinsic osmotic water permeability of the plasma membrane of *Xenopus laevis* oocytes makes this heterologous expression system ideal for quantitative studies of water permeability of select proteins. The water permeability of *Xenopus* oocytes increased ~15-fold following expression of AQP4, in line with previous reports (e.g., Fenton et al., 2010). The AQP4-mediated water permeability was not increased by PKG or PKA activation, nor was it reduced by inhibition of these protein kinases. These experiments were performed with each oocyte as its own control, thus solidifying the obtained data by exclusion of individual expression levels as a factor of variance. The sensitivity of the experimental system toward protein kinase-mediated changes in water permeability has previously been documented: PKC-activation reduced the water permeability of AQP4-expressing oocytes (Fenton et al., 2010; Moeller et al., 2009a) in line with observations in an AQP4-expressing mammalian cell line (Zelenina et al., 2002). We verified the presence of both cGMP-activated PKG and cAMP-activated PKA in *Xenopus* oocytes; evident as a robust PKG-induced activation of the epithelial Na^+-channel, ENaC (Nie et al., 2009) or as a PKA-induced activation of the voltage-gated K^+-channel KCNQ1/KCNE1 (Dilly et al., 2004; Grunnet et al., 2003). Site-directed mutagenesis of Ser^{111} to an alanine prevents a putative phosphorylation of this residue. Nevertheless, this mutated form of AQP4 (S111A) displayed unit water permeability identical to that of the wild type AQP4. Similarly, mimicking a Ser^{111} phosphorylation by introducing an aspartic acid residue in place of Ser^{111} did not increase the AQP4-mediated water permeability.

AQP4 is highly expressed in astrocytes of the mammalian central nervous system (Nielsen et al., 1997) and is a major contributor to the osmotic water permeability of the astrocyte plasma membrane (Solenov et al., 2004). To determine the PKG-dependent regulatory impact on AQP4 in a more native setting, we measured the effect of PKG activation on the osmotic water permeability of astrocytes in primary culture. To study water permeability in small, highly water permeable cells with a large surface to volume ratio, a fast sampling rate is of absolute necessity to obtain the initial linear cell swelling. This initial segment represents the osmotic water permeability of the astrocytic membrane. Our data show that the solution exchange rate in the microfluidic volume sensor exceeds that of the cell swelling and thus ensures that the rate-limiting step for the cell volume response is the water permeability of the cell and not that of the solution change (Heo et al., 2008; Solenov et al., 2004). We obtained

no evidence for a PKG-dependent effect on the water permeability of the AQP4-containing astrocytic membrane.

Taken together, our data demonstrate a complete absence of Ser^{111} phosphorylation-dependent increase in AQP4-mediated water permeability. This conclusion is in contrast to earlier reports of kinase-dependent gating of AQP4 (Gunnarson et al., 2005, 2008; Song and Gunnarson 2012). In these studies CaMKII, PKA, and PKG were all, based on similar approaches, proposed to lead to phosphorylation of AQP4 on Ser^{111} and thereby increase AQP4-mediated water permeability. Activation of the metabotropic glutamate receptors mGluR1/5 in the astrocytic membrane was suggested to induce a signaling cascade of Ca^{2+} release, activation of CaMKII and subsequent induction of NO-synthase and associated NO production. NO would in turn induce cGMP generation followed by PKG-dependent increase of AQP4-mediated water permeability (Gunnarson et al., 2008). No PKG-dependent increase in water permeability was observed upon expression of AQP4 with the Ser^{111} mutated to an alanine (Gunnarson et al., 2008). Based thereupon, phosphorylation of this residue was claimed as the regulatory switch. Although the reason for the contradictory data is not clear, a few technical issues may offer at least a partial explanation: (i) The data in Gunnarson et al. (2005, 2008), and Song and Gunnarson (2012) were obtained with a sample rate of one scan every 2 s, i.e., 0.5 Hz (data in present study obtained with continuous recording), (ii) the water permeability was calculated from the values obtained within the first 6–10 seconds after introduction of the osmotic challenge (we use the values obtained within the initial couple of seconds, where the cell swelling is linear and maximal and therefore represents the osmotic water permeability of the cell membrane), (iii) the authors performed their experiments at 10°C in Gunnarson et al. (2005), and (iv) did not provide verification that the speed of solution change exceeded that of the rate of volume change. Since the same cells never acted as their own control, one cannot rule out that minor unaccounted-for differences in cell size between cells transfected with different constructs or the native cells used for background-subtraction (as previously observed (Silberstein et al., 2004)) could have affected their calculated osmotic water permeabilities.

Ser^{111} is conserved in human, mouse and rat AQP4 and corresponds to Ser^{115} in the spinach aquaporin SoPIP2;1 (Gunnarson et al., 2008). The crystal structure of SoPIP2;1 was determined in an open and a closed confirmation and molecular dynamics simulations were performed on the basis of this crystal structure (Tornroth-Horsefield et al., 2006). The simulations recorded an open conformation of the water channel when a phosphate-moiety, *in silico*, was attached to Ser^{115}. The authors predicted this to be due to an interaction between the D-loop and the N-terminus which would anchor the loop onto the cytoplasmic entrance to the pore (Tornroth-Horsefield et al., 2006). The 1.8Å crystal structure of AQP4 was recently obtained in an *open* conformation despite no indication of the presence of a phosphate-moiety on Ser^{111} (Ho et al., 2009). The D-loop of the AQP4 was, in addition, deemed too short to serve the role of a gate (Ho et al., 2009) which thus argues against phosphorylation-dependent gating of AQP4 with Ser^{111} as the molecular switch.

In our molecular dynamics simulations on AQP4, we did not observe a significant difference between the water permeability of AQP4 and its phosphorylated form. The motion of the B-loop that contains the Ser^{111} and of the D-loop was restricted in either form, in line with the observation that the D-loop may be too short for a large structural change (Ho et al., 2009). The protonation of His^{95}, positioned above the channel pore opposite loop B, might be affected by the phosphorylation state of the Ser^{111}. To probe for this possibility, simulations of a doubly protonated His^{95} were carried out. However, no interaction between His^{95} and the phosphorylated serine was observed in the simulations. Accordingly, no significant difference in the calculated water permeability between the two forms of AQP4 was observed, leading us to infer that electrostatic interaction between the histidine (His^{95}) and the phosphorylated serine (Ser^{111}) did not affect the channel gating. Thus the simulations carried out in the present study do not indicate any effect of phosphorylation of Ser^{111} on movement of loops B and D and thus gating of AQP4.

Lack of phosphorylation-dependent changes of the water permeability of AQP4 could be caused by the absence of a functional outcome of a given phosphorylation or a complete lack of phosphorylation of the residue in question. It has been demonstrated that PKG and PKA are indeed able to phosphorylate Ser^{111}, *in vitro,* on a peptide corresponding to the sequence around Ser^{111} but determination of the phosphorylated state of this residue in the intact protein was not attempted (Gunnarson et al., 2008; Song and Gunnarson, 2012). To assess the latter possibility, we generated a custom-made phospho-specific antibody designed to recognize the epitope containing Ser^{111} only when this residue is phosphorylated. The antibody recognized a phosphorylated peptide containing the Ser^{111} while showing no immune-reactivity toward the non-phosphorylated peptide. We did not detect Ser^{111}-phosphorylated AQP4 in rat brain treated with an mGluR1/5 analog proposed to induce phosphorylation of this very residue (Gunnarson et al., 2008). We lack, however, a good positive control at the whole-protein level, and therefore cannot completely exclude that steric hindrance might block the epitope from antibody binding in the intact protein. With the phospho-specific antibody, we performed immunoblot on semi- and completely denatured AQP4 as well as immunohistochemistry on rat and mouse kidney slices that express high levels of AQP4 in specific cell types (data not

shown). From these experimental paradigms, one may expect three different levels of epitope accessibility, neither of which yielded a positive immune-response with this antibody. Taken together with the elaborate, yet unsuccessful, experimental effort to induce *in vivo* phosphorylation of Ser^{115} in SoPIP2;1 (Johansson et al., 1998), our data suggest that Ser^{111} remains unphosphorylated *in vivo*. Unfortunately, attempts to validate these data by means of mass spectrometry were unsuccessful, as the particular peptide fragment containing the Ser^{111} residue was not amenable to detection by mass spectrometry.

AQP4, as well as phosphorylation-dependent regulation thereof, has been suggested to be a possible mediator of K^+- and glutamate-induced cell swelling as well as cytotoxic brain edema formation. Curiously, experimental evidence to that effect is generally obtained upon addition of large, non-physiologically occurring osmotic gradients in the order of 100-200 mOsm (Gunnarson et al., 2005, 2008; Nicchia et al., 2000; Solenov et al., 2004; Song and Gunnarson, 2012). The calculated osmotic water permeabilities have then been inferred to represent physiologically applicable water transport. It should be noted that such osmotic gradients across the astrocytic membrane are unlikely to arise; the highly water-permeable astrocytes will remain in osmotic equilibrium with their surroundings upon small perturbations of transmembranous osmotic gradients well within a sub-second timescale. Note the rapidly-achieved equilibrium observed in astrocytes (both with and without AQP4 expression) upon challenge with a large osmotic gradient at 37°C (Solenov et al., 2004). Accordingly, the rate-limiting factor for astrocytic cell swelling will be either osmolyte accumulation or activity of water-translocating cotransporters (for review see MacAulay and Zeuthen (2010, 2012)). In fact, it was recently demonstrated that AQP4-deficient mice display *increased* stimulus-induced astrocytic cell swelling compared to their WT counterpart (Haj-Yasein et al., 2012), thus providing evidence against AQP4 as a mediator of astrocytic cell swelling during neuronal activity.

In conclusion, we detect no evidence in favor of phosphorylation-dependent gating of AQP4 via Ser^{111}, whether in cultured astrocytes or upon heterologous expression of AQP4 in oocytes (with or without an intact Ser^{111}). AQP4 phosphorylated at Ser^{111} was not detected *in vivo* and experimental mimicking of a phosphorylated Ser^{111}, whether with a mutational strategy or via molecular dynamics simulations, recorded no difference in the water permeability of AQP4. Thus, phosphorylation-dependent gating of AQP4 at Ser^{111} is not, as earlier proposed, the molecular switch for astrocytic cell swelling or brain edema formation.

Acknowledgment

Grant sponsors: Lundbeck Foundation (to N.M., M.A., and R.A.F.), Danish Medical Research Council (to N.M. and R.A.F.), Novo Nordisk Foundation (to N.M. and R.A.F.), National Institutes of Health; Grant number: DK\-77302 (to S.Z.H.); Grant sponsor: Max Planck Society (to S.K. and B.dG.).

The authors greatly value the technical assistance provided by Charlotte Goos Iversen, Catia Correa Goncalves Andersen, Mary Teeling, Inger-Merete Paulsen, and Bodil Kruse. The authors' gratitude goes to the inventors of the microfluidic volume sensor: Drs. Susan Z. Hua, Fred Sachs, and Steve Besch at University of Buffalo. The authors highly appreciate Dr. Hua's generosity of including Mette Assentoft into her laboratory to conduct the present experiments and the technical advice provided by Jason Rahimzadeh. The authors are grateful to Michael Lund Nielsen at the Copenhagen Protein Center for his willingness to perform the mass spectrometry and to Kamilla Angelo for technical assistance with the rat brain preparation. The authors thank Dr. Camilo Aponte Santamaria for the implementation of the collective diffusion constant measurement for Gromacs.

References

Ateya DA, Sachs F, Gottlieb PA, Besch S, Hua SZ. Volume cytometry: Microfluidic sensor for high-throughput screening in real time. Anal Chem 2005;77:1290–1294.

Berendsen HJC, Grigera JR, Straatsma TP. The missing term in effective pair potentials. J Phys Chem 1987;91:6269–6271.

Berger O, Edholm O, Jahnig F. Molecular dynamics simulations of a fluid bilayer of dipalmitoylphosphatidylcholine at full hydration, constant pressure, and constant temperature. Biophys J 1997;72:2002–2013.

Brahmachari S, Fung YK, Pahan K. Induction of glial fibrillary acidic protein expression in astrocytes by nitric oxide. J Neurosci 2006;26:4930–4939.

Bussi G, Donadio D, Parrinello M. Canonical sampling through velocity rescaling. J Chem Phys 2007;126:014101.

Darden T, York D, Pedersen L. Particle mesh Ewald—An N.Log(N) method for Ewald sums in large systems. J Chem Phys 1993;98:10089–10092.

Dilly KW, Kurokawa J, Terrenoire C, Reiken S, Lederer WJ, Marks AR, Kass RS. Overexpression of beta2-adrenergic receptors cAMP-dependent protein kinase phosphorylates and modulates slow delayed rectifier potassium channels expressed in murine heart: evidence for receptor/channel co-localization. J Biol Chem 2004;279:40778–40787.

Feenstra KA, Hess B, Berendsen HJC. Improving efficiency of large time-scale molecular dynamics simulations of hydrogen-rich systems. J Comput Chem 1999;20:786–798.

Fenton RA, Moeller HB, Zelenina M, Snaebjornsson MT, Holen T, MacAulay N. Differential water permeability and regulation of three aquaporin 4 isoforms. Cell Mol Life Sci 2010;67:829–840.

Friedman B, Schachtrup C, Tsai PS, Shih AY, Akassoglou K, Kleinfeld D, Lyden PD. Acute vascular disruption and aquaporin 4 loss after stroke. Stroke 2009;40:2182–2190.

Frydenlund DS, Bhardwaj A, Otsuka T, Mylonakou MN, Yasumura T, Davidson KG, Zeynalov E, Skare O, Laake P, Haug FM, Rash JE, Agre P, Ottersen OP, Amiry-Moghaddam M. Temporary loss of perivascular aquaporin-4 in neocortex after transient middle cerebral artery occlusion in mice. Proc Natl Acad Sci USA 2006;103:13532–13536.

Grunnet M, Jespersen T, MacAulay N, Jorgensen NK, Schmitt N, Pongs O, Olesen SP, Klaerke DA. KCNQ1 channels sense small changes in cell volume. J Physiol 2003;549:419–27.

Gunnarson E, Axehult G, Baturina G, Zelenin S, Zelenina M, Aperia A. Lead induces increased water permeability in astrocytes expressing aquaporin 4. Neuroscience 2005;136:105–114.

Gunnarson E, Zelenina M, Axehult G, Song Y, Bondar A, Krieger P, Brismar H, Zelenin S, Aperia A. Identification of a molecular target for glutamate regulation of astrocyte water permeability. Glia 2008;56:587–596.

Haj-Yasein NN, Jensen V, Ostby I, Omholt SW, Voipio J, Kaila K, Ottersen OP, Hvalby O, Nagelhus EA. Aquaporin-4 regulates extracellular space volume dynamics during high-frequency synaptic stimulation: A gene deletion study in mouse hippocampus. Glia 2012;60:867–874.

Heo J, Meng F, Hua SZ. Contribution of aquaporins to cellular water transport observed by a microfluidic cell volume sensor. Anal Chem 2008;80: 6974–6980.

Hess B. P-LINCS: A parallel linear constraint solver for molecular simulation. J Chem Theory Comput 2008;4:116–122.

Hess B, Kutzner C, van der Spoel D, Lindahl E. GROMACS 4: Algorithms for highly efficient, load-balanced, and scalable molecular simulation. J Chem Theory Comput 2008;4:435–447.

Ho JD, Yeh R, Sandstrom A, Chorny I, Harries WE, Robbins RA, Miercke LJ, Stroud RM. Crystal structure of human aquaporin 4 at 1.8 A and its mechanism of conductance. Proc Natl Acad Sci USA 2009;106:7437–7442.

Homeyer N, Horn AHC, Lanig H, Sticht H. AMBER force-field parameters for phosphorylated amino acids in different protonation states: Phosphoserine, phosphothreonine, phosphotyrosine, and phosphohistidine. J Mol Model 2006;12:281–289.

Johansson I, Karlsson M, Shukla VK, Chrispeels MJ, Larsson C, Kjellbom P. Water transport activity of the plasma membrane aquaporin PM28A is regulated by phosphorylation. Plant Cell 1998;10:451–459.

Konopacka A, Konopacki FA, Albrecht J. Protein kinase G is involved in ammonia-induced swelling of astrocytes. J Neurochem 2009;109:246–251.

Langan TJ, Plunkett RJ, Asada H, Kelly K, Kaseloo P. Long-term production of neurotrophic factors by astrocyte cultures from hemiparkinsonian rat brain. Glia 1995;14:174–184.

Lindorff-Larsen K, Piana S, Palmo K, Maragakis P, Klepeis JL, Dror RO, Shaw DE. Improved side-chain torsion potentials for the Amber ff99SB protein force field. Proteins 2010;78:1950–1958.

MacAulay N, Zeuthen T. Water transport between cns compartments: Contributions of aquaporins and cotransporters. Neuroscience 2010;168: 941–956.

MacAulay N, Zeuthen T. Glial K(+) clearance and cell swelling: Key roles for cotransporters and pumps. Neurochem Res 2012;37:2299–309.

Maciejewski PM, Peterson FC, Anderson PJ, Brooks CL. Mutation of serine-90 to glutamic-acid mimics phosphorylation of bovine prolactin. J Biol Chem 1995;270:27661–27665.

Meng S, Qiao M, Lin L, Del Bigio MR, Tomanek B, Tuor UI. Correspondence of AQP4 expression and hypoxic-ischaemic brain oedema monitored by magnetic resonance imaging in the immature and juvenile rat. Eur J Neurosci 2004;19:2261–2269.

Moe SE, Sorbo JG, Sogaard R, Zeuthen T, Ottersen P, Holen T. New isoforms of rat Aquaporin-4. Genomics 2008;91:367–377.

Moeller HB, Fenton RA, Zeuthen T, Macaulay N. Vasopressin-dependent short-term regulation of aquaporin 4 expressed in Xenopus oocytes. Neuroscience 2009a;164:1674–1684.

Moeller HB, MacAulay N, Knepper MA, Fenton RA. Role of multiple phosphorylation sites in the COOH-terminal tail of aquaporin-2 for water transport: Evidence against channel gating. Am J Physiol Renal Physiol 2009b;296:F649–F657.

Nicchia GP, Frigeri A, Liuzzi GM, Santacroce MP, Nico B, Procino G, Quondamatteo F, Herken R, Roncali L, Svelto M. Aquaporin-4-containing astrocytes sustain a temperature- and mercury-insensitive swelling in vitro. Glia 2000;31:29–38.

Nie HG, Chen L, Han DY, Li J, Song WF, Wei SP, Fang XH, Gu X, Matalon S, Ji HL. Regulation of epithelial sodium channels by cGMP/PKGII. J Physiol 2009;587:2663–2676.

Nielsen S, Nagelhus EA, Amiry-Moghaddam M, Bourque C, Agre P, Ottersen OP. Specialized membrane domains for water transport in glial cells: High-resolution immunogold cytochemistry of aquaporin-4 in rat brain. J Neurosci 1997;17:171–180.

Papadopoulos MC, Verkman AS. Aquaporin-4 gene disruption in mice reduces brain swelling and mortality in pneumococcal meningitis. J Biol Chem 2005;280:13906–13912.

Ribeiro Mde C, Hirt L, Bogousslavsky J, Regli L, Badaut J. Time course of aquaporin expression after transient focal cerebral ischemia in mice. J Neurosci Res 2006;83:1231–1240.

Rusinova R, Shen YM, Dolios G, Padovan J, Yang H, Kirchberger M, Wang R, Logothetis DE. Mass spectrometric analysis reveals a functionally important PKA phosphorylation site in a Kir3 channel subunit. Pflugers Arch 2009;458: 303–314.

Saadoun S, Papadopoulos MC, Krishna S. Water transport becomes uncoupled from K+ siphoning in brain contusion, bacterial meningitis, and brain tumours: immunohistochemical case review. J Clin Pathol 2003;56: 972–975.

Silberstein C, Bouley R, Huang Y, Fang P, Pastor-Soler N, Brown D, Van Hoek AN. Membrane organization and function of M1 and M23 isoforms of aquaporin-4 in epithelial cells. Am J Physiol Renal Physiol 2004;287: F501–F511.

Solenov E, Watanabe H, Manley GT, Verkman AS. Sevenfold-reduced osmotic water permeability in primary astrocyte cultures from AQP-4-deficient mice, measured by a fluorescence quenching method. Am J Physiol Cell Physiol 2004;286:C426–C432.

Song Y, Gunnarson E. Potassium dependent regulation of astrocyte water permeability is mediated by cAMP signaling. PloS One 2012;7:e34936.

Sorbo JG, Moe SE, Holen T. Early upregulation in nasal epithelium and strong expression in olfactory bulb glomeruli suggest a role for Aquaporin-4 in olfaction. FEBS Lett 2007;581:4884–4890.

Sporbert A, Mertsch K, Smolenski A, Haseloff RF, Schonfelder G, Paul M, Ruth P, Walter U, Blasig IE. Phosphorylation of vasodilator-stimulated phosphoprotein: a consequence of nitric oxide- and cGMP-mediated signal transduction in brain capillary endothelial cells and astrocytes. Brain Res Mol Brain Res 1999;67:258–266.

Tornroth-Horsefield S, Wang Y, Hedfalk K, Johanson U, Karlsson M, Tajkhorshid E, Neutze R, Kjellbom P. Structural mechanism of plant aquaporin gating. Nature 2006;439:688–694.

Walz T, Fujiyoshi Y, Engel A. The AQP structure and functional implications. Handb Exp Pharmacol 2009;190:31–56.

Wolf MG, Hoefling M, Aponte-Santamaria C, Grubmuller H, Groenhof G. g_membed: Efficient insertion of a membrane protein into an equilibrated lipid bilayer with minimal perturbation. J Comput Chem 2010;31:2169–2174.

Zador Z, Stiver S, Wang V, Manley GT. Role of aquaporin-4 in cerebral edema and stroke. Handb Exp Pharmacol 2009;190:159–170.

Zelenina M, Zelenin S, Bondar AA, Brismar H, Aperia A. Water permeability of aquaporin-4 is decreased by protein kinase C and dopamine. Am J Physiol Renal Physiol 2002;283:F309–F318.

Zeuthen T, Belhage B, Zeuthen E. Water transport by Na+-coupled cotransporters of glucose (SGLT1) and of iodide (NIS). The dependence of substrate size studied at high resolution. J Physiol 2006;570:485–499.

Zhao J, Moore AN, Clifton GL, Dash PK. Sulforaphane enhances aquaporin-4 expression and decreases cerebral edema following traumatic brain injury. J Neurosci Res 2005;82:499–506.

Zhu FQ, Tajkhorshid E, Schulten K. Collective diffusion model for water permeation through microscopic channels. Phys Rev Lett 2004;93:224501.

RESEARCH ARTICLE

Contributions of the Na^+/K^+-ATPase, NKCC1, and Kir4.1 to Hippocampal K^+ Clearance and Volume Responses

Brian Roland Larsen,[1] Mette Assentoft,[1] Maria L. Cotrina,[2] Susan Z. Hua,[3] Maiken Nedergaard,[2] Kai Kaila,[4,5] Juha Voipio,[4] and Nanna MacAulay[1]

Network activity in the brain is associated with a transient increase in extracellular K^+ concentration. The excess K^+ is removed from the extracellular space by mechanisms proposed to involve Kir4.1-mediated spatial buffering, the $Na^+/K^+/2Cl^-$ cotransporter 1 (NKCC1), and/or Na^+/K^+-ATPase activity. Their individual contribution to $[K^+]_o$ management has been of extended controversy. This study aimed, by several complementary approaches, to delineate the transport characteristics of Kir4.1, NKCC1, and Na^+/K^+-ATPase and to resolve their involvement in clearance of extracellular K^+ transients. Primary cultures of rat astrocytes displayed robust NKCC1 activity with $[K^+]_o$ increases above basal levels. Increased $[K^+]_o$ produced NKCC1-mediated swelling of cultured astrocytes and NKCC1 could thereby potentially act as a mechanism of K^+ clearance while concomitantly mediate the associated shrinkage of the extracellular space. In rat hippocampal slices, inhibition of NKCC1 failed to affect the rate of K^+ removal from the extracellular space while Kir4.1 enacted its spatial buffering only during a local $[K^+]_o$ increase. In contrast, inhibition of the different isoforms of Na^+/K^+-ATPase reduced post-stimulus clearance of K^+ transients. The astrocyte-characteristic $\alpha2\beta2$ subunit composition of Na^+/K^+-ATPase, when expressed in *Xenopus* oocytes, displayed a K^+ affinity and voltage-sensitivity that would render this subunit composition specifically geared for controlling $[K^+]_o$ during neuronal activity. In rat hippocampal slices, simultaneous measurements of the extracellular space volume revealed that neither Kir4.1, NKCC1, nor Na^+/K^+-ATPase accounted for the stimulus-induced shrinkage of the extracellular space. Thus, NKCC1 plays no role in activity-induced extracellular K^+ recovery in native hippocampal tissue while Kir4.1 and Na^+/K^+-ATPase serve temporally distinct roles.

GLIA 2014;62:608–622

Key words: extracellular ion homeostasis, cell volume changes in mammalian brain, ion transport

Introduction

Neuronal activity is associated with efflux of K^+ into brain extracellular space, where its accumulation can cause depolarization of neurons and glia and disturbance of neuronal signaling. Therefore, regulation of the extracellular K^+ concentration ($[K^+]_o$) is of vital importance for neuronal function. *In vitro* studies have shown that stimulation-induced increases in $[K^+]_o$ are paralleled by accumulation of K^+ in astrocytes, suggesting an astrocytic contribution to $[K^+]_o$ regulation (Ballanyi et al., 1987; Grafe and Ballanyi, 1987). Neuronal activity is, in addition, associated with shrinkage of the extracellular space (Dietzel et al., 1980; Ransom et al., 1985) probably due to astrocytic swelling (MacVicar et al., 2002). The molecular mechanism(s) responsible for clearance of the stimulus-evoked K^+ transient and the associated shrinkage of the extracellular space have been intensely debated during several decades (for review, see Hertz et al., 2013; MacAulay and Zeuthen, 2012) and their individual contributions remain to be quantified.

The concept of spatial buffering as a mechanism of K^+ clearance was originally coined by Orkand et al. (1966) and is often assigned a prominent role as a mechanism of K^+ clearance (Kofuji and Newman, 2004; Walz, 2000). The premise is based on influx of K^+ through a K^+ channel, that is,

View this article online at wileyonlinelibrary.com. DOI: 10.1002/glia.22629

Published online January 30, 2014 in Wiley Online Library (wileyonlinelibrary.com). Received Nov 5, 2013, Accepted for publication Dec 23, 2013.

Address correspondence to Nanna MacAulay, Department of Cellular and Molecular Medicine, Faculty of Health and Medical Sciences, University of Copenhagen, Blegdamsvej 3, 2200 Copenhagen, Denmark. E-mail: macaulay@sund.ku.dk

From the [1]Department of Cellular and Molecular Medicine, Faculty of Health and Medical Sciences, University of Copenhagen, Copenhagen, Denmark; [2]School of Medicine and Dentistry, University of Rochester Medical Center, Rochester, New York; [3]Department of Mechanical and Aerospace Engineering, University of Buffalo, Buffalo, New York; [4]Department of Biosciences, University of Helsinki, Helsinki, Finland; [5]Neuroscience Center, University of Helsinki, Helsinki, Finland.

the astrocytic Kir4.1 (Kofuji and Newman, 2004; MacAulay and Zeuthen, 2012). The positive charge entering as K^+ spreads electrotonically through the cytoplasm and exits again as K^+ at locations distant from the active neurons (Newman et al., 1984) with no associated overall increase in the intracellular K^+ concentration (Orkand et al., 1966; Walz, 2000). Although the existence of spatial buffering of K^+ has been documented (Karwoski et al., 1989; Strohschein et al., 2011), its quantitative contribution to K^+ clearance is uncertain.

Involvement of the Na^+/K^+-ATPase in clearance of K^+ from the extracellular space following neuronal activity has been demonstrated (D'Ambrosio et al., 2002; Ransom et al., 2000) although the contribution of the different α and β isoforms of the Na^+/K^+-ATPase remains unresolved.

Kir4.1-dependent influx of K^+ was proposed to functionally couple with aquaporin-4 (AQP4) to mediate the associated flux of water required for astrocytic cell swelling (Amiry-Moghaddam and Ottersen, 2003; Nagelhus et al., 2004; Strohschein et al., 2011). This coupling was recently rejected as neither AQP4 nor Kir4.1 appeared to be required for stimulus-induced shrinkage of the extracellular space (Haj-Yasein et al., 2011, 2012). The stoichiometry of the Na^+/K^+-ATPase ($3Na^+$:$2K^+$) generates an efflux of one osmotic particle per turnover and is therefore unlikely to directly provide the osmotic driving force for an accompanying cell swelling. The $Na^+/K^+/2Cl^-$ cotransporter 1 (NKCC1) has been indicated as a mechanism involved in stimulus-evoked astrocytic cell swelling (MacVicar and Hochman, 1991; MacVicar et al., 2002; Ransom et al., 1985) and may therefore partake in the clearance of excess K^+ from the extracellular space (MacVicar et al., 2002; Walz, 2000). This study aimed to determine the molecular characteristics of the K^+ transporting proteins in cell-based experimental systems and subsequently quantify their relative contribution to clearance of stimulus-evoked K^+ transients and the associated shrinkage of extracellular space in brain slices.

Materials and Methods

Heterologous Expression in Xenopus laevis Oocytes

Rat Na^+/K^+-ATPase $\alpha1$, $\alpha2$, $\alpha3$, $\beta1$, and $\beta2$ subunit isoforms and rat NKCC1 were subcloned into the oocyte expression vector pXOOM, linearized downstream from the poly-A segment, and *in vitro* transcribed using T7 mMessage machine according to manufacturer's instructions (Ambion, Austin, TX). cRNA was extracted with MEGAclear (Ambion) and micro-injected into defolliculated *X. laevis* oocytes: 10–20 ng $\alpha1$–3 RNA/oocyte in combination with 3–6 ng $\beta1$ or $\beta2$ RNA/oocyte (10:3 ratio) or 50 ng NKCC1 RNA/oocyte. *X. laevis* frogs were obtained from Nasco (Fort Atkinson, WI) or National center for Scientific Research (France). The surgical protocol, by which the oocytes were retrieved, was approved by The Danish National Committee for Animal Studies. The preparation of defolliculated oocytes was performed as described in (Moeller et al., 2009) and the oocytes were kept in Kulori medium (in mM): 90 NaCl, 1 KCl, 1 $CaCl_2$, 1 $MgCl_2$, 5 HEPES (pH 7.4) for 4–5 days at 19°C prior to experiments.

Primary Cultures of Rat Astrocytes

Astrocytes for radioactive tracer experiments: cortical rat astrocytes were cultured from dissected cerebral cortices of P7–P8 rat pups (Sprague–Dawley, Taconic, Denmark). The dissected cortices were dissociated mechanically by passing the tissue through an 80 μm nylon sieve into Dulbecco's modified Eagle's medium (DMEM) (D-5030, Sigma–Aldrich) containing an additional 6 mM D-glucose, 2.5 mM L-glutamine, 26.2 mM $NaHCO_3$, 100,000 IU/L of penicillin, and 20% fetal bovine serum (catalog nr 04-007-1a, lot 516714, Biological Industries, Israel). Single cells were generated by trituration with a syringe equipped with a steel cannula and plated in 24-well tissue culture plates (734-2325, VWR, Denmark). The fetal bovine serum concentration was sequentially reduced to 15% and 10% on the second and third week of culture. dB-cAMP (0.25 mM) (D-0627, Sigma-Aldrich) was added to the culture medium in the third week of culture to obtain morphologically differentiated astrocytes (Su et al., 2000). Immunocytochemical staining for glial fibrillary acidic protein (GFAP), a marker protein for astroglial cells, illustrated that >95% of the cells present in culture were astrocytes (data not shown). The astrocytes were kept at 37°C with an atmosphere of 5% CO_2 and were used for experiments 3–4 weeks after plating.

Astrocytes for volume measurements: adult male Sprague–Dawley rats (250–300 g) were used for the astrocytic preparation as described in detail in (Langan et al., 1995). These cultures have previously been used for volume measurements in (Assentoft et al., 2013; Ateya et al., 2005). In brief, adult astrocytes were isolated from gelatin-sponge implants left in the animal for 3 days. Sponges were subsequently removed, minced, and triturated followed by trypsination and passage through a nylon mesh with pore diameter of 20 μm. The astrocytes were maintained in DMEM supplemented with 10% fetal bovine serum and 1% penicillin/streptomycin. Cells between passage 5 and 15 were used and experiments performed 2–5 days after passage.

Electrophysiology of Oocytes

Conventional two-electrode voltage clamp studies were performed with a DAGAN CA-1B High Performance oocyte clamp (DAGAN, Minneapolis, MN) with Digidata 1322A interface controlled by pCLAMP software, version 9.2 (Molecular Devices, Burlingame, CA). Electrodes were pulled from borosilicate glass capillaries to a resistance of 1–5 MΩ when filled with 1 M KCl. The current traces were obtained by stepping the clamp potential from −50 mV to test potentials ranging from 0 to −100 mV in 20 mV increments (200-ms pulses). Recordings were low pass-filtered at 500 Hz and sampled at 2 kHz. The perfusion solution consisted of (in mM): 30 choline chloride (ChCl), 70 NaCl, 1 $MgCl_2$, 1 $CaCl_2$, 10 HEPES (pH 7.4), with KCl substituting for ChCl to vary the K^+ concentration. For each individual oocyte, the membrane currents were obtained in a range of test solutions containing increasing concentrations of K^+ from which the membrane currents obtained at 0 mM KCl were subsequently subtracted to isolate the K^+-sensitive currents. To

obtain the Na^+/K^+-ATPase-mediated currents, the experimental series was repeated in the presence of 1 mM ouabain (O-3125, Sigma–Aldrich).

Radioactive Uptake

Transport activity of NKCC1 and the Na^+/K^+-ATPase was determined as the bumetanide-sensitive (NKCC1) or ouabain-sensitive (Na^+/K^+-ATPase) influx of the radioactive K^+ congener $^{86}Rb^+$ (NEZ072001MC, Perkin Elmer, Germany). Oocytes were pre-incubated at room temperature in (in mM): 30 ChCl, 70 NaCl, 1 $MgCl_2$, 1 $CaCl_2$, 10 HEPES (at pH 7.4) for 30 min, 10 oocytes per condition. The oocytes were subsequently transferred to isosmotic solutions in which KCl substituted for ChCl to obtain different $[K^+]_o$ with 2 μCi/mL $^{86}Rb^+$ added. Bumetanide (10 μM) (B3023, Sigma-Aldrich) or 1 μL/mL ethanol (vehicle control) was included in the uptake solutions. The uptake experiment was performed at room temperature for 5 min which we previously demonstrated was at a time point in which time-linearity was maintained (Zeuthen and MacAulay, 2012). The assay was terminated with three brief washes in ice-cold media containing 30 mM KCl prior to individual solubilization in scintillation vials with 200 μL 10% sodium dodecyl sulfate (SDS). The radioactivity present was determined by liquid scintillation counting with Opti Fluor scintillation liquid (6013199, Perkin Elmer) in a Tri-Carb 2900TR Liquid Scintillation Analyzer (Packard). The obtained counts were corrected for the varying amount of K^+ present in the uptake solution.

Primary cultures of rat astrocytes grown in 24-well plates were allowed to equilibrate at 37°C for 5 min in solution containing (in mM): 30 ChCl, 104 NaCl, 1.2 $CaCl_2$, 1 $MgCl_2$, 5 D-glucose, and 20 HEPES (pH 7.4). $^{86}Rb^+$ tracer uptake took place at 37°C for a period of 20 s in an isosmotic solution in which KCl substituted for ChCl to obtain the required $[K^+]_o$, with 2 μCi/mL $^{86}Rb^+$ present in the given solution. For each K^+ concentration, a control uptake experiment was performed in triplicate in parallel with experiments with bumetanide (10 μM) or ouabain (1 mM), with all solutions containing 1 μL/mL ethanol as a vehicle control for bumetanide. The experiment was terminated by aspiration of the $^{86}Rb^+$-containing medium followed by three rapid rinses with a solution containing 30 mM KCl, 10 μM bumetanide, 1 mM ouabain, and 50 μM $BaCl_2$ to minimize leakage of $^{86}Rb^+$. The cells were lyzed in 250 μL 1 M NaOH, 100 μL transferred to scintillation tubes, while the rest was used for protein content determination (BioRad DC Protein Assay cat. no. 500-0116, BioRad). The radioactive content was determined by liquid scintillation counting with UltimaGold™ XR (6013119, Perkin Elmer) in a Tri-Carb 2900TR Liquid Scintillation Analyzer (Packard). The obtained counts were corrected for the varying amount of K^+ present in the uptake solution.

Microfluidic Cell Volume Sensor

A microfluidic cell volume sensor was used to study volume changes in astrocytes, as previously described (Ateya et al., 2005). Astrocytes were grown on a microscope slide that was inverted over the sensor chip thereby creating a flow chamber with a fixed volume of 60 nL. A sinusoidal current of 50 Hz, 1 μA was provided to the two outer electrodes in the chamber and the voltage was measured between the two inner electrodes. An increase in cell volume will increase the chamber resistance and thus an increase in voltage serves as the functional read-out of cell swelling. The solutions containing the different K^+ concentrations were created from two isosmolar stock solutions: a 0 mM K^+ stock consisting of (in mM): 129 NaCl, 30 ChCl, 1 $MgCl_2$, 1.2 $CaCl_2$, 5 D-glucose, 20 HEPES, 24.15 mannitol, and a 30 mM K^+ stock consisting of (in mM): 114 NaCl, 30 KCl, 1 $MgCl_2$, 1.2 $CaCl_2$, 5 glucose, 20 HEPES, and 36.2 mannitol. The concentrations of NaCl and mannitol in the two solutions were adjusted to obtain identical conductivity and osmolarity (verified with a cryoscopic osmometer [Gonotec, Berlin, Germany] and a conductivity meter [Thermo Scientific]). The flow rate of the solution (~30 μL/min) was controlled by adjusting hydraulic pressure at the inlet.

Brain Slices and Solutions

Experiments were performed on male Wistar rats at P21–P30. Rats were anesthetized using gaseous 2-Bromo-2-Chloro-1,1,1-Trifluoroethane (B-4388, Sigma-Aldrich). Following decapitation, the brain was quickly removed and placed into ice-cold cutting solution containing (in mM): 87 NaCl, 70 sucrose, 2.5 KCl, 0.5 $CaCl_2$, 25 $NaHCO_3$, 1.1 NaH_2PO_4, 7 $MgSO_4$, and 25 D-glucose, equilibrated with 95% O_2, 5% CO_2. Oblique sagittal (transverse) hippocampal slices (400 μm) were cut with a Campden Vibrating Microtome (7000SMZ, Campden Instruments, UK). Slices were transferred to the standard solution containing (in mM): 124 NaCl, 3 KCl, 2 $CaCl_2$, 25 $NaHCO_3$, 1.1 NaH_2PO_4, 2 $MgSO_4$, and 10 D-glucose, and equilibrated with 95% O_2, 5% CO_2 (pH 7.4 at the experimental temperature of 33–34°C) and left to recover at 34°C for 30 min and then kept at room temperature. In experiments involving $BaCl_2$, NaH_2PO_4 was replaced with NaCl and $MgSO_4$ replaced with $MgCl_2$ to prevent precipitation. All experiments were approved by the Ethics Committee for Animal Research at the University of Helsinki and complied with the policy of the Society for Neuroscience.

Ion-Sensitive Microelectrodes and Electrophysiological Recordings in Slices

Electrophysiological recordings were performed in a custom-made submerged-type recording chamber (volume 800 μL, 33–34°C) with continuous superfusion of both sides of the slice at a flow rate of 2 mL/min. Recordings were performed within stratum radiatum of the CA1 region. High-frequency stimulation (HFS) was delivered by a bipolar electrode inserted into the stratum radiatum in the vicinity ($\leq$500 μm) of the recording site. Stimulation trains (10–20 V, 60–80 μs pulses at 20 Hz for 10 s) were delivered at 5-min intervals. The resulting extracellular field potentials were recorded with glass capillary microelectrodes pulled to resistances of 1–10 MΩ when filled with the standard solution (see above). This electrode served as reference signal for the ion-sensitive microelectrodes. Ion-sensitive microelectrodes were prepared from thin walled non-filamented glass capillaries (GC150T-7.5, Harvard Apparatus) pulled to obtain a tip diameter in the range of 1–2 μm (Voipio et al., 1994). The capillaries were then silanized with gaseous *N,N*-dimethyltrimethylsilylamine (41716, Sigma–Aldrich) at 200°C for 20 min prior to being filled with the selected backfilling solution and a short column of liquid membrane solution. Potassium-sensitive

microelectrodes were made with a valinomycin-based membrane solution (99373, Potassium Ionophore I Cocktail B, Sigma-Aldrich) and backfilled with 150 mM NaCl, 3 mM KCl. The tetramethylammonium (TMA^+)-sensitive microelectrodes were generated with a membrane solution consisting of 50 mg/mL potassium tetrakis (4-chlorophenyl) borate (60591, Sigma–Aldrich) in 1,2-dimethyl-3-nitrobenzene (40870, Sigma-Aldrich) and backfilled with 150 mM TMA-Cl (Nicholson and Phillips, 1981; Voipio et al., 1994). For recordings of extracellular volume changes by means of these TMA^+-sensitive electrodes, 1.5 mM TMA-Cl (stock solution, 5 M, Sigma-Aldrich) was added to the recording solution. For simultaneous recordings of $[K^+]_o$ and extracellular volume changes, the valinomycin-containing electrodes were used to monitor $[K^+]_o$ while TMA^+-sensitive electrodes monitored changes in extracellular space volume. The tips of the recording and reference electrodes were placed $\leq$ tens of μm from each other in the core of the slice. In experiments designed to exclusively monitor $[K^+]_o$, TMA^+-sensitive electrodes were used. These electrodes act as K^+-sensors in the absence of TMA^+ in the recording solution (Voipio et al., 1994). The ion-sensitive microelectrodes were calibrated at the end of the experiments and the recorded signals were converted off line to obtain the K^+ concentration and % change in extracellular space (Voipio et al., 1994). Focal application of K^+ by means of iontophoresis (the release of substances through the application of current) was performed with a glass capillary microelectrode, similar to the one recording extracellular field potentials, filled with 1 M KCl. To prevent leakage, a continuous backing current of -1 nA was applied. K^+ was delivered to the slice by application of a 0–100 nA current for 5 s at 10-min intervals. In the iontophoresis experiments, the recording solution contained a cocktail of inhibitors to prevent spiking and activation of glutamate and GABA receptors: DL-2-amino-5-phosphonopentanoic acid (AP-5, 40 μM), 2,3-dioxo-6-nitro-1,2,3,4-tetrahydrobenzo[f]quinoxaline-7-sulfonamide disodium salt (NBQX, 10 μM), picrotoxin (PiTX, 100 μM), (2S)$-$3-[[(1S)$-$1-(3,4-dichlorophenyl)ethyl]amino-2-hydroxypropyl] (phenylmethyl) phosphinic acid (CGP-55845, 1 μM), tetrodotoxin (TTX, 1 μM), all from Tocris Cookson (Bristol, UK). For all experiments, three consecutive control responses were recorded at intervals of 5 min (iontophoresis; 10 min) prior to bath application of drug. Wash-in of TMA^+ was estimated to be completed after $\sim$6 min. All drug traces used for illustration and quantification were recorded $\sim$7 min after bath application of the drug with exception of (1) the iontophoretic experiments where the slice was exposed to Ba^{2+} for $\sim$15 min prior to recording the response and (2) the 50 μM ouabain, with which the traces were recorded after $\sim$3 min to limit slice damage observed during extended exposure (at this time point extracellular $[K^+]_o$ had stabilized, indicating that ouabain had reached its full effect). With exception of 50 μM ouabain, a second response to drug was recorded 5 min later (10 min for iontophoretic experiments) to ensure that the drug had reached its full effect. All recorded signals were anti-alias filtered, sampled at 1 kHz and stored for off-line analysis with WinEDR (courtesy of Dr. John Dempster, University of Strathclyde, Glasgow, UK) and GraphPad Prism 5.0 (GraphPad Software).

Quantification of K^+ Clearance Rate

The maximum rate of K^+ clearance activated by an experimentally evoked transient rise in $[K^+]_o$ is proportional to the rate of fall in $[K^+]_o$ that is seen immediately after termination of stimulation-induced or iontophoretic release of K^+ into the extracellular space. In our experiments, the fall in $[K^+]_o$ during the first 1 (iontophoresis) or 2 s (stimulus) of K^+ clearance was linear. Therefore, we quantified the initial post-stimulus rate of fall in $[K^+]_o$ (in mM/s) and used it as a direct measure of K^+ clearance in the initial post-stimulus phase. The extracellular space volume changes during this interval were small, and little affected by the applied inhibitors, and therefore did not affect the quantification. We did not use the time constant or half-time of $[K^+]_o$ recovery, since addition of inhibitors of K^+-translocating mechanisms may alter the kinetics of the recovery phase by, for example, increasing peak $[K^+]_o$ and/or generating a post-clearance undershoot in $[K^+]_o$, as has been reported for the Kir4.1 inhibitor Ba^{2+} (Bay and Butt, 2012; Jauch et al., 2002; Oakley et al., 1992). These additional effects of inhibitors may indirectly affect the time constant of the clearance while not interfering with the rate of K^+ clearance (in mM/s).

Statistics

All data are given as mean $\pm$ SEM. Statistical significance was tested with either Student's *t*-test or one-way ANOVA with Dunnett's or Tukey's multiple comparison *post hoc* test, as indicated in figure legends. *P* values <0.05 were considered statistically significant. Data on astrocytes and oocytes were obtained from at least three different animal preparations.

Results

K^+ Transport Properties of NKCC1 and Na^+/K^+-ATPase

For any molecular mechanism involved in the clearance of K^+ from the brain extracellular space, a certain prerequisite should be met: The transport protein must increase its activity in response to an increase in $[K^+]_o$ above the basal level of $\sim$3 mM $[K^+]_o$. Primary cultures of rat astrocytes were used to determine the K^+-activation properties of NKCC1 and the Na^+/K^+-ATPase. The transport rates were determined by uptake experiments with $^{86}Rb^+$, a radioactive congener of K^+, as the bumetanide-sensitive (NKCC1) or ouabain-sensitive (Na^+/K^+-ATPase) uptake. Time-dependent saturation occurred after approximately 30 s of transport activity (Fig. 1A, insert). The subsequent uptake measurements were therefore performed for 20 s to ensure that time-dependent saturation would not obscure the factual transport limit and thus skew the apparent $K_{0.5}$ obtained for the transport proteins (all listed $K_{0.5}$ values are apparent affinities). NKCC1 displayed increased turnover velocity as a function of $[K^+]_o$ (1–30 mM), with a $K_{0.5} = 21.3 \pm 2.7$ mM, $n = 4$ (Fig. 1A). Earlier studies performed with $^{86}Rb^+$-uptake periods outside the linear range, arrived at lower $K_{0.5(K^+)}$ for NKCC1 (Tas et al., 1987). For illustrative purposes, we therefore allowed a 10-min long uptake period in an otherwise identical experiment and obtained a $K_{0.5}$ for K^+ of 1.9 ± 0.2 mM,

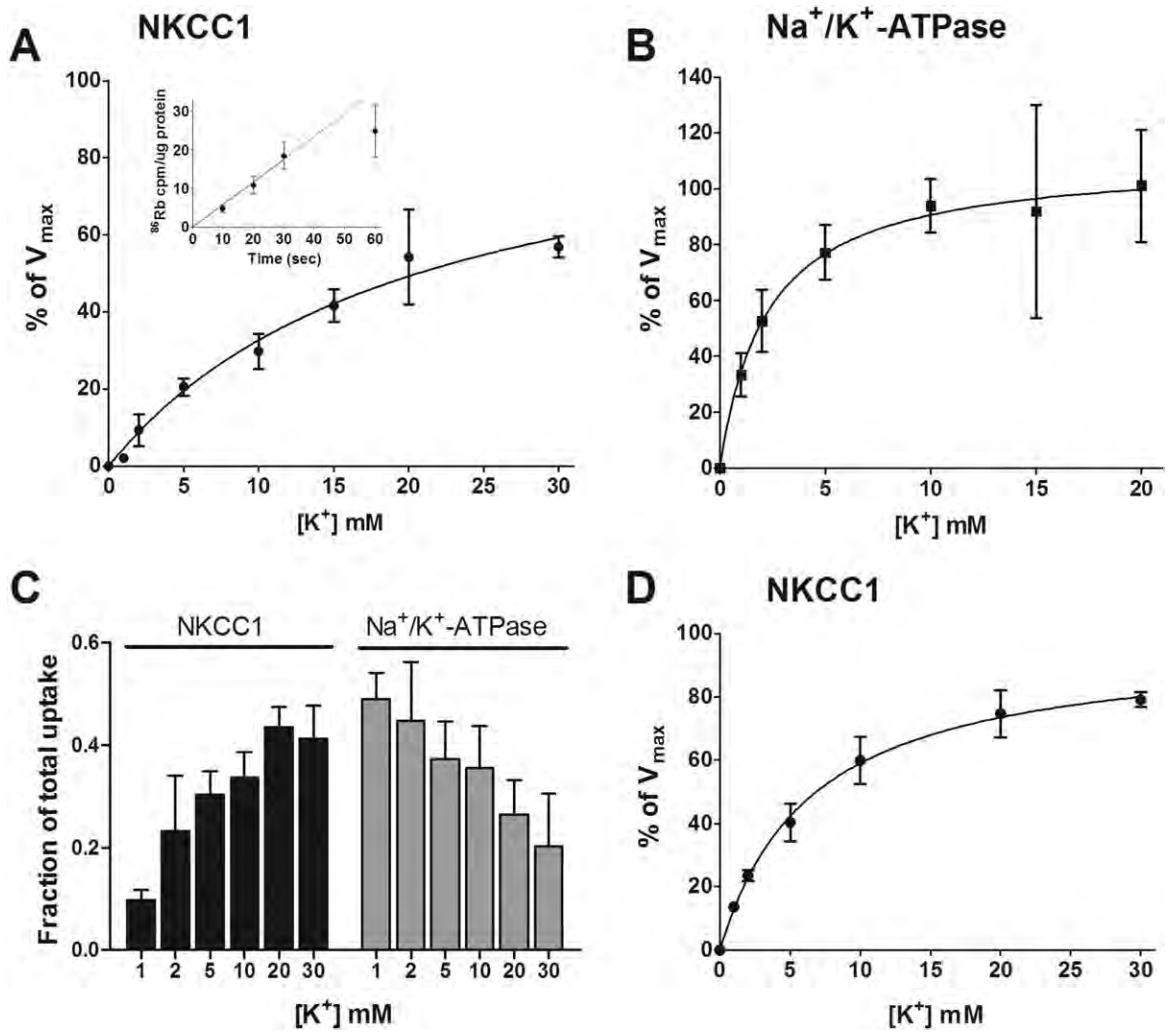

FIGURE 1: K^+-stimulated activity of NKCC1 and the Na^+/K^+-ATPase. (A–C) $^{86}Rb^+$ uptake in primary cultures of rat astrocytes: The NKCC1-dependent uptake was obtained as the bumetanide-sensitive (10 μM) fraction (A) after ensuring time-linearity (insert) and the Na^+/K^+-ATPase-dependent uptake as the ouabain-sensitive (1 mM) fraction (B). The individual experiments were fitted according to Michaelis–Menten kinetics and plotted as the average % of V_{max} as a function of $[K^+]_o$ ($n = 4$ experiments performed in triplicate with the $K_{0.5}$ obtained from each individual experiment prior to averaging). (C) The fractional contribution of NKCC1 and Na^+/K^+-ATPase to the total overall uptake at each K^+ concentration. (D) The bumetanide-sensitive (10 μM) uptake in rNKCC1-expressing *X. laevis* oocytes was fitted according to Michaelis–Menten kinetics and plotted as the average % of V_{max} as a function of $[K^+]_o$ whereas the $K_{0.5}$ was obtained from each individual experiment prior to averaging ($n = 3$ experiments with 10 oocytes per condition).

$n = 3$ (data not shown), similar to that obtained by Tas et al. (1987).

The Na^+/K^+-ATPase activity of cultured astrocytes is likely to consist of a mix of α- and β isoforms, most likely $\alpha 1$ and $\alpha 2$ (Juhaszova and Blaustein, 1997) in combination with the accessory β subunit, either $\beta 1$ or $\beta 2$. The apparent affinity of the Na^+/K^+-ATPase for K^+ ($K_{0.5} = 2.0 \pm 0.7$ mM, $n = 4$) was higher than that of NKCC1. Although saturation was approached already at 5 mM $[K^+]_o$, full saturation was not reached until an extracellular concentration of 10 mM K^+ (Fig. 1B). Thus, K^+ transport into cultured astrocytes at low to basal extracellular concentrations of K^+ (i.e., 1–5 mM) was predominantly performed by the Na^+/K^+-ATPase. The contribution of the Na^+/K^+-ATPase was roughly equal to that of NKCC1 at 10 mM $[K^+]$, above which NKCC1 became the primary mediator of the inwardly directed K^+ transport, Fig. 1C. Notably, a contribution of spatial buffering through Kir4.1 to K^+ uptake cannot be determined in a culture bathed in extracellular solution containing K^+, as the requirements for spatial buffering are not fulfilled in this experimental setting.

In addition, we determined the K^+-dependency of NKCC1 (bumetanide-sensitive fraction of the $^{86}Rb^+$ uptake) upon heterologous expression of rat NKCC1 in *X. laevis* oocytes (Fig. 1D). Although the $K_{0.5}$ was lower (7.3 ± 1.3 mM, $n = 3$) than that obtained in astrocytes, the data support

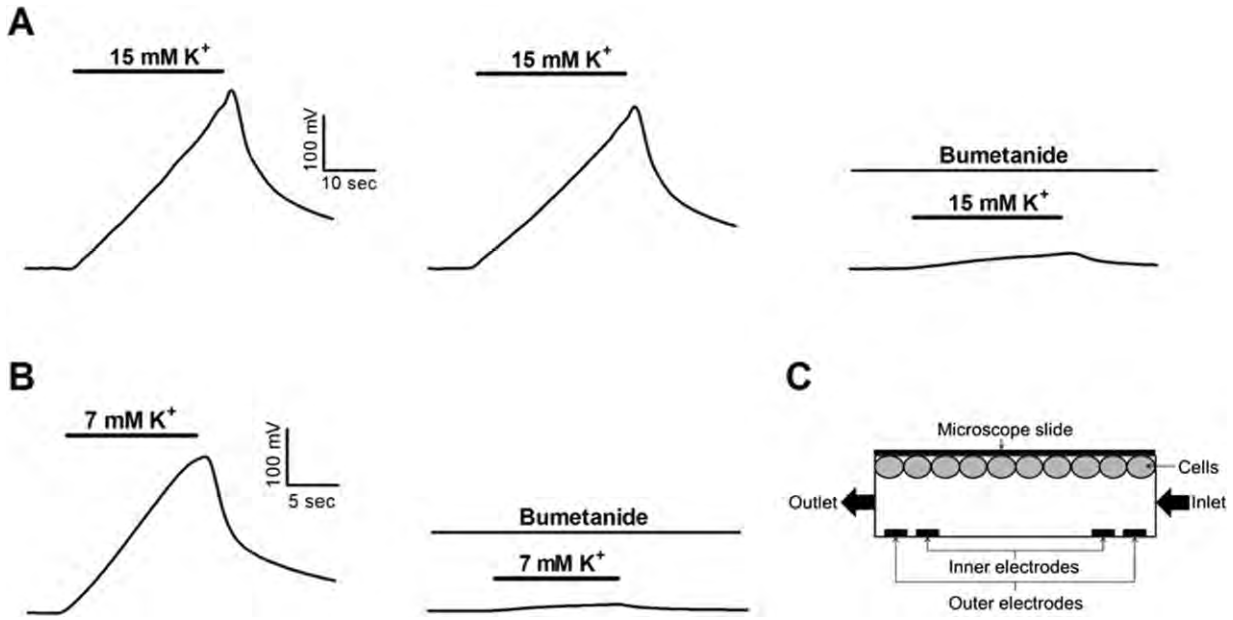

FIGURE 2: K^+-induced NKCC1-mediated astrocytic cell swelling. Stable baseline recordings of cell volume of cultured astrocytes were obtained in a microfluidic cell volume sensor with a control solution containing 0 mM K^+. (A) The cells were abruptly exposed to an isosmotic test solution containing 15 mM K^+ as indicated by the black bar in the left panel. Following return to 0 mM K^+ for 15 min, exposure to 15 mM K^+ induced a similar rate of astrocytic cell swelling (middle panel) compared with the one obtained in the initial trace. The K^+-induced astrocytic cell swelling was abolished by addition of bumetanide (10 μM), right panel. (B) As in (A) but with 3 mM K^+ in the control solution followed by an isosmotic challenge with a test solution containing 7 mM K^+ (left panel). The K^+-induced astrocytic cell swelling was abolished by addition of bumetanide (10 μM), right panel. (C) A schematic drawing of the microfluidic cell volume sensor with the two outer electrodes, between which the current is passed, and the two inner electrodes, between which the voltage is measured.

the conclusion from above; NKCC1 increases its transport activity along with K^+ concentrations that may be reached in extracellular microdomains affected by neuronal K^+ release.

NKCC1-Mediated Cellular Swelling in Astrocytes

The robust contribution of NKCC1 to the overall K^+ uptake in cultured astrocytes and its associated K^+-activation profile promote NKCC1 as a possible contributor to the clearance of stimulus-evoked K^+ in the central nervous system. NKCC1 may, possibly aided by its ability to cotransport water along with its substrate (Zeuthen and MacAulay, 2012), thus serve as a molecular mechanism contributing to removal of K^+ and stimulus-evoked astrocytic cell swelling. To determine the ability of NKCC1 to directly mediate astrocytic cell swelling upon an increase in extracellular K^+, we used a microfluidic cell volume sensor (Fig. 2C). This experimental device is based on cells placed in a small, closed chamber with application of a constant current through the chamber. Upon cell swelling, the free volume of the sensing chamber is reduced and the electric resistance therefore increased. The associated change in voltage is thus a sensitive and robust read-out of cell volume changes and is stable over the entire duration of the experiment (Ateya et al., 2005). With a transition from a K^+-free solution (equimolar replacement with choline) to an isosmotic solution containing 15 mM K^+, a rapid increase in cell volume was recorded (Fig. 2A, left panel). The K^+-induced volume increase could be repeated following a 15-min return to perfusion with the K^+-free control solution (Fig. 2A, middle panel). Inhibition of NKCC1 with bumetanide (10 μM) reduced the K^+-mediated increase in cell volume (Fig. 2A, right panel) to $3 \pm 1\%$ of control, $n = 9$. With a transition from an external solution containing 3 mM K^+ to an isosmolar solution containing 7 mM K^+, the cells still presented with a robust rise in volume (Fig. 2B). Bumetanide reduced the K^+-induced astrocytic cell swelling $1 \pm 1\%$ of control, $n = 7$. When situated in primary cultures of rat astrocytes, it is thus evident that NKCC1 is capable of removing extracellular K^+ and in the process cause rapid uptake of water as well.

Inhibition of NKCC1 Does Not Affect the Rate of K^+ Clearance Nor Extracellular Space Shrinkage in Hippocampal Slices

The contribution of NKCC1 to clearance of stimulus-evoked K^+ and the associated shrinkage of the extracellular space were determined in hippocampal slices of the rat. We used ion-sensitive microelectrodes to simultaneously record the concentration of extracellular K^+ (with a valinomycin-based liquid-membrane solution) and the relative size of the extracellular space (with a liquid-membrane solution sensitive to

the probe cation TMA^+) in the same local area. The tips of the two ion-sensitive electrodes and a field potential electrode were placed in CA1 stratum radiatum in the core of the slice (see Fig. 3A insert for a schematic drawing of the experimental design). TMA^+ (1.5 mM) was added to the superfusion solution and allowed to equilibrate into the slice prior to recording of the responses. TMA^+, being practically membrane-impermeable, increases its concentration upon shrinkage of the extracellular space and thus serves as a read-out for changes in extracellular space volume (Nicholson and Phillips, 1981; Voipio et al., 1994). Local electrical stimulation (20 Hz, 10 s) in the CA1 region of hippocampus gave rise to $[K^+]_o$ transients to 5–10 mM ($n = 4$, representative trace illustrated in Fig. 3A) that were paralleled by negative shifts in the extracellular field potential signal (not illustrated) and shrinkage of the extracellular space to 91.6–97.8% of control, $n = 4$ (representative trace illustrated in Fig. 3B). Both the $[K^+]_o$ and volume responses kept on rising until the end of the stimulation train and their recovery started promptly upon cessation of electrical stimulation. Inhibition of NKCC1 by bumetanide (10 μM) had no effect on the rate of K^+ clearance (see representative traces in Fig. 3A). For quantification of the post-stimulus K^+ clearance we used its initial rate (see Materials and Methods for details). During the 2-s quantification interval, marked by dashed lines in Fig. 3A, $[K^+]_o$ was a linear function of time and was cleared at a rate of 0.67 ± 0.16 mM/s, $n = 4$. The rate of K^+ clearance in the presence of bumetanide was normalized to that of the control trace and data are summarized in Fig. 3C, left panel, $n = 4$. Inhibition of NKCC1 had no effect on the shrinkage of the extracellular space either (gray line in Fig. 3B, data normalized and summarized in Fig. 3C, right panel, $n = 4$). Taken together, NKCC1 did not partake in post-stimulus K^+-recovery or the associated shrinkage of the extracellular space in hippocampus, despite the obvious capabilities thereof inherent in the molecular mechanism (Figs. 1 and 2).

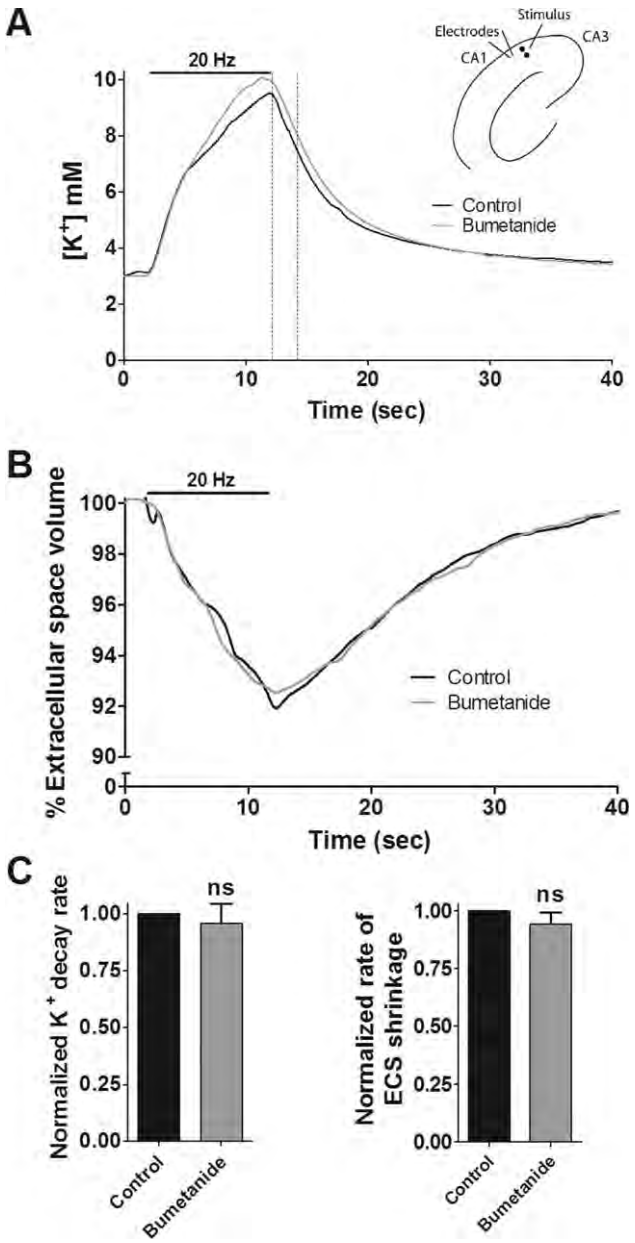

FIGURE 3: NKCC1 does not contribute to K^+-clearance and extracellular space shrinkage in hippocampal brain slices. Ion-sensitive microelectrodes were used to simultaneously measure extracellular $[K^+]_o$ and the relative size of the extracellular space (upon addition of 1.5 mM TMA^+ to the test solution) in rat hippocampal slices. (A) Electrical stimulation (10 s at 20 Hz) of stratum radiatum in CA1 (insert) generated field potentials. Representative traces of stimulus-evoked changes in $[K^+]_o$ prior (black trace) and post (gray trace) exposure to bumetanide (10 μM). The dashed lines mark the linear section ($r^2 \geq 0.99$ in all experiments) used for quantification of the K^+ decay rate. (B) Representative recordings of the relative extracellular space obtained simultaneously in the same local area as (A); the black trace illustrates the control trace and the gray trace the one obtained in the presence of bumetanide. (C) Normalized and summarized data on the post-stimulus $[K^+]_o$ decay rate (left panel) and the rate of extracellular space shrinkage (right panel): Bumetanide had no effect on the $[K^+]_o$ decay rate ($96.7 \pm 8.8\%$ of control, $n = 4$) or on the rate of stimulus-induced shrinkage of the extracellular space ($94.3 \pm 4.8\%$ of control, $n = 4$). Data presented as mean $\pm$ SEM and statistical significance determined with Student's paired *t*-test.

Kir4.1-Dependent Spatial Buffering as a Contributor to K^+ Clearance

The experimental design above was applied to resolve the role for Kir4.1 in stimulus-induced K^+ clearance and associated shrinkage of extracellular space in hippocampal slices. In this set of experiments, the stimulation parameters (20 Hz, 10 s) generated increases in the extracellular K^+ concentration to levels of 4–10 mM, $n = 5$. Inhibiton of Kir4.1 with 100 μM $BaCl_2$ (Ransom and Sontheimer, 1995) revealed no

statistically significant reduction of the post-stimulus K^+ decay rate (see representative traces in Fig. 4A, left panel). The decay rate (0.61 ± 0.15 mM/s, $n = 5$) was obtained from the initial 2 s of K^+ clearance, where the fall in $[K^+]_o$ was a linear function of time. The rate of clearance obtained in the presence of $BaCl_2$ was normalized to that of the control trace and data are summarized in Fig. 4A, right panel, $n = 5$. Inhibition of Kir4.1 did not affect the extracellular space volume changes during high-frequency stimulation (see representative traces in Fig. 4B, left panel, and summarized data in the right panel, $n = 3$).

The paradigm of spatial buffering relies on K^+ moving from distinct areas of high K^+ loads to more distant compartments where $[K^+]_o$ remains low. It can be argued that high-frequency stimulation, such as the one used in this experimental design, results in an area of increased $[K^+]_o$ which is simply too large to allow for spatial buffering to be observed at the site of recording. In essence, within the stimulated part of hippocampus, an area in which $[K^+]_o$ remains at its basal level may not occur and the prerequisite for spatial buffering will thus not be fulfilled. In the subsequent set of experiments, we therefore relied on a focal application of K^+ into the brain slice through iontophoresis via a glass capillary micropipette. In this way, we generated a constant point source of K^+ within the slice. To prevent spontaneous neuronal activity, a series of inhibitors were added to the artificial cerebrospinal fluid to block the action of the voltage-gated Na^+ channel (TTX), GABA- (PiTX, CGP-55845), and glutamate receptors (NBQX, AP-5). A 5-s pulse generated K^+ rises in the extracellular space in the range 6–15 mM, $n = 4$. The iontophoretic pulse generated comparable rises in $[K^+]_o$ during three consecutive control pulses (Fig. 4C, insert). Iontophoretic pulses applied following bath application of 100 μM $BaCl_2$ consistently generated an increase in peak $[K^+]_o$, as illustrated by the representative traces in Fig. 4C, left panel and summarized in the right panel. Addition of $BaCl_2$ increased the peak $[K^+]_o$ to $122.1 \pm 5.1\%$ of control, $n = 4$, $P < 0.01$. The ensuing rate of post-stimulus K^+ clearance rate was similar in the absence and presence of 100 μM $BaCl_2$ (see representative traces in Fig. 4C). The rate of clearance (3.81 ± 1.24 mM/s, $n = 4$) was quantified during the initial 1 s following the pulse, marked with dashed lines, where the falling of $[K^+]_o$ was a linear function of time (normalized data summarized in Fig. 4A, right panel, $n = 4$). To exclude that the recovery rate was affected by the higher peak K^+, a parallel quantification was performed at comparable $[K^+]_o$ concentrations (from the peak of the control trace, lasting 0.5 s during which both traces were in their linear phase). No Ba^{2+}-mediated change in the recovery rate of $[K^+]_o$ was detected with this mode of quantification (data not shown). It would thus appear that Kir4.1-dependent spatial buffering does not account for a significant contribution to the post-stimulus recovery of $[K^+]_o$ or to the associated shrinkage of the extracellular space. Kir4.1, however, partakes in the K^+ clearance taking place during the application of the iontophoretically applied $[K^+]_o$ increase.

Block of the Na^+/K^+-ATPase Compromises Extracellular K^+ Removal in a Dose-Dependent Manner Related to the Subunit Isoforms

With no evident involvement of neither NKCC1 nor Kir4.1 in post-stimulus $[K^+]_o$ recovery, we sought to determine the contribution of the various isoforms of the Na^+/K^+-ATPase to K^+ clearance following electrical stimulation. In this set of experiments, the high-frequency stimulation of the hippocampal slices (20 Hz, 10 s) generated, in control solution, increases in extracellular K^+ concentration in the range 4–13 mM, with a decay-rate of 0.73 ± 0.18 mM/s, $n = 7$. In rodents, the $\alpha1$ isoform of the Na^+/K^+-ATPase α-subunit displays a low sensitivity to the Na^+/K^+-ATPase inhibitor ouabain [around 1 mM ouabain is required to obtain a full block of $\alpha1$ activity, whereas the $\alpha2$ and $\alpha3$ isoforms are fully inhibited at 5 μM (Blanco et al., 1993)]. This difference allowed us to test the contribution of $\alpha2/\alpha3$ separately from that of $\alpha1$. It should be noted, however, that complete block of Na^+/K^+-ATPase activity compromised the slice viability and we therefore opted for partial inhibition of $\alpha1$ with an ouabain concentration of 50 μM, which roughly constitutes the IC_{50} for rat $\alpha1$ (Jewell and Lingrel, 1991). The basal level of K^+ in the extracellular space increased upon application of ouabain, as seen in the representative traces in Fig. 5A: 5 μM ouabain lead to a basal $[K^+]_o$ of 3.9 ± 0.4 mM, $n = 7$ and the 50 μM ouabain to a $[K^+]_o$ of 4.8 ± 0.8 mM, $n = 5$. The post-stimulus $[K^+]_o$ decay rate displayed a marked decrease following block of the $\alpha2/\alpha3$-subunits of the Na^+/K^+-ATPase (see representative trace, dark gray, in Fig. 5A). Additional application of ouabain (to 50 μM) led to a severely compromised K^+ clearance (light gray trace in Fig. 5A). The ouabain-dependent decrease in the rate of post-stimulus $[K^+]_o$ recovery was normalized to the control trace and summarized in Fig. 5C, left panel. The rate of decay was significantly reduced at both 5 μM ($69.3 \pm 9.3\%$ of control, $n = 7$, $P < 0.05$) and 50 μM ($31.5 \pm 7.8\%$ of control, $n = 5$, $P < 0.001$). Inhibition of Na^+/K^+-ATPase with 5 μM ouabain (block of $\alpha2/\alpha3$) did not affect the extracellular space volume changes during high-frequency stimulation (see representative traces in Fig. 5B, and summarized data in Fig. 5C, right panel, $n = 3$). Additional inhibition of Na^+/K^+-ATPase activity with 50 μM ouabain caused a tendency towards increased stimulus-induced extracellular space shrinkage, which is consistent with more pronounced and faster swelling of astrocytes when the Na^+/K^+-ATPase is less operational. These data demonstrate that the Na^+/K^+-ATPase-mediated K^+ removal does not, in itself, generate stimulus-induced cell

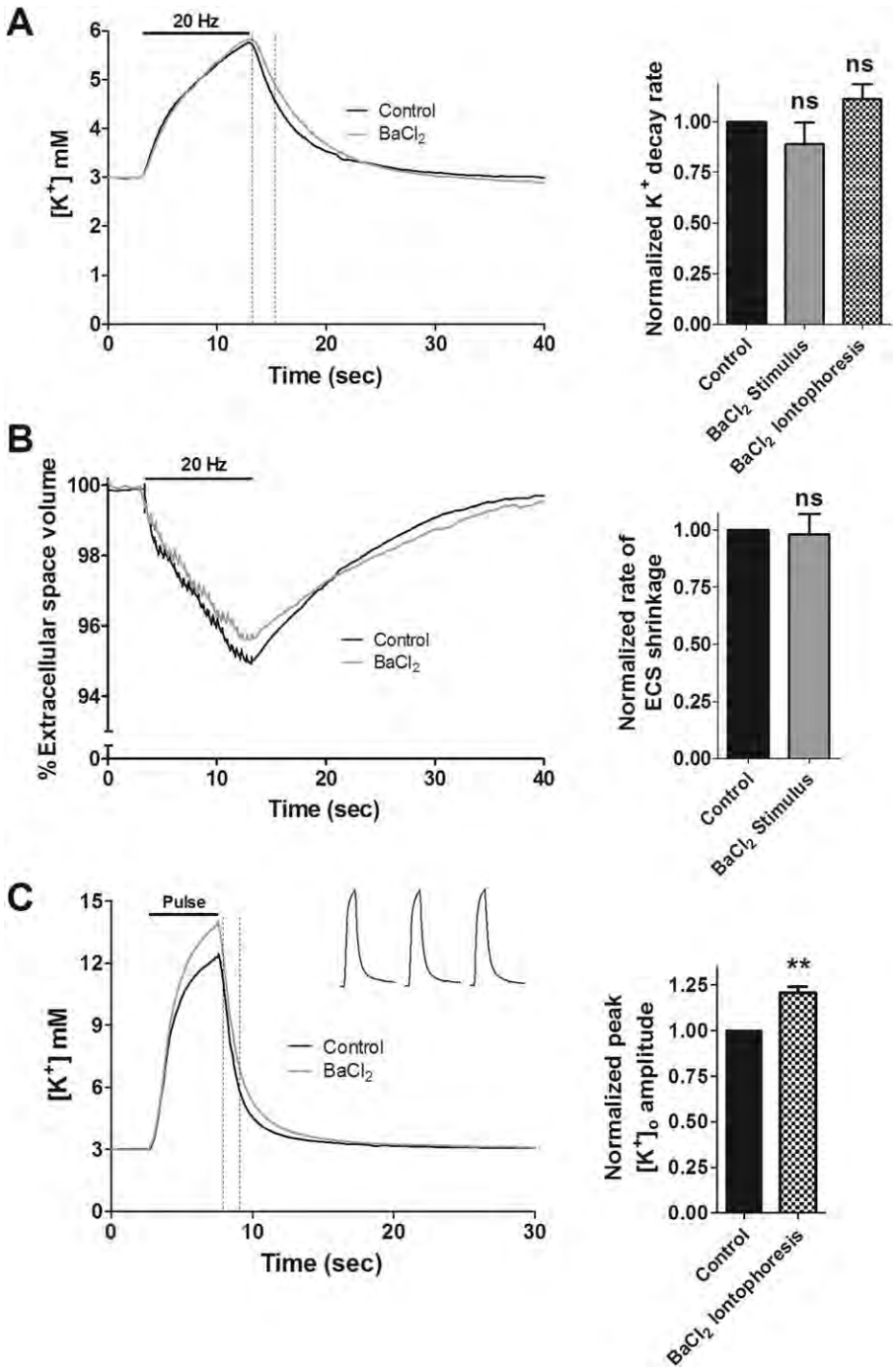

FIGURE 4: Kir4.1 does not contribute to post-stimulus K^+-clearance and extracellular space shrinkage in hippocampal brain slices. Ion-sensitive microelectrodes were used to determine the effect of Ba^{2+}-mediated inhibition of Kir4.1 on K^+ clearance and extracellular space shrinkage, essentially as in Fig. 3. (**A**) Representative traces of stimulus-evoked changes in $[K^+]_o$ prior (black trace) and post (gray trace) exposure to $BaCl_2$ (100 μM), left panel. The dashed lines mark the linear section (with $r^2 \geq 0.99$ in all experiments) used for quantification of the K^+ decay rate. The data obtained in the presence of $BaCl_2$ were normalized to control and summarized for the rate of decay of $[K^+]_o$ following stimulus (88.7 $\pm$ 10.6% of control, $n = 5$) and iontophoresis of K^+ (111.0 $\pm$ 7.4% of control, $n = 4$), right panel. (**B**) Representative recordings of the relative extracellular space obtained simultaneously in the same local area as (A); the black trace illustrates the control trace and the gray trace the one obtained in the presence of $BaCl_2$, left panel. The rate of stimulus-induced shrinkage of extracellular space obtained in the presence of $BaCl_2$ was normalized to control and summarized (98.0 $\pm$ 9.0% of control, $n = 3$) in the right panel (two of these were performed simultaneously with K^+ measurements and one was performed with individual monitoring of the extracellular space). (**C**) Focal application of K^+ was obtained with iontophoresis with a 5 s current pulse (indicated by the black bar) in the presence of an inhibitor cocktail containing (AP-5 40 μM, NBQX 10 μM, PiTX 100 μM, CGP-55845 1 μM, and TTX 1 μM). Consecutive iontophoretic pulses gave rise to identical increases in $[K^+]_o$ (insert). Representative traces of changes in $[K^+]_o$ prior (black trace) and post (gray trace) exposure to $BaCl_2$ (100 μM), left panel. The dashed lines mark the linear section (with $r^2 \geq 0.99$ in all experiments) used for quantification of the K^+ decay rate which, in this set of experiments, covers a span of 1 s due to the fast decay and thereby loss of linearity, see (A), right panel for summarized data. Peak $[K^+]_o$ values obtained in the presence of $BaCl_2$ were normalized to that of control and summarized (122.1 $\pm$ 5.1%, $n = 4$) in the right panel. Data presented as mean $\pm$ SEM and statistical significance determined with one-way ANOVA with Dunnett's multiple comparison *post hoc* test and Student's paired *t*-test (**, $P < 0.01$).

swelling (see representative trace in Fig. 5B insert and summarized data in Fig. 5C, right panel). It would thus appear that the combined action of different Na^+/K^+-ATPase isoforms is the key mechanism underlying uptake of neuronally released K^+ following electrical stimulation albeit without causing astrocytic cell swelling in the process.

The α2β2 Na^+/K^+-ATPase Subunit Composition Appears Geared for K^+ Clearance

Astrocytes express α1 and α2 as well as the accessory subunit, β1 and β2 whereas neurons express α1, α3, and possibly α2, all in combination with β1 (Cameron et al., 1994; Cholet et al., 2002; Juhaszova and Blaustein, 1997; Li et al., 2013; McGrail et al., 1991; Richards et al., 2007). It remains unknown what fractions of the different α isoforms are expressed at the cell membranes and to which β subunit the glial α isoforms associate. To determine the molecular characteristics of the different combinations of these subunits and isoforms, we expressed the various combinations of the rat Na^+/K^+-ATPase heterologously in *X. laevis* oocytes. The advantage thereof is the low background of *Xenopus* α and β subunits, compared with those heterologously expressed: the ouabain-sensitive currents of the uninjected oocytes amounted to <10% of those obtained in oocytes heterologously expressing the α1 and α2 isoforms of the rat Na^+/K^+-ATPase and <25% of those expressing the α3 isoform (data not shown). This expression system thereby provided us with the ability to determine the individual properties of the different combinations of the isoforms. The K^+-activation profile for each combination of Na^+/K^+-ATPase was determined by two-electrode voltage clamp with the *I/V* relationship established at each applied K^+ concentration. The experimental protocol was subsequently repeated in the presence of ouabain (1 mM) to extract the ouabain-sensitive current representing Na^+/K^+-ATPase activity. Representative current traces, obtained with 5 mM K^+ in the extracellular solution, for an α2β2-expressing oocyte are depicted in Fig. 6A in the absence (upper panel) and presence (lower panel) of ouabain (1 mM). The α1 isoform displayed a $K_{0.5}$ for K^+ of 0.25 ± 0.06 mM, $n = 7$ when co-expressed with the β1 accessory subunit and 0.67 ± 0.20 mM, $n = 7$ when co-expressed with β2. Both subunit compositions approached full saturation at an extracellular K^+ concentration around 2 mM, Fig. 6B. The $K_{0.5}$

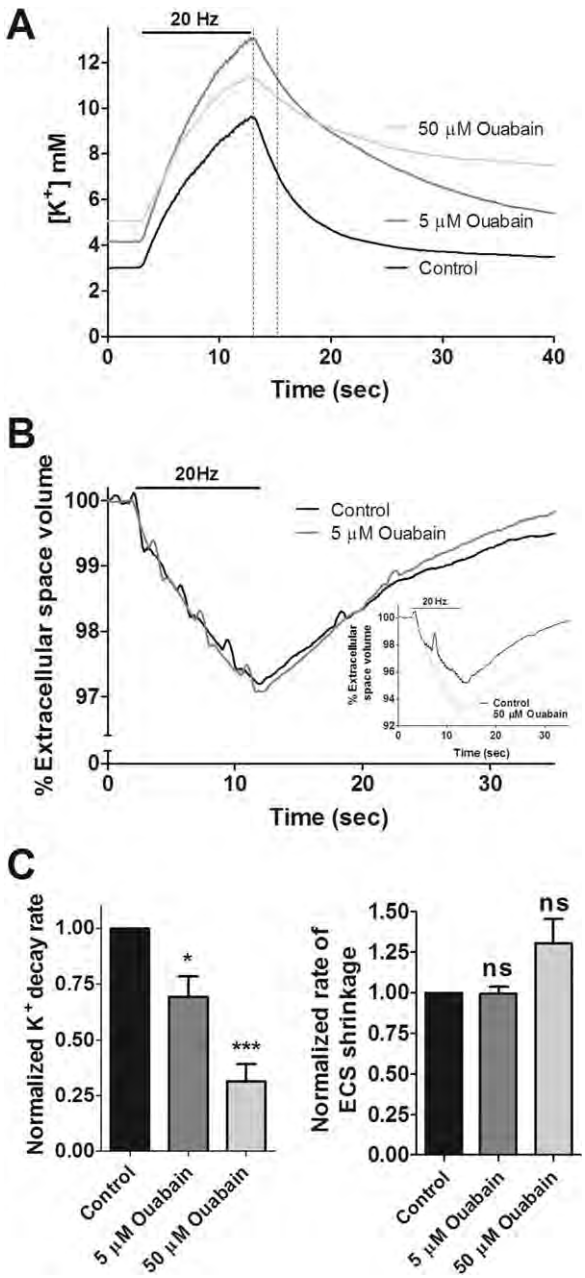

FIGURE 5: Inhibition of the Na^+/K^+-ATPase delays K^+-clearance in hippocampal brain slices. Ion-sensitive microelectrodes were used to determine the effect of ouabain on K^+ clearance following electrical stimulation, essentially as in Fig. 3. (A) Representative traces of stimulus-evoked changes in $[K^+]_o$ in control solution (black trace), after exposure to 5 μM ouabain (dark gray trace) and subsequently to 50 μM ouabain (light gray trace). The dashed lines mark the linear 2-s section (with $r^2 \geq 0.99$ in all experiments) used for quantification of the K^+ decay rate. (B) Representative recordings of the relative extracellular space in an independent experiment; the black trace illustrates the control trace and the gray trace the recording after application of 5 μM ouabain. Insert depicts a similar experiment obtained with 50 μM ouabain (light gray trace). (C) The $[K^+]_o$ decay rate obtained in the presence of ouabain was normalized to control and summarized ($69.3 \pm 9.3\%$ of control for 5 μM ouabain, $n = 7$ and $31.5 \pm 7.8\%$ of control for 50 μM ouabain, $n = 5$), left panel. The rate of stimulus-induced shrinkage of the extracellular space in the presence of ouabain was normalized to control and summarized ($99.3 \pm 4.4\%$ of control, $n = 3$ for 5 μM ouabain and $131 \pm 15\%$ of control, $n = 4$ for 50 μM ouabain), right panel. Data presented as mean ± SEM and statistical significance determined with one-way ANOVA with Dunnett's multiple comparison *post hoc* test (*, $P < 0.05$, ***, $P < 0.001$).

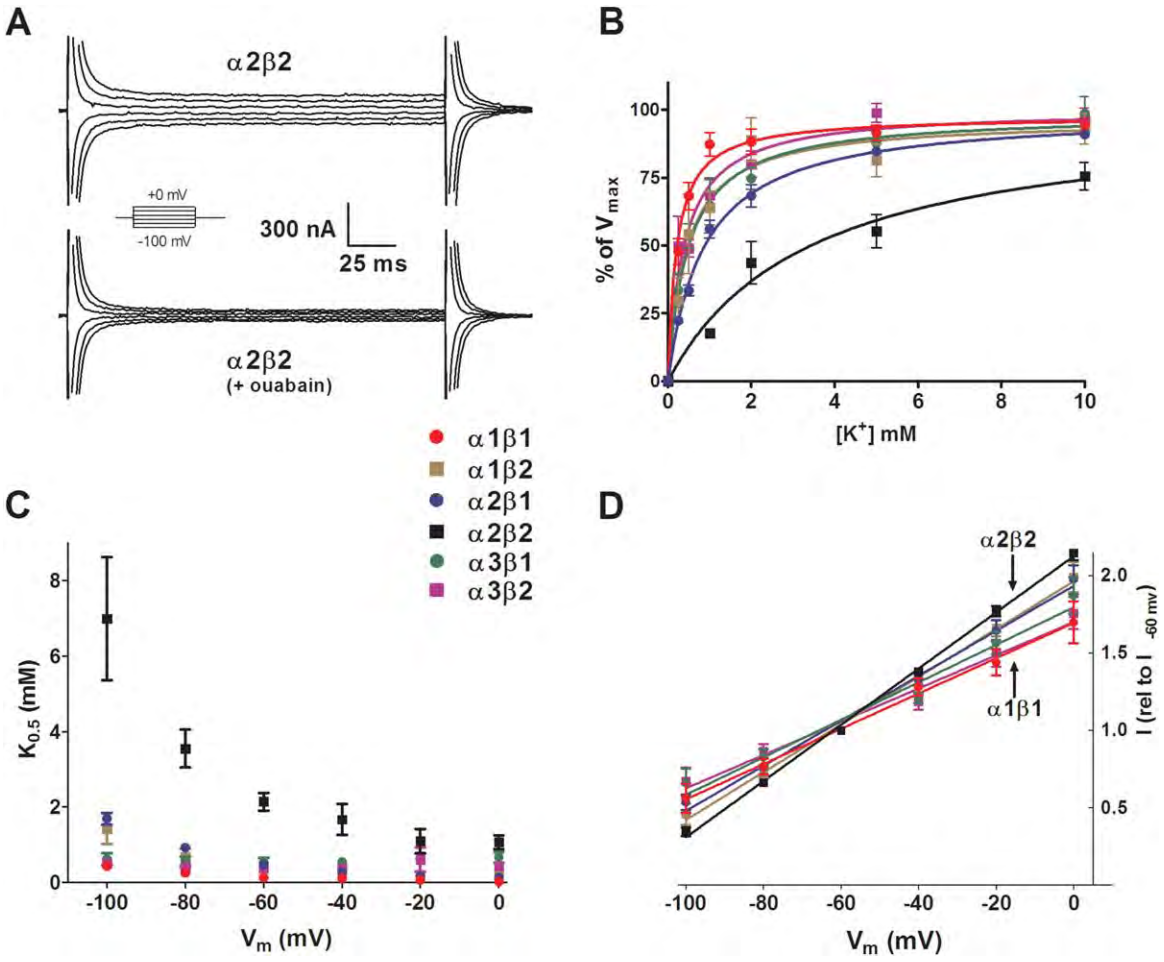

FIGURE 6: The subunit constellation of the Na^+/K^+-ATPase determines its K^+- and voltage-sensitivity. Various subunit isoform compositions of the Na^+/K^+-ATPase (α1β1, α1β2, α2β1, α2β2, α3β1, α3β2) were heterologously expressed in *X. laevis* oocytes and their activity determined with two-electrode voltage clamp. (A) From a holding potential of −50 mV, the membrane potential was stepped to 0 mV and subsequently in 20 mV increments to −100 mV for 200 ms (step protocol depicted in insert). The panel illustrates representative current traces from an α2β2-expressing oocyte prior to (upper trace) and following exposure to 1 mM ouabain (lower trace). (B) The Na^+/K^+-ATPase activity was determined as a function of $[K^+]_o$ (at $V_m = -80$ mV) and fitted according to Michaelis–Menten kinetics. The graph depicts the obtained activity at each $[K^+]_o$ as % of $V_{max} \pm$ SEM whereas the affinity constants were obtained from each individual oocyte prior to averaging, $n = 4–7$). (C) The $K_{0.5}$s for each subunit isoform composition was plotted as a function of the membrane potential (V_m), $n = 4–7$. (D) The ouabain-sensitive *I/V* relationships for each of the subunit compositions were obtained in the presence of 5 mM K^+ ($n = 6–8$ of each). Data were normalized to the current obtained at a membrane potential of −60 mV. Data presented as mean ± SEM and statistical significance determined with one-way ANOVA with Tukey's Multiple Comparison *post hoc* test or Student's *t*-test.

for K^+ of the α3 isoform was similar to that of α1, whether co-expressed with β1 (0.55 ± 0.13 mM, $n = 4$) or β2 (0.40 ± 0.08 mM, $n = 4$). The molecular combination of α2 with β1 yielded a $K_{0.5}$ for K^+ of 0.91 ± 0.08 mM, $n = 7$, which was comparable to those obtained with the α1 and α3 isoforms. In contrast, the α2β2 combination displayed a significantly higher $K_{0.5}$ for K^+ of 3.6 ± 0.5 mM, $n = 5$ ($P < 0.001$) and only approached saturation with extracellular K^+ concentrations of 10 mM. The low K^+ affinity of α2β2 thus provides this constellation of the Na^+/K^+-ATPase with the aforementioned requirement of increased transport activity upon a stimulus-induced rise in $[K^+]_o$ level in the brain. In contrast, the remaining subunit isoform combinations will respond only slightly to increments above the basal 3 mM $[K^+]_o$.

An increase in $[K^+]_o$ will promote a depolarization of the astrocytic and neuronal cell membranes. We therefore determined the $K_{0.5}$ for K^+ as a function of the membrane potential, Fig. 6C. The $K_{0.5}$ for K^+ of the α3 isoform combinations was not affected by changes in membrane potential whereas $K_{0.5}$ for K^+ decreased for all α1 and α2 isoform combinations as the membrane depolarized ($P < 0.05$). The effect was most prominently observed for α2β2. In addition, all isoform constellations displayed increased activity rate upon depolarization of the cell membrane in test solutions containing 5 mM K^+, $n = 6–8$ of each isoform combination,

Fig. 6D. The voltage-dependence of $\alpha2\beta2$ was, however, significantly more pronounced than that of $\alpha1\beta1$ (in 10^{-3} I_{rel}/mV; 18.2 ± 0.8 for $\alpha2\beta2$ *vs.* 11.4 ± 2.1 for $\alpha1\beta1$, $n = 6$, $P < 0.05$) and the $\alpha2\beta2$ subunit composition will thus increase its activity prominently as the astrocytic cell membrane depolarizes.

Discussion

We have in this study demonstrated that NKCC1 does not contribute to removal of K^+ from the extracellular space following neuronal activity in the rat hippocampus, whereas the combined action of the Na^+/K^+-ATPase isoforms acts as key contributor. Although Kir4.1 did not contribute to post-stimulus K^+ clearance, the peak $[K^+]_o$ was partially dependent on the action of Kir4.1 under conditions favoring spatial buffering. The concept of spatial buffering of K^+ via Kir4.1 has been forwarded as an important means of *post-stimulus* recovery of the extracellular K^+ concentration (Kofuji and Newman, 2004; Walz, 2000). It has been convincingly demonstrated that K^+ taken up in a local area of the astrocytic syncytium or retinal Müller cell is subsequently released at a distant site via Kir4.1 (Karwoski et al., 1989; Strohschein et al., 2011). A quantitative contribution of Kir4.1-mediated spatial buffering to K^+ clearance is however uncertain: a range of experimental approaches with pharmacological block or genetic deletion of Kir4.1 have demonstrated minor, if any, delay in the rate of post-stimulus $[K^+]_o$ recovery (Chever et al., 2010; D'Ambrosio et al., 2002; Karwoski et al., 1989; Meeks and Mennerick, 2007; Ransom et al., 2000) although another study reported decreased post-stimulus $[K^+]_o$ recovery in the Kir4.1 knock-out animal (Haj-Yasein et al., 2011).

Upon high-frequency stimulation of brain slice preparations, it is likely that the extracellular K^+ concentration is increased in a large volume of the tissue. The resultant global $[K^+]_o$ increase may prevent spatial buffering and a stimulation paradigm as the one used in this study and in (Chever et al., 2010; Haj-Yasein et al., 2011; Meeks and Mennerick, 2007; Ransom et al., 2000) may thus be ill-suited to experimentally determine the contribution of Kir4.1-mediated spatial buffering to clearance of excess $[K^+]_o$. To ensure an optimal experimental setting for detection of spatial buffering of K^+, we therefore applied K^+ focally by means of iontophoresis. Inhibition of Kir4.1 with 100 μM $BaCl_2$ did not significantly delay *post-stimulus* $[K^+]_o$ recovery but caused an increase in the peak $[K^+]_o$ *during* the K^+ application, the latter of which in agreement with an earlier report (Jauch et al., 2002). This observation aligns well with previous studies in retina, an experimental preparation conducive to Kir4.1-mediated spatial buffering due to its geometry and localized K^+ release: Kir4.1-mediated K^+ release into the vitreal body was apparent *during* the light stimulus whereas the vitreal K^+ concentration declined during post-stimulus $[K^+]_o$-recovery (Karwoski et al., 1989). In addition, a Ba^{2+}-mediated delay in K^+ clearance in the inner plexiform layer of the retina was observed only during the light-evoked stimulus whereas the rate of post-light stimulus clearance of K^+ seemed unaffected by inhibition of Kir4.1 (Karwoski et al., 1989; Oakley et al., 1992). Thus, it appears that Kir4.1-mediated spatial buffering enacts its function throughout the phase of continuous delivery of K^+ that takes place *during* neuronal activity and not in the post-stimulus phase of the $[K^+]_o$ recovery.

In this experimental setting, inhibition of the Na^+/K^+-ATPase caused a substantial delay in post-stimulus recovery of $[K^+]_o$ but did not prevent the stimulus-induced shrinkage of the extracellular space. The Na^+/K^+-ATPase thus appears as a prime molecular mechanism responsible for clearance of stimulus-induced increase in $[K^+]_o$ in agreement with previous reports on optic nerve and hippocampus (D'Ambrosio et al., 2002; Ransom et al., 2000; Vaillend et al., 2002). The ability of the Na^+/K^+-ATPase to regulate $[K^+]_o$ in hippocampus was recently demonstrated; astrocytic Ca^{2+} signaling stimulated Na^+/K^+-ATPase activity and thereby caused a reduction of $[K^+]_o$ (Wang et al., 2012). We demonstrate a partial role for $\alpha2/\alpha3$ in post-stimulus recovery of $[K^+]_o$. Complete inhibition of all three isoforms of the Na^+/K^+-ATPase compromised slice viability but partial inhibition of $\alpha1$ (in addition to the full inhibition of $\alpha2/\alpha3$) led to a further reduction in the rate of K^+ clearance. A problematic nature of the experimental design is the continued presence of ouabain in the test solution prior to induction of the stimulus protocol. This prolonged inhibition of Na^+/K^+-ATPase activity ($\geq$3 min) increased the baseline level of K^+ in the extracellular space of the brain slice, as observed here and in (D'Ambrosio et al., 2002; Ransom et al., 2000), which may affect the rate of K^+ clearance in a manner unknown.

The cell-specific expression pattern of the Na^+/K^+-ATPase α isoforms and the accessory β isoforms in the central nervous system remains unresolved due to the contradictory evidence in the literature. One emerging picture, however, assigns $\alpha2$ and $\beta2$ to glial cells, $\alpha3$ to neurons and $\alpha1$ and $\beta1$ to both cell types although some $\alpha2$ staining has been reported in neurons (Cameron et al., 1994; Cholet et al., 2002; Juhaszova and Blaustein, 1997; Li et al., 2013; McGrail et al., 1991; Richards et al., 2007). We took advantage of the *X. laevis* expression system to determine the isoform-specific characteristics of the different combinations of the Na^+/K^+-ATPase isoforms without significant contribution from contaminating native isoforms. The activity of $\alpha1$ and $\alpha3$ was saturated already at basal extracellular K^+ concentrations, whether combined with $\beta1$ or $\beta2$. When paired with $\beta1$, $\alpha2$ displayed a tendency towards lower K^+ affinity than $\alpha1$, as previously observed (Blanco, 2005; Horisberger and

Kharoubi-Hess, 2002; Jewell and Lingrel, 1991), although in this study the difference did not reach statistical significance. However, upon replacement of the household $\beta1$ isoform with $\beta2$, the K^+ affinity of $\alpha2$ shifted towards lower affinity, which is in agreement with observations on the human isoforms of the Na^+/K^+-ATPase (Crambert et al., 2000). Similarly, the voltage-sensitivity of $\alpha2$ appeared more pronounced than that of $\alpha1$ when paired with $\beta1$ (Horisberger and Kharoubi-Hess, 2002) although upon pairing of $\alpha2$ with $\beta2$, the voltage-sensitivity became significantly stronger than that obtained with $\alpha1\beta1$. Notably, the apparent affinity for K^+ of the $\alpha1$ and $\alpha2$ isoforms (in combination with either β isoform but most prominently for $\alpha2\beta2$) increased as the membrane potential became more depolarized, that is, at highly depolarized membrane potentials, these Na^+/K^+-ATPase isoforms will reach their maximal transport rates at lower K^+ concentrations. Although the underlying transporter kinetics of this voltage-induced shift in $K_{0.5(K+)}$ have yet to be resolved, one may speculate that $\alpha2\beta2$ in this manner is ensured of maximum transport activity during conditions of raised $[K^+]_o$. The $\alpha2\beta2$ isoform constellation characteristic to glial cells thereby exhibited increased Na^+/K^+-ATPase activity (i) along physiologically relevant K^+ increments and (ii) along the membrane depolarization inevitably associated with increased $[K^+]_o$. Taken together with the proposed localization of $\alpha2$ in glial leaflets surrounding dendritic spines (Cholet et al., 2002), $\alpha2\beta2$, although not as a single major contributor, appears specifically geared to respond efficiently to stimulus-evoked increase of K^+ in the extracellular space.

Inhibition of NKCC1 has earlier been proposed to reduce stimulus-evoked shrinkage of the extracellular space in hippocampus and optic nerve (MacVicar and Hochman, 1991; MacVicar et al., 2002; Ransom et al., 1985). NKCC1 would, as such, act as a potential additional mechanism for post-stimulus $[K^+]_o$ recovery (MacVicar et al., 2002; Walz, 2000). Partly due to uncertainty regarding rat NKCC1's K^+ affinity and therefore its ability to increase its activity along physiologically occurring $[K^+]_o$ increments, its putative involvement in K^+ clearance has remained unresolved. We determined the apparent affinity of rat NKCC1 for K^+ with radioactive uptake experiments at a time point at which the uptake was a linear function of time and thus yielded a reliable $K_{0.5}$. The rat NKCC1, whether expressed natively in cultured astrocytes or heterologously in *Xenopus* oocytes, displayed increasing transporter activity along K^+ increments expected to occur in extracellular microdomains affected by neuronal K^+ release, albeit with different $K_{0.5}$s. The different ionic compositions of intra- and extracellular solutions, putative accessory proteins, as well as the different membrane potentials of the two cell types may well underlie the differences in apparent affinity constants obtained in these two cellular systems. Either way, NKCC1 appears able to increase its transport activity along physiologically occurring K^+ increases in the extracellular space. Taken together with the robust NKCC1-mediated increase in cultured astrocytic cell volume upon an abrupt isotonic increase in $[K^+]_o$, NKCC1 displayed features that could account for glial clearance of excess $[K^+]_o$ in association with a shrinkage of the extracellular space. Irrespective thereof, NKCC1 did not contribute to the regulation of stimulus-evoked $[K^+]_o$ transients or extracellular space volume changes in the hippocampal brain slice. Thus, while NKCC1 is highly expressed in cultured astrocytes [this study and (Su et al., 2002a, b; Walz, 1992)], absence of astrocytic NKCC1 expression in native rat brain tissue has previously been reported (Clayton et al., 1998; Plotkin et al., 1997) but see Randall et al. (1997). This pattern is in line with NKCC1 being recognized for its functional up regulation in cultured cells of different lineages (Raat et al., 1996). However, it is entirely possible that during brain pathologies, that is, epilepsy, stroke, and edema, NKCC1 may be up-regulated and under such conditions contribute to K^+ and water homeostasis.

The stimulus-evoked shrinkage of the extracellular space, taking place during the neuronal activity, terminates with the stimulus-induced $[K^+]_o$ increase, that is, the post-stimulus K^+ recovery is associated with a *normalization* of the size of the extracellular space. Therefore, it must be emphasized that the mechanism responsible for post-stimulus restoration of basal $[K^+]_o$ does not mediate net influx of osmotic particles. The Na^+/K^+-ATPase activity is associated with a net loss of intracellular osmotic particles and we, accordingly, verified that Na^+/K^+-ATPase-mediated K^+ clearance did not, in itself, produce the stimulus-induced shrinkage of the extracellular space. In fact, in the presence of 50 μM ouabain, we observed a tendency towards *increased* stimulus-induced extracellular space shrinkage which could be due to the Na^+/K^+-ATPase acting to dampen cell swelling during clearance of stimulus induced $[K^+]_o$ or, alternatively, simply reflect a decrease in the basal size of the extracellular space following inhibition of the Na^+/K^+-ATPase. Either way, K^+-clearance via the Na^+/K^+-ATPase does not mediate the observed stimulus-induced shrinkage of the extracellular space. The extracellular space volume response remained intact following pharmacological blockade of Kir4.1, in agreement with a previous report performed with Kir4.1$^{-/-}$ mice (Haj-Yasein et al., 2011). Genetic deletion of AQP4, in addition, has failed to diminish stimulus-induced shrinkage of the extracellular space (Haj-Yasein et al., 2012). A functional coupling of Kir4.1 and AQP4, in terms of stimulus-evoked glial cell swelling, therefore cannot be reconciled with published experimental data nor with the concept of Kir4.1-mediated spatial buffering precluding intracellular accumulation of ions (and thus osmotic particles). The molecular mechanism underlying the stimulus-evoked shrinkage of the extracellular space, which has recurrently been observed (Dietzel et al., 1980; Ransom

et al., 1985) thus remains elusive. However, it has been speculated (Nagelhus et al., 2004) and recently demonstrated (Florence et al., 2012) that astrocytic bicarbonate transport may be activated by K^+-induced depolarization of the astrocytic membrane and subsequently lead to astrocytic cell swelling. Bicarbonate transport activity, which has not been addressed in this study, thus may partially underlie the observed stimulus-induced shrinkage of the extracellular space.

In conclusion, we have demonstrated that NKCC1 does not contribute to K^+ clearance following neuronal activity in the hippocampus whereas the Na^+/K^+-ATPase acts as a key mechanism. Kir4.1 enacts its contribution to K^+-buffering during local delivery of K^+ to the extracellular space. We must, however, emphasize that different clearance mechanisms may dominate in other brain regions. Increased Na^+/K^+-ATPase activity generates intracellular K^+ accumulation and its molecular characteristics therefore aligns well with the reported transient increase in intracellular K^+ concentration of astrocytes during the burst of activity which, however, is immediately followed by post-stimulus restoration of neuronal $[K^+]_i$ (Ballanyi et al., 1987; Grafe and Ballanyi, 1987). The $\alpha 2\beta 2$ isoform constellation characteristic to Na^+/K^+-ATPase in glial cells appears to be specifically geared to respond to excess extracellular K^+ due to its lower K^+ affinity and higher voltage-sensitivity.

Acknowledgment

Grant sponsor: Lundbeck Foundation (to N.M. and B.R.L.), The Academy of Finland (K.K.), and The Sigrid Jusélius Foundation (K.K., J.V.).

The authors greatly value the technical assistance provided by Charlotte Goos Iversen and Catia Correa Goncalves Andersen. Our gratitude goes to Prof. H. Waagepetersen and H. M. Nielsen for technical assistance with generation of primary cultures of astrocytes, Dr. T.H. Braunstein for assistance in GFAP staining of astrocytes, Dr. G. Blanco at University of Kansas Medical Center for providing the cDNA encoding the various α and β isoforms of the Na^+/K^+-ATPase and to the inventors of the microfluidic volume sensor; Drs. S. Z. Hua, F. Sachs, and S. Besch at University of Buffalo. Thanks to Professor Sabina Hrabetova for critical reading of the manuscript.

References

Amiry-Moghaddam M, Ottersen OP. 2003. The molecular basis of water transport in the brain. Nat Rev Neurosci 4:991–1001.

Assentoft M, Kaptan S, Fenton RA, Hua SZ, de Groot BL, MacAulay N. 2013. Phosphorylation of rat aquaporin-4 at Ser111 is not required for channel gating. Glia 61:1101–1112.

Ateya DA, Sachs F, Gottlieb PA, Besch S, Hua SZ. 2005. Volume cytometry: Microfluidic sensor for high-throughput screening in real time. Anal Chem 77: 1290–1294.

Ballanyi K, Grafe P, ten Bruggencate G. 1987. Ion activities and potassium uptake mechanisms of glial cells in guinea-pig olfactory cortex slices. J Physiol 382:159–174.

Bay V, Butt AM. 2012. Relationship between glial potassium regulation and axon excitability: A role for glial Kir4.1 channels. Glia 60:651–660.

Blanco G. 2005. Na,K-ATPase subunit heterogeneity as a mechanism for tissue-specific ion regulation. Semin Nephrol 25:292–303.

Blanco G, Xie ZJ, Mercer RW. 1993. Functional expression of the alpha 2 and alpha 3 isoforms of the Na,K-ATPase in baculovirus-infected insect cells. Proc Natl Acad Sci USA 90:1824–1828.

Cameron R, Klein L, Shyjan A, Rakic P, Levenson R. 1994. Neurons and astroglia express distinct subsets of Na,K-ATPase alpha and beta subunits. Brain Res Mol Brain Res 21:333–343.

Chever O, Djukic B, McCarthy KD, Amzica F. 2010. Implication of Kir4.1 channel in excess potassium clearance: An in vivo study on anesthetized glial-conditional Kir4.1 knock-out mice. J Neurosci 30:15769–15777.

Cholet N, Pellerin L, Magistretti PJ, Hamel E. 2002. Similar perisynaptic glial localization for the Na^+,K^+-ATPase $\alpha 2$ subunit and the glutamate transporters GLAST and GLT-1 in the rat somatosensory cortex. Cereb Cortex 12: 515–525.

Clayton GH, Owens GC, Wolff JS, Roderic LS. 1998. Ontogeny of cation–Cl^- cotransporter expression in rat neocortex. Dev Brain Res 109:281–292.

Crambert G, Hasler U, Beggah AT, Yu C, Modyanov NN, Horisberger J-D, Lelièvre L, Geering K. 2000. Transport and pharmacological properties of nine different human Na,K-ATPase isozymes. J Biol Chem 275:1976–1986.

D'Ambrosio R, Gordon DS, Winn HR. 2002. Differential role of KIR channel and Na^+/K^+-pump in the regulation of extracellular K^+ in rat hippocampus. J Neurophysiol 87:87–102.

Dietzel I, Heinemann U, Hofmeier G, Lux HD. 1980. Transient changes in the size of the extracellular space in the sensorimotor cortex of cats in relation to stimulus-induced changes in potassium concentration. Exp Brain Res 40:432–439.

Florence CM, Baillie LD, Mulligan SJ. 2012. Dynamic volume changes in astrocytes are an intrinsic phenomenon mediated by bicarbonate ion flux. PLoS One 7:e51124.

Grafe P, Ballanyi K. 1987. Cellular mechanisms of potassium homeostasis in the mammalian nervous system. Can J Physiol Pharmacol 65:1038–1042.

Haj-Yasein NN, Jensen V, Ostby I, Omholt SW, Voipio J, Kaila K, Ottersen OP, Hvalby O, Nagelhus EA. 2012. Aquaporin-4 regulates extracellular space volume dynamics during high-frequency synaptic stimulation: A gene deletion study in mouse hippocampus. Glia 60:867–874.

Haj-Yasein NN, Jensen V, Vindedal GF, Gundersen GA, Klungland A, Ottersen OP, Hvalby O, Nagelhus EA. 2011. Evidence that compromised K^+ spatial buffering contributes to the epileptogenic effect of mutations in the human Kir4.1 gene (KCNJ10). Glia 59:1635–1642.

Hertz L, Xu J, Song D, Yan E, Gu L, Peng L. 2013. Astrocytic and neuronal accumulation of elevated extracellular K^+ with a 2/3 K^+/Na^+ flux ratio—Consequences for energy metabolism, osmolarity and higher brain function. Front Comput Neurosci 7:114.

Horisberger J-D, Kharoubi-Hess S. 2002. Functional differences between α subunit isoforms of the rat Na,K-ATPase expressed in Xenopus oocytes. J Physiol 539:669–680.

Jauch R, Windmüller O, Lehmann T-N, Heinemann U, Gabriel S. 2002. Effects of barium, furosemide, ouabaine and 4,4′-diisothiocyanatostilbene-2,2′-disulfonic acid (DIDS) on ionophoretically-induced changes in extracellular potassium concentration in hippocampal slices from rats and from patients with epilepsy. Brain Res 925:18–27.

Jewell EA, Lingrel JB. 1991. Comparison of the substrate dependence properties of the rat Na,K-ATPase alpha 1, alpha 2, and alpha 3 isoforms expressed in HeLa cells. J Biol Chem 266:16925–16930.

Juhaszova M, Blaustein MP. 1997. Na+ pump low and high ouabain affinity α subunit isoforms are differently distributed in cells. Proc Natl Acad Sci USA 94:1800–1805.

Karwoski C, Lu H-K, Newman E. 1989. Spatial buffering of light-evoked potassium increases by retinal Müller (Glial) cells. Science 244:578–580.

Kofuji P, Newman EA. 2004. Potassium buffering in the central nervous system. Neuroscience 129:1043–1054.

Langan T, Plunkett R, Asada H, Kelly K, Kaseloo P. 1995. Long-term production of neurotrophic factors by astrocyte cultures from hemiparkinsonian rat brain. Glia 14:174–184.

Li B, Hertz L, Peng L. 2013. Cell-Specific mRNA Alterations in Na^+, K^+-ATPase α and β isoforms and FXYD in mice treated chronically with carbamazepine, an anti-bipolar drug. Neurochem Res 38:834–841.

MacAulay N, Zeuthen T. 2012. Glial K^+ clearance and cell swelling: Key roles for cotransporters and pumps. Neurochem Res 37:2299–2309.

MacVicar B, Hochman D. 1991. Imaging of synaptically evoked intrinsic optical signals in hippocampal slices. J Neurosci 11:1458–1469.

MacVicar BA, Feighan D, Brown A, Ransom B. 2002. Intrinsic optical signals in the rat optic nerve: Role for K(+) uptake via NKCC1 and swelling of astrocytes. Glia 37:114–123.

McGrail K, Phillips J, Sweadner K. 1991. Immunofluorescent localization of three Na,K-ATPase isozymes in the rat central nervous system: Both neurons and glia can express more than one Na,K-ATPase. J Neurosci 11:381–391.

Meeks JP, Mennerick S. 2007. Astrocyte membrane responses and potassium accumulation during neuronal activity. Hippocampus 17:1100–1108.

Moeller HB, Fenton RA, Zeuthen T, MacAulay N. 2009. Vasopressin-dependent short-term regulation of aquaporin 4 expressed in Xenopus oocytes. Neuroscience 164:1674–1684.

Nagelhus EA, Mathiisen TM, Ottersen OP. 2004. Aquaporin-4 in the central nervous system: Cellular and subcellular distribution and coexpression with KIR4.1. Neuroscience 129:905–913.

Newman E, Frambach D, Odette L. 1984. Control of extracellular potassium levels by retinal glial cell K^+ siphoning. Science 225:1174–1175.

Nicholson C, Phillips JM. 1981. Ion diffusion modified by tortuosity and volume fraction in the extracellular microenvironment of the rat cerebellum. J Physiol 321:225–257.

Oakley II B, Katz BJ, Xu Z, Zheng J. 1992. Spatial buffering of extracellular potassium by Müller (glial) cells in the toad retina. Exp Eye Res 55: 539–550.

Orkand R, Nicholls J, Kuffler SW. 1966. Effect of nerve impulses on the membrane potential of glial cells in the central nervous system of amphibia. J Neurophysiol 29:788–806.

Plotkin M, Kaplan M, Peterson L, Gullans S, Hebert S, Delpire E. 1997. Expression of the Na(+)-K(+)−2Cl- cotransporter BSC2 in the nervous system. Am J Physiol Cell 272:C173–C183.

Randall J, Thorne T, Delpire E. 1997. Partial cloning and characterization ofSlc12a2: The gene encoding the secretory Na^+-K^+-2Cl−cotransporter. Am J Physiol 273:C1267–C1277.

Ransom B, Yamate C, Connors B. 1985. Activity-dependent shrinkage of extracellular space in rat optic nerve: A developmental study. J Neurosci 5: 532–535.

Ransom CB, Ransom BR, Sontheimer H. 2000. Activity-dependent extracellular K^+ accumulation in rat optic nerve: The role of glial and axonal Na^+ pumps. J Physiol 522:427–442.

Ransom CB, Sontheimer H. 1995. Biophysical and pharmacological characterization of inwardly rectifying K^+ currents in rat spinal cord astrocytes. J Neurophysiol 73:333–346.

Richards KS, Bommert K, Szabo G, Miles R. 2007. Differential expression of Na^+/K^+-ATPase α-subunits in mouse hippocampal interneurones and pyramidal cells. J Physiol 585:491–505.

Raat N, Delpire E, van Os C, Bindels R. 1996. Culturing induced expression of basolateral Na^+-K^+-2Cl- cotransporter BSC2 in proximal tubule, aortic endothelium, and vascular smooth muscle. Pflugers Arch 431:458–460.

Strohschein S, Hüttmann K, Gabriel S, Binder DK, Heinemann U, Steinhäuser C. 2011. Impact of aquaporin-4 channels on K^+ buffering and gap junction coupling in the hippocampus. Glia 59:973–980.

Su G, Haworth RA, Dempsey RJ, Sun D. 2000. Regulation of Na^+-K^+-Cl−cotransporter in primary astrocytes by dibutyryl cAMP and high [K+]o. Am J Physiol 279:C1710–C1721.

Su G, Kintner DB, Flagella M, Shull GE, Sun D. 2002a. Astrocytes from Na(+)-K(+)-Cl(-) cotransporter-null mice exhibit absence of swelling and decrease in EAA release. Am J Physiol Cell Physiol 282:C1147–C1160.

Su G, Kintner DB, Sun D. 2002b. Contribution of Na^+-K^+-Cl−cotransporter to high-$[K^+]$o- induced swelling and EAA release in astrocytes. Am J Physiol 282:C1136–C1146.

Tas P, Massa P, Kress H, Koschel K. 1987. Characterization of an $Na^+/K^+/Cl$-co-transport in primary cultures of rat astrocytes. Biochem Biophys Acta 903: 411–416.

Vaillend C, Mason SE, Cuttle MF, Alger BE. 2002. Mechanisms of neuronal hyperexcitability caused by partial inhibition of Na^+-K^+-ATPases in the rat CA1 hippocampal region. J Neurophysiol 88:2963–2978.

Voipio J, Pasternack M, MacLeod K. 1994. Ion-sensitive microelectrodes. In: Ogden D, editor. Microelectrode techniques—The plymouth workshop handbook, 2nd ed. Cambridge: The Company of Biologists Limited. pp 275–316.

Walz W. 1992. Role of Na/K/Cl cotransport in astrocytes. Can J Physiol Pharmacol 70:S260–S262.

Walz W. 2000. Role of astrocytes in the clearance of excess extracellular potassium. Neurochem Int 36:291–300.

Wang F, Smith NA, Xu Q, Fujita T, Baba A, Matsuda T, Takano T, Bekar L, Nedergaard M. 2012. Astrocytes modulate neural network activity by Ca2+-dependent uptake of extracellular K^+. Sci Signal 5:ra26.

Zeuthen T, MacAulay N. 2012. Cotransport of water by Na^+–K^+–2Cl− cotransporters expressed in Xenopus oocytes: NKCC1 versus NKCC2. J Physiol 590:1139–1154.

Neurobiology of Disease

Chloride Cotransporters as a Molecular Mechanism underlying Spreading Depolarization-Induced Dendritic Beading

Annette B. Steffensen,[1] Jeremy Sword,[2] Deborah Croom,[2] Sergei A. Kirov,[2,3] and Nanna MacAulay[1]

[1]Department of Cellular and Molecular Medicine, Faculty of Health and Medical Sciences, University of Copenhagen, DK-2200 Copenhagen, Denmark, and [2]Brain and Behavior Discovery Institute and [3]Department of Neurosurgery, Medical College of Georgia, Georgia Regents University, Augusta, Georgia 30912

Spreading depolarizations (SDs) are waves of sustained neuronal and glial depolarization that propagate massive disruptions of ion gradients through the brain. SD is associated with migraine aura and recently recognized as a novel mechanism of injury in stroke and brain trauma patients. SD leads to neuronal swelling as assessed in real time with two-photon laser scanning microscopy (2PLSM). Pyramidal neurons do not express aquaporins and thus display low inherent water permeability, yet SD rapidly induces focal swelling (beading) along the dendritic shaft by unidentified molecular mechanisms. To address this issue, we induced SD in murine hippocampal slices by focal KCl microinjection and visualized the ensuing beading of dendrites expressing EGFP by 2PLSM. We confirmed that dendritic beading failed to arise during large (100 mOsm) hyposmotic challenges, underscoring that neuronal swelling does not occur as a simple osmotic event. SD-induced dendritic beading was not prevented by pharmacological interference with the cytoskeleton, supporting the notion that dendritic beading may result entirely from excessive water influx. Dendritic beading was strictly dependent on the presence of Cl^-, and, accordingly, combined blockade of Cl^--coupled transporters led to a significant reduction in dendritic beading without interfering with SD. Furthermore, our *in vivo* data showed a strong inhibition of dendritic beading during pharmacological blockage of these cotransporters. We propose that SD-induced dendritic beading takes place as a consequence of the altered driving forces and thus activity for these cotransporters, which by transport of water during their translocation mechanism may generate dendritic beading independently of osmotic forces.

Key words: **Cl-cotransporters; cotransporters; dendritic beading; neuronal swelling; spreading depression; two-photon microscopy**

Significance Statement

Spreading depolarization occurs during pathological conditions such as stroke, brain injury, and migraine and is characterized as a wave of massive ion translocation between intracellular and extracellular space in association with recurrent transient focal swelling (beading) of dendrites. Numerous ion channels have been demonstrated to be involved in generation and propagation of spreading depolarization, but the molecular machinery responsible for the dendritic beading has remained elusive. Using real-time *in vitro* and *in vivo* two-photon laser scanning microscopy, we have identified the transport mechanisms involved in the detrimental focal swelling of dendrites. These findings have clear clinical significance because they may point to a new class of pharmacological targets for prevention of neuronal swelling that consequently will serve as neuroprotective agents.

Introduction

Spreading depolarization (SD) is a fundamental pathological event in the brain that occurs as a wave of neuronal and glial depolarization invading the cortex at a rate of 2–6 mm/min (Leao, 1944; Dreier, 2011). The extracellular negative slow potential change between −5 and −30 mV serves as a robust measure of SD because it directly reflects the depolarization of a large population of cortical neurons (Canals et al., 2005). The full spectrum from short-lasting to very long-lasting SD waves has been

Received Jan. 30, 2015; revised July 3, 2015; accepted July 27, 2015.

Author contributions: S.A.K. and N.M. designed research; A.B.S., J.S., D.C., and S.A.K. performed research; A.B.S., J.S., D.C., and S.A.K. analyzed data; A.B.S., S.A.K., and N.M. wrote the paper.

This work was supported by National Institutes of Health Grant NS083858, American Heart Association Grant 12GRNT16570006 (S.A.K.), and Thorberg's Foundation (N.M.). We thank Libby Perry and Brendan Marshall of the Electron Microscopy Core at the Medical College of Georgia, Georgia Regents University for assistance with electron microscopy.

Correspondence should be addressed to either of the following: Dr. Sergei A. Kirov, Department of Neurosurgery, and Brain and Behavior Discovery Institute, Georgia Regents University, 1120 15th Street, CB-3706, Augusta, GA 30912-2630, E-mail: skirov13@gmail.com; or Dr. Nanna MacAulay, Department of Cellular and Molecular Medicine, Faculty of Health and Medical Sciences, University of Copenhagen, Blegdamsvej 3, Copenhagen, DK-2200, Denmark, E-mail: macaulay@sund.ku.dk.

DOI:10.1523/JNEUROSCI.0400-15.2015

 0270-6474/15/3512172-16$15.00/0

observed in association with cerebral pathologies, such as migraine aura, stroke, and traumatic brain injury, not only in experimental animals but also in patients (Hadjikhani et al., 2001; Oliveira-Ferreira et al., 2010; Hartings et al., 2011a; Dreier and Reiffurth, 2015). Moreover, multiple or prolonged SDs may instigate secondary neuronal damage in patients experiencing acute cerebral injuries (Dreier et al., 2006; Hartings et al., 2011b; Lauritzen et al., 2011).

Ionic changes between the extracellular and intracellular compartments during SD are massive, with a sharp increase of $[K^+]_o$ and a severe drop of $[Na^+]_o$, $[Ca^{2+}]_o$, $[Cl^-]_o$, and pH_o (Kraig and Nicholson, 1978; Hansen and Zeuthen, 1981; Mutch and Hansen, 1984; Menna et al., 2000; Windmüller et al., 2005). During SD, the interstitial space shrinks dramatically (Pérez-Pinzón et al., 1995; Mazel et al., 2002), reflecting abrupt cytotoxic edema manifested by profound neuronal swelling and dendritic beading with spine loss (Takano et al., 2007; Murphy et al., 2008; Risher et al., 2012) and attendant synaptic failure and neuronal damage (Somjen, 2001; Douglas et al., 2011; Chen et al., 2012). It appears that the transient or terminal nature of SD-induced dendritic beading depends on the metabolic status of the tissue invaded by this SD (Li and Murphy, 2008; Risher et al., 2010; Sword et al., 2013). Dendritic preservation is required for successful neuroprotection strategies (Iyirhiaro et al., 2008), and uncoupling of dendritic beading from SD should thus protect dendrites from terminal injury.

However, the molecular mechanisms generating the focal volume increase underlying SD-induced dendritic beading have remained elusive. Simple osmotically obliged water entry during SD is unlikely to cause beading because membranes of pyramidal neurons display low intrinsic osmotic water permeability caused by lack of expression of membrane-bound aquaporins (Andrew et al., 2007; Papadopoulos and Verkman, 2013). Therefore, we hypothesized that dendritic beading, at least in part, occurs secondary to the large SD-induced changes in ion and lactate concentrations. A range of cotransport proteins carry the inherent ability to cotransport water along their translocation mechanism in a manner independent of transmembrane osmotic forces (for review, see MacAulay and Zeuthen, 2010). Consequently, we propose that SD-induced alterations in transmembrane ion and lactate concentrations activate select cotransporters that then act as the molecular mechanisms responsible for dendritic bead formation. Here using two-photon laser scanning microscopy (2PLSM) imaging in hippocampal slices and *in vivo*, we search for evidence that Cl^--coupled and lactate transporters participate in SD-induced dendritic beading.

Materials and Methods

Brain slice preparation and solutions. All procedures followed National Institutes of Health guidelines for the humane care and use of laboratory animals and underwent yearly review by the Animal Care and Use Committee at the Medical College of Georgia, Georgia Regents University. Brain slices (400 μm) were made from 35 male and female adult mice (45–70 d old) according to standard protocols (Kirov et al., 2004). We used 32 heterozygous mice of B6.Cg–Tg(Thy1–EGFP)MJrs [GFP-M] strain, two heterozygous mice of B6.129P–*Cx3cr1*^{tm1Litt}/J [CX3CR1–EGFP] strain, and one wild-type mouse. Founders of the GFP-M colony were kindly provided by Dr. J. Sanes (Harvard University, Boston, MA). This strain of mice expresses the enhanced green fluorescent protein (EGFP) in sparse subsets of neocortical and hippocampal pyramidal neurons (Feng et al., 2000). The founding mice of the CX3CR1–EGFP colony were purchased from The Jackson Laboratory. These mice express EGFP in microglia under control of the endogenous *Cx3cr1* locus encoding the chemokine (C-X3-C) receptor 1 (CX3CR1; also known as fractalkine receptor; Jung et al., 2000). Mice were anesthetized deeply with halothane (2-bromo-2-chloro-1,1,1-trifluoroethane) and decapitated. The brain was quickly removed and placed in cold, oxygenated (95% O_2/5% CO_2) sucrose-based artificial CSF (aCSF; in mM: 1 NaH_2PO_4, 25 $NaHCO_3$, 10 glucose, 210 sucrose, 2.5 KCl, and 8 $MgSO_4$, pH 7.4). Transverse slices, including hippocampus, subiculum, and neocortex, were cut with a vibrating-blade microtome (VT1000S; Leica) and submerged in oxygenated standard aCSF (in mM: 1 NaH_2PO_4, 25 $NaHCO_3$, 10 glucose, 120 NaCl, 2.5 KCl, 1.3 $MgSO_4$, and 2.5 $CaCl_2$, pH 7.4) to recover at room temperature for a minimum of 1 h before recordings. For the hyposmolar experiments, 50 mM NaCl was replaced with mannitol in the isosmolar mannitol-containing aCSF (in mM: 1 NaH_2PO_4, 25 $NaHCO_3$, 10 glucose, 100 mannitol, 70 NaCl, 2.5 KCl, 1.3 $MgSO_4$, and 2.5 $CaCl_2$, pH 7.4). The hyposmolar aCSF was created by removal of the mannitol to obtain a "pure" osmotic challenge while avoiding alterations in ionic strength during the actual hyposmotic challenge and thus shifts in driving forces for the Na^+ and Cl^--driven transporters. The aCSF with a low-Cl^- concentration contained the following (in mM): 1 NaH_2PO_4, 25 $NaHCO_3$, 10 glucose, 120 $NaCH_3SO_4$, 2.5 KCH_3SO_4, 1.2 $MgSO_4$, and 1.2 $CaCl_2$, pH 7.4.

In vitro *imaging and electrophysiological recording.* A slice was placed into a submersion-type imaging/recording chamber (RC-29; 629 μl working volume; Warner Instruments) mounted on the Luigs & Neumann microscope stage. The slice was held down by an anchor (SHD-27LP/2; Warner Instruments) and superfused with oxygenated aCSF at 30–32°C, using a recirculating system with a flow rate of 7–8 ml/min controlled by two peristaltic pumps (Watson-Marlow). Temperature was monitored by a thermistor probe within 1 mm of the slice and maintained by an in-line solution heater/cooler (CL-100; Warner Instruments) with a bipolar temperature controller (TA-29; Warner Instruments). Images of apical dendrites of hippocampal CA1 pyramidal neurons were acquired in the area of the stratum radiatum localized between the recording microelectrode and the injection micropipette at a depth of ≥80 μm from the cut slice surface in which there was no trace of injured dendrites (Kirov et al., 1999; Davies et al., 2007). The field EPSPs (fEPSPs) were evoked by a concentric bipolar stimulating electrode (25 μm pole separation; FHC) placed in the middle of the stratum radiatum, and recorded with a glass microelectrode (filled with 0.9% NaCl, 1–2 MΩ). Evoked fEPSPs in healthy slices had a sigmoidal input/output response function and a stable response at half-maximal stimulation. The stimulating electrode was subsequently removed, and the first SD was induced by pressure injection of ~1.5 nl of 1 M KCl (25 psi, 100 ms) using a Picospritzer (Parker Hannifin; Aiba et al., 2012) with an injection micropipette (1–2 MΩ) positioned ~ 400 μm downstream of aCSF flow from the recording electrode. This experimental design was intended to prevent significant spread of the focally administered KCl into the imaging area. The extracellular negative direct current (DC) potential shift indicated SD. To obtain consecutive SDs, three near-instantaneous KCl injections were used to generate the second and third SD, with a 20 min recovery period between each SD. In low-Cl^- aCSF, six instantaneous KCl injections were required to evoke SD. Signals were recorded with a MultiClamp 200B amplifier (Molecular Devices). fEPSPs were filtered at 2 kHz and DC potential at 400 Hz, sampled at 10 kHz with a Digidata 1322A interface board, and analyzed with pClamp 10 software (Molecular Devices).

Preparation of mice for in vivo *imaging and electrophysiology.* Craniotomy for the optical window followed standard protocols (Risher et al., 2010). Ten heterozygous GFP-M male and female adult mice (56–70 d old) were used for *in vivo* experiments. Mice were anesthetized with an intraperitoneal injection of urethane (1.5 mg/g body weight). During surgery, body temperature was maintained at 37°C with a heating pad (Sunbeam). The trachea was cannulated, and mice were ventilated mechanically with an SAR-830 ventilator (CWE) throughout the experiment. Blood oxygen saturation level (>90%) and heart rate (450–650 beats/min) were monitored continuously with a MouseOx pulse oximeter (STARR Life Sciences). The skin covering the cranium above the somatosensory cortex was removed. A custom-made 1.3-cm-diameter plastic ring was glued with dental acrylic cement (Co-Oral-Ite Dental) to stabilize the head during the craniotomy and imaging using a mouse

head holder attached to a base plate. A dental drill (Midwest Stylus Mini 540S; DENTSPLY International) with 0.5 mm round bit was used to thin the circumference of a 2- to 4-mm-diameter circular region of the skull over the somatosensory cortex (centered at stereotaxic coordinates −1.8 mm from bregma and 2.8 mm lateral). The thinned bone was lifted up with forceps. An optical chamber was constructed by covering the intact dura with a cortex aCSF containing the following (in mM): 135 NaCl, 5.4 KCl, 1 $MgCl_2$, 1.8 $CaCl_2$, and 10 HEPES, pH 7.3. The chamber was left open to facilitate access with a glass microelectrode and a KCl-injection micropipette for SD induction. After installation of the Ag/AgCl pellet reference electrode (A-M Systems) under the skin above the nasal bone, the base plate containing the head holder with the mouse resting on a heating blanket was affixed to the Luigs & Neumann microscope stage for imaging. Rectal temperature was monitored continuously with an IT-18 thermocouple (AD Instruments) and a Fluke 51 thermometer, and maintained at 37°C with a heating blanket (Harvard Apparatus). Hydration was maintained by intraperitoneal injection of 100 μl of 0.9% NaCl with 20 mM glucose at 1 h intervals. Depth of anesthesia was assessed by toe pinch and heart rate monitoring, maintained with 10% of the initial urethane dose if necessary. A 0.1 ml bolus of 5% (w/v) Texas Red Dextran (70 kDa) in 0.9% NaCl was injected into the tail vein for blood flow visualization. The cortical slow DC potential was recorded with a glass microelectrode (filled with 0.9% NaCl, 1–2 MΩ) inserted through the dura to the site of imaged dendrites within layer I of the somatosensory cortex. SDs were induced by focal pressure injection of <5 nl of 1 M KCl with a Picospritzer (Parker Hannifin) using a micropipette inserted through the dura to the depth of 200–300 μm within 2 mm away from the site of imaged dendrites. Signals were recorded with a MultiClamp 200B amplifier, filtered at 1 kHz, digitized at 10 kHz with a Digidata 1322A interface board, and analyzed with pClamp 10 (Molecular Devices).

2PLSM. Images were collected with infrared-optimized 40×/0.8 numerical aperture (NA) water-immersion objective (Carl Zeiss) using the Zeiss LSM 510 NLO META multiphoton system mounted on the motorized upright Axioscope 2FS microscope. The scan module was coupled directly with a titanium:sapphire broadband, mode-locked laser (Mai-Tai; Spectra-Physics) tuned to 910 nm for two-photon excitation. Emitted light was detected by internal photomultiplier tubes of the scan module with the pinhole entirely opened. Three-dimensional (3D) time-lapse images were taken at 1 μm increments using a 3× optical zoom, yielding a nominal spatial resolution of 6.8 pixels/μm (12 bits/pixel, 0.9 μs pixel time) across a 75 × 75 μm imaging field. To monitor structural changes, image stacks consisting of 18–20 sections were acquired every 30 s after SD during the first 3 min or until full recovery of beading was observed. Each section takes ~1 s to acquire, and therefore the time point "10 s" refers to the middle time point of imaging of a new stack, which takes ~18–20 s to acquire. When experimental conditions caused a shift in the focal plane, it was adjusted and re-centered before subsequent data acquisition (Risher et al., 2009, 2010).

Laser speckle imaging. Two-dimensional (2D) maps of cerebral blood flow with high spatiotemporal resolution were acquired by laser speckle imaging as described previously (Dunn et al., 2001; Sigler et al., 2008; Risher et al., 2010). Briefly, the cortical surface was illuminated through an anamorphic beam expander (Edmund Optics) by a 785 nm StockerYale laser (ProPhotonix) at an angle of ~30° and imaged with a 4×/0.075 NA objective (Zeiss). Real-time speckle imaging was used with custom-written LabView software (National Instruments) (Yang et al., 2011) and modified for use with the Dalsa Pantera 1M60 camera (Dalsa) using the XCLIB DLL library (EPIX). The software processes ~10 fps at an exposure time of 20 ms in our setup using the NVIDIA Quadro FX 1700 graphics card CUDA (NVIDIA) on the graphics processing unit. Laser speckle contrast was obtained by dividing the SD image by the mean of each raw image with a 5 × 5 pixel sliding window for immediate display (Yang et al., 2011). Fifty frames were saved individually as 32 bit images in LabView and averaged offline using NIH ImageJ to obtain a single image for figures.

Image analysis from 2PLSM. Images were examined and analyzed with NIH ImageJ. The Scientific Volume Imaging Huygens Professional image deconvolution software was used to process images before analyses. All *in vivo* experiments and the experiments involving cytoskeletal rearrangements were quantified by an investigator blind to the experimental conditions. All other 2PLSM data were not coded for analyses. The formation of focal swelling or beading along the dendritic shaft was identified by rounded regions extending beyond the initial diameter of the dendrite separated from each other by thin dendritic segments ("beads-on-a-string" appearance). The recovery was defined as the disappearance of rounded "beaded" regions. The amount of dendritic beading in an imaging field was quantified as reported previously (Murphy et al., 2008; Sword et al., 2013). Briefly, 2D maximum intensity projections (MIPs) of 3D image stacks were aligned between different time points before and during SD. To quantify the extent of dendritic beading, each MIP image was divided into 6 × 6 squares (12.5 × 12.5 μm), and only the squares containing dendrites were counted and the percentage of squares containing beaded dendrites was calculated. Individual sections through 3D stacks were also examined and compared with pre-SD images to distinguish dendritic beads from sphere-shaped axonal boutons and dendrites imaged in cross-section.

To measure relative changes in the size of dendritic beads between experimental conditions, we used 2D MIPs of 3D image stacks to manually trace the cross-sectional area of individual dendritic beads. Analysis of changes in the lateral dimensions simplified the interpretation of morphometric data imposed by the low axial resolution of 2PLSM (~2 μm) compared with the lateral resolution (~0.4 μm). Such morphometric analysis was adequate to determine relative volume changes, which underestimated the actual volume changes assuming they are approximately isotropic.

Electron microscopy and image analysis. Slices were fixed rapidly during 8 s of microwave irradiation in mixed aldehydes (2% glutaraldehyde, 4% paraformaldehyde in 0.1 M cacodylate buffer, pH 7.4, and containing 2 mM $CaCl_2$ and 4 mM $MgCl_2$) and stored overnight in fixative at room temperature (Jensen and Harris, 1989). A small piece of tissue containing the CA1 region of the hippocampus was microdissected from the slice and subsequently processed with standard microwave-enhanced procedures through osmium, uranyl acetate, dehydration with a graded ethanol series, and embedding in Epon–Araldite resin (Kirov et al., 1999). Thin sections from the middle of the stratum radiatum at an optimal depth of 150–200 μm beneath the slice surface were cut with a diamond knife on a Leica EM UC6 ultramicrotome (Leica), collected on pioloform-coated copper Synaptek slot grids (Electron Microscopy Sciences), and stained with uranyl acetate and lead citrate. These protocols produced well stained and readily identifiable neuronal processes (see Fig. 2*G*). Five fields were photographed in each slice (total 25 fields) at the JEOL 1230 transmission electron microscope (JEOL). Images were captured digitally at a magnification of 3000× using the Gatan UltraScan 4000 camera (Gatan). The images were randomized, coded, and analyzed blind as to condition. Each image provided ~225 μm^2 (1125 μm^2 in total per condition) to evaluate microtubule disassembly. Each dendritic profile was scored as having microtubules present or completely devoid of them.

Chemicals. Latrunculin A and Texas Red Dextran were from Invitrogen, and Taxol was from Tocris Bioscience. All other drugs and chemicals were from Sigma. Furosemide (final concentration of 1 mM), 4-hydroxycinnamate (4-CIN; final concentration of 0.5 mM), and ouabain (final concentration of 100 μM) were dissolved directly into the aCSF. 4,4′-Diisothiocyanatostilbene-2,2′-disulphonic acid (DIDS; 15 mg) was dispersed in 300 μl of water and then solubilized at 300 μM in aCSF. Taxol (final concentration of 1.5 μM) and Latrunculin A (final concentration of 1.5 μM) were dissolved in DMSO to a stock solution of 500 μM each. aCSF solutions and drug mixtures were made fresh each day. Solutions containing Latrunculin A and Taxol were made immediately before their experimental application. All solutions and drugs were applied to the slices for 15 min (osmotic solutions, low-Cl^- aCSF, a mixture of furosemide, DIDS, and 4-CIN) or for 45 min (Taxol/Latrunculin A, furosemide, DIDS, or 4-CIN). The mixture of furosemide, DIDS, and 4-CIN in the cortex aCSF was applied directly to the cortex with dura intact for ~120 min.

Statistics. Statistica (StatSoft), SigmaStat (Systat), or GraphPrism 6.0 (GraphPad Software) was used to evaluate significant differences be-

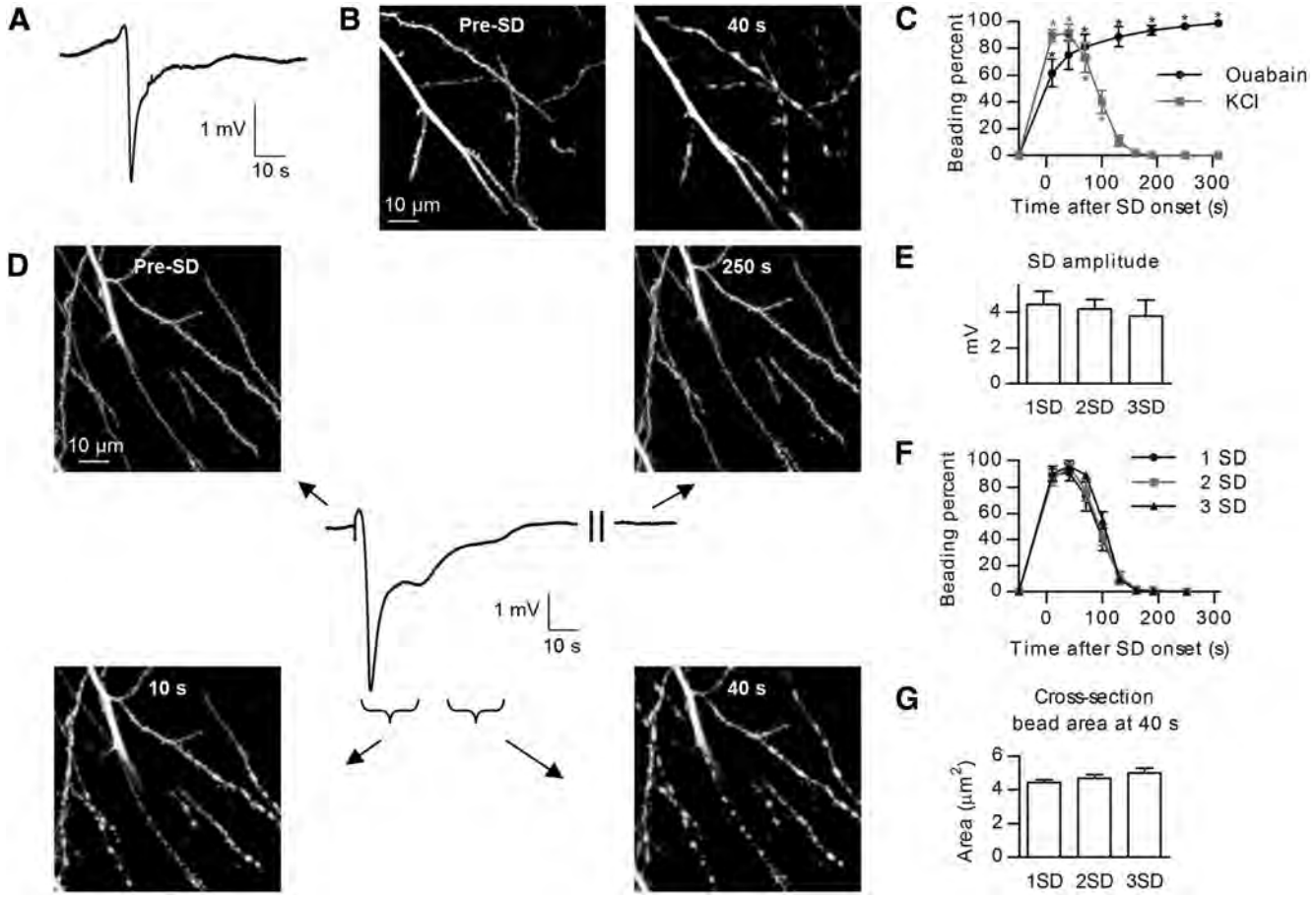

Figure 1. SD-induced dendritic beading in hippocampal slices. ***A***, Representative DC potential recording at the imaging site during exposure to ouabain-containing aCSF. The negative deflection in the DC trace represents the SD. ***B***, 2PLSM MIP images of apical dendrites of CA1 pyramidal neurons in the stratum radiatum before and 40 s after onset of terminal long-lasting SD evoked by exposure to 100 μM ouabain. ***C***, The fraction of beaded dendrites during SD evoked either by chemical ischemia with ouabain (black symbols, $n = 6$ slices) or by KCl microinjection (gray symbols, $n = 6$ slices) in normoxic hippocampus. Values are based on manually scored beading percentages in imaging fields using a 6×6 grid (Sword et al., 2013). Asterisks indicate significant difference from the time point before SD (one-way RM-ANOVA with Tukey's *post hoc* test); $*p < 0.001$. ***D***, 2PLSM MIP image sequence reveals transient dendritic beading during a passage of normoxic KCl-induced SD. Images were taken shortly before (Pre-SD), during initiation (10 s), and 40 and 250 s after onset of the short-lasting SD shown in the middle. Arrows specify time points on the recording when corresponding image stacks were taken, with braces indicating acquisition duration of each stack. The DC potential fully recovered to the baseline as neurons repolarized. ***E***, Quantified amplitudes of three consecutive KCl-induced SDs ($n = 6$ slices, one-way RM-ANOVA with Tukey's *post hoc* test). ***F***, Summary from three consecutive SDs showing that dendrites undergo similar beading and recovery during each round of SD ($n = 6$ slices, two-way RM-ANOVA with Tukey's *post hoc* test). ***G***, Summary from 34 beads in six slices showing identical increase in bead cross-section area at the same dendritic location as measured at 40 s after onset of each of three consecutive SDs (one-way RM-ANOVA with Tukey's *post hoc* test).

tween conditions. Unpaired and paired Student's *t* tests, Wilcoxon's signed-rank test, and one-way and two-way repeated-measures (RM) ANOVA, followed by the Tukey's or Sidak's multiple comparison *post hoc* tests were used when applicable. The χ^2 test was used to analyze data arranged in contingency tables. Data are presented as mean ± SEM, and the significance criterion was set at $p < 0.05$. For clarity of small panel figures, one asterisk signifies all significance levels, whereas the exact significance level is stated in Results.

Results

Generation of SD and dendritic beading in brain slices

Live brain slices allow real-time imaging of fully arborized neurons deep under the cut surface in which the native tissue architecture and cellular milieu is preserved. Anoxic or terminal SD, similar to an SD wave ignited *in vivo* in the severely energy-deprived ischemic core, can be initiated in slices during simulated global ischemia induced by oxygen/glucose deprivation (OGD) or by exposure to ouabain, which, like OGD, inhibits the Na^+/K^+-ATPase (Balestrino et al., 1999; Anderson et al., 2005). Initially, we induced SD by ouabain application (100 μM; for a representative SD recording, see Fig. 1*A*). Apical dendrites of hippocampal CA1 pyramidal neurons were imaged first in control aCSF and then during ouabain-induced SD (Fig. 1*B*). Dendritic beading occurred at the onset of SD, with the fraction of beaded dendrites increasing to 98.9 ± 1.1% at 310 s after SD initiation ($n = 6$ slices from 4 mice, $p < 0.001$; Fig. 1*C*, black symbols). As expected from previous studies, there was no recovery of dendritic beading during a wash in control aCSF (data not shown; Douglas et al., 2011). Because in normal healthy cortex and in moderately metabolically stressed ischemic penumbra SD-induced dendritic beading is transient (Takano et al., 2007; Risher et al., 2010), it was desirable to find experimental conditions that would allow the repeated trigger of transient SD-induced dendritic beading in the same slice. Normoxic SD can be evoked repetitively in slices by briefly elevating $[K^+]_o$ in the aCSF superfusate (Anderson and Andrew, 2002; Zhou et al., 2010) or by focal pressure injection of small quantities of 1 M KCl (Aiba et al., 2012). However, it was unknown whether transient dendritic beading could be triggered repetitively in the same slice by subsequent normoxic SDs. Focal pressure injection of KCl reliably triggered SD, and dendrites underwent a rapid cycle of beading

and recovery that coincided with the passage of SD (Fig. 1*D*). Beading was maximal at 40 s after the start of SD, with the fraction of beaded dendrites reaching 91.6 ± 6.4% ($n = 6$ slices from 4 mice) with complete recovery obtained by 220 s (Fig. 1*C*, gray symbols). The three consecutive KCl pressure injections (20 min interval) yielded SDs of comparable amplitude (4.4 ± 0.7 mV for first SD, 4.2 ± 0.5 mV for second SD, and 3.8 ± 0.9 mV for third SD, $n = 6$ slices, $p = 0.79$; Fig. 1*E*). The time course of SD-induced beading was similar during these consecutive KCl applications, with a maximal fraction of beaded dendrites at 40 s (91.6 ± 6.4% for first SD, 96.2 ± 1.9% for second SD, and 96.2 ± 3.8% for third SD, $n = 6$ slices, $p = 0.95$) and a complete recovery at 220 s after SD start (Fig. 1*F*). The size of dendritic beads at 40 s was also similar between the three consecutive depolarizations, with the cross-sectional area of individual dendritic beads reaching 4.4 ± 0.2, 4.7 ± 0.2, and 5.0 ± 0.3 μm^2, respectively ($n = 34$ beads in 6 slices, $p = 0.06$; Fig. 1*G*). Thus, we established that transient dendritic beading can be triggered reliably in slices by subsequent rounds of focal KCl microinjections without accumulating dendritic injury. Therefore, we used this experimental approach to determine molecular mechanisms underlying dendritic beading.

Cytoskeletal rearrangement is not required for dendritic beading

Even during normoxic SD, the energy demand of the Na^+/K^+-ATPase increases so markedly (LaManna and Rosenthal, 1975) that the ATP concentration falls to ~50% (Mies and Paschen, 1984). Such sharp reduction in ATP might trigger unregulated polymerization of monomeric globular actin to polymeric filamentous actin (Atkinson et al., 2004) and may thus contribute to beading (Gisselsson et al., 2005). In addition, dendritic $[Ca^{2+}]$ rises into the micromolar range during the course of SD (Dietz et al., 2008), which may interfere with microtubule stability. Therefore, to elucidate the role of cytoskeletal rearrangement in SD-induced dendritic beading, we stabilized microtubules with Taxol (Bird, 1984) and inhibited actin polymerization with Latrunculin A (Spector et al., 1983). First, SD was induced by focal KCl microinjection, and control dendritic beading was observed with 2PLSM (Fig. 2*A*). The slice subsequently recovered before exposure to aCSF containing 1.5 μM Taxol and 1.5 μM Latrunculin A. Then a second SD of similar amplitude was triggered with KCl (5.3 ± 0.6 vs 5.2 ± 0.7 mV, $n = 5$ slices from 5 mice, $p = 0.80$; Fig. 2*B*). Dendritic beading readily occurred in the presence of Taxol and Latrunculin A (Fig. 2*C*). There was no difference in the amount of SD-induced beading between control aCSF and aCSF containing toxins (76.7 ± 9.8 vs 89.6 ± 1.0% at 40 s, $n = 5$ slices, $p = 0.17$; Fig. 2*D*). Likewise, the size of dendritic beads at 40 s after SD initiation in control aCSF was not affected by pretreatment with Taxol and Latrunculin A (4.9 ± 0.3 vs 5.1 ± 0.3 μm^2, $n = 60$ beads in 5 slices, $p = 0.19$; Fig. 2*E*). These findings suggest that cytoskeletal rearrangements do not underlie formation of SD-induced dendritic beading.

To ensure that microtubules were stabilized and actin polymerization was indeed sufficiently abolished under our experimental conditions, we designed positive control experiments to independently verify the drug actions. Apparently, dendritic microtubules disassemble when intracellular $[Ca^{2+}]$ increases to the micromolar range (Schliwa et al., 1981), and several ultrastructural studies have revealed disintegration of microtubules inside swollen dendrites immediately after ischemia (Yamamoto et al., 1986, 1990). Therefore, we used chemical ischemia to verify whether Taxol could prevent microtubule fragmentation during ouabain-induced SD, which is by itself a much stronger noxious stimuli than KCl-induced SD. Slices were fixed rapidly during microwave irradiation in mixed aldehydes immediately after confirmation of dendritic integrity in control conditions or validation of dendritic beading by ouabain-induced SD in the absence or presence of 0.5 and 1.5 μM Taxol (Fig. 2*F*). The occurrence of microtubules in the cross-sectioned dendritic profiles was determined by EM (Fig. 2*G*), and the dendritic profiles were scored either as having microtubules or devoid of them (Fig. 2*H*). In control slices not exposed to SD, microtubules were clearly detectable in 84% of dendritic profiles, whereas in slices exposed to ouabain-induced SD only 31% of dendritic profiles contained microtubulus ($p < 0.001$; Fig. 2*H*). When SD was induced in the presence of 0.5 μM Taxol, 67% of cross-sectioned dendrites had microtubules. The number of dendrites with microtubules was significantly higher than in slices with ouabain-induced SD ($p < 0.001$), but this number was still significantly less than in the control condition ($p < 0.01$; Fig. 2*H*), indicating intermediate protection. However, quantification revealed a similar percentage of dendritic profiles with microtubules in the control and after ouabain-induced SD in the presence of 1.5 μM Taxol (84 vs 78%, respectively, $p = 0.3$; Fig. 2*H*), suggesting that, at this concentration, Taxol blocked microtubule fragmentation during ouabain-induced SD.

It has been reported that agents blocking actin polymerization were effective at inhibiting microglial process extension in slices (Hines et al., 2009). Therefore, we monitored activated microglia within 70 μm of the cut slice surface and confirmed that microglial processes were continuously undergoing cycles of extension and retraction (Fig. 2*I*) as shown *in vivo* (Nimmerjahn et al., 2005; Masuda et al., 2011). Bath application of Latrunculin A, even at a lower concentration (0.5 μM), reliably stopped microglia process activity (Fig. 2*J*; $n = 2$ slices from 2 mice). Next, we used two-photon excitation to create discrete circular microlesion and monitor outgrowth of microglia processes toward lesion as reported in previous studies in slices (Hines et al., 2009). The laser intensity was kept comparable between all experiments. After detection of robust microglia response to the injury (Fig. 2*K*), we superfused the same slice with aCSF containing 0.5 μM Latrunculin A and then created another microlesion away from the site of initial damage. Application of Latrunculin A for 14–66 min completely blocked process extension to the new lesion site (Fig. 2*L*; $n = 5$ slices from 2 mice). These observations indicate that Taxol and Latrunculin A exerted their inhibitory effect under our experimental conditions but failed to block SD-induced dendritic beading.

Dendritic beading does not occur as osmotically induced swelling

Dendritic beading is associated with increased dendritic volume (Hasbani et al., 1998) and therefore necessarily with a flux of water into the dendrites (Kirov et al., 2004; Andrew et al., 2007; also note the watery cytoplasm of swollen cross-sectioned dendrites after ouabain-induced SD shown in the middle and the right panels of Fig. 2*G*). During SD, the physiological transmembrane ion gradients are greatly altered. Thus, osmotic particles could potentially accumulate intracellularly and promote passive flux of water from the extracellular space into the dendrites. To mimic such an event, we introduced an extracellular hyposmotic challenge of 100 mOsm and monitored dendrites by 2PLSM (Fig. 3). The slice was initially kept in control aCSF (left panel, Control). To preserve the ionic strength of the aCSF and thus ionic driving forces during changes in aCSF osmolarity, the slice was

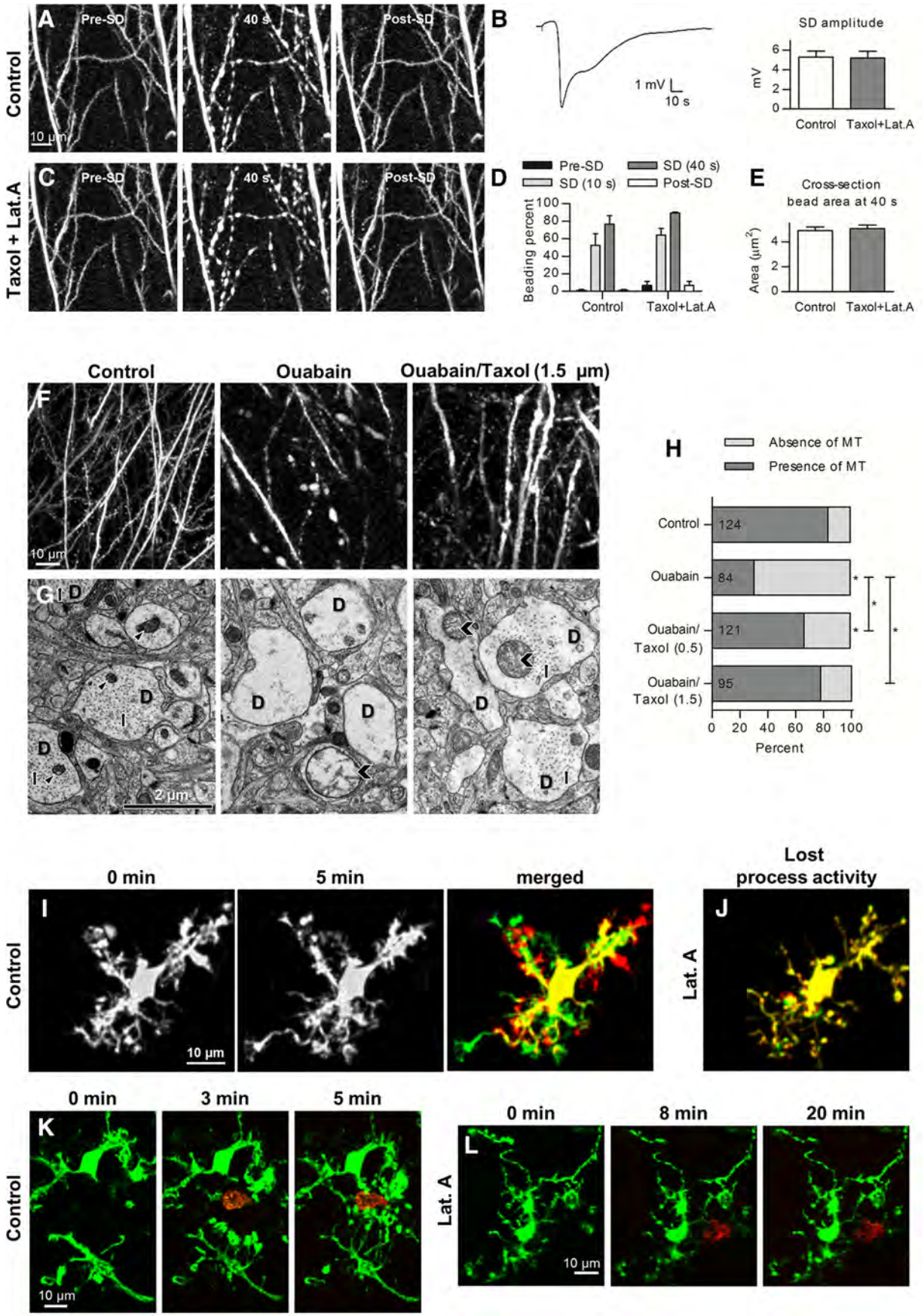

Figure 2. SD-induced beading was not prevented by pharmacological interference with dendritic cytoskeleton. ***A***, 2PLSM MIP control images of dendrites showing rapid beading and recovery during the passage of normoxic KCl-induced SD. ***B***, Representative DC potential recording and quantified amplitude before and after 45 min pretreatment with (*Figure legend continues.*)

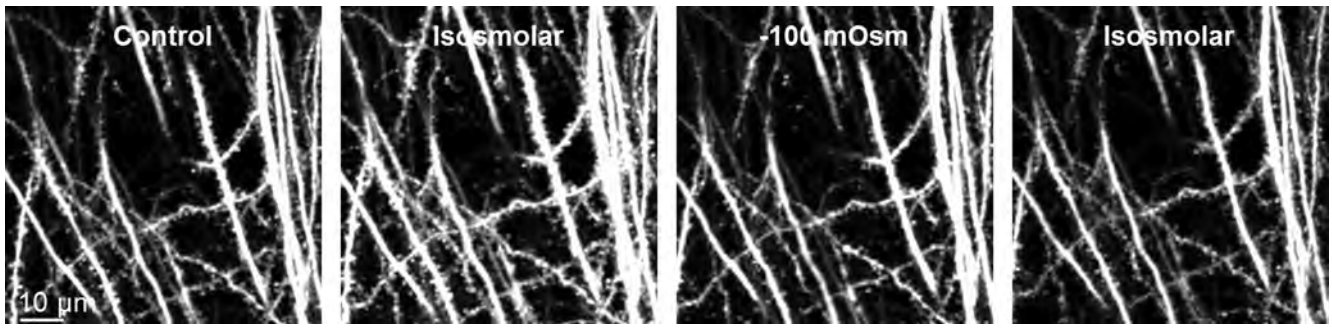

Figure 3. Dendrites withstand severe hyposmotic challenge. Representative 2PLSM MIP image sequence showing dendritic structural stability during superfusion of slices with control aCSF, after 15 min of isosmolar mannitol-containing aCSF, after 15 min of exposure to hyposmotic aCSF (−100 mOsm), and then after 15 min of return of isosmolar aCSF ($n = 4$ slices from 2 mice).

then superfused with an isosmolar mannitol-containing aCSF (50 mM NaCl replaced with 100 mM mannitol; second panel, Isosmolar). When the slice was subsequently exposed to the aCSF in which the 100 mM mannitol was removed, the slice would encounter an abrupt 100 mOsm hyposmotic challenge with no simultaneous changes in ionic driving forces and/or membrane potential (third panel, −100 mOsm). After the hyposmotic challenge, the slice was reexposed to the isosmolar mannitol-containing aCSF (right panel, Isosmolar). During the first minutes of the hyposmotic stress, a slow shift in the focal plane of the optical sections was observed, revealing the expected slice swelling. However, there was no dendritic beading observed during the hyposmotic challenge, indicating that SD-induced dendritic beading does not occur as a simple osmotic event after the ionic movements during SD.

←

(*Figure legend continued.*) 1.5 µM Taxol and 1.5 µM Latrunculin A (Lat.A; $n = 5$ slices, paired *t* test). ***C***, 2PLSM MIP image sequence of the same dendrites reveals transient beading during the passage of SD induced after pretreatment with Taxol and Latrunculin A. ***D***, SD-induced dendritic beading in control aCSF is similar to the beading after pretreatment with Taxol and Latrunculin A ($n = 5$ slices, two-way RM-ANOVA and Sidak's *post hoc* test), post-SD quantified at 250 s. ***E***, At 40 s after SD onset, the size of beads measured at the same dendritic location was not affected by pretreatment with Taxol and Latrunculin A ($n = 60$ beads in 5 slices, paired *t* test). ***F***, 2PLSM MIP images of dendrites in control and after onset of terminal long-lasting SD evoked by 100 µM ouabain. Dendrites become beaded precisely coinciding with the passage of ouabain-induced SD elicited in standard aCSF (middle) or aCSF containing 1.5 µM Taxol (right). ***G***, Corresponding ultrastructural components of dendritic structure from the slices shown in ***F***. EM images of neuropil in the CA1 region of the stratum radiatum were acquired in the middle of the slice ~200 µm below the cut surface. Morphologically healthy neuropil in control slices (left) had dendrites (D) with intact cytoplasm, microtubules (arrows), and non-swollen mitochondria (arrowheads). Disrupted neuropil after ouabain-induced SD (middle) had swollen dendrites (D) devoid of microtubules in their watery cytoplasm that contained severely swollen mitochondria (chevron). Dendrites (D) and mitochondria (chevrons) were swollen after the passage of ouabain-induced SD in aCSF containing 1.5 µM Taxol (right), but microtubule arrays (arrows) remained intact. ***H***, Percentage of dendritic profiles containing microtubules (MT) in control conditions and after passage of ouabain-induced SD triggered in standard aCSF or aCSF containing either 0.5 or 1.5 µM Taxol. The number of dendritic profiles that were analyzed in each condition is indicated within each bar. Asterisks above bars indicate significant difference from control condition (χ^2 test). Asterisks above braces indicate significant difference between SD-triggered microtubule loss in standard aCSF and aCSF containing 0.5 and 1.5 µM Taxol (χ^2 test). *$p < 0.01$. ***I***, Activated microglia morphology and dynamics near the cut slice surface. MIPs of image stacks acquired during time-lapse recording at the beginning (left) and 5 min later (middle) are overlaid in the right. Overlay image shows abundant extension (green) and retraction (red) of microglial processes. ***J***, Overlay showing the merged images of microglia captured at 10 and 15 min after 0.5 µM Latrunculin A application reveals lost process activity. ***K***, Image sequence showing extension of microglia processes (green) toward laser lesion (red) indicated by an autofluorescence of lipofuscin produced by peroxidation of lipids during membrane breakdown (Hines et al., 2009). Left (0 min) is control image just before laser lesion. The middle and right show processes outgrowth toward the lesion at 3 and 5 min after injury. ***L***, Extension of microglia processes in the same slice shown in ***K*** was blocked by 0.5 µM Latrunculin A treatment. Left is control image of microglia acquired at 14 min of Latrunculin A application, with the middle and right showing lack of processes outgrowth to the lesion site after 8 and 20 min of laser ablation, respectively.

Chloride is required for SD-induced dendritic beading

To determine the requirement of Cl^- flux for dendritic beading, we triggered SD in slices superfused with a low-Cl^- containing aCSF (2.4 mM Cl^-). First, transient dendritic beading was observed in control aCSF during a passage of normoxic SD triggered by a focal KCl microinjection (Fig. 4*A*). Then, after recovery in control aCSF, the slice was exposed to a low-Cl^- aCSF, followed by induction of the second SD, which was of similar amplitude to the control SD and SD evoked after subsequent reperfusion with the control aCSF (normalized to control, 0.8 ± 0.2 in low-Cl^- aCSF and 1.2 ± 0.1 after wash, $n = 5$ slices from 2 mice, $p = 0.08$; Fig. 4*D*). Nevertheless, the amount of dendritic beading in the imaging field was decreased visibly (Fig. 4*B*). Indeed, quantification revealed significant reduction of beading in the low-Cl^- aCSF in which the average beading percentage only reached ~25% of beading in control aCSF at 40 s after start of SD (87.2 ± 3.8% in control vs 21.7 ± 3.0% in low-Cl^- aCSF, $n = 5$ slices, $p < 0.001$; Fig. 4*E*). However, a small fraction of the dendrites persisted in beading despite the low extracellular Cl^- concentration. Still, the size of the remaining beads in the low-Cl^- aCSF was reduced significantly by 42.1 ± 3.3% at 40 s after SD start compared with the control (4.4 ± 0.3 vs 2.5 ± 0.2 μm^2, $n = 30$ beads from 5 slices, $p < 0.001$; Fig. 4*F*). After wash with control aCSF, the amount of transient SD-induced dendritic beading (94.4 ± 1.5% at 40 s, $n = 5$ slices; Fig. 4*C*,*E*) and the size of the beads (4.8 ± 0.3 μm^2, $n = 30$ beads from 5 slices; Fig. 4*F*) returned to the control values obtained before the exposure to the low-Cl^- aCSF. These data suggest that the generation and amplitude of normoxic SD did not require the presence of extracellular Cl^-, whereas the molecular mechanism underlying dendritic beading was Cl^--dependent.

To ensure that the Cl^- dependency of dendritic beading was not restricted to normoxic KCl-induced SD, we determined the effect of Cl^- removal on dendritic beading evoked by terminal ouabain-induced SD. As quantified in Figure 4*G*, irreversible beading resulting from ouabain-induced SD was delayed significantly in low-Cl^- aCSF. Dendritic beading in control aCSF happened at the onset of ouabain-induced SD (Fig. 1*A*–*C*), and it was complete by 310 s after SD initiation (Fig. 4*G*). Intriguingly, within this timeframe, no beading occurred in slices superfused with low-Cl^- aCSF: at 8 min after ouabain-induced SD, a mere 10.0 ± 8.3% fraction of beaded dendrites was detected, with the amount of beading slowly increasing as a function of time, with five of six slices display-

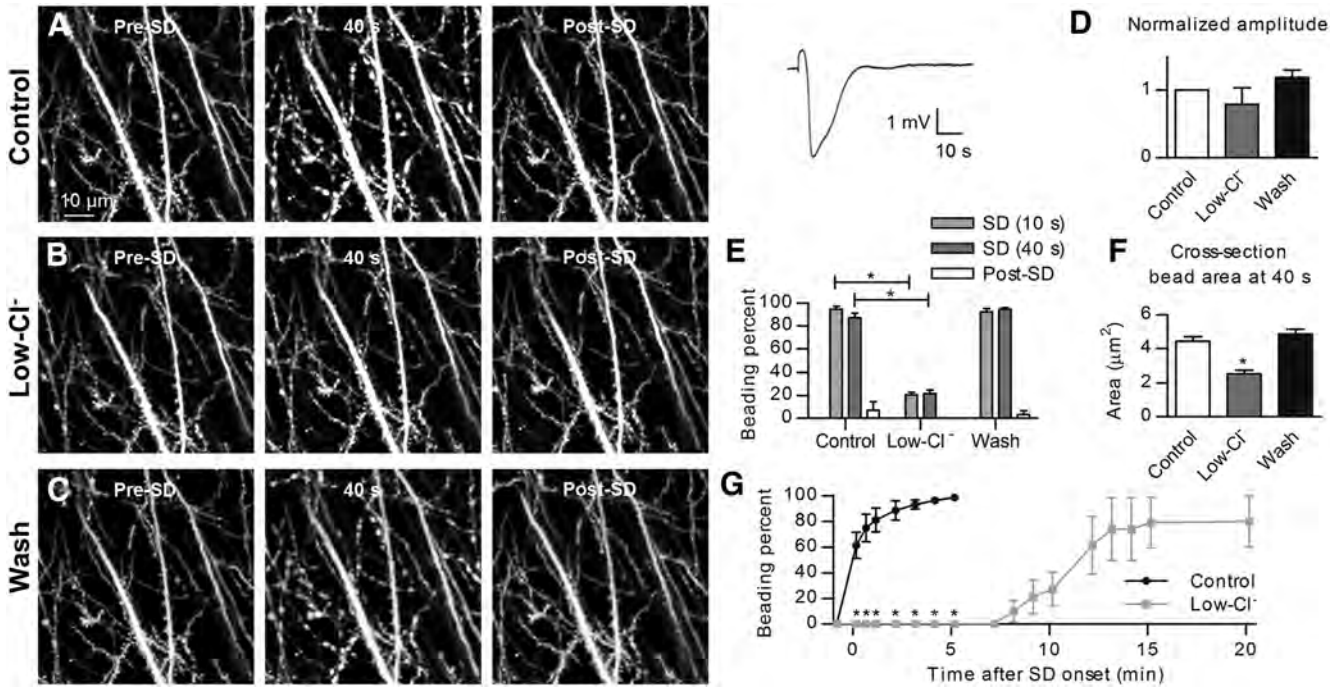

Figure 4. SD-induced dendritic beading is reduced in low-Cl^- aCSF. ***A***, Transient dendritic beading in control aCSF during passage of SD. Corresponding SD is shown to the right. ***B***, 2PLSM MIP image sequence of the same dendrites reveals the lack of SD-evoked beading after 15 min of superfusion with a low-Cl^- aCSF. ***C***, SD-triggered dendritic beading returns after 15 min of exposure to control aCSF (wash). ***D***, Control KCl-induced SD amplitudes varied in this set of experiments, and amplitudes were accordingly normalized before quantification. The amplitude did not change significantly in low-Cl^- aCSF ($n = 5$ slices, one-way RM-ANOVA with Tukey's *post hoc* test). ***E***, SD-induced beading was significantly reduced in low-Cl^- aCSF ($n = 5$ slices, two-way RM-ANOVA with Tukey's *post hoc* test), post-SD quantified at 160 s. Pre-SD fraction of dendritic beading was determined as $0 \pm 0\%$ for all conditions and therefore not visible. $^*p < 0.001$. ***F***, Summary of measurements from 30 beads in five slices reveals significant reduction in the beading size in low-Cl^- aCSF at 40 s after SD onset (one-way RM-ANOVA with Tukey's *post hoc* test). $^*p < 0.001$. ***G***, Onset of dendritic beading evoked by ouabain-induced SD is delayed in low-Cl^- aCSF (gray symbols) compared with ouabain-induced SDs in normal aCSF (control, black symbols; $n = 12$ slices, two-way RM-ANOVA with Tukey's *post hoc* test). $^*p < 0.05$.

ing complete beading after 20 min. However, ouabain-induced SDs obtained in low-Cl^- aCSF displayed ~60% smaller amplitude than those obtained in control aCSF (3.1 ± 0.5 vs 1.2 ± 0.2 mV, $p < 0.01$, $n = 7$ slices from 4 mice). Together, these data suggest that the molecular mechanism underlying SD-induced dendritic beading required Cl^- in the extracellular solution whether the SD was triggered by focal KCl microinjection or by exposure to ouabain.

Cotransporters may underlie the generation of dendritic beading

Because beading is not driven by passive osmotic forces and requires the presence of extracellular Cl^-, we hypothesized that the SD-induced dendritic beading takes place as a consequence of the altered driving forces for Cl^--dependent cotransporters. A range of cotransporters have been demonstrated to transport water during their translocation mechanism in a manner independent of osmotic forces (Zeuthen, 1994; Zeuthen and MacAulay, 2012; for review, see MacAulay et al., 2004; MacAulay and Zeuthen, 2010) and could thereby induce dendritic beading despite the low osmotic water permeability of the neuronal plasma membrane. To test this hypothesis, we inhibited two cation-chloride cotransporters expressed in neurons, the K^+/Cl^- cotransporter 2 (KCC2) and the $Na^+/K^+/2Cl^-$ cotransporter 1 (NKCC1; DeFazio et al., 2000; Blaesse et al., 2009) during SD induction. First SD (3.9 ± 0.3 mV) was triggered in control aCSF by focal KCl microinjection, followed by 20 min recovery. Then the slice was pretreated with 1 mM furosemide (blocker of both KCC2 and NKCC1; Payne, 1997; Kakazu et al., 1999) before the induction of a second SD of similar amplitude (4.0 ± 0.4 mV, $n = 6$ slices from 5 mice, $p = 0.67$). Dendritic beading occurred in both conditions (Fig. 5*A*) but the amount of beading was reduced significantly by furosemide at 10 s after SD onset ($81.1 \pm 6.0\%$ in control aCSF vs $51.8 \pm 9.0\%$ in furosemide, $n = 6$ slices, $p < 0.01$; Fig. 5*B*). The cross-section bead area decreased by $21.5 \pm 2.8\%$ as measured at 40 s after SD onset ($5.4 \pm 0.2\ \mu m^2$ in control vs $4.1 \pm 0.2\ \mu m^2$ in furosemide, $n = 36$ beads from 6 slices, $p < 0.001$; Fig. 5*C*).

The anion exchanger 3 (AE3), which is also expressed in neurons, transports HCO_3^- and Cl^- in opposite directions and therefore requires the presence of Cl^- to engage in cotransport activity (Kopito et al., 1989; Alper, 2009). In an experimental design similar to the one described above, the amount of dendritic beading at 40 s after SD onset was reduced significantly by $29.0 \pm 6.7\%$ (89.2 ± 4.1 vs $62.7 \pm 5.7\%$, $n = 6$ slices from 4 mice, $p < 0.001$; Fig. 5*D*,*E*) in the presence of the AE3 inhibitor DIDS (300 μM; Kopito et al., 1989) without affecting the SD amplitude (4.5 ± 0.6 vs 4.6 ± 0.2 mV, $n = 6$ slices, $p = 0.90$). Moreover, the size of DIDS-persistent dendritic beads at 40 s after SD onset was also reduced significantly by $13.6 \pm 2.5\%$ (5.3 ± 0.3 vs $4.5 \pm 0.2\ \mu m^2$, $n = 36$ beads from 6 slices, $p < 0.001$; Fig. 5*F*).

SD-elicited extracellular acidification and increased levels of lactate should increase the function of the neuronal monocarboxylate transporter 2 (MCT2; Halestrap, 2013). Therefore, we hypothesized that MCT2 could also participate in the dendritic beading by cotransporting water molecules during lactate and proton clearance from the extracellular space (Zeuthen et al., 1996). We quantified dendritic beading in the control aCSF and then after exposure to the MCT2 inhibitor 4-CIN (0.5 mM; Bröer

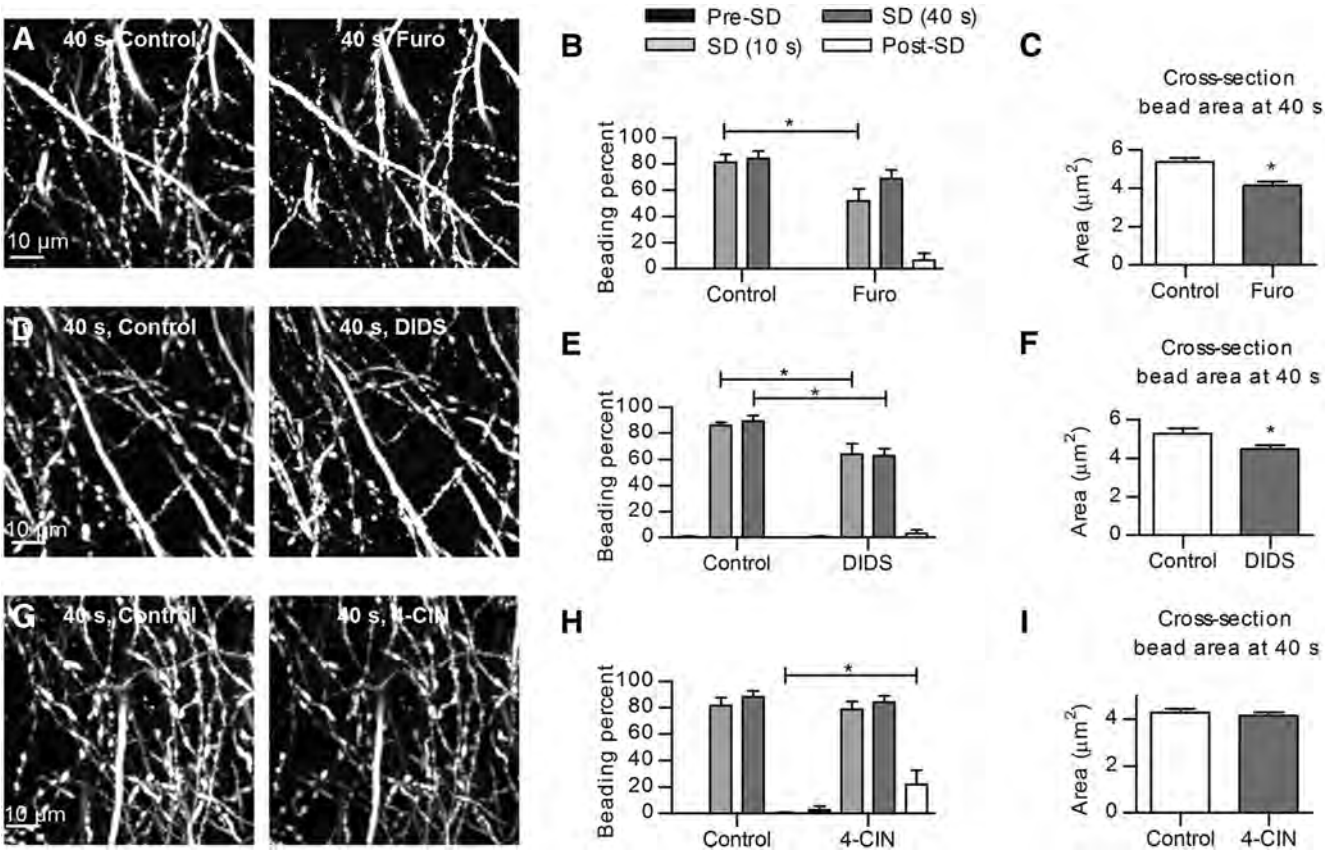

Figure 5. SD-induced dendritic beading is attenuated by separate inhibition of three different classes of cotransporters. ***A***, Representative 2PLSM MIP images of dendritic beading at 40 s after SD onset elicited before (control) and 45 min after pretreatment with 1 mM furosemide. ***B***, Beading before and after furosemide treatment shows significant difference at 10 s after SD onset ($n = 6$ slices, two-way RM-ANOVA and Sidak's *post hoc* test), post-SD quantified at 250 s. *$p < 0.01$. ***C***, Quantification of the size of beads at 40 s after SD onset reveals significant reduction in the cross-section bead area in furosemide-containing aCSF ($n = 36$ beads in 6 slices, paired *t* test). *$p < 0.001$. ***D***, Representative images of beaded dendrites at 40 s after SD onset in control condition and after 45 min of pretreatment with 300 μM DIDS. ***E***, SD-induced beading was significantly reduced in DIDS-containing aCSF at 10 and 40 s after SD onset ($n = 6$ slices, two-way RM-ANOVA and Sidak's *post hoc* test), post-SD quantified at 250 s. *$p < 0.001$. ***F***, The size of beads at 40 s after SD initiation in DIDS-containing aCSF was significantly decreased ($n = 36$ beads in 6 slices, paired *t* test). *$p < 0.001$. ***G***, 2PLSM MIP images showing dendritic beads of similar sizes at 40 s after SD onset evoked in control condition and after 45 min of pretreatment with 0.5 mM 4-CIN. ***H***, SD-induced dendritic beading percentage was unaffected by 4-CIN, whereas a slower recovery of beading was observed in 4-CIN-containing aCSF compared with control ($n = 7$ slices, two-way RM-ANOVA and Sidak's *post hoc* test), post-SD quantified at 250 s. *$p < 0.01$. ***I***, Summary from 36 beads in 6 slices demonstrating no significant decrease in the size of beads at 40 s during SD after 4-CIN pretreatment (Wilcoxon's signed-rank test, $p = 0.07$).

et al., 1999) in an experimental design as above. The maximal fraction of dendrites beaded at 40 s during SD was not altered by the inhibition of MCT2 (87.9 ± 4.7 vs 83.9 ± 4.8%, $n = 7$ slices from 3 mice, $p = 0.92$; Fig. 5*G*,*H*) nor were the amplitude of SD changed (3.5 ± 0.3 vs 3.7 ± 0.4 mV, $n = 7$ slices, $p = 0.15$) or the cross-section area of the beads at 40 s after SD induction (4.3 ± 0.1 vs 4.2 ± 0.2 μm^2, $n = 72$ beads from 6 slices, $p = 0.07$; Fig. 5*I*). However, at 250 s after SD initiation, 21.8 ± 11.0% of beading remained during 4-CIN treatment, whereas beading had returned to 0.5 ± 0.5% in the control condition ($n = 7$ slices, $p < 0.01$; Fig. 5*H*).

Together, these data suggest that the disturbance of ion homeostasis during SD could alter the activity of these cotransport proteins which thereby contribute to intracellular water accumulation and generation of dendritic beading.

Inhibition of NKCC1, KCC2, AE3, and MCT2 reduces dendritic beading in slices

Because blockers against these classes of cotransporters independently diminished the extent of SD-induced dendritic beading or reduced their recovery, we hypothesized that additive contribution of these cotransporters to dendritic beading might be reduced to an even greater degree by a mixture of all three inhibitors: furosemide, DIDS, and 4-CIN. Control dendritic beading was elicited by KCl-induced SD (Fig. 6*A*), followed by 20 min recovery and subsequent exposure to aCSF containing furosemide (1 mM), DIDS (300 μM), and 4-CIN (0.5 mM). The second SD of amplitude similar to the control SD elicited in the presence of the drug mixture (3.0 ± 0.7 vs 2.8 ± 0.4 mV, $n = 6$ slices from 3 mice, $p = 0.61$; Fig. 6*B*) resulted in less prominent beading (Fig. 6*C*). The maximal degree of dendritic beading at 40 s after SD initiation was reduced significantly by 19.2 ± 2.7% (94.7 ± 2.7 vs 76.6 ± 3.6%, $n = 6$ slices, $p < 0.01$; Fig. 6*D*) and the cross-section area of remaining beads was decreased by 45.5 ± 4.3% (4.2 ± 0.2 vs 2.2 ± 0.2 μm^2, $n = 36$ beads from 6 slices, $p < 0.001$; Fig. 6*E*). At 250 s after SD initiation, the fraction of beaded dendrites was 42.2 ± 8.7% in the drug mixture containing aCSF compared with 0.9 ± 0.9% of beading that remained in the control aCSF ($n = 6$ slices, $p < 0.001$; Fig. 6*D*). Therefore, inhibition of these selected cotransporters does not affect generation and amplitude of SD but reduces the fraction of beaded dendrites by ~20% and the cross-section area of the remaining beads by ~50%. These data indicate that cotransporter activity, at least in part, mediates the formation of SD-induced dendritic beading.

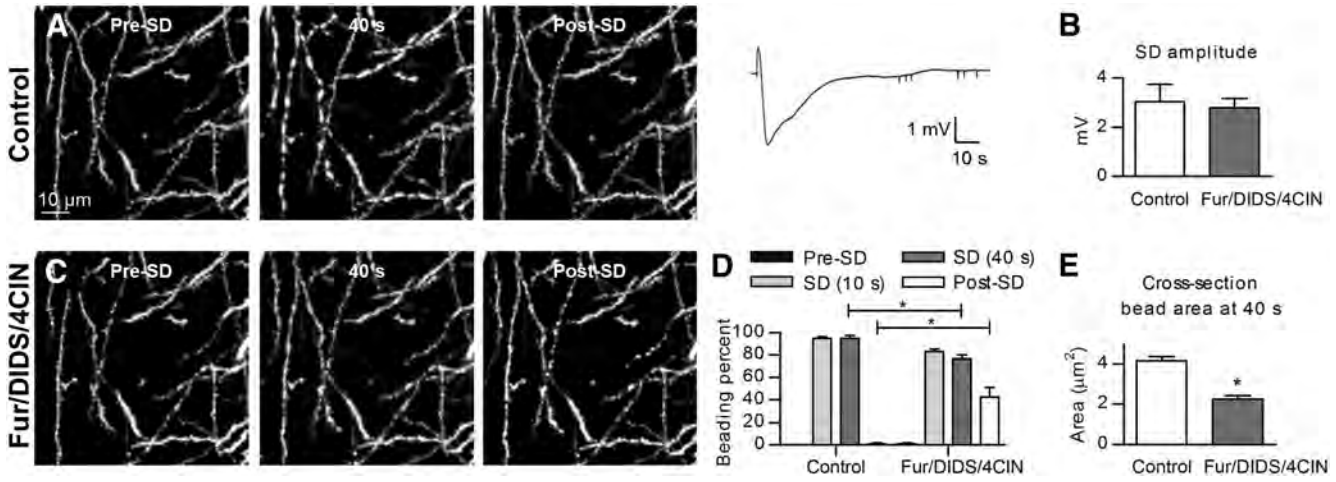

Figure 6. Mixture of furosemide (Fur), DIDS, and 4-CIN inhibits dendritic beading in slices. ***A***, 2PLSM MIP control image sequence of transient dendritic beading during passage of KCl-induced SD (shown to the right). ***B***, Amplitude of KCl-evoked SD was not different before and after pretreatment with drug mixture ($n = 6$ slices, paired t test). ***C***, 2PLSM MIP image sequence of the same dendrites exhibiting reduced beading during the second SD evoked 15 min after pretreatment of the slice with a mixture of inhibitors of cotransport proteins. The brief drug mixture incubation time was chosen to optimize image quality before induction of the second SD. ***D***, SD-induced dendritic beading shows diminished maximal fraction of beaded dendrites at 40 s after SD onset alongside slower dendritic recovery in the drug mixture containing aCSF ($n = 6$ slices, two-way RM-ANOVA and Sidak's *post hoc* test), post-SD quantified at 250 s. $*p < 0.01$. ***E***, Quantification of cross-section area of beads 40 s after SD onset before and after the three drug mixture application illustrates reduced beading area after drug exposure ($n = 36$ beads in 6 slices, paired t test). $*p < 0.001$.

Inhibition of NKCC1, KCC2, AE3, and MCT2 effectively reduces dendritic beading *in vivo*

Although slice preparations offer the advantage of rapid introduction of drugs with known concentrations and the precise control of pO_2, pCO_2, pH, and temperature, slices lack circulation and are obviously not as intact as highly relevant life and disease models with *in vivo* preparations. Therefore, we corroborated *in vivo* whether pharmacological inhibition of these cotransporters by a mixture of furosemide, DIDS, and 4-CIN would diminish SD-induced beading. The same methodological approach was used, although 2PLSM images were taken through the cranial window over the somatosensory cortex of the mouse. Previously, several studies in mice have reported that normoxic SD induces vasoconstriction/hypoperfusion and that it takes ~1 h for blood flow to recover to initial values (Ayata et al., 2004; Chang et al., 2010). Hence, 2D maps of cerebral blood flow acquired by laser speckle imaging was used to confirm return of blood flow to baseline when SDs were evoked with an ~1 h time interval (Fig. 7*A*) and to ensure sustainability of circulation throughout the experiment. As expected, when the first SD invaded the imaging field, rapid transient dendritic beading was observed (Fig. 7*B*; Takano et al., 2007; Sword et al., 2013). Initial time control experiments with three consecutive SDs elicited at 59 ± 7 min apart illustrated a tendency toward reduced amplitude of the second SD and a reduction of the third SD amplitude (17.9 ± 0.7 vs 16.4 ± 1.2 and 13.8 ± 1.1 mV, $n = 4$ mice, $p < 0.05$; Fig. 7*B–D*, bottom panels for representative SD traces and *E* for summarized SD amplitudes). However, these experiments revealed a similar degree of transient dendritic beading (100 ± 0% for first SD, 96.5 ± 2.5% for second SD, and 99.2 ± 0.8% for third SD, $p < 0.001$, compared with pre-SD beading percentages; Fig. 7*B–D*, summarized in *F*, $n = 4$ mice). Together, these results illustrate that our *in vivo* preparation was viable and sufficiently robust to act as its own control and thus could be used to determine the effect of cotransporter inhibition on SD-induced dendritic beading *in vivo*.

Cerebral blood flow was monitored with laser speckle imaging before each SD to ensure lack of drug effects on blood flow and its recovery to baseline after SD (Fig. 8*A*). To test the contribution of NKCC1, KCC2, AE3, and MCT2 to formation of SD-induced dendritic beading *in vivo*, a control SD was initially induced (18.1 ± 1.0 mV; Fig. 8*B*, bottom panel for representative trace and *F* for summarized data). Then, a cortex aCSF containing furosemide (1 mM), DIDS (300 µM), and 4-CIN (0.5 mM) was applied directly to the cortical surface with the dura intact. The amplitude of subsequent SDs obtained at 69 ± 3 min of drug exposure was 13.9 ± 1.2 mV, whereas the third SD induced at 138 ± 7 min of drug application yielded a reduced amplitude of 10.3 ± 1.1 mV ($n = 6$ mice, $p < 0.001$; Fig. 8*C–E*, bottom panel for representative trace and *F* for summarized data). However, the amplitude of this third SD was not significantly different from the amplitude of the third SD obtained in the time control experiments ($p = 0.07$) or the amplitude of the fourth SD recorded 30 min after 3× washout of drugs (10.6 ± 1.3 mV, $n = 3$ mice, $p = 0.77$; Fig. 8*E*, bottom panel for representative trace and *F* for summarized data). Therefore, the drug mixture does not appear to interfere directly with the mechanisms that trigger SD. Additionally, we observed comparable levels of DC electroencephalographic (EEG) signal before control SD and after 2 h of drug mixture application. To confirm this observation, we calculated the power spectrum amplitude (mV^2/Hz) in the 0.3–3 Hz band of DC EEG activity that is typical for urethane anesthesia (Mohajerani et al., 2010). DC EEG recordings were analyzed by selecting homologous 3 min segments during the periodic activity reported in urethane-anesthetized mice (Clement et al., 2008; Pagliardini et al., 2013). The power spectrums of EEG signals were similar before control SD and before the third SD at 135 ± 7 min of drug application ($n = 6$ mice, $p = 0.63$), indicating no significant drug-induced effects on cortical function.

Dendritic beading in the imaging field was unaffected by the drug mixture at 1 h exposure, but it was reduced visibly during the passage of the third SD induced after 2 h exposure to the drug mixture (Fig. 8*D*, summarized in *G*). Accordingly, the amount of dendritic beading in the imaging field was 90.5 ± 5.1% during the control SD, but it was significantly reduced by 65.5 ± 10.3% after

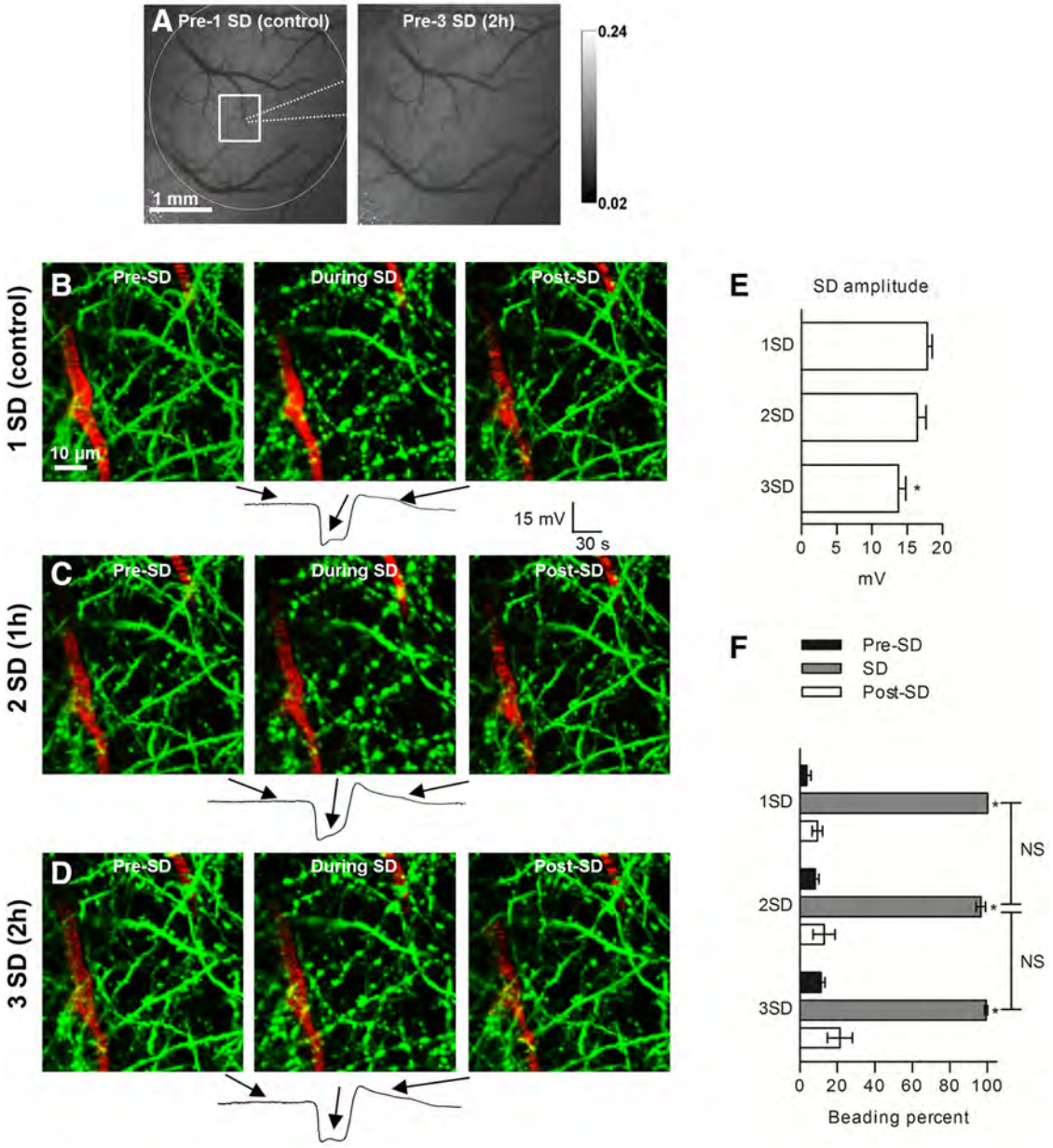

Figure 7. Several rounds of normoxic SD *in vivo* result in a similar pattern of reversible dendritic beading. ***A***, Grayscale image sequence of laser speckle contrast reveals cortical vasculature directly below the open craniotomy with flowing vessels appearing dark. Edges of the craniotomy (dashed circle), placement of recording electrode (dotted line), and 2PLSM imaging area (square) are indicated in the first image acquired before control SD at the beginning of experiment. Blood flow is stable, as seen in the second image acquired ~2 h later just before the third SD. ***B***, 2PLSM MIP image sequence of EGFP-positive dendrites (green) and flowing blood vessels (red; blood plasma labeled with Texas Red Dextran) showing rapid beading and recovery of dendrites during passage of control SD. SD was induced with focal KCl microinjection away from the imaging field. Arrows correspond to various time points on the recording of SD obtained with a glass microelectrode placed next to the imaged dendrites. ***C***, ***D***, 2PLSM MIP image sequence of the same dendrites exhibiting similar beading during the second and third SDs elicited at ~1 h time intervals after the control SD. ***E***, Quantified SD amplitudes from four mice indicate a tendency toward reduced amplitude for the second SD with significant decrease in the amplitude of the third SD (one-way RM-ANOVA with Tukey's *post hoc* test). *$p < 0.05$. ***F***, Summary from 12 SDs in four animals shows that dendrites undergo similar rounds of transient beading during the passage of three SDs evoked every ~1 h. Asterisks at each bar during SD indicate significant difference from the time point before and after SD (one-way RM-ANOVA with Tukey's *post hoc* test). *$p < 0.001$.

2 h exposure to the transport inhibitors (90.5 ± 5.1 vs 34.3 ± 10.6%, $n = 6$ mice, $p < 0.001$; Fig. 8*G*). However, the SD evoked after the washout procedure induced beading similar to that of the control SD (97.6 ± 2.4%, $n = 3$ mice; Fig. 8*E*, summarized in *G*), indicating that drug-mediated inhibition of SD-induced dendritic beading indeed occurred in a reversible manner. After this post-wash SD induction, a fraction of the dendritic beading remained, with the dendrites in one of the three tested animals resisting recovery. This observation indicates that, at this late experimental time point, SD induction may lead to some degree of partial terminal dendritic beading. Remarkably, in one animal, when the drug mixture was reapplied for 2 h after the first wash, SD-induced beading was, once more, reduced by nearly 50%, followed by partial restoring of SD-induced beading (87.5%) after a second wash procedure. Together, these data provide strong evidence that combined pharmacological inhibition of NKCC1, KCC2, AE3, and MCT2 is sufficient for reduction of SD-induced dendritic beading *in vivo*.

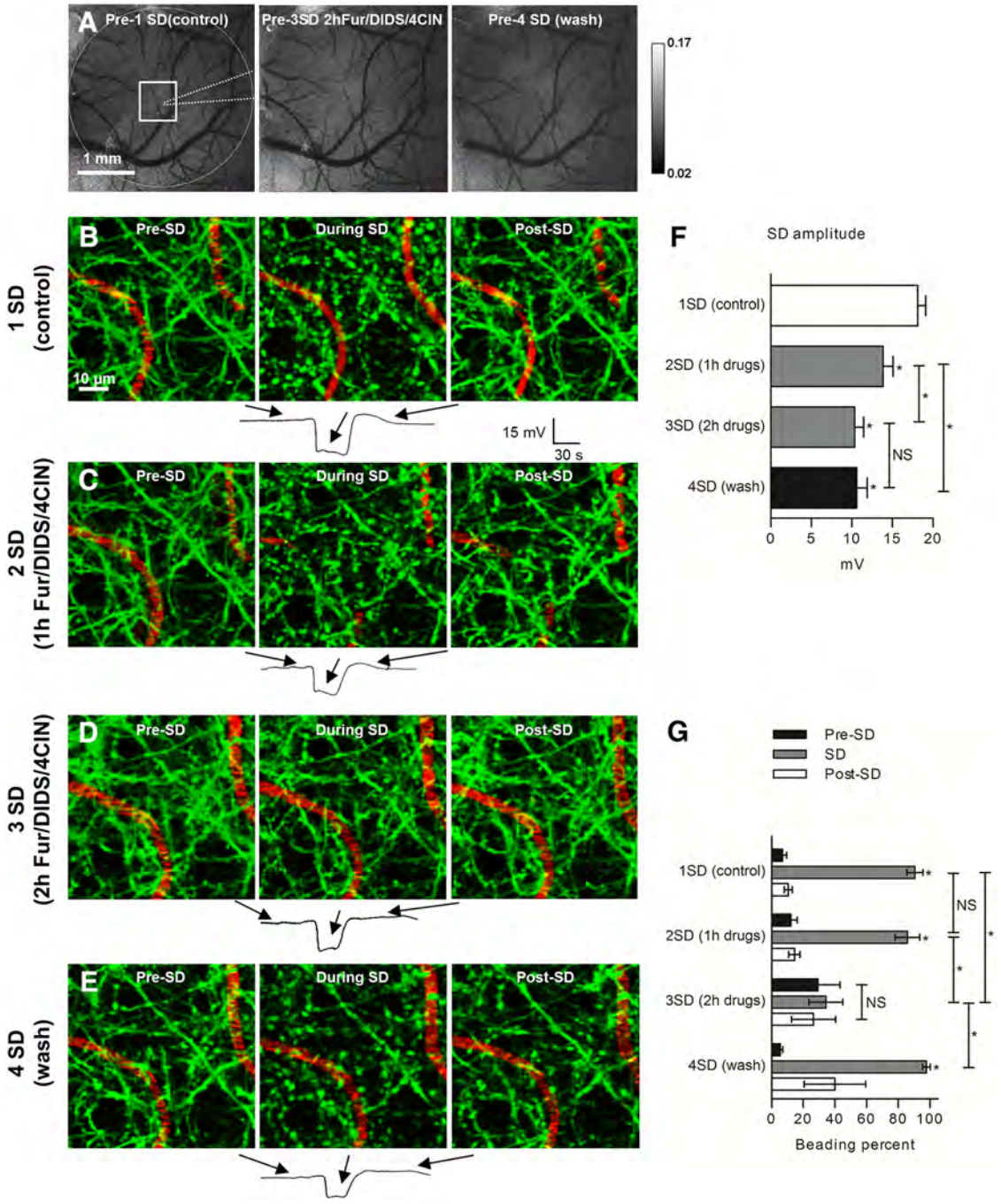

Figure 8. A three-drug mixture of furosemide (Fur), DIDS, and 4-CIN inhibited SD-induced dendritic beading *in vivo*. ***A***, Representative grayscale sequence of laser speckle contrast images taken before induction of SDs in control, ~2 h after drug mixture application, and 30 min after three times washout of drugs with cortex aCSF. Edges of craniotomy (dashed circle), placement of recording electrode (dotted line), and 2PLSM imaging area (square) are indicated in the control image acquired at the beginning of experiment. ***B***, 2PLSM MIP image sequence of EGFP-positive dendrites (green) and flowing blood vessels (red) showing rapid beading and recovery of dendrites during passage of control SD. Each image corresponds with a time point indicated on the respective SD recording from a glass microelectrode placed next to imaged dendrites. ***C***, 2PLSM MIP image sequence shows same dendrites undergoing rapid beading during the passage of the second SD induced after ~1 h of three-drug mixture application to the open craniotomy. ***D***, Dendritic structure remained mostly unchanged (lack of beading) during the passage of the third SD induced after ~2 h of three-drug mixture application. ***E***, Wash of the exposed cortex three times with cortex aCSF once again revealed a rapidly reversible beading with the passage of SD at 30 min after wash. ***F***, Quantification of the SD amplitudes from six mice indicates significant decrease in the subsequent SD amplitudes with no significant difference between SD elicited at ~2 h of the three-drug mixture application and SD elicited 30 min after washout of drugs (one-way RM-ANOVA with Tukey's *post hoc* test). $*p < 0.01$. ***G***, Quantification of SD-induced dendritic beading reveals that beading was significantly reduced after ~2 h of three-drug mixture application ($n = 6$ mice). In three mice that were tested at 30 min after washing three times with cortex aCSF, the drug effect was reversible. Asterisks at the bar during SD indicate significant difference from the time points Pre-SD and Post-SD. The amount of beading during the third SD elicited in the three-drug mixture was not significantly different from Pre-SD and Post-SD (one-way RM-ANOVA with Tukey's *post hoc* test). Asterisks above the braces indicate significant difference between the amount of beading during SD elicited at ~2 h in drug mixture from SDs elicited at all other time points during the experiment (one-way RM-ANOVA with Tukey's *post hoc* test). $*p < 0.001$.

Discussion

We have demonstrated that SD generation and the ensuing dendritic beading occur by distinct sets of molecular mechanisms and that the latter does not require cytoskeletal rearrangements and evolves independently of osmotic water transport. Rather, select neuronal cotransporters mediate the SD-induced dendritic beading.

SD is triggered by noxious stimuli, such as elevated potassium, glutamate, hypoxia, and ouabain (Balestrino et al., 1999; Hasbani et al., 2001). Once SD is triggered, its course is dictated by underlying ion currents without regard to the noxious stimulus that set the process in motion (Dreier, 2011). Attempts to define a specific ion channel responsible for SD have failed because several ion channels cooperate in initiation, propagation, and its maintenance (Somjen, 2004). SD leads to cytotoxic edema with associated focal swelling or beading along the dendritic shaft separated from each other by thin dendritic segments. Here, we took advantage of the spatial and temporal resolution afforded by 2PLSM to directly quantify, in real time, the parameters of SD-induced dendritic beading with simultaneous monitoring of SD amplitudes. By choosing KCl microinjection as a noxious stimulus to trigger SD, we were able to reliably induce consecutive SDs in the same slice or animal, which allowed for direct assessment of drug-induced alterations in SD-induced dendritic beading.

Cytoskeletal rearrangements have been anticipated to underlie dendritic beading. Previous studies have revealed disrupted microtubules within dendritic beads (Kirov et al., 2004; Hoskison et al., 2007) and accumulated actin filaments (Gisselsson et al., 2005). In our experiments, SD-induced dendritic beading was not prevented by pharmacological interference with cytoskeletal rearrangements. This observation is in agreement with a previous study (Hoskison and Shuttleworth, 2006) that suggested that both initial disruption of microtubules and dendritic beading may result directly from excessive water influx. SD-induced dendritic beading could thus result from Ca^{2+}-independent events, such as excessive influx of Na^+ and Cl^- with obligatory osmotic water uptake (Hasbani et al., 1998; Kirov et al., 2004). When a severe prolonged hyposmotic challenge was used to mimic such osmotic driving forces, dendrites nevertheless resisted volume change. This finding is in agreement with neurons lacking aquaporin expression (Papadopoulos and Verkman, 2013) and their resistance toward volume changes during acute osmotic stress in slices (Andrew et al., 2007). Contrarily, cultured or dissociated neurons respond readily to acute osmotic challenges and return to their initial volume over a matter of minutes (Pasantes-Morales et al., 1993; Aitken et al., 1998). Therefore, in acute brain slices, as used in the present study, SD-induced osmotically obliged passive water transport did not appear as the transmembrane route for the water influx causing the SD-induced dendritic beading.

Near-complete removal of Cl^- from the aCSF did not affect the amplitude of KCl-induced SD, whereas ouabain-induced SD displayed reduced amplitude. The latter observation agrees with a previous report demonstrating low-Cl^- aCSF-dependent reduction of hypoxia-induced SD amplitude (Müller, 2000). Reduced SD amplitude might reflect fewer implicated neurons near the microelectrode tip, thus lesser disturbance of transmembrane ion gradients within the imaging field that could affect dendritic beading. However, we have observed significant variations in SD amplitude among slices (1–5 mV) which all induced comparable patterns of beading, indicating that the size of the SD amplitude does not directly affect formation of dendritic beads.

Despite the robust SD amplitude observed in the low-Cl^- aCSF, SD-induced dendritic beading was severely impaired, whether SD was triggered by focal KCl microinjection or by ouabain, suggesting separation of the molecular pathways underlying SD and dendritic beading. This finding also indicates that SD-induced beading during depolarization occurs via a common mechanism, independently of the nature of the noxious stimulus used to trigger SD. This finding underscores the likelihood that the molecular machinery underlying dendritic beading will also be set in motion during pathological events, such as cerebral ischemia and migraine. Notably, a much-delayed irreversible dendritic beading did occur in the low-Cl^- ouabain-containing aCSF. This beading likely took place via a distinct molecular mechanism, possibly caused by cation influx driven by Gibbs–Donnan forces and insufficient cation efflux caused by prolonged inhibition of the Na^+/K^+-ATPase (Dreier et al., 2013).

A previous comprehensive study (Müller and Somjen, 1999), based on indirect assessment of dendritic beading, yielded conflicting data regarding the Cl^- dependence of hypoxia-mediated SD-induced dendritic beading: beading in brain slices required the presence of Cl^- when assessed as changes in tissue electrical resistance or light scattering, but bead formation occurred in a Cl^--independent manner when assessed with tetramethyl-ammonium (TMA^+)-sensitive microelectrodes. It was concluded that SD-induced dendritic beading occurred independently of Cl^-, because the TMA^+-sensitive microelectrodes were deemed the more reliable experimental approach to assess changes in the interstitial space (Müller and Somjen, 1999). Here, by real-time monitoring of SD-induced dendritic beading with 2PLMS, we have provided direct evidence that extracellular Cl^- is not a requirement for SD generation but is essential for the molecular mechanisms underlying SD-induced dendritic beading.

A range of cotransporters carry the inherent ability to transport water along with translocation of their respective substrates in a manner independent of osmotic driving forces (MacAulay and Zeuthen, 2010). During SD, the driving forces, and thus activity and/or transport direction, for many of these cotransporters alter with the massive shifts in lactate and ion concentrations and pH: increase of $[K^+]_o$ and $[lactate]_o$ and decrease in $[Na^+]_o$ and $[Cl^-]_o$ with the extracellular pH after a brief alkaline transient at the onset of SD succeeded by prolonged acidification (Mutch and Hansen, 1984; Müller and Somjen, 2000; Müller, 2000). Several cotransporters of these substrates are expressed in dendrites: the cation/chloride transporters KCC2 and NKCC1 (Payne et al., 1996; Plotkin et al., 1997), the bicarbonate/chloride exchanger AE3 (Kopito et al., 1989), and the H^+-coupled monocarboxylate transporter MCT2 (Pierre et al., 2002). Among these cotransporters, NKCC1 and other isoforms of KCC and MCT have been documented to cotransport water along their translocation pathway (Zeuthen, 1994; Zeuthen et al., 1996; Zeuthen and MacAulay, 2012) and thus share the ability to induce dendritic water influx with their SD-induced increased activity. Accordingly, and in line with the requirement for $[Cl^-]_o$, we observed a robust reduction in SD-induced dendritic beading on combined inhibition of these cotransporters in both slice and *in vivo* preparations. It should be noted that the quantification of changes in the size of dendritic beads after inhibition of cotransporters is most likely an underestimate (see Materials and Methods). The pharmacological tools used may not be entirely specific to the tested transporters and may act on other targets, such as the $GABA_A$ receptor and the oxidative metabolism pathways (Korpi and Lüddens, 1997; Del Prete et al., 2004). However, none of the inhibitors used affected cortical function, blood flow, or SD am-

plitudes, providing additional evidence for separate molecular machinery generating the membrane depolarization and dendritic beading. In the *in vivo* experiments, application of cotransport inhibitors did partly reduce the amplitude of the SD, as detected previously with DIDS and furosemide on hypoxia-induced SD in slices (do Carmo and Martins-Ferreira, 1984; Müller, 2000), while providing near-complete prevention of dendritic beading after sufficient time for drug penetration through the dura into the cortex. Notably, after washout of inhibitors in the *in vivo* experiments, SD-induced dendritic beading returned to control level but the SD amplitude remained decreased, indicating that the smaller SD amplitude was not the sole cause for reduced SD-induced beading in the presence of cotransport inhibitors. Our results align with previous data on hypoxia-mediated SD-induced changes in dendritic beading (assessed with light reflectance) in which separate inhibition of KCC/NKCC1 yielded little changes in SD-induced dendritic beading (Müller and Somjen, 1999). Conversely, with the increased sensitivity of 2PLSM, we detected a bicarbonate transporter-dependent contribution to dendritic beading that was not observed in the study by Müller and Somjen (1999). In our study, however, combined inhibition of KCCs, NKCC1, MCTs, and bicarbonate transporters yielded substantial (in slices) and almost complete (*in vivo*) blockage of SD-induced dendritic beading. Therefore, we propose that SD-mediated shifts in ion concentrations and pH alter the driving forces, transport direction, and/or activity of the tested cotransporters. These cotransporters share the ability to mediate dendritic water influx in a manner independent of osmotic forces and thereby promote dendritic beading despite the low inherent osmotic water permeability of the neuronal membrane. It was reported recently that the Cl^- channel SLC26A11 contributes to neuronal cell body swelling after pharmacologically induced increased $[Na^+]_i$ (Rungta et al., 2015). Given the negligible osmotic water permeability of the neuronal membrane (Andrew et al., 2007; Papadopoulos and Verkman, 2013), it will be of future interest to address the mechanism of water entry after SLC26A11 activation.

We conclude that SD-induced dendritic beading does not require cytoskeletal rearrangement and is independent of osmotic forces. Extracellular $[Cl^-]$ was not critical for SD generation but was essential for the ensuing dendritic beading that, at least in part, took place as a consequence of altered driving forces, transport direction, and activity of select neuronal cotransporters. These cotransporters share the ability to cotransport water during their translocation mechanism, in a manner independent of osmotic forces, thereby contributing to SD-induced dendritic beading. Using this experimental approach, we provided evidence for the SD generation and the dendritic beading occurring by separate molecular mechanisms.

References

Aiba I, Carlson AP, Sheline CT, Shuttleworth CW (2012) Synaptic release and extracellular actions of Zn^{2+} limit propagation of spreading depression and related events in vitro and in vivo. J Neurophysiol 107:1032–1041. Medline

Aitken PG, Borgdorff AJ, Juta AJA, Kiehart DP, Somjen GG, Wadman WJ (1998) Volume changes induced by osmotic stress in freshly isolated rat hippocampal neurons. Pflugers Arch 436:991–998. Medline

Alper SL (2009) Molecular physiology and genetics of Na^+-independent SLC4 anion exchangers. J Exp Biol 212:1672–1683. CrossRef Medline

Anderson TR, Andrew RD (2002) Spreading depression: imaging and blockade in the rat neocortical brain slice. J Neurophysiol 88:2713–2725. CrossRef Medline

Anderson TR, Jarvis CR, Biedermann AJ, Molnar C, Andrew RD (2005) Blocking the anoxic depolarization protects without functional compromise following simulated stroke in cortical brain slices. J Neurophysiol 93:963–979. Medline

Andrew RD, Labron MW, Boehnke SE, Carnduff L, Kirov SA (2007) Physiological evidence that pyramidal neurons lack functional water channels. Cereb Cortex 17:787–802. Medline

Atkinson SJ, Hosford MA, Molitoris BA (2004) Mechanism of actin polymerization in cellular ATP depletion. J Biol Chem 279:5194–5199. CrossRef Medline

Ayata C, Shin HK, Salomone S, Ozdemir-Gursoy Y, Boas DA, Dunn AK, Moskowitz MA (2004) Pronounced hypoperfusion during spreading depression in mouse cortex. J Cereb Blood Flow Metab 24:1172–1182. Medline

Balestrino M, Young J, Aitken P (1999) Block of (Na^+, K^+) ATPase with ouabain induces spreading depression-like depolarization in hippocampal slices. Brain Res 838:37–44. CrossRef Medline

Bird MM (1984) The effects of taxol on embryonic chick tectum maintained in culture: an electron microscope study. J Ultrastruct Res 89:123–135. CrossRef Medline

Blaesse P, Airaksinen MS, Rivera C, Kaila K (2009) Cation-chloride cotransporters and neuronal function. Neuron 61:820–838. CrossRef Medline

Bröer S, Bröer A, Schneider HP, Stegen C, Halestrap AP, Deitmer JW (1999) Characterization of the high-affinity monocarboxylate transporter MCT2 in *Xenopus laevis* oocytes. Biochem J 341:529–535. CrossRef Medline

Canals S, Makarova I, López-Aguado L, Largo C, Ibarz JM, Herreras O (2005) Longitudinal depolarization gradients along the somatodendritic axis of CA1 pyramidal cells: a novel feature of spreading depression. J Neurophysiol 94:943–951. CrossRef Medline

Chang JC, Shook LL, Biag J, Nguyen EN, Toga AW, Charles AC, Brennan KC (2010) Biphasic direct current shift, haemoglobin desaturation and neurovascular uncoupling in cortical spreading depression. Brain 133:996–1012. CrossRef Medline

Chen S, Mohajerani MH, Xie Y, Murphy TH (2012) Optogenetic analysis of neuronal excitability during global ischemia reveals selective deficits in sensory processing following reperfusion in mouse cortex. J Neurosci 32:13510–13519. CrossRef Medline

Clement EA, Richard A, Thwaites M, Ailon J, Peters S, Dickson CT (2008) Cyclic and sleep-like spontaneous alternations of brain state under urethane anaesthesia. PLoS One 3:e2004. CrossRef Medline

Davies ML, Kirov SA, Andrew RD (2007) Whole isolated neocortical and hippocampal preparations and their use in imaging studies. J Neurosci Methods 166:203–216. CrossRef Medline

DeFazio RA, Keros S, Quick MW, Hablitz JJ (2000) Potassium-coupled chloride cotransport controls intracellular chloride in rat neocortical pyramidal neurons. J Neurosci 20:8069–8076. Medline

Del Prete E, Lutz TA, Scharrer E (2004) Inhibition of glucose oxidation by α-cyano-4-hydroxycinnamic acid stimulates feeding in rats. Physiol Behav 80:489–498. CrossRef Medline

Dietz RM, Weiss JH, Shuttleworth CW (2008) Zn^{2+} influx is critical for some forms of spreading depression in brain slices. J Neurosci 28:8014–8024. CrossRef Medline

do Carmo RJ, Martins-Ferreira H (1984) Spreading depression of Leao probed with ion-selective microelectrodes in isolated chick retina. An Acad Bras Ciênc 56:401–421. Medline

Douglas HA, Callaway JK, Sword J, Kirov SA, Andrew RD (2011) Potent inhibition of anoxic depolarization by the sodium channel blocker dibucaine. J Neurophysiol 105:1482–1494. CrossRef Medline

Dreier JP (2011) The role of spreading depression, spreading depolarization and spreading ischemia in neurological disease. Nat Med 17:439–447. CrossRef Medline

Dreier JP, Reiffurth C (2015) The stroke-migraine depolarization continuum. Neuron 86:902–922. CrossRef Medline

Dreier JP, Woitzik J, Fabricius M, Bhatia R, Major S, Drenckhahn C, Lehmann TN, Sarrafzadeh A, Willumsen L, Hartings JA, Sakowitz OW, Seemann JH, Thieme A, Lauritzen M, Strong AJ (2006) Delayed ischaemic neurological deficits after subarachnoid haemorrhage are associated with clusters of spreading depolarizations. Brain 129:3224–3237. CrossRef Medline

Dreier JP, Isele T, Reiffurth C, Offenhauser N, Kirov SA, Dahlem MA, Herreras O (2013) Is spreading depolarization characterized by an abrupt, massive release of gibbs free energy from the human brain cortex? Neuroscientist 19:25–42. CrossRef Medline

Dunn AK, Bolay H, Moskowitz MA, Boas DA (2001) Dynamic imaging of

cerebral blood flow using laser speckle. J Cereb Blood Flow Metab 21:195–201. Medline

Feng G, Mellor RH, Bernstein M, Keller-Peck C, Nguyen QT, Wallace M, Nerbonne JM, Lichtman JW, Sanes JR (2000) Imaging neuronal subsets in transgenic mice expressing multiple spectral variants of GFP. Neuron 28:41–51. CrossRef Medline

Gisselsson LL, Matus A, Wieloch T (2005) Actin redistribution underlies the sparing effect of mild hypothermia on dendritic spine morphology after in vitro ischemia. J Cereb Blood Flow Metab 25:1346–1355. CrossRef Medline

Hadjikhani N, Sanchez Del Rio M, Wu O, Schwartz D, Bakker D, Fischl B, Kwong KK, Cutrer FM, Rosen BR, Tootell RB, Sorensen AG, Moskowitz MA (2001) Mechanisms of migraine aura revealed by functional MRI in human visual cortex. Proc Natl Acad Sci U S A 98:4687–4692. CrossRef Medline

Halestrap AP (2013) The SLC16 gene family—structure, role and regulation in health and disease. Mol Aspects Med 34:337–349. CrossRef Medline

Hansen AJ, Zeuthen T (1981) Extracellular ion concentrations during spreading depression and ischemia in the rat brain cortex. Acta Physiol Scand 113:437–445. CrossRef Medline

Hartings JA, Bullock MR, Okonkwo DO, Murray LS, Murray GD, Fabricius M, Maas AI, Woitzik J, Sakowitz O, Mathern B, Roozenbeek B, Lingsma H, Dreier JP, Puccio AM, Shutter LA, Pahl C, Strong AJ (2011a) Spreading depolarisations and outcome after traumatic brain injury: a prospective observational study. Lancet Neurol 10:1058–1064. CrossRef Medline

Hartings JA, Watanabe T, Bullock MR, Okonkwo DO, Fabricius M, Woitzik J, Dreier JP, Puccio A, Shutter LA, Pahl C, Strong AJ (2011b) Spreading depolarizations have prolonged direct current shifts and are associated with poor outcome in brain trauma. Brain 134:1529–1540. CrossRef Medline

Hasbani MJ, Hyrc KL, Faddis BT, Romano C, Goldberg MP (1998) Distinct roles for sodium, chloride, and calcium in excitotoxic dendritic injury and recovery. Exp Neurol 154:241–258. CrossRef Medline

Hasbani MJ, Schlief ML, Fisher DA, Goldberg MP (2001) Dendritic spines lost during glutamate receptor activation reemerge at original sites of synaptic contact. J Neurosci 21:2393–2403. Medline

Hines DJ, Hines RM, Mulligan SJ, Macvicar BA (2009) Microglia processes block the spread of damage in the brain and require functional chloride channels. Glia 57:1610–1618. CrossRef Medline

Hoskison MM, Shuttleworth CW (2006) Microtubule disruption, not calpain-dependent loss of MAP2, contributes to enduring NMDA-induced dendritic dysfunction in acute hippocampal slices. Exp Neurol 202:302–312. CrossRef Medline

Hoskison MM, Yanagawa Y, Obata K, Shuttleworth CW (2007) Calcium-dependent NMDA-induced dendritic injury and MAP2 loss in acute hippocampal slices. Neuroscience 145:66–79. CrossRef Medline

Iyirhiaro GO, Brust TB, Rashidian J, Galehdar Z, Osman A, Phillips M, Slack RS, Macvicar BA, Park DS (2008) Delayed combinatorial treatment with flavopiridol and minocycline provides longer term protection for neuronal soma but not dendrites following global ischemia. J Neurochem 105:703–713. CrossRef Medline

Jensen FE, Harris KM (1989) Preservation of neuronal ultrastructure in hippocampal slices using rapid microwave-enhanced fixation. J Neurosci Methods 29:217–230. CrossRef Medline

Jung S, Aliberti J, Graemmel P, Sunshine MJ, Kreutzberg GW, Sher A, Littman DR (2000) Analysis of fractalkine receptor CX3CR1 function by targeted deletion and green fluorescent protein reporter gene insertion. Mol Cell Biol 20:4106–4114. CrossRef Medline

Kakazu Y, Akaike N, Komiyama S, Nabekura J (1999) Regulation of intracellular chloride by cotransporters in developing lateral superior olive neurons. J Neurosci 19:2843–2851. Medline

Kirov SA, Sorra KE, Harris KM (1999) Slices have more synapses than perfusion-fixed hippocampus from both young and mature rats. J Neurosci 19:2876–2886. Medline

Kirov SA, Petrak LJ, Fiala JC, Harris KM (2004) Dendritic spines disappear with chilling but proliferate excessively upon rewarming of mature hippocampus. Neuroscience 127:69–80. CrossRef Medline

Kopito RR, Lee BS, Simmons DM, Lindsey AE, Morgans CW, Schneider K (1989) Regulation of intracellular pH by a neuronal homolog of the erythrocyte anion exchanger. Cell 59:927–937. CrossRef Medline

Korpi ER, Lüddens H (1997) Furosemide interactions with brain GABAA receptors. Br J Pharmacol 120:741–748. CrossRef Medline

Kraig RP, Nicholson C (1978) Extracellular ionic variations during spreading depression. Neuroscience 3:1045–1059. CrossRef Medline

LaManna JC, Rosenthal M (1975) Effect of ouabain and phenobarbital on oxidative metabolic activity associated with spreading cortical depression in cats. Brain Res 88:145–149. CrossRef Medline

Lauritzen M, Dreier JP, Fabricius M, Hartings JA, Graf R, Strong AJ (2011) Clinical relevance of cortical spreading depression in neurological disorders: migraine, malignant stroke, subarachnoid and intracranial hemorrhage, and traumatic brain injury. J Cereb Blood Flow Metab 31:17–35. CrossRef Medline

Leao AAP (1944) Pial circulation and spreading depression of activity in the cerebral cortex. J Neurophysiol 7:391–396.

Li P, Murphy TH (2008) Two-photon imaging during prolonged middle cerebral artery occlusion in mice reveals recovery of dendritic structure after reperfusion. J Neurosci 28:11970–11979. CrossRef Medline

MacAulay N, Zeuthen T (2010) Water transport between CNS compartments: contributions of aquaporins and cotransporters. Neuroscience 168:941–956. CrossRef Medline

MacAulay N, Hamann S, Zeuthen T (2004) Water transport in the brain: role of cotransporters. Neuroscience 129:1029–1042. CrossRef

Masuda T, Croom D, Hida H, Kirov SA (2011) Capillary blood flow around microglial somata determines dynamics of microglial processes in ischemic conditions. Glia 59:1744–1753. CrossRef Medline

Mazel T, Richter F, Vargová L, Syková E (2002) Changes in extracellular space volume and geometry induced by cortical spreading depression in immature and adult rats. Physiol Res 51:S85–S93. Medline

Menna G, Tong CK, Chesler M (2000) Extracellular pH changes and accompanying cation shifts during ouabain-induced spreading depression. J Neurophysiol 83:1338–1345. Medline

Mies G, Paschen W (1984) Regional changes of blood flow, glucose, and ATP content determined on brain sections during a single passage of spreading depression in rat brain cortex. Exp Neurol 84:249–258. CrossRef Medline

Mohajerani MH, McVea DA, Fingas M, Murphy TH (2010) Mirrored bilateral slow-wave cortical activity within local circuits revealed by fast bihemispheric voltage-sensitive dye imaging in anesthetized and awake mice. J Neurosci 30:3745–3751. CrossRef Medline

Müller M (2000) Effects of chloride transport inhibition and chloride substitution on neuron function and on hypoxic spreading-depression-like depolarization in rat hippocampal slices. Neuroscience 97:33–45. CrossRef Medline

Müller M, Somjen GG (1999) Intrinsic optical signals in rat hippocampal slices during hypoxia-induced spreading depression-like depolarization. J Neurophysiol 82:1818–1831. Medline

Müller M, Somjen GG (2000) Na^+ and K^+ concentrations, extra-and intracellular voltages, and the effect of TTX in hypoxic rat hippocampal slices. J Neurophysiol 83:735–745.

Murphy TH, Li P, Betts K, Liu R (2008) Two-photon imaging of stroke onset in vivo reveals that NMDA-receptor independent ischemic depolarization is the major cause of rapid reversible damage to dendrites and spines. J Neurosci 28:1756–1772. CrossRef Medline

Mutch WAC, Hansen AJ (1984) Extracellular pH changes during spreading depression and cerebral ischemia: mechanisms of brain pH regulation. J Cereb Blood Flow Metab 4:17–27. CrossRef Medline

Nimmerjahn A, Kirchhoff F, Helmchen F (2005) Resting microglial cells are highly dynamic surveillants of brain parenchyma in vivo. Science 308:1314–1318. CrossRef Medline

Oliveira-Ferreira AI, Milakara D, Alam M, Jorks D, Major S, Hartings JA, Lückl J, Martus P, Graf R, Dohmen C, Bohner G, Woitzik J, Dreier JP (2010) Experimental and preliminary clinical evidence of an ischemic zone with prolonged negative DC shifts surrounded by a normally perfused tissue belt with persistent electrocorticographic depression. J Cereb Blood Flow Metab 30:1504–1519. CrossRef Medline

Pagliardini S, Gosgnach S, Dickson CT (2013) Spontaneous sleep-like brain state alternations and breathing characteristics in urethane anesthetized mice. PLoS One 8:e70411. CrossRef Medline

Papadopoulos MC, Verkman AS (2013) Aquaporin water channels in the nervous system. Nat Rev Neurosci 14:265–277. CrossRef Medline

Pasantes-Morales H, Maar TE, Morán J (1993) Cell volume regulation in cultured cerebellar granule neurons. J Neurosci Res 34:219–224. CrossRef Medline

Payne JA (1997) Functional characterization of the neuronal-specific K-Cl

cotransporter: implications for $[K^+]_o$ regulation. Am J Physiol Cell Physiol 273:C1516–C1525.

Payne JA, Stevenson TJ, Donaldson LF (1996) Molecular characterization of a putative K-Cl cotransporter in rat brain A neuronal-specific isoform. J Biol Chem 271:16245–16252. CrossRef Medline

Pérez-Pinzón MA, Tao L, Nicholson C (1995) Extracellular potassium, volume fraction, and tortuosity in rat hippocampal CA1, CA3, and cortical slices during ischemia. J Neurophysiol 74:565–573. Medline

Pierre K, Magistretti PJ, Pellerin L (2002) MCT2 is a major neuronal monocarboxylate transporter in the adult mouse brain. J Cereb Blood Flow Metab 22:586–595. Medline

Plotkin MD, Kaplan MR, Peterson LN, Gullans SR, Hebert SC, Delpire E (1997) Expression of the Na^+-K^+-$2Cl^-$ cotransporter BSC2 in the nervous system. Am J Physiol Cell Physiol 41:C173.

Risher WC, Andrew RD, Kirov SA (2009) Real-time passive volume responses of astrocytes to acute osmotic and ischemic stress in cortical slices and in vivo revealed by two-photon microscopy. Glia 57:207–221. CrossRef Medline

Risher WC, Ard D, Yuan J, Kirov SA (2010) Recurrent spontaneous spreading depolarizations facilitate acute dendritic injury in the ischemic penumbra. J Neurosci 30:9859–9868. CrossRef Medline

Risher WC, Croom D, Kirov SA (2012) Persistent astroglial swelling accompanies rapid reversible dendritic injury during stroke-induced spreading depolarizations. Glia 60:1709–1720. CrossRef Medline

Rungta RL, Choi HB, Tyson JR, Malik A, Dissing-Olesen L, Lin PJ, Cain SM, Cullis PR, Snutch TP, MacVicar BA (2015) The cellular mechanisms of neuronal swelling underlying cytotoxic edema. Cell 161:610–621. CrossRef Medline

Schliwa M, Euteneuer U, Bulinski JC, Izant JG (1981) Calcium lability of cytoplasmic microtubules and its modulation by microtubule-associated proteins. Proc Natl Acad Sci U S A 78:1037–1041. CrossRef Medline

Sigler A, Goroshkov A, Murphy TH (2008) Hardware and methodology for targeting single brain arterioles for photothrombotic stroke on an upright microscope. J Neurosci Methods 170:35–44. CrossRef Medline

Somjen GG (2001) Mechanisms of spreading depression and hypoxic spreading depression-like depolarization. Physiol Rev 81:1065–1096. Medline

Somjen GG (2004) Ions in the brain: normal function, seizures, and stroke. New York: Oxford UP.

Spector I, Shochet NR, Kashman Y, Groweiss A (1983) Latrunculins: novel marine toxins that disrupt microfilament organization in cultured cells. Science 219:493–495. CrossRef Medline

Sword J, Masuda T, Croom D, Kirov SA (2013) Evolution of neuronal and astroglial disruption in the peri-contusional cortex of mice revealed by in vivo two-photon imaging. Brain 136:1446–1461. CrossRef Medline

Takano T, Tian GF, Peng W, Lou N, Lovatt D, Hansen AJ, Kasischke KA, Nedergaard M (2007) Cortical spreading depression causes and coincides with tissue hypoxia. Nat Neurosci 10:754–762. CrossRef Medline

Windmüller O, Lindauer U, Foddis M, Einhäupl KM, Dirnagl U, Heinemann U, Dreier JP (2005) Ion changes in spreading ischaemia induce rat middle cerebral artery constriction in the absence of NO. Brain 128:2042–2051. CrossRef Medline

Yamamoto K, Morimoto K, Yanagihara T (1986) Cerebral ischemia in the gerbil: transmission electron microscopic and immunoelectron microscopic investigation. Brain Res 384:1–10. CrossRef Medline

Yamamoto K, Hayakawa T, Mogami H, Akai F, Yanagihara T (1990) Ultrastructural investigation of the CA1 region of the hippocampus after transient cerebral ischemia in gerbils. Acta Neuropathol 80:487–492. CrossRef Medline

Yang O, Cuccia D, Choi B (2011) Real-time blood flow visualization using the graphics processing unit. J Biomed Optics 16:016009. CrossRef

Zeuthen T (1994) Cotransport of K^+, Cl^- and H_2O by membrane proteins from choroid plexus epithelium of *Necturus maculosus*. J Physiol 478:203–219. CrossRef Medline

Zeuthen T, MacAulay N (2012) Cotransport of water by Na^+-K^+-$2Cl^-$ cotransporters expressed in *Xenopus oocytes*: NKCC1 versus NKCC2. J Physiol 590:1139–1154. CrossRef Medline

Zeuthen T, Hamann S, La Cour M (1996) Cotransport of H^+, lactate and H_2O by membrane proteins in retinal pigment epithelium of bullfrog. J Physiol 497:3–17. CrossRef

Zhou N, Gordon GR, Feighan D, MacVicar BA (2010) Transient swelling, acidification, and mitochondrial depolarization occurs in neurons but not astrocytes during spreading depression. Cereb Cortex 20:2614–2624. CrossRef Medline

THE JOURNAL OF BIOLOGICAL CHEMISTRY VOL. 291, NO. 36, pp. 19184–19195, September 2, 2016

Aquaporin 4 as a NH_3 Channel*

Received for publication, May 25, 2016, and in revised form, July 8, 2016 Published, JBC Papers in Press, July 19, 2016, DOI 10.1074/jbc.M116.740217

Mette Assentoft[‡1,2], Shreyas Kaptan[§1,3], Hans-Peter Schneider[¶], Joachim W. Deitmer[¶4], Bert L. de Groot[§3], and Nanna MacAulay[‡5]

From the [‡]Department of Neuroscience and Pharmacology, University of Copenhagen, 2200 Copenhagen, Denmark, [§]Computational Biomolecular Dynamics Group, Max Planck Institute for Biophysical Chemistry, 37077 Gottingen, Germany, and [¶]Division of General Zoology, Department of Biology, University of Kaiserslautern, 67653 Kaiserslautern, Germany

Ammonia is a biologically potent molecule, and the regulation of ammonia levels in the mammalian body is, therefore, strictly controlled. The molecular paths of ammonia permeation across plasma membranes remain ill-defined, but the structural similarity of water and NH_3 has pointed to the aquaporins as putative NH_3-permeable pores. Accordingly, a range of aquaporins from mammals, plants, fungi, and protozoans demonstrates ammonia permeability. Aquaporin 4 (AQP4) is highly expressed at perivascular glia end-feet in the mammalian brain and may, with this prominent localization at the blood-brain-interface, participate in the exchange of ammonia, which is required to sustain the glutamate-glutamine cycle. Here we observe that AQP4-expressing *Xenopus* oocytes display a reflection coefficient <1 for NH_4Cl at pH 8.0, at which pH an increased amount of the ammonia occurs in the form of NH_3. Taken together with an NH_4Cl-mediated intracellular alkalization (or lesser acidification) of AQP4-expressing oocytes, these data suggest that NH_3 is able to permeate the pore of AQP4. Exposure to NH_4Cl increased the membrane currents to a similar extent in uninjected oocytes and in oocytes expressing AQP4, indicating that the ionic NH_4^+ did not permeate AQP4. Molecular dynamics simulations revealed partial pore permeation events of NH_3 but not of NH_4^+ and a reduced energy barrier for NH_3 permeation through AQP4 compared with that of a cholesterol-containing lipid bilayer, suggesting AQP4 as a favored transmembrane route for NH_3. Our data propose that AQP4 belongs to the growing list of NH_3-permeable water channels.

Ammonia is an integral constituent in cell metabolism, but its homeostasis is, due to the biological toxicity of ammonia (1–4), highly regulated around 10–35 μM in plasma (5). Ammonia is a base and thus exists in two forms: NH_3 (ammonia) or NH_4^+ (ammonium ion). Henceforward, the term ammonia will be used as a general form, whereas NH_3 and NH_4^+ will be used when referring to a specific form. At physiological pH, its pK_a of 9.25 dictates that ~1.5% of the ammonia is found as NH_3, whereas the rest exists as NH_4^+, the latter of which absolutely requires membrane transporters or channels to cross the plasma membrane. Although dedicated NH_4^+ transport proteins have been identified (6), NH_4^+ is, due to its resemblance to K^+, in addition transported by a range of K^+ transporters and channels, such as the Na^+/K^+-ATPase, the $Na^+/K^+/2Cl^-$ cotransporter, the K^+/Cl^- cotransporter, and inwardly rectifying, voltage-, and Ca^{2+}-activated K^+ channels (7–16). The permeability of NH_4^+ through K^+ channels usually amounts to ~10–20% of the permeability of K^+ (7). It was long believed that NH_3 could permeate the cell membrane by simple diffusion because of its small size and lack of electric charges. NH_3 is, however, a polar molecule with a dipole moment of 1.47 D (close to that of water = 1.85 D; see Fig. 1 for a structural comparison) and may thus permeate poorly through lipid bilayers. Indeed, plasma membranes with poor NH_3 permeability have been demonstrated (17–19), indicating that membrane transport proteins may facilitate NH_3 permeation. The structural similarity of water and NH_3 points to water channels, the aquaporins, as putative NH_3-permeable pores; the plant aquaporins of the tonoplast intrinsic membrane protein (TIP) family, the nodulin-26 like intrinsic protein (NIP) family, and aquaporins from the human-pathogenic protozoans *Plasmodium falciparum*, *Toxoplasma gondii*, and *Trypanosoma brucei* have indeed been shown to allow NH_3 permeation (20–26). The 13 mammalian aquaporins are classified into three families based on their permeability profile and sequence homology: the aquaporins (AQP0, AQP1, AQP2, AQP4,[6] AQP5, AQP6, and AQP8), the aquaglyceroporins (AQP3, AQP7, AQP9, and AQP10), which in addition to water are permeable to small hydrophilic molecules such as urea and glycerol, and the unorthodox aquaporins (AQP11 and AQP12), which share little sequence homology with the other aquaporins (27, 28). Several of both the aquaporins and aquaglyceroporins have been reported to be permeable to ammonia as well as water; AQP1, AQP3, AQP6, AQP7, AQP8, and AQP9 have been found to be permeable for NH_3 (21, 22, 29–31), although the NH_3 permeability of AQP1 has been questioned (21, 22, 32), whereas AQP0, AQP2, AQP5, and AQP4 have been reported to lack NH_3 permeability (29, 31). The sensitivity of the different experimental approaches employed to determine the NH_3 permeability is not defined, and it is possible that, as most K^+

* The authors declare that they have no conflicts of interest with the contents of this article.

[1] Both authors contributed equally.
[2] Supported by the Danish Medical Research Council.
[3] Supported by the Max Planck Society and the German Research Foundation via the SFB 803 (Project A03).
[4] Supported by the Deutsche Forschungsgemeinschaft (DE 231/24-2).

[5] To whom correspondence should be addressed: Dept of Neuroscience and Pharmacology, University of Copenhagen, Blegdamsvej 3, Bldg. 22.3, 2200 Copenhagen N, Denmark. Tel.: 45-35327566; E-mail: macaulay@sund.ku.dk.

[6] The abbreviations used are: AQP4, aquaporin 4; US, umbrella sampling; PMF, potential of mean force; POPC, 1-palmitoyl-2-oleoyl-sn-glycero-3-phosphocholine.

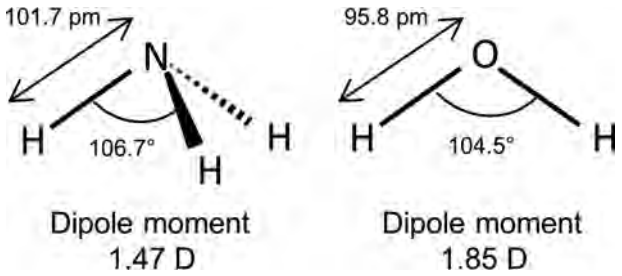

FIGURE 1. **The Lewis structure of NH_3 (*left*) and H_2O (*right*).** NH_3 and H_2O have several similarities including dipole moment (1.47 D for NH_3 and 1.85 for H_2O), tetrahedral electronic structure, bond angle (106.7° for NH_3 and 104.5° for H_2O), and bond length (101.7 pm for NH_3 and 95.8 pm for H_2O).

channels are permeable to NH_4^+, NH_3 permeability may be a general feature in most aquaporins, albeit to a varying degree and, therefore, to a variable degree of detectability. In support of a common water and NH_3 permeability pathway, a H^+-coupled NH_3 co-transporter (SLC4A11) has been demonstrated to allow for water permeation (33, 34).

During acute liver failure, ammonia levels increase in the plasma followed by brain accumulation approaching 5 mM in severe cases (35). This ammonia rise is thought to be the key factor in the pathogenesis of hepatic encephalitis and affects a range of brain functions, *i.e.* cerebral blood flow, cerebral glucose metabolic rate, synaptic transmission, glutamate homeostasis, and cell volume regulation (36–41). However, the paths of ammonia entry into the brain as well as into the cellular compartments of the brain are unresolved. The robust expression of AQP4 at the perivascular glial end-feet surrounding the brain capillaries (42) and the ammonia-dependent regulation of AQP4 membrane expression (43, 44) may suggest AQP4 as a possible entry point of NH_3 into the glial compartments. In the present study, we therefore determine the ammonia permeability of AQP4 by both experimental approaches and molecular dynamics simulations.

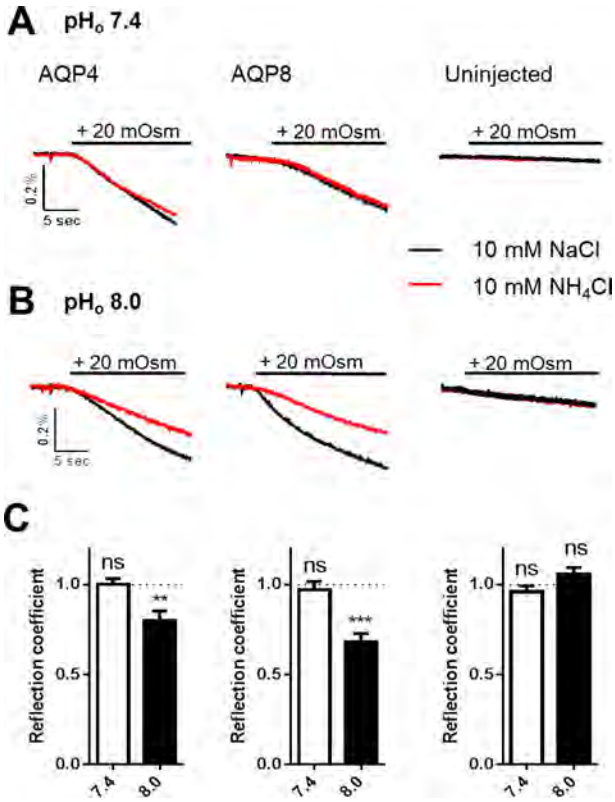

FIGURE 2. **The reflection coefficient is reduced for ammonia in AQP4- and AQP8-expressing oocytes.** *A* and *B*, volume traces from an AQP4-expressing, AQP8-expressing, or uninjected oocyte challenged with a hyperosmotic gradient of 20 mOsM (marked with a *black bar*) of either 10 mM NaCl (*black trace*) or 10 mM NH_4Cl (*red trace*) at pH$_o$ 7.4 (*A*) or pH$_o$ 8.0 (*B*). *C*, A summary of the reflection coefficients for ammonia for AQP4-expressing (*left panel*), AQP8-expressing (*middle panel*), and uninjected oocytes (*right panel*) at pH$_o$ 7.4 and pH$_o$ 8.0. The reflection coefficient is calculated from two control measurements (10 mM NaCl as the osmolyte) and two measurements using 10 mM NH_4Cl as the osmolyte for each oocyte; $n = 7$–12. Statistical significance was determined with paired Student's *t* test. **, $p < 0.01$; ***, $p < 0.001$; *ns*, not significant.

Results

A Low Reflection Coefficient of Ammonia Indicates Ammonia Permeability in AQP4—To determine whether ammonia permeates AQP4, we monitored the ability of ammonia to drive osmotic water flux in *Xenopus* oocytes expressing AQP4 and, as a positive control, the ammonia-permeable AQP8 (22, 31, 45, 46). An inherent advantage in this heterologous expression system is the low intrinsic water permeability of the native oocyte membrane; expression of AQP4 increases the osmotic water permeability of the oocyte membrane ~20-fold (47, 48), thus providing a robust signal-to-noise ratio. AQP4- and AQP8-expressing oocytes exposed to an osmotic challenge consisting of the impermeable osmolyte NaCl (10 mM; 20 mOsM) therefore, as opposed to uninjected oocytes, displayed robust cell shrinkage (water permeabilities at pH 7.4 in $\times 10^{-3}$ cm/s: 2.99 ± 0.49, $n = 12$ for AQP4, 2.04 ± 0.39, $n = 9$ for AQP8, and 0.14 ± 0.01, $n = 7$ for uninjected oocytes, $p < 0.05$ for both AQP4 and AQP8 when compared with uninjected); see the representative traces in *black* in Fig. 2*A*. To obtain the reflection coefficient of ammonia, the same oocytes were then exposed to an identical osmotic challenge of 20 mOsM but obtained with NH_4Cl (10 mM) as the osmolyte. Both oocytes expressing AQP4 and AQP8 as well as uninjected oocytes responded to the osmotic challenge in a manner essentially identical to that observed with NaCl as the osmolyte (water permeabilities with NH_4Cl as the osmolyte in $\times 10^{-3}$ cm/s: 3.04 ± 0.42, $n = 12$ for AQP4, 1.94 ± 0.37, $n = 9$ for AQP8, and 0.13 ± 0.01, $n = 7$ for uninjected oocytes, $p < 0.05$ for both AQP4 and AQP8 when compared with uninjected); see the representative traces in *red* in Fig. 2*A*. The reflection coefficient for ammonia at pH 7.4, $\sigma_{7.4}$, was therefore not significantly different from 1 (1.00 ± 0.03, $n = 12$ for AQP4, 0.96 ± 0.04, $n = 9$ for AQP8, and 0.96 ± 0.03, $n = 7$ for uninjected oocytes), illustrated as *white bars* in Fig. 2*C*. Of the 10 mM NH_4Cl, only 0.14 mM exists as NH_3 at pH 7.4 and the reminder exists as NH_4^+ (according to the Henderson-Hasselbalch equation). To increase the fraction of NH_3 in the test solution without changing the ammonia concentration, a parallel experimental series was carried out with test solutions of pH 8.0, in which the NH_3 concentration is 4-fold higher (0.56 mM). The slightly basic test solutions did not significantly affect the water permeability obtained with NaCl as the osmolyte (water permeabilities at pH 8.0 in $\times 10^{-3}$ cm/s: 2.34 ± 0.28 $n = 12$ for AQP4, 1.16 ± 0.25, $n = 9$ for AQP8, and 0.23 ± 0.04, $n = 7$ for uninjected oocytes); see the representative traces in *black*

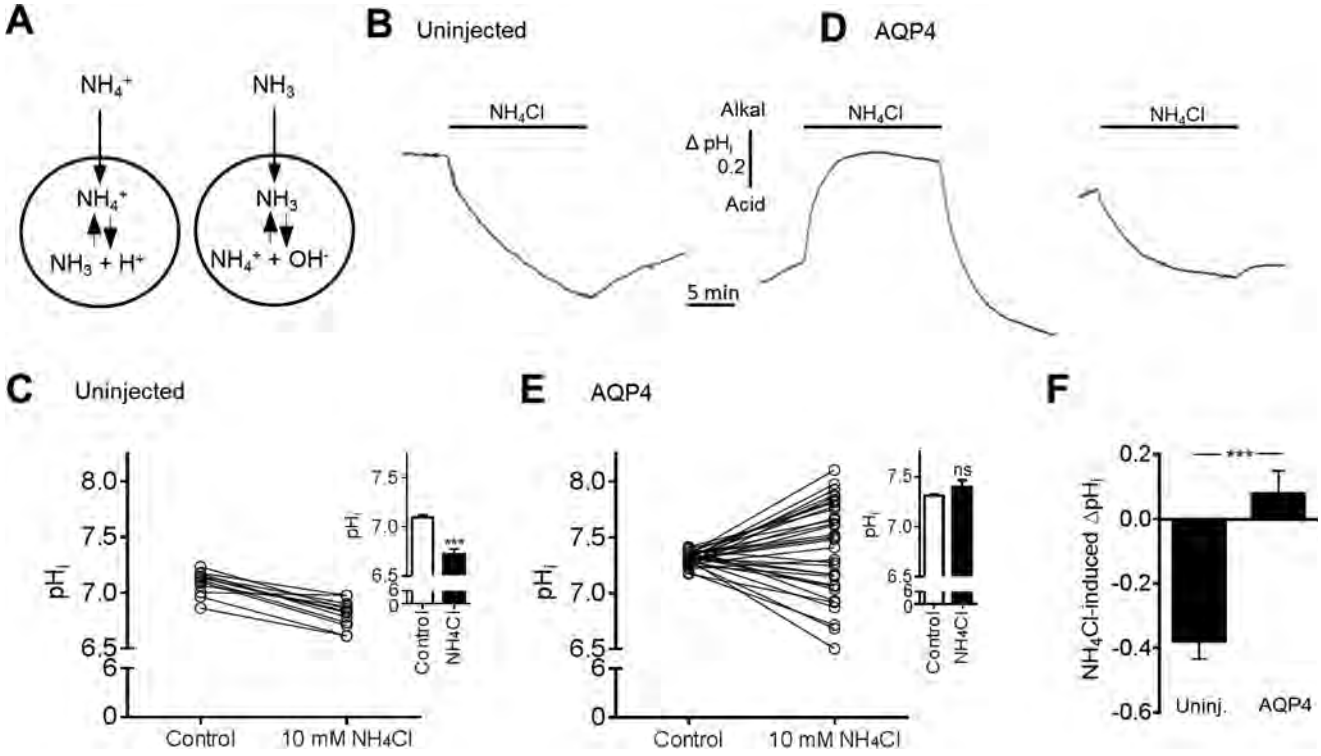

FIGURE 3. **pH_i changes in response to exposure to ammonia in uninjected and in AQP4-expressing oocytes.** *A*, transport of ammonia as either NH_4^+ or NH_3. If NH_4^+ crosses the cell membrane, it will cause an intracellular acidification, whereas influx of NH_3 will cause an intracellular alkalization. *B* and *D*, pH_i traces from an uninjected oocyte (*B*) and from two AQP4-expressing oocytes (*D*) exposed to 10 mM NH_4Cl (marked with a *black bar*). *C*, overview of the individual pH_i changes in uninjected oocytes after 15 min of exposure to 10 mM NH_4Cl, summarized in the *inset*, $n = 15$. *E*, overview of the individual pH_i changes in AQP4-expressing oocytes after 15 min of exposure to 10 mM NH_4Cl, summarized in the *inset*, $n = 33$. *F*, overview of the NH_4Cl-induced ΔpH_i in uninjected (*Uninj.*) oocytes ($n = 15$) and AQP4-expressing oocytes ($n = 33$). Statistical significance was determined with paired Student's *t* test (unpaired Student's *t* test in *panel F*). ***, $p < 0.001$; *ns*, not significant.

in Fig. 2*B*. These results demonstrate that the higher pH of the extracellular solution in itself did not affect the water permeability of either the AQPs or the native plasma membrane. An osmotic challenge based on NH_4Cl (at pH 8.0) provided a cell shrinkage of the uninjected oocytes identical to that obtained with NaCl; see the *red trace* in Fig. 2*B*, *right panel*, for a representative trace. Oppositely, the osmotic water permeability was significantly smaller for both AQP4- and AQP8-expressing oocytes when obtained with NH_4Cl instead of NaCl; see the *red traces* in Fig. 2*B*, *left* and *middle panels*, for representative traces. The reflection coefficient for NH_4Cl at pH 8, $\sigma_{8.0}$, was, therefore, significantly <1 for the AQP-expressing oocytes (0.80 ± 0.05, $n = 12$ for AQP4, $p < 0.01$ and 0.68 ± 0.04, $n = 9$ for AQP8, $p < 0.001$), whereas for the uninjected oocytes, $\sigma_{8.0}$ was not significantly different from 1 (1.07 ± 0.04, $n = 8$), summarized as *black bars* in Fig. 2*C*. These data suggest that at pH 8.0, at which the test solutions contain a significant NH_3 content, we detect ammonia permeation into the pore of the expressed aquaporins, thus preventing ammonia from exerting the full osmotic force as observed with the impermeable NaCl.

AQP4 Alters the pH_i Response to Ammonia Treatment of Oocytes—Cellular influx of NH_3 causes intracellular alkalinization, whereas NH_4^+ influx causes intracellular acidification, as illustrated in Fig. 3*A*. To further resolve the ability of ammonia to permeate AQP4, we monitored the intracellular pH of uninjected and AQP4-expressing oocytes with a H^+-sensitive microelectrode during the addition of ammonia to the extracellular solution. A stable pH_i baseline was obtained in control solution before exposure of the oocytes to an isosmotic solution containing 10 mM NH_4Cl for 15 min. NH_4Cl caused an intracellular acidification of all uninjected oocytes (representative trace in Fig. 3*B* and summarized data in Fig. 3*C*; compare pH_i of 7.10 ± 0.02 in control solution with 6.72 ± 0.06 in the presence of ammonia, $n = 15$, $p < 0.001$, *inset*). AQP4-expressing oocytes responded in a graded manner with the majority of the tested oocytes responding to NH_4Cl with either a robust intracellular alkalization or a lesser acidification than observed with the uninjected oocytes (representative traces are illustrated in Fig. 3*D*; summarized data are in Fig. 3*E*, $n = 33$). 6 of the 33 tested oocytes responded with a pH_i change that fell within the confidence interval of the pH_i change observed in the uninjected oocytes (ΔpH_i of −0.38 (CI −0.49 to −0.26) pH units, $n = 15$). Summarized data illustrate that the intracellular acidification observed in uninjected oocytes was abolished in the AQP4-expression oocytes; compare pH_i of 7.31 ± 0.01 in control solution with 7.39 ± 0.07 in NH_4Cl-containing solution, $n = 33$, $p = 0.26$, Fig. 3*E*, *inset*. The NH_4Cl-induced pH_i change in AQP4-expressing oocytes (0.08 ± 0.07 pH units, $n = 33$) was thus significantly different from that obtained in uninjected oocytes (-0.38 ± 0.06 pH units, $n = 15$), $p < 0.001$, Fig. 3*F*. The observed alkalization (or lesser acidification) in a substantial fraction of the AQP4-expressing oocytes (27/33),

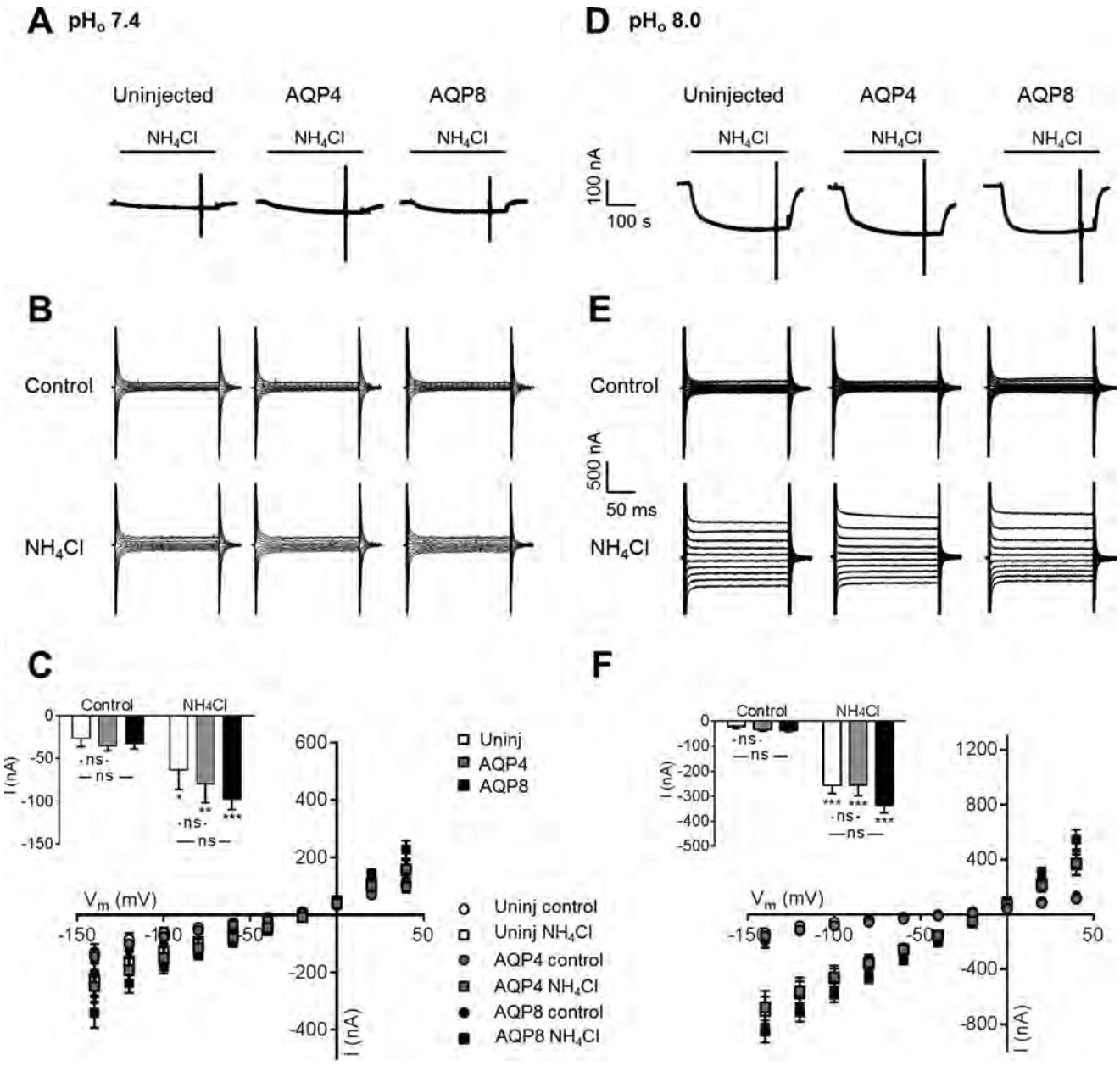

FIGURE 4. **No aquaporin-mediated NH_4^+ permeation.** *A* and *D*, representative current traces in uninjected (*left panel*), AQP4 (*middle panel*)-, and AQP8 (*right panel*)-expressing oocytes at pH$_o$ 7.4 (*A*) and pH$_o$ 8.0 (*D*) before and in the presence of 5 mM NH_4Cl, marked with a *black bar*. The currents were recorded from single oocytes at a holding potential of −50 mV. *B* and *E*, representative *I/V* relationships of uninjected (*left panels*), AQP4 (*middle panels*)-, or AQP8 (*right panels*)-expressing oocytes at pH$_o$ 7.4 (*B*) and pH$_o$ 8.0 (*E*) before and after 5 min of treatment with 5 mM NH_4Cl. *C* and *F*, summarized *I/V* relationships of uninjected (*Uninj.*) oocytes (*white*) and oocytes expressing AQP4 (*gray*) or AQP8 (*black*) before and after treatment with 5 mM NH_4Cl at pH$_o$ 7.4 (*C*) and pH$_o$ 8.0 (*F*), $n = 9$ of each, with the currents obtained at $V_m = -60$ mV summarized in the *insets*. Statistical significance was determined with two-way analysis of variance with Šídák's multiple comparison post hoc test. *, $p < 0.05$; **, $p < 0.01$; ***, $p < 0.001$; *ns*, not significant.

therefore, suggests that ammonia is able to permeate the pore of AQP4 in the form of NH_3.

Expression of AQP4 Does Not Induce NH_3/NH_4^+-dependent Membrane Current in Oocytes—To determine if AQP4 was permeable to NH_4^+, we monitored the current response of uninjected oocytes and AQP4- and AQP8-expressing oocytes during ammonia exposure. NH_4^+ membrane permeation results in a membrane current in voltage clamped oocytes which is absent with NH_3 permeation. At pH 7.4, isosmotic addition of 5 mM NH_4Cl to the test solution caused a small inward current in both uninjected oocytes and AQP-expressing oocytes; see the representative current traces in Fig. 4*A*. Voltage step protocols applied before and after the addition of ammonia illustrated comparable membrane currents in uninjected oocytes and AQP4- and AQP8-expressing oocytes both in control solution and after exposure to ammonia (see representative *I/V* current traces in Fig. 4*B*, summarized *I/V* relations in Fig. 4*C*, and summarized currents at −60 mV displayed as the inset); although the membrane current increased in the presence of ammonia for all tested oocytes (uninjected oocytes: compare −26.3 ± 9.9 nA with −63.7 ± 22.7 nA in the presence of ammonia, $n = 9$, $p < 0.05$; AQP4: compare −35.1 ± 6.0 nA with −79.9 ± 22.1

nA in the presence of ammonia, $n = 9$, $p < 0.05$; AQP8: compare -32.7 ± 6.0 nA with -97.5 ± 12.4 nA in the presence of ammonia, $n = 9$, $p < 0.001$), the increase observed in the AQP-expressing oocytes was not significantly different from that of the uninjected oocytes; see the Fig. 4*C inset*. To obtain an increased fractional NH_3 content, a parallel experimental series was carried out at pH_o 8.0. Although the ammonia-induced membrane currents intrinsic to the native oocyte membrane was enlarged at this extracellular alkalinization, the observed current pattern resembled that obtained at pH_o 7.4; see the representative current traces in Fig. 4*D*, representative *I*/*V* current traces in Fig. 4*E*, and the summarized *I*/*V* relations in Fig. 4*F* with an *inset* summarizing the current obtained at $V_m = -60$ mV (uninjected: compare -21.8 ± 8.0 nA with -256.4 ± 32.9 nA in the presence of ammonia, $n = 9$, $p < 0.05$; AQP4: compare -35.0 ± 5.5 nA with -255.7 ± 42.4 nA in the presence of ammonia, $n = 9$, $p < 0.05$; AQP8: compare -35.7 ± 6.4 nA with -336.3 ± 29.5 nA in the presence of ammonia, $n = 9$, $p < 0.001$). At pH_o 8.0 as well as pH_o 7.4, the ammonia-induced membrane currents were independent of aquaporin expression in the plasma membrane, which supports that AQP4- and AQP8-dependent ammonia permeation takes place via NH_3 rather than via NH_4^+.

Partial Ammonia Permeation Was Observed in Free Simulations—To obtain details on ammonia entry into the pore of AQP4 on a molecular scale, we performed molecular dynamics on this permeability event. Free simulations were initially carried out to observe the behavior of both NH_3 and NH_4^+ near the surface of AQP4. In these simulations we introduced, separately, 100 molecules each of NH_3 and NH_4^+ with appropriate neutralization for the latter. Each simulation was carried out for 500 ns. For any further analysis, only the latter 400 ns were considered to account for equilibration effects. We observed several partial permeation events of NH_3 entering the channel and exiting from the same end. Together, these partial permeation events cover almost the entire protein pore. In contrast, NH_4^+ never penetrated the pore to any significant extent. Remarkably, NH_4^+ showed high propensity to cluster around several anionic amino acids such as glutamate and aspartate on either protein surface (Fig. 5). Most of these clustering "hotspots" are placed closely to the opening of the channel pore.

The Free Energy Barrier for NH_3 Permeation through AQP4 Is Surmountable but Higher Than for Water Permeation—To determine the free energy profiles of NH_3 permeation via AQP4 *versus* via lipid membranes of different composition, we carried out umbrella sampling (US) simulations, in which we calculated the potential of mean force (PMF) for NH_3 permeation through the pore of AQP4. The uncertainty in the PMF calculation was ascertained using a bootstrapping algorithm as implemented in the g_wham tool from GROMACS and is illustrated as a *shaded margin around the PMF curves*, see Fig. 6*A*. The radius profile for the channel is shown for reference in Fig. 6*B*. To gauge the permeability of AQP4 to NH_3, we compared these PMFs to free energy profiles calculated across lipid bilayers. We used two lipid membranes for comparison; a pure 1-palmitoyl-2-oleoyl-sn-glycero-3-phosphocholine (POPC) bilayer and a hybrid bilayer with 20% cholesterol and 80% POPC. This latter comparison is shown in Fig. 6*A*. The free energy barrier for NH_3 permeation through AQP4 is comparable with that of the POPC pure membrane, whereas the barrier is ~3–4 kJ/mol lower in the AQP4 pore than in the lipid membrane containing 20% cholesterol. These results suggest that the free energy barrier of NH_3 permeation may indeed favor permeation through AQP4 rather than through a cholesterol-containing lipid membrane. The radius profile shown in Fig. 6*B* allows us to understand where the channel is narrowest. This can contribute to the entropic barrier for entering the channel and also to the overall loss of the hydrogen bonding from water as hydration of the NH_3 decreases in a narrow region of the channel. In addition to the channel pore profile, the pore-lining residues are illustrated in Fig. 6*C* as a histogram of their position along the *z* axis. These residues could potentially supplement the hydrogen bonding to the NH_3 depleted from the lack of hydration.

To compare the free energy barrier for NH_3 with that of water, we performed free simulations in the absence of NH_3 or NH_4^+ and calculated the PMF for water across AQP4 (Fig. 7*A*). The uncertainty in the PMF for these simulations is represented by the standard deviation of the PMF along the four monomers and illustrated as a *shaded margin around*

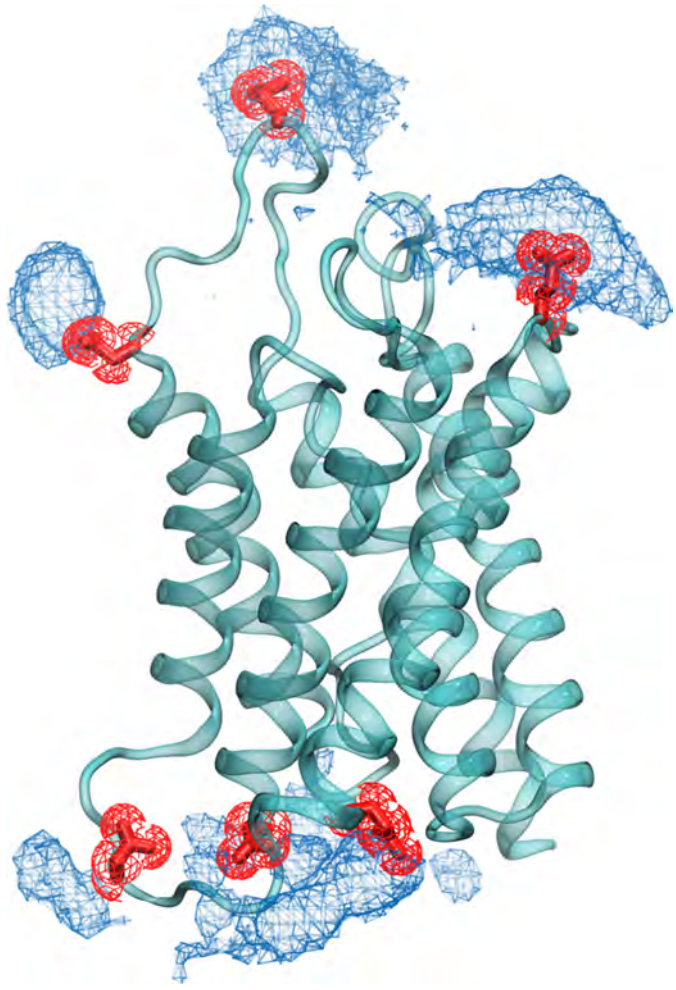

FIGURE 5. **Accumulation of NH_4^+ close to the channel surface.** In free simulations the NH_4^+ density (illustrated as *blue mesh*) is placed closely to the glutamate and aspartate residues on the protein surface, shown in *red licorice representation*.

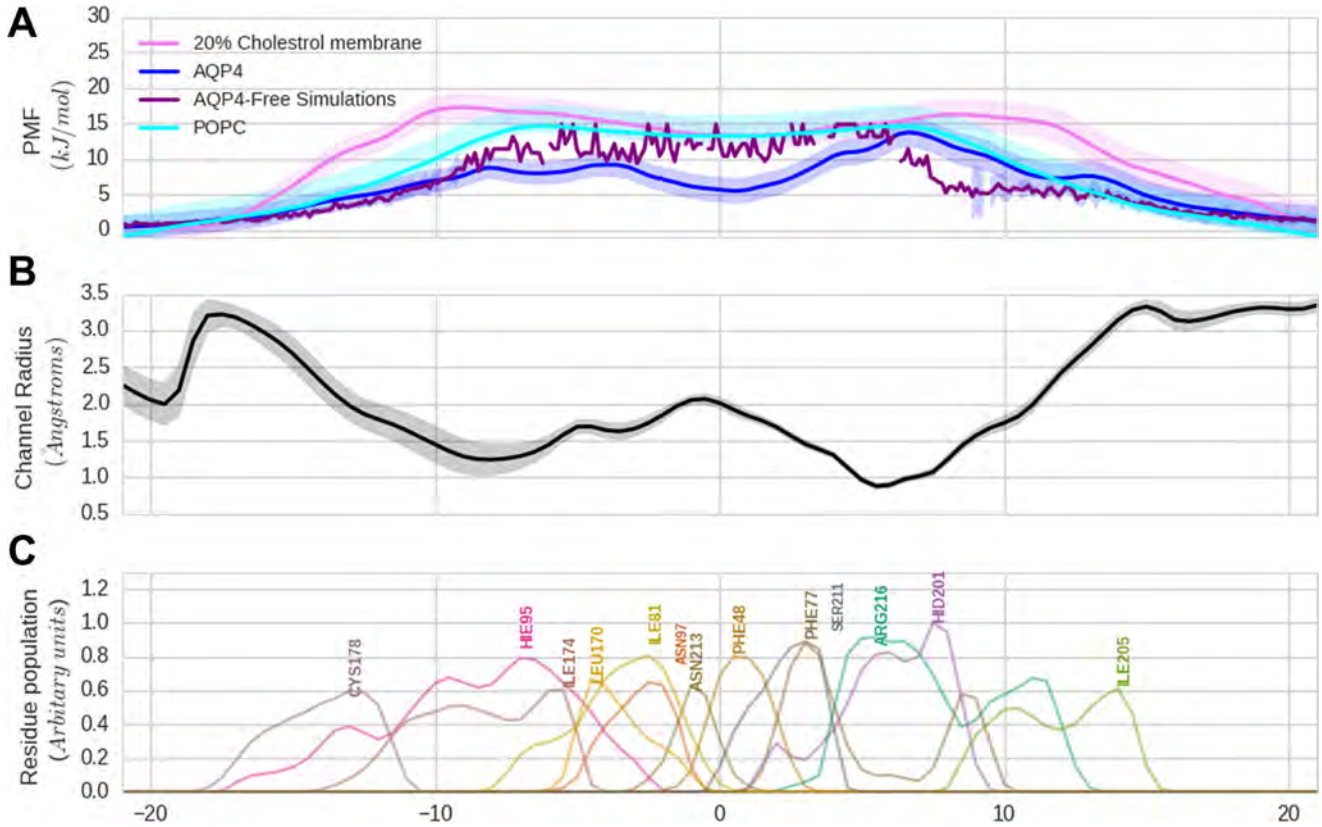

FIGURE 6. Potential of mean force for NH_3 permeation (*A*). Shown is a comparison of the PMF for NH_3 through the AQP4 channel with the membrane. The PMF of NH_3 through AQP4 is shown in *blue*. The PMF for NH_3 through a pure POPC lipid bilayer is shown in *cyan*. The PMF for NH_3 through a lipid bilayer with 20% cholesterol is shown in *purple*. The uncertainty measured via bootstrapping is shown in the *shaded region around the curves*. The *broken violet curve* is the PMF for NH_3 through AQP4 extracted from the free simulations. *B*, radius profile of the AQP4 pore along the channel axis. The *shaded region* represents the standard deviation in the profile over the simulation trajectory. *C*, population histogram of the important pore lining residues along the channel axis.

the PMF curve in Fig. 7*A*. The differences in the free energy profile for NH_3 compared with water are illustrated as a *hatched region* in Fig. 7*A* and points to the fact that water is preferred to ammonia for channel entry along almost the entire channel axis. To understand the origin of contribution of protein-NH_3 and NH_3-water hydrogen bonding to the PMF, we calculated the average number of hydrogen bonds of NH_3 with pore-lining amino acid residues from the US windows (Fig. 7*B*). The overall loss of hydrogen-bonding energy for the system as a whole observed when NH_3 enters the channel, by convention a positive number, is shown in Fig. 7*C*. This loss is quantified by use of the US windows by comparing the total hydrogen-bonding energy of a water-filled AQP4 pore against a pore in which NH_3 was introduced. For calculating the hydrogen-bonding energy of the water-filled pore, we took into account the protein and the 30 water molecules nearest to the channel center. We found that these consistently accounted for all the hydration inside the channel pore. The choice of this smaller number allowed us to minimize the fluctuations in the evaluation of hydrogen bonding energy. In the case of the US simulation windows, we chose only the first 29 water molecules to account for the presence of NH_3, which sterically replaces approximately one water molecule in the pore. An average over the trajectories in each window was used to calculate the mean difference in the hydrogen-bonding energy, and the standard error indicated the uncertainty in the estimation of the difference in energy thus obtained.

Discussion

In the present study we observed an ability of NH_3, but not NH_4^+, to gain access to the pore of AQP4 in a manner suggesting that AQP4 may belong to the growing number of aquaporins acting as NH_3 channels. The permeation of small hydrophobic molecules such as CO_2 or O_2 is expected to take place via passive diffusion across the lipid bilayer. In contrast, charged or polar molecules such as ions or water require a dedicated channel for their optimal conduction across the membrane. NH_3 presents an intriguing intermediate case with a capacity for hydrogen-bonding and low polarity. Thus, deciphering the permeation path of NH_3 across the lipid bilayer requires further study. Hub *et al.* (49) have shown that NH_3 experiences a low barrier (~6 kT or about 14 kJ/mol) for its passage across pure lipid membranes such as those composed of phosphatidylethanolamine or phosphocholine lipids. However, pure lipid membranes are generally only present in synthetic setups and do not represent a physiological situation. Biological membranes are often complex assemblies made up of several lipid types and sterols. Animal membranes, in particular, are rich in cholesterol, which can drastically alter the permeation properties of small molecules. Additionally, the cell membrane may be obstructed for entry due to high concentration of proteins or

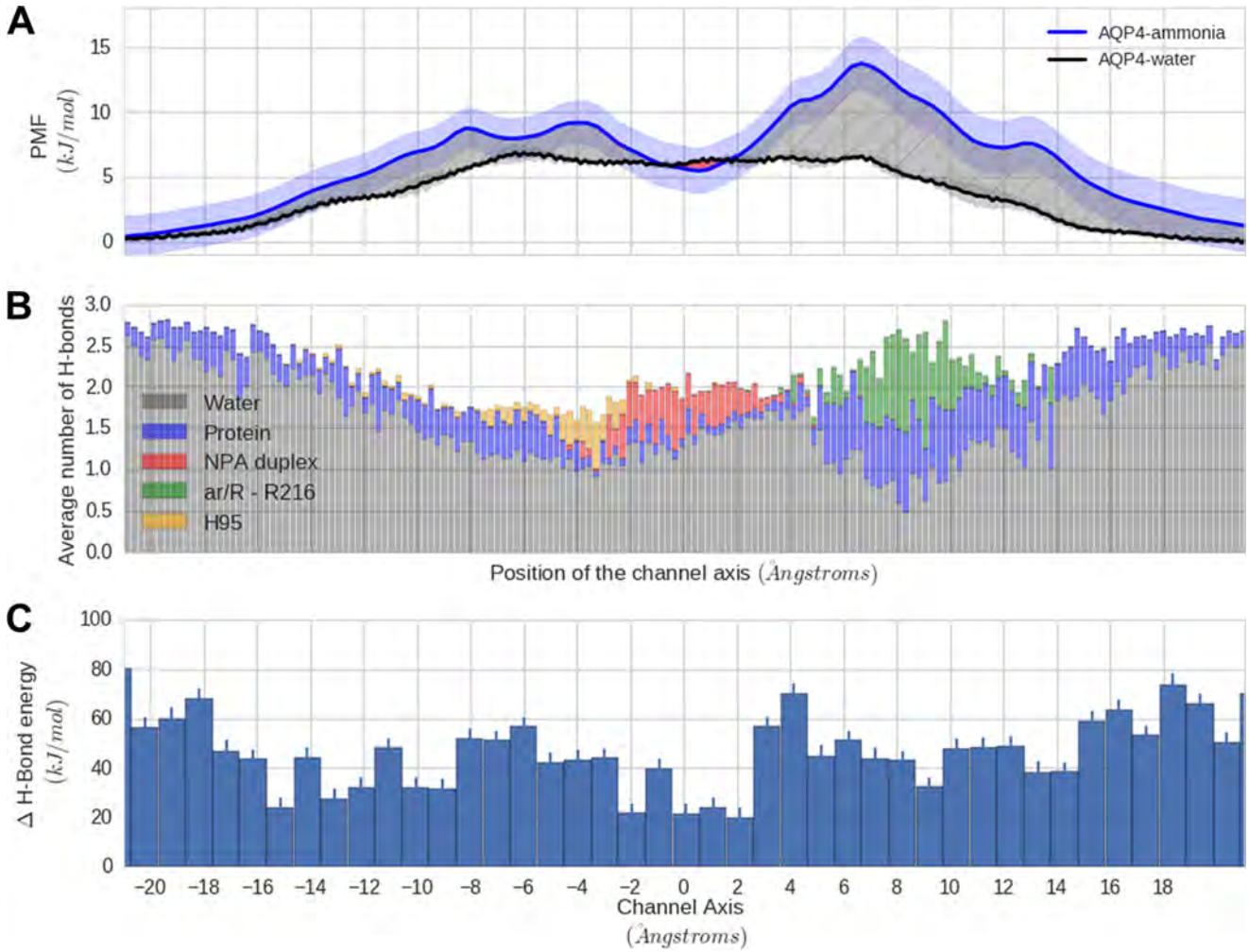

FIGURE 7. **Comparison of water and NH$_3$ permeation in AQP4.** *A*, NH$_3$ has a significantly larger (~5 kJ/mol) free energy barrier over water in AQP4 calculated from free simulations. *B*, as NH$_3$ loses hydration via hydrogen bonding on its entry into the channel, the average number of hydrogen bonds to the channel axis. *C*, hydrogen bonding energy (*HBE*) difference for water and NH$_3$ along the channel axis (HBE$_{NH3}$ − HBE$_{water}$). The positive difference indicates that hydrogen bonding with water is favored in the channel.

even because of glycosylation of lipids or protein covering the membrane surface. This might make an otherwise convenient means of diffusive passage less accessible. Thus, it might be necessary to take into account alternative means available for NH$_3$ conductance. Sometimes, these alternative routes might be as or more effective than passive membrane diffusion. Aquaporins have been long speculated to be involved in gas transport across cell membranes, and a range of aquaporins from plants, protozans, and mammals have been demonstrated to share the ability of NH$_3$ permeation in addition to their intrinsic water permeability (20–26, 29–31, 46, 50). Our experimental data show NH$_3$ permeation through AQP4 expressed in *Xenopus* oocytes measured as a reduced reflection coefficient of NH$_4$Cl and as the ability of NH$_4$Cl to promote intracellular alkalinization of AQP4-expressing oocytes. A low reflection coefficient ($\sigma < 1$) suggests that the osmolyte in question gains access to the aqueous pore and, therefore, is unable to osmotically extract water from the cell as efficiently as that of a non-permeable (reflected) osmolyte. We were, however, unable to detect a reduced reflection coefficient at pH 7.4, at which the NH$_3$ content in our 10 mM NH$_4$Cl-containing test solution was exceedingly low. At pH 8.0, the NH$_3$ fraction was calculated to reach 0.56 mM, and under these conditions oocytes expressing either AQP4 or AQP8 (a well established NH$_3$ channel (Refs. 22, 31, 45, and 46)) both displayed a lower osmotic water permeability with NH$_4$Cl as the osmolyte. The water permeability of the native oocyte membrane was unaffected by the choice of osmolyte and pH$_o$, indicating that the observed changes in water permeability originated in the expressed AQPs and suggests NH$_3$ permeation through both AQP4 and AQP8. Exposure of uninjected oocytes to NH$_4$Cl persistently caused an intracellular acidification, as previously observed (22, 30, 51–54), which is assigned to NH_4^+ entry through still unidentified pathways, presumably cation-selective ion channels (53, 55). Although a small fraction of the AQP4-microinjected oocytes displayed a similar acidification, the majority of the tested AQP4-expressing oocytes displayed either a lesser acidification or a robust alkalization upon exposure to ammonia with no obvious correlation to initial pH$_i$ or days in culture. We, therefore, cannot explain the graded response in these oocytes, which was also observed in AQP1-expressing oocytes (30). The exact placement of the electrode tip could affect the extent of

detection of a given pH_i change, and different levels of AQP4 expression in the tested oocytes likely affects the level of alkalization (functional AQP4 expression was tested for all oocytes by a simple, non-quantitative swelling assay that reveals the presence of an aquaporin in the oocyte membrane but not its abundance). This alkalization (or lesser acidification) suggests the ability of AQP4 to allow permeation of NH_3. The observed AQP4-mediated NH_3 permeation is at odds with previous reports by Boron and co-workers (29, 31) who were unable to demonstrate NH_3 permeability in AQP4-expressing oocytes. In those studies, NH_3 permeation was evaluated by monitoring the pH_o at the external face of the oocyte plasma membrane with a blunt microelectrode pushed against the surface of an AQP-expressing oocyte. A reason for the discrepancy with our result may rely on the 20-fold difference in applied NH_4Cl (0.5 mM in Refs. 29 and 31) *versus* 10 mM in this study. At the low NH_4Cl concentration employed by Boron and co-workers (29, 31), only 0.007 mM exists as NH_3 and in case AQP4 has a lower NH_3 permeability capacity than the other tested aquaporins, it may simply be experimentally undetectable at this concentration.

Exposing oocytes to NH_4Cl increased the transmembrane currents, irrespective of the presence of an aquaporin in the plasma membrane, by as yet unidentified pathways (52). We detected, however, no significant difference between the currents obtained in AQP4-expressing oocytes and uninjected oocytes at either of the tested pH values, indicating a lack of NH_4^+ permeation through AQP4. There was a tendency (although statistical significance was not reached in the present study) for the ammonia-induced transmembrane current to be slightly increased in the AQP8-expressing oocytes compared with that of the uninjected oocytes, as previously observed in oocytes expressing AQP8 and other ammonia-permeable aquaporins (22, 26, 32).

To shed light on the thermodynamic parameters that govern the NH_3 permeation in AQP4, we employed molecular simulations. US simulations show that the free energy barrier of ~14 kJ/mol (~6 kT) for NH_3 permeation through AQP4 is surmountable at room temperature. At higher temperatures such as at 37 °C, the attempt rate could encourage the permeation even further. The magnitude of this barrier is comparable with the one associated with a POPC lipid bilayer. Interestingly, the addition of cholesterol to this lipid makes the barrier rise up to ~20 kJ/mol, which is ~5 kJ/mol larger than the free energy barrier for AQP4. The permeation barrier increase observed upon the addition of cholesterol is to be expected, as cholesterol has a tendency to "thicken" the membrane by ordering the lipid tails and closing the small gaps in lipid tails that facilitate diffusion of the gas (49). This might have a real physiological effect *in vivo*, making the AQP4, rather than the plasma membrane, a favored route for NH_3 permeation. Also, 20% cholesterol is a lower limit of the sterol portion in the membrane, and an increased percentage could, therefore, lead to an even further increase in the relative passage of NH_3 through AQP4. In the sub-microsecond time scale employed for the free simulations, we observed partial permeation events of NH_3 through AQP4 that together span almost the complete AQP4 pore. The free simulations are hampered by the potential lack of sampling of putative permeation events due to the finite simulation time. Spontaneous barrier crossing in an unbiased, "free" MD simulation is a stochastic event that may or may not happen in a finite simulation time. Therefore, we took the more systematic approach of US that computes the energetic profile for solute permeation. The US method, due to the enforcement on the coordinate of ammonia across the permeation pathway, ensures that the relevant thermodynamic information concerning permeation is recovered. The barrier of ~14 kJ/mol (6 kT) observed using this method is surmountable under physiological conditions, indicating that the channel is a viable means of permeation. Indeed, the statistics collected from several partial entries of ammonia in the channel allowed us to compare the PMF calculated from the US method to the PMF from the partial permeations (Fig. 6*A*). The barrier, as calculated by the two methods, is remarkably similar, further strengthening the hypothesis that ammonia permeates the channel by diffusion. Thus, overall, the molecular dynamics simulations support the permeation of ammonia across AQP4 at physiological conditions as compared with the lipid bilayer, especially in a lipid environment rich in cholesterol.

AQP4 seems to facilitate the transport of NH_3 by stabilizing the molecule in the channel pore. In the highly conserved and narrow aromatic/arginine (ar/R) region of the protein, we observe several stabilizing hydrogen bonding interactions that seem to partially replace the loss of hydration for NH_3. However, this dehydration appears quite significant (~5 kJ/mol) and seems to be contributed due to a lack of replacement of the hydrogen bonding in the channel compared with the bulk. This "hydrophobic" effect seems to underlie the favored permeation of water over NH_3 through AQP4, as was previously reported to be the main permeation barrier for apolar gas molecules such as O_2 and CO_2 (56). The only region where the PMF for ammonia dips below the PMF for water is close to the asparagine-proline-alanine (NPA) duplex. This dip can be explained based on the enthalpic contribution of hydrogen bonding to the total free energy. We observe that in this region difference in enthalpy of hydrogen bonding of water compared with NH_3 reaches its minimum. Additionally, AQP4 seems to provide a platform for attracting NH_4^+ due to the preponderance of the acidic amino acids that decorate its either face. Speculatively, this could be a potential mechanism to facilitate the conversion of excess NH_4^+ into NH_3. The presence of the negatively charged surface amino acids could thus be of physiological relevance, as these residues could be catalytic sites for accelerating the rate of both forward and backward conversion of NH_3 to NH_4^+ and hence lead to a locally enhanced concentration of NH_3.

NH_4^+ is readily transported by a range of K^+ transporting mechanisms (7–16), whereas NH_3, probably due to its resemblance to water, appears to cross cell membranes by facilitated diffusion through a range of aquaporins, among which we here propose that AQP4 is featured. The cerebral glutamate-glutamine cycle encompasses vesicular release of glutamate from the presynapse with subsequent astrocytic uptake, amidation of glutamate to glutamine (a process requiring free ammonia), shuttling of glutamine to the neuronal structures, and its hydrolyzation to glutamate and ammonia. Due to the toxic property of ammonia, operation of the glutamate-glutamine cycle thus requires that astrocytes exhibit an efficient way of accumulat-

ing and removing ammonia (57). AQP4 is robustly expressed at the perivascular glial end-feet and covers ~50% of the surface area of this membrane (42, 58). It may, with this prime location at the interface between the brain and the blood, participate in facilitation of NH_3 permeation across the glial membrane both under physiological conditions and during hyperammonemia. Hyperammonemia occurs in association with various pathologies, among these acute liver failure, and associates with metabolic alkalosis (59). Increased plasma ammonia levels in combination with alkaline pH will thus, in combination, increase the fraction of ammonia existing as NH_3 and, therefore, even further enhance the AQP4-mediated brain accumulation of ammonia that is consistently observed during hepatic encephalopathy (35). AQP4 may, therefore, be a potential pharmaceutical target in the attempt to limit brain ammonia accumulation during hepatic encephalopathy.

Experimental Procedures

Molecular Biology—Rat AQP4.M23 and rat AQP8 was subcloned into the oocyte expression vector pXOOM, linearized downstream from the poly-A segment, and *in vitro* transcribed using T7 mMessage Machine (Ambion, Austin, TX) according to the manufacturer's instructions. MEGAclear (Ambion) was used to extract the cRNA before micro-injection into defolliculated *Xenopus laevis* oocytes.

Oocyte Preparation—X. laevis frogs were obtained from Nasco (Fort Atkinson, WI) or Xenopus Express (Le Bourg, Vernassal, France). All animal protocols comply with the European Community guidelines for the use of experimental animals, and were approved and performed under a license issued for the use of experimental animals by the Danish Ministry of Justice (Dyreforsøgstilsynet) or by The Landesuntersuchungsamt Rheinland-Pfalz (Koblenz, Germany). Oocytes were surgically removed, and their follicular membrane was removed by incubation in Kulori medium (90 mM NaCl, 1 mM KCl, 1 mM $CaCl_2$, 1 mM $MgCl_2$, 5 mM HEPES, pH 7.4) containing 10 mg/ml collagenase (Type 1, Worthington, Lakewood, NJ) and 1 mg/ml trypsin inhibitor (Sigma) as previously described (48). The oocytes were kept in Kulori medium at 18 °C to recover until the following day, at which time they were microinjected with cRNA encoding AQP4 or AQP8 (25 ng RNA/oocyte) and left at 18 °C for 3–5 days before experiments. All oocyte experiments were performed at room temperature.

Oocyte Volume Measurements—The experimental setup for measuring water permeability of oocytes has been described in detail previously (60). Briefly, the oocyte was placed in a small chamber with a glass bottom and perfused with a control solution at room temperature (95 mM NaCl, 2 mM KCl, 1 mM $CaCl_2$, 1 mM $MgCl_2$, 10 mM HEPES, 5 mM choline chloride, pH 7.4 or pH 8.0). The oocyte was viewed from below via a long distance objective, and oocyte images were captured continuously at a rate of 25 images/s. To determine the water permeability, the oocytes were challenged with a hyperosmotic solution (control solution containing either additional 20 mosM NaCl (10 mM) or 20 mosM NH_4Cl (10 mM)), osmolarities of all solutions verified with an accuracy of 1 mosM with an osmometer Type 15 (Löser Messtechnik, Berlin, Germany), and the water permeability was calculated as,

$$L_p = \frac{-J_v}{A \cdot \Delta\pi \cdot V_w} \quad \text{(Eq. 1)}$$

where Jv is the water flux during the osmotic challenge, A is the true membrane surface area (about nine times the apparent area due to membrane folding (Ref. 61), $\Delta\pi$ is the osmotic challenge, V_w is the partial molal volume of water (18 cm^3/mol), and L_p is the water permeability given in units of (cm/s).

The reflection coefficient for NH_4^+/NH_3, as previously described (22), was calculated as,

$$\sigma_s = \frac{L_{p,s}}{L_p} \quad \text{(Eq. 2)}$$

where $L_{p,s}$ is the apparent water permeability obtained with s as the osmolyte, in the present study NH[inf]4Cl, and L_p as the true osmotic water permeability obtained with an impermeable osmolyte, in the present study NaCl.

Electrophysiology—Conventional two-electrode voltage clamp studies were performed with a DAGAN CA-1B High Performance oocyte clamp (DAGAN, Minneapolis, MN) with DigiData 1322A interface controlled by pCLAMP software, version 9.2 (Axon Instruments, Burlingame, CA). The membrane potential was clamped at −50 mV and the current-voltage (I/V) relationship was determined by stepping the clamp potential from −50 mV to test potentials ranging from +40 mV to −120 mV in 20-mV increments (100-ms pulses). Currents measured at the holding potential were sampled at 5 Hz, and currents measured at the test potentials were low pass-filtered at 1 kHz and sampled at 2 kHz.

Intracellular pH Measurements—Changes in pH_i in oocytes were determined with ion-selective microelectrodes under voltage-clamp conditions. For measurement of intracellular pH and membrane potential, double-barreled microelectrodes were used; the manufacture and application have been described in detail previously (62). Electrodes were superfused with control solution (100 mM NaCl, 2 mM KCl, 1 mM $CaCl_2$, 1 mM $MgCl_2$, 10 mM HEPES, pH 7.4) for calibration, and after a stable electrode potential was reached, control solution pH 7.0 was applied until the electrode again reached a stable potential. The subsequent measurements of oocyte pH_i were stored digitally using homemade phosphocholine software. For two-electrode voltage clamp, a borosilicate glass capillary, 1.5 mm in diameter, was pulled to a micropipette and backfilled with 3 M KCl. This electrode was used for current injection and was connected to the head-stage of an Axoclamp 2A amplifier (Molecular Devices, Sunnyvale, CA). The actual membrane voltage was recorded by the reference barrel of the double-barreled pH-sensitive microelectrode. Oocytes were clamped to a holding potential of −40 mV. A stable pH_i baseline was obtained in control solution (100 mM NaCl, 2 mM KCl, 1 mM $CaCl_2$, 1 mM $MgCl_2$, 10 mM choline chloride, 10 mM HEPES, pH 7.4) before exposure of the oocytes to an isosmotic solution containing 10 mM NH_4Cl replacing choline chloride. Optimal pH_i changes were detected when the ion-selective electrode was located near the inner surface of the plasma membrane as described previously (63).

Molecular Dynamics Simulations—Molecular dynamics simulations were carried out with the software GROMACS 5.0

(64). The CHARMM36 force field was used for the AQP4 protein, ions, ammonia, ammonium, and the lipid parameters (65). The AQP4 protein was embedded in a patch with 361 POPC lipids and was solvated with ~27,000 CHARMM TIP3P explicit water molecules (66). The choice of the lipids was motivated by phosphocholine lipids (with mixed saturated-unsaturated tails) as the dominant lipids in eukaryotic cell membranes (67). Throughout the simulations, temperature and pressure were maintained at 310 K, 5 degrees above the lipid critical temperature and at 1 atm with a v-rescale thermostat and a Parrinello-Rahman barostat (68). An ionic strength of 150 mM NaCl was maintained to mimic physiological conditions. Explicit electrostatics were used with the Particle Mesh Ewald method for simulating long range interactions (69) with a cut-off of 1.2 nm, whereas the short range van der Waals interactions were simulated using a shift function with a switch at 0.8 nm and the cutoff at 1 nm. The crystal structure with a resolution of 0.18 nm (PDB code 3GD8) was used as the protein model (70). The package WHATIF (71) was used to predict the protonation of the protein residues at neutral pH conditions. Later analysis was carried out using GROMACS tools, the MDANALYSIS library (72), and the HOLE2.0 suite of programs (73).

Umbrella Sampling Simulations—To calculate the free energy profile of ammonia across the AQP4 channel, we used the US-enhanced sampling technique, as implemented in GROMACS. We used the WHAM algorithm to calculate the resulting PMF, and the statistical uncertainty associated with it was calculated via bootstrapping (74). To have unambiguous comparison between multiple profiles, we used a radial flat bottom potential as implemented in GROMACS 5.0 to constrain the ammonia molecule subjected to umbrella "pulling." This allowed us to take into account entropic and concentration effects of entering the channel from a given "bulk" volume surrounding the channel. The sampling itself was carried out with 280 windows, spread across 7 nm across and beyond the channel, with each window as small as 0.025 nm. A harmonic force of 500 $kJ{\cdot}mol^{-1}{\cdot}nm^{-1}$ was used to restrain the ammonia molecule in a given window. Each window was simulated for 6 ns, of which the first nanosecond was discarded during analysis to account for equilibration.

Statistics—Data are presented as the means ± S.E. Student's *t* test or analysis of variance with Šidák's multiple comparison post hoc test were used for the statistical analysis (GraphPrism 6.0, GraphPad, CA). A probability level of $p < 0.05$ was considered statistically significant. All oocyte experiments were carried out on individual oocytes obtained from at least three different animal donors.

Author Contributions—N. M. and M. A. designed, performed, and analyzed the experiments shown in Figs 2 and 4. B. L. de G. and S. K. designed, performed, and analyzed the experiments shown in Figs. 5–7. J. W. D. and H. P. S. designed, performed, and analyzed the experiments shown in Fig. 3. N. M., M. A., B. L. de G., and S. K. wrote the majority of the paper.

Acknowledgments—We greatly value the technical assistance provided by Charlotte Goos Iversen and Catia Correa Goncalves Andersen.

References

1. Rangroo Thrane, V., Thrane, A. S., Wang, F., Cotrina, M. L., Smith, N. A., Chen, M., Xu, Q., Kang, N., Fujita, T., Nagelhus, E. A., and Nedergaard, M. (2013) Ammonia triggers neuronal disinhibition and seizures by impairing astrocyte potassium buffering. *Nat. Med.* **19,** 1643–1648
2. Butterworth, R. F. (2002) Pathophysiology of hepatic encephalopathy: a new look at ammonia. *Metab. Brain Dis.* **17,** 221–227
3. Butterworth, R. F., Giguere, J. F., Michaud, J., Lavoie, J., and Layrargues, G. P. (1987) Ammonia: key factor in the pathogenesis of hepatic encephalopathy. *Neurochem. Pathol.* **6,** 1–12
4. Laursen, H., and Diemer, N. H. (1980) Morphometry of astrocyte and oligodendrocyte ultrastructure after portocaval anastomosis in the rat. *Acta Neuropathol.* **51,** 65–70
5. Cohn, R. M., and Roth, K. S. (2004) Hyperammonemia, bane of the brain. *Clin. Pediatr. (Phila.)* **43,** 683–689
6. Caner, T., Abdulnour-Nakhoul, S., Brown, K., Islam, M. T., Hamm, L. L., and Nakhoul, N. L. (2015) Mechanisms of ammonia and ammonium transport by rhesus-associated glycoproteins. *Am. J. Physiol. Cell Physiol.* **309,** C747–C758
7. Choe, H., Sackin, H., and Palmer, L. G. (2000) Permeation properties of inward-rectifier potassium channels and their molecular determinants. *J. Gen. Physiol.* **115,** 391–404
8. Chepilko, S., Zhou, H., Sackin, H., and Palmer, L. G. (1995) Permeation and gating properties of a cloned renal K^+ channel. *Am. J. Physiol.* **268,** C389–C401
9. Zhou, H., Tate, S. S., and Palmer, L. G. (1994) Primary structure and functional properties of an epithelial K channel. *Am. J. Physiol.* **266,** C809–C824
10. Edvinsson, J. M., Shah, A. J., and Palmer, L. G. (2011) Kir4.1 K^+ channels are regulated by external cations. *Channels* **5,** 269–279
11. Bachmann, O., Wüchner, K., Rossmann, H., Leipziger, J., Osikowska, B., Colledge, W. H., Ratcliff, R., Evans, M. J., Gregor, M., and Seidler, U. (2003) Expression and regulation of the Na^+-K^+-$2Cl^-$ cotransporter NKCC1 in the normal and CFTR-deficient murine colon. *J. Physiol.* **549,** 525–536
12. Bergeron, M. J., Gagnon, E., Wallendorff, B., Lapointe, J. Y., and Isenring, P. (2003) Ammonium transport and pH regulation by K^+-Cl^- cotransporters. *Am. J. Physiol. Renal Physiol.* **285,** F68–F78
13. Kinne, R., Kinne-Saffran, E., Schütz, H., and Schölermann, B. (1986) Ammonium transport in medullary thick ascending limb of rabbit kidney: involvement of the Na^+,K^+,Cl^- cotransporter. *J. Membr. Biol.* **94,** 279–284
14. Kurtz, I., and Balaban, R. S. (1986) Ammonium as a substrate for Na^+-K^+-ATPase in rabbit proximal tubules. *Am. J. Physiol.* **250,** F497–F502
15. Watts, B. A., 3rd, and Good, D. W. (1994) Effects of ammonium on intracellular pH in rat medullary thick ascending limb: mechanisms of apical membrane NH_4^+ transport. *J. Gen. Physiol.* **103,** 917–936
16. Blatz, A. L., and Magleby, K. L. (1984) Ion conductance and selectivity of single calcium-activated potassium channels in cultured rat muscle. *J. Gen. Physiol.* **84,** 1–23
17. Hamm, L. L., Trigg, D., Martin, D., Gillespie, C., and Buerkert, J. (1985) Transport of ammonia in the rabbit cortical collecting tubule. *J. Clin. Invest.* **75,** 478–485
18. Boron, W. F., Waisbren, S. J., Modlin, I. M., and Geibel, J. P. (1994) Unique permeability barrier of the apical surface of parietal and chief cells in isolated perfused gastric glands. *J. Exp. Biol.* **196,** 347–360
19. Yip, K. P., and Kurtz, I. (1995) NH_3 permeability of principal cells and intercalated cells measured by confocal fluorescence imaging. *Am. J. Physiol.* **269,** F545–F550
20. Loqué, D., Ludewig, U., Yuan, L., and von Wirén, N. (2005) Tonoplast intrinsic proteins AtTIP2;1 and AtTIP2;3 facilitate NH_3 transport into the vacuole. *Plant Physiol.* **137,** 671–680
21. Jahn, T. P., Møller, A. L., Zeuthen, T., Holm, L. M., Klaerke, D. A., Mohsin, B., Kühlbrandt, W., and Schjoerring, J. K. (2004) Aquaporin homologues in plants and mammals transport ammonia. *FEBS Lett.* **574,** 31–36
22. Holm, L. M., Jahn, T. P., Møller, A. L., Schjoerring, J. K., Ferri, D., Klaerke, D. A., and Zeuthen, T. (2005) NH_3 and NH_4^+ permeability in aquaporin-expressing *Xenopus* oocytes. *Pflugers Arch.* **450,** 415–428

23. Dynowski, M., Mayer, M., Moran, O., and Ludewig, U. (2008) Molecular determinants of ammonia and urea conductance in plant aquaporin homologs. *FEBS Lett.* **582,** 2458–2462
24. Bertl, A., and Kaldenhoff, R. (2007) Function of a separate NH_3-pore in Aquaporin TIP2;2 from wheat. *FEBS Lett.* **581,** 5413–5417
25. Hwang, J. H., Ellingson, S. R., and Roberts, D. M. (2010) Ammonia permeability of the soybean nodulin 26 channel. *FEBS Lett.* **584,** 4339–4343
26. Zeuthen, T., Wu, B., Pavlovic-Djuranovic, S., Holm, L. M., Uzcategui, N. L., Duszenko, M., Kun, J. F., Schultz, J. E., and Beitz, E. (2006) Ammonia permeability of the aquaglyceroporins from *Plasmodium falciparum*, *Toxoplasma gondii*, and *Trypanosoma brucei*. *Mol. Microbiol.* **61,** 1598–1608
27. Benga, O., and Huber, V. J. (2012) Brain water channel proteins in health and disease. *Mol. Aspects Med.* **33,** 562–578
28. Gomes, D., Agasse, A., Thiébaud, P., Delrot, S., Gerós, H., and Chaumont, F. (2009) Aquaporins are multifunctional water and solute transporters highly divergent in living organisms. *Biochim. Biophys. Acta* **1788,** 1213–1228
29. Musa-Aziz, R., Chen, L. M., Pelletier, M. F., and Boron, W. F. (2009) Relative CO_2/NH_3 selectivities of AQP1, AQP4, AQP5, AmtB, and RhAG. *Proc. Natl. Acad. Sci. U.S.A.* **106,** 5406–5411
30. Nakhoul, N. L., Hering-Smith, K. S., Abdulnour-Nakhoul, S. M., and Hamm, L. L. (2001) Transport of NH_3/NH in oocytes expressing aquaporin-1. *Am. J. Physiol. Renal Physiol.* **281,** F255–F263
31. Geyer, R. R., Musa-Aziz, R., Qin, X., and Boron, W. F. (2013) Relative CO_2/NH_3 selectivities of mammalian aquaporins 0–9. *Am. J. Physiol. Cell Physiol.* **304,** C985–C994
32. Beitz, E., Wu, B., Holm, L. M., Schultz, J. E., and Zeuthen, T. (2006) Point mutations in the aromatic/arginine region in aquaporin 1 allow passage of urea, glycerol, ammonia, and protons. *Proc. Natl. Acad. Sci. U.S.A.* **103,** 269–274
33. Vilas, G. L., Loganathan, S. K., Liu, J., Riau, A. K., Young, J. D., Mehta, J. S., Vithana, E. N., and Casey, J. R. (2013) Transmembrane water-flux through SLC4A11: a route defective in genetic corneal diseases. *Hum. Mol. Genet.* **22,** 4579–4590
34. Zhang, W., Ogando, D. G., Bonanno, J. A., and Obukhov, A. G. (2015) Human SLC4A11 is a novel NH_3/H^+ co-transporter. *J. Biol. Chem.* **290,** 16894–16905
35. Swain, M., Butterworth, R. F., and Blei, A. T. (1992) Ammonia and related amino acids in the pathogenesis of brain edema in acute ischemic liver failure in rats. *Hepatology* **15,** 449–453
36. Lockwood, A. H., Murphy, B. W., Donnelly, K. Z., Mahl, T. C., and Perini, S. (1993) Positron-emission tomographic localization of abnormalities of brain metabolism in patients with minimal hepatic encephalopathy. *Hepatology* **18,** 1061–1068
37. Rose, C. (2006) Effect of ammonia on astrocytic glutamate uptake/release mechanisms. *J. Neurochem.* **97,** 11–15
38. Rose, C., Kresse, W., and Kettenmann, H. (2005) Acute insult of ammonia leads to calcium-dependent glutamate release from cultured astrocytes, an effect of pH. *J. Biol. Chem.* **280,** 20937–20944
39. Søgaard, R., Novak, I., and MacAulay, N. (2012) Elevated ammonium levels: differential acute effects on three glutamate transporter isoforms. *Am. J. Physiol. Cell Physiol.* **302,** C880–C891
40. Norenberg, M. D., Rao, K. V., and Jayakumar, A. R. (2005) Mechanisms of ammonia-induced astrocyte swelling. *Metab. Brain Dis.* **20,** 303–318
41. O'Carroll, R. E., Hayes, P. C., Ebmeier, K. P., Dougall, N., Murray, C., Best, J. J., Bouchier, I. A., and Goodwin, G. M. (1991) Regional cerebral blood flow and cognitive function in patients with chronic liver disease. *Lancet* **337,** 1250–1253
42. Nielsen, S., Nagelhus, E. A., Amiry-Moghaddam, M., Bourque, C., Agre, P., and Ottersen, O. P. (1997) Specialized membrane domains for water transport in glial cells: high-resolution immunogold cytochemistry of aquaporin-4 in rat brain. *J. Neurosci.* **17,** 171–180
43. Bodega, G., Suárez, I., López-Fernández, L. A., García, M. I., Köber, M., Penedo, M., Luna, M., Juárez, S., Ciordia, S., Oria, M., Córdoba, J., and Fernández, B. (2012) Ammonia induces aquaporin-4 rearrangement in the plasma membrane of cultured astrocytes. *Neurochem. Int.* **61,** 1314–1324
44. Rama Rao, K. V., Chen, M., Simard, J. M., and Norenberg, M. D. (2003) Increased aquaporin-4 expression in ammonia-treated cultured astrocytes. *Neuroreport* **14,** 2379–2382
45. Liu, K., Nagase, H., Huang, C. G., Calamita, G., and Agre, P. (2006) Purification and functional characterization of aquaporin-8. *Biol. Cell* **98,** 153–161
46. Saparov, S. M., Liu, K., Agre, P., and Pohl, P. (2007) Fast and selective ammonia transport by aquaporin-8. *J. Biol. Chem.* **282,** 5296–5301
47. Meinild, A. K., Klaerke, D. A., and Zeuthen, T. (1998) Bidirectional water fluxes and specificity for small hydrophilic molecules in aquaporins 0–5. *J. Biol. Chem.* **273,** 32446–32451
48. Fenton, R. A., Moeller, H. B., Zelenina, M., Snaebjornsson, M. T., Holen, T., and MacAulay, N. (2010) Differential water permeability and regulation of three aquaporin 4 isoforms. *Cell. Mol. Life Sci.* **67,** 829–840
49. Hub, J. S., Winkler, F. K., Merrick, M., and de Groot, B. L. (2010) Potentials of mean force and permeabilities for carbon dioxide, ammonia, and water flux across a rhesus protein channel and lipid membranes. *J. Am. Chem. Soc.* **132,** 13251–13263
50. Kirscht, A., Kaptan, S. S., Bienert, G. P., Chaumont, F., Nissen, P., de Groot, B. L., Kjellbom, P., Gourdon, P., and Johanson, U. (2016) crystal structure of an ammonia-permeable aquaporin. *PLoS Biol.* **14,** e1002411
51. Burckhardt, B. C., and Frömter, E. (1992) Pathways of NH_3/ NH_4^+ permeation across *Xenopus laevis* oocyte cell membrane. *Pflugers Archiv.* **420,** 83–86
52. Boldt, M., Burckhardt, G., and Burckhardt, B. C. (2003) NH_4^+ conductance in *Xenopus laevis* oocytes. III. Effect of NH_3. *Pflugers Archiv.* **446,** 652–657
53. Cougnon, M., Bouyer, P., Hulin, P., Anagnostopoulos, T., and Planelles, G. (1996) Further investigation of ionic diffusive properties and of NH_4^+ pathways in *Xenopus laevis* oocyte cell membrane. *Pflugers Archiv.* **431,** 658–667
54. Sasaki, S., Ishibashi, K., Nagai, T., and Marumo, F. (1992) Regulation mechanisms of intracellular pH of *Xenopus laevis* oocyte. *Biochim. Biophys. Acta* **1137,** 45–51
55. Burckhardt, B. C., and Burckhardt, G. (1997) NH_4^+ conductance in *Xenopus laevis* oocytes. I. Basic observations. *Pflugers Archiv.* **434,** 306–312
56. Hub, J. S., and de Groot, B. L. (2008) Mechanism of selectivity in aquaporins and aquaglyceroporins. *Proc. Natl. Acad. Sci. U.S.A.* **105,** 1198–1203
57. Bak, L. K., Schousboe, A., and Waagepetersen, H. S. (2006) The glutamate/GABA-glutamine cycle: aspects of transport, neurotransmitter homeostasis, and ammonia transfer. *J. Neurochem.* **98,** 641–653
58. Wolburg, H. (1995) Orthogonal arrays of intramembranous particles: a review with special reference to astrocytes. *J. Hirnforsch.* **36,** 239–258
59. Adeva, M. M., Souto, G., Blanco, N., and Donapetry, C. (2012) Ammonium metabolism in humans. *Metab. Clin. Exp.* **61,** 1495–1511
60. Zeuthen, T., Belhage, B., and Zeuthen, E. (2006) Water transport by Na^+-coupled cotransporters of glucose (SGLT1) and of iodide (NIS): the dependence of substrate size studied at high resolution. *J. Physiol.* **570,** 485–499
61. Zampighi, G. A., Kreman, M., Boorer, K. J., Loo, D. D., Bezanilla, F., Chandy, G., Hall, J. E., and Wright, E. M. (1995) A method for determining the unitary functional capacity of cloned channels and transporters expressed in *Xenopus laevis* oocytes. *J. Membr. Biol.* **148,** 65–78
62. Deitmer, J. W. (1991) Electrogenic sodium-dependent bicarbonate secretion by glial cells of the leech central nervous system. *J. Gen. Physiol.* **98,** 637–655
63. Bröer, S., Schneider, H. P., Bröer, A., Rahman, B., Hamprecht, B., and Deitmer, J. W. (1998) Characterization of the monocarboxylate transporter 1 expressed in *Xenopus laevis* oocytes by changes in cytosolic pH. *Biochem. J.* **333,** 167–174
64. Abraham, M. J., Murtola, T., Schulz, R., Pall, S., Smith, J. C., Hess, B., and Lindahl, E. (2015) GROMACS: high performance molecular simulations through multi-level parallelism from laptops to supercomputers. *SoftwareX* **1–2,** 19–25
65. Huang, J., and MacKerell, A. D., Jr.(2013) CHARMM36 all-atom additive protein force field: validation based on comparison to NMR data. *J. Comput. Chem.* **34,** 2135–2145
66. Jorgensen, W. L., Chandrasekhar, J., Madura, J. D., Impey, R. W., and Klein, M. L. (1983) Comparison of simple potential functions for simulating liquid water. *J. Chem. Phys.* **79,** 926–935

67. van Meer, G., Voelker, D. R., and Feigenson, G. W. (2008) Membrane lipids: where they are and how they behave. *Nat. Rev. Mol. Cell Biol.* **9,** 112–124
68. Bussi, G., Donadio, D., and Parrinello, M. (2007) Canonical sampling through velocity rescaling. *J. Chem. Phys.* **126,** 014101
69. Darden, T., York, D., and Pedersen, L. (1993) Particle mesh Ewald: an N. log(N) method for Ewald sums in large systems. *J. Chem. Phys.* **98,** 10089–10092
70. Ho, J. D., Yeh, R., Sandstrom, A., Chorny, I., Harries, W. E., Robbins, R. A., Miercke, L. J., and Stroud, R. M. (2009) Crystal structure of human aquaporin 4 at 1.8 angstrom and its mechanism of conductance. *Proc. Natl. Acad. Sci. U.S.A.* **106,** 7437–7442
71. Vriend, G. (1990) What if: a molecular modeling and drug design program. *J. Mol. Graph.* **8,** 52–56
72. Michaud-Agrawal, N., Denning, E. J., Woolf, T. B., and Beckstein, O. (2011) Software news and updates MDAnalysis: a toolkit for the analysis of molecular dynamics simulations. *J. Comput. Chem.* **32,** 2319–2327
73. Smart, O. S., Goodfellow, J. M., and Wallace, B. A. (1993) The pore dimensions of gramicidin-A. *Biophys. J.* **65,** 2455–2460
74. Hub, J. S., Aponte-Santamaría, C., Grubmüller, H., and de Groot, B. L. (2010) Voltage-regulated water flux through aquaporin channels *in silico*. *Biophys. J.* **99,** L97–L99

Received: 15 February 2017 | Revised: 9 June 2017 | Accepted: 23 June 2017

DOI: 10.1002/glia.23187

GLIA
WILEY

RESEARCH ARTICLE

Activity-dependent astrocyte swelling is mediated by pH-regulating mechanisms

Brian Roland Larsen | Nanna MacAulay

Faculty of Health and Medical Sciences, Center for Neuroscience, University of Copenhagen, Copenhagen, Denmark

Correspondence
Nanna MacAulay, Faculty of Health and Medical Sciences, Center for Neuroscience, University of Copenhagen, Blegdamsvej 3, 2200 Copenhagen N, Denmark.
Email: macaulay@sund.ku.dk

Funding information
Lundbeck Foundation, Grant/Award Number: R151-2013-14120; Novo Nordisk Foundation, Grant/Award Number: NNF15OC0017052

Abstract

During neuronal activity in the mammalian brain, the K^+ released into the synaptic space is initially buffered by the astrocytic compartment. In parallel, the extracellular space (ECS) shrinks, presumably due to astrocytic cell swelling. With the $Na^+/K^+/2Cl^-$ cotransporter and the Kir4.1/AQP4 complex not required for the astrocytic cell swelling in the hippocampus, the molecular mechanisms underlying the activity-dependent ECS shrinkage have remained unresolved. To identify these molecular mechanisms, we employed ion-sensitive microelectrodes to measure changes in ECS, $[K^+]_o$ and $[H^+]_o/pH_o$ during electrical stimulation of rat hippocampal slices. Transporters and receptors responding directly to the K^+ and glutamate released into the extracellular space (the K^+/Cl^- cotransporter, KCC, glutamate transporters and G protein-coupled receptors) did not modulate the extracellular space dynamics. The HCO_3^--transporting mechanism, which in astrocytes mainly constitutes the electrogenic Na^+/HCO_3^- cotransporter 1 (NBCe1), is activated by the K^+-mediated depolarization of the astrocytic membrane. Inhibition of this transporter reduced the ECS shrinkage by ~25% without affecting the K^+ transients, pointing to NBCe1 as a key contributor to the stimulus-induced astrocytic cell swelling. Inhibition of the monocarboxylate cotransporters (MCT), like-wise, reduced the ECS shrinkage by ~25% without compromising the K^+ transients. Isosmotic reduction of extracellular Cl^- revealed a requirement for this ion in parts of the ECS shrinkage. Taken together, the stimulus-evoked astrocytic cell swelling does not appear to occur as a *direct effect* of the K^+ clearance, as earlier proposed, but partly via the pH-regulating transport mechanisms activated by the K^+-induced astrocytic depolarization and the activity-dependent metabolism.

KEYWORDS
extracellular space dynamics, MCT, NBCe1, volume regulation, water transport

1 | INTRODUCTION

During synaptic activity, K^+ is released into the extracellular space of the brain. To prevent wide-spread depolarization caused by K^+ accumulation, the surrounding glia cells take up K^+ by means of the Na^+/K^+-ATPase, to a certain extent aided by Kir4.1-mediated spatial buffering (Hertz, Song, Xu, Peng, & Gibbs, 2015; Kofuji & Newman, 2004; Larsen et al., 2014; Larsen, Holm, Vilsen, & MacAulay, 2016; Walz, 2000). Glial cells thus act as K^+ sinks during neuronal activity. The network activity and resultant rise in extracellular $[K^+]$ occurs in parallel to a shrinkage of the ECS, a phenomenon attributed to swelling of adjacent cells (Connors, Ransom, Kunis, & Gutnick, 1982; Dietzel, Heinemann, Hofmeier, & Lux, 1980; Ransom, Yamate, & Connors, 1985). The cell swelling has been assigned to astrocytic structures as it persists in enucleated optic nerve (MacVicar, Feighan, Brown, & Ransom, 2002) and is absent in optic nerve of young rats at a developmental age prior to maturation of glial cells (Ransom et al., 1985), although a contribution from the neuronal compartment cannot be excluded (Pál, Nyitrai, Kardos, & Héja, 2013). However, the molecular mechanisms underlying the activity-dependent glia cell swelling remain unresolved: As the ECS shrinkage parallels the stimulus-induced $[K^+]_o$ transients, K^+-transporting mechanisms such as the $Na^+/K^+/2Cl^-$ cotransporter type 1 (NKCC1) and the inwardly rectifying K^+ channel Kir4.1 were proposed as molecular candidates underlying the glial cell swelling (MacAulay & Zeuthen, 2012; Nagelhus, Mathiisen, & Ottersen, 2004). NKCC1 via its ability to translocate water (Zeuthen & MacAulay, 2012a) and Kir4.1 via an association with AQP4 (Nagelhus et al., 2004). Experimental evidence, however, illustrated that NKCC1 was not involved in stimulus-induced ECS shrinkage in rat

hippocampal brain slices (Larsen et al., 2014; Pál et al., 2013), which aligned well with the negligible NKCC1 expression in astrocytes in vivo (Plotkin et al., 1997; Zhang et al., 2014), despite its robust expression in cultured astrocytes (Larsen et al., 2014; Su, Haworth, Dempsey, & Sun, 2000; Walz, 1992). Both genetic ablation (Haj-Yasein et al., 2011) and pharmacological experiments (Larsen et al., 2014) revealed that activity-dependent glial swelling occurred independently of Kir4.1-mediated spatial buffering, thus ruling out its contribution to this phenomenon. Astrocytes express high levels of the water channel AQP4 in their endfeet (Nielsen et al., 1997), which could provide a direct entry-way for water provided an osmotic gradient favoring astrocytic water influx. However, mice with genetic ablation of AQP4 presented with either identical (*stratum pyramidale*) or even *increased* (*stratum radiatum*) stimulus-induced ECS shrinkage in the hippocampal brain region (Haj-Yasein et al., 2012), thereby ruling out AQP4 as a molecular mediator of activity-induced glia cell swelling. Taken together, the activity-dependent extracellular space shrinkage does not appear to be directly coupled to the mechanism of K^+ clearance from the extracellular space and may, in addition, not exclusively rely on a simple build-up of osmotic particles. As the K^+ transients often occur alongside synaptic glutamate release and extracellular pH fluctuations, we set out to determine the role of membrane transporters, regulated by these factors, in extracellular space shrinkage in the face of neuronal network activity.

2 | MATERIALS AND METHODS

2.1 | Brain slices and solutions

Experiments were performed on male rats (Sprague-Dawley, Janvier Labs, France) at P21-P30. Rats were anaesthetized using gaseous 2-Bromo-2-Chloro-1,1,1-Trifluoroethane (B-4388, Sigma-Aldrich, Germany). Following decapitation, the brain was quickly removed and placed into ice-cold cutting solution containing (in mM): 87 NaCl, 70 sucrose, 2.5 KCl, 0.5 $CaCl_2$, 25 $NaHCO_3$, 1.1 NaH_2PO_4, 7 $MgCl_2$, and 25 D-glucose, equilibrated with gaseous 95% O_2, 5% CO_2. Oblique sagittal (transverse) hippocampal slices (400 μm) were cut with a Campden Vibrating Microtome (7000SMZ-2, Campden Instruments, UK). Slices were transferred to the standard artificial cerebrospinal fluid (aCSF) solution containing (in mM): 124 NaCl, 3 KCl, 2 $CaCl_2$, 25 $NaHCO_3$, 1.1 NaH_2PO_4, 2 $MgCl_2$ and 10 D-glucose, and equilibrated with 95% O_2, 5% CO_2 (pH 7.4 at the experimental temperature of 33–34°C) and left to recover at 34°C for 30 min and then kept at room temperature. For experiments with reduction in Cl^-, the aCSF contained (in mM): 124 Na-gluconate, 3 KCl, 2 $CaCl_2$, 25 $NaHCO_3$, 1.1 NaH_2PO_4, 2 $MgCl_2$, 10 D-glucose, osmolarity adjusted with mannitol (5–10 mM) and tested with an osmometer (Löser, Type 15) to ensure isosmotic conditions (±1–2 mOsm of standard aCSF).

2.2 | Ion-sensitive microelectrodes and electrophysiological recordings in slices

Electrophysiological recordings were carried out in a submerged-type recording chamber (Brain Slice Chamber 1, Scientific Systems Design, Digitimer Ltd, UK) at an experimental temperature of 33–34°C and a continuous superfusion at a flow rate of 2.2 ml/min. Recordings were performed within *stratum radiatum* of the CA1 region. High-frequency stimulation (HFS) was delivered by a concentric bipolar tungsten electrode (TM33CCNON, World Precision Instruments, UK) inserted into the stratum radiatum in the vicinity (≤500 μm) of the recording site. Stimulation trains (20–23 V at 20 Hz for 3 s) were delivered at 10 min intervals. The resulting extracellular field potentials were recorded with thin-walled filamented glass capillary microelectrodes (GC150TF-7.5, Harvard Apparatus, MA) pulled to resistances of 15–25 MΩ when filled with the standard solution (see above). This electrode served as reference signal for the ion-sensitive microelectrodes. Ion-sensitive microelectrodes were prepared from thin-walled nonfilamented glass capillaries (GC150T–7.5, Harvard Apparatus, MA) pulled to obtain a tip diameter in the range of 1–2 μm (Voipio, Pasternack, & MacLeod, 1994). The capillaries were then silanized internally with gaseous N,N-dimethyltrimethylsilylamine (cat. no. 41716, Sigma Aldrich, Germany) and baked at 180°C for 20 min prior to being backfilled. The electrodes were backfilled with a solution pending on the type of measurement, containing either 150 mM tetramethylammonium (TMA^+) chloride (for extracellular space volume measurements), 150 mM NaCl, 3 mM KCl (for extracellular K^+ measurements), or 150 mM NaCl, 20 mM HEPES, 10 mM NaOH (for extracellular pH/H^+ measurements). The tip of the capillary was afterwards filled with a short column of either TMA^+/K^+-sensitive liquid membrane solution (IE190, World Precision Instruments, UK), or H^+-sensitive liquid membrane solution (Hydrogen ionophore II—cocktail A, cat. no. 95297, Sigma Aldrich, Germany). For experiments with TMA^+, 1.5 mM TMA-Cl was included in the test solution. Note that the TMA^+/K^+ membrane is highly sensitive to quarternary ions, such as TMA^+, however in the absence of such ions it becomes selective to K^+ ions, and can therefore be used for both measurements.

The tips of the ion-sensitive electrode and the reference electrode were placed within a few microns at the exact same depth in the core of the slice. Distance was ensured via Sensapex micromanipulators (SMX series, Sensapex, Finland), which provide precise μm *x*,*y*,*z* coordinates, by placing the electrode tips closely together above the slice and afterwards moving into the tissue maintaining this narrow distance. The ion-sensitive signal and the field potential signal were both recorded via an ION-01M amplifier and headstage (NPI electronics, Germany). All recorded signals were filtered at 250 Hz, sampled at 500 Hz and stored for off-line analysis with WinEDR (courtesy of Dr. John Dempster, University of Strathclyde, Glasgow, UK) and GraphPad Prism 7.0 (GraphPad Software, CA). The ion-sensitive microelectrodes were calibrated at the end of the experiments and the recorded signals were converted off line to obtain either the % volume change, the K^+ concentration, or the mV change corresponding to Δ1.0 pH (Voipio et al., 1994). For all experiments, at least three consecutive control responses were recorded at intervals of 10 min prior to bath application of drug. Time estimates of drug penetration into the recording site in the brain slice were obtained by determination of the wash-in time of TMA^+, which will shift the potential of the electrode due to the nature of the liquid membrane (see above). The exact diffusion

properties within the brain slice tissue are likely to differ between drugs but their transit time in the perfusion system should be identical. Using these time estimates, drugs were allowed to enter the slice and then incubate for either 1 min (TBOA), 6–7 min (LY341495, amiloride, and 4-CIN), 8–9 min (DIDS), or 16 min (furosemide).

2.3 | Drugs

Furosemide (cat. no. F4381, Sigma Aldrich) used at 1 mM to block KCC and NKCC transporters, DIDS, 4,4′-Diisothiocyanato-2,2′-stilbenedisulfonic acid (cat. no. D3514, Sigma Aldrich) used at 300 μM to block bicarbonate transporters and anion-exchangers, and 4-CIN, α-cyano-4-hydroxycinnamic acid (cat. no. C2020, Sigma Aldrich) used at 500 μM to block monocarboxylate transporters were dissolved directly in aCSF prior to use. DL-TBOA, DL-*threo*-β-Benzyloxyaspartic acid (cat. no. 1223, Tocris) used at 200 μM to block the glutamate transporters (EAAT1–5) and amiloride (cat. no. A7419, Sigma Aldrich) used at 100 μM to block NHE1 were prepared in stocks of 100 mM in DMSO. LY341495, (2*S*)-2-Amino-2-[(1*S*,2*S*)-2-carboxycycloprop-1-yl]-3-(xanth-9-yl) propanoic acid (cat. no 4062, Tocris) used at 95 μM to block mGluR1–5, 7–8 was prepared in stock of 95 mM in dH_2O.

2.4 | Statistics

All data are given as mean ± *SEM*. Statistical significance was tested with Student's *t*-test or one-way ANOVA with Tukey's multiple comparison post hoc test, as indicated in figure legends. p values $< .05$ were considered statistically significant. The number of experiments, *n*, signifies individual brain slices and are mentioned in the Result section, whereas the number of animals from which these slices have been obtained are included in the Figure legends.

3 | RESULTS

To evaluate the contribution of different molecular transport mechanisms in extracellular space shrinkage during neuronal activity, we approximated a native setting by employing acute hippocampal slices from rat. The relative change in size of the extracellular space (ΔECS) during electrical stimulation of the CA1 Schaffer collaterals was monitored with tetramethyl ammonium (TMA^+)-sensitive microelectrodes upon bath application of 1.5 mM TMA^+ and the K^+ transients recorded with K^+-sensitive microelectrodes (see Figure 1a for a schematic of the experimental design). Electrical stimulation (20Hz, 3 s) of the slice gave rise to field potentials (a representative of which is illustrated in Figure 1a) and caused transient $[K^+]_o$ increases of 2–10 mM. The associated stimulus-induced increase in TMA^+ concentration represented a robust and stable read-out of the extracellular space shrinkage (2–14% in this experimental series). Consecutive stimuli (at 10 min intervals) resulted in identical relative changes of the extracellular space and K^+ transients (and pH shifts, see later, Figure 1b–d), thereby allowing an experimental pharmacological strategy, in which each slice served as its own control. To limit changes in basal ion concentrations and pH following prolonged inhibitor application, the slice was exposed

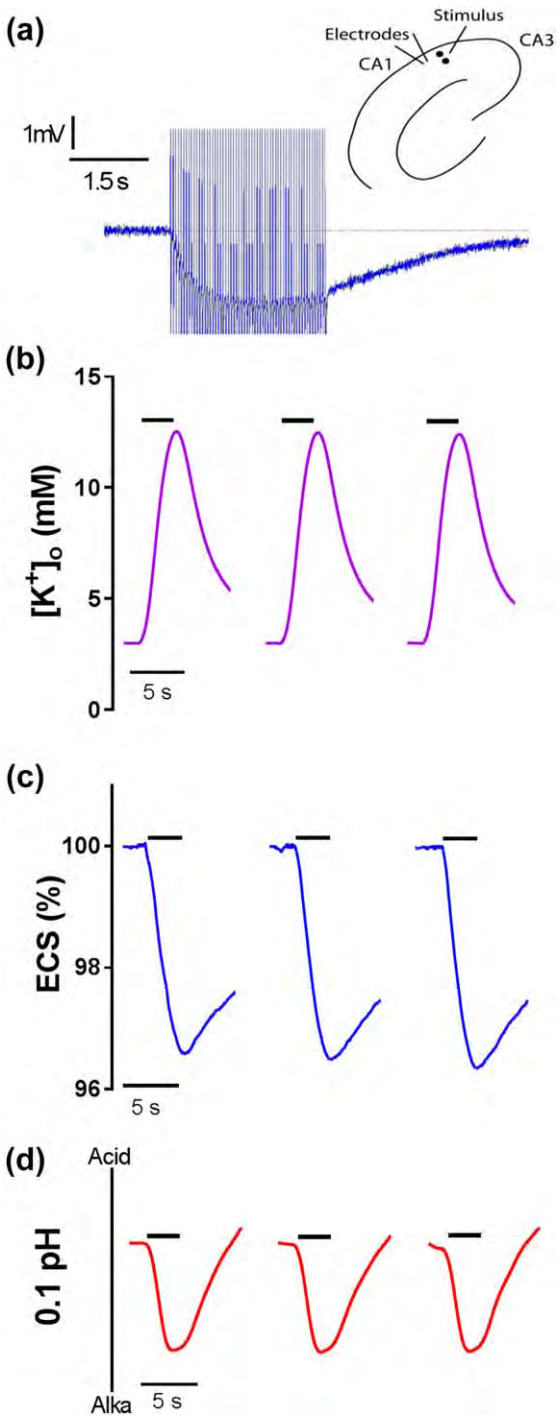

FIGURE 1 Ion-sensitive microelectrodes were employed to measure either extracellular K^+, the relative size of the ECS or pH (H^+). (a) Rat hippocampal slices were electrically stimulated in the Schaffer collaterals of CA1 *stratum radiatum*, with the ion-sensitive- and reference electrodes placed further along the Schaffer collateral pathway. A representative recording of the reference field potential is shown. (b–d) Representative traces of stimulus-evoked changes are shown for $[K^+]_o$ (b), the relative size of ECS (c) and pH_o (d), recorded at 10 min intervals to illustrate equal amplitudes in the various scenarios over time. The black bar above the respective traces represents 20 Hz stimulation [Color figure can be viewed at wileyonlinelibrary.com]

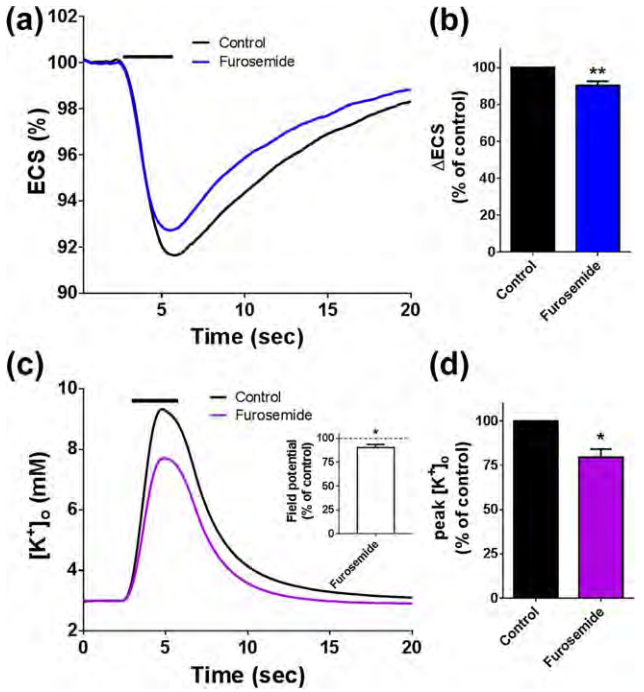

FIGURE 2 KCC-mediated contribution to K^+ and ECS dynamics measured with ion-sensitive microelectrodes. (a) Representative traces of stimulus-evoked changes in ECS prior to and after exposure to 1 mM furosemide. (b) The amplitude of the ECS change in the presence of furosemide was normalized to the control and summarized ($n = 7$ slices from 7 rats). (c) Representative traces of stimulus-evoked changes in extracellular K^+ prior to and after exposure to 1 mM furosemide. Insert shows the normalized and summarized peak amplitude of the reference field potential in the presence of furosemide (90.1 ± 3.6% of control, $n = 12$ slices from 12 rats). (d) The peak level of $[K^+]_o$ in the presence of furosemide was normalized to the control and summarized ($n = 5$ slices from 5 rats). The black bar above the respective traces represents 20 Hz stimulation. Statistical significance was tested with Student's paired *t* test. *; $p < .05$, **; $p < .01$ [Color figure can be viewed at wileyonlinelibrary.com]

to minimal incubation time of the pharmacological agents (see Materials and Methods section).

3.1 | The K^+/Cl^- cotransporter affects the neuronal activity but does not contribute to stimulus-induced extracellular space shrinkage

Astrocytes express the K^+/Cl^- cotransporter, KCC (Le Rouzic et al., 2006; Pearson, Lu, Mount, & Delpire, 2001), which is generally poised to expel its substrates from the cell. However, when faced with increased extracellular K^+ concentrations, KCCs may revert to inwardly directed transport and could as such contribute to K^+ clearance and/or extracellular space shrinkage. A stimulus-induced volume trace was obtained in the hippocampal slice and repeated after bath application of the KCC inhibitor furosemide (1 mM; Gillen, Brill, Payne, & Forbush, 1996; Race et al., 1999)), see representative traces in Figure 2a. The peak ΔECS was reduced in the presence of furosemide (to 90.3 ± 2.4% of control, $n = 7$, $p < .01$), normalized and summarized data in Figure 2b. Furosemide has previously been proposed to affect neuronal signaling, and thereby alter the K^+ release, via its effect on the neuronal KCC (Löscher, Puskarjov, & Kaila, 2013; Staley, 2002), which indirectly could cause the observed reduction in extracellular space shrinkage. Consequently, we determined the K^+ dynamics in the presence of furosemide and observed a reduced peak $[K^+]_o$ amplitude (79.5 ± 4.5% of control, $n = 5$, $p < .05$), representative traces in Figure 2c and normalized and summarized data in Figure 2d. Although these results, at first approximation, suggested KCC-dependent glial volume changes, the reduced amplitude of the field potentials recorded during the stimulation paradigm (90.1 ± 3.6% of controls, $n = 12$, $p < .05$, see insert in Figure 2c), revealed a compromised excitability (further illustrated by the diminished K^+ release) from the neuronal population upon application of furosemide. The data, when taken together, exclude a significant contribution of KCC in stimulus-induced K^+ clearance and glial volume dynamics.

3.2 | Glutamate transporter activity and metabotropic glutamatergic cell signaling are not required for stimulus-induced glia cell swelling

The glutamate released into the synaptic space during stimulation of the hippocampal neuronal population is swiftly cleared from the extracellular space by the action of the Na^+-coupled glutamate transporters, GLT1 and GLAST, highly expressed in the neighbor astrocytes (Danbolt, 2001). To test if this transport activity caused glia cell swelling, the effect of bath application of the noncompetitive glutamate transport blocker TBOA (200 μM; IC_{50} for TBOA ~6 μM for GLT1 and ~70 μM for GLAST (Shigeri et al., 2001; Shimamoto et al., 1998; Waagepetersen, Shimamoto, & Schousboe, 2001)) was evaluated. Prolonged exposure of TBOA leads to spontaneous activity due to inefficient removal of glutamate (Campbell & Hablitz, 2004; Karus, Mondragão, Ziemens, & Rose, 2015; Tsukada, Iino, Takayasu, Shimamoto, & Ozawa, 2005). Consequently, we recorded the stimulus-induced ΔECS 1 min after introduction of TBOA into the experimental chamber, at which point no spontaneous activity was detected. Exposure to TBOA led to a significant increase in stimulus-induced ΔECS (143.6 ± 9.9% of control, $n = 8$, $p < .05$), see representative traces in Figure 3a and normalized and summarized data in Figure 3b, despite undisturbed field potential amplitudes (Figure 3a, insert). The increased ΔECS most likely reflects the increased K^+ transients observed upon inhibition of the glutamate transporters, illustrated as dashed traces in Figure 3a (adapted from Larsen et al. (2016)). Although the TBOA-mediated effect on the K^+ transients complicates direct quantification, these data indicate a lack of glutamate transporter-mediated glia cell swelling in the present context. The glutamate released into the extracellular space acts, in addition, on the metabotropic glutamate receptors (mGluR), also present in the astrocytic compartment (Aronica et al., 2000; Schools & Kimelberg, 1999). To test if inhibition of the mGluRs prevented stimulus-induced ECS shrinkage, the inhibitor LY341495 (95 μM; IC_{50}s ranging from 0.001 to 22 μM (Fitzjohn et al., 1998)) was bath applied during the stimulation paradigm. Inhibitor application did not affect the field

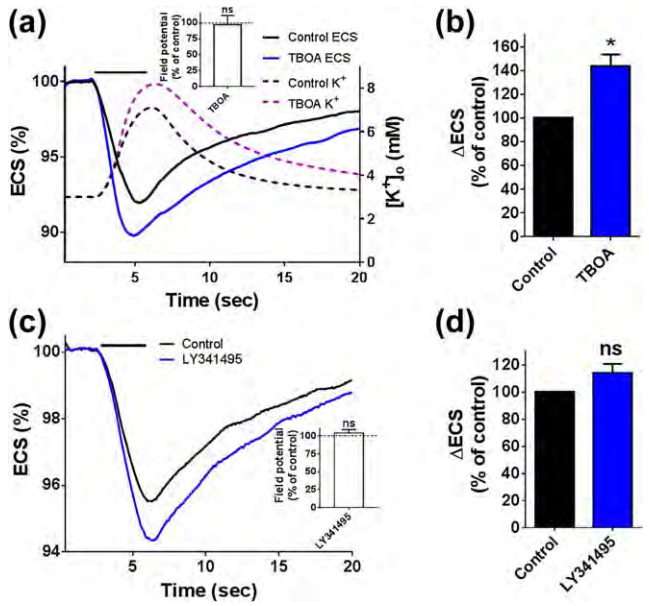

FIGURE 3 Glutamate transporter/receptor-mediated contribution to K^+ and ECS dynamics measured with ion-sensitive microelectrodes. (a) Representative traces of stimulus-induced changes in the ECS prior to and after exposure to TBOA. Additionally, the stimulus-induced changes in $[K^+]_o$ prior to and after exposure to TBOA are illustrated, courtesy of Larsen et al. (2016). Insert shows the normalized and summarized peak amplitude of the reference field potential in the presence of TBOA (96.7 ± 14.7% of control, $n = 8$ slices from 6 rats). (b) The change in ECS in the presence of TBOA was normalized to the control and summarized ($n = 8$ slices from 6 rats). (c) Representative traces of stimulus-evoked changes in ECS before and following addition of LY341495. Insert shows the normalized and summarized peak amplitude of the reference field potential in the presence of LY341495 (104.2 ± 4.7% of control, $n = 4$ slices from 3 rats). (d) The change in ECS in the presence of LY341495 was normalized to the control and summarized ($n = 4$ slices from 3 rats). The black bar above the respective traces represents 20 Hz stimulation. Statistical significance was tested with Student's paired *t* test. *; $p < .05$, ns; not significant [Color figure can be viewed at wileyonlinelibrary.com]

potential amplitude (insert) or the stimulus-induced ECS shrinkage (ΔECS: 114.2 ± 6.7% of control, $n = 4$, $p = .13$), see representative traces in Figure 3c and normalized and summarized data in Figure 3d, thus excluding mGluRs as mediators of stimulus-induced glia cell swelling.

3.3 | The pH-regulating Na^+-coupled bicarbonate cotransporter mediates stimulus-induced extracellular space shrinkage

As the stimulus-induced extracellular space shrinkage apparently did not arise via action of the membrane transport proteins involved in clearance of synaptically released K^+ and glutamate (this study and (Larsen et al., 2014)), it must thus be promoted by alternative transport mechanisms. During neuronal stimulation, the K^+ transient is mirrored by the shrinkage of ECS. The temporal pattern of these extracellular dynamics is, in addition, mimicked by pH changes in the extracellular space, see Figure 4a for representative K^+, ΔECS and pH traces recorded in separate rat hippocampal slices with K^+-, TMA^+-, and pH-sensitive microelectrodes. The extracellular space is rapidly alkalinized at the onset of the electrical stimulation followed by a slower acidic shift in the wake of network activity. While the responses (K^+, ECS, pH) peak in parallel, the return to baseline occurs noticeably faster for $[K^+]_o$ than for ΔECS and, even more pronounced, for the pH changes. The parallel transients may suggest that molecular transport mechanisms influenced by/influencing pH could be mediators of stimulus-induced glial cell volume changes. To test if the Na^+/H^+ exchanger (NHE1), which is expressed in astrocytes (Hwang et al., 2008; Theparambil, Ruminot, Schneider, Shull, & Deitmer, 2014), modulates the stimulus-induced extracellular space dynamics, amiloride (100 μM; Pizzonia, Ransom, & Pappas, 1996)) was bath applied during the stimulus paradigm. Amiloride had no effect on the field potentials (insert) or the ΔECS amplitude during stimulation (108.7 ± 4.5% of control, $n = 7$, $p = .1$), see representative traces in Figure 4b and normalized and summarized data in Figure 4c. The electrogenic Na^+/HCO_3^- cotransporter 1 (NBCe1) is the major astrocytic bicarbonate transporter (Theparambil et al., 2014; Zhang et al., 2014). The membrane depolarization that occurs as a consequence of stimulus-induced rise in $[K^+]_o$ promotes inwardly directed Na^+-driven HCO_3^- cotransport (Deitmer & Szatkowski, 1990; Theparambil et al., 2014) which could modulate the glia cell volume. Inhibition of bicarbonate transporters by application of DIDS (300 μM; McAlear, Liu, Williams, McNicholas-Bevensee, & Bevensee, 2006)) caused a significant reduction in the stimulus-induced ECS change (to 72.9 ± 5.1% of control, $n = 9$, $p < .001$), see representative traces in Figure 4d and normalized and summarized data in Figure 4e, with no effect on the field potential amplitude (insert). Application of DIDS (at the applied time scale) did not affect the stimulus-induced peak $[K^+]_o$ transient (95.2 ± 3.7% of control, $n = 8$, $p = .23$), see Figure 4f for representative traces and Figure 4g for normalized and summarized data. These results suggest that NBCe1 activity did indeed modulate the stimulus-induced ΔECS directly. We verified the action of DIDS on NBCe1 by recording pH in the extracellular space during the stimulus. Application of DIDS caused an enhanced peak alkalization (131.3 ± 4% of control, $n = 7$, $p < .001$), see Figure 4h for representative traces and normalized and summarized data in Figure 4i. This shift in peak alkalization is indicative of prevention of NBCe1 from transporting HCO_3^- into the astrocytes, causing accumulation of extracellular HCO_3^- during the stimulus phase and thereby a larger alkaline shift. Comparison of the difference between the peak alkaline shift and the subsequent peak acidic shift, revealed that DIDS did not cause a significant change in the post-stimulus acidification of the extracellular space (99.5 ± 2.5% of control, $n = 7$, $p = .85$). These data support the notion of NBCe1 acting out its role during the stimulus-induced increase in K^+ and the associated alkalization of the extracellular space, and causing astrocytic cell swelling in the process.

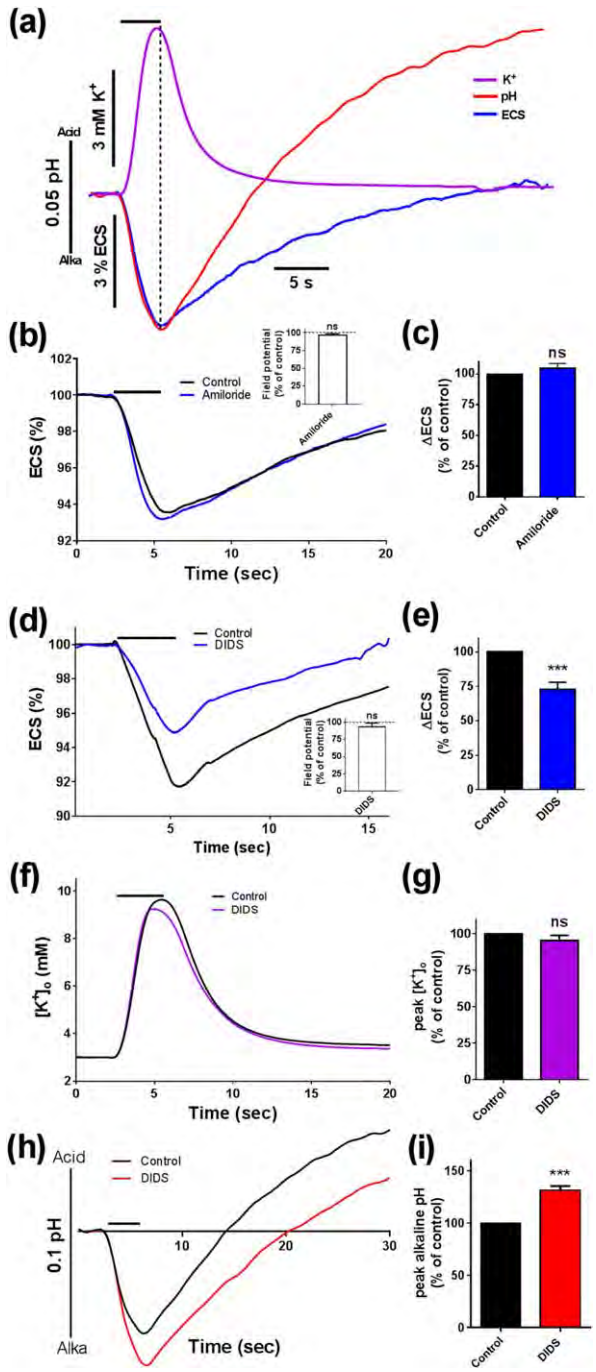

FIGURE 4 Bicarbonate transporter-mediated contribution to K^+, ECS, and pH_o dynamics measured with ion-sensitive microelectrodes. (a) Comparison of three representative traces of ECS, $[K^+]_o$, and pH_o from three individual experiments. (b) Representative traces of stimulus-induced changes in the ECS prior to and following application of amiloride. Insert shows the normalized and summarized peak amplitude of the reference field potential in the presence of amiloride (96.6 ± 2.1% of control, $n = 7$ slices from 6 rats). (c) The change in the ECS in the presence of amiloride was normalized to the control and summarized ($n = 7$ slices from 6 rats). (d) Representative traces of stimulus-induced changes in the ECS prior to and after exposure to DIDS. Insert shows the normalized and summarized peak amplitude of the reference field potential in the presence of DIDS (93.5 ± 5.4% of control, $n = 24$ slices from 15 rats). (e) The change in the ECS in the presence of DIDS was normalized to the control and summarized ($n = 9$ slices from 7 rats). (f) Representative traces of stimulus-induced changes in extracellular K^+ before and after application of DIDS. (g) The change in $[K^+]_o$ in the presence of DIDS was normalized to the control and summarized ($n = 8$ slices from 4 rats). (h) Representative traces of stimulus-induced changes in extracellular pH prior to and after exposure to DIDS. (i) The peak of the initial fast alkaline shift in pH_o in the presence of DIDS was normalized to the control and summarized ($n = 7$ slices from 4 rats). The black bar above the respective traces represents 20 Hz stimulation. Statistical significance was tested with Student's paired t test. ***; $p < .001$, ns; not significant [Color figure can be viewed at wileyonlinelibrary.com]

3.4 | The lactate-transporting MCTs mediate stimulus-induced extracellular space shrinkage

During the initial phase (seconds) of neuronal activation, the lactate concentration in the extracellular space may drop on a time scale comparable to the ECS changes (prior to the delayed and prolonged build-up of lactate) (Hu & Wilson, 1997; Mangia et al., 2003). This rapid lactate fluctuation indicates a possible activation of the H^+-coupled monocarboxylate transporters (MCTs), of which several isoforms are present on neurons and glia (Bergersen et al., 2001; Leino, Gerhart, & Drewes, 1999; Pierre, Magistretti, & Pellerin, 2002; Pierre, Pellerin, Debernardi, Riederer, & Magistretti, 2000; Rafiki, Boulland, Halestrap, Ottersen, & Bergersen, 2003). To determine if these transporters contribute to stimulus-induced extracellular space shrinkage, we bath-applied the MCT inhibitor 4-CIN (500 μM; Dimmer, Friedrich, Lang, Deitmer, & Bröer, 2000; Fox, Meredith, & Halestrap, 2000)) during the stimulation paradigm and obtained a significant decrease in the ECS shrinkage (to 74.8 ± 4.6% of control, $n = 6$, $p < .01$), see representative traces in Figure 5a and normalized and summarized data in Figure 5b. 4-CIN did not compromise the field potential amplitude (Figure 5a, insert) or the K^+ transients (102.6 ± 7.4% of controls, $n = 5$, $p = .75$), see representative traces in Figure 5c and normalized and summarized data in Figure 5d, indicating that MCT activation affects the extracellular space shrinkage directly. While not being considered a pH-regulating mechanism, MCTs hold the capability of influencing pH due to the cotransport of H^+. Inhibition of MCTs with 4-CIN slightly but significantly reduced the stimulus-induced alkaline shift (to 90.0 ± 2.6% of control, $n = 7$, $p < .01$), see representative traces in Figure 5e and normalized and summarized data in Figure 5f. This reduction aligns well with an initial inwardly directed transport of lactate and a concomitant removal of acid equivalents from the extracellular space, which is prevented in the presence of the inhibitor. The difference between stimulus-induced peak alkaline and subsequent peak acidic change was reduced in the presence of 4-CIN (to 87.8 ± 1.5% of control, $n = 7$, $p < .001$), suggesting a role for MCTs also in the post-stimulus lactate and pH alterations. Furthermore, we noticed that as the test solution containing 4-CIN washed in, the pH baseline acidified by 0.040 ± 0.006 pH units ($p < .01$, $n = 7$). This baseline shift is not illustrated in Figure 5e, in which only stimulus-induced pH changes are quantified. Taken together, these data promote MCTs as participants in stimulus-induced shrinkage of the extracellular space.

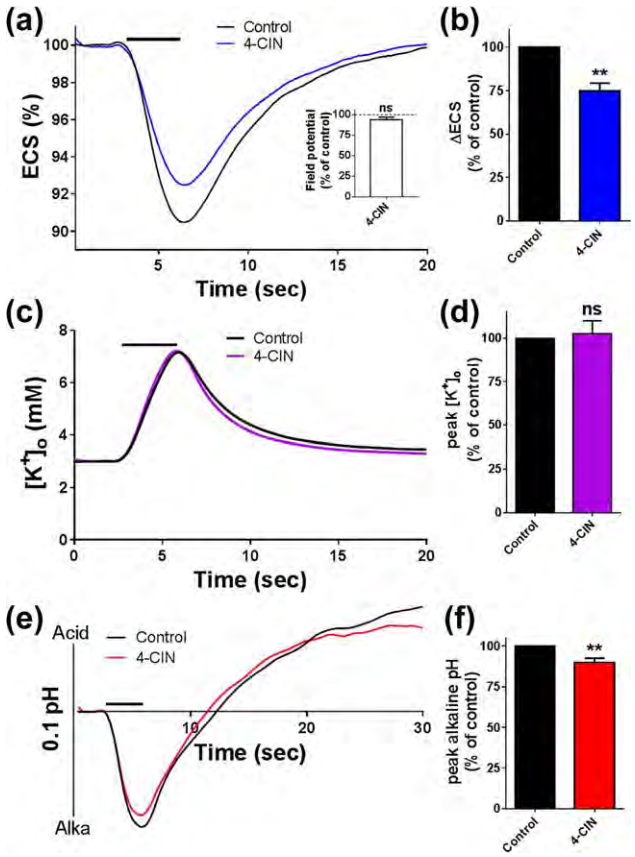

FIGURE 5 Monocarboxylate transporter-mediated contribution to K^+, ECS, and pH_o dynamics measured with ion-sensitive microelectrodes. (a) Representative traces of stimulus-induced changes in the ECS before and after exposure to 4-CIN. Insert shows the normalized and summarized peak amplitude of the reference field potential in the presence of 4-CIN (93.4 ± 3.4% of control, $n = 18$ slices from 12 rats). (b) The changes in the ECS in the presence of 4-CIN was normalized to the control and summarized ($n = 6$ slices from 5 rats). (c) Representative traces of stimulus-induced changes in $[K^+]_o$ prior to and after application of 4-CIN. (d) The change in $[K^+]_o$ in the presence of 4-CIN was normalized to the control and summarized ($n = 5$ slices from 3 rats). (e) Representative traces of stimulus-induced changes in pH_o prior to and after exposure to 4-CIN. (f) The peak of the initial fast alkaline shift in pH_o in the presence of 4-CIN was normalized to the control and summarized ($n = 7$ slices from 4 rats). The black bar above the respective traces represents 20 Hz stimulation. Statistical significance was tested with Student's paired *t* test. **; $p < .01$, ns; not significant [Color figure can be viewed at wileyonlinelibrary.com]

3.5 | The extracellular chloride concentration influences the extracellular space dynamics

Glial KCl accumulation has been suggested as a main event for cellular swelling, although the specific entryway for both K^+ and Cl^- has remained unresolved. To elucidate a role for Cl^- in stimulus-induced glial volume changes, we measured the stimulus-induced ΔECS in rat hippocampal slices with the TMA^+-sensitive microelectrodes and varying $[Cl^-]_o$. First, in the presence of basal $[Cl^-]_o$ (standard aCSF, 131 mM Cl^-) and subsequently in a low-$[Cl^-]_o$ solution (11 mM Cl^- for $[K^+]_o$ and pH_o measurements, and 12.5 mM for ECS measurements due to the addition of 1.5 mM TMA-Cl, equimolar replacement with gluconate). Reduction of extracellular $[Cl^-]$ modulated the stimulus-induced ECS dynamics two-fold: At *the end of the electrical stimulation*, where the ΔECS peaks in control aCSF, we consistently observed a reduction of the stimulus-induced ECS shrinkage upon reduction of $[Cl^-]_o$ (to 70 ± 6% of control, $n = 11$, $p < .001$), see Figure 6a for representative traces and normalized and summarized data in 6B, insert shows an extended trace. However, this initial reduction appeared as a "shoulder" in ECS dynamics, as the extracellular space volume then further decreased with the *maximal amplitude* significantly increased compared with that obtained in control solution (174.3 ± 18.3% of control, $n = 11$, $p < .01$), see Figure 6a for the representative traces and Figure 6c for normalized and summarized data. The return to baseline was delayed in the low-$[Cl^-]_o$ solution, as illustrated in the extended trace in Figure 6a, insert. The extracellular space dynamics were completely restored upon re-introduction of the control solution (*data not shown*). As one could well imagine that such severe reduction in $[Cl^-]_o$ could affect neuronal activity, we quantified the stimulus-induced field potentials obtained in this experimental series. Field potential amplitudes obtained in the low-$[Cl^-]_o$ solutions were 2.5-fold higher than those obtained in the control condition (Figure 6d, insert). To obtain the ΔECS as a function of the neuronal activity, we therefore quantified the percent change in ECS per mV of the corresponding field potential. This approach revealed a ΔECS of 4.9 ± 0.7% per mV in the control solution versus a significantly lower ΔECS of 1.3 ± 0.3% per mV in the low-$[Cl^-]_o$ solution ($n = 11$ of each, $p < .001$). The data illustrate a $[Cl^-]_o$-dependent fraction of the stimulus-induced extracellular space shrinkage and implicates this anion in the ECS dynamics.

To further explore the impact of Cl^- on extracellular dynamics, we addressed the K^+ transients in conditions of low $[Cl^-]_o$. The stimulus-induced peak $[K^+]_o$ increased upon removal of Cl^- from the test solution (to 217.7 ± 5.7% of control at the end of stimulation, $n = 5$, $p < .001$), see representative traces in Figure 6d and normalized and summarized data in Figure 6e. The $[K^+]_o$ continued to rise after the termination of the stimulus (to 269.7 ± 15.3% of control at the maximum amplitude, $n = 5$, $p < .001$), summarized in Figure 6f. Consequently, at *stimulus-end* we have *more* K^+ in the extracellular space (Figure 6d,e) compared with controls but a *smaller* ECS change (Figure 6a,b), which underscores the importance of Cl^- in stimulus-induced ECS shrinkage of the hippocampus. The Cl^--dependent pH_o response largely mirrored that of the K^+ transients with increased extracellular alkalization in low-$[Cl^-]_o$ solutions (to 197.1 ± 15.2% of control at the end of stimulation, $n = 7$, $p < .001$), see representative traces in Figure 6g and normalized and summarized data in Figure 6h. The pH alkalization increased further to 239.2 ± 33.3% of control at its maximal amplitude, $n = 7$, $p < .01$, summarized in Figure 6i (see insert for an extended trace). In control conditions, ΔECS, K^+ and pH transients peaked around the end of the electrical stimulation (see Figure 4a). In the low-$[Cl^-]_o$ conditions, in contrast, the enhanced responses reach their peaks seconds after end of stimulation, see comparison of the stimulus-induced ΔECS, K^+ and pH responses as representative traces in Figure 6j (combination of the representative traces from Figure 6a,d,

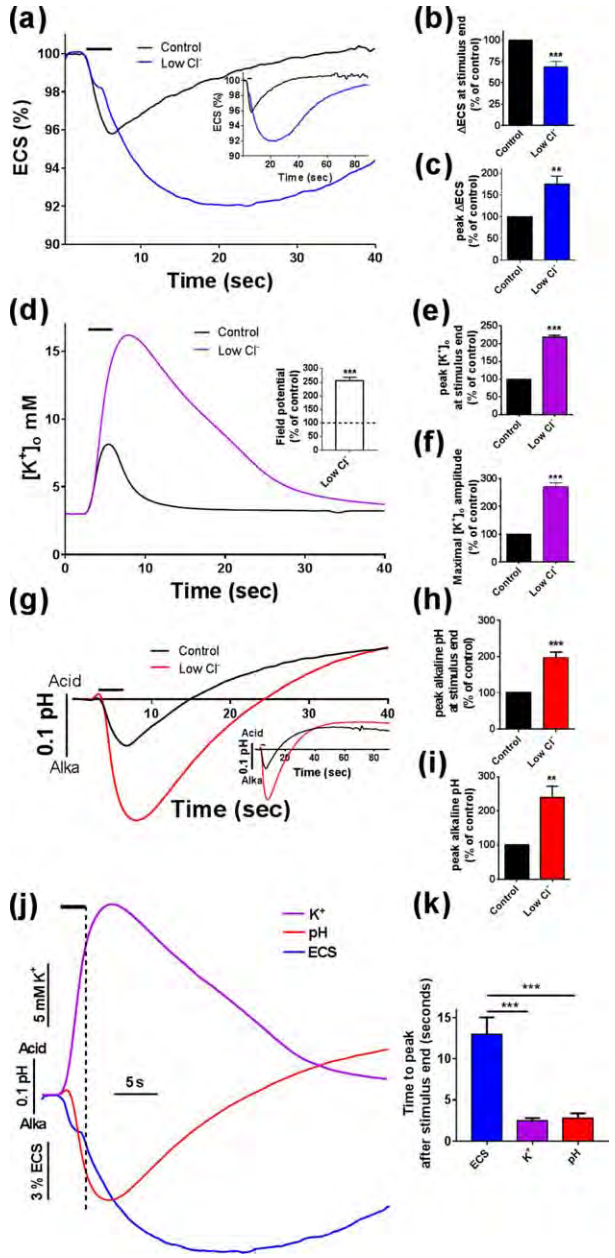

FIGURE 6 Cl^--dependent changes in K^+, ECS, and pH_o dynamics measured with ion-sensitive microelectrodes. (a) Representative traces of stimulus-induced changes in the ECS before and after exposure to low Cl^- containing aCSF. Insert shows the ECS transients on a longer time scale. (b, c) The change in ECS at the end of stimulation (b) or at the peak (c) was normalized to the control and summarized ($n = 11$ slices from 7 rats). (d) Representative traces of stimulus-induced changes in $[K^+]_o$ prior to and following exposure to low Cl^- containing aCSF. Insert shows the normalized and summarized peak amplitude of the reference field potential at the end of stimulation in the presence of low Cl^- containing aCSF (254 ± 13.4% of control, $n = 23$ slices from 13 rats). (e, f) The change in $[K^+]_o$ at the end of stimulation (e) or at the peak (f) was normalized to the control and summarized ($n = 5$ slices from 3 rats). (g) Representative traces of stimulus-induced changes in pH_o before and after exposure to low Cl^- containing aCSF. Insert shows the pH transient on a longer time scale. (h, i) The initial fast alkaline shift in pH_o at the end of stimulation (h) or at the peak (i) was normalized to the control and summarized ($n = 7$ slices from 3 rats). (j) Temporal comparison of the ECS, $[K^+]_o$, and pH_o dynamics during electrical stimulation of the hippocampal slice in the presence of low Cl^- containing aCSF, from the experiments shown in panels a, d, g. (k) Comparison of the time to reach the peak change in ECS ($n = 11$ slices from 7 rats), $[K^+]_o$ ($n = 5$ slices from 3 rats), and alkaline pH_o ($n = 7$ slices from 3 rats) *after the end* of electrical stimulation. The black bar above the respective traces represents 20 Hz stimulation. Statistical significance was tested with Student's paired *t* test or one-way ANOVA with Tukey's multiple comparison post hoc test. **; $p < .01$, ***; $p < .001$ [Color figure can be viewed at wileyonlinelibrary.com]

g) and the summarized time from end of stimulus to peak response in Figure 6k (ECS: 13.0 ± 2.0 s, K^+: 2.5 ± 0.3 s, and pH: 2.8 ± 0.6 s, $n = 11$, 5 and 7, respectively, $p < .001$). Thus with severely reduced $[Cl^-]_o$, the ECS shrinkage follows a temporal pattern distinct from that of the $[K^+]_o$ and $[pH]_o$. Severe reduction of Cl^- in the bath solution thus enhances and extents the stimulus-induced K^+ and pH transients and the related shrinkage of the extracellular space but, in addition, appears to be required for parts of the activity-dependent ECS shrinkage, although via unidentified transport mechanisms.

4 | DISCUSSION

In this study, we show that the ECS shrinkage observed during neuronal network activity in rat hippocampal slices does not directly depend on the molecular mechanisms responsible for K^+ clearance but occurs, in part, by the action of bicarbonate and lactate cotransporters and, in part, by an unidentified transport mechanism relying on the presence of Cl^- in the extracellular space. Stimulus-induced extracellular space shrinkage has been assigned to cellular swelling of the glial compartment (Connors et al., 1982; MacVicar et al., 2002; Ransom et al., 1985), as was additionally illustrated in slices bathed in high $[K^+]_o$ by direct visualization of the fluorescent astrocytes (Florence, Baillie, & Mulligan, 2012). Nevertheless, swelling of the neurons may well constitute a portion of this event (Pál et al., 2013), as evident during cortical spreading depolarization (Steffensen, Sword, Croom, Kirov, & MacAulay, 2015). Historically, the activity-induced glial cell swelling has been inferred to occur in direct relation to the molecular machinery underlying K^+ clearance in the extracellular space, partly based on results obtained in cultured astrocytes (Hertz et al., 2013; Kofuji & Newman, 2004; Nagelhus et al., 2004; Su, Kintner, Flagella, Shull, & Sun, 2002; Tas, Massa, Kress, & Koschel, 1987; Walz, 1992). Although NKCC1 is sparsely expressed *in vivo* in hippocampal/cortical astrocytes (Plotkin et al., 1997; Zhang et al., 2014), it appears to be highly expressed following culturing of the astrocytes (Larsen et al., 2014; Su et al., 2000; Walz, 1992; Walz & Hertz, 1984), a phenomenon also observed in other cell types (Raat, Delpire, van Os, & Bindels, 1996). The observation that cultured astrocytes readily swell, in a NKCC1-mediated fashion, when faced with increased K^+ in the surrounding solution (Larsen et al., 2014), suggested a putative role for NKCC1 in clearance of K^+ from the extracellular space and associated glia cell swelling (Hertz & Chen, 2016; Hertz

et al., 2013; Kofuji & Newman, 2004; MacAulay & Zeuthen, 2012). Recent observations, however, illustrated that neither NKCC1 (rat), Kir4.1 (rat/mouse), nor AQP4 (mouse) were required for stimulus-induced extracellular space shrinkage in the hippocampus (Haj-Yasein et al., 2011, 2012; Larsen et al., 2014), although at present, it is unclear whether inter-species differences could exist. We were thus prompted to explore alternative molecular mechanisms. The independence of AQP4 as an osmotically-driven pathway for stimulus-induced astrocytic water influx (Haj-Yasein et al., 2012) promoted water-translocating cotransporters (MacAulay & Zeuthen, 2010; Zeuthen & MacAulay, 2012b) as a molecular means to induce glia cell swelling. The water-transporting KCCs (Zeuthen, 1994), of which KCC1, 3, and 4 appear to be expressed in astrocytes (as well as neurons) while KCC2 is exclusive to the neuronal compartment (Le Rouzic et al., 2006; Zhang et al., 2014), are generally outwardly directed but may reverse if faced with high extracellular $[K^+]$. Although, at first glance, inhibition of KCC transport activity reduced the stimulus-induced ECS shrinkage, as previously observed (MacVicar et al., 2002; Pál et al., 2013; Ransom et al., 1985), it did, however, also result in a decreased $[K^+]_o$ amplitude as a consequence of reduced neuronal activity (apparent as reduced field potential amplitude), in agreement with (Holthoff & Witte, 1996). Thus, the impaired ECS shrinkage is likely explained by a loss of neuronal activity and therefore cannot be directly assigned to KCC-mediated cell swelling.

With neuronal activity, the extracellular space concentrations of not only K^+ but also a range of other solutes fluctuates. These changes affect the driving forces for the assigned cotransporters and therefore their activity and/or direction of transport and could, as a byproduct, lead to cell swelling of the glial or neuronal compartment. The majority of the excitatory synapses in the central nervous system release glutamate into the extracellular space, which is swiftly cleared by the astrocytic compartment via the glutamate transporters (Danbolt, 2001), an isoform of which has been demonstrated to belong to the water-translocating cotransporters (EAAT1; MacAulay, Gether, Klærke, & Zeuthen, 2001). Although cell culture and *in vitro/ex vivo* studies have demonstrated both glutamate transporter-mediated cell swelling (Izumi, Kirby, Benz, Olney, & Zorumski, 1999; Koyama et al., 2000; Pál et al., 2013; Schneider, Baethmann, & Kempski, 1992) and metabotropic glutamate receptor-induced cell swelling (Hansson, Johansson, Westergren, & Rönnbäck, 1994), we observed no reduction of stimulus-induced extracellular space shrinkage upon inhibition of either of these membrane proteins. Notably, inhibition of the glutamate transporters amplified the volume dynamics, which we assigned to the increased K^+ transients observed in the presence of the glutamate transporter inhibitor, TBOA (Larsen et al., 2016). We cannot, however, exclude that the TBOA-enhanced K^+ transients may mask a small contribution of the glutamate transporters to the extracellular space shrinkage.

Neuronal activity in hippocampal slices is associated with pH fluctuations in the extracellular space, leading to a fast alkaline shift followed by a slower acidic shift at the end of stimulation, in agreement with previous reports (Syková, 1997; Voipio & Kaila, 1993). The underlying mechanisms of the alkaline shift remain disputed (Chesler, 2003): Among the possible manners of extracellular alkalization are HCO_3^- efflux through GABA-A receptors (Chen & Chesler, 1992; Kaila, Paalasmaa, Taira, & Voipio, 1992; Kaila & Voipio, 1987) and H^+ uptake via Ca^{2+}/H^+-ATPase activity (Paalasmaa, Taira, Voipio, & Kaila, 1994). The stoichiometry of the glutamate transporters include 1 H^+ (Zerangue & Kavanaugh, 1996), the removal of which from the extracellular space will contribute to the observed alkalization. As several Cl^- channels, in addition to the GABA-A receptor, appear to be permeable to HCO_3^- (Kunzelmann, Gerlach, Fröbe, & Greger, 1991; Qu & Hartzell, 2008), one of these being the glutamate transporters with their associated anion conductance (Kanai, Trotti, Berger, & Hediger, 2002), the extracellular HCO_3^- accumulation may well, in part, originate through these transport mechanisms. Proliferation and differentiation of glial cells alter the pH response in the CNS of rats (Jendelová & Syková, 1991; Xiong & Stringer, 2000) akin to how management of extracellular K^+ and the phenomenon of ECS shrinkage develop along with maturation of glia cells (Connors et al., 1982; Ransom et al., 1985): A more pronounced alkaline shift is observed in both spinal cord and hippocampus of young rats and the following acidic shift increases with gliogenesis (Jendelová & Syková, 1991; Xiong & Stringer, 2000). These observations support a suggested role of glia cells in the extracellular pH management (Chesler, 2003; Chesler & Kraig, 1989). We discovered a good match in the temporal profile of K^+ transients, ECS changes, and pH changes during hippocampal stimulation, suggesting pH alterations as a missing link between stimulus-induced K^+ transients and the associated ECS shrinkage.

The electrogenic NBCe1 is the dominant astrocytic bicarbonate transporter with a proposed stoichiometry of symport of 1 Na^+:2 HCO_3^- (Deitmer & Schlue, 1989; Theparambil et al., 2014; Zhang et al., 2014). At rest, NBCe1 probably extrudes net HCO_3^-, although the predicted reversal potential of the bicarbonate transport lies in the vicinity of the astrocytic membrane potential, thus allowing for reversal upon increased $[HCO_3^-]_o$, increased $[H^+]_i$, and/or membrane depolarization (Theparambil & Deitmer, 2015; Theparambil, Naoshin, Thyssen, & Deitmer, 2015; Theparambil et al., 2014). Notably, astrocytic membrane depolarization, as for example occurs with stimulus-induced K^+ transients, has thus repeatedly been shown to induce inwardly directed transport activity of NBCe1 (Brookes & Turner, 1994; Chesler & Kraig, 1989; Deitmer & Szatkowski, 1990; Pappas & Ransom, 1994; Theparambil et al., 2014). In the present study, acute inhibition of NBCe1 with DIDS had no effect on the stimulus-induced K^+ transients or field potentials at the tested time scale but increased the extracellular alkalization (in line with reduced removal of HCO_3- from the extracellular space) and reduced the stimulus-induced extracellular space shrinkage by around 25%. DIDS also affects other bicarbonate transporters, Cl^- channels and, in high concentrations, MCTs (Dimmer et al., 2000) and we therefore cannot exclude that a part of the response could be due to other transport mechanisms than NBCe1 (despite the brief exposure of the inhibitor). However, with the observed DIDS-induced shift in the alkaline transient (which points to a pH-regulating transport mechanism as the DIDS target) and the astrocytic membrane being dominated by K^+ conductance (indicating an absence of Cl^- channels) (Kuffler, Nicholls, & Orkand, 1966; Ransom & Goldring, 1973), our data

indicate NBCs (probably the main astrocytic bicarbonate transporter, NBCe1) as a mediator of activity-induced glia cell swelling, indirectly prompted by K^+-mediated astrocytic membrane depolarization. Although the ability of NBCe1 to cotransport water remains unresolved, we propose that inwardly directed NBCe1-mediated transport (of 1 Na^+ and 2 HCO_3^-) leads to concomitant water accumulation, as observed for a range of other cotransport mechanisms (for review, see MacAulay & Zeuthen, 2010). These data aligns well with an earlier hypothesis (Nagelhus et al., 2004) and a report on intrinsic optical signaling on rat hippocampal brain slices, in which DIDS reduced the optical signaling associated with electrical stimulation (Pál et al., 2013). Two-photon imaging of rat hippocampal brain slices with SR101-labelled astrocytes demonstrated astrocyte cell swelling upon bath application of a test solution containing an additional 3 mM K^+: The cell swelling required the presence of HCO_3^- in the bath solution and was severely reduced by application of DIDS (Florence et al., 2012). The astrocytic bicarbonate transporter thus appears to be activated by neuronal activity or by exposure to increased $[K^+]_o$, resulting in extracellular space shrinkage, at least in part due to glia cell swelling, irrespective of the mode of data acquisition.

The lactate concentration fluctuates in the extracellular space during neuronal activity, as observed in rats and humans with a brief dip during the initial seconds of neuronal activity followed by a prolonged increase in extracellular lactate concentration (Barros, 2013; Hu & Wilson, 1997; Mangia et al., 2003), as a consequence of increased cell metabolism (Barros, 2013). The initial brief drop in extracellular lactate concentration may well be induced by MCT-mediated uptake of lactate (prior to the onset of stimulus-induced glial lactate production), possibly partly into the astrocytic compartment. Astrocytes express MCT1 and MCT4, as indicated by immunolabeled tissue sections of mice and rats (Bergersen et al., 2001; Leino et al., 1999; Pierre et al., 2000; Rafiki et al., 2003), as well as humans (MCT1) (Chiry et al., 2006). In contrast, MCT2 appears exclusively neuronal (Bergersen et al., 2001; Pierre et al., 2000, 2002; Rafiki et al., 2003). Interestingly, the astrocytic MCT4 is weakly expressed at P7 but reaches adult levels at P14 (Rafiki et al., 2003), not unlike the development of ECS shrinkage with glial proliferation and maturation (Connors et al., 1982; Ransom et al., 1985). In support of this notion, acute inhibition of MCTs with 4-CIN caused 25% reduction in stimulus-induced extracellular space shrinkage with undisturbed field potential amplitude and K^+ dynamics. 4-CIN may have additional targets despite our brief incubation time (Emmons, 1999; Halestrap, 1975) and we therefore cannot exclude that part of the 4-CIN-evoked changes in ΔECS could be assigned to alternative transport mechanisms. We did, however, observe a shift in the stimulus-evoked extracellular pH transients, which aligned with MCTs as a prominent target for 4-CIN (less extracellular H^+ being removed by the H^+-coupled lactate cotransporter following its inhibition). Efficient astrocyte lactate uptake has been reported in a slice preparation (Gandhi, Cruz, Ball, & Dienel, 2009) and with at least one isoform of the MCTs (MCT1) carrying water along its translocation pathway (Zeuthen, Hamann, & la Cour, 1996), this transport activity could lead to cotransporter-mediated glia cell swelling. Such lactate-dependent glia cell swelling was previously observed in C6 glioma cells and primary cultured rat astrocytes (Bender, Young, & Norenberg, 1997; Ringel, Chang, Staub, Baethmann, & Plesnila, 2000), the latter of which required 200 mOsm mannitol to prevent, thus underscoring the ability of MCT to cotransport water. While there is some disagreement in the literature as to the exact potency of 4-CIN toward the MCTs, it appears that all of them would be, at least partially, affected by the 500 μM concentration applied in our approach (Dimmer et al., 2000; Fox et al., 2000). Therefore, we may underestimate the full contribution of MCT but our data suggest a role for MCTs in stimulus-induced extracellular space shrinkage.

With the combined action of the bicarbonate and lactate transporters contributing to roughly half of the stimulus-induced ECS shrinkage, the remaining fraction remained unaccounted for. We determined the importance of Cl^- in this process by severely reducing the Cl^- concentration of the test solution (equimolar replacement with gluconate) following the control trace. The field potential amplitude increased with acutely applied low-$[Cl^-]_o$ test solution, as earlier reported (Chebabo, Hester, Aitken, & Somjen, 1995; Huang, Bossut, & Somjen, 1997). Both the stimulus-induced K^+ transient and the resulting alkalization were amplified and the peak response slightly delayed in relation to stimulus end. The underlying reasons for these changes are currently unresolved. The extracellular space dynamics, however, responded in two distinct manners: At the end of the stimulation, the TMA^+ trace consistently displayed a "shoulder" at which the ΔECS was reduced by 30% (despite the increased K^+ and ΔpH amplitude) compared with the control trace, strongly suggesting Cl^- as a contributing factor in stimulus-induced extracellular space shrinkage, as earlier observed with intrinsic optical signaling (Holthoff & Witte, 1996; MacVicar et al., 2002). The extracellular space shrinkage subsequently continued to shrink, peaking at a time point around 10 s later than those of K^+ and pH and only slowly returning to baseline. It should be noted that it is challenging to fully speculate on the exact effect that a vastly reduced (120 mM *lower* $[Cl^-]_o$) would have on a number of transport mechanisms and that the (putative) Cl^- channel composition of astrocytes are not yet fully elucidated. These data, nevertheless, suggest an importance of Cl^- for complete glial cell swelling during hippocampal stimulation, possibly via an unidentified cotransport mechanism.

In conclusion, it has been evident for decades that the extracellular space in the central nervous system shrinks during neuronal activity arising following electrical stimulation. This (at least in part) glial cell swelling was originally inferred to be directly associated with the molecular mechanisms governing K^+ management. Here, we report that the activity-evoked extracellular space alkalization, in association with K^+-dependent depolarization of the astrocytic compartment, drives inwardly directed Na^+-coupled bicarbonate transport, which together with brief activation of the MCTs, produces half of the observed glia cell swelling, most likely via cotransport of water during their transport cycle. These transport mechanisms do not require Cl^- as a substrate and the fraction of the cellular swelling relying on extracellular Cl^- must thus involve other, yet unresolved, molecular pathways leading to stimulus-induced glial cell swelling.

ACKNOWLEDGMENT

This study was funded by the Lundbeck Foundation (R151–2013-14120) and the Novo Nordisk Foundation (NNF15OC0017052).

REFERENCES

Aronica, E., Van Vliet, E. A., Mayboroda, O. A., Troost, D., Da Silva, F. H. L., & Gorter JA. (2000). Upregulation of metabotropic glutamate receptor subtype mGluR3 and mGluR5 in reactive astrocytes in a rat model of mesial temporal lobe epilepsy. *European Journal of Neuroscience*, *12*, 2333–2344. doi:10.1046/j.1460-9568.2000.00131.x

Barros, L. F. (2013). Metabolic signaling by lactate in the brain. *Trends in Neurosciences*, *36*, 396–404. doi:10.1016/j.tins.2013.04.002

Bender, A. S., Young, L. P., & Norenberg, M. D. (1997). Effect of lactic acid on l-glutamate uptake in cultured astrocytes: Mechanistic considerations. *Brain Research*, *750*, 59–66. doi:10.1016/S0006-8993(96)01331–5

Bergersen, L., Wærhaug, O., Helm, J., Thomas, M., Laake, P., Davies, A. J., … Ottersen, O. P. (2001). A novel postsynaptic density protein: The monocarboxylate transporter MCT2 is co-localized with δ-glutamate receptors in postsynaptic densities of parallel fiber–Purkinje cell synapses. *Experimental Brain Research*, *136*, 523–534. doi:10.1007/s002210000600

Brookes, N., & Turner, R. J. (1994). K(+)-induced alkalinization in mouse cerebral astrocytes mediated by reversal of electrogenic Na(+)-HCO3-cotransport. *American Journal of Physiology - Cell Physiology*, *267*, C1633–C1640.

Campbell, S. L., & Hablitz, J. J. (2004). Glutamate transporters regulate excitability in local networks in rat neocortex. *Neuroscience*, *127*, 625–635. doi:10.1016/j.neuroscience.2004.05.030

Chebabo, S. R., Hester, M. A., Aitken, P. G., & Somjen, G. G. (1995). Hypotonic exposure enhances synaptic transmission and triggers spreading depression in rat hippocampal tissue slices. *Brain Research*, *695*, 203–216. doi:10.1016/0006-8993(95)00778-O

Chen, J. C., & Chesler, M. (1992). Modulation of extracellular pH by glutamate and GABA in rat hippocampal slices. *Journal of Neurophysiology*, *67*, 29–36.

Chesler, M. (2003). Regulation and modulation of pH in the brain. *Physiological Reviews*, *83*, 1183–1221. doi:10.1152/physrev.00010.2003

Chesler, M., & Kraig, R. (1989). Intracellular pH transients of mammalian astrocytes. *The Journal of Neuroscience*, *9*, 2011–2019.

Chiry, O., Pellerin, L., Monnet-Tschudi, F., Fishbein, W. N., Merezhinskaya, N., Magistretti, P. J., & Clarke, S. (2006). Expression of the monocarboxylate transporter MCT1 in the adult human brain cortex. *Brain Research*, *1070*, 65–70. doi:10.1016/j.brainres.2005.11.064

Connors, B., Ransom, B., Kunis, D., & Gutnick, M. (1982). Activity-dependent K+ accumulation in the developing rat optic nerve. *Science*, *216*, 1341–1343.

Danbolt, N. C. (2001). Glutamate uptake. *Progress in Neurobiology*, *65*, 1–105. doi:10.1016/S0301-0082(00)00067–8

Deitmer, J. W., & Schlue, W. R. (1989). An inwardly directed electrogenic sodium-bicarbonate co-transport in leech glial cells. *The Journal of Physiology*, *411*, 179–194. doi:10.1113/jphysiol.1989.sp017567

Deitmer, J. W., & Szatkowski, M. (1990). Membrane potential dependence of intracellular pH regulation by identified glial cells in the leech central nervous system. *The Journal of Physiology*, *421*, 617–631. doi:10.1113/jphysiol.1990.sp017965

Dietzel, I., Heinemann, U., Hofmeier, G., & Lux, H. D. (1980). Transient changes in the size of the extracellular space in the sensorimotor cortex of cats in relation to stimulus-induced changes in potassium concentration. *Experimental Brain Research*, *40*, 432–439.

Dimmer, K.-S., Friedrich, B., Lang, F., Deitmer, J. W., & Bröer, S. (2000). The low-affinity monocarboxylate transporter MCT4 is adapted to the export of lactate in highly glycolytic cells. *Biochemical Journal*, *350*, 219–227. doi:10.1042/bj3500219

Emmons, C. (1999). Transport characteristics of the apical anion exchanger of rabbit cortical collecting duct β-cells. *American Journal of Physiology - Renal Physiology*, *276*, F635–F643.

Fitzjohn, S. M., Bortolotto, Z. A., Palmer, M. J., Doherty, A. J., Ornstein, P. L., Schoepp, D. D., … Collingridge, G. L. (1998). The potent mGlu receptor antagonist LY341495 identifies roles for both cloned and novel mGlu receptors in hippocampal synaptic plasticity. *Neuropharmacology*, *37*, 1445–1458. doi:10.1016/S0028-3908(98)00145–2

Florence, C. M., Baillie, L. D., & Mulligan, S. J. (2012). Dynamic volume changes in astrocytes are an intrinsic phenomenon mediated by bicarbonate ion flux. *PloS One*, *7*, e51124. doi:10.1371/journal.pone.0051124

Fox, J. E. M., Meredith, D., & Halestrap, A. P. (2000). Characterisation of human monocarboxylate transporter 4 substantiates its role in lactic acid efflux from skeletal muscle. *The Journal of Physiology*, *529*, 285–293. doi:10.1111/j.1469-7793.2000.00285.x

Gandhi, G. K., Cruz, N. F., Ball, K. K., & Dienel, G. A. (2009). Astrocytes are poised for lactate trafficking and release from activated brain and for supply of glucose to neurons. *Journal of Neurochemistry*, *111*, 522–536. doi:10.1111/j.1471-4159.2009.06333.x

Gillen, C. M., Brill, S., Payne, J. A., & Forbush, B. (1996). Molecular cloning and functional expression of the K-Cl cotransporter from rabbit, rat, and human: A new member of the cation-chloride cotransporter family. *Journal of Biological Chemistry*, *271*, 16237–16244. doi:10.1074/jbc.271.27.16237

Haj-Yasein, N. N., Jensen, V., Ostby, I., Omholt, S. W., Voipio, J., Kaila, K., … Nagelhus, E. A. (2012). Aquaporin-4 regulates extracellular space volume dynamics during high-frequency synaptic stimulation: A gene deletion study in mouse hippocampus. *Glia*, *60*, 867–874. doi:10.1002/glia.22319

Haj-Yasein, N. N., Jensen, V., Vindedal, G. F., Gundersen, G. A., Klungland, A., Ottersen, O. P., … Nagelhus, E. A. (2011). Evidence that compromised K+ spatial buffering contributes to the epileptogenic effect of mutations in the human Kir4.1 gene (KCNJ10). *Glia*, *59*, 1635–1642. doi:10.1002/glia.21205

Halestrap, A. P. (1975). The mitochondrial pyruvate carrier. Kinetics and specificity for substrates and inhibitors. *Biochemical Journal*, *148*, 85–96. doi:10.1042/bj1480085

Hansson, E., Johansson, B. B., Westergren, I., & Rönnbäck, L. (1994). Glutamate-induced swelling of single astroglial cells in primary culture. *Neuroscience*, *63*, 1057–1066. doi:10.1016/0306-4522(94)90572-X

Hertz, L., & Chen, Y. (2016). Importance of astrocytes for potassium ion (K+) homeostasis in brain and glial effects of K+ and its transporters on learning. *Neuroscience and Biobehavioral Reviews*, *71*, 484–505. doi:10.1016/j.neubiorev.2016.09.018

Hertz, L., Song, D., Xu, J., Peng, L., & Gibbs, M. (2015). Role of the astrocytic Na+, K+-ATPase in K+ homeostasis in brain: K+ uptake, signaling pathways and substrate utilization. *Neurochemical Research*, *40*, 2505–2516. doi:10.1007/s11064-014-1505-x

Hertz, L., Xu, J., Song, D., Yan, E., Gu, L., & Peng, L. (2013). Astrocytic and neuronal accumulation of elevated extracellular K+ with a 2/3 K+/Na+ flux ratio - consequences for energy metabolism, osmolarity and higher brain function. *Frontiers in Computational Neuroscience*, *7*, 114. doi:10.3389/fncom.2013.00114

Holthoff, K., & Witte, O. (1996). Intrinsic optical signals in rat neocortical slices measured with near- infrared dark-field microscopy reveal changes in extracellular space. *The Journal of Neuroscience*, *16*, 2740–2749.

Hu, Y., & Wilson, G. S. (1997). Rapid changes in local extracellular rat brain glucose observed with an in vivo glucose sensor. *Journal of Neurochemistry*, *68*, 1745–1752. doi:10.1046/j.1471-4159.1997.68041745.x

Huang, R., Bossut, D. F., & Somjen, G. G. (1997). Enhancement of whole cell synaptic currents by low osmolarity and by low [NaCl] in rat hippocampal slices. *Journal of Neurophysiology*, *77*, 2349–2359.

Hwang, I. K., Yoo, K.-Y., An, S.-J., Li, H., Lee, C. H., Choi, J. H., … Won, M.-H. (2008). Late expression of Na+/H+ exchanger 1 (NHE1) and neuroprotective effects of NHE inhibitor in the gerbil hippocampal CA1 region induced by transient ischemia. *Experimental Neurology*, *212*, 314–323. doi:10.1016/j.expneurol.2008.04.007

Izumi, Y., Kirby, C. O., Benz, A. M., Olney, J. W., & Zorumski, C. F. (1999). Müller cell swelling, glutamate uptake, and excitotoxic neurodegeneration in the isolated rat retina. *Glia*, *25*, 379–389. doi:10.1002/(SICI)1098-1136(19990215)25:4 < 379::AID-GLIA7 > 3.0.CO;2-7

Jendelová, P., & Syková, E. (1991). Role of glia in K+ and pH homeostasis in the neonatal rat spinal cord. *Glia*, *4*, 56–63. doi:10.1002/glia.440040107

Kaila, K., Paalasmaa, P., Taira, T., & Voipio, J. (1992). pH transients due to monosynaptic activation of GABAA receptors in rat hippocampal slices. *Neuroreport*, *3*, 105–108.

Kaila, K., & Voipio, J. (1987). Postsynaptic fall in intracellular pH induced by GABA-activated bicarbonate conductance. *Nature*, *330*, 163–165.

Kanai, Y., Trotti, D., Berger, U. V., & Hediger, M. A. (2002). The high-affinity glutamate and neutral amino-acid transporter family. In M. E. A. Reith (Ed.), *Neurotransmitter transporters - structure, function and regulation* (2nd ed., pp. 255–312). Humana Press: Springer Science+ Business Media.

Karus, C., Mondragão, M. A., Ziemens, D., & Rose, C. R. (2015). Astrocytes restrict discharge duration and neuronal sodium loads during recurrent network activity. *Glia*, *63*, 936–957. doi:10.1002/glia.22793

Kofuji, P., & Newman, E. A. (2004). Potassium buffering in the central nervous system. *Neuroscience*, *129*, 1043–1054. doi:10.1016/j.neuroscience.2004.06.008

Koyama, Y., Ishibashi, T., Okamoto, T., Matsuda, T., Hashimoto, H., & Baba, A. (2000). Transient treatments with l-glutamate and threo-β-hydroxyaspartate induce swelling of rat cultured astrocytes. *Neurochemistry International*, *36*, 167–173. doi:10.1016/S0197-0186(99)00109–6

Kuffler, S. W., Nicholls, J. G., & Orkand, R. K. (1966). Physiological properties of glial cells in the central nervous system of amphibia. *Journal of Neurophysiology*, *29*, 768–787.

Kunzelmann, K., Gerlach, L., Fröbe, U., & Greger, R. (1991). Bicarbonate permeability of epithelial chloride channels. *Pflügers Archiv*, *417*, 616–621.

Larsen, B. R., Assentoft, M., Cotrina, M. L., Hua, S. Z., Nedergaard, M., Kaila, K., … MacAulay, N. (2014). Contributions of the Na+/K+-ATPase, NKCC1, and Kir4.1 to hippocampal K+ clearance and volume responses. *Glia*, *62*, 608–622. doi:10.1002/glia.22629

Larsen, B. R., Holm, R., Vilsen, B., & MacAulay, N. (2016). Glutamate transporter activity promotes enhanced Na+/K+-ATPase-mediated extracellular K+ management during neuronal activity. *The Journal of Physiology*, *594*, 6627–6641. doi:10.1113/JP272531

Le Rouzic, P., Ivanov, T. R., Stanley, P. J., Baudoin, F. M. H., Chan, F., Pinteaux, E., … Luckman, S. M. (2006). KCC3 and KCC4 expression in rat adult forebrain. *Brain Research*, *1110*, 39–45. doi:10.1016/j.brainres.2006.06.055

Leino, R. L., Gerhart, D. Z., & Drewes, L. R. (1999). Monocarboxylate transporter (MCT1) abundance in brains of suckling and adult rats: A quantitative electron microscopic immunogold study. *Developmental Brain Research*, *113*, 47–54. doi:10.1016/S0165-3806(98)00188–6

Löscher, W., Puskarjov, M., & Kaila, K. (2013). Cation-chloride cotransporters NKCC1 and KCC2 as potential targets for novel antiepileptic and antiepileptogenic treatments. *Neuropharmacology*, *69*, 62–74. doi:10.1016/j.neuropharm.2012.05.045

MacAulay, N., Gether, U., Klærke, D. A., & Zeuthen, T. (2001). Water transport by the human Na+-coupled glutamate cotransporter expressed in Xenopus oocytes. *The Journal of Physiology*, *530*, 367–378. doi:10.1111/j.1469-7793.2001.0367k.x

MacAulay, N., & Zeuthen, T. (2010). Water transport between CNS compartments: Contributions of aquaporins and cotransporters. *Neuroscience*, *168*, 941–956. doi:10.1016/j.neuroscience.2009.09.016

MacAulay, N., & Zeuthen, T. (2012). Glial K+ clearance and cell swelling: Key roles for cotransporters and pumps. *Neurochemical Research*, *37*, 2299–2309. doi:10.1007/s11064-012-0731-3

MacVicar, B. A., Feighan, D., Brown, A., & Ransom, B. (2002). Intrinsic optical signals in the rat optic nerve: Role for K(+) uptake via NKCC1 and swelling of astrocytes. *Glia*, *37*, 114–123.

Mangia, S., Garreffa, G., Bianciardi, M., Giove, F., Di Salle, F., & Maraviglia, B. (2003). The aerobic brain: Lactate decrease at the onset of neural activity. *Neuroscience*, *118*, 7–10. doi:10.1016/S0306-4522(02)00792–3

McAlear, S. D., Liu, X., Williams, J. B., McNicholas-Bevensee, C. M., & Bevensee, M. O. (2006). Electrogenic Na/HCO_3 cotransporter (NBCe1) variants expressed in *Xenopus* oocytes: Functional comparison and roles of the amino and carboxy termini. *The Journal of General Physiology*, *127*, 639–658. doi:10.1085/jgp.200609520

Nagelhus, E. A., Mathiisen, T. M., & Ottersen, O. P. (2004). Aquaporin-4 in the central nervous system: Cellular and subcellular distribution and coexpression with KIR4.1. *Neuroscience*, *129*, 905–913. doi:10.1016/j.neuroscience.2004.08.053

Nielsen, S., Arnulf Nagelhus, E., Amiry-Moghaddam, M., Bourque, C., Agre, P., & Petter Ottersen, O. (1997). Specialized membrane domains for water transport in glial cells: High-resolution immunogold cytochemistry of aquaporin-4 in rat brain. *The Journal of Neuroscience*, *17*, 171–180.

Paalasmaa, P., Taira, T., Voipio, J., & Kaila, K. (1994). Extracellular alkaline transients mediated by glutamate receptors in the rat hippocampal slice are not due to a proton conductance. *Journal of Neurophysiology*, *72*, 2031–2033.

Pál, I., Nyitrai, G., Kardos, J., & Héja, L. (2013). Neuronal and astroglial correlates underlying spatiotemporal intrinsic optical signal in the rat hippocampal slice. *PloS One*, *8*, e57694. doi:10.1371/journal.pone.0057694

Pappas, C. A., & Ransom, B. R. (1994). Depolarization-induced alkalinization (DIA) in rat hippocampal astrocytes. *Journal of Neurophysiology*, *72*, 2816–2826.

Pearson, M. M., Lu, J., Mount, D. B., & Delpire, E. (2001). Localization of the K+–Cl− cotransporter, KCC3, in the central and peripheral nervous systems: Expression in the choroid plexus, large neurons and white matter tracts. *Neuroscience*, *103*, 481–491. doi:10.1016/S0306-4522(00)00567–4

Pierre, K., Magistretti, P. J., & Pellerin, L. (2002). MCT2 is a major neuronal monocarboxylate transporter in the adult mouse brain. *Journal of Cerebral Blood Flow and Metabolism*, *22*, 586–595. doi:10.1097/00004647-200205000-00010

Pierre, K., Pellerin, L., Debernardi, R., Riederer, B. M., & Magistretti, P. J. (2000). Cell-specific localization of monocarboxylate transporters, MCT1 and MCT2, in the adult mouse brain revealed by double immunohistochemical labeling and confocal microscopy. *Neuroscience*, *100*, 617–627. doi:10.1016/S0306-4522(00)00294–3

Pizzonia, J. H., Ransom, B. R., & Pappas, C. A. (1996). Characterization of Na+/H+ exchange activity in cultured rat hippocampal astrocytes.

Journal of Neuroscience Research, *44*, 191–198. doi:10.1002/(SICI)1097-4547(19960415)44:2 < 191::AID-JNR12 > 3.0.CO;2-9

Plotkin, M., Kaplan, M., Peterson, L., Gullans, S., Hebert, S., & Delpire, E. (1997). Expression of the Na(+)-K(+)-2Cl- cotransporter BSC2 in the nervous system. *American Journal of Physiology - Cell Physiology*, *272*, C173–C183.

Qu, Z., & Hartzell, H. C. (2008). Bestrophin Cl− channels are highly permeable to HCO3−. *American Journal of Physiology - Cell Physiology*, *294*, C1371–C1377. doi:10.1152/ajpcell.00398.2007

Raat, N., Delpire, E., van Os, C., & Bindels, R. (1996). Culturing induced expression of basolateral Na+-K+-2Cl- cotransporter BSC2 in proximal tubule, aortic endothelium, and vascular smooth muscle. *Pflugers Archive*, *431*, 458–460.

Race, J. E., Makhlouf, F. N., Logue, P. J., Wilson, F. H., Dunham, P. B., & Holtzman, E. J. (1999). Molecular cloning and functional characterization of KCC3, a new K-Cl cotransporter. *American Journal of Physiology - Cell Physiology*, *277*, C1210–C1219.

Rafiki, A., Boulland, J. L., Halestrap, A. P., Ottersen, O. P., & Bergersen, L. (2003). Highly differential expression of the monocarboxylate transporters MCT2 and MCT4 in the developing rat brain. *Neuroscience*, *122*, 677–688. doi:10.1016/j.neuroscience.2003.08.040

Ransom, B., & Goldring, S. (1973). Slow depolarization in cells presumed to be glia in cerebral cortex of cat. *Journal of Neurophysiology*, *36*, 869–878.

Ransom, B., Yamate, C., & Connors, B. (1985). Activity-dependent shrinkage of extracellular space in rat optic nerve: A developmental study. *The Journal of Neuroscience*, *5*, 532–535.

Ringel, F., Chang, R. C. C., Staub, F., Baethmann, A., & Plesnila, N. (2000). Contribution of anion transporters to the acidosis-induced swelling and intracellular acidification of glial cells. *Journal of Neurochemistry*, *75*, 125–132. doi:10.1046/j.1471-4159.2000.0750125.x

Schneider, G.-H., Baethmann, A., & Kempski, O. (1992). Mechanisms of glial swelling induced by glutamate. *Canadian Journal of Physiology and Pharmacology*, *70*, S334–S343. doi:10.1139/y92-280

Schools, G. P., & Kimelberg, H. K. (1999). mGluR3 and mGluR5 are the predominant metabotropic glutamate receptor mRNAs expressed in hippocampal astrocytes acutely isolated from young rats. *Journal of Neuroscience Research*, *58*, 533–543. doi:10.1002/(SICI)1097-4547(19991115)58:4 < 533::AID-JNR6 > 3.0.CO;2-G

Shigeri, Y., Shimamoto, K., Yasuda-Kamatani, Y., Seal, R. P., Yumoto, N., Nakajima, T., & Amara, S. G. (2001). Effects of threo-β-hydroxyaspartate derivatives on excitatory amino acid transporters (EAAT4 and EAAT5). *Journal of Neurochemistry*, *79*, 297–302. doi:10.1046/j.1471-4159.2001.00588.x

Shimamoto, K., Lebrun, B., Yasuda-Kamatani, Y., Sakaitani, M., Shigeri, Y., Yumoto, N., & Nakajima, T. (1998). dl-threo-β-Benzyloxyaspartate, A potent blocker of excitatory amino acid transporters. *Molecular Pharmacology*, *53*, 195–201. doi:10.1124/mol.53.2.195

Staley, K. J. (2002). Diuretics as antiepileptic drugs: Should we go with the flow? *Epilepsy Currents*, *2*, 35–38. doi:10.1046/j.1535-7597.2002.00018.x

Steffensen, A. B., Sword, J., Croom, D., Kirov, S. A., & MacAulay, N. (2015). Chloride cotransporters as a molecular mechanism underlying spreading depolarization-induced dendritic beading. *The Journal of Neuroscience*, *35*, 12172–12187. doi:10.1523/jneurosci.0400-15.2015

Su, G., Haworth, R. A., Dempsey, R. J., & Sun, D. (2000). Regulation of Na+-K+-Cl−cotransporter in primary astrocytes by dibutyryl cAMP and high [K+]o. *American Journal of Physiology - Cell Physiology*, *279*, C1710–C1721.

Su, G., Kintner, D. B., Flagella, M., Shull, G. E., & Sun, D. (2002). Astrocytes from Na(+)-K(+)-Cl(-) cotransporter-null mice exhibit absence of swelling and decrease in EAA release. *American Journal of Physiology - Cell Physiology*, *282*, C1147–1160. doi:10.1152/ajpcell.00538.2001

Syková, E. (1997). The extracellular space in the CNS: Its regulation, volume and geometry in normal and pathological neuronal function. *The Neuroscientist*, *3*, 28–41. doi:10.1177/107385849700300113

Tas, P., Massa, P., Kress, H., & Koschel, K. (1987). Characterization of an Na+/K+/Cl- co-transport in primary cultures of rat astrocytes. *Biochemica et Biophysica Acta*, *903*, 411–416.

Theparambil, S. M., & Deitmer, J. W. (2015). High effective cytosolic H+ buffering in mouse cortical astrocytes attributable to fast bicarbonate transport. *Glia*, *63*, 1581–1594. doi:10.1002/glia.22829

Theparambil, S. M., Naoshin, Z., Thyssen, A., & Deitmer, J. W. (2015). Reversed electrogenic sodium bicarbonate cotransporter 1 is the major acid loader during recovery from cytosolic alkalosis in mouse cortical astrocytes. *The Journal of Physiology*, *593*, 3533–3547. doi:10.1113/JP270086

Theparambil, S. M., Ruminot, I., Schneider, H.-P., Shull, G. E., & Deitmer, J. W. (2014). The electrogenic sodium bicarbonate cotransporter NBCe1 is a high-affinity bicarbonate carrier in cortical astrocytes. *The Journal of Neuroscience*, *34*, 1148–1157. doi:10.1523/jneurosci.2377-13.2014

Tsukada, S., Iino, M., Takayasu, Y., Shimamoto, K., & Ozawa, S. (2005). Effects of a novel glutamate transporter blocker, (2S, 3S)-3-{3-[4-(trifluoromethyl)benzoylamino]benzyloxy}aspartate (TFB-TBOA), on activities of hippocampal neurons. *Neuropharmacology*, *48*, 479–491. doi:10.1016/j.neuropharm.2004.11.006

Voipio, J., & Kaila, K. (1993). Interstitial PCO2 and pH in rat hippocampal slices measured by means of a novel fast CO2/H(+)-sensitive microelectrode based on a PVC-gelled membrane. *Pflügers Archiv - European Journal of Physiology*, *423*, 193–201.

Voipio, J., Pasternack, M., & MacLeod, K. (1994). Ion-sensitive microelectrodes. In D. Ogden (Ed.), *Microelectrode techniques - the plymouth workshop handbook* (2nd ed., pp. 275–316). Cambridge, UK: The Company of Biologists Limited.

Waagepetersen, H., Shimamoto, K., & Schousboe, A. (2001). Comparison of effects of DL-Threo-β-benzyloxyaspartate (DL-TBOA) and L-trans-pyrrolidine-2,4-dicarboxylate (t-2,4-PDC) on uptake and release of [3H]D-aspartate in astrocytes and glutamatergic neurons. *Neurochemical Research*, *26*, 661–666. doi:10.1023/A:1010939304104

Walz, W. (1992). Role of Na/K/Cl cotransport in astrocytes. *Canadian Jounral of Physiology and Pharmacology*, *70*, S260–S262.

Walz, W. (2000). Role of astrocytes in the clearance of excess extracellular potassium. *Neurochemistry International*, *36*, 291–300. doi:10.1016/S0197-0186(99)00137–0

Walz, W, & Hertz, L. (1984). Intense furosemide-sensitive potassium accumulation in astrocytes in the presence of pathologically high extracellular potassium levels. *Journal of Cerebral Blood Flow and Metabolism*, *4*, 301–304.

Xiong, Z.-Q., & Stringer, J. L. (2000). Regulation of extracellular pH in the developing hippocampus. *Developmental Brain Research*, *122*, 113–117. doi:10.1016/S0165-3806(00)00057–2

Zerangue, N., & Kavanaugh, M. P. (1996). Flux coupling in a neuronal glutamate transporter. *Nature*, *383*, 634–637.

Zeuthen, T. (1994). Cotransport of K+, Cl- and H2O by membrane proteins from choroid plexus epithelium of Necturus maculosus. *The Journal of Physiology*, *478*, 203–219. doi:10.1113/jphysiol.1994.sp020243

Zeuthen, T., Hamann, S., & la Cour, M. (1996). Cotransport of H+, lactate and H2O by membrane proteins in retinal pigment epithelium of bullfrog. *The Journal of Physiology*, *497*, 3–17. doi:10.1113/jphysiol.1996.sp021745

Zeuthen, T, & MacAulay, N. (2012a). Cotransport of water by Na+–K+–2Cl− cotransporters expressed in Xenopus oocytes: NKCC1 versus NKCC2. *The Journal of Physiology*, *590*, 1139–1154. doi:10.1113/jphysiol.2011.226316

Zeuthen, T., & MacAulay, N. (2012b). Transport of water against its concentration gradient: Fact or fiction? *Wiley Interdisciplinary Reviews: Membrane Transport and Signaling*, *1*, 373–381. doi:10.1002/wmts.54

Zhang, Y., Chen, K., Sloan, S. A., Bennett, M. L., Scholze, A. R., O'Keeffe, S., … Wu, J. Q. (2014). An RNA-sequencing transcriptome and splicing database of glia, neurons, and vascular cells of the cerebral cortex. *The Journal of Neuroscience*, *34*, 11929–11947. doi:10.1523/jneurosci.1860-14.2014

How to cite this article: Larsen BR, MacAulay N. Activity-dependent astrocyte swelling is mediated by pH-regulating mechanisms. *Glia*. 2017;65:1668–1681. https://doi.org/10.1002/glia.23187

Original Article

JCBFM

Journal of Cerebral Blood Flow & Metabolism
0(00) 1–16

DOI: 10.1177/0271678X17736715
journals.sagepub.com/home/jcbfm
SAGE

Evaluating the involvement of cerebral microvascular endothelial Na^+/K^+-ATPase and Na^+-K^+-$2Cl^-$ co-transporter in electrolyte fluxes in an in vitro blood–brain barrier model of dehydration

Kasper Lykke[1], Mette Assentoft[1], Sofie Hørlyck[2], Hans CC Helms[2], Anca Stoica[1], Trine L Toft-Bertelsen[1], Katerina Tritsaris[3], Frederik Vilhardt[3], Birger Brodin[2] and Nanna MacAulay[1]

Abstract

The blood–brain barrier (BBB) is involved in brain water and salt homeostasis. Blood osmolarity increases during dehydration and water is osmotically extracted from the brain. The loss of water is less than expected from pure osmotic forces, due to brain electrolyte accumulation. Although the underlying molecular mechanisms are unresolved, the current model suggests the luminally expressed Na^+-K^+-$2Cl^-$ co-transporter 1 (NKCC1) as a key component, while the role of the Na^+/K^+-ATPase remains uninvestigated. To test the involvement of these proteins in brain electrolyte flux under mimicked dehydration, we employed a tight in vitro co-culture BBB model with primary cultures of brain endothelial cells and astrocytes. The Na^+/K^+-ATPase and the NKCC1 were both functionally dominant in the abluminal membrane. Exposure of the in vitro BBB model to conditions mimicking systemic dehydration, i.e. hyperosmotic conditions, vasopressin, or increased $[K^+]_o$ illustrated that NKCC1 activity was unaffected by exposure to vasopressin and to hyperosmotic conditions. Hyperosmotic conditions and increased K^+ concentrations enhanced the Na^+/K^+-ATPase activity, here determined to consist of the $\alpha1\beta1$ and $\alpha1\beta3$ isozymes. Abluminally expressed endothelial Na^+/K^+-ATPase, and not NKCC1, may therefore counteract osmotic brain water loss during systemic dehydration by promoting brain Na^+ accumulation.

Keywords

Blood–brain barrier, brain water homeostasis, dehydration, ion transport, volume regulation

Received 21 June 2017; Revised 9 August 2017; Accepted 13 September 2017

Introduction

Maintenance of the water balance is a fundamental requirement for the organism to function properly. In case of systemic dehydration, the blood volume drops and the plasma becomes hyperosmotic, thus causing osmotic extraction of water from various tissues including the brain. Although aquaporins are absent from cerebral endothelium[1] and its osmotic water permeability low,[2] significant amounts of brain water are extracted during systemic hyperosmolarity due to the large surface area of the cerebral vascular bed.[3] However, this water loss is counteracted by

[1]Department of Neuroscience, Faculty of Health and Medical Sciences, University of Copenhagen, Copenhagen, Denmark
[2]Department of Pharmacy, Faculty of Health and Medical Sciences, University of Copenhagen, Copenhagen, Denmark
[3]Department of Cellular and Molecular Medicine, Faculty of Health and Medical Sciences, University of Copenhagen, Copenhagen, Denmark

Corresponding author:
Nanna MacAulay, Department of Neuroscience, Faculty of Health and Medical Sciences, University of Copenhagen, Blegdamsvej 3, Copenhagen DK-2200, Denmark.
Email: macaulay@sund.ku.dk

cerebral accumulation of the osmolytes Na^+ and Cl^-, which enter the brain via unresolved volume regulatory mechanisms.[4,5] A proposed model suggests the endothelial $Na^+/K^+/2Cl^-$ cotransporter 1 (NKCC1), expressed predominantly at the luminal endothelial membrane, as a key component in brain electrolyte regulation.[6,7] NKCC1 could, in this capacity, and via its ability to cotransport water independently of osmotic forces,[8] serve as a molecular transport mechanism underlying dehydration-induced brain accumulation of Na^+ and Cl^- with associated water influx. However, as NKCC1 is notoriously upregulated in cultured cells[9,10] and its endothelial expression debated,[11,12] its precise role in brain microvasculature-dependent electrolyte flux is unresolved. An alternative endothelial ion transport mechanism involved in brain ion homeostasis is the Na^+/K^+-ATPase, which appears to be predominantly located on the abluminal side of the brain endothelium.[13,14] With this polarized localization, the Na^+/K^+-ATPase could partake in dehydration-induced Na^+ influx into the brain parenchyma. The Na^+/K^+-ATPase consists of one α and one β subunit, each represented by three different isoforms in the mammalian brain.[15] The Na^+/K^+-ATPase ion affinities and other kinetic and regulatory parameters depend on the catalytic α isoform and its associated β subunit.[9,16,17] The isoform-specific endothelial expression of the Na^+/K^+-ATPase, nevertheless, remains unresolved as does its response to factors changed upon systemic dehydration.

In addition to the cell shrinkage expected to occur with the increased plasma osmolarity during systemic dehydration, the antidiuretic hormone, vasopressin (AVP), is released both systemically and centrally.[18,19] Although the kidney is a key target,[20] vasopressin also leads to increased brain water accumulation through activation of the vasopressin $V1_a$ receptor ($V1_aR$).[21–23] $V_{1a}R$ may be expressed in the brain microvasculature[24] although its expression in the cerebral endothelium remains disputed.[12,25,26] The current model includes $V1_aR$ activation of the luminal NKCC1,[27] thus promoting dehydration-induced brain electrolyte accumulation.

Here we set out to determine the response of brain capillary endothelial NKCC1 and Na^+/K^+-ATPase to factors present during systemic dehydration and resolve their proposed contribution to dehydration-induced brain electrolyte accumulation.

Materials and methods

Cultivation of bovine brain endothelial cells, the bEnd3 cell-line, and rat astrocytes

Primary culture of brain microvasculature and astrocytes was used to approximate in vivo conditions in the in vitro co-culture BBB model, while an immortalized cell line was used for comparison. Astrocytes obtained from newborn rats potently induce barrier tightness in bovine endothelium.[28,29] The procedures for isolation of bovine capillaries and rat astrocytes and the culturing procedures were performed as previously described.[30] The protocol, by which the primary cells were obtained, complies with the European Community guidelines for the use of experimental animals and the results are reported in compliance with the ARRIVE guidelines. The bovine cerebral endothelial cells (BCECs) were passaged with a brief trypsinization and seeded (30,000 cells/cm^2) either in collagen/fibronectin-coated 96-well plates (Ca^{2+} signaling) or 24-well plates (radiotracer experiments), or (90,000 cells/cm^2) on collagen/fibronectin-coated transwell polycarbonate filter inserts (area = 1.12 cm^2, pore radius = 0.4 μm, Corning Life Sciences, NY) in a non-contact co-culture with astrocytes.[30] The murine endothelial cell line (bEnd3, ATCC® CRL-2299™) was cultured to confluency in DMEM (30-2002, ATCC) supplemented with 10% FBS (37°C, 5 % CO_2) and passages 30–37 were used for experiments.

Light and electron microscopy

To verify proper cell origin and culture purity in the in vitro BBB model, immunocytochemistry was performed on endothelial cells grown in the co-cultured BBB model, according to standard protocols. Employed primary antibodies were: rabbit α-vWF, 1:400 (ab6994), rabbit α-GFAP, 1:1000 (ab7260), and rabbit α-PDGFRβ, 1:100 (ab32570), all from Abcam, Cambridge, UK and with Alexa 488-conjugated goat-anti-rabbit IgG, 1:200 (Life Technologies, Carlsbad, CA) as the secondary antibody. Staining for filamentous actin employed Alexa 488-conjugated phalloidin, 1:200 (Molecular Probes, Leiden, The Netherlands). Preparations were counterstained with propidium iodide (Molecular Probes, Leiden, The Netherlands) and examined by confocal laser scanning microscopy (Zeiss LSM 510 laser confocal microscope, Carl Zeiss, Jena, Germany). To illustrate the Na^+/K^+-ATPase isoform distribution in bovine microvasculature and resolve putative contamination by astrocytic fragments in the isolated capillaries, we performed morphological analysis of bovine brain samples and isolated capillaries. Both were fixed in 4% paraformaldehyde in phosphate buffer, pH 7.4, and cryopreserved. Semi-thin or ultra-thin sections were produced with a Reichert Ultracut cryoultramicrotome (Leica, Glostrup, Denmark) and processed for either immunofluorescence following standard procedures, or for cryo-immunogold staining as described[31] using

polyclonal anti-Na^+/K^+-ATPase $\alpha 2$ antibodies, 1:1000 (16836-1-AP, Protein Tech, Chicago, IL) or mouse anti-pan-Na^+/K^+-ATPase α subunit, 1:200 (M7-PB-E9, Thermo Fisher Scientific) followed by 7 or 13 nm gold-conjugated goat anti-rabbit or goat anti-mouse antibodies. Immunofluorescence slides were examined in a Zeiss LSM 510 confocal laser scanning microscope using a C-Apochromat 63× 1.2 water immersion objective (Carl Zeiss, Thornwood, NY) and the 488-nm line of the argon laser or 543-nm line of the helium–neon laser for the excitation of Alexa488- or 568-conjugated secondary antibodies and phalloidin (Molecular Probes); 1024×1024-pixel images at 8-bit resolution were imported into Adobe Photoshop (Adobe Systems, Mountain View, CA) for compilation. Ultra-thin sections were examined in a Philips CM100 electron microscope (Eindhoven, The Netherlands) and images acquired with a side-mounted Olympus Veleta camera with a resolution of 2048×2048 pixels. For both light and electron microscopy, controls included omission of primary antibodies or the use of irrelevant, isotype-matched antibodies and produced no or only low levels of staining.

Oocyte preparation and in vitro transcription

To obtain a scenario in which we could determine the activity of a given protein in isolation, we employed *Xenopus laevis* oocytes. Oocytes were obtained from frogs (Nasco, Fort Atkinson, WI) and prepared as previously described.[32] The protocol complies with the European Community guidelines for the use of experimental animals and the experiments were approved by The Danish National Committee for Animal Studies. The results are reported in compliance with the ARRIVE guidelines. cDNA encoding rat NKCC1 (from P. Blaesse and K. Kaila, Helsinki University), rat Na^+/K^+-ATPase $\alpha 1$ and $\beta 1$ subunit (from G. Blanco, University of Kansas), rat AQP4.M23 (from S. Nielsen, Aalborg University) in the oocyte expression vector pXOOM, and the human $V_{1a}R$ (from M. J. Brownstein, NIMH, Bethesda) in the oocyte expression vector pNB1 were linearized downstream from the poly-A segment and in vitro transcribed using T7 mMessage Machine (Ambion, Austin, TX). The cRNA was extracted with MEGAclear (Ambion, Austin, TX) and microinjected into defolliculated *Xenopus* oocytes (in ng RNA/oocyte: 25 rNKCC1 ± 16 $hV_{1a}R$; 10 Na^+/K^+-ATPase α1-2 and 3 β1-2 ± 8 rAQP4). The oocytes were kept in Kulori medium (in mM: 90 NaCl, 1 KCl, 1 $CaCl_2$, 1 $MgCl_2$, 5 Hepes, pH 7.4) for four to six days at 19°C prior to experiments. Oocyte membrane preparations were obtained as previously described.[17]

Radioactive flux experiments

K^+ transport is used as the functional read-out of NKCC1 and Na^+/K^+-ATPase activity. Their activity was measured at 37°C (oocytes at room temperature, RT) as bumetanide-sensitive (10 μM[33]) and ouabain-sensitive (1 mM[34]) K^+ uptake using (2–6 μCi/ml) $^{86}Rb^+$ (NEZ072, PerkinElmer) as a tracer for K^+. $^{86}Rb^+$ quantification was determined with Ultima Gold XR scintillation liquid (PerkinElmer, Skovlunde, Denmark) using a Tri-Carb Liquid Scintillation Analyzer (PerkinElmer). The K^+ uptake rates were calculated from the $^{86}Rb^+$ flux data and the tracer dilution, where indicated. Primary endothelial monocultures or bEnd3 cells cultured in 24-well plates were pretreated in ((in mM): 145 or 139 NaCl (primary culture or bEnd3), 3 KCl, 1.2 $CaCl_2$, 1 $MgCl_2$, 5 D-glucose, 20 Hepes; pH 7.4; 317 or 307 mOsm) for 5–30 min prior to 5 min exposure to identical media containing $^{86}Rb^+$ (± ouabain, ± bumetanide, or ± [Arg^8]-vasopressin (AVP), (Sigma-Aldrich), or vehicle). Osmolarities of the test media were determined with an osmometer, Type 15 (Löser; Berlin, Germany). For studies of Na^+/K^+-ATPase K^+ affinity, cells were washed in K^+-free medium (containing in mM: 127 NaCl, 20 choline chloride, 1.2 $CaCl_2$, 1 $MgCl_2$, 5 D-glucose, 20 Hepes; pH 7.4, 317 mOsm) prior to exposure to isosmotic medium with different concentrations of KCl (equimolar substitution with choline chloride). The assays were terminated by rapid wash with cold assay buffer containing 10 μM bumetanide, 1 mM ouabain and 1 mM $BaCl_2$. The cells were lysed with 1 mM NaOH and protein concentration determined.[35] For the co-cultured endothelial cells, the transendothelial electrical resistance (TEER) was measured at RT prior to all experiments, using an Endohm-12 cup electrode chamber (World Precision Instruments, Sarasota, FL) connected to a Millicell-ERS device (Millipore, MA). The uptake experiments were carried out in TES-buffered DMEM-comp without FBS[30] and the $^{86}Rb^+$ was added to the luminal and/or abluminal side by media change. In hyperosmotic experiments, the endothelial cells were pretreated for 30 min, in absence of astrocytes, with glucose-containing Hepes and bicarbonate-buffered Hank's balanced salt solution (HBSS, Thermo-Fisher) supplemented with mannitol (70 mM) in both chambers for an isosmotic treatment, or with 170 mM mannitol in both chambers for hyperosmotic (Δ100 mOsm) treatment, prior to introduction of the tracer. The assays were terminated by rapid wash of the filter support with cold isosmotic HBSS containing 10 μM bumetanide, 1 mM ouabain and 1 mM $BaCl_2$, and the radioactive content of the filter determined. The uptake assays in *Xenopus* oocytes were carried out for 5–10 oocytes in

((in mM): 5 KCl, 95 NaCl, 1 $MgCl_2$, 1 $CaCl_2$, 10 Hepes, pH 7.4, 207 mOsm). The oocytes were either preincubated (30 min) in control solution, in a K^+-free solution (equimolar substitution with choline chloride), or in a 100 mOsm hyperosmotic solution (addition of 100 mOsm mannitol). The oocytes were exposed to the tracer for 5–10 min (± bumetanide, ± ouabain, or ± vasopressin). The assays were terminated by rapid wash in cold $^{86}Rb^+$-free assay solution and the oocytes individually dissolved in 200 µl 10 % SDS prior to quantification of the radioactive content.

Ca^{2+} signaling

To determine the activity of the G protein-coupled vasopressin receptor, intracellular calcium measurements were performed on primary monoculture of bovine endothelial cells grown in 96-well plates with Fura2-AM (5 µM, Life Technologies, Carlsbad, CA).[36] Excitation was conducted alternatingly at 340 nm and 380 nm and emission was measured at 510 nm with a NOVOstar microplate reader (BMG Labtech, Germany). Vasopressin (Sigma-Aldrich) and ATP (Tocris Bioscience, Bristol, UK) was added automatically from stock solutions to final concentrations of 1 µM and 100 µM. Autofluorescence values were subtracted from the experimentally achieved emission values and changes in $[Ca^{2+}]_i$ were calculated as 340:380 nm ratios.

Oocyte volume measurements

The experimental setup for measuring and calculating water permeability of oocytes has been described in detail previously.[37] Briefly, the oocytes were placed in a small chamber with a glass bottom and perfused with a control solution (in mM: 100 NaCl, 2 KCl, 1 $CaCl_2$, 1 $MgCl_2$, 10 Hepes, pH 7.4, RT). Oocyte images were captured from below at a rate of 25 images/s. The oocytes were challenged with a hyperosmotic solution (addition of 100 mOsm mannitol) for determination of water permeability and cell volume changes.

Quantitative PCR

Total RNA from primary endothelial cells cultured as monolayers or as co-cultures on filter inserts was purified using the RNeasy mini and micro kit (Qiagen, Copenhagen, Denmark), treated with DNase, reverse transcribed (0.2 µg RNA) and amplified by qPCR as previously described.[38] Primers were from Baddela et al.[39] or designed using NCBI's pick primer software: ATP1A1 (NM_001076798.1); F: GGAATGGGTGTT GCCCTGAG; R: TGAGCTTCCGGACTTCGTCA (106 bp), ATP1A2 (NM_001081524.1); ATCCCCGA GATCACCCCTTT; R: TTCACCAGCTTGTCCGTC TG (188 bp), ATP1A3 (XM_002695074.5); F: AT TGTCCTCTGGCTCCGTGA; R: GGTACCGGTT GTCATTGGGG (128 bp), ATP1B1 (NM_00103 5334.1); F: GGAGTTTTTGGGCAGGACCG; R: CCGCCAGGCAGCCATAAAAA (77 bp), ATP1B2 (NM_174677.2); F: TGGACAGCCCTGTGTCTT CA; R: TTGCCGTTTGCAGGGAACAT (147), ATP 1B3 (NM_001035393.2); F: TACAACCGGACAAC CGGAGA; R: GAGTCTGAAGCATGGCCCAC (133 bp), GFAP (NM_174065.2); F: CACAGGAAA GGAAGAGGCTG; R: AGTGTTTCCTGGGTCAG GTG (138 bp). For reference genes, we employed GAPDH (NM_001034034.2); F: GTGAAGGTCGG AGTGAACGG; R: TTGATGGCGACGATGTCCA C (92 bp) and RPS18 (NM_001033614.2); F: GAG GTGGAACGTGTGATCACCATT; R: TGTATTT CCCGTCCTTCACGTCCT (100 bp). The primer annealing temperature was 60°C. The optimum concentration for each primer set was 200 nM, except for GAPDH (300 nM) and the amplification efficiencies were 90–99% for all primer sets. GenEx (MultiD Analyses AB, Sweden) was used for data analysis, including testing for best reference gene combinations.

SDS-PAGE and Western blot

Bovine grey matter tissue, purified capillaries, and co-cultured endothelial cells were lysed in RIPA buffer (150 mM NaCl, 1% Triton X-100, 0.5% Na deoxycholate, 0.1% SDS, 5 mM EDTA, 50 mM Tris, pH 8, supplemented with 0.4 mM Pefabloc and 8 µM Leupeptin (Sigma-Aldrich)) and sonicated with Sonoplus mini20 (Bandelin electronic, Berlin, Germany). Protein concentration was determined using DC Protein Assay (Bio-Rad, Hercules, CA). The expression of Na^+/K^+-ATPase isoforms was analyzed by SDS-PAGE and immunoblotting on Immobilon-FL PVDF membranes (Millipore, MA) using: mouse anti-α1 a6F, 1:60 (DSHB, Iowa City, IA); rabbit anti-α2 07-674, 1:500 (Millipore, MA); mouse anti-α3 XVIF9-G10, 1:1000 (Thermo-Fisher); chicken anti-GAPDH AB2302, 1:2000 (Millipore, MA) diluted in Odyssey blocking buffer:PBS-T 1:1 (LI-COR, Lincoln, NE). Detection was performed using fluorophore-conjugated secondary antibodies (LI-COR) and scanned on an Odyssey CLx imaging system.

Data analysis

All functional assays were performed on batches of cells obtained from at least three different animals (primary cell culture and *Xenopus* oocyte batches). The *n* refers to the number of individual experiments, each carried out with 3–4 wells/condition for mammalian cells, 5–10

oocytes, or batches of purified capillaries. Data are shown as mean ± SEM, unless otherwise stated. K^+-dependent Na^+/K^+-ATPase activity was approximated to Michaelis–Menten kinetics, and K_M for K^+ and the maximal uptake rate V_{max} were calculated using non-linear regression: $V = V_{max} \cdot [K^+]_o/(K_M + [K^+]_o)$, where V is the ouabain-sensitive K^+ uptake rate. Statistical analysis was performed with GraphPad Prism 6.0 (La Jolla, CA) as indicated in the figure legends and $p < 0.05$ was considered statistically significant.

Results

Brain endothelial cells, co-cultured with astrocytes, generate electrically tight monolayers and express endothelial cell marker proteins

To approximate the in vivo blood–brain barrier with proper endothelial polarization and monolayer tightness, we employed a co-culture in vitro BBB model. A non-contact co-culture configuration (Figure 1(a)) was chosen to facilitate determination of endothelial ion transport from both the luminal and the abluminal compartment.[30] The primary endothelial cultures were immunolabelled with antibodies towards an endothelial marker (vWF), an astrocyte marker (GFAP), and a pericyte marker (PDGFRβ) in order to verify cell origin and culture purity, Figure 1(b). The average TEER measured in all in vitro BBB co-culture models included in the present study was 1609 ± 476 (SD) $\Omega \cdot cm^2$, $n = 248$ individual wells from 18 experiments (Figure 1(c)), which falls within the range of the estimated in vivo BBB TEER of 1500–1870 $\Omega \cdot cm^2$.[40,41]

We initially determined the transendothelial flux of K^+ (in the form of its radioactive congener $^{86}Rb^+$) in the luminal-to-abluminal and abluminal-to-luminal direction. The bidirectional fluxes were of equal magnitude and dependent on the TEER (Figure 2(a)), a phenomenon commonly observed for small paracellular tracers like mannitol.[42,43] The transendothelial K^+ flux was not affected by addition of inhibitors of NKCC1 (bumetanide) and the Na^+/K^+-ATPase (ouabain) to the luminal or abluminal side (Figure 2(a)). These results indicate that transendothelial K^+ flux occurs predominantly via the paracellular pathway in the co-cultured endothelial monolayers.

We therefore, instead, determined the uptake rates across each endothelial membrane by adding $^{86}Rb^+$ to either the luminal or the abluminal compartment, followed by determination of the intracellular $^{86}Rb^+$ accumulation. The intracellular accumulation of the

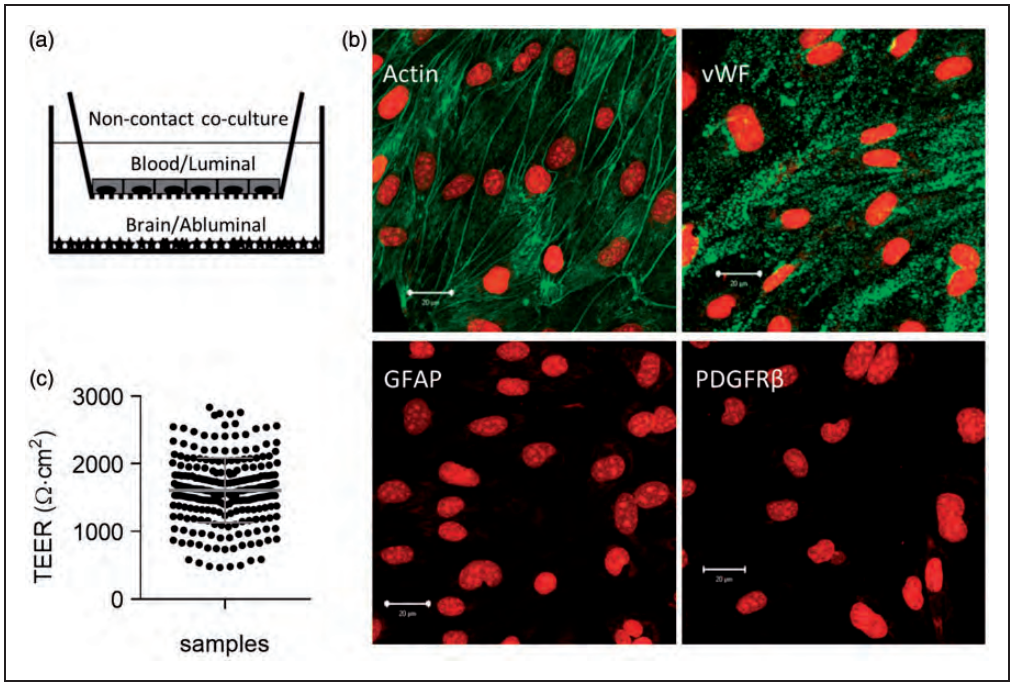

Figure 1. (a) Illustration of the primary cultured bovine capillary endothelial cells (rectangles) and astrocyte (stars) in vitro non-contact co-culture model of the BBB. (b) Immunocytochemistry with antibodies targeting filamentous actin, von Willbrand's factor (vWF), glial fibrillary acidic protein (GFAP) and platelet-derived growth factor recetor β (PDGFRβ) in the co-cultured endothelial cells (green). Visualization of cell nuclei with propidium iodide (red). Scale bars: 20 μm. (c) TEER values for the co-cultured endothelial cells ($n = 248$ individual wells from 18 experiments, error bars indicate SD).

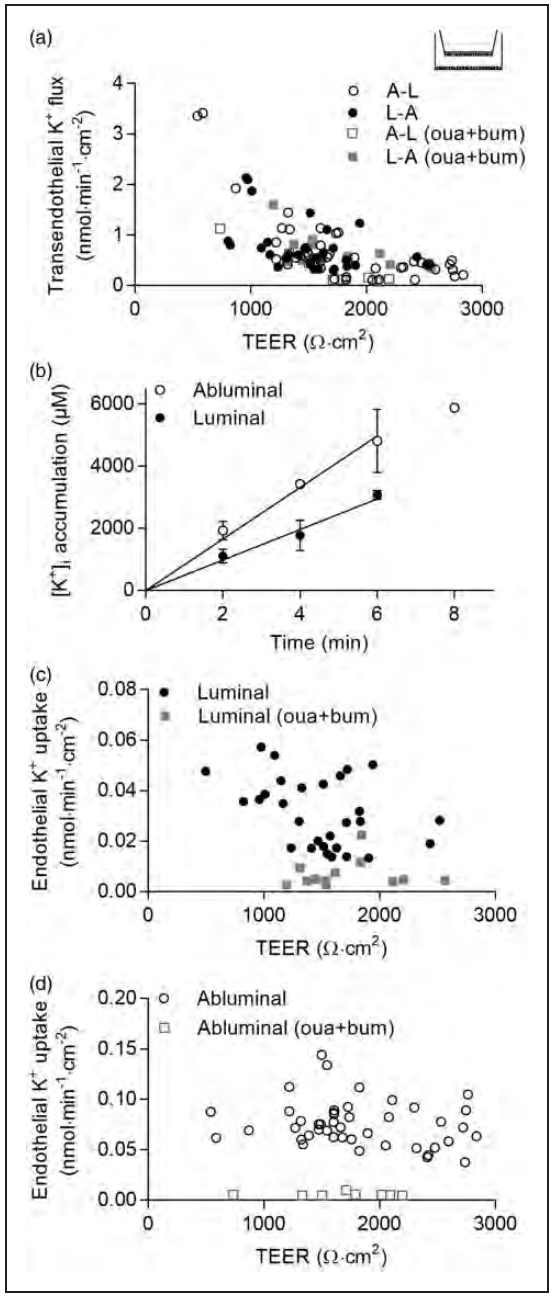

Figure 2. K^+ flux studies in the in vitro co-culture BBB model using $^{86}Rb^+$ as a tracer for K^+. (a) Transendothelial K^+ flux as a function of TEER. A–L: Abluminal to luminal flux; L–A: Luminal to abluminal flux. Flux was measured for 2–6 min in the presence ($n = 3$) or absence ($n = 7$–8) of ouabain (1 mM) and bumetanide (10 μM). (b) Endothelial K^+ accumulation from luminal or abluminal uptake as a function of time. Data are shown as mean ± SD from a representative experiment carried out with three wells per time point. (c) Endothelial K^+ uptake from the luminal side as a function of TEER value. Uptake was measured in the presence or absence of ouabain (1 mM) and bumetanide (10 μM). Combined data from $n = 14$ experiments. (d) as in (c) but conducted from the abluminal side, combined data from $n = 14$ experiments. Oua: ouabain, bum: bumetanide.

radioisotope occurred as a linear function of time, at least until 6 min, regardless of whether the isotope was added to the luminal or abluminal side (Figure 2(b)). All subsequent uptake assays were therefore performed in a 5-min experimental window. In this time window, the amount of total transendothelial isotope crossing was negligible (< 0.1% of total isotope) in endothelial cells with TEER above 500 $\Omega \cdot cm^2$ and this TEER value was therefore employed as the cut-off value for measuring luminal and abluminal K^+-transporting mechanisms.

The luminal and abluminal endothelial K^+ uptake rates showed no TEER dependency and were completely blocked by simultaneous addition of ouabain and bumetanide (Figure 2(c) and (d)), indicating that NKCC1 and the Na^+/K^+-ATPase act as the major endothelial inwardly directed K^+-transporting mechanisms in the in vitro co-culture BBB model.

The differences in luminal and abluminal transport rates indicate dominant abluminal expression of NKCC1 and the Na^+/K^+-ATPase

The luminal and abluminal K^+ uptake rates were determined to estimate the relative contributions of NKCC1 and the Na^+/K^+-ATPase at the two membranes. The abluminal NKCC1 activity was 7-fold higher than the luminal NKCC1 activity ($p < 0.001$, Figure 3(a)), while the abluminal Na^+/K^+-ATPase activity was 3.7-fold higher than the luminal Na^+/K^+-ATPase activity ($p < 0.01$, Figure 3(b)). The luminal NKCC1-mediated K^+ uptake was not significantly different from the luminal Na^+/K^+-ATPase-mediated K^+ uptake, $p = 0.98$, and neither was the abluminal NKCC1-mediated K^+ uptake significantly different from the abluminal Na^+/K^+-ATPase-mediated K^+ uptake, $p = 0.82$, two-way ANOVA followed by Šídák's multiple comparison (Figure 3(a) and (b)). These results indicate a polarization of the brain endothelium in vitro, with a dominant abluminal expression of NKCC1 and the Na^+/K^+-ATPase, each contributing to ~50% of the K^+ uptake at both membranes.

Vasopressin does not affect NKCC1 and Na^+/K^+-ATPase activity in the endothelial cells

To resolve if a vasopressin-dependent regulatory pathway induces NKCC1-mediated activity, vasopressin was applied to both sides of the in vitro co-culture BBB model prior to measuring the bumetanide-sensitive K^+ uptake from both the luminal and the abluminal face of the endothelial cell layer. Vasopressin did not influence neither luminal NKCC1 activity ($p = 0.62$, Figure 4(a)) nor abluminal NKCC1 activity ($p = 0.99$, Figure 4(b)). To consolidate this observation, we tested the effect of vasopressin on

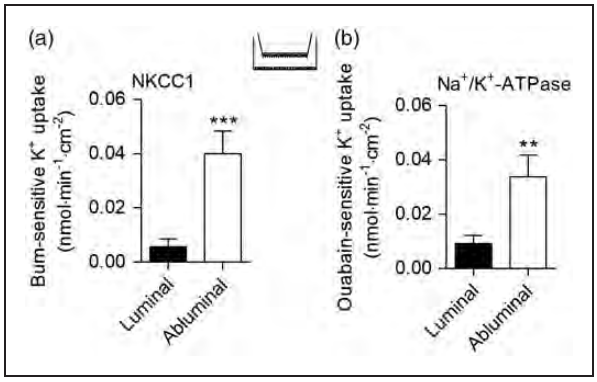

Figure 3. NKCC1 and Na^+/K^+-ATPase activity in the in vitro co-culture BBB model. (a) Luminal and abluminal NKCC1 activity assessed as bumetanide-sensitive K^+ uptake. The co-cultured endothelial cells were assayed for co-transporter activity for 5 min in medium containing bumetanide (0 or 10 μM) at the same side as tracer. (b) Luminal and abluminal Na^+/K^+-ATPase activity assessed as ouabain-sensitive K^+ uptake in co-culture models exposed to medium containing ouabain (0 or 1 mM) at the same side as the tracer for 5 min. Data are shown as means ± SEM with $n = 3$. Statistical significances were determined using two-way ANOVA followed by Šídák's multiple comparisons test. $^{**}p < 0.01$, $^{***}p < 0.001$.

both NKCC1 and Na^+/K^+-ATPase activity in monocultures of bovine capillary endothelium (in the absence of astrocytes). Vasopressin did not increase NKCC1 activity ($p = 0.051$, Figure 4(c)) or Na^+/K^+-ATPase activity ($p = 0.88$, Figure 4(d)). Similar lack of vasopressin-dependent transport activity was obtained using an immortalized endothelial cell line from mouse brain, bEnd3 (NKCC1 activity; $p = 0.95$, Figure 4(e) and the Na^+/K^+-ATPase activity; $p = 0.64$, Figure 4(f)).

To test if $V_{1a}R$ is functionally present in primary monoculture of bovine endothelium pre-loaded with the Ca^{2+} indicator Fura2-AM, the intracellular Ca^{2+} response was monitored upon addition of vasopressin to the test medium. No vasopressin-dependent intracellular Ca^{2+} response was observed, whereas addition of the positive control, ATP, to the extracellular medium produced a robust Ca^{2+} response (Figure 4(g)). To ensure biological activity of the employed batch of vasopressin, we (in another project carried out simultaneously[44]) tested the vasopressin-mediated inositol phosphate (IP) production in $hV_{1a}R$-expressing COS-7 cells. As illustrated in Figure 4(h), the $V_{1a}R$ responded correctly to addition of vasopressin to the test medium with an EC_{50} of 0.68 nM (figure adapted from Lykke et al.[44]). These data indicate that the $V_{1a}R$ is not functionally expressed in the cultured endothelial cells employed in these experiments.

To obtain an experimental scenario in which we could ensure co-expression of $V_{1a}R$ and NKCC1, we co-expressed these in the *Xenopus laevis* oocyte expression system and determined NKCC1 activity by means of K^+ ($^{86}Rb^+$) uptake. The background K^+ uptake (uninjected oocytes) was unaffected by the addition of vasopressin as was the K^+ uptake in $V_{1a}R$/NKCC1-expressing oocytes kept in basal solution during the uptake, ($97.8 \pm 4.8\%$ of control, $p = 1.0$, Figure 4(i)). As NKCC1 is known to be activated by shrinkage of the oocytes,[45] we additionally tested if the activity of pre-activated NKCC1 could be further enhanced by activation of the vasopressin receptor. Although NKCC1 was robustly activated in a bumetanide-sensitive manner by cell shrinkage (9.3 ± 0.3 fold, $p < 0.001$), this activation was not further enhanced upon activation of $V_{1a}R$ (9.1 ± 0.4 fold, $p > 0.99$). Taken together, our data suggest that vasopressin, via activation of $V_{1a}R$, does not directly activate NKCC1 (or the Na^+/K^+-ATPase).

Cell shrinkage activates NKCC1 differentially depending on the experimental system

To test if cell shrinkage could directly affect the two transport systems and thus lead to brain ion and water influx, the in vitro co-culture BBB model was exposed to an isosmotic or hyperosmotic (+100 mOsm) solution (luminal and abluminal) prior to determination of NKCC1- and Na^+/K^+-ATPase-mediated activity in the respective test solutions. The transporter activity determined following the hyperosmotic challenge was not significantly different from the control situation for NKCC1 ($p = 0.48$, Figure 5(a)) or for the Na^+/K^+-ATPase ($p = 0.07$, Figure 5(b)), although the latter displayed a tendency towards increased activity. The hyperosmotic preincubation period reduced the TEER down to 19 $\Omega \cdot cm^2$ (n = 2 wells), which, however, should not affect the cellular uptake as the isotope was added to both sides simultaneously. As cell shrinkage-induced NKCC1 activity previously has been demonstrated in cultured cells,[6,45] we determined the effect of NKCC1 in the immortalized bEnd3 cell line. We did indeed find a 2.5-fold increase in NKCC1 activity upon a 100 mOsm hyperosmotic treatment ($p < 0.05$, Figure 5(c)). Hyperosmotic activation of heterologously expressed NKCC1 was confirmed in NKCC1-expressing *Xenopus* oocytes, in which the K^+ uptake increased 60-fold ($p < 0.01$) with preincubation of the oocytes in an additional 100 mOsm mannitol (or by preincubation in K^+ free solution), Figure 5(d). These data show that the NKCC1 is indeed activated by cell shrinkage upon heterologous expression in *Xenopus* oocytes and in an immortalized endothelial cell line, whereas we detected no hyperosmolar-induced activation of NKCC1 in the tight in vitro co-culture BBB model.

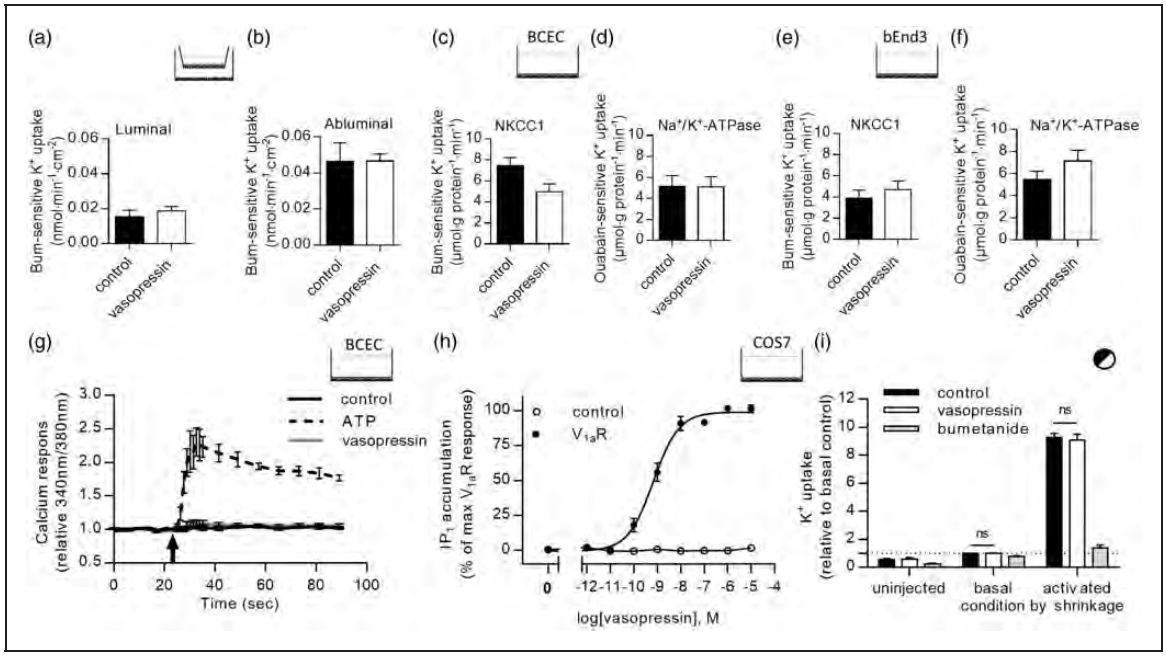

Figure 4. Effects of vasopressin on NKCC1 and Na^+/K^+-ATPase activity. (a) Luminal and (b) abluminal NKCC1 activity in bovine endothelial cells of the in vitro co-culture BBB model treated for 5 min with bumetanide (0 or 10 μM) on the same side as $^{86}Rb^+$ ± vasopressin (AVP) (1 μM) in both chambers ($n = 3$). Effects of vasopressin on (c) NKCC1 activity and (d) Na^+/K^+-ATPase activity in bovine capillary endothelial monocultures (BCEC) or (e–f) the bEnd3 cell line. Primary endothelial monocultures and bEnd3 cells were pretreated in isosmotic Hepes buffered media for 5 min before assayed in identical media containing $^{86}Rb^+$ with or without bumetanide (10 μM) or ouabain (1 mM) ± vasopressin (1 μM) for 5 min ($n = 5$). One-way ANOVA followed by Dunnett's multiple comparisons test was applied to test for vasopressin-mediated increase in NKCC1 or Na^+/K^+-ATPase activity. (g) Ca^{2+} response as a function of time determined in primary cultured endothelial monocultures loaded with Fura2-AM and treated with vasopressin (1 μM), ATP (100 μM), or control buffer. (h) Dose-dependent stimulation of IP_1 response by vasopressin in $hV_{1a}R$-transfected COS7 cells (figure adapted from Lykke et al.,[44] n = 7). (i) Vasopressin-mediated stimulation of NKCC1 activity in $hV_{1a}R$/rNKCC1-expressing oocytes. Uninjected or $hV_{1a}R$/rNKCC1-expressing oocytes were pretreated for 30 min in Hepes-buffered medium containing 0 or 5 mM K^+ (to obtain cell shrinkage) before assayed in isosmotic media containing 5 mM K^+, $^{86}Rb^+$ ± vasopressin (1 μM) or bumetanide (10 μM) for 5 min. Data are normalized to control oocytes under basal conditions (n=3) and analyzed by two-way ANOVA followed by Šídák's multiple comparison test. Ns: not significant.

The Na^+/K^+-ATPase is activated by hyperosmolar-induced cell shrinkage

We expressed the Na^+/K^+-ATPase in *Xenopus* oocytes to resolve whether the tendency towards hyperosmolar-induced increase in Na^+/K^+-ATPase activity observed in the in vitro BBB model (Figure 5(b)) could be solidified in an isolated system. To facilitate cell shrinkage, the $\alpha 1\beta 1$ isoform combination of the Na^+/K^+-ATPase was co-expressed with aquaporin 4 (AQP4). As illustrated in the representative traces in Figure 5(e), the AQP4-expressing oocytes shrunk at a faster rate than that of the non-aquaporin-expressing oocytes ($6.9 \pm 0.8\%$ shrinkage after 10 min compared to $1.6 \pm 0.2\%$ in the control oocytes, $p < 0.001$, Figure 5(e), right panel). Expression of the Na^+/K^+-ATPase together with AQP4 increased the ouabain-sensitive K^+ uptake compared to oocytes only expressing AQP4 ($p < 0.001$, Figure 5(f)). Exposure to a hyperosmotic solution (+100 mOsm mannitol) increased the ouabain-sensitive uptake of Na^+/K^+-ATPase/AQP4-expressing oocytes by 1.8-fold ($p < 0.05$, Figure 5(g)). This hyperosmolar-mediated increase in activity of the $\alpha 1\beta 1$ isoform combination of the Na^+/K^+-ATPase indicates that the tendency of hyperosmolar-mediated ouabain-sensitive K^+ uptake found in the in vitro co-culture BBB model (Figure 5(b)) may well arise from increased Na^+/K^+-ATPase activity.

K^+ affinity of the Na^+/K^+-ATPase suggests physiologically relevant regulation

To investigate if brain endothelial Na^+/K^+-ATPase activity is regulated by the expected increase in parenchymal K^+ during osmotic extraction of brain water and, as a consequence, regulate Na^+ flux into the brain, we determined the ouabain-sensitive apparent K^+ affinity in the primary-cultured endothelial monolayer (Figure 6). The measured K_M of 2.1 ± 0.7 mM, n

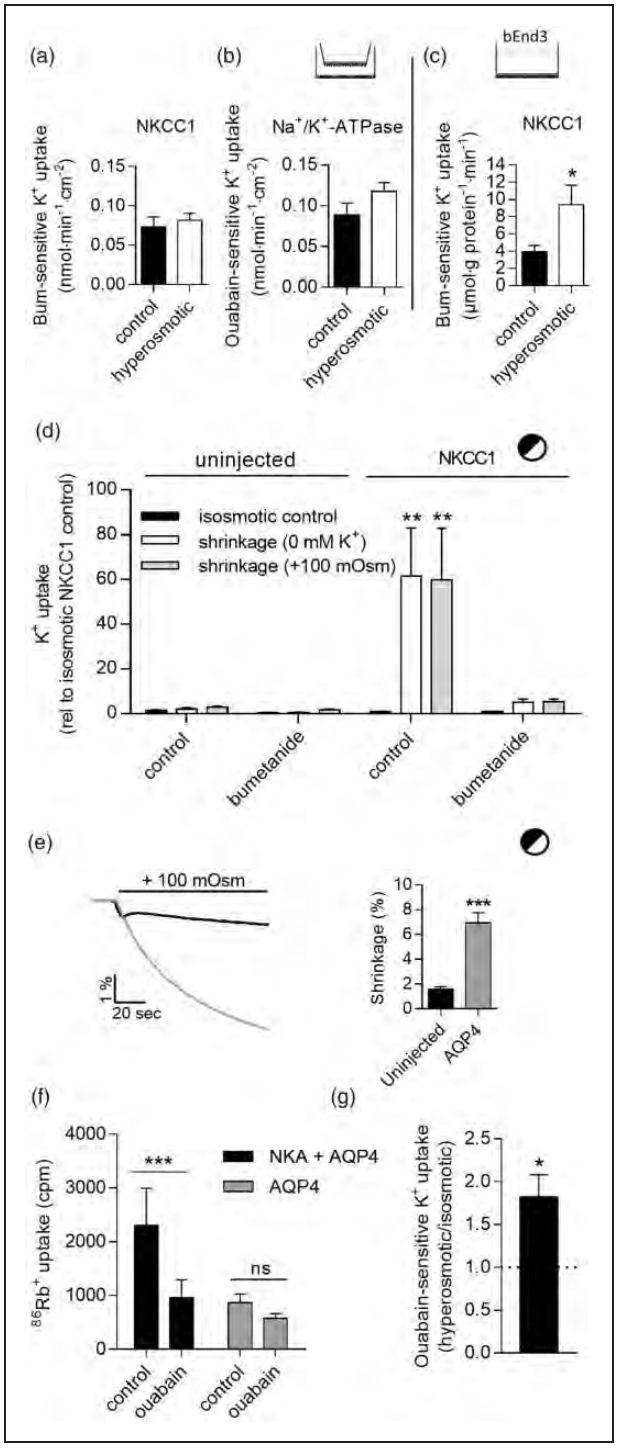

Figure 5. Hyperosmotic regulation of NKCC1 and Na^+/K^+-ATPase. (a) Bumetanide-sensitive and (b) ouabain-sensitive K^+ uptake in the endothelial cells of the in vitro co-culture BBB model pretreated with isosmotic or hyperosmotic test solution (+100 mOsm mannitol) for 30 min before assayed in identical solution containing $^{86}Rb^+$ ± bumetanide (0 or 10 µM) or ouabain (0 or 1 mM) for 5 min, $n = 4$. (c) Bumetanide-sensitive activity in the bEnd3 cell line pretreated with isosmotic test solution or 100 mOsm hypertonic test solution for 30 min before assayed in identical solution containing $^{86}Rb^+$ + bumetanide (0 or 10 µM) for 5 min, $n = 5$. Statistical significant differences between isosmotic control and hyperosmotic treatment were evaluated by unpaired Student's *t*-test. (d) Hyperosmotic regulation of NKCC1 expressed in oocytes. Uninjected or rNKCC1-expressing oocytes were pretreated for 30 min in oocyte buffer containing 0 or 5 mM K^+ before assayed in isosmotic medium containing 5 mM K^+, $^{86}Rb^+$ + bumetanide (0 or 10 µM) or ouabain (0 or 1 mM) for 5 min or assayed without pretreatment in an equal uptake solution but with addition of 100 mOsm mannitol. Data are normalized to control oocytes under basal conditions ($n = 3$) and analyzed by two-way ANOVA followed by Šídák's multiple comparison test. (e) Volume traces obtained from AQP4-expressing oocytes (grey) or uninjected oocytes (black) challenged with a hyperosmotic gradient of 100 mOsm. Right panel indicates total shrinkage after 10 min. $n = 9$–11. (f) K^+ uptake in Na^+/K^+-ATPase(NKA)/AQP4- or AQP4-expressing oocytes assayed in isosmotic test solution containing $^{86}Rb^+$ ± ouabain (1 mM), shown is a representative experiment of $n = 8$, error bars as SD. (g) Hyperosmotic (+100 mOsm mannitol)-mediated increase in ouabain-sensitive K^+ uptake in Na^+/K^+-ATPase/AQP4-expressing oocytes ($n = 6$). *$p < 0.05$, ** $p < 0.01$, ***$p < 0.001$, ns: not significant.

$= 4$, is in a range which allows increased Na^+/K^+-ATPase activity during incidents of raised parenchymal extracellular K^+ concentrations.

Na^+/K^+-ATPase of the $\alpha 1\beta 1$ and $\alpha 1\beta 3$ isoform combinations dominate in brain capillaries

To determine the endothelial Na^+/K^+-ATPase isoform distribution in the endothelial compartment, the mRNA encoding the Na^+/K^+-ATPase subunit isoforms were quantified by qPCR in freshly isolated bovine cerebral capillaries. mRNA from the two α subunits $\alpha 1$, $\alpha 2$, and the three β subunits $\beta 1$, $\beta 2$ and $\beta 3$ were detected in the samples, whereas the $\alpha 3$ transcript was absent (Figure 7(a)). $\alpha 2$ and $\beta 2$ constitute the typical astrocytic isoforms[15] and their presence could be due to astrocytic endfeet remnants in the capillary fraction, as also indicated by GFAP transcript in the capillary fraction (data not shown). We further determined the relative abundance of the different Na^+/K^+-ATPase isoforms in both endothelial monocultures and co-cultures relative to purified capillaries. The transcript levels in the cultured endothelial cells were normalized to the transcript levels in the parent capillary isolation (across three different batches of brain capillaries). $\alpha 3$ remained undetected. However, both $\alpha 2$ and $\beta 2$ (and GFAP, data not shown) were barely detectable in the cultured endothelial cells (Figure 7(b)), suggesting that the $\alpha 2$ and $\beta 2$ transcripts in capillaries were due to the presence of astrocyte endfeet remnants.

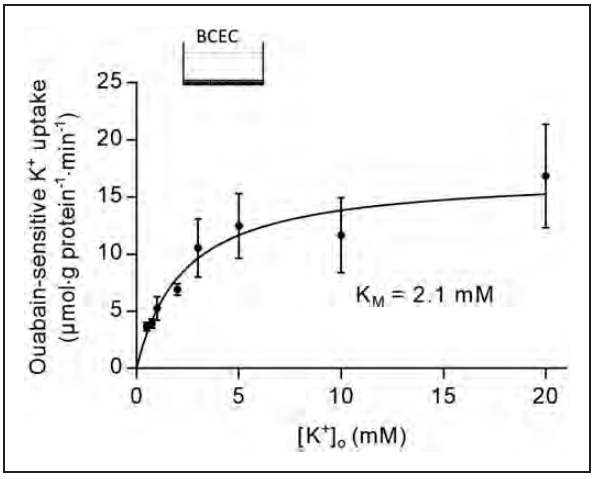

Figure 6. K^+ affinity of the Na^+/K^+-ATPases in primary cultured endothelial monocultures (BCEC) assessed as ouabain-sensitive K^+ uptake (with $^{86}Rb^+$ as the tracer). Cells were pre-treated in Hepes-buffered medium containing 3 mM K^+ for 5 min and then rapidly washed in K^+-free buffer before assayed in isosmotic buffer containing K^+ (0.5 to 20 mM) ± ouabain (1 mM). Data and K_M are shown as means ± SEM ($n = 4$) and curve fits were approximated to Michaelis–Menten kinetics for individual experiments using prior to averaging the K_Ms.

The mRNA levels of $\alpha1$ and $\beta1/\beta3$ showed an expression profile comparable to the isolated capillaries (although with a small reduction in $\beta1$). These transcript data indicate that $\alpha1$ and $\beta1/\beta3$ are the predominant Na^+/K^+-ATPase isoforms expressed in brain endothelial cells and that this favored isoform abundance is upheld in cell culture under our experimental conditions.

The transcript data were substantiated by Western blotting, which showed expression of Na^+/K^+-ATPase $\alpha1$ and $\alpha2$ in purified capillaries (Figure 7(c)), while only $\alpha1$ was detected in the endothelial cells grown as co-culture with astrocytes (Figure 7(d)).

The difference in expression of Na^+/K^+-ATPase isoforms between isolated capillaries and cultured endothelial cells derived from them suggests astrocytic remnants in the isolated capillaries, which would be absent from cultured cells. To answer this question, we applied morphological analysis to resolve the endothelial distribution of Na^+/K^+-ATPase in vivo by immunofluorescence and cryo-immunogold labeling of in situ or isolated bovine capillaries. Na^+/K^+-ATPase $\alpha2$ staining was clearly not endothelial in origin. Rather, $\alpha2$ immunoreactivity was confined to severed (from the isolation procedure) astroglial foot processes remaining associated with the outer aspect of the endothelial basement membrane (Figure 7(e) to (i)). A pan-Na^+/K^+-ATPase α subunit mAb, in addition to the astrocytic basement membrane stain observed above, also indicated immunoreactivity at the abluminal portion of endothelial cells (Figure 7(j)), presumably indicating $\alpha1$ subunit expression in the endothelial cells. Taken together, with $\alpha3$ transcript absent from the endothelium and $\alpha2$ localized to the astrocytic endfeet, $\alpha1$ thus appears as the predominant α-isoform in abluminal membrane of bovine brain capillaries with $\beta1$ and $\beta3$ as the preferred accessory subunits.

Discussion

In the present study, we have demonstrated that the Na^+/K^+-ATPase, but not the NKCC1, is subject to functional regulation upon treatments mimicking dehydration in a tight in vitro co-culture model of the BBB. To access both membranes of the endothelial cell layer, we employed a non-contact in vitro endothelial/astrocytic co-culture model of the blood–brain barrier with TEER similar to estimates of the in vivo BBB TEER (1500-1870 $\Omega \cdot cm^2$).[40,41] This tightness of the endothelial cell layer is crucial for proper induction of the BBB properties and allowed us to determine the transport rate from each side of the endothelium in isolation. Functional expression of NKCC1 and the Na^+/K^+-ATPase was primarily detected at the astrocytic compartment-facing side of the endothelial cell layer, thus denoted the abluminal side of the in vitro BBB model. This abluminally located NKCC1-mediated activity is in agreement with a previous study,[46] while others have found predominantly luminal NKCC1 expression.[7,47] The contrasting localization of NKCC1 may arise from differences in the monolayer tightness of the in vitro BBB model and underscores the importance of employing models with high TEER values to ensure proper BBB characteristics. Immunohistochemical studies of rat brain indicated scarce expression of NKCC1 in the cerebral endothelium in vivo,[11] which aligns well with transcriptome studies detecting limited mRNA encoding NKCC1 in this cell type.[12] With NKCC1 notoriously upregulated upon cell cultivation[10] and the limited specificity of a range of commercially available NKCC1 antibodies, it remains unresolved to what extent NKCC1 is functionally expressed in brain microvascular endothelium in vivo under certain conditions. Nevertheless, the dominant expression of NKCC1 at the abluminal side of the endothelium and a predicted inwardly-directed ion transport is challenging to reconcile with the current model based on NKCC1 serving as the molecular mechanism underlying dehydration-induced ion and water accumulation in the brain.

The antidiuretic hormone vasopressin increases in the plasma of patients experiencing stroke and intracranial injuries[48,49] and promotes enhanced endothelial water flux[50] and edema formation[51] in a manner sensitive to $V_{1a}R$ antagonism.[21,22] The vasopressin-mediated

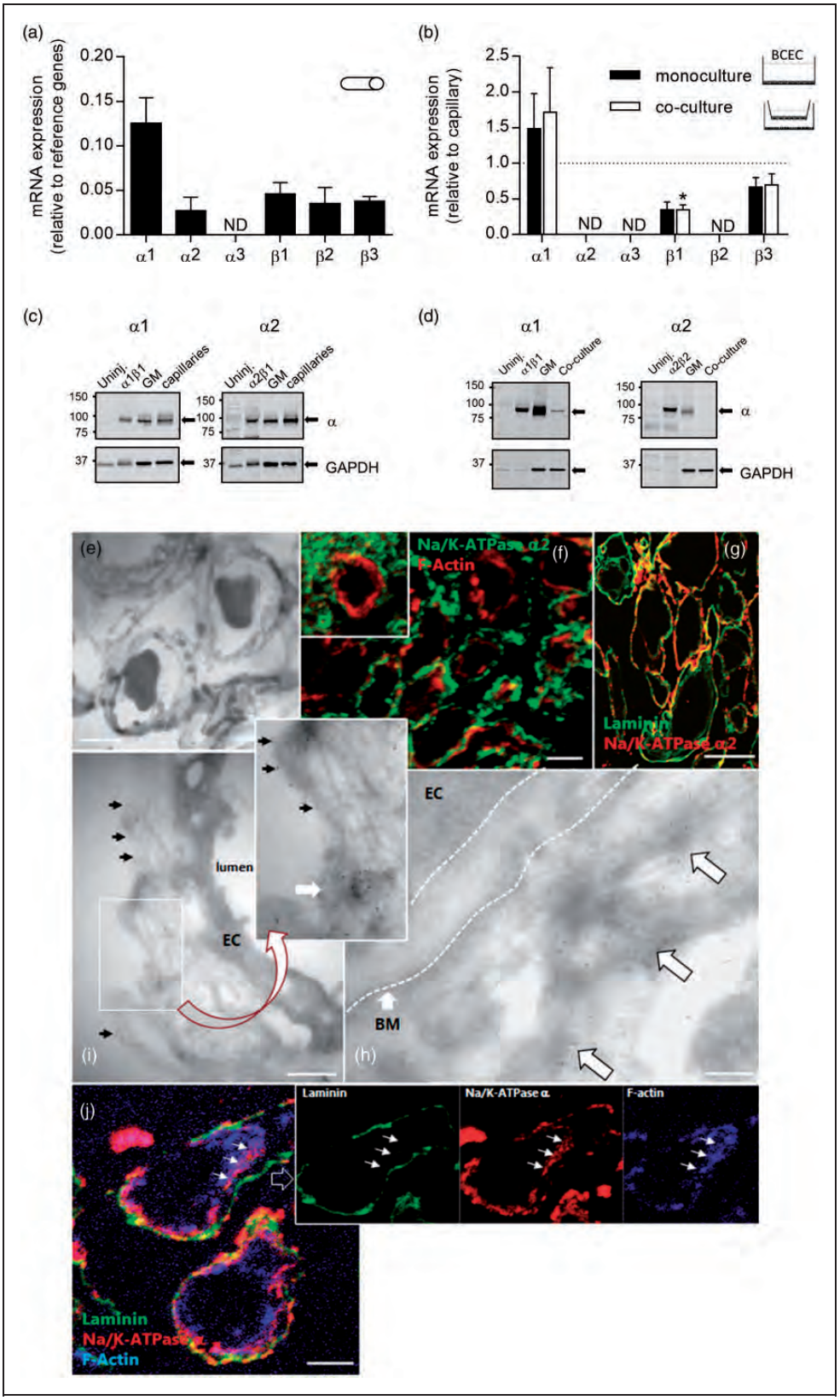

Figure 7. Na^+/K^+-ATPase subunit expression in the cerebral endothelium. (a) qPCR quantification of Na^+/K^+-ATPase subunit mRNA in purified bovine cortical capillaries normalized to reference genes (see materials and methods). (b) mRNA levels in primary cultured cerebral endothelial cells (monoculture (BCEC) or co-culture), normalized to reference genes and quantified relative to the

endothelial water flux could thus occur via the V_{1a}R-dependent NKCC1 activation, proposed in the current model.[27] We were, however, unable to detect vasopressin-mediated activation of NKCC1 activity, whether determined in monocultures or co-cultures of brain endothelial cells (*in vitro* BBB models) or in *Xenopus* oocytes co-expressing NKCC1 and the vasopressin receptor. Biological activity of the vasopressin was therefore verified in V_{1a}R-expressing COS-7 cells in a parallel experimental series, which illustrated V_{1a}R-dependent down-regulation of AQP4 in V_{1a}R/AQP4-expressing oocytes.[44] Ca^{2+} imaging revealed lack of V_{1a}R activity in the primary cultures of bovine cerebral endothelium, which aligns well with low levels of V_{1a}R transcript in cerebral endothelium[12,25] and lack of V_{1a}R expression in capillary endothelial membrane as determined by immunohistochemistry and autoradiography.[26,52] Although we are unaware of the experimental explanation to the diversion from the report by O'Donnell et al.[27] in which V_{1a}R-mediated NKCC1 activation was demonstrated,[27] a partial reason may be exposure of the co-culture to the glucocorticoid dexamethasone in order to induce BBB properties:[30] Dexamethasone exposure may abolish the vasopressin-dependent stimulation of NKCC1 activity.[53] However, neither endothelial monoculture, the bEnd3 cell line, nor V_{1a}R/NKCC1-expressing oocytes were exposed to this compound.

Ultrastructural determination of distribution of Na^+/K^+-ATPase reaction products at the microvascular endothelium has revealed predominant accumulation at the abluminal membrane[13,14,54] although luminal membrane Na^+/K^+-ATPase has been proposed as well.[55–57] A possible reason for this discrepancy is the variable tissue fixation, which has been shown to alter the levels of the Na^+/K^+-ATPase reaction products at the two endothelial membranes,[55] while the enzyme distribution may be rearranged upon cultivation in vitro.[54] These biochemical methods, however, does not reveal the isoform-specific distribution of the Na^+/K^+-ATPase. Western blot analysis of isolated brain microvessels (possibly including remnants of astrocytic endfeet and nerve endings) has previously detected expression of all tested isoforms (α1–3 and β1–2).[58] Our combined results from qPCR, Western Blot, and light/electron microscopy identified endothelial expression of α1 on the abluminal membrane in predicted combination with β1 or β3. α3 transcript was absent in the capillary fractions and electron microscopy illustrated that the detected α2 originated from the astrocytic endfeet tightly wrapped around the purified capillaries. In an earlier study, brain microvessels contained slightly more total α subunit (α1–3) but significantly less total β subunit (β1–2) in comparison to that of whole brain homogenate.[58] Since the subunit stoichiometry for functionally active Na^+/K^+-ATPases is 1α:1β, this apparent lack of β subunit implies that a substantial fraction of the total capillary β isoform could be assigned to β3, which was not included in the aforementioned analysis.[58] Altogether, we therefore propose that the Na^+/K^+-ATPase of bovine brain capillaries mainly consists of $\alpha1\beta1$ and $\alpha1\beta3$. In

Figure 7. Continued
corresponding capillary preparation ($n = 3$). Differences in mRNA expression relative to the capillary preparation were determined by one-way ANOVA followed by Dunnett's multiple comparison test. *$p < 0.05$, ND: not detectable. (c–d) Western blot analysis of Na^+/K^+-ATPase α subunits in isolated capillaries (c) and co-cultured endothelial cells (d). Membrane preparations from *Xenopus* oocytes expressing the individual Na^+/K^+-ATPase α isoforms (as indicated) were used as positive controls with uninjected oocytes serving as the negative control. The endogenous expression of isoforms was validated in isolated bovine grey matter (GM). (e) TEM of isolated bovine brain capillaries, bar 2 μm. (f) Cryosections of isolated bovine brain capillaries were processed for immunofluorescence to visualize F-actin (endothelial cells; red) and Na^+/K^+-ATPase α2 subunit (green). Inset; bovine brain capillary in situ stained for the same. Note the lack of co-localization between the two antigens in both cases. Bar, 10 μm. (g) Immunofluorescence of isolated capillaries to show endothelial basement membrane (laminin; green) and Na^+/K^+-ATPase α2 subunit (red) immunoreactivity. Note there is no α2 subunit staining within the circumference delineated by the basement membrane. Bar, 10 μm. (h) Cryoimmunogold staining of Na^+/K^+-ATPase α2 subunit in bovine brain shows that endothelial cells (EC) are devoid of α2 immunoreactivity, which is almost exclusively localized to astroglial foot processes (h; arrows), which envelope that vessel on the abluminal side of the basement membrane (BM; marked with stippled line). Bar, 200 nm. (i) Separation of α2 staining (i; arrows) from the endothelium is particularly evident in isolated capillaries where the subendothelial matrix has expanded (during the isolation process) to displace the basement membrane some distance from the endothelium. Inset shows the boxed region in (i) at higher magnification to reveal the astroglial foot processes with α2 immunoreactivity (open arrow). Bar, 500 nm. (j) Immunofluorescence on isolated capillaries with anti-pan-Na^+/K^+-ATPase α subunit (red) and polyclonal rabbit anti-laminin (green) antibodies counterstained with Alexa-conjugated phalloidin (blue) to visualize endothelial F-actin. The pan-Na^+/K^+-ATPase mAb displays immunoreactivity similar to α2 staining; astroglial processes associated with the exterior of the basement membrane (laminin; green), but in addition, shows immunoreactivity at the basolateral part of the endothelial cells (arrows), likely representing the Na^+/K^+-ATPase α1 subunit. Bar, 5 μm.

support of this isoform distribution, the ouabain-sensitivity of Na^+/K^+-ATPase activity in rat brain endothelial cells ($IC_{50} \approx 10\,\mu M$[59]) resembles that of the rodent $\alpha 1$ isoform[60] and an RNA-seq transcriptome database lists robust mRNA levels of the $\alpha 1$, $\beta 1$ and $\beta 3$ subunit isoforms in mouse brain vascular cells.[12] Cultivation of the bovine brain capillary endothelium (both in the in vitro co-culture BBB model and as primary endothelial monoculture) preserved the expression of $\alpha 1$ and $\beta 1/\beta 3$. Taken together with the dominant abluminal Na^+/K^+-ATPase activity in the tight in vitro co-culture BBB model, this finding supports the relevance of this model for determination of cerebral microvasculature endothelial Na^+/K^+-ATPase transport characteristics.

Different isoform combinations of the Na^+/K^+-ATPase display distinct kinetic characteristics, such as apparent ion affinities.[9,15,16,61] For the endothelial Na^+/K^+-ATPase to increase its activity in response to dehydration-induced osmotic extraction of water and associated predicted fluctuations in parenchymal $[K^+]_o$ (and other ions) and thus maintain the cerebral K^+ homeostasis, its isoform expression should be of a combination which renders the Na^+/K^+-ATPase sensitive to $[K^+]_o$ in the parenchyma.[62] Such K^+-mediated increase in Na^+/K^+-ATPase activity is accompanied by Na^+ flux from the endothelium to the brain and this net parenchymal accumulation of electrolytes thus counteracts the osmotic brain water loss, given parallel accumulation of a counter ion. With a K_M for K^+ of 2.1 mM in the primary endothelial cultures, in agreement with previous reports,[59,62,63] the Na^+/K^+-ATPase displays the ability to react to increased $[K^+]$. In contrast, the neuronal Na^+/K^+-ATPase activity saturates at the basal $[K^+]_o$ of around 3 mM.[63] Of the two isoform combinations predicted to dominate the endothelial Na^+/K^+-ATPase activity, the $\alpha 1\beta 1$ isoform combination has an apparent K^+ affinity in the range of 1 mM[9,16,61,64] and thus approaches saturation at basal parenchymal $[K^+]_o$. The $\alpha 1\beta 3$ isoform combination is less well studied and apparent K^+ affinities in the range 1–3 mM have been reported.[61,65] The $\alpha 1\beta 3$ isoform combination could then, in part, underlie the apparent K^+ affinity observed in cultured or freshly isolated cerebral microvascular endothelial cells. With such relatively low K^+ affinity of an endothelial abluminal Na^+/K^+-ATPase, excess K^+ could be efficiently cleared from the brain tissue during intraparenchymal K^+ fluctuations and thus serve to protect the neurons from global prolonged K^+-mediated depolarization during dehydration. The endothelial Na^+/K^+-ATPase is, in addition, likely to be prone to regulation by a range of systemic volume-regulating hormones such as angiotensin and noradrenalin[66,67] and in that manner further counteract brain water loss during systemic dehydration.

Endothelial cell shrinkage is predicted to occur during systemic dehydration and the Na^+/K^+-ATPase activity in the in vitro co-culture BBB model displayed a tendency towards hyperosmolar activation. Such shrinkage-induced activation reached statistical significance in heterologously expressed Na^+/K^+-ATPase $\alpha 1\beta 1$ isozyme in oocytes. This Na^+/K^+-ATPase isoform may therefore be subject to direct activation by hyperosmotic stress and could in that manner increase the brain Na^+ content during dehydration. NKCC1, on the other hand, is recognized to be activated by cell shrinkage in cell lines and heterologous expression systems via activation of the WNK and SPAK/OSR1 kinases.[68,69] We observed this shrinkage-evoked activation in NKCC1-expressing oocytes and in the immortalized endothelial cell line, bEnd3, but not in the tight in vitro co-culture BBB model from acutely isolated endothelial cells. This discrepancy may suggest that NKCC1 is fully activated at basal conditions in the brain endothelium and/or that the regulatory kinases involved in cell shrinkage-activation of NKCC1 may be reduced in the brain endothelium. Although heterologous expression systems and immortalized cell lines are useful for a wide range of experimental approaches and biophysical characterization of transport proteins, they may not fully recapitulate what is observed in vivo or in in vitro systems approximating in vivo conditions. It must, however, be emphasized that despite the proper induction of important BBB characteristics in the co-culture in vitro BBB model, this experimental setup remains a model of a complex cellular system and may not fully recapitulate in vivo conditions. Although it would be desirable to test the hypothesis arising from the present study in an in vivo setting, the difficulty regarding determination of transport activity at the abluminal endothelial membrane and the severe complications arising from in vivo inhibition of the Na^+/K^+-ATPase will certainly make it a challenging endeavor.

In conclusion, in an in vitro co-culture BBB model with TEER values resembling that of the in vivo BBB, we detected abluminal localization of NKCC1 and lack of hyperosmolar- and vasopressin receptor-mediated NKCC1 activation. This finding, taken together with low expression of NKCC1 and $V_{1a}R$ in cerebral endothelium, suggests a limited role of NKCC1 in dehydration-induced brain electrolyte accumulation and thus contrasts with the current model of dehydration-induced brain electrolyte accumulation. The abluminal localization of the Na^+/K^+-ATPase (of the $\alpha 1\beta 1$ and $\alpha 1\beta 3$ isozymes) and its activation by dehydration-induced K^+ fluctuations and cell shrinkage, instead, predicts this ion transporter to enhance cerebral Na^+ accumulation during systemic dehydration and thereby reduce osmotic brain water loss in vivo.

Funding

The author(s) disclosed receipt of the following financial support for the research, authorship, and/or publication of this article: This study was supported by the Sapere Aude program under the Danish Medical Research Council (grant number 0602-02344B FSS) to NM, Læge Sofus Carl Emil Friis og hustru Olga Doris Friis' legat (to NM), the Carlsberg Foundation (CF15-0070) to NM and the Faculty of Health and Medical Sciences, University of Copenhagen (to NM).

Acknowledgements

We thank Carina Lynnerup Pedersen, Charlotte Goos Iversen for technical assistance and Professor Kjeld Møllgård for expert histological guidance.

Declaration of conflicting interests

The author(s) declared no potential conflicts of interest with respect to the research, authorship, and/or publication of this article.

Authors' contributions

KL, MA, SH, HCCH, AS, TLTB, KT, FV, BB, NM Made a substantial contribution to the concept and design, acquisition of data or analysis and interpretation of data. KL, MA, SH, HCCH, AS, KT, FV, BB, NM Drafted the article or revised it critically for important intellectual content. KL, MA, SH, HCCH, AS, TLTB, KT, FV, BB, NM Approved the version to be published.

References

1. Haj-Yasein NN, Vindedal GF, Eilert-Olsen M, et al. Glial-conditional deletion of aquaporin-4 (Aqp4) reduces blood-brain water uptake and confers barrier function on perivascular astrocyte endfeet. *Proc Natl Acad Sci U S A* 2011; 108: 17815–17820.
2. Paulson OB, Hertz MM, Bolwig TG, et al. Filtration and diffusion of water across the blood-brain barrier in man. *Microvasc Res* 1977; 13: 113–124.
3. Nag S and Begley D. Blood-brain barrier, exchange of metabolites and gases. In: Kalimo H (ed.) Blood-brain barrier, exchange of metabolites and gases. *Pathology and genetics: Cerebrovascular diseases* 2005; 22–29.
4. Cserr HF, DePasquale M and Patlak CS. Regulation of brain water and electrolytes during acute hyperosmolality in rats. *Am J Physiol* 1987; 253: F522–F529.
5. Cserr HF, DePasquale M and Patlak CS. Volume regulatory influx of electrolytes from plasma to brain during acute hyperosmolality. *Am J Physiol* 1987; 253: F530–F537.
6. O'Donnell ME. Role of Na-K-Cl cotransport in vascular endothelial cell volume regulation. *Am J Physiol* 1993; 264: C1316–C1326.
7. O'Donnell ME, Tran L, Lam TI, et al. Bumetanide inhibition of the blood-brain barrier Na-K-Cl cotransporter reduces edema formation in the rat middle cerebral artery occlusion model of stroke. *J Cereb Blood Flow Metab* 2004; 24: 1046–1056.
8. Zeuthen T and MacAulay N. Cotransport of water by Na(+)-K(+)-2Cl(-) cotransporters expressed in Xenopus oocytes: NKCC1 versus NKCC2. *J Physiol* 2012; 590: 1139–1154.
9. Larsen BR, Assentoft M, Cotrina ML, et al. Contributions of the Na(+)/K(+)-ATPase, NKCC1, and Kir4.1 to hippocampal K(+) clearance and volume responses. *Glia* 2014; 62: 608–622.
10. Raat NJ, Delpire E, van Os CH, et al. Culturing induced expression of basolateral Na+-K+-2Cl- cotransporter BSC2 in proximal tubule, aortic endothelium, and vascular smooth muscle. *Pflugers Arch* 1996; 431: 458–460.
11. Plotkin MD, Kaplan MR, Peterson LN, et al. Expression of the Na(+)-K(+)-2Cl- cotransporter BSC2 in the nervous system. *Am J Physiol* 1997; 272: C173–C183.
12. Zhang Y, Chen K, Sloan SA, et al. An RNA-sequencing transcriptome and splicing database of glia, neurons, and vascular cells of the cerebral cortex. *J Neurosci* 2014; 34: 11929–11947.
13. Betz AL, Firth JA and Goldstein GW. Polarity of the blood-brain barrier: distribution of enzymes between the luminal and antiluminal membranes of brain capillary endothelial cells. *Brain Res* 1980; 192: 17–28.
14. Kato S and Nakamura H. Ultrastructural and ultracytochemical studies on the blood-brain barrier in chronic relapsing experimental allergic encephalomyelitis. *Acta Neuropathol* 1989; 77: 455–464.
15. Larsen BR, Stoica A and MacAulay N. Managing brain extracellular K(+) during neuronal activity: the physiological role of the Na(+)/K(+)-ATPase subunit isoforms. *Front Physiol* 2016; 7: 141.
16. Blanco G. Na,K-ATPase subunit heterogeneity as a mechanism for tissue-specific ion regulation. *Semin Nephrol* 2005; 25: 292–303.
17. Larsen BR, Holm R, Vilsen B, et al. Glutamate transporter activity promotes enhanced Na+/K+-ATPase-mediated extracellular K+ management during neuronal activity. *J Physiol* 2016; 594: 6627–6641.
18. Demotes-Mainard J, Chauveau J, Rodriguez F, et al. Septal release of vasopressin in response to osmotic, hypovolemic and electrical stimulation in rats. *Brain Res* 1986; 381: 314–321.
19. Jojart I, Joo F, Siklos L, et al. Immunoelectronhistochemical evidence for innervation of brain microvessels by vasopressin-immunoreactive neurons in the rat. *Neurosci Lett* 1984; 51: 259–264.
20. Kortenoeven ML and Fenton RA. Renal aquaporins and water balance disorders. *Biochim Biophys Acta* 2014; 1840: 1533–1549.
21. Kleindienst A, Dunbar JG, Glisson R, et al. The role of vasopressin V1A receptors in cytotoxic brain edema formation following brain injury. *Acta Neurochir* 2013; 155: 151–164.
22. Liu X, Nakayama S, Amiry-Moghaddam M, et al. Arginine-vasopressin V1 but not V2 receptor antagonism modulates infarct volume, brain water content, and aquaporin-4 expression following experimental stroke. *Neurocrit Care* 2010; 12: 124–131.

23. Rosenberg GA, Estrada E and Kyner WT. The effect of arginine vasopressin and V1 receptor antagonist on brain water in cat. *Neurosci Lett* 1988; 95: 241–245.
24. Pearlmutter AF, Szkrybalo M, Kim Y, et al. Arginine vasopressin receptors in pig cerebral microvessels, cerebral cortex and hippocampus. *Neurosci Lett* 1988; 87: 121–126.
25. Daneman R, Zhou L, Agalliu D, et al. The mouse blood-brain barrier transcriptome: a new resource for understanding the development and function of brain endothelial cells. *PLoS One* 2010; 5: e13741.
26. Szmydynger-Chodobska J, Chung I, Kozniewska E, et al. Increased expression of vasopressin v1a receptors after traumatic brain injury. *J Neurotrauma* 2004; 21: 1090–1102.
27. O'Donnell ME, Duong V, Suvatne J, et al. Arginine vasopressin stimulation of cerebral microvascular endothelial cell Na-K-Cl cotransporter activity is V1 receptor and [Ca] dependent. *Am J Physiol Cell Physiol* 2005; 289: C283–C292.
28. Deli MA, Abraham CS, Kataoka Y, et al. Permeability studies on in vitro blood-brain barrier models: physiology, pathology, and pharmacology. *Cell Mol Neurobiol* 2005; 25: 59–127.
29. Helms HC, Abbott NJ, Burek M, et al. In vitro models of the blood-brain barrier: an overview of commonly used brain endothelial cell culture models and guidelines for their use. *J Cereb Blood Flow Metab* 2016; 36: 862–890.
30. Helms HC and Brodin B. Generation of primary cultures of bovine brain endothelial cells and setup of cocultures with rat astrocytes. *Methods Mol Biol* 2014; 1135: 365–382.
31. Vilhardt F, Nielsen M, Sandvig K, et al. Urokinase-type plasminogen activator receptor is internalized by different mechanisms in polarized and nonpolarized Madin-Darby canine kidney epithelial cells. *Mol Biol Cell* 1999; 10: 179–195.
32. Fenton RA, Moeller HB, Zelenina M, et al. Differential water permeability and regulation of three aquaporin 4 isoforms. *Cell Mol Life Sci* 2010; 67: 829–840.
33. Lykke K, Tollner K, Feit PW, et al. The search for NKCC1-selective drugs for the treatment of epilepsy: structure-function relationship of bumetanide and various bumetanide derivatives in inhibiting the human cation-chloride cotransporter NKCC1A. *Epilepsy Behav* 2016; 59: 42–49.
34. Stoica A, Larsen BR, Assentoft M, et al. The alpha2beta2 isoform combination dominates the astrocytic Na+/K+ -ATPase activity and is rendered nonfunctional by the alpha2.G301R familial hemiplegic migraine type 2-associated mutation. *Glia*, Epub ahead of print 2017.
35. Lowry OH, Rosebrough NJ, Farr AL, et al. Protein measurement with the Folin phenol reagent. *J Biol Chem* 1951; 193: 265–275.
36. Hunt BD and Lambert DG. Ratiometric [Ca(2)(+)]i measurements in adherent cell-lines using the NOVOstar microplate reader. *Methods Mol Biol* 2013; 937: 111–120.
37. Zeuthen T, Belhage B and Zeuthen E. Water transport by Na+-coupled cotransporters of glucose (SGLT1) and of iodide (NIS). The dependence of substrate size studied at high resolution. *J Physiol* 2006; 570: 485–499.
38. Sorensen CE, Tritsaris K, Reibel J, et al. Elevated p16ink4a expression in human labial salivary glands as a potential correlate of cognitive aging in late midlife. *PLoS One* 2016; 11: e0152612.
39. Baddela VS, Baufeld A, Yenuganti VR, et al. Suitable housekeeping genes for normalization of transcript abundance analysis by real-time RT-PCR in cultured bovine granulosa cells during hypoxia and differential cell plating density. *Reprod Biol Endocrinol* 2014; 12: 118.
40. Crone C and Olesen SP. Electrical resistance of brain microvascular endothelium. *Brain Res* 1982; 241: 49–55.
41. Butt AM, Jones HC and Abbott NJ. Electrical resistance across the blood-brain barrier in anaesthetized rats: a developmental study. *J Physiol* 1990; 429: 47–62.
42. Helms HC, Hersom M, Kuhlmann LB, et al. An electrically tight in vitro blood-brain barrier model displays net brain-to-blood efflux of substrates for the ABC transporters, P-gp, Bcrp and Mrp-1. *AAPS J* 2014; 16: 1046–1055.
43. Patabendige A, Skinner RA, Morgan L, et al. A detailed method for preparation of a functional and flexible blood-brain barrier model using porcine brain endothelial cells. *Brain Res* 2013; 1521: 16–30.
44. Lykke K, Assentoft M, Fenton RA, et al. Vasopressin receptors V1a and V2 are not osmosensors. *Physiol Rep* 2015; 3: pii: e12519.
45. Haas M. Properties and diversity of (Na-K-Cl) cotransporters. *Annu Rev Physiol* 1989; 51: 443–457.
46. Abbruscato TJ, Lopez SP, Roder K, et al. Regulation of blood-brain barrier Na,K,2Cl-cotransporter through phosphorylation during in vitro stroke conditions and nicotine exposure. *J Pharmacol Exp Ther* 2004; 310: 459–468.
47. Sun D, Lytle C and O'Donnell ME. Astroglial cell-induced expression of Na-K-Cl cotransporter in brain microvascular endothelial cells. *Am J Physiol* 1995; 269: C1506–C1512.
48. Miura M, Takagi S, Matsukado Y, et al. Influence of vasopressin level on osmotic pressure and sodium concentration in plasma and cerebrospinal fluid in patients with intracranial lesions. *Neurol Med Chir* 1989; 29: 806–810.
49. Barreca T, Gandolfo C, Corsini G, et al. Evaluation of the secretory pattern of plasma arginine vasopressin in stroke patients. *Cerebrovasc Dis* 2001; 11: 113–118.
50. Rosenberg GA, Kyner WT, Fenstermacher JD, et al. Effect of vasopressin on ependymal and capillary permeability to tritiated water in cat. *Am J Physiol* 1986; 251: F485–F489.
51. Liu XF, Shi YM and Lin BC. Mechanism of action of arginine vasopressin on acute ischemic brain edema. *Chin Med J* 1991; 104: 480–483.
52. Kretzschmar R, Landgraf R, Gjedde A, et al. Vasopressin binds to microvessels from rat hippocampus. *Brain Res* 1986; 380: 325–330.

53. Putney LK, Brandt JD and O'Donnell ME. Effects of dexamethasone on sodium-potassium-chloride cotransport in trabecular meshwork cells. *Invest Ophthalmol Vis Sci* 1997; 38: 1229–1240.
54. Vorbrodt AW and Trowbridge RS. Ultracytochemical characteristics of cultured goat brain microvascular endothelial cells [corrected]. *J Histochem Cytochem* 1991; 39: 1555–1563.
55. Manoonkitiwongsa PS, Schultz RL, Wareesangtip W, et al. Luminal localization of blood-brain barrier sodium, potassium adenosine triphosphatase is dependent on fixation. *J Histochem Cytochem* 2000; 48: 859–865.
56. Sanchez del Pino MM, Hawkins RA and Peterson DR. Biochemical discrimination between luminal and abluminal enzyme and transport activities of the blood-brain barrier. *J Biol Chem* 1995; 270: 14907–14912.
57. Vorbrodt AW, Lossinsky AS and Wisniewski HM. Cytochemical localization of ouabain-sensitive, K+-dependent p-nitro-phenylphosphatase (transport ATPase) in the mouse central and peripheral nervous systems. *Brain Res* 1982; 243: 225–234.
58. Zlokovic BV, Mackic JB, Wang L, et al. Differential expression of Na,K-ATPase alpha and beta subunit isoforms at the blood-brain barrier and the choroid plexus. *J Biol Chem* 1993; 268: 8019–8025.
59. Goldstein GW. Relation of potassium transport to oxidative metabolism in isolated brain capillaries. *J Physiol* 1979; 286: 185–195.
60. Jewell EA and Lingrel JB. Comparison of the substrate dependence properties of the rat Na,K-ATPase alpha 1, alpha 2, and alpha 3 isoforms expressed in HeLa cells. *J Biol Chem* 1991; 266: 16925–16930.
61. Crambert G, Hasler U, Beggah AT, et al. Transport and pharmacological properties of nine different human Na, K-ATPase isozymes. *J Biol Chem* 2000; 275: 1976–1986.
62. Lin JD. Potassium transport in isolated cerebral microvessels from the rat. *Jpn J Physiol* 1985; 35: 817–830.
63. Schielke GP, Moises HC and Betz AL. Potassium activation of the Na,K-pump in isolated brain microvessels and synaptosomes. *Brain Res* 1990; 524: 291–296.
64. Munzer JS, Daly SE, Jewell-Motz EA, et al. Tissue- and isoform-specific kinetic behavior of the Na,K-ATPase. *J Biol Chem* 1994; 269: 16668–16676.
65. Yu C, Xie Z, Askari A, et al. Enzymatic properties of human Na,K-ATPase alpha1beta3 isozyme. *Arch Biochem Biophys* 1997; 345: 143–149.
66. Muscella A, Aloisi F, Marsigliante S, et al. Angiotensin II modulates the activity of Na+,K+-ATPase in cultured rat astrocytes via the AT1 receptor and protein kinase C-delta activation. *J Neurochem* 2000; 74: 1325–1331.
67. Taub M and Cutuli F. Data on Na,K-ATPase in primary cultures of renal proximal tubule cells treated with catecholamines. *Data Brief* 2016; 6: 419–422.
68. Alessi DR, Zhang J, Khanna A, et al. The WNK-SPAK/OSR1 pathway: master regulator of cation-chloride cotransporters. *Sci Signal* 2014; 7: re3.
69. Gagnon KB, England R and Delpire E. Characterization of SPAK and OSR1, regulatory kinases of the Na-K-2Cl cotransporter. *Mol Cell Biol* 2006; 26: 689–698.

nature COMMUNICATIONS

ARTICLE

DOI: 10.1038/s41467-018-04677-9 OPEN

Cotransporter-mediated water transport underlying cerebrospinal fluid formation

Annette B. Steffensen[1], Eva K. Oernbo[1], Anca Stoica[1], Niklas J. Gerkau[2], Dagne Barbuskaite[3], Katerina Tritsaris[3], Christine R. Rose[2] & Nanna MacAulay[1]

Cerebrospinal fluid (CSF) production occurs at a rate of 500 ml per day in the adult human. Conventional osmotic forces do not suffice to support such production rate and the molecular mechanisms underlying this fluid production remain elusive. Using ex vivo choroid plexus live imaging and isotope flux in combination with in vivo CSF production determination in mice, we identify a key component in the CSF production machinery. The $Na^+/K^+/2Cl^-$ cotransporter (NKCC1) expressed in the luminal membrane of choroid plexus contributes approximately half of the CSF production, via its unusual outward transport direction and its unique ability to directly couple water transport to ion translocation. We thereby establish the concept of cotransport of water as a missing link in the search for molecular pathways sustaining CSF production and redefine the current model of this pivotal physiological process. Our results provide a rational pharmacological target for pathologies involving disturbed brain fluid dynamics.

[1] Department of Neuroscience, Faculty of Health and Medical Sciences, University of Copenhagen, Noerre Allé 14, 2200 Copenhagen, Denmark. [2] Institute of Neurobiology, Heinrich Heine University Duesseldorf, Universitaetsstrasse 1, 40225 Duesseldorf, Germany. [3] Department of Cellular and Molecular Medicine, Faculty of Health and Medical Sciences, University of Copenhagen, Noerre Allé 14, 2200 Copenhagen, Denmark. Correspondence and requests for materials should be addressed to N.M. (email: macaulay@sund.ku.dk)

The mammalian brain is bathed in the cerebrospinal fluid (CSF), which is continuously produced at a rate of approximately 500 ml fluid per day in the adult human[1]. Prior to exiting the brain, the CSF travels through the ventricular system and part of it re-enters the brain via the para-vascular route along the large arteries and penetrating arterioles[2,3]. The CSF is predominantly produced by the choroid plexus, an epithelial monolayer resting on highly vascularized connective tissue and located at the base of each of the four ventricles[4–7]. The molecular mechanisms underlying this choroidal fluid production remain unresolved. Dysregulation of CSF production or clearance may lead to brain water accumulation and raised intracranial pressure, as evident in patients with hydrocephalus. Hydrocephalus most commonly occurs as a consequence of obstructed CSF outflow, and is routinely treated by insertion of a ventriculo-peritoneal shunt diverting the excessive fluid from the ventricles into the peritoneal cavity in the abdomen[8]. However, in certain choroidal pathologies, such as choroid plexus hyperplasia, choroid plexus papilloma, and posthemorrhagic hydrocephalus, the increased intracranial pressure occurs, at least in part, from CSF overproduction[6,9,10]. The molecular mechanisms underlying the pathologic increase in CSF production remain elusive. Insight into the transport mechanisms underlying brain CSF accumulation could provide a rational therapeutic target to reduce this pathologic brain fluid accumulation.

The CSF production is generally assumed to take place by transport of osmotically active ions (e.g. sodium by the Na^+/K^+-ATPase[11,12]) followed by osmotically obliged, passive movement of water, partly via the water channel aquaporin 1 (AQP1) expressed at the luminal membrane of the choroid plexus[13,14]. However, several observations suggest that such a simple osmotic model may not be adequate: (1) The CSF production declined by a mere 20% in the AQP1 knock-out mice, partly ascribed to the 80% reduction of central venous blood pressure in these mice[15]. (2) With the known osmotic water permeability across the choroid plexus, detailed calculations have demonstrated that the osmolarity of the CSF must exceed that of the plasma by as much as 250 mOsm (in contrast to the measured difference in osmolarity of 5−10 mOsm[16,17]) in order for the CSF to be produced at the observed rate by simple osmosis[18]. (3) The choroid plexus has the ability to produce CSF against an oppositely directed osmotic gradient[18–21]. Taken together, conventional aquaporin-mediated osmotic water transport does not suffice to sustain the rates of CSF production consistently observed in mammals.

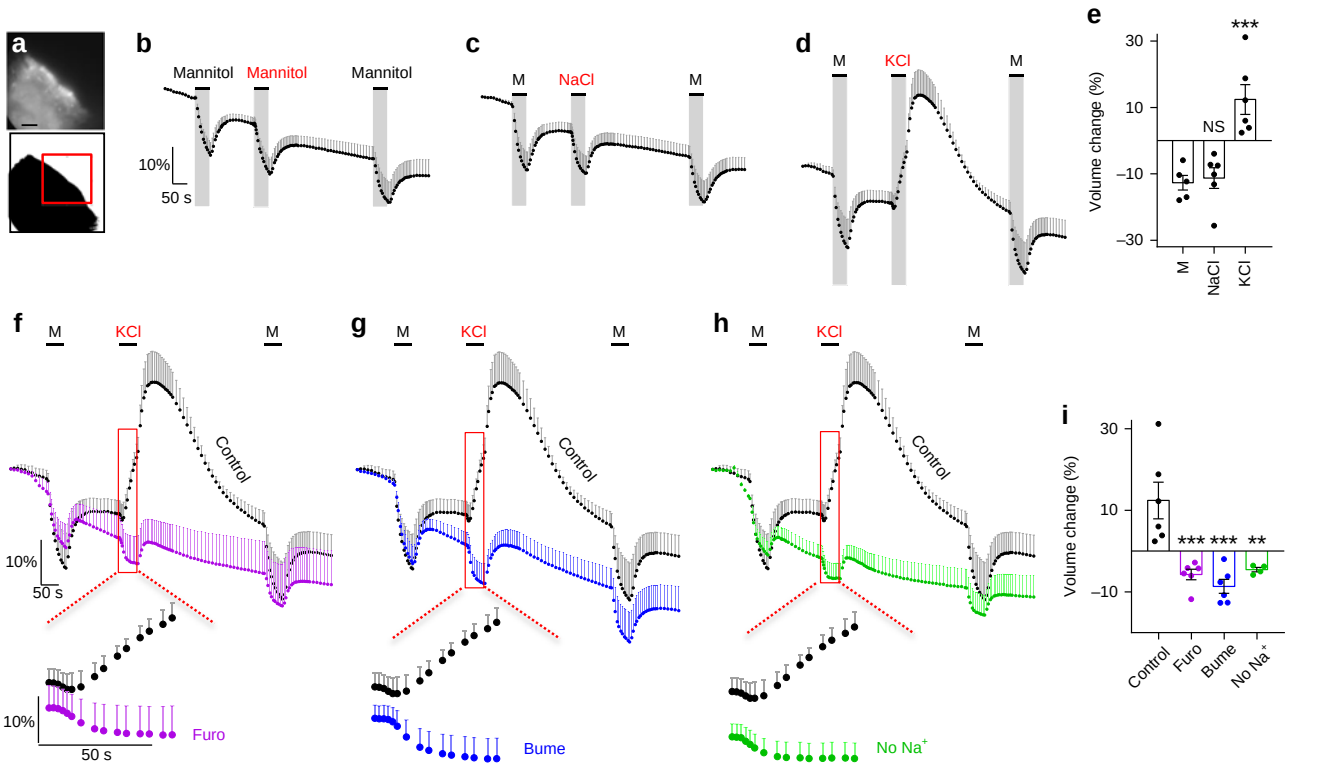

Fig. 1 Cotransporter-mediated active water transport against an osmotic gradient. **a** Image of calcein fluorescence in mouse choroid plexus (CP, top) and the converted image (bottom) with indication of the region of interest (red box). Scale bar = 60 µm. **b** Volume changes of CPs challenged with a 100 mOsm gradient of mannitol (M), indicated by the extended bars ($n = 5$ CPs from five mice). **c** CPs challenged with a 100 mOsm gradient of first mannitol (M), then NaCl, and finally mannitol, indicated by the extended bars ($n = 6$ CPs from six mice). **d** CPs challenged with a 100 mOsm gradient of first mannitol (M), then KCl, and finally mannitol, indicated by the extended bars ($n = 6$ CPs from six mice). **e** Summary of the second volume change induced by identical osmotic gradients. **f** CPs challenged with 100 mOsm KCl alone (control, black symbols, data from **d**) or in the presence of 1 mM furosemide (purple symbols, $n = 6$ CPs from six mice). Inset magnifies the area of interest where furosemide blocks the KCl-induced swelling. **g** CPs challenged with 100 mOsm alone (control, black symbols, data from **d**) or in the presence of 10 µM bumetanide (blue symbols, $n = 6$ CPs from six mice). Inset magnifies the area of interest where bumetanide blocks the KCl-induced swelling. **h** CPs challenged with 100 mOsm KCl (control, black symbols, data from **d**) and in the absence of Na^+ in the test solution (green symbols, $n = 4$ CPs from four mice). Inset magnifies the area of interest where lack of Na^+ blocks the KCl-induced swelling. **i** Summary of the second volume change induced by KCl alone or with drug application/Na^+ omission. Error bars represent standard error of the mean and statistical significance was tested with one-way ANOVA followed by Tukey's multiple comparisons test. In panel **e**, the asterisks refer to a comparison to the mannitol-mediated shrinkage and in panel **i**, the asterisks refer to a comparison to the KCl-mediated swelling. $^{**}P < 0.01$, $^{***}P < 0.001$, NS not significant

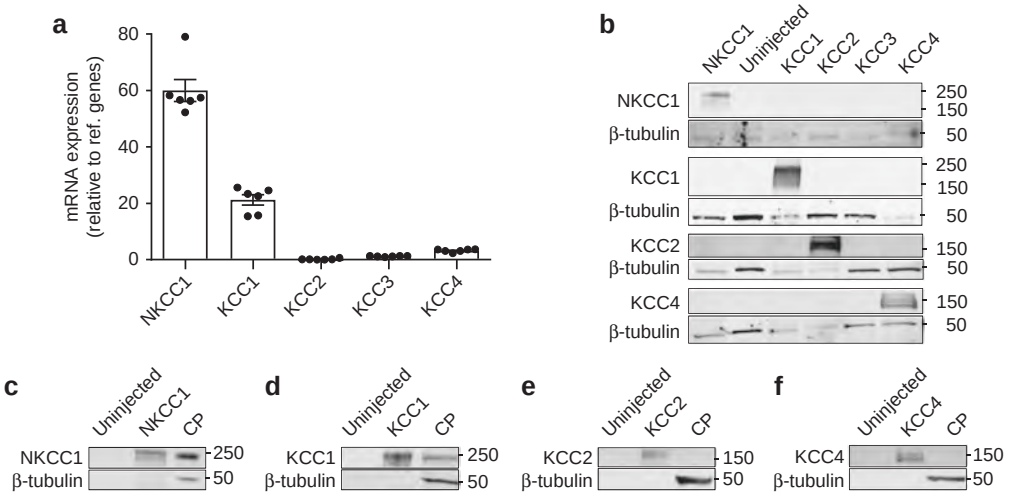

Fig. 2 NKCC1 and KCC1 are expressed in mouse choroid plexus. **a** mRNA expression levels of NKCC1 and the four KCC isoforms in mouse choroid plexuses. The five target genes were normalized to two reference genes, GAPDH and H2AFZT, and presented as relative expression; NKCC1 = 60.0 ± 3.9, KCC1 = 21.2 ± 1.8, KCC2 = 0.2 ± 0.1, KCC3 = 1.2 ± 0.1, and KCC4 = 3.2 ± 0.2 ($n = 6$ mice), error bars represent standard error of the mean. **b** Representative western blots to verify antibody specificity. NKCC1 and KCC1-4 were expressed in *Xenopus laevis* oocytes and purified membranes from these and uninjected oocytes were exposed to SDS-PAGE followed by western blot ($n = 3$ experiments). **c**–**f** Western blots of lysates from mouse choroid plexus demonstrated expression of NKCC1 (**c**) and KCC1 (**d**), while KCC2 (**e**) and KCC4 (**f**) were not detected. Beta-tubulin was employed as loading control ($n = 3$ experiments)

A number of cotransporter proteins have the inherent ability to cotransport water along with the ions/solutes in the translocation mechanism (for review see refs. [18,22]). The coupling between water translocation and substrate transport takes place within the protein itself in a manner that permits water to be transported independently of, and even against, an osmotic gradient[23]. Examples of such water-translocating cotransporters are the $Na^+/K^+/2Cl^-$ cotransporter 1 (NKCC1) and the K^+/Cl^- cotransporters (KCCs)[24–26]. Isoforms of these transport proteins have been detected in the choroid plexus epithelium[27–29], although their exact isoform distribution, relative expression, and membrane targeting remain largely unknown, as are their ability to transport water independently of an osmotic gradient in the choroid plexus tissue and their contribution to CSF production in vivo. In the present study, we introduce the water-translocating cotransporter, NKCC1, as the main contributor to CSF formation in the mouse choroid plexus.

Results

Choroidal cotransport of water against an osmotic gradient. To determine if membrane transport mechanisms in the luminal membrane of choroid plexus carry an inherent ability to translocate water against an osmotic gradient, ex vivo mouse choroid plexus was monitored by live imaging during exposure to osmotic challenges. The acutely isolated choroid plexus was loaded with calcein-AM and the water movement determined as two-dimensional volume changes occurring as movement of the choroid plexus upon exposure to a hyperosmotic challenge of 100 mOsm (Fig. 1a). Three consecutive applications of 100 mOsm (100 mM) mannitol led to robust and reproducible shrinkage of choroid plexus ($n = 5$, Fig. 1b). This pattern was replicated with NaCl as the osmolyte (100 mOsm, 55 mM) during the second application ($n = 6$, Fig. 1c) while keeping mannitol application as a reference for the first and last osmotic challenge. In contrast, application of a 100 mOsm hyperosmolar challenge introduced via addition of KCl (55 mM) generated an abrupt choroid plexus volume increase ($n = 6$, Fig. 1d), indicating that water was transported *into* the choroid plexus despite the large oppositely directed osmotic gradient. It should be noted that the volume increase occurred instantaneously prior to significant changes in intracellular parameters[22,25]. Summarized data from the second osmolyte application illustrate that the volume decrease obtained upon application of 100 mOsm mannitol (12.7 ± 2.2%, $n = 5$) or NaCl (11.3 ± 3.1%, $n = 6$) $P = 0.96$, df = 14, $q = 0.4$) reached comparable levels (Fig. 1e), while application of an identical osmotic challenge given in the form of KCl produced a volume *increase* of 12.4 ± 4.5%, $n = 6$ (one-way ANOVA followed by Tukey's multiple comparisons test, $P = 0.0006$, df = 14, $q = 6.9$, Fig. 1e). These results indicate that choroid plexus contains transport mechanisms capable of transporting water independently of, and even against, the direction of an applied osmotic gradient. To determine the involvement of cation-chloride cotransporters (CCCs) in the K^+-mediated transport of water against an experimentally applied osmotic gradient, we continued the experimental series described above with the inclusion of pharmacological agents. Application of furosemide (1 mM inhibits both KCCs and NKCCs[30]) completely blocked the K^+-mediated choroid plexus volume increase: The tissue responded in a passive manner, as when challenged with mannitol as the osmolyte (shrinkage of 5.7 ± 1.3%, one-way ANOVA followed by Tukey's multiple comparisons test, $P = 0.0006$, df = 18, $q = 6.9$, $n = 6$, Fig. 1f). For illustrative purposes, the volume traces obtained in control solution in the previous figure (Fig. 1d) are included in black. Inclusion of bumetanide (10 µM inhibits NKCC1[31], 8.6 ± 1.7% shrinkage, one-way ANOVA followed by Tukey's multiple comparisons test, $P = 0.0001$, df = 18, $q = 8.0$, $n = 6$, Fig. 1g) or removal of Na^+ from the test solution (equiosmolar replacement with choline; 4.5 ± 0.5% shrinkage, one-way ANOVA followed by Tukey's multiple comparisons test, $P = 0.0037$, df = 18, $q = 5.8$, $n = 4$, Fig. 1h) likewise abolished the K^+-mediated water accumulation. Data are summarized in Fig. 1i. Increased $[K^+]_e$ thus promoted inwardly directed ion transport by NKCC1, which by its ability to cotransport water during its translocation mechanism contributed to intracellular water accumulation against a substantial osmotic gradient. Cotransporter-mediated water transport is thereby indeed able to move water across the choroid plexus membrane in a manner independent of an osmotic gradient.

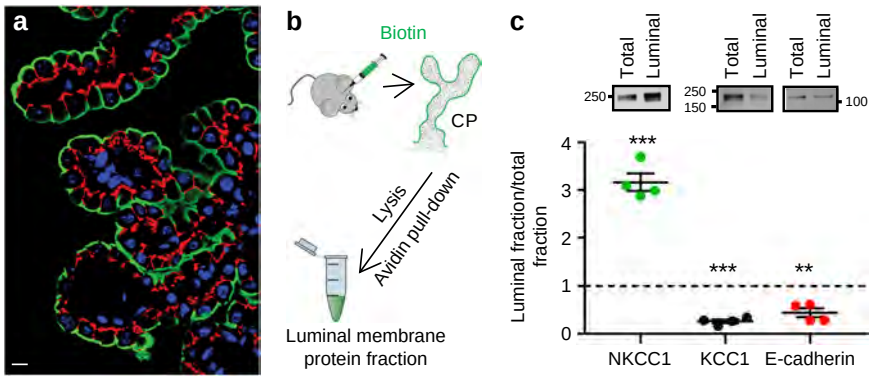

Fig. 3 NKCC1 is located at the luminal membrane facing the ventricles. **a** Immunostaining of mouse choroid plexus illustrated expression of NKCC1 in the membrane facing the lumen (green) with E-cadherin (red) as a basolateral marker and nuclei in blue. Scale bar = 10 µm. Previously unpublished image generously provided by Dr. Jeppe Praetorius. **b** Schematic illustration of the luminal surface biotinylation of mouse choroid plexus in situ. **c** Representative western blots showing expression of NKCC1, KCC1, and E-cadherin in total tissue fraction (F_t) and purified biotinylated (luminal) membrane protein fraction (F_l). Below is depicted the quantification of protein abundance represented as luminal membrane/total protein fraction ($n = 4$ mice). NKCC1 was expressed significantly higher in the purified luminal membrane fraction while KCC1 and E-cadherin were predominantly in the total fraction. Error bars represent standard error of the mean and statistical significance was determined with one-sample *t* test and comparison to equal distribution; $F_l/F_t = 1$ and the asterisks refer to a value significantly different from 1. $^{**}P < 0.01$, $^{***}P \leq 0.001$

NKCC1 and KCC1 are expressed in choroid plexus. To determine the isoform-specific expression profile of NKCC1 and the KCCs in mouse choroid plexus, we initially performed quantitative PCR on mRNA purified from acutely isolated tissue. Normalization of the obtained quantities of mRNA encoding NKCC1 and KCC1-4 to two reference genes illustrated a robust expression of NKCC1 and, although to a lesser extent, KCC1, while KCC2-4 mRNA expression was minor or below detection limit ($n = 6$, Fig. 2a). Prior to determination of the protein expression of the CCCs in choroid plexus tissue, we verified that the employed antibodies exclusively recognized their targeted isoform. To this end, NKCC1 and KCC1-4 were individually expressed in *Xenopus laevis* oocytes and purified membranes containing each isoform were exposed to SDS-PAGE followed by western blot with antibodies targeting each of these transport proteins. As evident from Fig. 2b, the employed antibodies recognized only their respective target protein with no isoform cross-reaction ($n = 3$). We were, however, unsuccessful with all five KCC3 antibodies tested, none of which properly recognized KCC3, either due to poor epitope recognition or lack of KCC3 expression in the oocytes. Western blotting of lysates from mouse choroid plexus demonstrated robust immunoreaction with antibodies targeting NKCC1 and KCC1, while KCC2 and KCC4 were below detection limit in this tissue ($n = 3$, Fig. 2c, f). None of the five tested KCC3 antibodies provided indications of immunoreactivity in the choroid plexus tissue, indicating either lack of choroidal expression of this isoform or poor epitope recognition. Taken together, mRNA and protein analysis illustrate robust expression of NKCC1 and KCC1 in the mouse choroid plexus and negligible expression of KCC2-4.

NKCC1 is localized to the luminal membrane in choroid plexus. Localization of NKCC1 and KCC1 to the luminal membrane of the choroid plexus is required in order for these to directly transport water into the ventricular lumen. Immunohistochemical staining of mouse choroid plexus verified the localization of NKCC1 at the luminal membrane (green, Fig. 3a). Three antibodies directed towards KCC1 produced only diffusive, and therefore inconclusive, staining in choroid plexus tissue. To determine the membrane targeting of KCC1 in an alternative fashion, we performed surface biotinylation of the choroid plexus. Rupture of the choroidal tissue during the isolation procedure yielded undesirable access of the biotin to the basolateral membrane. Instead, selective biotinylation of the lumen-facing choroidal membrane was obtained by ventricular delivery of biotin in the intact animal, prior to isolation of the choroid plexus and purification of the biotinylated proteins (see Fig. 3b for a diagram of the procedure). Densitometric analysis of the western blots of the biotinylated membrane protein fraction relative to the total membrane protein fraction illustrated NKCC1 enrichment in the biotinylated (luminal) membrane fraction (F_l) compared to the total membrane fraction (F_t) (Fig. 3c, left panels, $F_l/F_t = 3.2 \pm 0.2$, $n = 4$, one-sample *t* test and comparison to equal distribution; $F_l/F_t = 1$, $P = 0.001$, $t = 11.82$, df = 3). In contrast, abundance of KCC1 was significantly lower in the biotinylated fraction (Fig. 3c, middle panels, $F_l/F_t = 0.3 \pm 0.0$, $n = 4$, one-sample *t* test and comparison to equal distribution; $F_l/F_t = 1$, $P < 0.001$, $t = 20.1$, df = 3) and resembled the pattern obtained with E-cadherin, a basolaterally located membrane protein[32] (Fig. 3c, right panels, $F_l/F_t = 0.4 \pm 0.1$, $n = 4$, one-sample *t* test and comparison to equal distribution; $F_l/F_t = 1$, $P = 0.009$, $t = 6$, df = 3). Therefore, NKCC1, not KCC1, is localized to the luminal membrane of choroid plexus, from which it could indeed participate in CSF production.

NKCC1 is poised for outwardly directed transport. The NKCC1 transport is inwardly directed in most cell types[33] while production of CSF necessitates outwardly directed transport of ions and water. To reveal the choroidal NKCC1 transport direction, we determined the ion concentrations of Na^+, K^+, and Cl^- in choroid plexus epithelial cells and CSF of mice. CSF was extracted from anesthetized and artificially ventilated mice by a glass capillary inserted in cisterna magna. Immediately thereafter, each mouse was sacrificed, choroid plexus isolated ($n = 4$), and the ion concentrations determined with flame photometry (Na^+ and K^+) or by colorimetry (Cl^-). The obtained ion concentrations (CSF: 150 ± 1 mM Na^+, 3 ± 0 mM K^+, 100 ± 6 mM Cl^- and in the choroid plexus epithelial cells: 31 ± 5 mM Na^+, 141 ± 12 mM K^+, and 35 ± 9 mM Cl^-, $n = 4$) illustrate that the intracellular Na^+ and Cl^- concentrations are substantially higher than the 5−15 mM range usually observed in most mammalian cells[34]. Calculation of the Gibbs free energy using the obtained ion

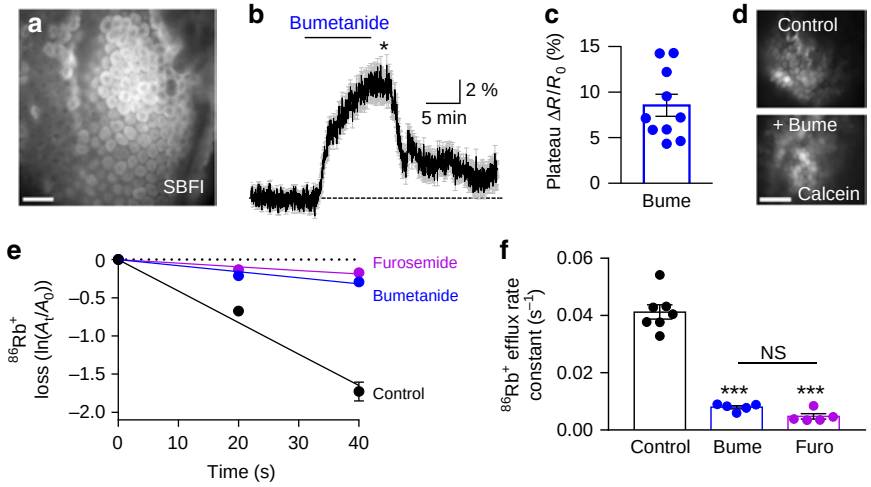

Fig. 4 NKCC1 is poised for outward transport in the luminal membrane. **a** Image of SBFI fluorescence of the choroid plexus taken with wide-field fluorescence microscope. Scale bar = 40 µm. **b** Representative sodium signals of choroid plexus during 10 min baseline, 10 min application of the NKCC1 inhibitor bumetanide (10 µM), and 20 min washout. Gray lines represent the SBFI ratio obtained from 40 single cells during one experiment, black line represents an average of these cells. **c** Average bumetanide-induced increase in SBFI ratio of choroid plexus cells, indicative of increased intracellular sodium concentration ($n = 10$ CPs from ten mice). **d** Representative images of calcein fluorescence of the choroid plexus either after 10 min in aCSF (top panel) or after 10 min of bumetanide treatment (bottom panel, time point marked as * in **b**). Scale bar = 40 µm. **e** Loss of $^{86}Rb^+$ from choroid plexus as a function of time in control settings (black, $n = 7$ CPs from seven mice) or with treatment of either bumetanide (20 µM, blue, $n = 5$ CPs from five mice) or furosemide (1 mM, violet, $n = 5$ CPs from five mice). *Y*-axis is the natural logarithm of amount of $^{86}Rb^+$ left in choroid plexus at time t (A_t) divided by the amount at time 0 (A_0). **f** Efflux rate constants for $^{86}Rb^+$ in control (0.041 ± 0.003 s^{-1}, $n = 7$ CPs from seven mice), in the presence of bumetanide (0.008 ± 0.001 s^{-1}, $n = 5$ CPs from five mice), or furosemide (0.005 ± 0.001 s^{-1}, $n = 5$ CPs from five mice). Error bars represent standard error of the mean and statistical significance was tested with one-way ANOVA followed by Tukey's multiple comparisons test and the asterisks above the bars indicate comparison to the control while the comparison between the two test solutions is indicated with a line above the relevant bars. ***$P < 0.0001$, NS not significant ($P = 0.526$)

concentrations (see Methods) yields $\Delta G = 448$ J mol^{-1}, which indicates an outwardly directed transport of NKCC1 in the lumen-facing membrane of mouse choroid plexus epithelial cells under physiological conditions. To experimentally determine the transport direction of NKCC1 in choroid plexus epithelial cells, we performed wide-field Na^+ imaging on ex vivo choroid plexus, loaded with SBFI-AM (sodium-binding benzofuran isophthalate acetoxymethyl ester) (Fig. 4a). In choroid plexus kept in control aCSF, $[Na^+]_i$ was stable and did not undergo detectable fluctuations (Fig. 4b). Upon inhibition of NKCC1 (10 µM bumetanide), however, the SBFI fluorescence ratio increased by 8.5 ± 1.2% within 10 min ($n = 10$, Fig. 4b, c), revealing an increase in $[Na^+]_i$. This increase indicates outwardly directed NKCC1-mediated Na^+ transport. Upon 20 min washout of bumetanide, the $[Na^+]_i$ returned towards baseline (2.4 ± 0.6%, $n = 5$, Fig. 4b), reflecting re-establishment of Na^+ export by the NKCC1. Bumetanide did not compromise cell viability (confirmed by uptake of calcein-AM as a marker of cell health[35], Fig. 4d, $n = 4$ of each condition), indicating that the observed increase in $[Na^+]_i$ did not result from unspecific influx of Na^+, but was indeed due to blocking of NKCC1 transport activity. The unique transport direction of NKCC1 was verified with efflux experiments with $^{86}Rb^+$, a congener for K^+, from pre-loaded ex vivo choroid plexus. The $^{86}Rb^+$ efflux decreased approximately 85% after exposure to either bumetanide (20 µM, $n = 5$, one-way ANOVA followed by Tukey's multiple comparisons, $P < 0.0001$, df = 14, $q = 17.6$) or furosemide (1 mM, $n = 5$, one-way ANOVA followed by Tukey's multiple comparisons, $P < 0.0001$, df = 14, $q = 19.3$) (Fig. 4e, f), indicating that the K^+ efflux was predominantly orchestrated by NKCC1. Together, these results show that the ion concentrations of choroid plexus epithelial cells uniquely dictate outwardly directed transport of NKCC1, which thus could act as a contributor to CSF production.

NKCC1 significantly contributes to CSF production in vivo. To determine the contribution of NKCC1 to CSF production in vivo, we performed experiments on anesthetized mice placed in a stereotaxic frame during ventriculo-cisternal perfusion (modified from refs. [15,36]). In this experimental approach, aCSF containing fluorescent dye (dextran) is perfused via a cannula through the lateral ventricle of the mouse (0.7 µl min^{-1}) with simultaneous fluid collection by a glass capillary from the cisterna magna at 5-min intervals (Fig. 5a). The dilution of the fluorescent dye represents the rate of CSF production. As our experimental protocol was based on employing each mouse as its own control, it was an absolute requirement to record a sustained rate of CSF production throughout the prolonged experimental procedure (125 min). To obtain such standard, the animals were artificially ventilated, their heart rate, respiratory partial pressure of carbon dioxide, and arterial oxygen saturation were monitored, and their core temperature maintained (see Methods). A representative time control experiment is depicted in Fig. 5b, in which the dextran gradually appeared in the CSF samples and a stable dilution obtained after approximately 40 min. The last two samples prior to the solution change (60 min, marked in red in Fig. 5b) were employed to calculate the CSF production rate of 0.66 ± 0.02 µl min^{-1} ($n = 18$, Fig. 5b inset). A similar CSF production rate (0.60 ± 0.02 µl min^{-1}, $n = 6$, $P = 0.21$, $t = 1.3$, df = 22, t test) was obtained in a set of animals anesthetized with isoflurane rather than ketamine/xylazine (see Methods). The vehicle (DMSO)-containing aCSF delivered to the lateral ventricle was replaced with new DMSO-containing aCSF at the time point marked "solution change". After 60 min additional sample time, the last two sample points (blue in Fig. 5b) were normalized to the original baseline (the red points) revealing a slight (although non-significant) drop of baseline to 92.2 ± 3.3% during the course of the experiment ($n = 6$, one-way ANOVA followed by Tukey's

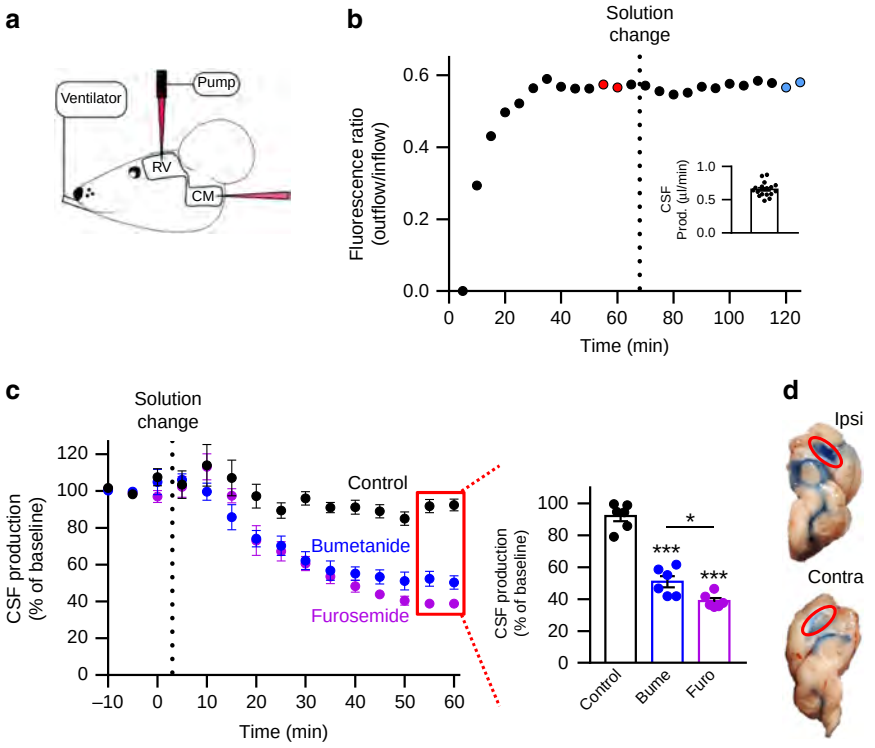

Fig. 5 NKCC1 acts as a significant contributor to in vivo CSF production. **a** Schematic drawing of the infusion of aCSF containing dextran (dark red cannula) into the right lateral ventricle (RV) and collection of the diluted dextran (light red cannula) at cisterna magna (CM) of a ventilated mouse. **b** Representative time course of the fluorescence ratio of dextran (outflow/inflow) during a control ventriculo-cisternal perfusion. After stable baseline (60 min), the dextran/DMSO aCSF-solution was changed within 5–10 min. Inset depicts the average CSF production rate ($n = 18$ mice). **c** Summarized data from ventriculo-cisternal perfusion illustrating CSF production (percentage of baseline) as a function of time. Data normalized to the average of the two last samples before solution change. Control perfusion with the DMSO-vehicle is shown in black ($n = 6$ mice), treatment with bumetanide in blue ($n = 6$ mice), and furosemide (n = 6 mice) in purple. Inset illustrates the summarized CSF production rates after 60 min exposure to vehicle (black), bumetanide (blue), or furosemide (purple) normalized to own control. **d** Mid-sagittal section of a mouse brain after unilateral injection of Evans Blue revealed staining mainly in the injected, right lateral ventricle (top panel) compared to the contralateral ventricle (bottom image). Error bars represent standard error of the mean and statistical significance was tested with one-way ANOVA followed by Tukey's multiple comparisons test with asterisks above the bars indicating comparison to control perfusion and comparison between test solutions indicated by lines above the respective bars. *$P < 0.05$, ***$P < 0.001$

multiple comparisons, $P = 0.06$, $t = 2.4$, df = 5, Fig. 5c), demonstrating rather stable CSF production throughout the experimental procedure. To determine the quantitative contribution of NKCC1 to CSF production, aCSF including bumetanide (100 µM) was introduced with the solution change, which reduced the CSF production to 51.0 ± 3.5% of baseline ($n = 6$, one-way ANOVA followed by Tukey's multiple comparisons, $P < 0.0001$, df = 15, $q = 13.9$, Fig. 5c). Inclusion of the NKCC1/KCC inhibitor furosemide (2 mM) reduced the CSF production to 38.8 ± 1.8% of baseline ($n = 6$, one-way ANOVA followed by Tukey's multiple comparisons, $P < 0.0001$, df = 15, $q = 18.0$, Fig. 5c), slightly more than that observed with bumetanide (one-way ANOVA followed by Tukey's multiple comparisons, $P = 0.03$, df = 15, $q = 4.1$). Based on these results, it is evident that NKCC1 is a substantial contributor to the molecular machinery underlying CSF production in an in vivo experimental setting. While this dilution method reflects CSF production of all origins (all four choroid plexuses in addition to trans-capillary fluid production), delivery of a pharmacologic inhibitor via the cannula placed in one lateral ventricle may not reach the transport mechanisms expressed in the choroid plexus at the base of the contralateral ventricle. To obtain an estimate of the reach of such one-sided drug delivery, Evans blue was infused into one lateral ventricle in a manner mimicking the experimental approach above, prior to isolation of the brain. As evident in Fig. 5d, staining was predominantly observed in the perfused lateral ventricle with little staining in the contralateral one. We therefore predict partial inhibition of the cotransporters in the contralateral choroid plexus and that our data thus represent an underestimate of the role of NKCC1 in CSF production.

Live imaging shows NKCC1-mediated CSF production. To obtain a swift and less-invasive manner of revealing NKCC1-mediated CSF production, we developed an in vivo imaging strategy based on the LI-COR Pearl Trilogy small animal imaging system. This method allows imaging of anesthetized animals immediately after lateral ventricular delivery of a fluorescent dye (IRDye 800CW carboxylate). The ventricular dye redistribution is employed as a proxy of CSF production, although diffusion of the dye is expected to contribute to its redistribution. Figure 6a illustrates the head of a white mouse (obtained as a white light image) immediately after ventricular delivery of the fluorescent probe (superimposing of pseudo-color fluorescence). The red square indicates the area of interest, in which the dye intensity is determined as a function of time (representing movement of CSF) (Fig. 6b, d). After 5-min pre-injection of inhibitor (or vehicle) the fluorescent dye was injected into one lateral ventricle along with inhibitor (or vehicle)-injection, and the mouse rapidly placed in the LI-COR Pearl (exactly 1 min lapse from injection to first image acquisition); see Fig. 6d for representative images. The

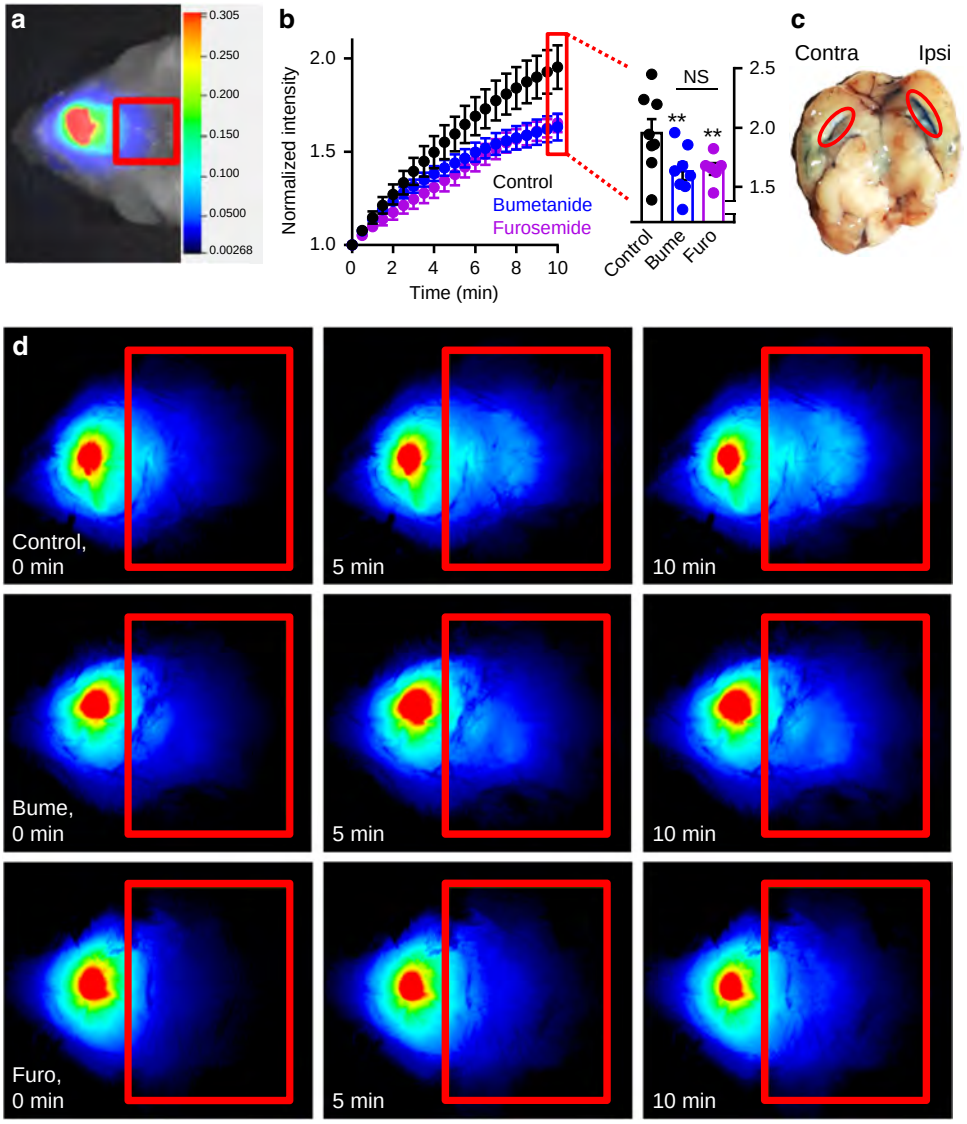

Fig. 6 Live imaging determines significant NKCC1 contribution to in vivo CSF production. **a** Illustration of pseudo-color fluorescence superimposed on a white light image from a white mouse after ventricular injection of 10 µM IRDye 800CW carboxylate dye. The dye content is quantified in the red box, placed in line with lambda. The intensity scale is arbitrary units and applies to all images. **b** Intensity of images were quantified and normalized to the first image (0 min) for control (vehicle, black), bumetanide (blue), or furosemide (purple) and plotted as a function of time. Inset illustrates summarized data at the 10-min time point; the fluorescence intensity of control mice reached 1.95 ± 0.12 ($n = 8$ mice), furosemide-treated 1.65 ± 0.05 ($n = 6$ mice), and bumetanide 1.63 ± 0.07 ($n = 8$ mice). **c** Unilateral injection of Evans Blue revealed staining mainly in the injected, right lateral ventricle (red oval) compared to the contralateral ventricle. **d** Representative images at 0, 5, and 10 min for control condition (top panels), bumetanide treatment (middle panels), and furosemide treatment (bottom panels). Error bars represent standard error of the mean and statistical significance was evaluated with two-way ANOVA (RM) followed by Tukey's multiple comparisons test. Asterisks above the bars indicate comparison to control while comparisons between test solutions are indicated with a line above the respective bars. $^{**}P < 0.01$, NS: not significant ($P = 0.98$)

fluorescence intensity recorded in the area of interest was normalized to the intensity of the first image, summarized, and illustrated as a function of time (Fig. 6b). Inclusion of bumetanide (100 µM, $n = 8$, two-way analysis of variance (ANOVA) (repeated measures (RM)) followed by Tukey's multiple comparisons test, $P = 0.0018$, df = 399, $q = 4.9$) or furosemide (2 mM, $n = 6$, two-way ANOVA (RM) followed by Tukey's multiple comparisons test, $P = 0.0083$, df = 399, $q = 4.2$) significantly decreased the movement of dye compared to control, indicative of NKCC1-mediated movement of ventricular fluorescence and thus CSF flow. Of note, injection of Evans blue, in a manner and quantity mimicking the experimental approach above, predominantly stained the ipsilateral ventricle (Fig. 6c), indicative of a putative underestimation of the inhibitor-sensitive movement of the fluorescent dye.

Discussion

Here, we have demonstrated, by complementary ex vivo and in vivo experimentation, that the high production rate of CSF is sustained by NKCC1 via its inherent ability to cotransport water along with its directional ion translocation in a manner independent of osmotic driving forces. This unconventional means of fluid secretion underlying CSF production represents a paradigm shift in the field and provides a long-needed rational therapeutic target towards brain pathologies involving disturbances in brain water homeostasis and increased intracranial pressure.

The limitations of a conventional osmotic model for CSF production are apparent from three independent lines of evidence: The minimal effects of genetic deletion of AQP1, the low osmotic water permeability of the epithelium, and the ability of

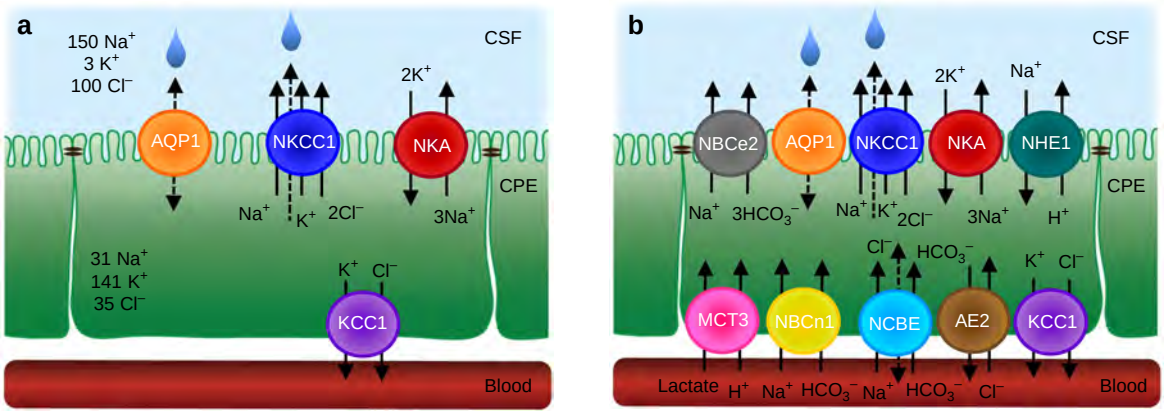

Fig. 7 Schematic drawing of transporters in a choroid plexus epithelial cell. **a** The drawing depicts the selective expression of NKCC1 at the luminal membrane and indicates its unique outward transport direction, due to the high intracellular concentration of Na^+ and Cl^- in this tissue (ion concentrations given in mM). The NKCC1-mediated cotransport of water is indicated with a dashed arrow. The Na^+/K^+-ATPase and AQP1[14] are indicated on the luminal membrane of the choroid plexus epithelium (CPE), while KCC1 is localized to the basolateral membrane facing the vascular compartment (this study). **b** The drawing includes the many other coupled transporters localized to the choroidal epithelial membranes[1]. Note that NCBE may also be referred to as NBCn2

the choroid plexus epithelium to transport water uphill against a transepithelial osmotic gradient. Firstly, discovery of AQP1 in the lumen-facing membrane of choroid plexus initially promoted its implication in CSF production[13,15,27]. A slightly reduced CSF production was observed in AQP1$^{-/-}$ mice, although accompanied by a severe drop in venous blood pressure in these animals[15]. With the general view that CSF originates from the vascular compartment[37,38], taken together with a fivefold higher arterial flow in choroid plexus compared to that of the brain as a whole[12], such AQP1-dependent reduction in blood pressure[15] is anticipated to contribute to the reduced CSF production observed in AQP1$^{-/-}$ mice. Secondly, it has been assumed that CSF production takes place via conventional osmotic water transport following a ventricular build-up of osmotic particles through activity of choroidal membrane transport mechanisms, such as the Na^+/K^+-ATPase, cotransporters, and/or ion channels[1,4,13]. Concerted action of these transport mechanisms renders the CSF approximately 5−10 mOsm hyperosmolar relative to plasma[16,17]. With the established water permeability of the choroid plexus epithelium[39], calculations dictate that the transepithelial osmotic gradient entailed to sustain the high CSF production rate would need to be about 50 times greater than that observed[18]. Thirdly, while the rate of CSF production indeed increases with raised ventricular osmolarity, CSF production continues even when the ventricular fluid is hyposmotic to plasma[18–21]. In goat, the in vivo CSF production continued despite opposing osmotic gradients of up to 100 mOsm[20].

Simple osmotically obliged water entry into the ventricle is therefore insufficient to sustain the well-established rate of CSF production and here we propose cotransport of water as the molecular mechanism underlying CSF production. Our research group earlier demonstrated that cotransporters function as unconventional water transporters carrying 300–500 water molecules along with the transported solutes per transport cycle[18,22], rendering the combined solute and water transport near-isotonic. NKCC1 is prominently featured among these and has in complementary cell systems been demonstrated to cotransport water[24,26]. Here, we reveal that the mouse choroid plexus displays the ability to transport water against a significant osmotic gradient in a K^+-induced, NKCC1-mediated manner. While the high $[K^+]_o$ strongly favors inward transport by NKCC1, and thus robust cell swelling, the high $[Na^+]_o$ is, although to a lesser degree, likely to do so as well. However, with the low apparent affinity of NKCC1 for K^+[40], the inwardly directed transport under conditions of high $[Na^+]_o$ and low $[K^+]_o$ and the resulting NKCC1-mediated cell swelling will be limited and thus likely masked by the parallel osmotically induced cell shrinkage. Our data align with an earlier study on salamander choroid plexus, performed with ion-sensitive microelectrodes, which, however, relied on the KCC for movement of water independently of the prevalent osmotic gradient[25]. It should be emphasized that the NKCC1-mediated component of CSF production is a molecular property within the transport protein and not a result of unstirred layers around the protein or changes in intracellular osmolarity[22].

Our expression studies of mRNA and protein were conducted on pooled tissue obtained from the lateral and the fourth choroid plexuses from mouse (to obtain sufficient tissue) and revealed robust expression of NKCC1. The observation of NKCC1 localization in the lumen-facing membrane of mouse aligns with reports on human[27] and rat[41] choroid plexus. We observed KCC1 expression at the mRNA[42,43] and protein level and localized it to the basolateral membrane, while KCC2-4 mRNA and protein expression was negligible or below detection limit in our samples. Lack of KCC2 mRNA and protein in choroid plexus confirms previous studies[42,44], whereas a few reports have assigned KCC3 and KCC4 protein to choroidal tissue[28,29] despite absence or downregulation after birth of mRNA encoding these isoforms (this study and ref. [43]). We speculate that the discrepancy might arise from insufficient antibody specificity, by the developmental changes in KCC mRNA expression[43], and/or the distinct expression profile of the different choroid plexuses[45]. We are, nevertheless, left with the conclusion that in adult mouse choroid plexus, NKCC1 is expressed in the membrane facing the ventricular lumen and KCC1 in the basolateral membrane. The remarkably high intracellular concentrations of Na^+ (~30 mM) and Cl^- (~35 mM) in the mouse choroidal epithelium align with values obtained in rat[1,46] and suffice to promote outwardly directed NKCC1 transport. This atypical NKCC1 transport direction was experimentally verified by complementary techniques, aligns with rat tissue[47], and supports the notion that NKCC1 is uniquely well-suited to participate in CSF production via its outwardly directed transport in the choroid plexus epithelium (see summary Fig. 7a). This is in contrast to other epithelia and cell types, in which NKCC1 is generally poised towards

inwardly directed transport[48,49]. NKCC1 is therefore detected on the basolateral membrane of other secretory epithelia[33].

Optimal CSF production relies on sustained physiological parameters in the anesthetized animal. We therefore propose that to reliably measure the rate of CSF production and assign quantitative contributions of different transport mechanisms, it is crucial to make every effort to maintain core body temperature and ensure proper artificial ventilation of the animal, and hence physiological values for arterial partial pressure of carbon dioxide and oxygen, arterial pH, heart rate, and blood pressure. Of note, ventilated mice had a significantly higher CSF production rate of 0.66 ± 0.02 µl min^{-1} than determined earlier in non-ventilated mice (0.38 ± 0.02 µl min^{-1} [15]) and in our unpublished pilot experiments. Determination of CSF production by the ventriculo-cisternal perfusion method relies on dilution of ventricularly delivered dextran by the newly produced CSF. This method, however, cannot distinguish between CSF formed by the choroid plexus (presumably the majority[4–7]) and that entering the ventricles via the ependymal cell layer following its secretion across the capillary wall in the reminder of the brain[50]. The endothelial expression of NKCC1 is negligible[41], and the bumetanide-sensitive fraction of the CSF production is therefore assigned to the highly NKCC1-expressing choroid plexus. Inhibition of NKCC1 (upon intraventricular delivery of inhibitor) decreased CSF production by 50% in mice, the quantitative importance underscored by a similar finding in dogs[51]. Notably, intravenous delivery of CCC inhibitors consistently fail to affect CSF production rate[9,52,53], in alignment with the luminal membrane expression of NKCC1 illustrated in summary Fig. 7a. The ventricular perfusion rate was set to approximately the same speed as the CSF production rate, thereby expecting a 1:1 dilution of the applied inhibitors. While we therefore increased the inhibitor concentration in the in vivo experimentation compared to that employed ex vivo, we cannot exclude a lower concentration of inhibitor reaching the choroid plexus epithelium at the base of the ventricles, due to the continuous production of CSF and the ensuing wash out. Taken together with limited reach of the applied inhibitor to the contralateral ventricle (illustrated with Evans blue), we predict that our results may underestimate the quantitative contribution of NKCC1 to CSF production and that NKCC1 may represent even more than the observed half of the CSF production machinery.

While in larger animal models, it would be technically feasible to place cannulas in both lateral ventricles and apply double lateral perfusion (to determine the full contribution of NKCC1), it is highly likely that other luminally -expressed membrane transport mechanisms such as Na^+-coupled bicarbonate transporters and the Na^+/K^+-ATPase also contribute to CSF production[4,13,14], and may potentially cotransport water. Figure 7b illustrates a summary of the coupled transporters expressed in the choroid plexus[14,54]. The involvement of bicarbonate transporters has been investigated via inhibition of the carbonic anhydrase by acetazolamide[55,56]. As this treatment appears highly vasoconstrictive especially in choroid plexus[57], the ensuing decreased choroidal blood flow, which in itself lowers CSF production[38], may complicate delineation of the direct role of the bicarbonate transporters. The slightly increased effect of furosemide over that of bumetanide in the ventricular-cisternal perfusion experiment, despite the lack of KCCs in the luminal membrane of the choroid plexus, may be assigned to the low-affinity inhibitory action of furosemide on carbonic anhydrase[52] and potentially on chloride/bicarbonate exchange[58]. The less invasive and rapid whole animal imaging qualitatively confirmed the role of NKCC1 in CSF production.

Notably, genetic deletion of NKCC1 is predicted to cause severe alterations in choroidal epithelium ion concentrations, and therefore in the driving forces and activity of other choroidal transport mechanisms (which could add a substantial confounding element to data obtained in the $NKCC1^{-/-}$ mouse model). While $NKCC1^{-/-}$ mice are viable, they, in addition, display a range of physiological deficits[59] and we therefore relied on the well-tested action of bumetanide. With such a specific and effective inhibitor, the advantage of the pharmacological approach is the acuteness of the transporter inhibition, maintenance of normal epithelial ion concentrations, the ability to employ each mouse as its own control, and the guarantee of no developmental effects (as observed for the $NCBE/NBCn2^{-/-}$ mice, in which the luminally localized Na^+/H^+ exchanger (NHE1) trafficked to the opposite choroidal membrane[60]).

In support of the proposed importance of NKCC1 in CSF production, a recent report convincingly demonstrated hyperactivation of NKCC1 by inflammatory markers in the CSF in an animal model of intraventricular hemorrhage[9]. This condition is well-known to promote posthemorrhagic hydrocephalus in patients[61], and the increased NKCC1 activity in the animal model yielded bumetanide-sensitive ventriculomegaly. NKCC1, via its direct contribution to brain water accumulation, thus represents a promising pharmacological target in brain pathologies involving disturbed water dynamics and increased intracranial pressure, the lack of which precludes efficient pharmacological treatment of a range of patients.

Taken together, our results challenge the general conception that simple, passive movement of water suffices to support the high CSF production rate. NKCC1-mediated cotransport of water ultimately provides a molecular mechanism by which the CSF production can take place independently of an osmotic gradient in a manner dictated by the prevailing ion gradients, generated and maintained by the concerted action of the Na^+/K^+-ATPase and the wealth of other ion transporters and channels expressed in choroid plexus. While the present study addressed the molecular mechanisms of fluid flow from the choroidal epithelial cell to the ventricle, future studies must delineate the transport mechanisms underlying ion and fluid flow across the basolateral membrane. Of immediate interest in this context is the orchestrated synergy between several bicarbonate transporters[14], the expression of which is illustrated in Fig. 7b.

Methods

Experimental animals. All procedures involving animal experimentation conformed to European guidelines, complied with all relevant ethical regulations, and were approved by the Danish Animal Experiments Inspectorate with permission no. 2016-15-0201-00944. Adult male B6JBOM (Taconic) or C57BL6J (Janvier Labs) mice were used for the animal experimentation in ages ranging from 8 to 12 weeks. Housed with 12:12 light cycle and access to water and food ad libitum. Sample size for the in vivo studies was chosen using the formula[62]: sample size = $2SD^2(1.96 + 0.842)^2/d^2$ with 80% power and type 1 error and using SD (standard deviation) = 0.06 from ref. [15] and d (effect size) = 0.11 combined from refs. [15,51].

Isolation of choroid plexus from mouse brain. Choroid plexus (CP) was isolated after cervical dislocation, decapitation and rapid removal and placement of the brain in cold artificial CSF solution (aCSF-HEPES) containing (in mM: 120 NaCl, 2.5 KCl, 2.5 $CaCl_2$, 1.3 $MgSO_4$, 1 NaH_2PO_4, 10 glucose, 17 Na-HEPES, pH 7.4). The brains were kept in ice-cold aCSF-HEPES for a minimum of 10 min to cool the tissue and ease dissection. Choroid plexus was isolated from the lateral and the fourth ventricles (the latter only employed in expression studies and ex vivo volume live imaging) after removal of the most lateral 2−3 mm of the brain hemispheres followed by separation of the two brain hemispheres.

Live imaging. Following isolation, the choroid plexus was stored in ice-cold aCSF-HEPES up to 3 h prior to experiments and mounted on glass coverslips coated with Cell-Tak® (BD Biosciences), prepared according to the manufacturer's instructions (1 part 2 M Na_2CO_3:9 parts Cell-Tak, addition of 2% isopropanol to decrease surface tension, washed twice in aCSF after 30 min drying period). The coverslip was placed in the closed laminar perfusion chamber (Warner instruments) prior to loading with 16.67 µM calcein-AM (Life tech), 8–10 min loading followed by a 6–7 min washout period to remove excess dye. Live imaging was performed at 37 °C on

choroid plexus mounted on an inverted Nikon T2000 microscope stage with a ×60 1.4 NA plan Fluor objective placed underneath the coverslip with immersion oil. The tissue was superfused with aCSF-HEPES at a flow rate of 1 ml min^{-1} and swift solution change was ensured with a PC-16 controller (Bioscience Tools). Hyperosmolar solutions were obtained by addition of 100 mOsm mannitol (100 mM), NaCl (55 mM), or KCl (55 mM). Na^+-free aCSF-HEPES (in mM: 120 cholineCl, 2.5 KCl, 2.5 $CaCl_2$, 1.3 $MgSO_4$, KH_2PO_4, 17 HEPES, 10 glucose (15 mannitol to obtain ~290 mOsm), pH 7.4). Osmolarities were determined with an accuracy of 1 mOsm with an osmometer Type 15 (Löser Messtechnik). The fluorophore was excited by light of a wavelength of 495 ± 15 nm delivered by a polychrome IV monochromator (Photonics). The emitted fluorescence of wave lengths 510–535 nm was recorded for 2–10 ms at a frequency of 1–5 s with a 12-bit cooled monochrome CCD (Charge-Coupled Device) camera and analyzed with FEI Live Acquisition software. Each choroid plexus was randomly assigned and all image analyses were blinded to the experimental conditions. Images of mouse choroid plexus were converted into black, and background into white using ImageJ percentile threshold adjustment. The 2D changes in the black to white ratio were used to measure relative changes in the size of the choroid plexus. These values represent an underestimation of the actual 3D volume changes, assuming these are approximately isotropic but with the relative comparisons employed in this study, this limitation does not affect the outcome of our data.

mRNA quantification. Total RNA from mouse choroid plexus in RNAlater (R0901, Sigma-Aldrich) was purified with the RNeasy micro kit (Qiagen) and the RNase-free DNase set (Qiagen), according to the manufacturer's instruction. A total of 0.5 µg total RNA or 1 µg cRNA was used for reverse transcription using the Omniscript RT mini kit (Qiagen) (cDNA from cRNA was diluted 1:50,000 before further use). cDNA was amplified by quantitative PCR conducted using LightCycler 480 SYBR Green I Master Mix (Roche Applied Sciences). Reactions were carried out in triplicates on a Stratagene Mx3005P QPCR system from Agilent Technologies. The following primer pairs were applied for amplification of targets: 5′-GCAAGACTCCAACTCAGCCAC-3′ (forward) and 5′-ACCTCCATCATC AAAAAGCCACC-3′ (reverse) to generate an *SLC12A2* product of 158 bp; 5′-GCCCCAACCTTACTGCTGAC-3′ (forward) and 5′-TCTCCTTTAGGCCGA GGGTG -3′ (reverse) to generate an *SLC12A4* product of 150 bp; 5′-TGCTCA TTGCCGGACTCATT-3′ (forward) and 5′-CCACGTTCTGATCCTGGTCC-3′ (reverse) to generate an *SLC12A5* product of 195 bp; 5′-CAGCTGGGGGCTCATA CTTC-3′ (forward) and 5′-ACTCCGAAAGATGGCAGCTC-3′ (reverse) to generate an *SLC12A6* product of 170 bp; 5′-AGCTCAACGGCGTAGTTCTC-3′ (forward) and 5′-CTGTTCAGCCCTTCCGTCAG-3′ (reverse) to generate an *SLC12A7* product of 136 bp; 5′-CCGGGTTCCTATAAATACGGACTG-3′ (forward) and 5′-CAATCTCCACTTTGCCACTGC-3′ (reverse) to generate a Glyceraldehyd-3-phosphate (*GAPDH*) product of 195 bp; 5′-CTCCGGAAAGG CCAAGACAA-3′ (forward) and 5′-TTTGACGCATTTCCTGCCAAC-3′ (reverse) to generate an H2A family, member Z (*H2AFZ*) product of 198 bp.

Primers were designed using NCBI's pick primer software. The optimum concentration for each primer set was determined to 200 nM. The initial melting was performed at 95 °C for 10 min. During the subsequent 40 amplification cycles, the melting temperature was 95 °C (20 s), the primer annealing temperature was 60 °C (22 s), and the elongation temperature was 72 °C (20 s). After completed amplification, melting curves were generated to confirm amplification specificity. Standard curves of 4× serial dilutions of cDNA were made using either reverse transcribed cRNA (target genes) or total RNA from mouse choroid plexus (reference genes) in order to determine the amplification efficiencies for each of the utilized primer-sets (*SLC12A2* 104.3%; *SLC12A4* 95.1%; *SLC12A5* 101.2%; *SLC12A6* 101.8%; *SLC12A7* 96.1%, *GAPDH* 100.5%; and *H2AFZ* 97.6%). GenEx (MultiD Analyses AB) was used for data analysis including testing for best reference gene combinations. Target genes are normalized to *GAPDH* and *H2AFZT* and presented as relative expression.

Protein expression in oocytes and membrane preparations. Oocytes from *Xenopus laevis* were obtained from frogs purchased from Nasco (Fort Atkinson) or purchased from Ecocyte Bioscience (Germany). The oocytes were surgically removed from anesthetized (2 g l^{-1} Tricain, 3-aminobenzoic acid ethyl ester, Sigma-Aldrich A-5040) frogs. The follicular membrane was removed by incubation in Kulori medium (90 mM NaCl, 1 mM KCl, 1 mM $CaCl_2$, 1 mM $MgCl_2$, 5 mM HEPES, pH 7.4, 182 mOsm) containing 10 mg ml^{-1} collagenase (type 1, Worthington, NJ, USA) and trypsin inhibitor (1 mg ml^{-1}, Sigma-Aldrich, Denmark) for 1 h, prior to wash in Kulori medium containing 0.1% bovine serum albumin (Sigma, Denmark) and incubated in 100 mM K_2HPO_4 with 0.1% BSA for 1 h. The oocytes were kept in Kulori medium until experiments. cDNA encoding rNKCC1 was obtained from Professor Kai Kaila (University of Helsinki, Finland) and cDNA encoding mKCC1-4 was obtained from Professor Hans Gerd NothWang (Carl von Ossietzky University of Oldenburg, Germany) and all sequences were verified prior to use (Eurofins Genomics). cRNA was prepared from linearized plasmids using the mMESSAGE mMACHINE T7 kit (Ambion) and extracted with MEGAclear (Ambion), according to the manufacturer's instructions, prior to microinjection of 50 ng cRNA per oocyte with a Nanoject microinjector (Drummond Scientific Company). The oocytes were kept at 19 °C for 5 days after which membrane preparations were obtained by homogenization of 20–40 oocytes expressing each construct in 1 ml buffer containing (in mM: 5 $MgCl_2$, 5 NaH_2PO_4, 1 EDTA, 80 sucrose, 20 Tris, pH 7.48, containing the protease inhibitors leupeptin (8 µM) and pefabloc (0.4 mM), both from Sigma-Aldrich). The supernatant was recovered following 10 min centrifugation at 250 × *g* and subsequently centrifuged at 14,000 × *g* for 20 min to obtain the total membrane fraction.

Western blotting. Isolated choroid plexuses (laterals and fourth) were pooled from each mouse and sonicated on ice (3 × 10 s at 70%, Sonopuls, Bandelin) in phosphate-buffered saline (PBS). Western blotting was performed using precast SDS-PAGE gels (Mini-PROTEAN, Biorad) and immobilon FL-membranes (Merck Millipore). Both primary and secondary antibodies were diluted in Odyssey blocking buffer (LI-COR Biosciences):PBS-T at 1:1. Signals were detected with an Odyssey CLx imaging system and image analysis was performed using Image Studio 5 (both from LI-COR Biosciences). Full blots with original markers are included as Supplementary Fig. 1. Primary antibodies: anti-β-tubulin; MAB3408 (Millipore, 1:500), anti-e-cadherin; 610181 (BD BioSciences, 1:5000), anti-NKCC1; sc-21545 (Santa Cruz, 1:500), anti-KCC1&3 [63–66] (kind gift from Professor Thomas J. Jentsch, Max Delbrück Center For Molecular Medicine, Berlin, Germany, 1:500), anti-KCC2; 07-432 (Millipore, 1:1000), anti-KCC3&4 [67] (kind gift from Professor Jinwei Zhang, University of Dundee, UK, 2 µg ml^{-1}), other anti-KCC3 tested; HPA034563 (Atlas, 1:200), H00009990-A01 (Abnova, 1:1000), and sc-19424 (Santa Cruz, 1:200). Secondary antibodies; IRDye 800CW donkey anti-goat; P/N 926-32214, IRDye 680RD donkey anti-mouse; P/N 926-68072, IRDye 800CW donkey anti-rabbit; P/N 926-32213, and IRDye 800CW goat anti-rabbit; P/N 926-32211. All from LI-COR Biosciences, 1:10,000-1:15,000.

Cell surface biotinylation. Mice were anesthetized with isoflurane, placed in the prone position in a stereotaxic frame (Harvard Apparatus), a dorsal midline incision was made over the skull and upper cervical spine to expose the cranium, after which a brain infusion cannula (Brain infusion kit 3, Alzet) was placed in the lateral ventricle using the coordinates: 1.0 mm lateral to the midline, 0.5 mm posterior to bregma, and 2.5 mm ventral into the brain. After sacrificing the mouse by cervical dislocation, 1.5 mg EZ-link Sulfo-NHS-SS biotin (Thermo Fisher) in 100 µl biotin buffer (in mM: 125 NaCl, 2 $CaCl_2$, 10 triethanolamine, pH 7.5) was injected to the ventricle and the mouse left on ice for 15 min followed by isolation of choroid plexus. After isolation and quenching to remove excess biotin, the choroid plexus was transferred to a lysis buffer (in mM: 150 NaCl, 5 EDTA, 50 Tris-HCl, 1% Triton X-100, 0.05% SDS, 0.4 pefabloc and 8 µM leupeptin) for 30 min, all according to the manufacturer's instructions. The samples were sonicated 3 × 10 s at 70% (Sonopuls, Bandelin) and centrifuged at 10,000 × *g* for 5 min at 4 °C. An aliquot was removed (total fraction) before proceeding with the biotin (luminal) fraction purified on NeutrAvidin (Thermo Fisher) columns (Pierce).

Tissue preparation and immunostaining. Sections obtained from tissue from male C57BL/b mice from Taconic (Denmark) were immunostained with anti-NKCC1(kind gift from Professor Turner[68], 1:4000) and anti-e-cadherin; 610181 (BD Biosciences, 1:2000), prior to labeling with secondary antibody; donkey anti-mouse; Alexa555 (Invitrogen, 1:1000), donkey anti-rabbit; Alexa488 (Invitrogen, 1:1000) and nuclear staining with Topro3 (Invitrogen, 1:1000). Anti-KCC1 tested; HPA041138 (Atlas Antibodies), anti-KCC1 (kind gift from Professor Thomas J. Jentsch), and ab115607 (Abcam). The digital images were acquired with a DM IRE2 inverted confocal microscope (Leica Microsystems).

Ion content determination. To obtain enough material, samples from four mice were pooled for each of the four experiments. Mice were anesthetized with xylazine (only one initial intraperitoneal (i.p.) injection; 1 mg ml^{-1} and 0.1 ml per 10 g body weight, 37 °C, ScanVet). 5−10 min later, it was followed by an i.p. injection with ketamine (10 mg ml^{-1} and 0.1 ml per 10 g body weight + 150 µl for mice <30 g and 200 µl for mice >30 g, 37 °C, MDS Animal Health). With intervals of 25−35 min, the mouse was re-dosed with ketamine (up to 50% of start dose, as needed to sustain anesthesia). Anesthetized mice, after tracheotomy, were placed in a stereotaxic frame and clear CSF collected from cisterna magna. Immediately after decapitation, blood was collected and choroid plexus isolated, weighed, dried at 105 °C, and extracted in 0.1 M HNO_3 on a horizontal shaker table (200 rpm, 72 h, room temperature)[69]. The ion concentrations of the choroid plexus were calculated based on previous observations of choroid plexus epithelium containing 79% water and 8.5% blood[69]. Na^+ and K^+ content was quantified by flame photometry (Instrument Laboratory 943) while Cl^- concentration was quantified by a colorimetric method using QuantiChrom™ Chloride Assay Kit (MEDIBENA Life Science & Diagnostic Solution). Gibbs free energy for NKCC1 was calculated as Eq. 1

$$\Delta G = RT \times \ln \frac{[Na^+]_i \times [K^+]_i \times ([Cl^-]_i)^2}{[Na^+]_o \times [K^+]_o \times ([Cl^-]_o)^2}, \quad (1)$$

where R = gas constant (8.314 J mol^{-1}), T = temperature (at 37 °C; 310.15 K), $[X]_i$ = intracellular ion concentration, and $[X]_o$ = ion concentration in CSF.

Imaging of intracellular sodium and cell viability. For Na^+ imaging of choroid plexus bathed in aCSF-HEPES, the epithelial cells were loaded (~20 min) with the membrane-permeable form of SBFI (sodium-binding benzofuran isophthalate acetoxymethyl (AM) ester, 200 µM, Teflabs) To this end, the dye was pressure-applied (5 s) directly onto the cells on several positions[70]. Afterwards, the tissue was perfused with aCSF-HEPES for at least 20 min to allow for de-esterification of the dye before imaging experiments were commenced. Wide-field Na^+ imaging was performed utilizing a variable scan digital imaging system (Nikon NIS-Elements v4.3, Nikon) attached to an upright microscope (Nikon Eclipse FN-PT, Nikon GmbH). The microscope was equipped with a ×40/N.A. 0.8 LUMPlanFI water immersion objective (Olympus Deutschland GmbH) and an orca FLASH V2 camera (Hamamatsu Photonics Deutschland GmbH). SBFI was alternatively excited at 340 and 380 nm. Images were obtained at 1 Hz and emission was collected >440 nm. Fluorescence was evaluated in regions of interest (ROIs), representing single cells. Signals were background-corrected as follows: The fluorescence intensities obtained at each excitation wavelength (340/380 nm) were dynamically subtracted frame by frame by the respective fluorescence emissions of a ROI in the field of view, which was free of SBFI-labeling (background). After background subtraction, the fluorescence ratio (F_{340}/F_{380}) was calculated from individual ROIs and analyzed using OriginPro Software (OriginLab Corporation v.9.0). For imaging of cell survival of the choroid plexus after bumetanide treatment, the epithelial cells were loaded with Calcein-AM (500 µM, Sigma-Aldrich) as described for SBFI loading. This was done after 10 min of bumetanide treatment, right before the blocker washout (or after 10 min of aCSF as a control). Calcein was excited at 488 nm, emission was collected 510 nm. Each choroid plexus was randomly assigned to each group.

$^{86}Rb^+$ efflux experiments. Choroid plexus was isolated as above, initially in cold aCSF (in mM: 120 NaCl, 2.5 KCl, 2.5 $CaCl_2$, 1.3 $MgSO_4$, 1 NaH_2PO_4, 25 $NaHCO_3$, 10 glucose, pH 7.4, equilibrated with 95% O_2/5% CO_2) but allowed to recover at 37 °C for 5–10 min before beginning of the experiment. Choroidal isotope accumulation was performed by a 10 min incubation in equilibrated (95% O_2/5% CO_2) aCSF-based isotope medium (2 µCi ml^{-1} $^{86}Rb^+$, NEZ07200 (congener for K^+ transport) and 8 µCi ml^{-1} ^{3}H-mannitol, NET101 (extracellular marker), both from PerkinElmer), followed by 15 s wash prior to incubation in 0.5 ml equilibrated (95% O_2/5% CO_2) efflux medium (aCSF containing 20 µM bumetanide, 1 mM furosemide or vehicle (DMSO), each choroid plexus randomly assigned to each group). 0.2 ml of the efflux medium was collected into scintillation vials every 20 s (time points: 0, 20, and 40 s) and replaced with fresh aCSF. At the end of the experiment, choroid plexus was solubilized at room temperature with 1 ml Solvable (6NE9100, PerkinElmer) in the leftover efflux medium. The isotope content was determined by liquid scintillation counting with Ultima Gold^{TM} XR scintillation liquid (6013119, PerkinElmer) in a Tri-Carb 2900TR Liquid Scintillation Analyzer (Packard). The choroid plexus $^{86}Rb^+$ content corrected for ^{3}H-mannitol (extracellular background) was calculated for each time point, and the natural logarithm of the choroid plexus content A_t/A_0 was plotted against time[47]. Slopes indicating the $^{86}Rb^+$ efflux rate constants (s^{-1}) were determined from linear regression analysis.

Ventriculo-cisternal perfusion. Mice were anaesthetized with ketamine and xylazine (as described above) during the experimental procedure and their body temperature monitored and maintained at approximately 37 °C using a homeothermic system (Harvard Apparatus). To obtain near-physiological conditions, the mice were ventilated (VentElite, Harvard Apparatus) after tracheotomy and settings continuously optimized for each animal using a capnograph (Type 340, Harvard Apparatus) and a pulse oximeter (MouseOx® Plus, Starr Life Sciences), each calibrated with respiratory partial pressure of carbon dioxide and arterial oxygen saturation (ABL800 FLEX, Radiometer). Ventilation of a ~25 g mouse; approximately 150 µl per breath of a mix of 0.1 l min^{-1} O_2 and 0.9 l min^{-1} air and approximately 150 breath per min, sight = 10 % increase in tidal volume and Positive End-Expiratory Pressure (PEEP) = 2 cm H_2O. The heart rate was continuously monitored (MouseOx® Plus, Starr Life Sciences). After tracheotomy, 1 ml of warmed 0.9% NaCl was injected subcutaneously to decrease risk of dehydration. The infusion cannula was placed as described in the biotinylation method, and was glued to the scull (with superglue, Pelikan). The perfusion solution was heated to 37 °C in an inline heater (SF-28, Warner Instruments) before entering the infusion cannula. A micropipette held in a 5° position was introduced into the cisterna magna. After observing CSF in the micropipette, infusion of equilibrated (95% O_2/5% CO_2) aCSF (containing 1−2 mg ml^{-1} tetramethylrhodamine isothiocyanate-dextran (TRITC-dextran MW 155,000, T1287 Sigma-Aldrich) or 0.03 % w/v Evans blue (314-13-6 Sigma-Aldrich)) and 0.1% DMSO was initiated at a rate of ~ 0.7 µl min^{-1}. Addition of dextran and vehicle (DMSO) increased the osmolarity of the aCSF by approximately 20 mOsm. The final osmolarity of the aCSF employed for the ventricular-cisternal perfusion thus amounted to approximately 313 mOsm, designed to match the mouse plasma osmolarity (313 ± 2 mOsm, $n = 5$ mice) in order to limit osmotically induced experimental confounders into the experimental paradigm. An extra set of mice were anaesthetized with isoflurane (0.5–1.5 %) at the time of CSF production rate determination. Anesthesia was induced as above (to facility the tracheometry) but the animal transferred to isoflurane immediately thereafter with no subsequent additional ketamine injections. In this manner, the animal had not been subjected to ketamine/xylazine for at least 2 h and the dominant anesthesia predicted to be isoflurane. After an hour of infusion, the animals anesthetized with the standard ketamine/xylazine described above were exposed to a new aCSF solution containing either 2 mM furosemide, 100 µM bumetanide (expected ventricular concentrations of 1 mM and 50 µM) or the vehicle, DMSO (animals were randomly assigned to these groups). The solution change took 5–10 min. Outflow was collected in 5-min intervals by introducing a second micropipette into the fixed cisterna magna micropipette and the fluorescent content measured in a microplate photometer (Fluoroskan Ascent, Thermo Labsystems). The production rate of CSF was calculated from the equation:

$$V_p = r_i \times \frac{C_i - C_o}{C_o}, \quad (2)$$

where V_p = CSF production rate (µl min^{-1}), r_i = infusion rate (µl min^{-1}), C_i = fluorescence of inflow solution, C_o = fluorescence of outflow solution.

In vivo live imaging. Ventricular injections were done as above, except with variation in the ventricular depth: A cannula was placed 2.5 mm into the brain and 2 µl aCSF with vehicle(DMSO)/inhibitor (2 mM furosemide or 100 µM bumetanide, animals were randomly assigned to these groups) was injected during 2 s. Within 5 min, the cannula was removed and a new placed 2.2 mm into the brain and the second solution injected. This second cannula contained aCSF with vehicle/inhibitor, as above, in addition to a carboxylate dye (10 µM IRDye 800CW, P/N 929-08972, LI-COR Biosciences). With a lapse of 1 min after injection, the first image was obtained on the Pearl Trilogy Small Animal Imaging System (800 nm channel, 85 µm resolution, and 30 s intervals, LI-COR Biosciences). At the termination of each experiment, a white field image was taken. Due to the swift protocol, these mice were not ventilated. Images were analyzed using Image Studio 5.2 and the region of interest defined as a square, starting at lambda. For test of whether the injected solution reached both ventricles, 0.03% w/v Evans blue (314-13-6, Sigma-Aldrich) dissolved in aCSF was injected in a manner mimicking the injection of fluorescent dye.

Chemicals. Chemicals were freshly dissolved prior to each experimental day. Furosemide (F4381, Sigma-Aldrich) was dissolved directly into the aCSF while a stock solution (100 mM in DMSO) was prepared with bumetanide (B3023, Sigma-Aldrich).

Statistics. Data analysis and statistical tests were carried out with GraphPrism 7.0 (GraphPad Software). One-sample *t* test, one-way or two-way (RM)ANOVA followed by the Tukey's multiple comparisons post hoc test were employed as indicated in figure legends. Data are obtained from choroid plexus from individual animals and presented as mean ± SEM with significance set at $P < 0.05$.

Data availability. We confirm that all relevant data from this study are available from the corresponding author upon request.

Received: 26 January 2018 Accepted: 14 May 2018
Published online: 04 June 2018

References

1. Damkier, H. H., Brown, P. D. & Praetorius, J. Cerebrospinal fluid secretion by the choroid plexus. *Phys. Rev.* **93**, 1847–1892 (2013).
2. Iliff, J. J. et al. A paravascular pathway facilitates CSF flow through the brain parenchyma and the clearance of interstitial solutes, including amyloid β. *Sci. Trans. Med.* **4**, 147ra111 (2012).
3. Rennels, M. L., Gregory, T. F., Blaumanis, O. R., Fujimoto, K. & Grady, P. A. Evidence for a "paravascular" fluid circulation in the mammalian central nervous system, provided by the rapid distribution of tracer protein throughout the brain from the subarachnoid space. *Brain Res.* **326**, 47–63 (1985).
4. Spector, R., Keep, R. F., Snodgrass, S. R., Smith, Q. R. & Johanson, C. E. A balanced view of choroid plexus structure and function: focus on adult humans. *Exp. Neurol.* **267**, 78–86 (2015).
5. Milhorat, T. H., Hammock, M. K., Fenstermacher, J. D., Rall, D. P. & Levin, V. A. Cerebrospinal fluid production by the choroid plexus and brain. *Science* **173**, 330–332 (1971).
6. Hallaert, G. G. et al. Endoscopic coagulation of choroid plexus hyperplasia. *J. Neurosur.: Ped.* **9**, 169–177 (2012).
7. Abbott, N. J. Evidence for bulk flow of brain interstitial fluid: significance for physiology and pathology. *Neurochem. Int.* **45**, 545–552 (2004).
8. Ziebell, M., Wetterslev, J., Tisell, M., Gluud, C. & Juhler, M. Flow-regulated versus differential pressure-regulated shunt valves for adult patients with

normal pressure hydrocephalus. *Cochrane Database Syst. Rev.* **5**, CD009706 (2013).
9. Karimy, J. K. et al. Inflammation-dependent cerebrospinal fluid hypersecretion by the choroid plexus epithelium in posthemorrhagic hydrocephalus. *Nat. Med.* **23**, 997–1003 (2017).
10. Ducros, A. & Biousse, V. Headache arising from idiopathic changes in CSF pressure. *Lancet Neurol.* **14**, 655–668 (2015).
11. Davson, H. F. & Segal, M. B. The effects of some inhibitors and accelerators of sodium transport on the turnover of 22Na in the cerebrospinal fluid and the brain. *J. Physiol.* **209**, 131–153 (1970).
12. Welch, K. Secretion of cerebrospinal fluid by choroid plexus of the rabbit. *Am. J. Phys.* **205**, 617–624 (1963).
13. Hladky, S. B. & Barrand, M. A. Fluid and ion transfer across the blood−brain and blood−cerebrospinal fluid barriers; a comparative account of mechanisms and roles. *Fluids Barriers CNS* **13**, 19 (2016).
14. Praetorius, J. & Damkier, H. H. Transport across the choroid plexus epithelium. *Am. J. Phys.—Cell Phys.* **312**, C673–C686 (2017).
15. Oshio, K., Watanabe, H., Song, Y., Verkman, A. S. & Manley, G. T. Reduced cerebrospinal fluid production and intracranial pressure in mice lacking choroid plexus water channel Aquaporin-1. *FASEB J.* **19**, 76–78 (2005).
16. Cserr, H. F. Physiology of the choroid plexus. *Phys. Rev.* **51**, 273–311 (1971).
17. Pollay, M. & Curl, F. Secretion of cerebrospinal fluid by the ventricular ependyma of the rabbit. *Am. J. Phys.* **213**, 1031–1038 (1967).
18. MacAulay, N. & Zeuthen, T. Water transport between CNS compartments: contributions of aquaporins and cotransporters. *Neuroscience* **168**, 941–956 (2010).
19. Curl, F. D. & Pollay, M. Transport of water and electrolytes between brain and ventricular fluid in the rabbit. *Exp. Neurol.* **20**, 558–574 (1968).
20. Heisey, S. R., Held, D. & Pappenheimer, J. R. Bulk flow and diffusion in the cerebrospinal fluid system of the goat. *Am. J. Phys.* **203**, 775–781 (1962).
21. Welch, K. E. A. S., Sadler, K. E. I. T. & Gold, G. E. R. A. Volume flow across choroidal ependyma of the rabbit. *Am. J. Phys.* **210**, 232–236 (1966).
22. Zeuthen, T. & MacAulay, N. Transport of water against its concentration gradient: fact or fiction? *WIREs Membr. Transp. Signal.* **1**, 373–381 (2012).
23. Choe, S., Rosenberg, J. M., Abramson, J., Wright, E. M. & Grabe, M. Water permeation through the sodium-dependent galactose cotransporter vSGLT. *Biophys. J.* **99**, L56–L58 (2010).
24. Hamann, S., Herrera-Perez, J. J., Zeuthen, T. & Alvarez-Leefmans, F. J. Cotransport of water by the Na+-K+-2Cl- cotransporter NKCC1 in mammalian epithelial cells. *J. Phys.* **588**, 4089–4101 (2010).
25. Zeuthen, T. Cotransport of K^+, Cl^- and H_2O by membrane proteins from choroid plexus epithelium of Necturus maculosus. *J. Phys.* **478**, 203–219 (1994).
26. Zeuthen, T. & MacAulay, N. Cotransport of water by Na^+-K^+-$2Cl^-$ cotransporters expressed in Xenopus oocytes: NKCC1 versus NKCC2. *J. Phys.* **590**, 1139–1154 (2012).
27. Praetorius, J. & Nielsen, S. Distribution of sodium transporters and aquaporin-1 in the human choroid plexus. *Am. J. Phys.—Cell Phys.* **291**, C59–C67 (2006).
28. Pearson, M. M., Lu, J., Mount, D. B. & Delpire, E. Localization of the K + -Cl- cotransporter, KCC3, in the central and peripheral nervous systems: expression in the choroid plexus, large neurons and white matter tracts. *Neuroscience* **103**, 481–491 (2001).
29. Karadsheh, M. F., Byun, N., Mount, D. B. & Delpire, E. Localization of the KCC4 potassium-chloride cotransporter in the nervous system. *Neuroscience* **123**, 381–391 (2004).
30. Payne, J. A., Rivera, C., Voipio, J. & Kaila, K. Cation-chloride co-transporters in neuronal communication, development and trauma. *Trends Neurosci.* **26**, 199–206 (2003).
31. Lykke, K. et al. The search for NKCC1-selective drugs for the treatment of epilepsy: Structure-function relationship of bumetanide and various bumetanide derivatives in inhibiting the human cation-chloride cotransporter NKCC1A. *Epilepsy Behav.* **59**, 42–49 (2016).
32. Christensen, I. B., Gyldenholm, T., Damkier, H. H., & Praetorius, J. Polarization of membrane associated proteins in the choroid plexus epithelium from normal and slc4a10 knockout mice. *Front. Physiol.* **4**, 344 (2013).
33. Haas, M. & Forbush, B. III The Na-K-Cl cotransporter of secretory epithelia. *Annu. Rev. Phys.* **62**, 515–534 (2000).
34. Alberts, B. et al. *Transport Across Cell Membranes in Essential Cell Biology* Vol. 385 (Garland Science, New York, 2013).
35. Bratosin, D., Mitrofan, L., Palii, C., Estaquier, J. Ã. & Montreuil, J. Novel fluorescence assay using calcein-AM for the determination of human erythrocyte viability and aging. *Cytometry* **66**, 78–84 (2005).
36. Pappenheimer, J. R., Heisey, S. R. & Jordan, E. F. Perfusion of the cerebral ventricular system in unanesthetized goats. *Am. J. Phys.* **203**, 763–774 (1962).
37. Ames, A. III, Higashi, K. F. & Nesbett, F. B. Effects of Pco2 acetazolamide and ouabain on volume and composition of choroid-plexus fluid. *J. Phys.* **181**, 516–524 (1965).
38. Carey, M. E. & Vela, A. R. Effect of systemic arterial hypotension on the rate of cerebrospinal fluid formation in dogs. *J. Neurosurg.* **41**, 350–355 (1974).
39. House, C. R. *Water Transport in Cells and Tissues* (E. Arnold, London, 1974).
40. Larsen, B. R. et al. Contributions of the Na+/K+-ATPase, NKCC1, and Kir4. 1 to hippocampal K + clearance and volume responses. *Glia* **62**, 608–622 (2014).
41. Plotkin, M. D. et al. Expression of the Na (+)-K (+)-2Cl-cotransporter BSC2 in the nervous system. *Am. J. Phys.—Cell Phys.* **272**, 173–183 (1997).
42. Kanaka, C. et al. The differential expression patterns of messenger RNAs encoding K-Cl cotransporters (KCC1, 2) and Na-K-2Cl cotransporter (NKCC1) in the rat nervous system. *Neuroscience* **104**, 933–946 (2001).
43. Li, H., Tornberg, J., Kaila, K., Airaksinen, M. S. & Rivera, C. Patterns of cation-chloride cotransporter expression during embryonic rodent CNS development. *Eur. J. Neurosci.* **16**, 2358–2370 (2002).
44. Markkanen, M. et al. Distribution of neuronal KCC2a and KCC2b isoforms in mouse CNS. *J. Comp. Neurol.* **522**, 1897–1914 (2014).
45. Lun, M. P. et al. Spatially heterogeneous choroid plexus transcriptomes encode positional identity and contribute to regional CSF production. *J. Neurosci.* **35**, 4903–4916 (2015).
46. Murphy, V. A. & Johanson, C. E. Na (+)-H+exchange in choroid plexus and CSF in acute metabolic acidosis or alkalosis. *Am. J. Phys.—Ren. Phys.* **258**, F1528–F1537 (1990).
47. Keep, R. F., Xiang, J. I. A. N. & Betz, A. L. Potassium cotransport at the rat choroid plexus. *Am. J. Phys.—Cell Phys.* **267**, C1616–C1622 (1994).
48. Untiet, V. et al. Glutamate transporter-associated anion channels adjust intracellular chloride concentrations during glial maturation. *Glia* **65**, 388–400 (2017).
49. Cong, D., Zhu, W., Kuo, S., Hu, S. & Sun, D. Ion transporters in brain tumors. *Curr. Med. Chem.* **22**, 1171–1181 (2015).
50. Oreskovic, D. & Klarica, M. The formation of cerebrospinal fluid: nearly a hundred years of interpretations and misinterpretations. *Brain Res. Rev.* **64**, 241–262 (2010).
51. Javaheri, S. & Wagner, K. R. Bumetanide decreases canine cerebrospinal fluid production. In vivo evidence for NaCl cotransport in the central nervous system. *J. Clin. Inv.* **92**, 2257 (1993).
52. Vogh, B. P. & Langham, M. R. Jr. The effect of furosemide and bumetanide on cerebrospinal fluid formation. *Brain Res.* **221**, 171–183 (1981).
53. Vogh, B. P. & Doyle, A. S. The effect of carbonic anhydrase inhibitors and other drugs on sodium entry to cerebrospinal fluid. *J. Pharm. Exp. Ther.* **217**, 51–56 (1981).
54. Philp, N. J., Yoon, H. & Lombardi, L. Mouse MCT3 gene is expressed preferentially in retinal pigment and choroid plexus epithelia. *Am. J. Phys.—Cell Phys.* **280**, C1319–C1326 (2001).
55. Tschirgi, R. D., Frost, R. W. & Taylor, J. L. Inhibition of cerebrospinal fluid formation by a carbonic anhydrase inhibitor, 2-acetylamino-1, 3, 4-thiadiazole-5-sulfonamide (Diamox). *Proc. Soc. Exp. Biol. Med.* **87**, 373–376 (1954).
56. Kister, S. J. Carbonic anhydrase inhibition. VI. The effect of acetazolamide on cerebrospinal fluid flow. *J. Pharmacol. Exp. Ther.* **117**, 402–405 (1956).
57. Macri, F. J., Politoff, A., Rubin, R., Dixon, R. & Rall, D. Preferential vasoconstrictor properties of acetazolamide on the arteries of the choroid plexus. *Int. J. Neuropharm.* **5**, 109–115 (1966).
58. Kimelberg, H. K., Rose, J. W., Barron, K. D., Waniewski, R. A. & Cragoe, E. J. Astrocytic swelling in traumatic-hypoxic brain injury. *Mol. Chem. Neuropath.* **11**, 1–31 (1989).
59. Delpire, E. & Mount, D. B. Human and murine phenotypes associated with defects in cation-chloride cotransport. *Ann. Rev. Phys.* **64**, 803–843 (2002).
60. Damkier, H. H., Prasad, V., Hübner, C. A. & Praetorius, J. Nhe1 is a luminal Na + /H + exchanger in mouse choroid plexus and is targeted to the basolateral membrane in Ncbe/Nbcn2-null mice. *Am. J. Phys.—Cell Phys.* **296**, C1291–C1300 (2009).
61. Bu, Y. et al. Mechanisms of hydrocephalus after intraventricular haemorrhage in adults. *Stroke Vasc. Neurol.* **1**, 23–27 (2016).
62. Charan, J. & Kantharia, N. D. How to calculate sample size in animal studies? *J. Pharmacol. Pharmacother.* **4**, 303 (2013).
63. Rust, M. B. et al. Disruption of erythroid K-Cl cotransporters alters erythrocyte volume and partially rescues erythrocyte dehydration in SAD mice. *J. Clin. Invest.* **117**, 1708–1717 (2007).
64. Hübner, C. A. et al. Disruption of KCC2 reveals an essential role of K-Cl cotransport already in early synaptic inhibition. *Neuron* **30**, 515–524 (2001).
65. Boettger, T. et al. Deafness and renal tubular acidosis in mice lacking the K-Cl co-transporter Kcc4. *Nature* **416**, 874–878 (2002).
66. Boettger, T. et al. Loss of K-Cl co-transporter KCC3 causes deafness, neurodegeneration and reduced seizure threshold. *EMBO J.* **22**, 5422–5434 (2003).

67. de los Heros, P. et al. The WNK-regulated SPAK/OSR1 kinases directly phosphorylate and inhibit the K+-Cl- co-transporters. *Biochem. J.* **458**, 559–573 (2014).
68. Kurihara, K., Moore-Hoon, M. L., Saitoh, M. & Turner, R. J. Characterization of a phosphorylation event resulting in upregulation of the salivary Na+-K+-2Cl- cotransporter. *Am. J. Phys.—Cell Phys.* **277**, C1184–C1193 (1999).
69. Johanson, C. E., Reed, D. J. & Woodbury, D. M. Active transport of sodium and potassium by the choroid plexus of the rat. *J. Phys.* **241**, 359 (1974).
70. Meier, S. D., Kovalchuk, Y. & Rose, C. R. Properties of the new fluorescent Na + indicator CoroNa Green: comparison with SBFI and confocal Na+ imaging. *J. Neurosci. Methods* **155**, 251–259 (2006).

Acknowledgements

We thank Mette Assentoft, Micael Loenstrup, Kristofffer Racz, and Carina Lynnerup Pedersen for expert technical assistance and Professor Jeppe Praetorius, Aarhus University, Denmark for providing the immunostaining of NKCC1 in choroid plexus. We are grateful to Professor Thomas J. Jentsch, University of Hamburg, Germany for kindly providing the KCC1 and KCC3 antibodies and Professor Jinwei Zhang, University of Dundee, Scotland for kindly providing the KCC3 and KCC4 antibodies. We thank Professor Thomas Zeuthen for critical reading of the manuscript. This work was supported by Thorberg's Foundation (53.734), Novo Nordisk Foundation; Tandem program (NNF17OC0024718), the Danish Medical Research Council, Sapere Aude program (0602-02344B), Vera and Carl Johan Michaelsen's Scholarship, the Augustinus Foundation, Doctor Sofus Carl Emil Friis og hustru Olga Doris Friis' scholarship, and the Carlsberg Foundation (CF15-0070).

Author contributions

A.B.S., K.T., C.R.R., and N.M. designed the research; A.B.S., E.K.O, A.S., N.J.G., D.B., K. T., and C.R.R. performed research and analyzed the data; A.B.S. and N.M. drafted the manuscript and all authors contributed to the final version of the manuscript.

Additional information

Supplementary Information accompanies this paper at https://doi.org/10.1038/s41467-018-04677-9.

Competing interests: The authors declare no competing interests.

Reprints and permission information is available online at http://npg.nature.com/reprintsandpermissions/

Publisher's note: Springer Nature remains neutral with regard to jurisdictional claims in published maps and institutional affiliations.

Oernbo *et al. Fluids Barriers CNS (2018) 15:27*
https://doi.org/10.1186/s12987-018-0111-8

Fluids and Barriers of the CNS

RESEARCH

Open Access

Cerebral influx of Na^+ and Cl^- as the osmotherapy-mediated rebound response in rats

Eva Kjer Oernbo[1], Kasper Lykke[1,5], Annette Buur Steffensen[1], Kathrin Töllner[2,3], Christina Kruuse[4], Martin Fredensborg Rath[1], Wolfgang Löscher[2,3] and Nanna MacAulay[1,6*]

Abstract

Background: Cerebral edema can cause life-threatening increase in intracranial pressure. Besides surgical craniectomy performed in severe cases, osmotherapy may be employed to lower the intracranial pressure by osmotic extraction of cerebral fluid upon intravenous infusion of mannitol or NaCl. A so-called rebound effect can, however, hinder continuous reduction in cerebral fluid by yet unresolved mechanisms.

Methods: We determined the brain water and electrolyte content in healthy rats treated with osmotherapy. Osmotherapy (elevated plasma osmolarity) was mediated by intraperitoneal injection of NaCl or mannitol with inclusion of pharmacological inhibitors of selected ion-transporters present at the capillary lumen or choroidal membranes. Brain barrier integrity was determined by fluorescence detection following intravenous delivery of Na^+-fluorescein.

Results: NaCl was slightly more efficient than mannitol as an osmotic agent. The brain water loss was only ~60% of that predicted from ideal osmotic behavior, which could be accounted for by cerebral Na^+ and Cl^- accumulation. This electrolyte accumulation represented the majority of the rebound response, which was unaffected by the employed pharmacological agents. The brain barriers remained intact during the elevated plasma osmolarity.

Conclusions: A brain volume regulatory response occurs during osmotherapy, leading to the rebound response. This response involves brain accumulation of Na^+ and Cl^- and takes place by unresolved molecular mechanisms that do not include the common ion-transporting mechanisms located in the capillary endothelium at the blood–brain barrier and in the choroid plexus epithelium at the blood–CSF barrier. Future identification of these ion-transporting routes could provide a pharmacological target to prevent the rebound effect associated with the widely used osmotherapy.

Keywords: Osmotherapy, Rebound effect, Brain edema, Brain barriers, Ion-transporting mechanisms

Background

The ion and fluid homeostasis in the mammalian brain is tightly controlled to preserve the intracranial pressure (ICP) within a normal range. Cerebral edema, as occurring in pathologies such as traumatic brain injury and stroke, can cause the ICP to rise to life-threateningly high levels [1]. In severe cases, a decompressive craniectomy can be initiated to lower the ICP [2]. Alternatively, osmotherapy can be used to osmotically extract cerebral fluid into the blood circulation by intravenous (i.v.) infusion of mannitol or NaCl [3], although it remains disputed which of these osmotic agents is most efficient for brain water extraction. The initial target when applying osmotherapy is a plasma osmolarity up to 320 mOsm but depending on the clinical circumstances, this recommended value may be exceeded [1]. Osmotherapy induces an immediate loss of brain fluid, which can, however, be reduced or even reversed due to yet incompletely understood mechanisms; a phenomenon referred to as the rebound

*Correspondence: macaulay@sund.ku.dk
[6] Department of Neuroscience, Faculty of Health and Medical Sciences, University of Copenhagen, Blegdamsvej 3, 2200 Copenhagen, Denmark
Full list of author information is available at the end of the article

effect [4, 5]. The rebound effect has been suggested to arise from a compensatory accumulation of cerebral osmolytes, generating an osmotic gradient favoring fluid movement back into the brain particularly upon dilution of the plasma osmolarity by renal excretion and/or withdrawal of the osmotic agent [4, 5]. It remains uncertain to what extent brain ion accumulation participates in the rebound response, and if so, which molecular transporting mechanisms contribute to this volume regulatory response. The secretion of ions may take place at one or both of the two major interfaces between the brain and blood: the capillary endothelium forming the blood–brain barrier (BBB) and/or the cerebrospinal fluid (CSF)-secreting choroid plexus epithelium, which forms the blood–CSF barrier (BCSFB) [6, 7]. The capillary endothelium and the choroid plexus epithelium express several ion-transporting mechanisms, i.e. the Na^+–K^+–$2Cl^-$ co-transporter 1 (NKCC1), the Na^+–H^+ anti-porter 1 (NHE1), Na^+-coupled bicarbonate transporters (NBCs), and the amiloride-sensitive Na^+ channel (ENaC) [8–10]. These transport mechanisms may be potential candidates for brain ion and water regulation, and could, as such, participate in electrolyte translocation from blood to brain during the elevated blood osmolarity resulting from osmotherapy treatment. Inhibition of a subset of these ion transporters has been associated with improved outcome in an experimental animal model of stroke [11, 12], which may indicate involvement of such transport mechanisms in brain ion and water dynamics. Here, we employed in vivo investigations of healthy non-edematous rats to obtain the brain volume regulatory response to increased plasma osmolarity in the absence of pathological events, such as stroke/haemorrhage, and investigate a putative role of a range of transport mechanisms in the brain volume regulatory gain of ions.

Methods

Animals

This study was performed in accordance with the European Community guidelines for the use of experimental animals using protocols approved either by the Lower Saxony State Office for Consumer Protection and Food Safety (Niedersachsen, Germany) or Supervisory Authority on Animal Testing (Danish Veterinary and Food Administration, Denmark). To avoid variation due to mixed gender, only female Sprague–Dawley rats were employed, aged 9–13 weeks (Taconic A/S, Lille Skensved, Denmark or Janvier Labs, Le Genest-Saint-Isle, France). Whether the present findings hold for male rats as well will require further studies in the future. Rats were housed in groups of 2–5 per cage (Tp III cages, 22 °C, 12:12 h light/dark cycle) with access to unlimited water and standard altromin rodent diet. The allocation of rats into the treatment groups was randomized, and all experiments were reported in compliance with the ARRIVE guidelines (Animal Research: Reporting in Vivo Experiments) [13].

Brain water extraction by elevated plasma osmolarity

Rats were anesthetized using isoflurane inhalation mixed in O_2 (1.5–5%, 1 l/min) and anaesthesia was maintained throughout the entire experiment. The body temperature was controlled to 37 °C using an electric heating pad (Harvard Apparatus, Holliston, MA, US) and monitored by a rectal probe during the entire procedure. To avoid systemic regulation of blood osmolytes upon hyperosmotic treatment, a functional nephrectomy was performed immediately prior to the initiation of the experiment in all animals except for naïve animals, which were not exposed to isosmolar- or hyperosmolar treatment but underwent anaesthesia induction shortly before decapitation, see Table 1 for grouping of experimental animals. In brief, laparotomy incision areas were treated with local analgesia [2–4 drops 2% tetracaine (Sigma-Aldrich, Brøndbyvester, Denmark, T7508) or xylocaine (1 mg/ml, AstraZeneca A/S, Copenhagen, Denmark, N01BB02)/bupivacaine (0.5 mg/ml, Amgros I/S, Copenhagen, Denmark, N01BB01) (both in 0.9% w/v NaCl)] prior to opening of the abdominal cavity either from the dorsal or the ventral side in the fully anesthetized animals. The renal artery and vein were ligated using non-absorbable suture. For rats given ventral incision, a catheter (for i.p. delivery, see below) was placed during suturing of the incision, while for rats with dorsal incisions, the smaller openings were closed with metal wound clamps immediately after i.p. delivery. The rats received a single i.p. bolus of a physiological NaCl solution (0.9% w/v NaCl) as an isosmolar control treatment, while an equiosmolar bolus of NaCl (1.17 g/kg, 1 M [14]) or mannitol (7.29 g/kg, dissolved in 0.9% w/v NaCl; 2 M) was given to elevate the plasma osmolarity to a similar extent. All solutions were heated to 37 °C and delivered as 2 ml/100 g body weight. We employed i.p. delivery of the osmotic agent as this delivery route gives similar plasma osmolarities as i.v. delivery [14]. For i.v. inhibitor experiments, a catheter was inserted into the tail vein and an inhibitor mixture containing bumetanide (10 mg/kg [11], Sigma-Aldrich, B3023), amiloride (6 mg/kg [15], Sigma-Aldrich, A7410), and methazolamide (20 mg/kg [16], Sigma-Aldrich, SML0720) or vehicle (specified below) was injected 5 min prior to i.p. treatment with isosmolar- or hyperosmolar NaCl, see Table 1 for grouping of experimental animals. Inhibitors were given in a mixture to minimize the number of rats used for experiments. While drug concentrations in the blood are difficult to assess due to unspecific binding to tissue

Table 1 Overview of experimental animal groups

Experiment	Label	Osmotic agent	Treatment	Delivery route	# rats
Brain water and ion quantification	Control	–	Vehicle	i.v.	9
		–	Inhibitors	i.v.	7
		–	Vehicle	i.c.v.	6
		–	Inhibitors	i.c.v.	6
	Osmotherapy	NaCl (i.p.)	Vehicle	i.v.	9
		NaCl (i.p.)	Inhibitors	i.v.	8
		NaCl (i.p.)	3× vehicle	i.v.	4
		NaCl (i.p.)	3× inhibitors	i.v.	4
		NaCl (i.p.)	Vehicle	i.c.v.	6
		NaCl (i.p.)	Inhibitors	i.c.v.	6
		Mannitol (i.p.)	–	–	6
	Naïve	–	–	–	3
Brain barrier permeability	Control	–	NaFl	i.v.	3
	Osmotherapy	NaCl (i.p.)	NaFl	i.v.	3
	Naïve	–	–	–	3
Monitoring of ICP		–	Evans blue	i.c.v.	3
Blood pressure measurement		–	Vehicle	i.v.	3
		–	Inhibitors	i.v.	3

i.p., intraperitoneal; i.v., intravenous; i.c.v., intra(cerebro)ventricular; 3×, triple doses; NaFl, Na^+-fluorescein

and blood proteins, we estimate maximal blood concentrations of 0.4 mM for bumetanide and amiloride, and 1.2 mM for methazolamide based on estimated blood volume of 7% of the rat body weight (average: 233 g). In a few experiments, rats were given a triple inhibitor or vehicle dose into the tail vein. In this case, a bolus injection of inhibitors or vehicle was given 20 min and 5 min before and 15 min after delivery of isosmolar or hyperosmolar NaCl. In other experiments, rats were positioned in a stereotactic frame (Stoelting, Wood Dale, IL, US, 51500) and a micro drill (CircuitMedic, Haverhill, MA, US, 110-4102) employed to induce a burr hole in the skull (coordinates from bregma: 1.4 mm lateral, 0.8 mm posterior). A Hamilton syringe (G27, Agntho's AB, Lidingö, Sweden, 2100521) filled with inhibitor mixture (bumetanide: 33 µM, amiloride and methazolamide: 167 µM, final ventricular concentrations estimated to be 20 and 100 µM [17–22]) or vehicle dissolved in equilibrated (95% O_2/5% CO_2) artificial CSF (aCSF) (120 mM NaCl, 2.5 mM KCl, 1.3 mM $MgSO_4 \times 7$ H_2O, 1 mM NaH_2PO_4, 25 mM $NaHCO_3$, 10 mM glucose $\times$ H_2O, 2.5 mM $CaCl_2$, pH 7.4 at 37 °C) was fastened to the stereotactic apparatus and introduced into the right lateral ventricle (4.7 mm ventral). Two min prior to isosmolar or hyperosmolar i.p. treatment, 6 µl inhibitor or vehicle solution was injected in 2 s (volume and rate adjusted to hit both lateral ventricles), see Table 1 for grouping of experimental animals. To maintain an optimal intraventricular inhibitor dose, inhibitor or vehicle solution was injected into the ventricular system every 15 min. All the experiments were terminated by decapitation of the animal 1 h after i.p. injection of osmotic agent or physiological saline. A 1 h treatment period was chosen according to the reported near stabilization of plasma osmolarity and brain volume within 30 min after a hyperosmolar challenge [14]. All inhibitor solutions were made freshly each day (some from frozen stock solutions). Bumetanide and methazolamide were dissolved in 0.1 M NaOH (pH adjusted with 0.1 M HCl to pH 11 and 9, respectively) and diluted to 10 mg/ml for injection into the tail vein, while amiloride was dissolved in heated water at 10 mg/ml. Inhibitors, which were introduced into the ventricular system, were dissolved in DMSO (final concentration of 0.2% in aCSF).

Brain water and electrolyte quantification

The brain was removed immediately after decapitation. The olfactory bulbs and medulla oblongata were discarded and the remaining brain tissue was placed in a pre-weighed porcelain evaporation beaker and weighed within minutes after isolation to reduce loss of brain water. Brain tissue was homogenized in the pre-weighed evaporation beaker using a steel pestle and dried at 100 °C for 3–4 days to a constant mass for determination of the brain water content. The dried brain tissue (75–130 mg) was extracted in 1 ml 0.75 M HNO_3 on a horizontal shaker table for 3 days at room temperature (RT). The Cl^- content in the brain extracts was quantified by

a colorimetric method using a QuantiChrom™ Chloride Assay Kit (MEDIBENA Life Science & Diagnostic Solution, Vienna, Austria), while the Na^+ and K^+ content was quantified using flame photometry (Instrument Laboratory 943, Bedford, MA, US).

Plasma osmolarity and ion quantification

A heparin-coated tube (Jørgen Kruuse A/S, Langeskov, Denmark) was filled with pooled blood (venous and arterial) from the neck region upon decapitation of the rats. Blood samples were kept cold for maximal 4 h until centrifugation at 1300*g* for 10 min at RT. The plasma layer was collected and stored at − 20 °C. The plasma osmolarity was determined by a freezing point depression osmometer (Löser, Berlin, Germany), while the content of Na^+, Cl^-, urea and creatinine was measured using a RAPIDLab® blood gas analyzer (Siemens, Münich, Germany) or flame photometer (Instrument Laboratory 943).

Analysis of data

If assuming that the barriers between blood and brain behave as semipermeable membranes, i.e. permeable only to water but not to solutes, a new steady state in brain water content V_h (h; hyperosmolar, in ml/g dry weight) mediated by an elevated plasma osmolarity C^h_{osm} (mOsm) can be given by Eq. 1 as described in [14], where V_i is brain water content (i; isosmolar, in ml/g dry weight) in rats with isosmolar plasma osmolarity C^i_{osm} (mOsm).

$$V_h = V_i \cdot \frac{C^i_{osm}}{C^h_{osm}} \quad (1)$$

If the brain water loss is less than predicted by Eq. 1, this will imply that the brain gains osmotically active solutes given that the plasma and brain water is in osmotic equilibrium. The predicted gain of electrolytes, ΔQ (mmol/kg dry weight), can then be given by

$$\Delta Q = V_h \cdot C^h_{osm} - V_i \cdot C^i_{osm} \quad (2)$$

Brain barrier permeability

To assess the paracellular permeability of the brain barriers, anaesthetized rats were subjected to a functional nephrectomy. The experiments were initiated as above, after which a 4% Na^+-fluorescein (Sigma-Aldrich, F63772) solution (2 ml/kg, 0.25 ml/min, dissolved in 0.9% w/v NaCl) was infused into the femoral vein through a catheter; Na^+-fluorescein is a marker of paracellular permeability and has been used to identify paracellular BBB disruption by osmotic shock [23]. Five min hereafter, isosmolar or hyperosmolar NaCl was injected into the abdominal cavity as described above, see Table 1 for grouping of experimental animals. Rats were decapitated after 1 h, and the brains were removed immediately and frozen on crushed solid CO_2. Coronal sections (12 µm) were cut in a cryostat and mounted on slides. Na^+-fluorescein was visualized using an Axioplan 2 epifluoresence microscope (Carl Zeiss Vision, München-Halbergmoos, Germany) equipped with a Plan Neofluar and an AxioCam MR digital camera by use of the AxioVision 4.4 software (Carl Zeiss Vision, Birkerød, Denmark). Image acquisition was performed in a blinded fashion. Representative images were captured of brain regions comprising the neocortex, hippocampus, thalamus, and the lateral ventricle. The pineal gland was used as an internal positive control due to its lack of BBB [24]. Phase contrast images were included to visualize brain structures in transmitted light. Image processing (brightness and contrast) was performed using Adobe Photoshop (San Jose, CA, US).

Monitoring of ICP

In order to monitor the ICP of the anaesthetized rats, a micro drill (1 mm bit) was applied to manually induce a burr hole into the skull until transparency was observed. The thin skull layer was gently ruptured using a 0.6 mm bit (without disruption of dura mater) after which a tweezer was employed to remove skull flakes. An epidural probe (Plastics One, Roanoke, VA, US, C313GS-5-3UP, 0 mm below pedestal) was gently placed onto dura mater, and fastened to the skull by cement (GC, Kortrijk, Belgium, Fuji I, 000136). ICP fluctuations were detected by PicoLog Recorder software (Pico Technology, Cambridgeshire, UK). To ensure proper probe insertion in the epidural space, the jugular vein was compressed before the beginning of each experiment and a raised ICP detected as a positive control. An Evans blue (Sigma-Aldrich, E2129) solution (0.003% w/v in 0.9% w/v NaCl) was infused into the right lateral ventricle (6 µl in total, 3 µl/s) using a Hamilton syringe, while ICP recordings were collected, see Table 1 for grouping of experimental animals. 10 min after intraventricular injections, rats were euthanized by decapitation. The brains were isolated and cerebral hemispheres separated to confirm intraventricular Evans blue staining.

Blood pressure measurement

Female Sprague–Dawley rats (22–28 weeks) were anaesthetized with chloral hydrate (400 mg/kg, i.p.), see Table 1 for grouping of experimental animals. A catheter was inserted into the left femoral artery to measure the intra-arterial blood pressure (BioSys software, TSE Systems, Bad Homburg, Germany). The intra-arterial blood pressure was monitored until 1 h after i.v. injection of inhibitors (10 mg/kg bumetanide, 6 mg/kg amiloride and

20 mg/kg methazolamide) or vehicle, and experiments were terminated by decapitation of the rats.

Statistical analysis

All data are given as mean values ± standard error of mean (SEM). To evaluate statistically significant differences between mean values of two groups, an unpaired two-tailed Student's t-test was applied, while a one-way analysis of variance (ANOVA) followed by Dunnett's or Tukey's multiple comparisons post hoc test was applied to compare mean values of multiple groups. Comparison of two factors was evaluated by a two-way ANOVA followed by Tukey's multiple comparisons post hoc test. $p < 0.05$ was considered statistically significant. All statistical analyses were performed in GraphPad Prism 7.0 (GraphPad Software, Inc., La Jolla, CA, US) and indicated in the respective figure legend.

Results

Osmotherapy caused cerebral water loss and influx of Na^+ and Cl^-

To determine the effect of osmotherapy on the brain water and electrolyte content, we employed a rat in vivo model in which the plasma osmolarity was elevated by i.p. injection of NaCl (1.17 g/kg, 2 ml/100 g body weight). To isolate the effect of brain volume regulation, rats were functionally nephrectomized prior to the procedure, the success of which was evident from the increased plasma content of creatinine and urea in these animals compared to naïve rats, which had not undergone nephrectomy (Fig. 1a, b, see figure legend for values). The plasma osmolarity in the nephrectomized rats treated with isosmolar NaCl (303 ± 1 mOsm, n = 9, termed 'control' henceforward) was not significantly different from that of the naïve rats (298 ± 1 mOsm, n = 3, Fig. 1c), indicating that the extended experimental protocol in itself did not interfere with plasma osmolarity. Following a single bolus injection with hyperosmotic NaCl (termed 'osmotherapy' henceforward), the plasma osmolarity was increased to 355 ± 1 mOsm after 1 h (n = 9, $p < 0.001$, Fig. 1c), with an associated increase in the plasma content of Na^+ and Cl^- (n = 9, $p < 0.001$, Fig. 1d, e, see figure legend for values).

The brain water content of the naïve rats, which were not exposed to isosmolar or hyperosmolar treatment, (3.72 ± 0.03 ml/g dry weight, n = 3) was slightly lower than that of the control rats exposed to the isosmolar NaCl treatment (3.79 ± 0.01 ml/g dry weight, n = 9, $p < 0.05$, Fig. 2a), while osmotherapy caused a 9% reduction in the brain water content (to 3.46 ± 0.01, n = 9, $p < 0.001$, Fig. 2a). However, this reduction in brain water content amounted to only ~60% of that predicted from ideal osmotic behavior (calculated according to Eq. 1 and illustrated as a dashed red line in Fig. 2a), which indicates that volume regulation takes place. The osmotherapy-mediated reduction in the brain water loss was associated with an increase in brain electrolyte content, with a 15% increase in brain Na^+ ($p < 0.001$, Fig. 2b) and a 31% increase in brain Cl^- ($p < 0.001$, Fig. 2c) (see figure legend for values). There was a minor 2% increase in the brain K^+ content (control: 463 ± 2 mmol/kg dry weight vs. osmotherapy: 471 ± 2 mmol/kg dry weight, n = 9, $p < 0.05$). The brain Na^+ and Cl^- content in control rats was not significantly different from that obtained in naïve rats, Fig. 2b, c, see figure legend for values. The total increase in osmolyte content represented by Na^+, Cl^-, and K^+, $\Delta Q_{observed}$, amounted to 79 mmol/kg dry weight, which represents 104% of the predicted osmolyte gain, $\Delta Q_{predicted} = 76$ mmol/kg dry weight (Eq. 2). The osmotherapy-mediated gain of brain Na^+ and Cl^-, and to a minor extent K^+, can thereby account for the reduction in brain water loss observed 1 h after administration of the hyperosmolar challenge.

NaCl is slightly more potent than mannitol in osmotherapy

To determine the potency of osmotherapy conducted with NaCl vs. mannitol, we performed a parallel experimental series with mannitol as the osmotic agent. The increased Na^+ and Cl^- plasma concentration observed with NaCl infusion (as above, $p < 0.001$), was absent, and even slightly reversed compared to control rats upon i.p. delivery of mannitol (7.29 g/kg, 2 ml/100 g body weight) ($p < 0.001$ for Na^+ and $p < 0.05$ for Cl^-, Fig. 2d, e, see figure legend for values). Mannitol treatment yielded a plasma osmolarity (356 ± 3 mOsm, n = 6) similar to that obtained in rats treated with NaCl (355 ± 1 mOsm, n = 9, Fig. 1c, $p = 0.71$). Mannitol efficiently reduced the brain water content (to 3.51 ± 0.02 ml/g dry weight, $p < 0.001$), although slightly less effectively than NaCl ($p < 0.05$), Fig. 2a. Osmotherapy performed with mannitol increased the brain Na^+ content by 6% ($p < 0.001$), which was less than with NaCl as the osmotic agent (15%, $p < 0.001$), Fig. 2b. The brain Cl^- content, in contrast, increased to a similar extent upon treatment with either of the osmolytes (31% with NaCl, $p < 0.001$ and 38% with mannitol, $p < 0.001$, Fig. 2c), which was also evident for the brain K^+ content ($p = 0.23$; 2% with NaCl, n = 9, $p < 0.01$, and 3% with mannitol, n = 6, $p < 0.001$). Osmotherapy thus reduced the brain water content, but promoted brain electrolyte accumulation (predominantly in the form of Na^+ and Cl^-) irrespective of the osmotic agent employed, with NaCl being slightly more effective than mannitol for brain water extraction under our experimental conditions.

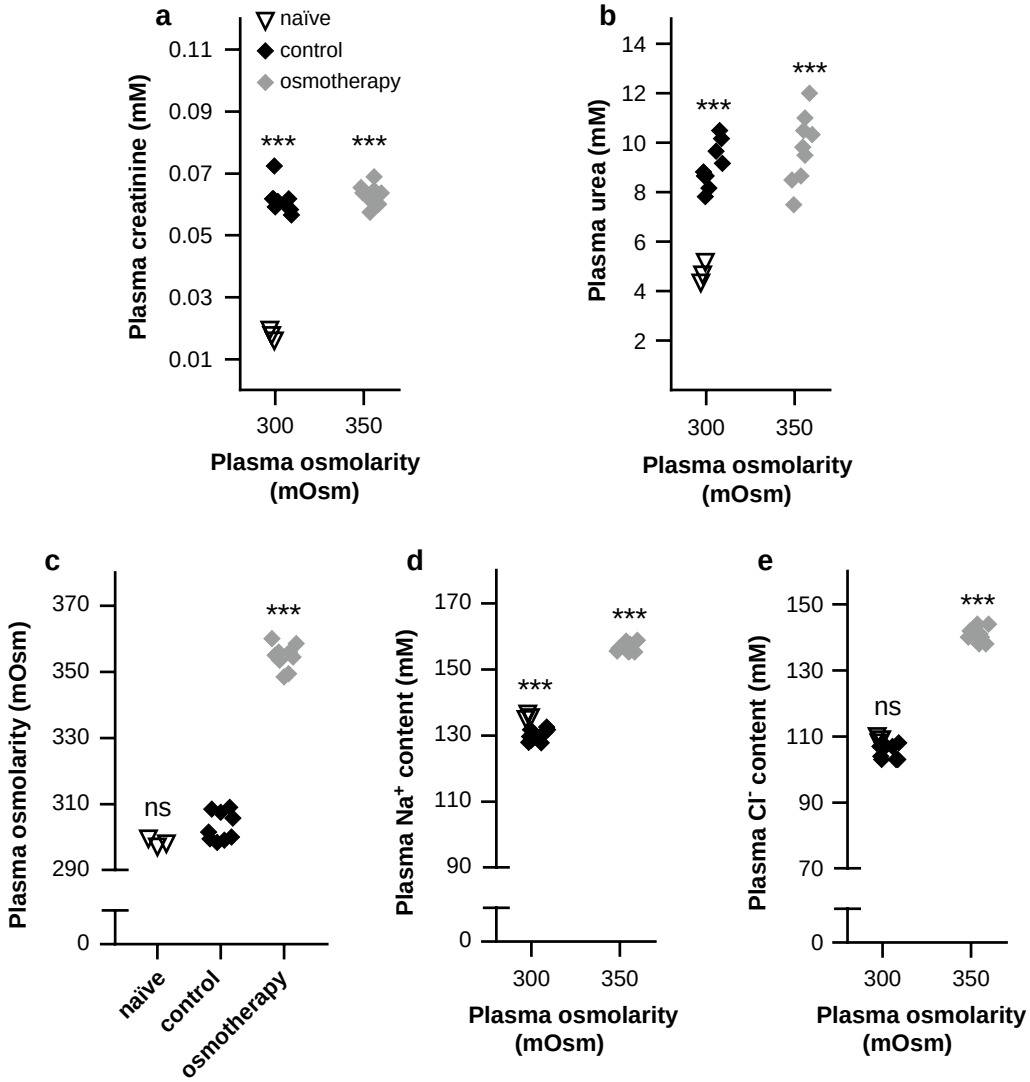

Fig. 1 Plasma electrolyte concentrations in response to NaCl osmotherapy (elevated plasma osmolarity). A functional nephrectomy was performed in rats prior to i.p. treatment with isosmolar NaCl (control) or hyperosmolar NaCl (osmotherapy) and compared to non-operated naïve rats. **a** Plasma creatinine concentrations (in mM) in naïve rats (0.018 ± 0.001, n = 3), control rats (0.061 ± 0.002, n = 9), and osmotherapy-treated rats (0.063 ± 0.001, n = 9). **b** Plasma urea concentrations (in mM) in naïve rats (4.7 ± 0.2, n = 3), control rats (9.1 ± 0.3, n = 9), and rats exposed to osmotherapy (9.7 ± 0.5, n = 9). **c** Plasma osmolarity (in mOsm) of naïve rats (n = 3), control rats (n = 9), and rats exposed to osmotherapy (n = 9). **d**, **e** The plasma electrolyte concentrations (in mM) in naïve rats (135.6 ± 0.5 Na^+ and 109.0 ± 0.6 Cl^-, n = 3), control rats (130.0 ± 0.6 Na^+ and 105.6 ± 0.7 Cl^-, n = 9) and rats exposed to osmotherapy (156.5 ± 0.5 Na^+ and 140.7 ± 0.8 Cl^-, n = 9). Statistically significant differences were determined by a one-way ANOVA with Dunnett's multiple comparisons post hoc test in **a**, **b** and Tukey's multiple comparisons post hoc test in **c**–**e**. Asterisk above the scatter plots indicates statistical significance compared to naïve rats (**a**, **b**) or control rats (**c**–**e**). ***p < 0.001, *ns* not significant

Inhibitors of ion-transporting mechanisms at the blood-side membranes of the BBB capillary endothelium and choroid plexus had no effect on the brain water loss or electrolyte gain upon osmotherapy

To identify the molecular mechanisms governing the hyperosmotic-induced brain ion accumulation and resulting volume regulation, the experimental regime from above (with NaCl as the osmotic agent) was repeated in rats during i.v. exposure to a mixture of inhibitors targeting a selection of ion-transporting mechanisms expressed in the BBB capillary endothelium and the blood-facing side of the choroid plexus. The diuretic compound bumetanide was applied for NKCC1 inhibition [25], amiloride to target NHE1 and ENaC [19], while the carbonic anhydrase inhibitor methazolamide [16] was applied to indirectly inhibit the NBCs. Importantly,

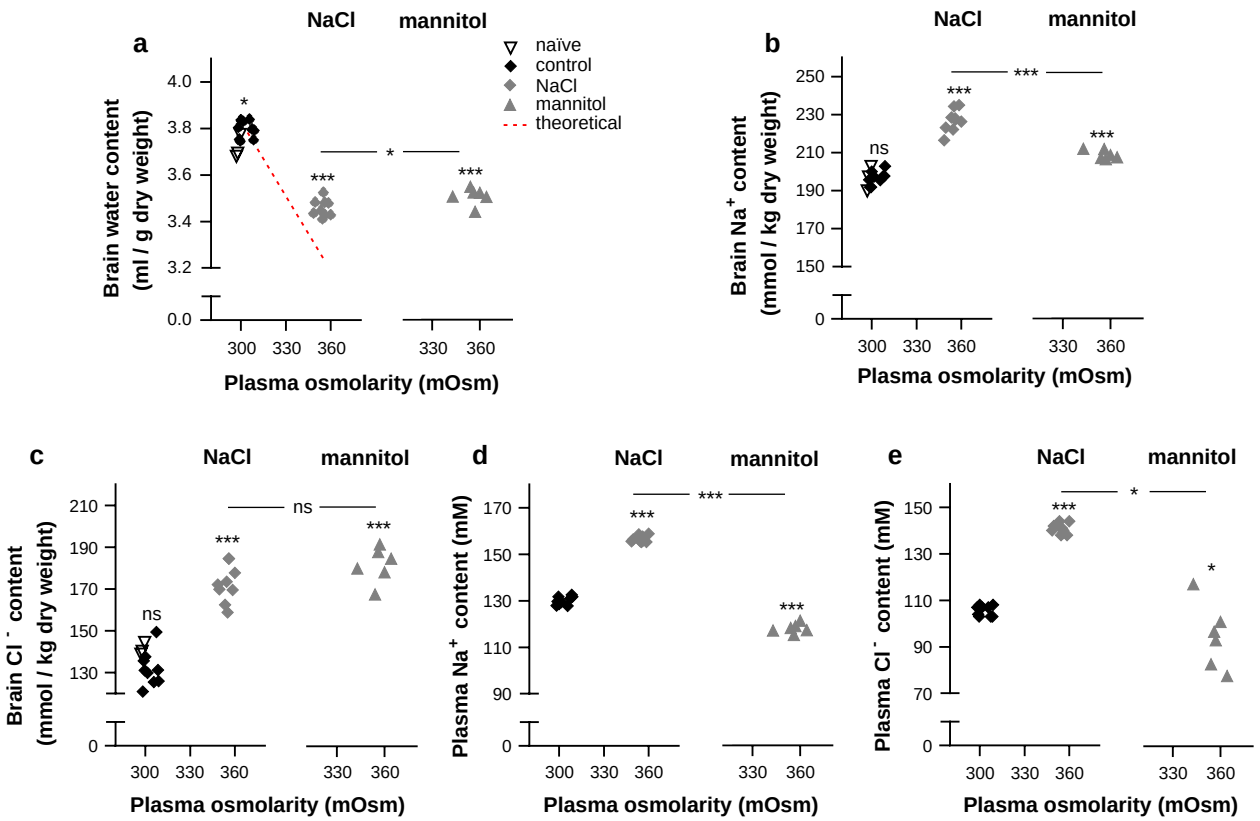

Fig. 2 Osmotherapy-induced brain water loss and electrolyte gain. Rats were treated with isosmolar NaCl (control), hyperosmolar NaCl (osmotherapy, denoted NaCl in legend), or mannitol. **a** The brain water content (in ml/g dry weight) in naïve (n = 3) and control (n = 9) rats, and in rats exposed to osmotherapy in the form of NaCl (n = 9) or mannitol (n = 6). The theoretical brain water loss assuming ideal osmotic behavior (to 3.24 ml/g dry weight, calculated by Eq. 1) is illustrated as a dashed red line. **b**, **c** The brain electrolyte content (in mmol/kg dry weight) shown for naïve rats (197 ± 4 Na^+ and 141 ± 2 Cl^-, n = 3), control rats (197 ± 1 Na^+ and 132 ± 3 Cl^-, n = 9), and rats exposed to NaCl-mediated osmotherapy (227 ± 2 Na^+ and 173 ± 3 Cl^-, n = 9) or mannitol-mediated osmotherapy (209 ± 1 Na^+ and 182 ± 3 Cl^-, n = 6). **d**, **e** Plasma electrolyte concentrations (in mM) for rats exposed to mannitol-mediated osmotherapy (117.9 ± 0.8 Na^+ and 94.9 ± 5.7 Cl^-, n = 6). Values from control rats and rats exposed to NaCl-mediated osmotherapy are from Fig. 1d, e and included for comparison. To determine whether means of naïve, control, and NaCl were statistically different from each other, a one-way ANOVA with Tukey's multiple comparisons post hoc test was performed. This statistical analysis was further performed to determine differences between means of control, NaCl, and mannitol groups [note; comparison of mannitol (no vehicle treatment) with either of the experimental NaCl groups (i.v. or intraventricular vehicle) provided similar results]. Asterisk above the scatter plot indicates statistical significance compared to control rats and asterisk within the lines indicates statistical significance between the indicated groups. *p < 0.05, ***p < 0.001

these inhibitors did not demonstrate an effect on the arterial blood pressure of anaesthetized rats compared with vehicle (at 1 h endpoint, n = 3, Fig. 3a).

A single i.v. dose of inhibitors did not alter the plasma osmolarity compared to vehicle treatment in either control rats (vehicle: 303 ± 1 mOsm vs. inhibitors: 303 ± 2 mOsm, n = 7–9, p = 0.76) or osmotherapy-treated rats (vehicle: 355 ± 1 mOsm vs. inhibitors: 357 ± 2 mOsm, n = 8–9, p = 0.35). Delivery of inhibitors did not affect the brain water, Na^+, and Cl^- content in control rats and failed to modulate the osmotherapy-induced changes in brain water, Na^+, and Cl^- content, Fig. 3b–d. The K^+ content was also unaffected by i.v. inhibitor application (in mmol/kg dry weight: control; vehicle: 463 ± 2 vs. inhibitors: 460 ± 2, osmotherapy; vehicle: 471 ± 2 vs. inhibitors: 474 ± 2, n = 7–9, p > 0.80). To increase the probability for the inhibitors to reach their targets in sufficient concentrations, we performed an additional experimental series with triple inhibitor application (20 min and 5 min prior to initiation of hyperosmotic treatment and 15 min after). These increased inhibitor doses did not affect the brain water content (Fig. 3b, inset). The unchanged electrolyte contents following inhibitor exposure aligns with the stable brain water content. These results suggest that NKCC1,

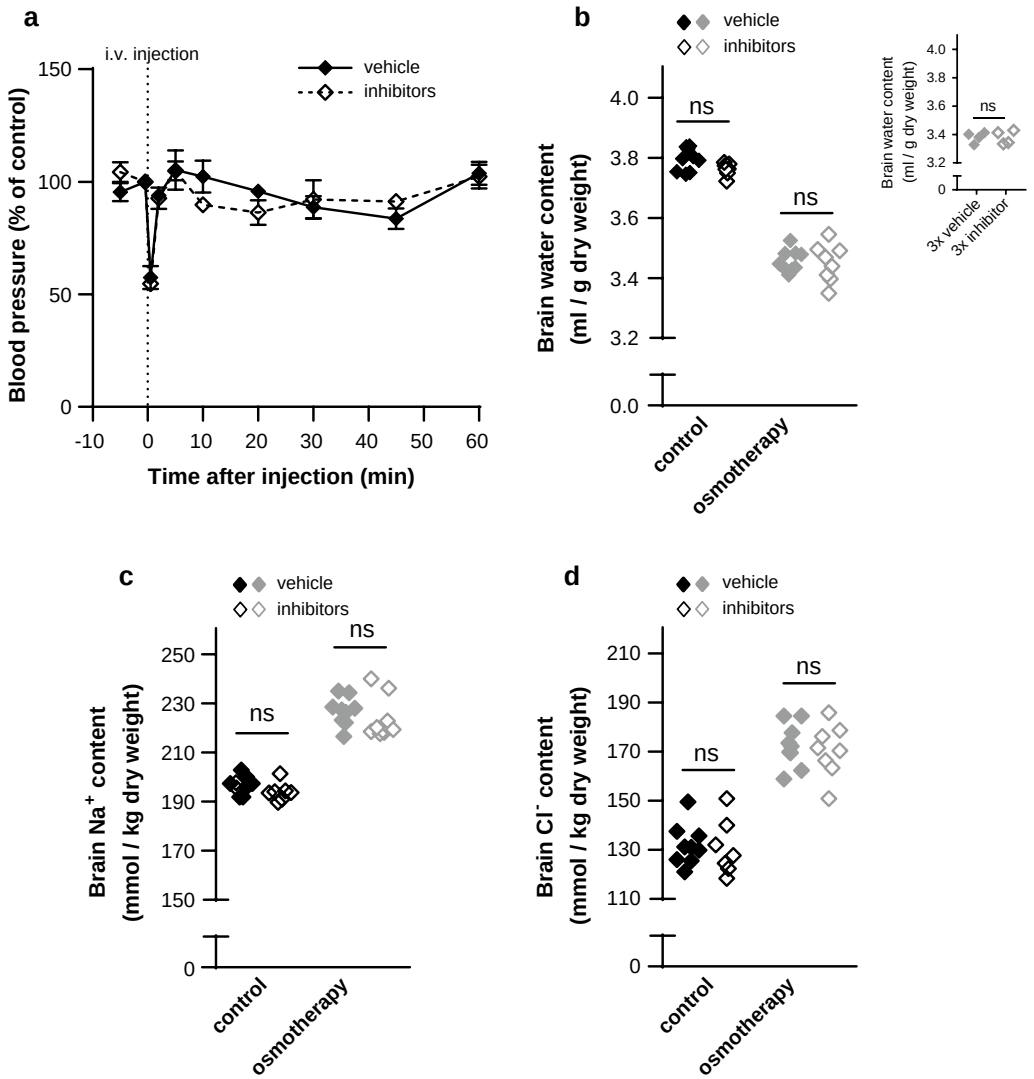

Fig. 3 Inhibitors of ion-transporting mechanisms at the blood-side membranes do not affect water loss and electrolyte gain. **a** The arterial blood pressure was measured before and until 1 h after i.v. treatment with vehicle or inhibitors (10 mg/kg bumetanide, 6 mg/kg amiloride, and 20 mg/kg methazolamide). Values are given as the percentage of arterial blood pressure from the last control measurement (corresponding to 30 s before i.v. injection). The arterial blood pressure did not differ significantly from control measurements after 1 h ($p > 0.90$). The end arterial blood pressure was unchanged following inhibitor delivery, $n = 3$ of each, $p > 0.90$. **b** The brain water content was unaffected by i.v. inhibitor application in control rats [in (ml/g dry weight): vehicle: 3.79 ± 0.01 vs. inhibitors: 3.76 ± 0.01] and in rats subjected to NaCl-mediated osmotherapy (vehicle: 3.46 ± 0.01 vs. inhibitors: 3.45 ± 0.02), $n = 7–9$. Inset: Brain water content in osmotherapy-treated rats exposed to triple doses of vehicle (3.38 ± 0.02) or inhibitors (3.38 ± 0.02), $n = 4$ of each. **c** The brain Na^+ content (in mmol/kg dry weight) in control rats (vehicle: 197 ± 1 vs. inhibitors: 194 ± 1) and in rats exposed to osmotherapy (vehicle: 227 ± 2 vs. inhibitors: 224 ± 3), $n = 7–9$. **d** The brain Cl^- content (in mmol/kg dry weight) in control rats (vehicle: 132 ± 3 vs. inhibitors: 131 ± 4) and in rats exposed to osmotherapy (vehicle: 173 ± 3 vs. inhibitors: 170 ± 4), $n = 7–9$. Vehicle values from control and osmotherapy-treated rats are from Fig. 2a–c and included for comparison. Statistically significant differences were determined by a two-way ANOVA with Tukey's multiple comparisons post hoc test, except for values in the inset of **b**, which were analyzed using a two-tailed un-paired Student's t-test. *ns* not significant

NHE1, ENaC, and NBCs localized at the blood-facing side of the BBB capillary endothelium and the choroidal membrane are not the primary access routes for brain electrolyte entry during osmotherapy and therefore not the molecular mechanisms underlying brain volume regulation under these conditions.

Osmotherapy-induced brain water loss and ion accumulation were unaffected by inhibitors of ion-transporting mechanisms at the CSF-facing choroidal membrane

Ion-transporting mechanisms localized at the other major interface; the ventricular side of the choroid plexus, may instead contribute to the volume regulatory gain of cerebral electrolytes upon administration of osmotherapy in the form of a hyperosmotic NaCl challenge. The select ion-transporting mechanisms expressed at the luminal membrane of the choroid plexus epithelium were targeted by injection of the inhibitor mixture (estimated ventricular concentrations of 20 μM bumetanide, 100 μM amiloride, and 100 μM methazolamide) directly into one of the lateral ventricles. Initially, the maximal inhibitor volume and infusion rate were chosen from two criteria: (1) both lateral ventricles should be exposed to inhibitors even though injections were given into only one of the lateral ventricles (verified with Evans blue, see Fig. 4a for a representative image) and (2) the ICP should remain fairly stable upon intraventricular inhibitor infusion (the ICP increased briefly to only a minor extent; 2.6 ± 0.7 mmHg, n = 3, Fig. 4b, with a brief compression of the jugular vein illustrated as a positive control).

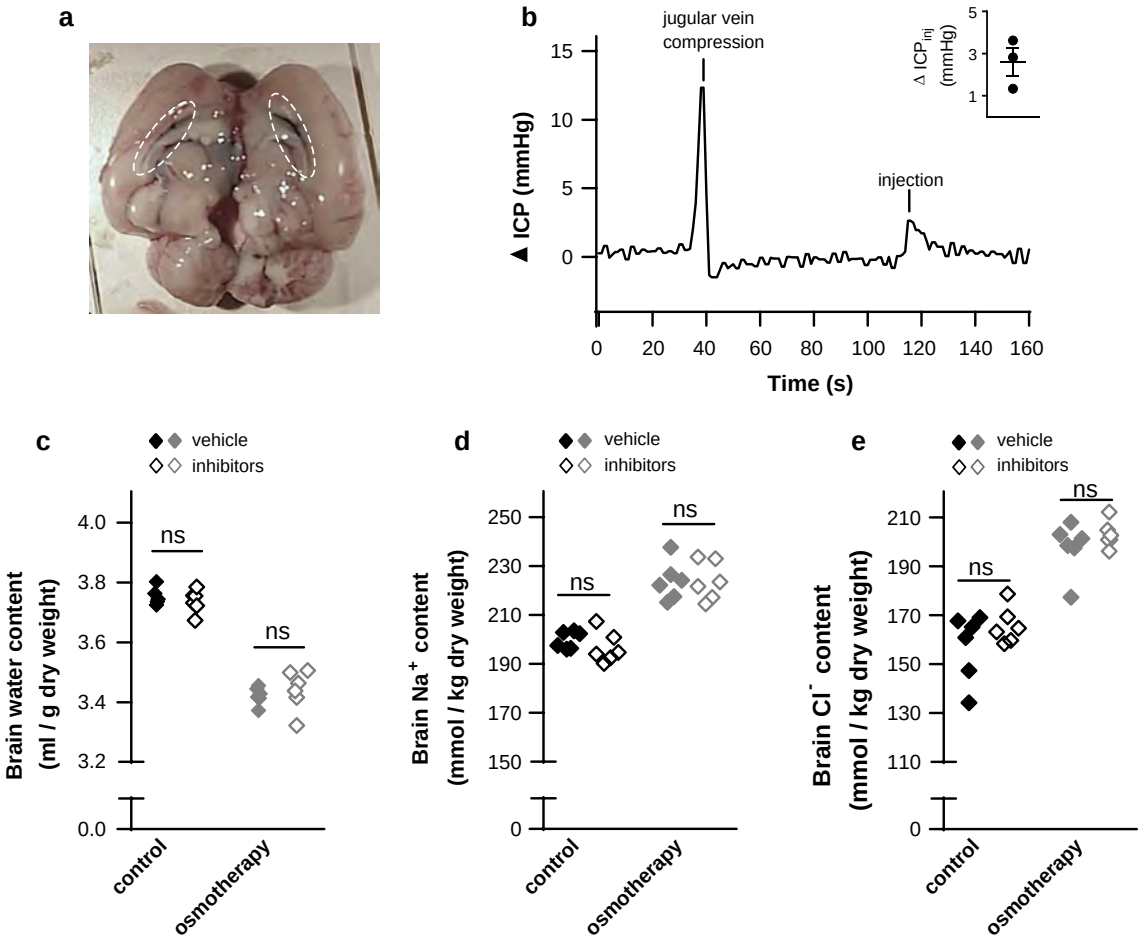

Fig. 4 Inhibition of choroidal ion-transporting mechanisms does not affect brain water loss or electrolyte gain. **a** Representative image of brain hemispheres following Evans blue injection into the right lateral ventricle (stained lateral ventricles highlighted in dashed ovals), n = 3. **b** A representative epidural ICP trace with jugular vein compression included as a positive control. The inset shows mean ΔICP ± SEM (mmHg) during intraventricular injection, n = 3. **c** Brain water content (in ml/g dry weight) of rats treated with intraventricular injections of vehicle or inhibitors prior to i.p. administration of isosmolar NaCl (control; vehicle: 3.75 ± 0.01 vs. inhibitors: 3.74 ± 0.02) or hyperosmolar NaCl (osmotherapy; vehicle: 3.42 ± 0.01 vs. inhibitors: 3.44 ± 0.03), n = 6 of each. **d** The brain Na^+ content (in mmol/kg dry weight) in control rats treated with vehicle (200 ± 1) or inhibitors (197 ± 3) and in osmotherapy-treated rats exposed to vehicle (224 ± 3) or inhibitors (224 ± 3), n = 6 of each. **e** The brain Cl^- content (in mmol/kg dry weight) in control rats treated with vehicle (162 ± 3) or inhibitors (166 ± 3) and in osmotherapy-treated rats exposed to vehicle (198 ± 4) or inhibitors (203 ± 2), n = 6 of each. Statistical significant differences were determined by a two-way ANOVA with Tukey's multiple comparisons post hoc test. *ns* not significant

Vehicle or inhibitors were thus injected into the ventricular system of anesthetized rats prior to osmotherapy followed by another drug application every 15 min during the 1 h experimental time period to maintain a maximal targeting effect despite risk of wash-out by the high ventricular CSF flow rate [26]. The plasma osmolarity was similar in vehicle- and inhibitor-treated rats exposed to isosmolar NaCl solution (vehicle: 297 ± 2 mOsm vs. inhibitors: 298 ± 2 mOsm, n = 6, p = 0.94) and in rats subjected to osmotherapy (vehicle: 347 ± 1 mOsm vs. inhibitors: 347 ± 2 mOsm, n = 6, p = 0.87). Osmotherapy led to a reduction in the brain water content and to an increased Na^+ (12%) and Cl^- (22%) content in the brain of vehicle-treated rats (n = 6, p < 0.001 for both, Fig. 4c–e), with an unaltered brain K^+ content (in mmol/kg dry weight: control: 472 ± 3 vs. osmotherapy: 471 ± 4, n = 6, p > 0.90). Intraventricular inhibitor application had no effect on the brain water content in control rats or in osmotherapy-treated rats, Fig. 4c. The brain Na^+ and Cl^- content in control- or osmotherapy-treated rats was, likewise, unaffected by inhibitor application into the lateral ventricles (n = 6, for all conditions, Fig. 4d, e), which was also seen for brain K^+ content (in mmol/kg dry weight: control; vehicle: 472 ± 3 vs. inhibitors: 469 ± 4, osmotherapy; vehicle: 471 ± 4 vs. inhibitors: 472 ± 2, n = 6, p > 0.90 for both). These results suggest that osmotherapy-mediated brain electrolyte influx does not originate from increased activity of choroidal transporters (NKCC1, NHE1, NBCs, or ENaC) expressed at the luminal CSF-facing side of the membrane.

The integrity of the brain barriers was preserved after osmotherapy treatment

To assess whether Na^+ and Cl^- entered the brain through a possible breach in the brain barriers in response to osmotherapy, we delivered Na^+-fluorescein i.v. 5 min prior to osmotherapy treatment (as above). Histological analysis of coronal brain sections (Fig. 5a) from the control rats revealed a weak background fluorescent signal in the brain parenchyma, as illustrated before [23], near-absence of Na^+-fluorescein in the neocortex, hippocampus, and thalamus, and minor staining in the lateral ventricle [23] (from choroid plexus with fenestrated blood capillaries), n = 3, Fig. 5c. Notably, the observed staining pattern was unaltered by osmotherapy treatment as illustrated in representative images of the neocortex, hippocampus, thalamus, and lateral ventricle, while no fluorescence was detected in naïve rats, which did not receive Na^+-fluorescein (n = 3, Fig. 5b–d). The pineal gland (Fig. 5e) served as

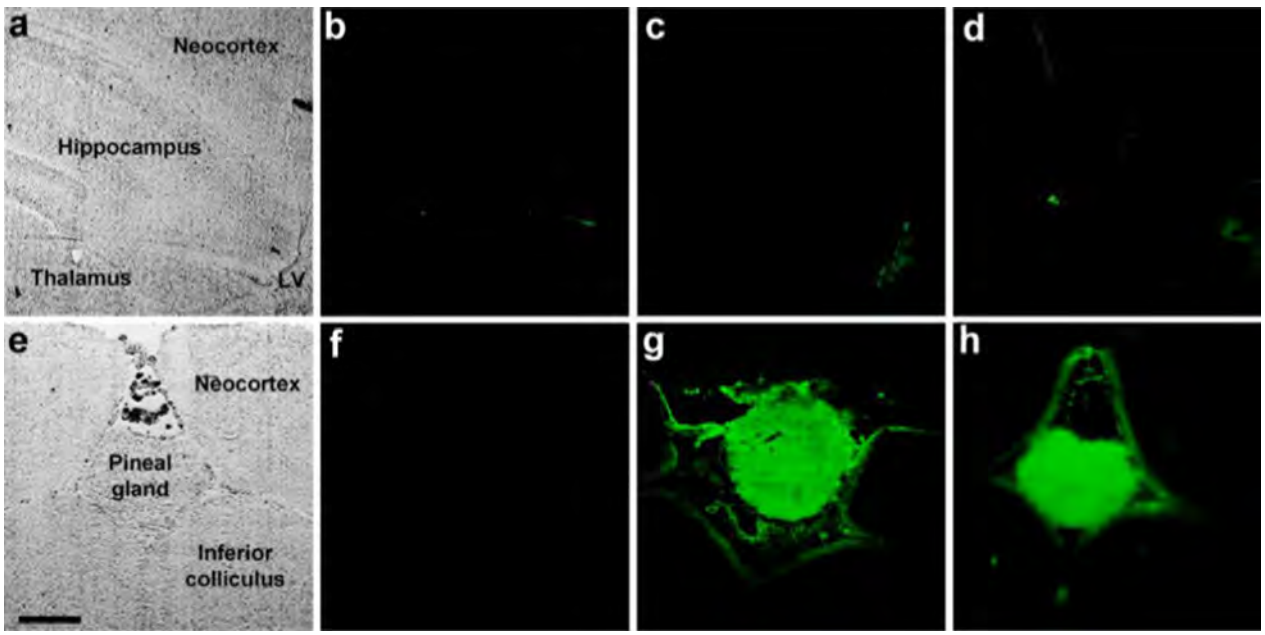

Fig. 5 Osmotherapy does not alter the brain barrier permeability. Na^+-fluorescein (green fluorescence) was injected into the blood circulation of rats prior to i.p. exposure of isosmolar NaCl (control) or hyperosmolar NaCl (osmotherapy). Naïve rats did not receive Na^+-fluorescein and were euthanized immediately after anaesthesia induction. **a**, **e** Phase contrast images illustrate structures of the brain regions of interest in transmitted white light. Representative images of Na^+-fluorescein in **b**–**d** hippocampus, thalamus, neocortex, and the lateral ventricle (LV) and **f**–**h** pineal gland (positive control) of naïve rats, control rats, and osmotherapy-treated rats, n = 3. Scale bar = 500 µm

a positive control due to the lack of BBB in this brain structure. Hence, Na^+-fluorescein was detected in the pineal gland of control rats and osmotherapy-treated rats, while no fluorescence was observed in the pineal gland of naïve rats, which did not receive Na^+-fluorescein (n = 3, Fig. 5f–h). The absence of osmotherapy-induced penetration of Na^+-fluorescein into the brain indicates that the integrity of the BBB and BCSFB remained intact during the applied osmotherapy treatment.

Discussion

We have demonstrated in rats that following osmotherapy (~ 50 mOsm increase in plasma osmolarity), water is osmotically extracted from the brain, although to a lesser extent than can be predicted from theoretical calculations. The reduced osmotic extraction was assigned predominantly to brain Na^+ and Cl^- accumulation (6–15% for Na^+ and 22–38% for Cl^-) and to a minor extent, if any, brain K^+ accumulation (up to 3% increase) as a function of increased plasma osmolarity, in agreement with an earlier report [14]. Notably, it is not simply the ion *concentration* that increases with the systemic hyperosmolarity but the actual ion *content*. These findings indicate that specific volume regulatory transporting mechanisms are activated in response to and/or as a consequence of increased plasma osmolarity. Employment of NaCl as the osmotic agent contributed to an increased Na^+ and Cl^- concentration in the plasma, which, in itself, could affect the brain electrolyte content. However, we observed that mannitol-mediated osmotherapy of identical magnitude and delivered volume led to similar effects on the brain electrolyte/water content [14], indicating that plasma hyperosmolarity, and not the increased plasma Na^+ and Cl^- concentrations, causes the brain electrolyte accumulation. Osmotic extraction of cerebral fluid was slightly more effective with NaCl as the osmotic agent, rather than mannitol, even though the cerebral accumulation of Na^+ was significantly higher in rats treated with NaCl. The reduced osmotic fluid extraction (and thus osmolyte increase) observed with mannitol as the osmotic agent may instead be explained by an unknown but substantial influx of other osmolytes, e.g. mannitol itself, which has previously been detected in the rat brain following mannitol-induced elevation in the plasma osmolarity [14]. With the similar Cl^- accumulation obtained with both NaCl and mannitol as the osmotic agent, one may, however, from the principle of electroneutrality, expect accumulation of another cationic electrolyte (or reduced retention of a different anion). Taken together, our findings indicate that the osmotherapy-induced rebound response may be regulated differently depending on the osmotic agent applied, although overlapping mechanisms, such as the observed gain of brain Na^+ and Cl^-, clearly exist.

According to theoretical considerations based on reflection coefficients of both osmotic agents, i.e. the relative impermeability across the BBB, NaCl treatment has been predicted to induce a larger osmotic response than mannitol [27], as confirmed by our findings. While previous findings demonstrated that NaCl was superior with regard to initial reduction of the ICP, maintenance of a lowered ICP [28, 29], and an increased cerebral water loss [29] in experimental animal models of brain injuries, other researchers observed an equal efficiency of NaCl or mannitol as the osmotic agent [30, 31], or a higher efficiency with mannitol in healthy animals [32]. Two of the latter observations may, however, be influenced by the unequal end plasma osmolarity induced by either osmotic agent [30, 32], which essentially prevents a comparative analysis. A line of clinical trials, mainly performed on patients with traumatic brain injury, reported that osmotherapy using NaCl solutions with additives (e.g. dextran, lactate, or hydroxyethyl starch solutions) [33–35] or NaCl alone [36] more effectively lowered the ICP compared with mannitol. While these reports support the findings from our animal experiments, two other clinical trials found an equal efficacy of the two osmotic agents on the ICP [37, 38]. However, a direct comparison between the few head-to-head studies carried out is challenged by the varying treatment strategies; (i) continuous or bolus injections, (ii) different doses/volumes of the osmotic agent, and (iii) different time windows, which altogether resulted in variable plasma osmolarities. In addition, diverse patient populations and outcome measurements [39] further hamper the comparison between clinical trials. It is, therefore, still questionable which osmotic agent is superior [1, 40] and animal/clinical studies, which allow direct comparison, are warranted. Mannitol remains the recommended standard osmotic agent for treatment of patients with severe head injury (Level II evidence), whereas hyperosmolar NaCl is recommended for children (Level III evidence) [41]. The choice of osmotic agent may, however, rather be based on side-effect profiles of the osmotic agents and how those will affect the clinical situation (comorbidities, age) [1].

Neither the signaling cascades, nor the molecular transport mechanisms, that couple systemic plasma hyperosmolarity to brain electrolyte accumulation have been identified. In the present study, we therefore introduced a mixture of inhibitors targeting ion-transporting proteins expressed in the BBB capillary endothelium and/or the choroid plexus epithelium, and determined their effect on osmotherapy-induced brain ion accumulation. While amiloride and methazolamide may target abluminal ion-transporting mechanisms [21, 42],

we expect insignificant bumetanide interaction at the abluminal membrane of the capillaries forming the BBB because of its poor BBB permeability [43, 44]. We failed to detect evidence in favor of NKCC1, NHE1, ENaC or carbonic anhydrase (indirectly targeting the bicarbonate transporters) located at the BBB endothelium or in choroid plexus participating in this brain volume regulation. Hence, we were unable to reproduce a previously reported reduction of hyperosmotic plasma-induced brain water extraction by methazolamide [14]. The reasons for this discrepancy are unclear, although the previous study employed a very high dose of methazolamide, which was delivered i.p. instead of i.v. as in the present study. We cannot rule out that the inhibitor concentrations applied in this study were not sufficient for effective blockage of the target proteins, even though a procedure with triple doses was incorporated to enhance inhibitor efficiency. The free unbound inhibitor concentration may, however, be significantly reduced by potential binding of inhibitors to plasma proteins, as shown for bumetanide [45]. We recently found that hyperosmotic conditions enhanced the activity of abluminal Na^+/K^+-ATPase in endothelial cells, which were co-cultured with astrocytes in an in vitro BBB model [46], indicating that this transport mechanism may counteract osmotic extraction from the brain by cerebral accumulation of Na^+ in response to a hyperosmotic challenge. With the damaging effect of pump inhibition, it is, however, not simple to verify this finding by currently available techniques in animal models in vivo: a direct effect of Na^+/K^+-ATPase inhibition is difficult to deduce, due to disruption of electrochemical gradients controlling secondary active and passive transporting mechanisms. The Na^+/K^+-ATPase expressed at the CSF-facing membrane of the choroid plexus could also be a potential candidate in brain volume regulation upon osmotherapy, since the Na^+/K^+-ATPase may contribute to CSF production [47], in addition to the recently reported significant contribution of NKCC1 in murine CSF production [48]. To this end, it is important to note that the wet-dry technique, employed to determine brain water content, favors parenchymal water content over CSF, as the major part of CSF is lost in the brain isolation process. If the ion-transporting mechanisms were to regulate the CSF production per se, and the equilibrium rate between CSF and brain interstitial fluid is slow, such regulatory functions could well be missed by this experimental design.

While the ion-transporting mechanisms (NKCC1, NHE1, NBCs, and ENaC) at the BBB capillary endothelium and choroid plexus epithelium were shown not to be involved in the osmotherapy-mediated translocation of Na^+ and Cl^- from the blood into the rat brain under our experimental conditions, Na^+ and Cl^- could instead enter the brain via paracellular transport routes, which may become available with hyperosmolar plasma. However, we demonstrated that the two major brain barriers, i.e. the BBB and BCSFB, appeared to remain intact upon osmotherapy, as we detected no changes in cerebral Na^+-fluorescein accumulation whether or not the animals had been exposed to osmotherapy. Notably, we cannot exclude that Na^+ and Cl^-, which are of a smaller molecular weight (22.99 Da and 35.45 Da) than Na^+-fluorescein (376.27 Da), can cross the brain barriers via a paracellular route *provided* that the given hyperosmotic challenge promoted an increase in the permeability of the brain barriers towards smaller permeants, while excluding the fluorescent dye. However, a previous study showed that a change in barrier function, corresponding to BBB opening towards mannitol and Na^+, occurred only with hyperosmotic challenges rendering the plasma osmolarity > 385 mOsm [49]. An alternative manner of accumulating brain electrolytes during conditions of elevated plasma osmolarity could be via increased bulk flow of CSF into the brain interstitial fluid [50] or via a potential regulation of fluid drainage at arachnoid granulations [51], dural lymphatic vessels [52, 53], and/or at glymphatic paravascular drainage routes [54]. Parenchymal cell volume regulation may, in addition, indirectly affect electrolyte movement across the brain barriers.

The present experimental protocol was designed to quantitatively resolve the *direct* consequences of increased plasma osmolarity (mimicked osmotherapy) on brain water and ion accumulation (hence the choice of nephrectomized animals, in which the inflicted change in plasma osmolarity could be tightly controlled). In various severities of stroke-induced brain edema in animal models, one may well expect altered BBB integrity (in the afflicted area) and potentially even altered expression/activity of membrane transporters in the BBB capillary endothelium. Such stroke-induced membrane transport responses could potentially affect ion and water accumulation during osmotherapy, and may serve to explain the observed beneficial effect of bumetanide treatment in an animal stroke model [11]. Future studies should therefore address whether the osmotherapy-mediated influx of cerebral Na^+ and Cl^- likewise contribute to the rebound response in animal models of stroke-induced cerebral edema.

Conclusions

While osmotherapy immediately lowers the ICP of patients with cerebral edema, a delayed rebound response can limit or even reverse the otherwise effective drainage. We here demonstrated that the mammalian brain loses less water than predicted from osmotically obliged water extraction when exposed to

hyperosmolar plasma; osmotherapy. This volume regulatory mechanism, the rebound effect, hinges on initiation of brain ion accumulation predominantly in the form of Na^+ and Cl^-. We propose that the brain ion accumulation occurs via transcellular pathways, one of which may well be hyperosmolar-induced abluminal Na^+/K^+-ATPase activity [46], rather than due to a hyperosmolar-induced breach in the brain barriers. In the absence of identified luminal transport mechanisms, altered bulk flow (CSF-to-parenchyma flow) or drainage ((g)lymphatic pathways) may well contribute to osmolarity-induced brain electrolyte accumulation. The transport mechanisms proposed to promote osmotherapy-induced brain ion accumulation remain unresolved, since we found no evidence of NKCC1, NHE1, ENaC, and NBCs appearing amongst these under our experimental conditions in healthy non-edematous rats. Future identification of such ion-transporting mechanisms might provide a useful therapeutic target for pharmacological prevention of the rebound effect during osmotherapy in patients experiencing brain edema.

Abbreviations

aCSF: artificial CSF; ANOVA: analysis of variance; BBB: blood–brain barrier; BCSFB: blood–CSF barrier; CSF: cerebrospinal fluid; ENaC: amiloride-sensitive Na^+ channel; ICP: intracranial pressure; i.p.: intraperitoneal; i.v.: intravenous; NBCs: Na^+-coupled bicarbonate transporters; NHE1: Na^+–H^+ anti-porter 1; NKCC1: Na^+–K^+–$2Cl^-$ co-transporter 1; RT: room temperature; SEM: standard error of mean.

Authors' contributions

EKO, KL, ABS, KT, MFR, WL, and NM contributed substantially to the design/concept of experiments, experimental performance, data analysis, or interpretation. EKO, KL, ABS, KT, CK MFR, WL, and NM drafted or critically revised the manuscript, and approved the version to be published. All authors read and approved the final manuscript.

Author details

[1] Department of Neuroscience, University of Copenhagen, Copenhagen, Denmark. [2] Department of Pharmacology, Toxicology, and Pharmacy, University of Veterinary Medicine Hannover, Hannover, Germany. [3] Center for Systems Neuroscience, Hannover, Germany. [4] Neurovascular Research Unit, Department of Neurology, Herlev Gentofte Hospital, University of Copenhagen, Herlev, Copenhagen, Denmark. [5] Present Address: AJVaccines, Copenhagen, Denmark. [6] Department of Neuroscience, Faculty of Health and Medical Sciences, University of Copenhagen, Blegdamsvej 3, 2200 Copenhagen, Denmark.

Acknowledgements

We thank Edith Kaczmarek, Kristoffer Racz, Rikke Lundorf, and Charlotte Mehlin for technical and surgical assistance and Prof. Dr. Andrea Tipold for measuring plasma electrolyte concentrations.

Competing interests

The authors declare that they have no competing interests.

Availability of data and materials

All material is available from the corresponding author on reasonable request.

Consent for publication

Not applicable.

Ethics approval and consent to participate

All experiments were performed in compliance with the Directive 2010/63/EU on the Protection of Animals used for Scientific Purposes. Approval Number 2016-15-0201-00944.

Funding

This study was funded by the Independent Research Fund Denmark (Sapere Aude, 0602-02344B FSS, to NM) and the Deutsche Forschungsgemeinschaft (Bonn, Germany, Lo 274/15-1, to WL).

Publisher's Note

Received: 8 June 2018 Accepted: 19 August 2018
Published online: 25 September 2018

References

1. Ropper AH. Management of raised intracranial pressure and hyperosmolar therapy. Pract Neurol. 2014;14:152–8.
2. Ucar T, Akyuz M, Kazan S, Tuncer R. Role of decompressive surgery in the management of severe head injuries: prognostic factors and patient selection. J Neurotrauma. 2005;22:1311–8.
3. McManus ML, Churchwell KB, Strange K. Regulation of cell volume in health and disease. N Engl J Med. 1995;333:1260–6.
4. Todd MM. Hyperosmolar therapy and the brain: a hundred years of hard-earned lessons. Anesthesiology. 2013;118:777–9.
5. Paczynski RP. Osmotherapy. Basic concepts and controversies. Crit Care Clin. 1997;13:105–29.
6. Abbott NJ, Ronnback L, Hansson E. Astrocyte–endothelial interactions at the blood–brain barrier. Nat Rev Neurosci. 2006;7:41–53.
7. Brown PD, Davies SL, Speake T, Millar ID. Molecular mechanisms of cerebrospinal fluid production. Neuroscience. 2004;129:957–70.
8. Hladky SB, Barrand MA. Fluid and ion transfer across the blood–brain and blood–cerebrospinal fluid barriers; a comparative account of mechanisms and roles. Fluids Barriers CNS. 2016;13:19.
9. Damkier HH, Brown PD, Praetorius J. Cerebrospinal fluid secretion by the choroid plexus. Physiol Rev. 2013;93:1847–92.
10. Kusche-Vihrog K, Jeggle P, Oberleithner H. The role of ENaC in vascular endothelium. Pflugers Arch. 2014;466:851–9.
11. O'Donnell ME, Tran L, Lam TI, Liu XB, Anderson SE. Bumetanide inhibition of the blood–brain barrier Na–K–Cl cotransporter reduces edema formation in the rat middle cerebral artery occlusion model of stroke. J Cereb Blood Flow Metab. 2004;24:1046–56.
12. O'Donnell ME, Chen YJ, Lam TI, Taylor KC, Walton JH, Anderson SE. Intravenous HOE-642 reduces brain edema and Na uptake in the rat permanent middle cerebral artery occlusion model of stroke: evidence for participation of the blood–brain barrier Na/H exchanger. J Cereb Blood Flow Metab. 2013;33:225–34.
13. Kilkenny C, Browne WJ, Cuthill IC, Emerson M, Altman DG. Improving bioscience research reporting: the ARRIVE guidelines for reporting animal research. J Pharmacol Pharmacother. 2010;1:94–9.
14. Cserr HF, DePasquale M, Patlak CS. Regulation of brain water and electrolytes during acute hyperosmolality in rats. Am J Physiol. 1987;253:F522–9.
15. Nordquist L, Isaksson B, Sjoquist M. The effect of amiloride during infusion of oxytocin in male sprague-dawley rats: a study of a possible intrarenal target site for oxytocin. Clin Exp Hypertens. 2008;30:151–8.
16. Gray WD, Rauh CE, Osterberg AC, Lipchuck LM. The anticonvulsant actions of methazolamide (a carbonic anhydrase inhibitor) and diphenylhydantoin. J Pharmacol Exp Ther. 1958;124:149–60.
17. Lykke K, Tollner K, Feit PW, Erker T, MacAulay N, Loscher W. The search for NKCC1-selective drugs for the treatment of epilepsy: structure–function relationship of bumetanide and various bumetanide derivatives in inhibiting the human cation-chloride cotransporter NKCC1A. Epilepsy Behav. 2016;59:42–9.
18. Bairamian D, Johanson CE, Parmelee JT, Epstein MH. Potassium cotransport with sodium and chloride in the choroid plexus. J Neurochem. 1991;56:1623–9.

19. Teiwes J, Toto RD. Epithelial sodium channel inhibition in cardiovascular disease. A potential role for amiloride. Am J Hypertens. 2007;20:109–17.
20. Nakamura K, Kamouchi M, Kitazono T, Kuroda J, Shono Y, Hagiwara N, Ago T, Ooboshi H, Ibayashi S, Iida M. Amiloride inhibits hydrogen peroxide-induced Ca^{2+} responses in human CNS pericytes. Microvasc Res. 2009;77:327–34.
21. Li M, Wang W, Mai H, Zhang X, Wang J, Gao Y, Wang Y, Deng G, Gao L, Zhou S, et al. Methazolamide improves neurological behavior by inhibition of neuron apoptosis in subarachnoid hemorrhage mice. Sci Rep. 2016;6:35055.
22. Sugrue MF, Gautheron P, Mallorga P, Nolan TE, Graham SL, Schwam H, Shepard KL, Smith RL. L-662,583 is a topically effective ocular hypotensive carbonic anhydrase inhibitor in experimental animals. Br J Pharmacol. 1990;99:59–64.
23. Hawkins BT, Egleton RD. Fluorescence imaging of blood–brain barrier disruption. J Neurosci Methods. 2006;151:262–7.
24. Moller M, van Deurs B, Westergaard E. Vascular permeability to proteins and peptides in the mouse pineal gland. Cell Tissue Res. 1978;195:1–15.
25. Russell JM. Sodium–potassium–chloride cotransport. Physiol Rev. 2000;80:211–76.
26. Karimy JK, Kahle KT, Kurland DB, Yu E, Gerzanich V, Simard JM. A novel method to study cerebrospinal fluid dynamics in rats. J Neurosci Methods. 2015;241:78–84.
27. Bhardwaj A, Ulatowski JA. Hypertonic saline solutions in brain injury. Curr Opin Crit Care. 2004;10:126–31.
28. Mirski AM, Denchev ID, Schnitzer SM, Hanley FD. Comparison between hypertonic saline and mannitol in the reduction of elevated intracranial pressure in a rodent model of acute cerebral injury. J Neurosurg Anesthesiol. 2000;12:334–44.
29. Qureshi AI, Wilson DA, Traystman RJ. Treatment of elevated intracranial pressure in experimental intracerebral hemorrhage: comparison between mannitol and hypertonic saline. Neurosurgery. 1999;44:1055–63.
30. Freshman SP, Battistella FD, Matteucci M, Wisner DH. Hypertonic saline (7.5%) versus mannitol: a comparison for treatment of acute head injuries. J Trauma. 1993;35:344–8.
31. Scheller MS, Zornow MH, Seok Y. A comparison of the cerebral and hemodynamic effects of mannitol and hypertonic saline in a rabbit model of acute cryogenic brain injury. J Neurosurg Anesthesiol. 1991;3:291–6.
32. Wang LC, Papangelou A, Lin C, Mirski MA, Gottschalk A, Toung TJ. Comparison of equivolume, equiosmolar solutions of mannitol and hypertonic saline with or without furosemide on brain water content in normal rats. Anesthesiology. 2013;118:903–13.
33. Battison C, Andrews PJ, Graham C, Petty T. Randomized, controlled trial on the effect of a 20% mannitol solution and a 7.5% saline/6% dextran solution on increased intracranial pressure after brain injury. Crit Care Med. 2005;33:196–202 **(discussion 257-198)**.
34. Harutjunyan L, Holz C, Rieger A, Menzel M, Grond S, Soukup J. Efficiency of 7.2% hypertonic saline hydroxyethyl starch 200/0.5 versus mannitol 15% in the treatment of increased intracranial pressure in neurosurgical patients—a randomized clinical trial [ISRCTN62699180]. Crit Care. 2005;9:R530–40.
35. Ichai C, Armando G, Orban JC, Berthier F, Rami L, Samat-Long C, Grimaud D, Leverve X. Sodium lactate versus mannitol in the treatment of intracranial hypertensive episodes in severe traumatic brain-injured patients. Intensive Care Med. 2009;35:471–9.
36. Oddo M, Levine JM, Frangos S, Carrera E, Maloney-Wilensky E, Pascual JL, Kofke WA, Mayer SA, LeRoux PD. Effect of mannitol and hypertonic saline on cerebral oxygenation in patients with severe traumatic brain injury and refractory intracranial hypertension. J Neurol Neurosurg Psychiatry. 2009;80:916–20.
37. Sakellaridis N, Pavlou E, Karatzas S, Chroni D, Vlachos K, Chatzopoulos K, Dimopoulou E, Kelesis C, Karaouli V. Comparison of mannitol and hypertonic saline in the treatment of severe brain injuries. J Neurosurg. 2011;114:545–8.
38. Cottenceau V, Masson F, Mahamid E, Petit L, Shik V, Sztark F, Zaaroor M, Soustiel JF. Comparison of effects of equiosmolar doses of mannitol and hypertonic saline on cerebral blood flow and metabolism in traumatic brain injury. J Neurotrauma. 2011;28:2003–12.
39. Asehnoune K, Lasocki S, Seguin P, Geeraerts T, Perrigault PF, Dahyot-Fizelier C, Paugam Burtz C, Cook F, Demeure Dit Latte D, Cinotti R, et al. Association between continuous hyperosmolar therapy and survival in patients with traumatic brain injury—a multicentre prospective cohort study and systematic review. Crit Care. 2017;21:328.
40. Burgess S, Abu-Laban RB, Slavik RS, Vu EN, Zed PJ. A systematic review of randomized controlled trials comparing hypertonic sodium solutions and mannitol for traumatic brain injury: implications for emergency department management. Ann Pharmacother. 2016;50:291–300.
41. Adelson PD, Bratton SL, Carney NA, Chesnut RM, du Coudray HE, Goldstein B, Kochanek PM, Miller HC, Partington MD, Selden NR, et al. Guidelines for the acute medical management of severe traumatic brain injury in infants, children, and adolescents. Chapter 11. Use of hyperosmolar therapy in the management of severe pediatric traumatic brain injury. Pediatr Crit Care Med. 2003;4:S40–4.
42. Durham-Lee JC, Mokkapati VU, Johnson KM, Nesic O. Amiloride improves locomotor recovery after spinal cord injury. J Neurotrauma. 2011;28:1319–26.
43. Brandt C, Nozadze M, Heuchert N, Rattka M, Loscher W. Disease-modifying effects of phenobarbital and the NKCC1 inhibitor bumetanide in the pilocarpine model of temporal lobe epilepsy. J Neurosci. 2010;30:8602–12.
44. Li Y, Cleary R, Kellogg M, Soul JS, Berry GT, Jensen FE. Sensitive isotope dilution liquid chromatography/tandem mass spectrometry method for quantitative analysis of bumetanide in serum and brain tissue. J Chromatogr B Analyt Technol Biomed Life Sci. 2011;879:998–1002.
45. Walker PC, Berry NS, Edwards DJ. Protein binding characteristics of bumetanide. Dev Pharmacol Ther. 1989;12:13–8.
46. Lykke K, Assentoft M, Horlyck S, Helms HC, Stoica A, Toft-Bertelsen TL, Tritsaris K, Vilhardt F, Brodin B, MacAulay N. Evaluating the involvement of cerebral microvascular endothelial Na(+)/K(+)-ATPase and Na(+)-K(+)-2Cl(−) co-transporter in electrolyte fluxes in an in vitro blood–brain barrier model of dehydration. J Cereb Blood Flow Metab. 2017. https://doi.org/10.1177/0271678X17736715.
47. Pollay M, Hisey B, Reynolds E, Tomkins P, Stevens FA, Smith R. Choroid plexus Na+/K+-activated adenosine triphosphatase and cerebrospinal fluid formation. Neurosurgery. 1985;17:768–72.
48. Steffensen AB, Oernbo EK, Stoica A, Gerkau NJ, Barbuskaite D, Tritsaris K, Rose CR, MacAulay N. Cotransporter-mediated water transport underlying cerebrospinal fluid formation. Nat Commun. 2018;9:2167.
49. Cserr HF, DePasquale M, Patlak CS. Volume regulatory influx of electrolytes from plasma to brain during acute hyperosmolality. Am J Physiol. 1987;253:F530–7.
50. Pullen RG, DePasquale M, Cserr HF. Bulk flow of cerebrospinal fluid into brain in response to acute hyperosmolality. Am J Physiol. 1987;253:F538–45.
51. Pollay M. The function and structure of the cerebrospinal fluid outflow system. Cerebrospinal Fluid Res. 2010;7:9.
52. Aspelund A, Antila S, Proulx ST, Karlsen TV, Karaman S, Detmar M, Wiig H, Alitalo K. A dural lymphatic vascular system that drains brain interstitial fluid and macromolecules. J Exp Med. 2015;212:991–9.
53. Louveau A, Smirnov I, Keyes TJ, Eccles JD, Rouhani SJ, Peske JD, Derecki NC, Castle D, Mandell JW, Lee KS, et al. Structural and functional features of central nervous system lymphatic vessels. Nature. 2015;523:337–41.
54. Iliff JJ, Wang M, Liao Y, Plogg BA, Peng W, Gundersen GA, Benveniste H, Vates GE, Deane R, Goldman SA, et al. A paravascular pathway facilitates CSF flow through the brain parenchyma and the clearance of interstitial solutes, including amyloid beta. Sci Transl Med. 2012;4:147ra111.

J Physiol 00.0 (2018) pp 1–15

The Journal of Physiology

Developmental maturation of activity-induced K^+ and pH transients and the associated extracellular space dynamics in the rat hippocampus

Brian Roland Larsen, Anca Stoica and Nanna MacAulay

Department of Neuroscience, Faculty of Health and Medical Sciences, University of Copenhagen, Copenhagen, Denmark

Edited by: David Wyllie & Maike Glitsch

Key points

- Neuronal activity induces fluctuation in extracellular space volume, $[K^+]_o$ and pH_o, the management of which influences neuronal function
- The neighbour astrocytes buffer the K^+ and pH and swell during the process, causing shrinkage of the extracellular space
- In the present study, we report the developmental rise of the homeostatic control of the extracellular space dynamics, for which regulation becomes tighter with maturation and thus is proposed to ensure efficient synaptic transmission in the mature animals
- The extracellular space dynamics of volume, $[K^+]_o$ and pH_o evolve independently with developmental maturation and, although all of them are inextricably tied to neuronal activity, they do not couple directly.

Abstract Neuronal activity in the mammalian central nervous system associates with transient extracellular space (ECS) dynamics involving elevated K^+ and pH and shrinkage of the ECS. These ECS properties affect membrane potentials, neurotransmitter concentrations and protein function and are thus anticipated to be under tight regulatory control. It remains unresolved to what extent these ECS dynamics are developmentally regulated as synaptic precision arises and whether they are directly or indirectly coupled. To resolve the development of homeostatic control of $[K^+]_o$, pH, and ECS and their interaction, we utilized ion-sensitive microelectrodes in electrically stimulated rat hippocampal slices from rats of different developmental stages (postnatal days 3–28). With the employed stimulation paradigm, the stimulus-evoked peak $[K^+]_o$ and pH_o transients were stable across age groups, until normalized to neuronal activity (field potential amplitude), in which case the K^+ and pH shifted significantly more in the younger animals. By contrast, ECS dynamics increased with age until normalized to the field potential, and thus correlated with neuronal activity. With age, the animals not only managed the peak $[K^+]_o$ better, but also displayed swifter post-stimulus removal of $[K^+]_o$, in correlation with the

Brian Roland Larsen has a MSc in molecular biomedicine and obtained his PhD at the University of Copenhagen in 2014. During the past 4 years, he has worked as a postdoctoral researcher in the MacAulay laboratory. His research focus has been on mammalian brain ion-homeostasis and astrocyte cell swelling, aiming to determine and characterize the molecular mechanisms underlying these crucial phenomena. In particular, he has concentrated on mechanism(s) of K^+ clearance such as the subunit constellations of the Na^+/K^+-ATPase and their biophysical properties, as well as transport mechanisms causing cellular water influx.

DOI: 10.1113/JP276768

increased expression of the α1-3 isoforms of the Na^+/K^+-ATPase, and a swifter return of ECS volume. The different ECS dynamics approached a near-identical temporal pattern in the more mature animals. In conclusion, although these phenomena are inextricably tied to neuronal activity, our data suggest that they do not couple directly.

(Received 3 July 2018; accepted after revision 22 October 2018; first published online 25 October 2018)
Corresponding author N. MacAulay: Department of Neuroscience, Faculty of Health and Medical Sciences, University of Copenhagen, Blegdamsvej 3, 2200 Copenhagen N, Denmark. Email: macaulay@sund.ku.dk

Introduction

Neuronal activity in the central nervous system associates with a rise in the extracellular concentration of K^+ ($[K^+]_o$). To prevent widespread neuronal membrane depolarization and associated disruption of synaptic function, it is paramount that K^+ is swiftly cleared from the extracellular space (ECS). The neighbouring astrocytes act as K^+ sinks during neuronal activity and take up a portion of the neuronally-released K^+ (Ballanyi *et al.* 1987; Grafe & Ballanyi, 1987), predominantly via the glia-specific K^+-sensitive $\alpha2\beta2$ isoform combination of the Na^+/K^+-ATPase, which is kinetically geared to respond to increased $[K^+]_o$ and the associated membrane depolarization (Ransom *et al.* 2000; D'Ambrosio *et al.* 2002; Larsen *et al.* 2014; Stoica *et al.* 2017). Following termination of neuronal activity, K^+ exits the astrocytic compartment and re-enters the neurons, presumably via the action of the neuronal $\alpha3$ Na^+/K^+-ATPase isoform (Coles & Schneider-Picard, 1989; Ransom *et al.* 2000; Larsen *et al.* 2016*b*). In the wake of neuronal stimulation, some studies report a transient undershoot of $[K^+]_o$ (Ransom *et al.* 2000; Chever *et al.* 2010), although this is not detected in other studies (Karwoski *et al.* 1989; D'Ambrosio *et al.* 2002; Meeks & Mennerick, 2007; Haj-Yasein *et al.* 2011; Larsen *et al.* 2014; Larsen *et al.* 2016*a*). This undershoot may be driven by activity of the $[Na^+]_i$-sensitive neuronal $\alpha3$ Na^+/K^+-ATPase (Ransom *et al.* 2000). The ECS shrinks during the K^+ transient, presumably as a result of astrocytic swelling (Dietzel *et al.* 1980; Connors *et al.* 1982; Ransom *et al.* 1985). Because K^+ transients and ECS shrinkage occur in parallel in mature tissue, ECS shrinkage was presumed to be directly coupled to the astrocytic K^+ and/or glutamate uptake (Schneider *et al.* 1992; Koyama *et al.* 2000; Kofuji & Newman, 2004; Nagelhus *et al.* 2004; MacAulay & Zeuthen, 2012; Pál *et al.* 2013). However, none of the proposed K^+-uptake mechanisms (the Na^+/K^+-ATPase, the $Na^+/K^+/2Cl^-$ cotransporter 1 (NKCC1) or the K^+ channel Kir4.1) appeared to be required for activity-evoked ECS shrinkage (Haj-Yasein *et al.* 2011; Larsen *et al.* 2014), and neither were the astrocytic aquaporin 4 (Haj-Yasein *et al.* 2012) or the glutamate transporters (Larsen & MacAulay, 2017). During neuronal activity, H^+ (pH) fluctuates, leading to a fast extracellular alkaline pH shift (Chen & Chesler, 1992; Voipio & Kaila, 1993; Syková, 1997; Makani & Chesler, 2010). With prolonged tetanic stimulation, the transient alkalization is followed by an acidosis after termination of neuronal activity, which is absent at lower firing rates (Makani & Chesler, 2007). The nature of the pH transients led us to identify pH-regulating transporters, mainly the electrogenic Na^+/bicarbonate cotransporter 1 (NBCe1) and the monocarboxylate transporters (MCTs), acting as mechanisms underlying a portion of the activity-evoked ECS shrinkage in rat hippocampal slices (Larsen & MacAulay, 2017). The NBCe1 is activated by the K^+-mediated cellular depolarization and the alkaline pH transient (Theparambil *et al.* 2014; Theparambil & Deitmer, 2015; Theparambil *et al.* 2015), whereas MCT is predicted to be activated by the K^+-mediated increase in metabolism (Wender *et al.* 2000; Choi *et al.* 2012; Brown & Ransom, 2015; Waitt *et al.* 2017). These findings suggest that K^+ clearance, pH changes and ECS shrinkage are linked but not directly coupled.

The homeostatic management of extracellular K^+ appears to mature with development in the rat optic nerve and hippocampus: In the adult tissue, the stimulus-induced $[K^+]_o$ transient remains within the K^+ ceiling level of ~12–15 mM, which is exceeded in the immature animal (in which K^+ transients up to 20 mM can be detected) (Connors *et al.* 1982; Ransom *et al.* 1985; Nixdorf-Bergweiler *et al.* 1994). Notably, in the young immature optic nerve of the rat [postnatal day (P)1–P2], the activity-evoked K^+ transient fails to associate with ECS shrinkage, which only becomes apparent as the rat matures (P8) and complete at P20–P21 (Connors *et al.* 1982; Ransom *et al.* 1985). This pattern is paralleled for $[K^+]_o$ regulation in the spinal cord of young rats compared to their more mature counterparts (Jendelová & Syková, 1991). This developmental regulation of $[K^+]_o$ management and ECS shrinkage appears to coincide with the proliferation, maturation and organization of glial cells (Ransom *et al.* 1985; Nixdorf-Bergweiler *et al.* 1994), with further morphological changes taking place during the fourth postnatal week (Nixdorf-Bergweiler *et al.* 1994). Taken together with the K^+-mediated cell swelling observed in enucleated rat optic nerve (MacVicar *et al.* 2002), these observations support the notion of glia cells comprising the cellular structures responsible for K^+ uptake and ECS shrinkage (Ransom *et al.*

1985). Analogous to the developmental profile of the activity-evoked K^+ and ECS transients, a shift in the H^+/pH transient was detected in the rat spinal cord from P3 to adult animals (Jendelová & Syková, 1991; Syková, 1997). However, the developmental profile of these ECS dynamics, and hence maturation of synaptic functionality, remains unresolved in grey matter tissue.

To determine the developmental maturation of K^+ management, ECS shrinkage and pH transients and their interaction in a grey matter tissue, we employed electric stimulation of acute slices of rat hippocampus and ion-sensitive microelectrodes to monitor the activity-evoked ECS dynamics. Although the peak $[K^+]_o$, ECS, and pH as a function of age correlated differentially with neuronal activity, restoration of extracellular $[K^+]_o$ became swifter with age, following elevated expression of the α isoforms of the Na^+/K^+-ATPase. The developmental profile of the K^+ transients was paralleled by fast return of ECS shrinkage but a slower normalization of the alkaline transient. In the more mature animals, the three different ECS dynamics approached a similar temporal pattern.

Methods

Ethical approval

The experiments were performed in accordance with the guidelines of the Danish Veterinary and Food Administration (Ministry of Environment and Food) and were approved by the animal facility at the Faculty of Health and Medical Sciences, University of Copenhagen. The animal experiments conform to the principles and regulations described in Grundy (2015). Experiments were performed on male and female rats (Sprague–Dawley, Janvier Labs, France) at P3–P28, housed in the animal facility at the Faculty of Health and Medical Sciences, University of Copenhagen with free access to food and water. Rats older than P11 were anaesthetized using gaseous 2-bromo-2-chloro-1, 1,1-trifluoroethane (halothane) (B-4388; Sigma-Aldrich, Hamburg, Germany) prior to decapitation. In total, 47 animals were used for electrophysiology experiments and 20 animals for hippocampal tissue collection.

Brain slices and solutions

Following decapitation, the brain was quickly removed and placed into ice-cold cutting solution containing (in mM): 87 NaCl, 70 sucrose, 2.5 KCl, 0.5 $CaCl_2$, 25 $NaHCO_3$, 1.1 NaH_2PO_4, 7 $MgCl_2$ and 25 D-glucose, equilibrated with gaseous 95% O_2, 5% CO_2. Oblique sagittal (transverse) hippocampal slices (400 μm) were cut with a Campden Vibrating Microtome (7000SMZ-2; Campden Instruments, Loughborough, UK). Slices were transferred to the standard artificial cerebrospinal fluid solution containing (in mM): 124 NaCl, 3 KCl, 2 $CaCl_2$, 25 $NaHCO_3$, 1.1 NaH_2PO_4, 2 $MgCl_2$ and 10 D-glucose, equilibrated with 95% O_2, 5% CO_2 (pH 7.4 at the experimental temperature of 33–34 °C) and left to recover at 34 °C for 30 min, and then maintained at room temperature.

Ion-sensitive microelectrodes and electrophysiological recordings in slices

Electrophysiological recordings were carried out in a submerged-type recording chamber (Brain Slice Chamber 1, Scientific Systems Design; Digitimer Ltd, Welwyn Garden City, UK) at an experimental temperature of 33–34 °C and a continuous superfusion at a flow rate of 2.2 mL min^{-1}. Recordings were performed within stratum radiatum of the CA1 region. High-frequency stimulation was delivered by a concentric bipolar tungsten electrode (TM33CCNON; World Precision Instruments, Hitchin, UK) inserted into the stratum radiatum in the vicinity ($\leq$300 μm) of the recording site. Stimulation trains (22 V at 20 Hz, each pulse of a duration of 80 μs, for 3 s) were delivered to the slice to activate the Schaffer collaterals. The resulting extracellular field potentials were recorded with thin-walled filamented glass capillary microelectrodes (GC150TF-7.5; Harvard Apparatus, Holliston, MA, USA) pulled to resistances of 15–25 MΩ when filled with the standard solution (see above). This electrode served as a reference signal for the ion-sensitive microelectrodes. Ion-sensitive microelectrodes were prepared from thin-walled non-filamented glass capillaries (GC150T-7.5; Harvard Apparatus) pulled to obtain a tip diameter in the range of 1–2 μm (Voipio *et al.* 1994). The capillaries were then silanized internally with gaseous *N*,*N*-dimethyltrimethylsilylamine (catalgue no. 41716; Sigma-Aldrich) and baked at 190°C for 20 min prior to being backfilled. The electrodes were backfilled with a solution depending on the type of measurement, containing either 150 mM tetramethylammonium (TMA^+) chloride (for extracellular space volume measurements), 150 mM NaCl and 3 mM KCl (for extracellular K^+ measurements), or 150 mM NaCl, 20 mM Hepes and 10 mM NaOH (for extracellular pH/H^+ measurements). The tip of the capillary was subsequently filled with a short column of either TMA^+/K^+-sensitive liquid membrane solution [50 mg mL^{-1} potassium tetrakis (4-chlorophenyl) borate (catalogue no. 60591; Sigma-Aldrich) in 1,2-dimethyl-3-nitrobenzene (catalogue no. 40870; Sigma-Aldrich)], or H^+-sensitive liquid membrane solution (Hydrogen ionophore II – cocktail A, catalogue no. 95297; Sigma-Aldrich). For experiments with TMA^+, 1.5 mM TMA-Cl was included in the test solution. Note that the TMA^+/K^+ membrane is highly sensitive to

quartenary ions, such as TMA^+; however, in the absence of such ions, it becomes selective to K^+ ions and can therefore be used for both measurements depending on the back-filling solution.

The tips of the ion-sensitive electrode and the reference electrode were placed within a few microns at the exact same depth in the core of the slice. Close distance was ensured via Sensapex micromanipulators (SMX series; Sensapex, Oulu, Finland), which provide precise (μm) *x*, *y*, *z* co-ordinates, by placing the electrode tips closely together above the slice and afterwards moving into the tissue maintaining this narrow distance aided by the *x*, *y*, *z* co-ordinates. The ion-sensitive signal and the field potential signal were both recorded via an ION-01M amplifier and headstage (NPI Electronic, Tamm, Germany). Online deduction of the field potential signal from that of the ion-sensitive electrode provided the traces employed for analysis. Recordings in slices were terminated and the data discarded if deviations (more than ∼15%, tested at >2 points along the recordings) in the original resistance of the ion-sensitive electrode were detected (indicating, for example, a change in tip-diameter or alterations in the tip liquid membrane column). All recorded signals were filtered at 250 Hz, sampled at 500 Hz and stored for off-line analysis with WinEDR (courtesy of Dr John Dempster, University of Strathclyde, Glasgow, UK) and Prism, version 7.0 (GraphPad Software Inc., La Jolla, CA, USA). At the end of the experiment, each ion-sensitive microelectrode was thoroughly calibrated to translate the signal in mV to either the percentage volume change, the K^+ concentration or pH; a detailed description is provided in Voipio *et al.* (1994). In brief, the conversion to concentration of the appropriate ion relies on finding the 'slope' (*S*) of the electrode response.

$$S = \frac{\Delta V}{\log\left(\frac{[test\ solution\ 2]}{[test\ solution\ 1]}\right)}$$

where ΔV is the response in mV and 'test solution' refers to the applied calibration solutions in mM of the appropriate ion. For an ideal electrode, *S* should approach Nernstian conditions. To calculate the relative percentage change in ECS shrinkage, the following approach was utilized. Data were offset to reach a baseline of 0 mV and this equation used with *X* representing the recording in mV:

$$V_{ECS}\ (\%) = 10^{\left(\frac{-X}{S}\right)} * 100\%$$

Notably, the employed experimental approach provides the relative ECS shrinkage but gives no information about the actual size of the ECS. For absolute values of the extracellular space fraction (α), the method developed by Nicholson & Phillips (1981) and Nicholson & Syková (1998) is required.

Tissue lysis, western blotting and semi-quantitative analysis

The hippocampi of rats aged P3–P22 were lysed in RIPA buffer (150 mM NaCl, 1% Triton X-100, 0.5% Na deoxycholate, 0.1% SDS, 5 mM EDTA, 50 mM Tris, pH 8) supplemented with 0.4 mM Pefabloc and 8 μM Leupeptin (both from Sigma-Aldrich) by sonication with a Sonoplus mini20 (Bandelin Electronic, Berlin, Germany). The total protein concentration was determined using the Bio-Rad DC Protein Assay (Bio-Rad, Hercules, CA, USA). The proteins were separated by SDS-PAGE on 4–20% polyacrylamide gels (TGX Gels; Bio-Rad) and electro-transferred on Immobilon-FL polyvinylidene fluoride membranes (Millipore, Billerica, MA, USA). The expression of Na^+/K^+-ATPase isoforms was analysed using the antibodies: mouse anti-α1 a6F (dilution 1:60; DSHB, Iowa City, IA, USA); rabbit anti-α2 07–674 (dilution 1:500; Millipore); mouse anti-α3 XVIF9-G10 (dilution 1:1000; Thermo Fisher, Waltham, MA, USA); chicken anti-GAPDH AB2302 (dilution 1:1000; Millipore); mouse anti-β tubulin MAB3408 (dilution 1:10,000; Millipore); and mouse anti-polyhistidine ab18184 (dilution 1:500; Abcam, Cambridge, UK) diluted in Odyssey blocking buffer: PBS-T 1:1 (Li-Cor, Lincoln, NE, USA). Following detection using fluorophore-conjugated secondary antibodies (Li-Cor), the membranes were scanned on an Odyssey CLx imaging system and band intensities were quantified using Image Studio software (Li-Cor). GAPDH and β tubulin were used as internal standards. The specificity of antibodies targeting the α subunit isoforms of the Na^+/K^+-ATPase was demonstrated previously upon expression of the three isoforms in *Xenopus laevis* oocytes followed by tests of cross-reactivity (Stoica *et al.* 2017). For the semi-quantitative analysis of Na^+/K^+-ATPase isoforms, polyhistidine-tagged versions of Na^+/K^+-ATPase isoforms α1, α2 and α3 expressed in *X. laevis* oocytes were used as standards for normalization as described previously (Stoica *et al.* 2017).

Statistical analysis

All data are reported as the mean ± SEM. Decay constants were obtained with the equation:

$$Y = (Y_0 - Plateau) * e^{(-K*X)} + plateau$$

where Y_0 is the *Y* value at the point where the time, *X*, is zero; *K* is the decay constant (in s^{-1}); and plateau denotes the *Y* value at 'infinite' time. The time constant τ can be calculated as the reciprocal of *K*, and the half-life λ as $\ln(2)/K$. The calculation was performed using Prism, version 7.0 (GraphPad Software Inc.) and analysed from the maximal peak (even when this occurred later than at stimulus end). Statistical significance was tested with Student's *t* test or one-way ANOVA with Tukey's or

Dunnett's multiple comparison *post hoc* test, as indicated. $P < 0.05$ was considered statistically significant. The number of experiments (n) signifies individual brain slices and is noted as appropriate, as is the number of animals from which these slices have been obtained in the figure legends.

Results

Optimal management of activity-evoked K^+ transients occurs during development

To evaluate the developmental maturation of regulation and control of K^+ dynamics associated with neuronal activity in an approximated native setting in the mammalian brain, we employed acute hippocampal slices from rats at different age groups, P3–P4, P7–P8, P10–P11, P13–P14 and P21–P28 (with the latter considered as adolescents). Activity-evoked K^+ transients were induced by electrical stimulation of the CA1 Schaffer collaterals (20 Hz, 3 s, as indicated by a black bar above the traces in all figures) and recorded with K^+- sensitive microelectrodes. Figure 1*A*–*E* illustrates representative K^+ traces and field potentials (inserts) obtained from the different age groups. The peak $[K^+]_o$ at the end of the stimulation period was not significantly different amongst the age groups (for summarized data, see Fig. 1*F*, $n = 6$–9 per age group). Although the $[K^+]_o$ in the younger age groups (P3–P4) appeared to peak at a time point later than stimulus end, quantification of this delayed maximum $[K^+]_o$ revealed no significant difference from the peak $[K^+]_o$ at stimulus end (Fig. 1*F*, insert). However, the younger age groups (P3–P4, P7–P8 and P10–P11) had smaller field potential amplitudes than the adolescent age group ($n = 6$–9, $P < 0.001$) (Fig. 1*G*). Normalization of the peak $[K^+]_o$ (at the stimulus end) to the field potential amplitude (in mV) illustrated that the K^+ transients at a given neuronal activity were significantly increased in the young age groups (P3–P4) compared to the adolescent age group ($n = 6$–9, $P < 0.001$) (Fig 1*H*). The delayed peak was not significantly different from the peak at stimulus end, when quantified relative to the field potential (Fig. 1*H*, insert). To reveal age-dependent differences in the post-stimulus K^+ clearance kinetics, we normalized the K^+ transients to the value at the end of the stimulation (Fig. 1*I*), revealing the distinct shape of the K^+ transients in each age group. To cement this observation, we quantified the decay constant of the K^+ transient for each individual experiment (from the point of maximal K^+ concentration; for an example of decay phase fit in a slice from a P21 rat, see Fig. 1*J*; for summarized data on the decay constants, see Fig. 1*K*). It was evident that the return to baseline occurred slower in the younger age groups than in the more mature rats ($n = 6$–9, $P < 0.001$). These results illustrate that the peak $[K^+]_o$ does not display age-related correlation with neuronal activity (in mV) and that the K^+ clearance machinery becomes more efficient with maturation, both with regard to the peak $[K^+]_o$/mV and the return to baseline value.

Increased expression of Na^+/K^+-ATPase coincides with maturation of K^+ management in the rat hippocampus

To determine whether the age-dependent increase in homeostatic control of K^+ correlated with expression of the Na^+/K^+-ATPase, we semi-quantified the expression level of the different α subunit isoforms of the Na^+/K^+-ATPase in hippocampal tissue from the different age groups by western blotting. The expression of all three isoforms increased stepwise with age (Fig. 2*A*–*C*). This standard western blot approach provides no insight into the relative expression level of each isoform because distinct antibody efficiency prevents inter-antibody comparisons. To gain novel insight into the relative protein expression of the different Na^+/K^+-ATPase isoforms, we utilized a polyhistidine-tag-based semi-quantitative approach (Stoica *et al.* 2017) to compare the expression of $\alpha3$ with that of $\alpha1$ and $\alpha2$. This approach relies on expression of polyhistidine-tagged Na^+/K^+-ATPase in *Xenopus* oocytes followed by parallel immunoblotting of the membrane fractions with an anti-polyhistidine antibody (Fig. 2*D*) and a specific α antibody (Fig. 2*E*–*G*). The ratio of these signals provided an efficiency factor for each antibody, which was subsequently employed to normalize the band intensities obtained in western blots of hippocampal tissue from the adolescent rats (P21+) (Fig. 2*E*–*G*). Semi-quantification of the different Na^+/K^+-ATPase isoforms in the adolescent rat hippocampus in this manner provided a ratio of $\alpha3$ to $\alpha2$ protein abundance of 6.3 ± 0.9 (Fig. 2*H*) and of $\alpha3$ to $\alpha1$ protein abundance of 20.8 ± 1.6 (Fig. 2*I*) ($n = 4$ of each). These results demonstrate that all three isoforms of the Na^+/K^+-ATPase are developmentally upregulated and that the neuronal $\alpha3$ isoform is the dominant Na^+/K^+-ATPase in hippocampus of adolescent rats.

Activity-evoked extracellular space shrinkage is present in all age groups and correlate with neuronal activity

To quantify the activity-evoked ECS shrinkage in the different age groups, we employed TMA^+-sensitive microelectrodes. These monitor the extracellular concentration of the membrane-impermeable TMA^+ (bath-applied), which increases with activity-evoked ECS shrinkage and represents a robust read-out of percentage change of ECS. Electrical stimulation of the Schaffer collaterals (as in Fig. 1) led to a transient ECS shrinkage. Figure 3*A*–*E*

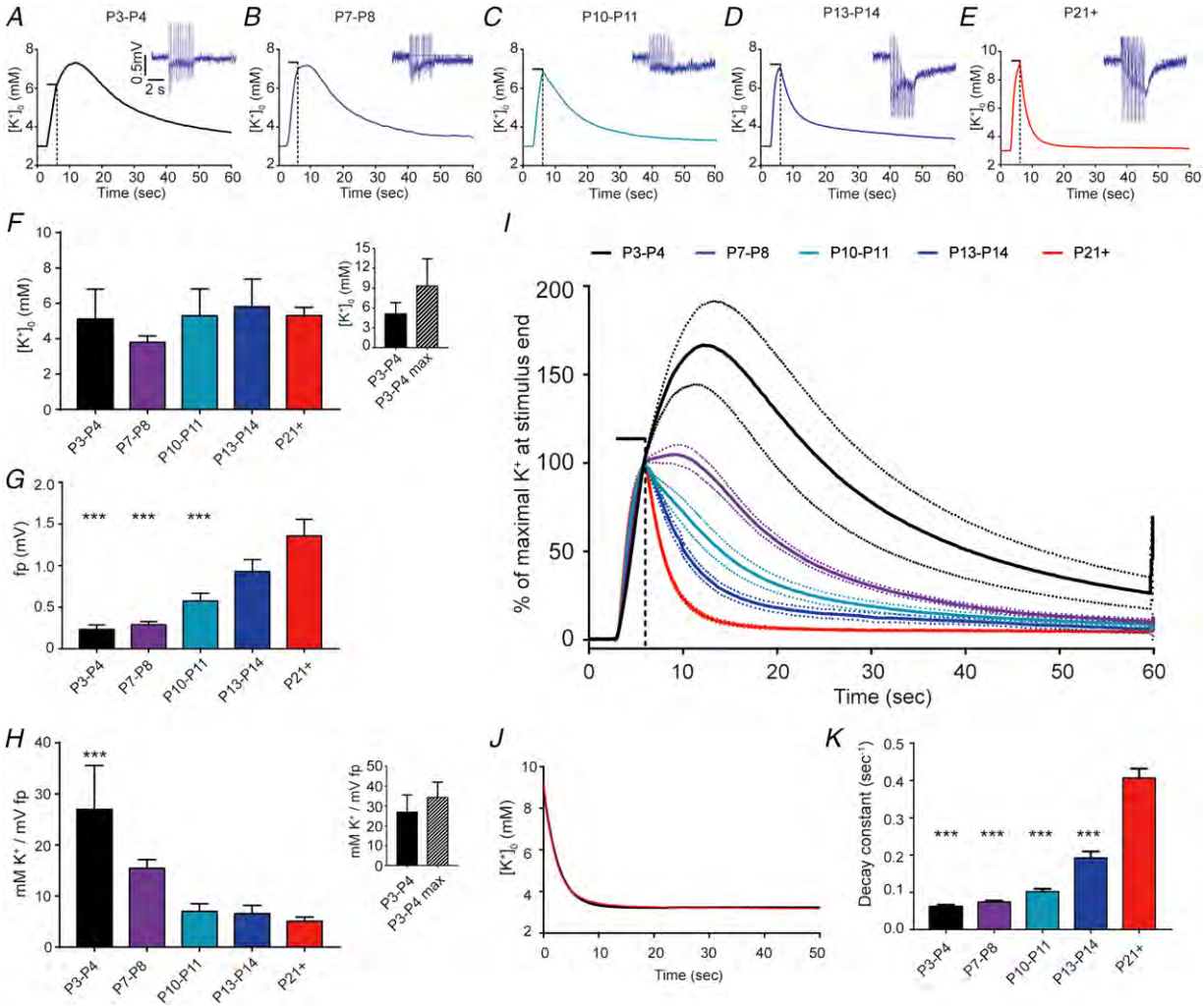

Figure 1. Development of K^+ regulation in rats
Ion-sensitive microelectrodes were utilized to record the extracellular K^+ concentration, and the corresponding field potential, in electrically stimulated hippocampal slices from rats of various age groups. *A–E*, representative traces of stimulus-evoked changes in $[K^+]_o$ for the different age groups tested; P3–P4 (*A*), P7–P8 (*B*), P10–P11 (*C*), P13–P14 (*D*) and P21+ (*E*), with representative field potentials as inserts. *F*, summarized data of the peak amplitude at the end of stimulation for the respective age groups (in mM) P3–P4: 5.1 ± 1.7; P7–P8: 3.8 ± 0.4; P10–P11: 5.3 ± 1.5; P13–P14: 5.8 ± 1.6; P21+: 5.3 ± 0.5. Insert: peak amplitude of P3-P4 at stimulus end and at the time of the maximal amplitude (9.3 ± 4.1 mM). *G*, summarized data of the amplitude of the field potential for the different age groups (in mV) P3–P4: 0.23 ± 0.05; P7–P8: 0.29 ± 0.04; P10–P11: 0.58 ± 0.09; P13–P14: 0.93 ± 0.14; P21+: 1.4 ± 0.20. *H*, peak $[K^+]_o$ amplitude at stimulus end was normalized to the corresponding field potential in each experiment and summarized (in mM/mV) P3–P4: 27.0 ± 8.6; P7–P8: 15.4 ± 1.7; P10–P11: 7.0 ± 1.5; P13–P14: 6.6 ± 1.6; P21+: 5.1 ± 0.80. Insert includes the maximal peak amplitude of P3–P4 normalized to the field potential (34.3 ± 7.8 mM/mV). *I*, single individual recordings were normalized to the K^+ amplitude at the end of stimulus and illustrated as the average (full line) and standard errors (dashed lines) within the age group allowing for direct comparison of their shape. *J*, representative example of fitting the return to baseline using a one-phase decay equation (black line) on a K^+ recording (red) from a P21 rat. *K*, comparison of the decay constant between the age groups (calculated from the individual recordings, in s^{-1}): P3–P4: 0.06 ± 0.01; P7–P8: 0.07 ± 0.01; P10–P11: 0.10 ± 0.01; P13–P14: 0.19 ± 0.02; P21+: 0.41 ± 0.02. The black bar above the respective traces represents 20 Hz stimulation. The number of experiments performed: P3–P4 (n = 6 slices from six animals); P7–P8 (n = 9 slices from nine animals); P10–P11 (n = 6 slices from six animals); P13–P14 (n = 7 slices from six animals); P21+ (n = 7 slices from four animals). Statistical significance was tested with one-way ANOVA with Dunnett's multiple comparison *post hoc* test and the asterisks refer to significant differences to the P21+ age group or with Student's paired t test (insert in *F* and *H*). ***$P < 0.001$.

illustrates representative volume traces obtained from the different age groups, with inserts of representative field potentials. The percentage ECS shrinkage measured at the end of the stimulation period was significantly smaller in the younger age groups compared to the adolescent rats (n = 5–8 per age group, $P < 0.001$ for P3–P4 and P7–8, $P < 0.05$ for P10–P11) (Fig. 3*F*). The ΔECS in the youngest age group (P3–P4) appeared to dip at stimulus end only to subsequently continue and reach maximal peak later, the latter of which is statistically different from that obtained at stimulus end (Fig. 3*F*, insert). The field potential amplitude of the young age groups (P3–P4 and P7–P8) was similarly smaller compared to the adolescent rats (n = 5–8 per age group, $P < 0.001$ for P3–P4 and P7–P8) (Fig. 3*G*). To relate the ECS dynamics to neuronal activity, the ΔECS was normalized to the field potential (in mV). These data illustrate that the ECS dynamics (quantified at stimulus end) associated with a given neuronal activity are stable across ages (n = 5–8 per age group) (Fig. 3*H*). In the youngest age group (P3–P4), the maximum ΔECS/mV (post-stimulus) was significantly larger than that obtained at stimulation end (Fig 3*H*, insert). To reveal age-dependent differences in the post-stimulus ECS dynamics, the volume traces were normalized to that obtained at stimulus end (Fig. 3*I*). Quantification of the decay constant (for a representative fitting of the decay phase of a P22 rat, see Fig. 3*J*) of the individual ECS transients illustrated that the extracellular space returned to baseline slower for the younger age groups (P3–P4, $P < 0.05$; P7–P8, $P < 0.01$; and P10–P11, $P < 0.05$) than for the adolescent (P21+) rats (Fig. 3*K*). These results illustrate that the ECS dynamics become swifter with maturation and that stimulus-evoked ECS changes are small in the immature animals but the peak of the ECS transients display age-related correlation with neuronal activity (in mV).

Activity-evoked extracellular pH transients are similar in all age groups but does not correlate with neuronal activity across maturation

Our earlier finding that extracellular pH transients occur in parallel to the activity-induced K^+ rise and contribute to regulation of ECS shrinkage in hippocampus (Larsen & MacAulay, 2017) prompted us to determine the age-dependent pH regulation. pH_o was monitored by H^+-sensitive microelectrodes during electrical stimulation of the Schaffer collaterals, as described above. Neuronal activity associated with

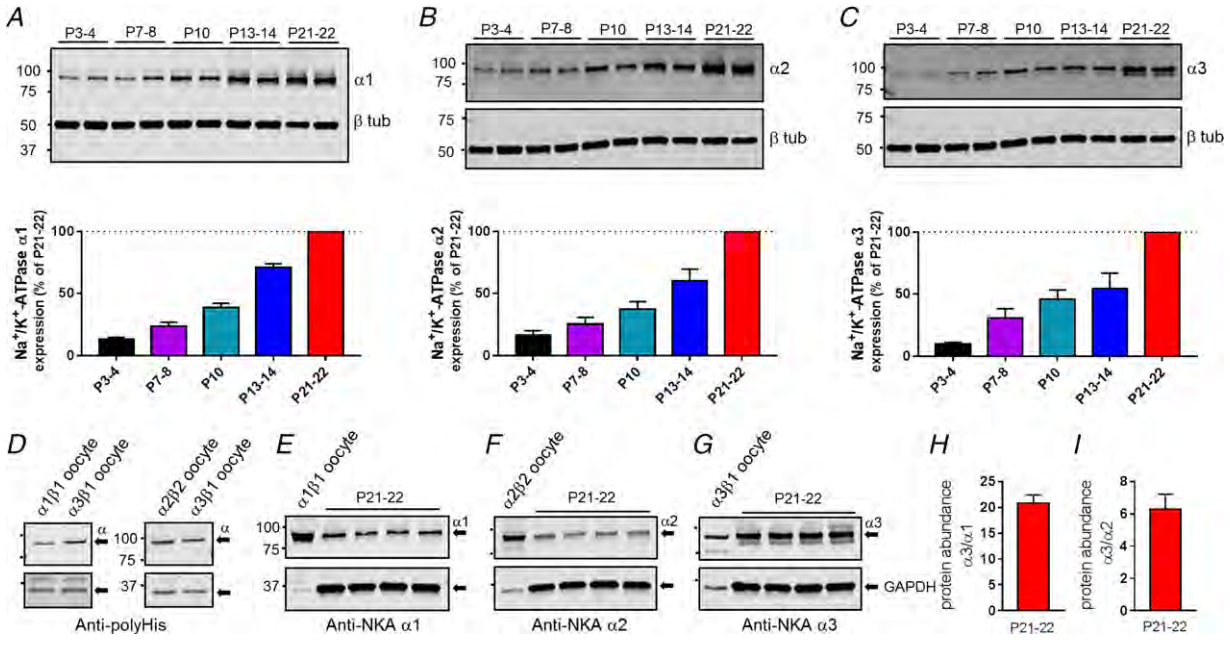

Figure 2. Na^+/K^+-ATPase subunit expression
Representative western blots showing the protein expression of Na^+/K^+-ATPase isoforms α1 (*A*), α2 (*B*) and α3 (*C*) across five different developmental time points of the rat hippocampus (upper). Lower: quantification and normalization of the signals to the values at age P21+. For semi-quantitative comparison of isoforms α1, α2 and α3, polyhistidine-tagged versions expressed in *Xenopus* oocytes were probed with an anti-polyhistidine antibody (*D*) and with isoform-specific antibodies (*E*, *F* and *G*, left lanes). The ratios of the thus detected signals were used to quantify Na^+/K^+-ATPase α1, α2,and α3 in P21+ rat hippocampal lysates (*E*, *F* and *G*). *H*, quantification of Na^+/K^+-ATPase α3 relative to α1. *I*, quantification of Na^+/K^+-ATPase α3 relative to α2 (n = 4 for all experiments). β tubulin and GAPDH was used as loading controls.

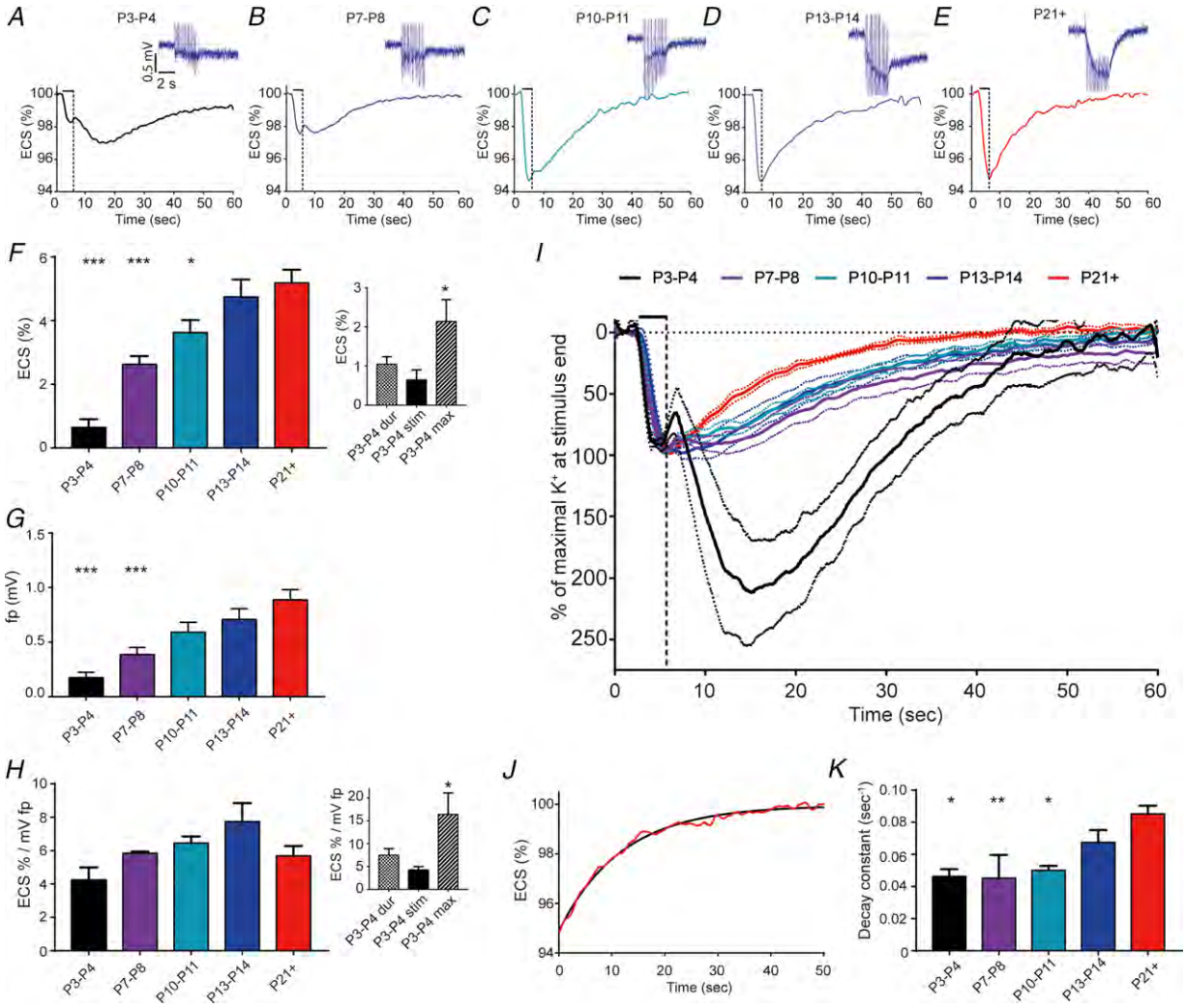

Figure 3. Development of ECS shrinkage dynamics in rats
Ion-sensitive microelectrodes were employed to record the ECS changes (as well as the associated field potential), in electrically stimulated hippocampal slices from rats of various age groups. *A–E*, representative traces of stimulus-evoked changes in ECS for the different age groups tested. P3–P4 (*A*), P7–P8 (*B*), P10–P11 (*C*), P13–P14 (*D*) and P21+ (*E*). Inserts show representative field potentials. *F*, summarized data of the peak ECS change at the end of stimulation for the respective age groups (as a percentage) P3–P4: 0.65 ± 0.26; P7–P8: 2.63 ± 0.26; P10–P11: 3.63 ± 0.39; P13–P14: 4.75 ± 0.55; P21+: 5.19 ± 0.41. Insert: P3–P4 ECS changes during the stimulation ('dur', 1.04 ± 0.19%), at the end of the stimulation ('stim'), and at the maximum ('max', 2.12 ± 0.56%). *G*, summarized data showing the amplitude of the field potential for the respective age groups (in mV) P3–P4: 0.18 ± 0.05; P7–P8: 0.39 ± 0.06; P10–P11: 0.59 ± 0.09; P13–P14: 0.71 ± 0.10; P21+: 0.9 ± 0.09. *H*, ECS amplitude was normalized to the corresponding field potential in each experiment and summarized (as a percentage/mV) P3–P4: 4.22 ± 0.78; P7–P8: 5.84 ± 0.10; P10–P11: 6.46 ± 0.40; P13–P14: 7.73 ± 1.11; P21+: 5.68 ± 0.59. Insert illustrates the normalized P3–P4 ECS changes during the stimulation (7.46 ± 1.45%/mV), at the end of the stimulation, and at the maximum (16.4 ± 4.67%/mV). *I*, single individual recordings were normalized to the ECS change at the end of stimulus, summarized (full line, standard error illustrated as dashed line) for each age group, allowing for direct comparison of their shape. *J*, representative example of fitting the return to baseline using a one-phase decay equation (black line) on an ECS recording (red) from a P22 rat. *K*, comparison of the decay constant calculated from the maximal peak between the age groups (calculated from the individual recordings, in s^{-1}): P3–P4: 0.048 ± 0.004; P7–P8: 0.047 ± 0.015; P10–P11: 0.052 ± 0.003; P13–P14: 0.069 ± 0.008; P21+: 0.087 ± 0.005. The black bar above the respective traces represents 20 Hz stimulation. The number of experiments performed: P3–P4 (n = 5 slices from five animals), P7–P8 (n = 7 slices from seven animals), P10–P11 (n = 6 slices from six animals), P13–P14 (n = 8 slices from eight animals), P21+ (n = 8 from seven animals). Statistical significance was tested with one-way ANOVA with Dunnett's multiple comparison *post hoc* test and the asterisks refer to significant differences to the P21+ age group (or to stimulus end inserts in F–G). *P < 0.05, **P < 0.01, ***P < 0.001.

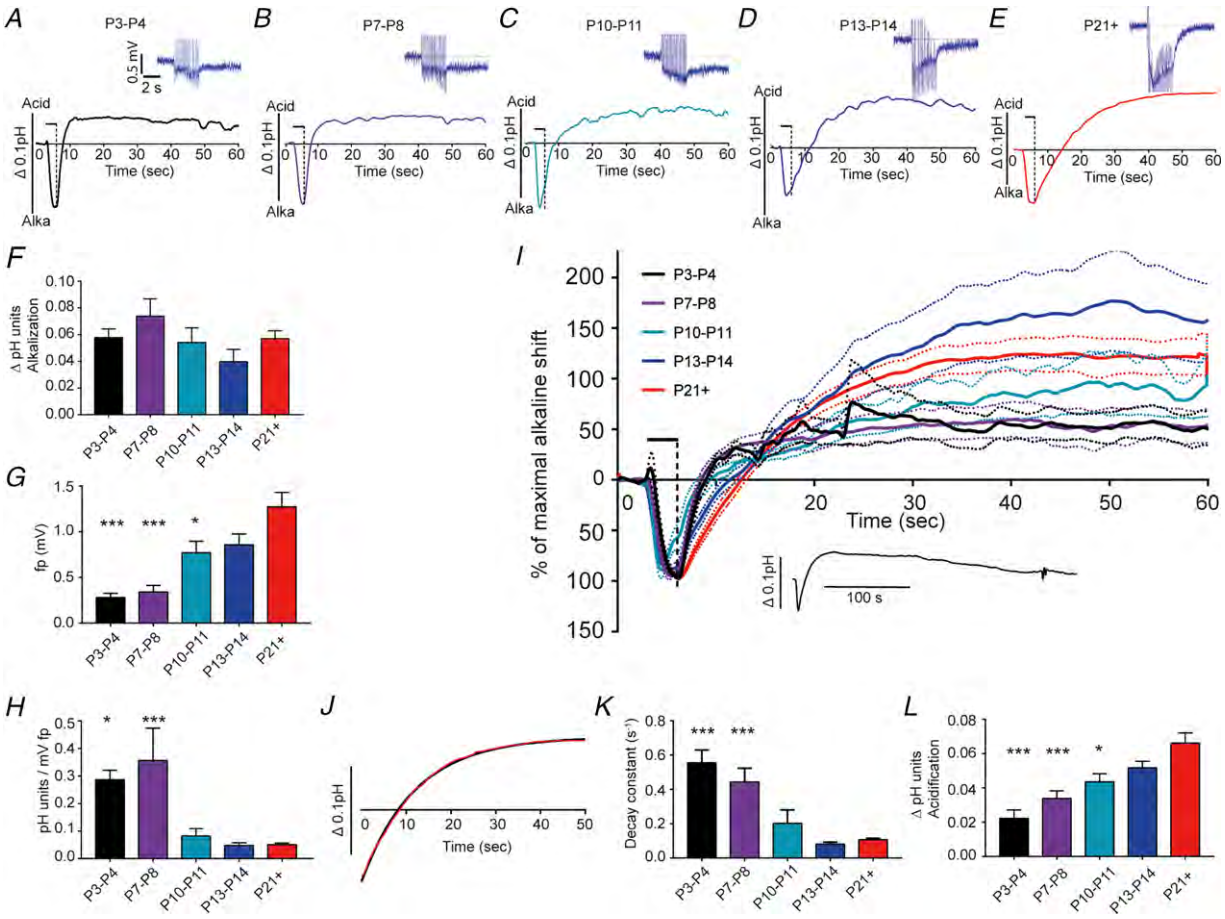

Figure 4. Development of extracellular pH transients in rats
Ion-sensitive microelectrodes were employed to record the pH shifts and the corresponding field potential, in electrically stimulated hippocampal slices from rats of various age groups. *A–E*, representative recordings of stimulus-evoked shifts in pH for the different age groups tested. P3–P4 (*A*), P7–P8 (*B*), P10–P11 (*C*), P13–P14 (*D*) and P21+ (*E*). Inserts show representative field potentials. *F*, summarized data of the peak alkaline shift for the respective age groups (in pH units) P3–P4: 0.058 ± 0.006; P7–P8: 0.074 ± 0.013; P10–P11: 0.054 ± 0.011; P13–P14: 0.040 ± 0.009; P21+: 0.057 ± 0.006. *G*, summarized data showing the amplitude of the field potential for the respective age groups (in mV) P3–P4: 0.28 ± 0.05; P7–P8: 0.34 ± 0.07; P10–P11: 0.77 ± 0.13; P13–P14: 0.86 ± 0.12; P21+: 1.3 ± 0.16. *H*, amplitude in pH of the alkaline shift was normalized to the corresponding field potential in each experiment and summarized (in pH/mV) P3–P4: 0.103 ± 0.030; P7–P8: 0.142 ± 0.044; P10–P11: 0.063 ± 0.012; P13–P14: 0.067 ± 0.009; P21+: 0.059 ± 0.006. *I*, single individual recordings were normalized to the maximal alkaline shift and summarized (full line with the standard errors illustrated as dashed lines) for each age group, allowing for direct comparison of their shape. Insert shows a longer recording from a P27 rat indicating the time it takes for the pH to fully recover following a stimulation train. *J*, representative example of fitting the return pH using a one-phase decay equation (black line) on a pH recording (red) from a P27 rat. *K*, comparison of the decay constant between the age groups (calculated from the individual recordings, in s^{-1}): P3–P4: 0.56 ± 0.07; P7–P8: 0.44 ± 0.08; P10–P11: 0.20 ± 0.08; P13–P14: 0.08 ± 0.01; P21+: 0.11 ± 0.01. *L*, summarized data of the maximal acidic shift relative to the initial baseline for the respective age groups (in pH units) P3–P4: 0.022 ± 0.005; P7–P8: 0.034 ± 0.004; P10–P11: 0.044 ± 0.005; P13–P14: 0.052 ± 0.004; P21+: 0.066 ± 0.006. The black bar above the respective traces represents 20 Hz stimulation. The number of experiments performed: P3–P4 ($n = 5$ slices from five animals), P7–P8 ($n = 6$ from six animals), P10–P11 ($n = 5$ from five animals), P13–P14 ($n = 7$ from seven animals); P21+ ($n = 9$ from six animals). Statistical significance was tested with one-way ANOVA with Dunnett's multiple comparison *post hoc* test and the asterisks refer to significant differences to the P21+ age group. $^{*}P < 0.05$, $^{***}P < 0.001$.

a swift alkalization followed by a return to baseline and a post-stimulus acidification. Figure 4*A*–*E* illustrates representative pH traces obtained from the different age groups, alongside representative field potentials (inserts). The peak alkalization was constant across the different age groups ($n = 5$–9 for each age group) (Fig. 4*F*). The quantification of field potential amplitude revealed smaller amplitudes in the younger age groups (P3–P4 and P7–P8, $P < 0.001$ and P10–P11, $P < 0.05$) (Fig. 4*G*). To relate the alkalization to neuronal activity, the ΔpH was normalized to the field potential (in mV). These data illustrate that the alkalization associated with a given neuronal activity is enlarged in the youngest age groups (P3–P4, $P < 0.05$ and P7–P8, $P < 0.001$) ($n = 5$–9) (Fig. 4*H*). To reveal age-dependent differences in the post-stimulus pH dynamics, the pH traces were normalized to that obtained at stimulus end (Fig. 5*I*). The re-acidification following alkalization was swifter for the youngest age groups as determined with comparisons of decay constants (for fitting example on a P27 rat, see Fig. 4*J*) ($n = 5$–9, P3–P4 and P7–P8, $P < 0.001$) (Fig. 4*K*). The extracellular pH displayed a post-stimulus acidification for all age groups (Fig. 4*I*), although this was less prominent in the younger age groups (P3–P4 and P7–P8, $P < 0.001$ and P10–P11, $P < 0.05$) (Fig. 4*L*). The return to baseline pH occurred at a much later time point (for a representative trace from a P21+ rat, see Fig. 4*I*, insert, average of 280 ± 23 s after stimulus end, $n = 8$ for P21+). These results illustrate that, with age, the extracellular alkalization/mV is diminished and the recovery from extracellular alkalization is prolonged.

Time comparison of K^+, ECS and pH transients

The three different stimulus-evoked alterations of the extracellular space (K^+, ECS shrinkage, and H^+/pH) occur alongside one another, triggered by the same electric stimulation that causes neuronal activity in the hippocampal slice. Although one of these (ECS) appeared to be insignificant in the young age group, the two others (K^+ and pH) displayed similarity across the age groups (prior to normalization to the field potential). To further determine a potential disconnect between these phenomena, we compared their time to peak (after stimulation initiation) across age groups (Fig. 5). The alkalization peaked near the end of stimulus for all age

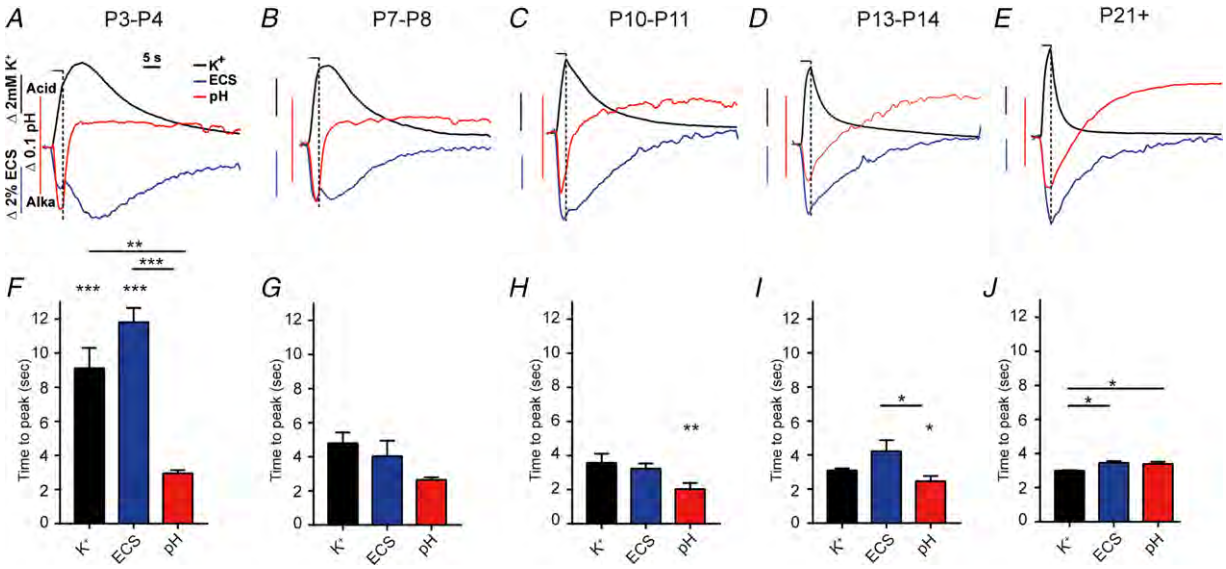

Figure 5. Comparison of the temporal aspect in the ionic transients
The data are a re-representation of the data acquired in Figs 1, 3 and 5, with the goal to analyse the time course of the ionic shifts. *A*–*E*, representative comparison of the different ionic transients (K^+, ECS, pH) for the different age groups. The black bar above the respective traces represents 20 Hz stimulation. *F*–*J*, summarized data of the time to reach the maximal response following the initiation of stimulation (in s). P3–P4: K^+: 9.1 ± 1.2, ECS: 11.8 ± 0.8, pH: 3.0 ± 0.2; P7–P8: K^+: 4.8 ± 0.6, ECS: 4.0 ± 0.9, pH: 2.6 ± 0.1; P10–P11: K^+: 3.5 ± 0.5, ECS: 3.2 ± 0.3, pH: 2.0 ± 0.4; P13–P14: K^+: 3.1 ± 0.1, ECS: 4.2 ± 0.7, pH: 2.5 ± 0.3; P21+: K^+: 3.0 ± 0.04, ECS: 3.5 ± 0.1, pH: 3.4 ± 0.1. The number of experiments can be found in the legends of Figs 1, 3 and 5. Statistical significance was tested with one-way ANOVA with Tukey's multiple comparison *post hoc* test, when comparing within the age groups, and with Dunnett's multiple comparison *post hoc* test when comparing between the age groups for each individual ion. The asterisks above the histograms refer to significant differences to the P21+ age group (Dunnett's), while asterisks above lines indicate comparisons between the indicated bars (Tukey's). $^*P < 0.05$, $^{**}P < 0.01$, $^{***}P < 0.001$.

groups, with a slightly swifter peak for the intermediate age groups (P10–P11, $P < 0.01$ and P13–14, $P < 0.05$) compared to the adolescent rats, whereas the K^+ and ΔECS peaked significantly later for the youngest age group (P3–P4, $P < 0.001$) compared to the more mature rats ($n = 5$–9 for each separate measurement in each age group) (Fig. 5*F*–*J*). Although all three parameters peaked at a similar time point in the intermediate age groups (P7–P8 and P10–P11), small differences were apparent in the older age groups (P13–14; $n = 7$–8, $P < 0.05$ for ECS *vs.* pH and P21+; $n = 7$–9, $P < 0.05$ for K^+ *vs.* pH and for K^+ *vs.* ECS) (Fig. 5*I*–*J*). Most noticeable, however, was the significant shift in the young rats (P3–P4) in the time to peak for the K^+ and ΔECS transients compared to that of the pH ($n = 5$–6, $P < 0.01$ for K^+ *vs.* pH and $P < 0.001$ for ECS *vs.* pH) (Fig. 5*F*). These results further support the notion that, although these activity-evoked transient changes in the extracellular space all happen during neuronal activity, their coupling appears to be of an indirect nature.

Discussion

In the present study, we show that management of activity-evoked extracellular K^+ transients becomes fine-tuned during development. The ECS shrinkage and pH transients associated with neuronal activity occur in parallel with the K^+ dynamics, although these three phenomena are not directly coupled.

The K^+ released into the extracellular space during neuronal activity is swiftly removed (Frankenhaeuser & Hodgkin, 1956). The neighbouring astrocytes act as temporary K^+ sinks primarily via the action of the Na^+/K^+-ATPase and, to a smaller extent, the K^+ channel Kir4.1 (Ballanyi *et al.* 1987; Grafe & Ballanyi, 1987; Ransom *et al.* 2000; Kofuji & Newman, 2004; MacAulay & Zeuthen, 2012; Larsen *et al.* 2014). Electrical stimulation of Schaffer collaterals in the rat hippocampus resulted in a brief rise in $[K^+]_o$ in all tested postnatal maturation levels. The oldest age group tested in the present study was rats of P21–P28. Brain slices from rodents of this age are frequently employed for electrophysiological recordings as a result of the presumed adult-like expression of most receptors involved in neurotransmission (Catania *et al.* 1994; Wenzel *et al.* 1997). The stimulus-evoked peak $[K^+]_o$ transient reached a similar level across all tested age groups, although, when normalized to the field potential amplitude, the young age groups (P3–P4 and P7–P8) displayed an elevated peak $[K^+]_o$ load, in agreement with findings in the rat spinal cord (Jendelová & Syková, 1991; Syková, 1997). Although the field potential represents neuronal activity, its amplitude will additionally be affected by ECS shrinkage, which will skew our data by a few percent. In addition, hippocampal slices from the younger age groups (P3–P10) displayed a slower return to $[K^+]_o$ baseline. This inadequate K^+ management in the younger animals correlated with elevated expression of all three α isoforms of the Na^+/K^+-ATPase during maturation and illustrates a tighter control of $[K^+]_o$ as the animal develops. The robust stepwise increase of protein expression of the different α subunits of the Na^+/K^+-ATPase continued in a similar fashion across the tested age groups of hippocampal tissue with no signs of saturation. Although the pattern of increased protein expression was similar for the three isoforms, a previous study showed that the mRNA transcript of $\alpha3$ reached adult levels at P7, whereas, in comparison, $\alpha1$ and $\alpha2$ only achieved the same at P25 (Orlowski & Lingrel, 1988). The hippocampal astrocytes predominantly express the K^+- and voltage-sensitive $\alpha2\beta2$ isoform of the Na^+/K^+-ATPase with a contribution from the $\alpha2\beta1$ isoform combination, which responds to the intracellular Na^+ transient that occurs with the Na^+-coupled glutamate re-uptake (Larsen *et al.* 2014; Larsen *et al.* 2016*a*; Larsen *et al.* 2016*b*; Stoica *et al.* 2017). Following stimulus end, K^+ returns to the neurons, presumably via the neuronal $\alpha3\beta1/\alpha1\beta1$ isoforms of the Na^+/K^+-ATPase (Ransom *et al.* 2000; Larsen *et al.* 2016*b*). Using our novel poly-his-tagged based method for semi-quantification of the different isoforms (Stoica *et al.* 2017), we revealed a higher protein expression of the neuronal $\alpha3$ isoform over that of the $\alpha1$ isoform (20-fold) and of the astrocytic $\alpha2$ isoform (6-fold) in the rat hippocampus. These findings indicate a powerful neuronal machinery to ensure return of the released K^+ to the original neuronal structure (Ballanyi *et al.* 1984; Coles *et al.* 1986; Ransom *et al.* 2000; Mondragão *et al.* 2016). Transcriptomics studies have revealed high but comparable levels of transcripts encoding the $\alpha2$ and $\alpha3$ isoforms in the cortex (Zhang *et al.* 2014) compared to that of $\alpha1$, although they did not reveal the significant difference in protein abundance of the distinct Na^+/K^+-ATPase isoforms. In addition to the Na^+/K^+-ATPase, Kir4.1-mediated buffering may contribute to removal of K^+ from the extracellular space (Walz, 2000; Kofuji & Newman, 2004; Larsen & MacAulay, 2014). The developmental profile of Kir4.1 expression in hippocampus mirrors that of the Na^+/K^+-ATPase, with low expression levels in the first postnatal weeks (Nwaobi *et al.* 2014). We therefore propose that the poor management of $[K^+]_o$ in the younger age groups is reflective of diffusion serving as a key mechanism for buffering of stimulus-evoked $[K^+]_o$ (Gardner-Medwin, 1983).

For decades, the extracellular space shrinkage has been presumed to occur as a function of the astrocytic clearance of $[K^+]_o$ (Kofuji & Newman, 2004; Nagelhus *et al.* 2004; MacAulay & Zeuthen, 2012). In the present study, we show that, although the stimulus-evoked $[K^+]_o$ arrived at similar levels across the different age groups, the associated ECS shrinkage at stimulus end was much smaller in the

younger age groups (as a percentage of P21+: ∼12.5 in P3–P4, ∼50.7 in P7–P8 and ∼69.9 in P10–P11). A similar dissociation was previously detected in the rat optic nerve, in which the ECS remained constant in tissue from young animals, despite elevated $[K^+]_o$ transients (Connors *et al.* 1982; Ransom *et al.* 1985). Curiously, the ECS shrinkage observed in the youngest age group (and a less pronounced version in P7–P8) displayed a double peak: one prior to stimulus end and a delayed, larger, prolonged peak. The delayed peak mirrors the similarly delayed peak $[K^+]_o$ in the P3–P4 age group and may well originate from this prolonged elevation in $[K^+]_o$ and the related membrane depolarization and/or distinct subset of membrane transporters expressed at the different levels of maturation. The occurrence of stimulus-evoked ECS shrinkage came with maturation of astrocytes and oligodendrocytes, supporting a glial origin of ECS shrinkage (Ransom *et al.* 1985). Upon normalization to the field potential amplitude in the rat hippocampus, the ECS shrinkage became of similar amplitude across the age groups, indicating a relation to neuronal activity (quantified as the field potential) rather than a direct function of the $[K^+]_o$. This lack of direct $[K^+]_o$-dependence of ECS shrinkage amplitude supports the lack of requirement for Kir4.1 and NKCC1 (Haj-Yasein *et al.* 2011; Larsen *et al.* 2014) in addition to KCCs and glutamate transporters/receptors (Larsen & MacAulay, 2017) in activity-evoked ECS shrinkage. We recently demonstrated the pH-regulating cotransporters of bicarbonate and lactate (NBCe1 and MCTs), presumably via their ability to cotransport water (Zeuthen & MacAulay, 2012), as molecular mechanisms underlying parts of the stimulus-evoked extracellular space shrinkage and, by extension, astrocytic cell swelling (Florence *et al.* 2012; Larsen & MacAulay, 2017). The remaining fraction of the stimulus-evoked ECS shrinkage has so far remained unexplained.

The stimulus-evoked peak alkaline transient occurring in parallel to $[K^+]_o$ and ECS dynamics was comparable across all age groups but larger in the young animals (P3–P4 and P7–P8) when normalized to field potential, in agreement with similar observations in rat spinal cord (Jendelová & Syková, 1991; Syková, 1997). The peak alkaline transient thus appears to correlate with the peak $[K^+]_o$ rather than neuronal activity as such. Although the alkaline transient has been proposed to occur via HCO_3^- permeability in $GABA_A$ receptors and/or glutamate transporters or, alternatively, to activity of the plasma membrane Ca^{2+}-ATPase (Chen & Chesler, 1992; Kaila *et al.* 1992; Paalasmaa *et al.* 1994), the latter was recently promoted as the dominant mediator of the ECS pH transient (Makani & Chesler, 2010). The alkaline transient was followed by a prolonged acidification, which increased with development. This acidification has been assigned to an artefact of the stimulation paradigm (Makani & Chesler, 2007) and thus may not occur in a physiological setting.

During neuronal activity, K^+ is released into the extracellular space as a function of Na^+-dependent neuronal depolarization, the ECS alkalinizes as a function of Ca^{2+}-ATPase activation, and the ECS shrinks (in part) as a function of NBCe1 activation by K^+-mediated astrocyte depolarization and ECS alkalization (Theparambil *et al.* 2014; Theparambil & Deitmer, 2015) and MCT (presumably via the instant metabolic demand) (Wender *et al.* 2000; Choi *et al.* 2012; Theparambil *et al.* 2016). Although these phenomena are all inextricably tied to neuronal activity, our data suggest that they do not couple *directly*. This notion is supported both by their distinct relation to field potential and by their individual time dependence. Most notable in regard to the latter, the pH transient peaked at comparable time points after stimulus initiation, whereas the peak K^+ transient and the peak ECS shrinkage displayed a delay in the youngest age group (P3–P4). The return to baseline of $[K^+]_o$ and ECS shrinkage became swifter with age, whereas the return of pH_o became slower, thus approaching a near-identical temporal pattern in the adolescent animals (Fig. 5*E*).

In conclusion, during the developmental phase, the regulation of the ECS dynamics becomes tighter. The stimulus-evoked peak $[K^+]_o$ as a function of neuronal activity is reduced and the return to baseline $[K^+]_o$ becomes swifter with maturity. However, the K^+ transient reached comparable peak concentrations in the ECS in all age groups, despite the fact that the steady-state ECS (α) (Nicholson & Phillips, 1981) is larger in the neocortex of young rats (P3–P4, ∼40% volume fraction) than in adults (∼20% volume fraction) (Bondareff & Pysh, 1968; Lehmenkühler *et al.* 1993). Accordingly, a comparable release of K^+ should promote a doubling of the $[K^+]_o$ in the older animals with smaller ECS. The similar peak value across the age groups may arise as a result of age-specific K^+ management: in the young animals with large ECS, diffusion away from the site of activity may dominate, whereas a powerful uptake machinery arises in the more mature animals with the developmental increase in expression of all three catalytic isoforms of the Na^+/K^+-ATPase managing the extracellular K^+ concentration. The activity-evoked ECS shrinkage (as a percentage) appears with developmental age. The smaller ECS in the more mature animals will, with a similar numerical change in H^+/HCO_3^- and K^+, yield a larger percentage change. The combination of a smaller volume fraction following maturation and the occurrence of stimulus-evoked ECS shrinkage is anticipated to enhance the biophysical effects of elevated K^+ and neurotransmitters, thus promoting more efficient synaptic transmission in the adult animals.

References

Ballanyi K, Grafe P, Reddy MM & Ten Bruggencate G (1984). Different types of potassium transport linked to carbachol and γ-aminobutyric acid actions in rat sympathetic neurons. *Neuroscience* **12**, 917–927.

Ballanyi K, Grafe P & ten Bruggencate G (1987). Ion activities and potassium uptake mechanisms of glial cells in guinea-pig olfactory cortex slices. *J Physiol* **382**, 159–174.

Bondareff W & Pysh JJ (1968). Distribution of the extracellular space during postnatal maturation of rat cerebral cortex. *Anat Rec* **160**, 773–780.

Brown AM & Ransom BR (2015). Astrocyte glycogen as an emergency fuel under conditions of glucose deprivation or intense neural activity. *Metab Brain Dis* **30**, 233–239.

Catania MV, Landwehrmeyer GB, Testa CM, Standaert DG, Penney JB & Young AB (1994). Metabotropic glutamate receptors are differentially regulated during development. *Neuroscience* **61**, 481–495.

Chen JC & Chesler M (1992). Modulation of extracellular pH by glutamate and GABA in rat hippocampal slices. *J Neurophysiol* **67**, 29–36.

Chever O, Djukic B, McCarthy KD & Amzica F (2010). Implication of Kir4.1 channel in excess potassium clearance: an in vivo study on anesthetized glial-conditional Kir4.1 knock-out mice. *J Neurosci* **30**, 15769–15777.

Choi HB, Gordon GRJ, Zhou N, Tai C, Rungta RL, Martinez J, Milner TA, Ryu JK, McLarnon JG, Tresguerres M, Levin LR, Buck J & MacVicar BA (2012). Metabolic communication between astrocytes and neurons via bicarbonate-responsive soluble adenylyl cyclase. *Neuron* **75**, 1094–1104.

Coles JA, Orkand RK, Yamate CL & Tsacopoulos M (1986). Free concentrations of Na, K, and Cl in the retina of the honeybee drone: stimulus-induced redistribution and homeostasis. *Ann NY Acad Sci* **481**, 303–317.

Coles JA & Schneider-Picard G (1989). Increase in glial intracellular K^+ in drone retina caused by photostimulation but not mediated by an increase in extracellular K^+. *Glia* **2**, 213–222.

Connors B, Ransom B, Kunis D & Gutnick M (1982). Activity-dependent K^+ accumulation in the developing rat optic nerve. *Science* **216**, 1341–1343.

D'Ambrosio R, Gordon DS & Winn HR (2002). Differential role of KIR channel and Na^+/K^+-pump in the regulation of extracellular K^+ in rat hippocampus. *J Neurophysiol* **87**, 87–102.

Dietzel I, Heinemann U, Hofmeier G & Lux HD (1980). Transient changes in the size of the extracellular space in the sensorimotor cortex of cats in relation to stimulus-induced changes in potassium concentration. *Exp Brain Res* **40**, 432–439.

Florence CM, Baillie LD & Mulligan SJ (2012). Dynamic volume changes in astrocytes are an intrinsic phenomenon mediated by bicarbonate ion flux. *PLoS ONE* **7**, e51124.

Frankenhaeuser B & Hodgkin AL (1956). The after-effects of impulses in the giant nerve fibres of Loligo. *J Physiol* **131**, 341–376.

Gardner-Medwin AR (1983). A study of the mechanisms by which potassium moves through brain tissue in the rat. *J Physiol* **335**, 353–374.

Grafe P & Ballanyi K (1987). Cellular mechanisms of potassium homeostasis in the mammalian nervous system. *Can J Physiol Pharmacol* **65**, 1038–1042.

Grundy D (2015). Principles and standards for reporting animal experiments in The Journal of Physiology and Experimental Physiology. *J Physiol* **593**, 2547–2549.

Haj-Yasein NN, Jensen V, Ostby I, Omholt SW, Voipio J, Kaila K, Ottersen OP, Hvalby O & Nagelhus EA (2012). Aquaporin-4 regulates extracellular space volume dynamics during high-frequency synaptic stimulation: a gene deletion study in mouse hippocampus. *Glia* **60**, 867–874.

Haj-Yasein NN, Jensen V, Vindedal GF, Gundersen GA, Klungland A, Ottersen OP, Hvalby O & Nagelhus EA (2011). Evidence that compromised K^+ spatial buffering contributes to the epileptogenic effect of mutations in the human Kir4.1 gene (KCNJ10). *Glia* **59**, 1635–1642.

Jendelová P & Syková E (1991). Role of glia in K^+ and pH homeostasis in the neonatal rat spinal cord. *Glia* **4**, 56–63.

Kaila K, Paalasmaa P, Taira T & Voipio J (1992). pH transients due to monosynaptic activation of GABAA receptors in rat hippocampal slices. *Neuroreport* **3**, 105–108.

Karwoski C, Lu H-K & Newman E (1989). Spatial buffering of light-evoked potassium increases by retinal Müller (glial) cells. *Science* **244**, 578–580.

Kofuji P & Newman EA (2004). Potassium buffering in the central nervous system. *Neuroscience* **129**, 1043–1054.

Koyama Y, Ishibashi T, Okamoto T, Matsuda T, Hashimoto H & Baba A (2000). Transient treatments with l-glutamate and threo-β-hydroxyaspartate induce swelling of rat cultured astrocytes. *Neurochem Int* **36**, 167–173.

Larsen BR, Assentoft M, Cotrina ML, Hua SZ, Nedergaard M, Kaila K, Voipio J & MacAulay N (2014). Contributions of the Na^+/K^+-ATPase, NKCC1, and Kir4.1 to hippocampal K^+ clearance and volume responses. *Glia* **62**, 608–622.

Larsen BR, Holm R, Vilsen B & MacAulay N (2016*a*). Glutamate transporter activity promotes enhanced Na^+/K^+-ATPase-mediated extracellular K+ management during neuronal activity. *J Physiol* **594**, 6627–6641.

Larsen BR & MacAulay N (2014). Kir4.1-mediated spatial buffering of K^+: Experimental challenges in determination of its temporal and quantitative contribution to K^+ clearance in the brain. *Channels* **8**, 544–550.

Larsen BR & MacAulay N (2017). Activity-dependent astrocyte swelling is mediated by pH-regulating mechanisms. *Glia* **65**, 1668–1681.

Larsen BR, Stoica A & MacAulay N (2016*b*). Managing brain extracellular K^+ during neuronal activity: the physiological role of the Na^+/K^+-ATPase subunit isoforms. *Front Physiol* **7**, PMC4841311.

Lehmenkühler A, Syková E, Svoboda J, Zilles K & Nicholson C (1993). Extracellular space parameters in the rat neocortex and subcortical white matter during postnatal development determined by diffusion analysis. *Neuroscience* **55**, 339–351.

MacAulay N & Zeuthen T (2012). Glial K^+ clearance and cell swelling: key roles for cotransporters and pumps. *Neurochem Res* **37**, 2299–2309.

MacVicar BA, Feighan D, Brown A & Ransom B (2002). Intrinsic optical signals in the rat optic nerve: role for K(+) uptake via NKCC1 and swelling of astrocytes. *Glia* **37**, 114–123.

Makani S & Chesler M (2007). Endogenous alkaline transients boost postsynaptic NMDA receptor responses in hippocampal CA1 pyramidal neurons. *J Neurosci* **27**, 7438–7446.

Makani S & Chesler M (2010). Rapid rise of extracellular pH evoked by neural activity is generated by the plasma membrane calcium ATPase. *J Neurophysiol* **103**, 667–676.

Meeks JP & Mennerick S (2007). Astrocyte membrane responses and potassium accumulation during neuronal activity. *Hippocampus* **17**, 1100–1108.

Mondragão MA, Schmidt H, Kleinhans C, Langer J, Kafitz KW & Rose CR (2016). Extrusion versus diffusion: mechanisms for recovery from sodium loads in mouse CA1 pyramidal neurons. *J Physiol* **594**, 5507–5527.

Nagelhus EA, Mathiisen TM & Ottersen OP (2004). Aquaporin-4 in the central nervous system: cellular and subcellular distribution and coexpression with KIR4.1. *Neuroscience* **129**, 905–913.

Nicholson C & Phillips JM (1981). Ion diffusion modified by tortuosity and volume fraction in the extracellular microenvironment of the rat cerebellum. *J Physiol* **321**, 225–257.

Nicholson C & Syková E (1998). Extracellular space structure revealed by diffusion analysis. *Trends Neurosci* **21**, 207–215.

Nixdorf-Bergweiler BE, Albrecht D & Heinemann U (1994). Developmental changes in the number, size, and orientation of GFAP-positive cells in the CA1 region of rat hippocampus. *Glia* **12**, 180–195.

Nwaobi SE, Lin E, Peramsetty SR & Olsen ML (2014). DNA methylation functions as a critical regulator of Kir4.1 expression during CNS development. *Glia* **62**, 411–427.

Orlowski J & Lingrel JB (1988). Tissue-specific and developmental regulation of rat Na,K-ATPase catalytic alpha isoform and beta subunit mRNAs. *J Biol Chem* **263**, 10436–10442.

Pál I, Nyitrai G, Kardos J & Héja L (2013). Neuronal and Astroglial correlates underlying spatiotemporal intrinsic optical signal in the rat hippocampal slice. *PLoS ONE* **8**, e57694.

Paalasmaa P, Taira T, Voipio J & Kaila K (1994). Extracellular alkaline transients mediated by glutamate receptors in the rat hippocampal slice are not due to a proton conductance. *J Neurophysiol* **72**, 2031–2033.

Ransom B, Yamate C & Connors B (1985). Activity-dependent shrinkage of extracellular space in rat optic nerve: a developmental study. *J Neurosci* **5**, 532–535.

Ransom CB, Ransom BR & Sontheimer H (2000). Activity-dependent extracellular K^+ accumulation in rat optic nerve: the role of glial and axonal Na^+ pumps. *J Physiol* **522**, 427–442.

Schneider G-H, Baethmann A & Kempski O (1992). Mechanisms of glial swelling induced by glutamate. *Can J Physiol Pharmacol* **70**, S334-S343.

Stoica A, Larsen BR, Assentoft M, Holm R, Holt LM, Vilhardt F, Vilsen B, Lykke-Hartmann K, Olsen ML & MacAulay N (2017). The $\alpha 2\beta 2$ isoform combination dominates the astrocytic Na^+/K^+-ATPase activity and is rendered nonfunctional by the α2.G301R familial hemiplegic migraine type 2-associated mutation. *Glia* **65**, 1777–1793.

Syková E (1997). The extracellular space in the CNS: its regulation, volume and geometry in normal and pathological neuronal function. *Neuroscientist* **3**, 28–41.

Theparambil SM & Deitmer JW (2015). High effective cytosolic H^+ buffering in mouse cortical astrocytes attributable to fast bicarbonate transport. *Glia* **63**, 1581–1594.

Theparambil SM, Naoshin Z, Thyssen A & Deitmer JW (2015). Reversed electrogenic sodium bicarbonate cotransporter 1 is the major acid loader during recovery from cytosolic alkalosis in mouse cortical astrocytes. *J Physiol* **593**, 3533–3547.

Theparambil SM, Ruminot I, Schneider H-P, Shull GE & Deitmer JW (2014). The electrogenic sodium bicarbonate cotransporter NBCe1 is a high-affinity bicarbonate carrier in cortical astrocytes. *J Neurosci* **34**, 1148–1157.

Theparambil SM, Weber T, Schmälzle J, Ruminot I & Deitmer JW (2016). Proton fall or bicarbonate rise: glycolytic rate in mouse astrocytes is paved by intracellular alkalinization. *J Biol Chem* **291**, 19108–19117.

Voipio J & Kaila K (1993). Interstitial PCO_2 and pH in rat hippocampal slices measured by means of a novel fast CO_2/H(+)-sensitive microelectrode based on a PVC-gelled membrane. *Pflügers Archiv* **423**, 193–201.

Voipio J, Pasternack M & MacLeod K (1994). Ion-sensitive microelectrodes. In *Microelectrode Techniques – The Plymouth Workshop Handbook, 2nd edn*, ed. Ogden D, pp. 275–316. The Company of Biologists Limited, Cambridge.

Waitt AE, Reed L, Ransom BR & Brown AM (2017). Emerging roles for glycogen in the CNS. *Front Mol Neurosci* **10**, https://doi.org/10.3389/fnmol.2017.00073.

Walz W (2000). Role of astrocytes in the clearance of excess extracellular potassium. *Neurochem Int* **36**, 291–300.

Wender R, Brown AM, Fern R, Swanson RA, Farrell K & Ransom BR (2000). Astrocytic glycogen influences axon function and survival during glucose deprivation in central white matter. *J Neurosci* **20**, 6804–6810.

Wenzel A, Fritschy JM, Mohler H & Benke D (1997). NMDA receptor heterogeneity during postnatal development of the rat brain: differential expression of the NR2A, NR2B, and NR2C subunit proteins. *J Neurochem* **68**, 469–478.

Zeuthen T & MacAulay N (2012). Transport of water against its concentration gradient: fact or fiction? *Wiley Interdisciplinary Reviews: Membrane Transport and Signaling* **1**, 373–381.

Zhang Y, Chen K, Sloan SA, Bennett ML, Scholze AR, O'Keeffe S, Phatnani HP, Guarnieri P, Caneda C, Ruderisch N, Deng S, Liddelow SA, Zhang C, Daneman R, Maniatis T, Barres BA & Wu JQ (2014). An RNA-sequencing transcriptome and splicing database of glia, neurons, and vascular cells of the cerebral cortex. *J Neurosci* **34**, 11929–11947.

Additional information

Competing interests

The authors declare that they have no competing interests.

Author contributions

All experiments were conducted at The University of Copenhagen, Denmark, in the laboratory of NM (Department of Neuroscience). NM and BRL conceived and designed the study. BRL and AS performed the experiments. BRL, AS, and NM analysed the data and wrote the manuscript. All authors are accountable for all aspects of the work and all persons designated as authors qualify for the authorship, and all those who qualify for authorship are listed. All authors read and approved the final version of the manuscript submitted for publication.

Funding

The study was supported by the Novo Nordisk Foundation (to NM; NNF15OC0017052).

Acknowledgements

We thank Professor Mitchell Chesler, New York University Langone, for critically reading the manuscript.